SPIE PRESS

SPIE

Multimodality Breast Imaging

Diagnosis and Treatment

E. Y. K. Ng
U. Rajendra Acharya
Rangaraj M. Rangayyan
Jasjit S. Suri
Editors

Multimodality Breast Imaging

Diagnosis and Treatment

Multimodality Breast Imaging
Diagnosis and Treatment

E. Y. K. Ng
U. Rajendra Acharya
Rangaraj M. Rangayyan
Jasjit S. Suri
Editors

SPIE
PRESS
Bellingham, Washington USA

Library of Congress Cataloging-in-Publication Data

Multimodality breast imaging : diagnosis and treatment / editors, E.Y.K. Ng, U. Rajendra Acharya, Rangaraj M. Rangayyan, and Jasjit S. Suri.
pages cm
Includes bibliographical references.
ISBN 978-0-8194-9294-4
1. Breast–Imaging. I. Ng, Y. K. Eddie, editor of collaboration. II. Acharya U, Rajendra, editor of collaboration. III. Rangayyan, Rangaraj M., editor of collaboration. IV. Suri, Jasjit S., editor of collaboration.
RG493.5.D52M85 2013
618.1′90754–dc23

2012042251

Published by
SPIE
P.O. Box 10
Bellingham, Washington 98227-0010 USA
Phone: +1 360.676.3290
Fax: +1 360.647.1445
Email: Books@spie.org
Web: http://spie.org

Cover background image courtesy of SuperSonic Imagine.

Printed in the United States of America.
First printing

Contents

Preface

Breast cancer is an abnormal growth of cells in the breast, usually in the inner lining of the milk ducts or lobules. It is currently the most common type of cancer in women in developed and developing countries. The number of women affected by breast cancer is gradually increasing and remains as a significant health concern. Hence, the early detection of breast cancer can improve the survival rate and quality of life. Therefore, today, newer modalities are available to more accurately detect breast cancer. Researchers are continuously working to develop novel techniques to detect early stages of breast cancer. This book covers breast cancer detection using different imaging modalities such as mammography, magnetic resonance imaging, computed tomography, positron emission tomography, ultrasonography, infrared imaging, and other modalities.

Architectural distortion is one of the major causes of false-negative findings in the detection of early stages of breast cancer. Chapter 1 presents methods for computer-aided detection of architectural distortion in mammograms acquired prior to the diagnosis of breast cancer in the interval between scheduled screening sessions. The results are promising and indicate that the proposed methods can detect architectural distortion in prior mammograms taken 15 months (on average) before clinical diagnosis of breast cancer, with a sensitivity of 0.8 at 5.2 false positives per patient.

A computer-aided system for the automated detection of normal, benign, and cancerous breasts using texture features extracted from digitized mammograms and data mining techniques is proposed in Chapter 2. The novelty of this work is to automatically classify the mammogram into normal, benign, and malignant classes using the texture features alone, with an efficiency of 93.3% and sensitivity of 92.3% using a fuzzy classifier.

Breast cancer diagnosis by combination of fuzzy systems and an ant colony optimization algorithm is proposed in Chapter 3. Results on the breast cancer diagnosis dataset from the University of California Irvine machine learning repository show that the proposed FUZZY-ACO would be capable of classifying cancer instances with a high accuracy rate and adequate interpretability of extracted rules.

Chapter 4 discusses a computer-aided diagnosis system tested on magnetic resonance datasets obtained from different scanners, with a variable temporal and spatial resolution and on both fat-sat and non–fat-sat images, and has shown promising results. This type of system could potentially be used for early diagnosis and staging of breast cancer to reduce reading time and to improve detection, especially of the smaller satellite nodules.

Imaging plays a pivotal role in the evaluation of metastatic spread of breast cancer disease. Chapter 5 gives an overview of the recent developments in breast cancer imaging, in terms of instrumentation and clinical applications. In addition, the theoretical framework behind advanced imaging modalities is highlighted to provide background knowledge to the reader, and potential future research directions are also presented.

The role of positron emission tomography is established in the practice of oncology. The advances in functional and molecular imaging techniques have increased the accuracy in the diagnostic evaluation of breast cancers and is discussed in detail in Chapter 6.

Chapter 7 discusses 3D whole-breast ultrasonography, which can provide the entire breast anatomy for later review. The 3D whole-breast ultrasound procedure and the training time are simpler and shorter than the traditional 2D US. It also provides interoperator consistency, and its reproducibility is better for follow-up studies.

Recent progress in medical ultrasound has paved the way for the evaluation of breast cancer. State-of-the-art high-resolution ultrasound can detect tiny breast lesions as small as 1–2 mm in size, and sometimes microcalcifications even less than 0.5 mm, or small carcinomas 3–6 mm in diameter. Chapter 8 presents an overview of the recent developments in ultrasound imaging of breast cancer, in terms of instrumentation and clinical applications.

Nonlinear features such as Lyapunov exponents are used to differentiate malignant and benign breast thermograms in Chapter 9. This work can be extended for classifying different stages of breast cancer. The authors are currently working toward these objectives.

A set of image features describing bilateral differences between left and right breast regions in thermograms is described in Chapter 10. These features are then used in a pattern classification stage to discriminate malignant cases from benign ones. Classification is performed by fuzzy if-then rules and applies a genetic algorithm to optimize the rule base, and secondly uses an ant colony optimization classification algorithm. Both approaches have shown good classification accuracy.

Infrared imaging has shown to be a promising technique for the early diagnosis of breast pathologies and as a screening technique. The concept of a combined diagnostic enables a high degree of specificity and sensibility in such diagnosis. Chapter 11 presents a concept of merging

information from the images with other modalities of examination, such as mammograms and ultrasound, in order to improve the early detection of breast pathologies, including cancer.

Chapter 12 discusses diffuse optical imaging, which makes use of diffuse light to probe deep tissues by taking advantage of low tissue absorption within the near-infrared wavelength range (650–900 nm). The optical measurements obtained can be used to calculate optical properties, namely absorption and scattering within tissues. This, in turn, can provide information about physiological parameters within tissues, such as oxy- and deoxy-haemoglobin, and water and lipid, all of which can be utilized in the detection, characterization, and therapy monitoring of breast cancer.

Cytopathology is a branch of pathology that studies and diagnoses diseases on the cellular level, using samples of free cells or tissue fragments. Chapter 13 describes the results of a study of the features that are used by physicians and computers to diagnose cancer based on features in fine-needle aspiration cytology images. It discusses the significance of a cytological feature in representing its true ability to discriminate benign and malignant conditions of a breast lump in the Wisconsin Diagnostic Breast Cancer database.

Only a small number of studies have been reported on breast radiofrequency ablation, and most of them have included the posterior surgical excision of the treated breast. Chapter 14 presents the future trends in the development of more-specific radiofrequency algorithms for breast cancer treatment, to improve the results, determine the setting of the specific indications for the technique, and expand the study of long-term results and survival.

Breast conserving therapy is the gold-standard option for patients with early-stage breast cancer. The surgical excision removes the entire tumor with a negative surgical margin and helps to preserve the breast tissue as far as possible. Chapter 15 explains minimally invasive ablative techniques, which may offer complete tumor ablation, with less psychological morbidity, better cosmetic results, and shorter hospital stay.

A microwave-based imaging modality is an emerging noninvasive medical imaging approach exploring the dielectric property of biological tissue that shows great potential in breast cancer detection. Chapter 16 discusses a correlated microwave acoustic imaging modality and numerical simulation using finite-difference time-domain analysis. It is clearly shown that a combination of microwave-based imaging modalities is expected to provide an efficient diagnostic method for breast cancer detection in the future.

Fluorescence-based bioassays are novel diagnostic tools that are available to clinicians for deciding future treatment and to researchers for monitoring biological functions that may lead to novel investigations.

The different aspects of photonic crystal fiber, its guiding mechanism, the refractive index law, etc. are analyzed and explained in Chapter 17. The proposed methodology is implemented in an array format of immuno recognition of specific proteins using a hollow-core photonic crystal fiber.

An overview of a quality-assurance program for digital mammography is discussed in Chapter 18. This overview includes the quality-control test procedures based on the American College of Radiology and the International Atomic Energy Agency. The role of medical physicists in the mammography quality-assurance programs, including acceptance, annual, and regular quality-control testing, is briefly presented.

In this book, we have made an honest effort to present information and methodologies for accurate diagnosis of breast cancer to help researchers, doctors, teachers, and students in biomedical science and engineering.

E. Y. K. Ng
U. Rajendra Acharya
Rangaraj M. Rangayyan
Jasjit S. Suri
January 2013

List of Contributors

Hiroyuki Abe
The University of Chicago Medicine, USA

U. Rajendra Acharya
Ngee Ann Polytechnic, Singapore and University of Malaya, Malaysia

Silvano Agliozzo
im3D S.p.A., Italy

Marcus C. Araújo
Federal University of Pernambuco, Brazil

Mohammad Ataei
University of Isfahan, Iran

Shantanu Banik
University of Calgary, Canada

Alberto Bert
im3D S.p.A., Italy

Luciete A. Bezerra
Federal University of Pernambuco, Brazil

Tiago B. Borschartt
Fluminense Federal University, Brazil

Ruey-Feng Chang
National Taiwan University, Taiwan

Jyotirmoy Chatterjee
Indian Institute of Technology Kharagpur, India

Chung-Ming Chen
National Taiwan University, Taiwan

Jie-Zhi Cheng
National Taiwan University, Taiwan

Yi-Hong Chou
Taipei Veterans Hospital, Taiwan and National Yang-Ming University, Taiwan

Aura Conci
Fluminense Federal University, Brazil

Massimo De Luca
Institute for Cancer Research and Treatment, Italy

José Luis del Cura
Basque Country University, Spain

J. E. Leo Desautels
University of Calgary, Canada

Jing Dong
Nanyang Technological University, Singapore

Mahnaz Etahadtavakol
Isfahan University of Medical Sciences, Iran

Tânia Aparecida Correia Furquim
Universidade de São Paulo, Brazil

Fei Gao
Nanyang Technological University, Singapore

Hrushikesh Garud
Indian Institute of Technology Kharagpur, India and Texas Instruments, India

Arindam Ghosh
Kharagpur Sub-Divisional Hospital, India

Valentina Giannini
Institute for Cancer Research and Treatment, Italy and Politecnico di Torino, Italy

Jun Hui Ho
Nanyang Technological University, Singapore

Andrew Tan Eik Hock
Singapore General Hospital, Singapore

Noriah Jamal
Malaysian Nuclear Agency, Malaysia

Kijoon Lee
Nanyang Technological University, Singapore

Rita C. F. Lima
Federal University of Pernambuco, Brazil

Zhiping Lin
Nanyang Technological University, Singapore

Caro Lucas
University of Tehran, Iran

Paulo R. M. Lyra
Federal University of Pernambuco, Brazil

Manjunatha Mahadevappa
Indian Institute of Technology Kharagpur, India

Filippo Molinari
Politecnico di Torino, Italy

Lia Morra
im3D S.p.A., Italy

Vadakke Matham Murukeshan
Nanyang Technological University, Singapore

E. Y. K. Ng
Nanyang Technological University, Singapore

Kwan-Hoong Ng
University of Malaya, Malaysia

Marília M. Oliveira
Federal University of Pernambuco, Brazil

Parasuraman Padmanabhan
Singapore BioImaging Consortium, Singapore

Saraswathi Padmanabhan
Nanyang Technological University, Singapore

Diego Persano
im3D S.p.A., Italy

Rangaraj M. Rangayyan
University of Calgary, Canada

Ajoy Kumar Ray
Indian Institute of Technology Kharagpur, India and Bengal Engineering and Science University, India

Daniele Regge
Institute for Cancer Research and Treatment, Italy

Roger Resmini
Fluminense Federal University, Brazil

Tiago L. Rolim
Federal University of Pernambuco, Brazil

Francisco G. S. Santos
Federal University of Pernambuco, Brazil

Ladjane C. Santos
Federal University of Pernambuco, Brazil

Gerald Schaefer
Loughborough University, United Kingdom

Debdoot Sheet
Indian Institute of Technology Kharagpur, India

Yi-Wei Shen
National Taiwan University, Taiwan

Vengalathunadakal Kuttinarayanan Shinoj
Nanyang Technological University, Singapore

S. Vinitha Sree
Nanyang Technological University, Singapore

Jasjit S. Suri
Global Biomedical Technologies Inc., CA, USA and Idaho State University, USA (Aff.)

Andrew Eik Hock Tan
Raffles Hospital, Singapore

Cher Heng Tan
Tan Tock Seng Hospital,
Singapore

Jen-Hong Tan
Ngee Ann Polytechnic,
Singapore

Chui-Mei Tiu
Taipei Veterans Hospital,
Taiwan and National Yang-Ming
University, Taiwan

Mariana J. A. Viana
Federal University of
Pernambuco, Brazil

Anna Vignati
Institute for Cancer
Research and Treatment,
Italy

Feng Wu
Chongqing Medical
University, China,
University of Oxford,
and Oxford University Hospitals,
Oxford, United Kingdom

Wanying Xie
Singapore General Hospital,
Singapore

Ye Xu
Philips Research, USA

Yuanjin Zheng
Nanyang Technological
University, Singapore

Acronyms and Abbreviations

ABSN	angles between surface normals
ABVS	Automated Breast Volume Scanner
ACO	ant colony optimization
ACR	American College of Radiology
ACS	ant colony system
AEC	automatic exposure control
AI	artificial intelligence
AJCC	American Joint Committee on Cancer
ALA	5-aminolevulinic acid
ANN	artificial neural network
ANOVA	analysis of variance
APC	antigen-presenting cell
APD	avalanche photodiode
ART	algebraic reconstruction technique
AUC	area under ROC curve
AUCEC	area under the contrast-enhancement curve
B + F	base + fog
BC	breast cancer
BCDSG	Breast Cancer Disease Site Group
BEM	boundary element method
BFGS	Broyden–Fletcher–Goldfarb–Shanno (method)
BHTE	bioheat transfer equation
BIRADS®	Breast Imaging Reporting and Data System
BIRADS-MRI	BIRADS for MRI
bpp	bits per pixel
BRCA-1, -2	breast cancer genes
BS	bone scintigraphy
BSE	breast self-examination
BWI	bound water index
CaCo	colorectal cancer
CAD	computer-aided diagnosis
CADe	computer-aided detection
CADx	computer-aided diagnosis
CAM	combined autocorrelation method

CBE	clinical breast examination
CCD	charge-coupled device
CDS	clinical decision support
CDSS	clinical decision support system
CDU	color Doppler ultrasound
CECT	contrast-enhanced computed tomography
CFD	computational fluid dynamics
CI	confidence interval
CLS	curvilinear structure
CMAI	correlated microwave acoustic imaging
CMM	coordinate measuring machine
CMOS	complementary metal-oxide semiconductor
CNS	central nervous system
CR	computed radiography
CR	contrast response
CT	computed tomography
CTL	cytotoxic T lymphocyte
CTS	chaotic time series
CW	continuous wave
CXR	chest radiology
DC	dendritic cells
DCE-MRI	dynamic contrast-enhanced MRI
DCIS	ductal carcinoma *in situ*
DCS	diffuse correlation spectroscopy
DD	density difference
DDSM	Digital Database for Screening Mammography
del	detector element
DeTr	decision tree
DICOM	Digital Imaging and Communications in Medicine
DM	digital mammography
DMD	digital micromirror device
DMIST	Digital Mammographic Imaging Screening Trial
DOI	diffuse optical imaging
DOS	diffuse optical spectroscopy
DOT	diffuse optical tomography
DR	digital radiology
DRS	diffuse reflectance spectroscopy
DW	diffusion weighted
E-M	expectation maximization
EGFR	epidermal growth factor receptor
EI	exposure index
EM	electromagnetic
EORTC	European Organization for Research and Treatment of Cancer

ER	estrogen receptor
ESAK	entrance surface air kerma
ESF	edge spread function
EW	evanescent wave
fat-sat	fat saturated
FCC	fibrocystic change
FD	frequency domain
FDG	fluorodeoxyglucose (^{18}F)
FDM	finite-difference method
fDOT	fluorescence diffuse optical tomography
FDTD	finite-difference time domain
FEM	finite-element method
FES	fluoro-17β-estradiol
FFDM	full-field digital mammography
FG	fibroglandular
FG	fractal geometry
FLDA	Fisher linear discriminant analysis
FN	false negative
FNA	fine-needle aspiration
FNAC	fine-needle aspiration cytology
FNN	false nearest neighbor
FP	false positive
FROC	free-response ROC
FS	feature selection
FUI	feature usability index
GLCM	gray-level co-occurrence matrix
GMM	Gaussian mixture model
GSDF	grayscale standard display function
GUI	graphical user interface
H&E	hematoxylin-eosin
HCC	hepatocellular carcinoma
HC-PCF	hollow-core photonic crystal fiber
HC/UFPE	Clinical Hospital of the Federal University of Pernambuco
HIFU	high-intensity focused ultrasound
HL7	health level 7
HNG	high nuclear grade
HRT	hormone replacement therapy
HSP	heat shock protein
HVL	half-value layer
IAEA	International Atomic Energy Agency
ICG	indocynanine-green
IDC	invasive ductal carcinoma

IFN	interferon
IG-NIRS	image-guided NIR spectroscopy
IM	internal mammary
ING	intermediate nuclear grade
IR	infrared
ITK	Insight Toolkit
IV	intravenous
JAFROC	jackknife alternative free-response ROC
JND	just-noticeable difference
k-NN	*k*-nearest neighbor
LA	laser ablation
LBP	local binary pattern
LC-VCO	inductor/capacitor voltage-controlled oscillator
LCIS	lobular carcinoma *in situ*
LE	Lyapunov exponent
LNG	low nuclear grade
LSM	least-square method
LTB	lesion-to-background (ratio)
LUT	lookup table
MCC	microcalcification
MD	mid-density
MGD	mean glandular dose
MGH	Massachusetts General Hospital
MIAS	Mammographic Image Analysis Society
MIP	maximum-intensity projection
MIPT	maximum-intensity projection over time
mIPT	mean-intensity projection over time
ML	maximum likelihood
MOF	microstructured optical fiber
MPV	mean pixel value
MQSA	Mammography Quality Standards Act
MR	magnetic resonance
MRI	magnetic resonance imaging
MRS	magnetic resonance spectroscopy
MTAI	microwave-induced thermoacoustic imaging
MTF	modulation transfer function
MWA	microwave ablation
MWI	microwave imaging
NADH	nicotinamide adenine dinucleotide plus hydrogen
NBC	Naïve Bayesian classifier
NICE	National Institute for Health and Clinical Excellence (UK)
NIR	near infrared

NPV	negative predictive value
OI	optical index
OO	object-oriented (model)
ORD	object-relational database
PASH	pseudo-angiomatous stromal hyperplasia
PBG	photonic bandgap
PBS	phosphate-buffered saline
PCF	photonic crystal fiber
PD	progressive disease
PEM	positron emission mammography
PET	positron emission tomography
PET-CT	PET with computed tomography
PDU	power Doppler ultrasound
PHA	phytohaemagglutinin
PMMA	poly(methyl methacrylate)
PMT	photomultiplier tube
PNN	probabilistic neural network
PO	pulse oximeter
PPIX	protoporphyrin IX
PPV	positive predictive value
PR	partial response
PR	progesterone receptor
QA	quality assurance
QAP	quality assurance program
QC	quality control
QDA	quadratic discriminant analysis
RBF	radial basis function
RECIST	response evaluation criteria in solid tumors
RF	radiofrequency
RFA	radiofrequency ablation
RI	refractive index
RI	resistivity index
ROC	receiver operating characteristic
ROI	region of interest
ROL	reference operating level
RPS	reconstructed phase space
S/C	signal-to-clutter ratio
SD	stable disease
SDNR	signal-difference-to-noise ratio
SEM	scanning electron microscope
SFM	screen-film mammography
SI	shape index
SID	source-to-image distance

SHH	Sacred Heart Hospital
SIRT	simultaneous iterative reconstruction technique
SLNB	sentinel lymph node biopsy
SMPTE	Society of Motion Picture and Television Engineers
SNR	signal-to-noise ratio
SPAD	single-photon avalanche diode
SPECT	single-photon emission computed tomography
SQP	sequential quadratic programming
std	standard deviation
STIR	short tau inversion recovery
StO_2	tissue oxygenation or oxygen saturation
SUVmax	maximum standardized uptake value
SUVmean	mean standardized uptake value
SVD	singular value decomposition
SVM	support vector machine
TBS	tris-buffered saline
TBST	tris-buffered saline/Tween
TD	time domain
TDE	time-delay embedding
TDLU	terminal ductalobular unit
THC	total haemoglobin concentration
THI	tissue harmonic imaging
TIL	tumor-infiltrating lymphocyte
TN	true negative
TNF	tumor necrosis factor
TP	true positive
TPSF	temporal point spread function
TS	time series
TSFC	texture shape feature coding
UCI	University of California Irvine
US	ultrasound/ultrasonography
US NCI	United States National Cancer Institute
USPIO	ultrasmall superparamagnetic iron oxide
UWB	ultrawideband
VAB	vacuum-assisted biopsy
VOI	volume of interest
WB	whole body
WDBC	Wisconsin Diagnostic Breast Cancer (database)
WFUSM	Wake Forest University School of Medicine
WHO	World Health Organization
WU	Washington University in St. Louis

Chapter 1
Detection of Architectural Distortion in Prior Mammograms Using Statistical Measures of Angular Spread[1]

Rangaraj M. Rangayyan, Shantanu Banik, and J. E. Leo Desautels
University of Calgary, Calgary, Alberta, Canada

[1]This chapter is a revised and expanded version of S. Banik, R. M. Rangayyan, and J. E. L. Desautels, "Measures of angular spread and entropy for the detection of architectural distortion in prior mammograms," *International Journal of Computer Assisted Radiology and Surgery* **8**(1), 121–134 (2013). Reproduced with kind permission from Springer Science+Business Media.

1.1 Introduction

Architectural distortion, a distortion of the architecture of breast parenchyma without being accompanied by increased density or a mass, is a mammographic sign of breast cancer.[1] Architectural distortion is an important finding in the detection of early stages of breast cancer.[2] However, subtlety and variability in appearance, and similarity in presentation to normal breast tissue patterns overlapped in the projected mammographic image impose challenges in the detection of architectural distortion. Architectural distortion is the most commonly missed abnormality in false-negative (FN) screening cases.[1] Several studies have indicated that architectural distortion accounts for 12% to 45% of breast cancer cases overlooked or misinterpreted in screening mammography.[3,4]

In terms of treatment of patients affected by breast cancer, only localized and nonmetastasized cancers are considered to be treatable and curable. In order to increase the possibility of survival, the detection of breast cancer at its early stages is of highest importance.[5] The use of computer-aided diagnosis (CAD) techniques by a radiologist could be as effective as double reading, and provide efficient and effective means of reducing errors and help in increasing sensitivity in the detection of breast cancer.[6–8] Numerous CAD techniques and systems have been proposed and developed to improve the sensitivity and accuracy of the detection of breast cancer. Several CAD techniques are found to be effective in detecting masses and calcifications; unfortunately, the same systems have demonstrated poor performance in the detection of subtle or indirect signs of possible malignancy, such as architectural distortion.[9] Several studies have indicated that a substantial portion of prior mammograms of cases of screen-detected cancer or interval-cancer cases[10–13] could contain subtle or minimal signs of abnormality.[14] Such signs of abnormality include hard-to-detect features or patterns that could indicate breast cancer at stages prior to the formation of a mass or tumor. Architectural distortion could appear at the initial stages of the formation of a breast mass or tumor, and has been found to be associated with breast malignancy in one-half to two-thirds of the cases in which it is present.[2] Increasing the sensitivity and accuracy in the detection of architectural distortion could lead to improvement in the prognosis of patients affected by breast cancer[15] and help in increasing the associated survival rate.

Development of CAD techniques for the detection of architectural distortion is a comparatively new field that has not been studied adequately. There is increasing interest in this area at present, indicated by the appearance of a relatively small number of publications addressing parts of the problem.[2,16–22] Furthermore, CAD of architectural distortion in prior mammograms, in particular those of interval-cancer cases, is an important approach that could facilitate early detection of breast cancer and warrants more attention.[10–14] Simultaneous analysis of current and prior mammograms could help in early detection of breast cancer and is usually practiced by radiologists in the detection of breast cancer;[23–25] the same procedure may be effective for CAD systems also.

Based on the hypothesis that screening mammograms obtained prior to the detection of breast cancer could contain subtle signs of early stages of breast cancer, development of CAD systems specifically designed for the analysis of prior mammograms of screen-detected or interval-cancer cases[12–14,26] could help in understanding the causes of FN error as well as developing strategies for the detection and treatment of breast diseases at their early stages, and lead to substantial improvement in the prognosis of the patient.[15]

The normally oriented texture pattern in the normal breast, which typically converges toward the nipple, is changed or distorted in the presence of architectural distortion.[27] The distorted pattern may include radiating or spiculating patterns or focal retraction at the edge of the breast parenchyma. Several methods may be required to capture and characterize the variety of textural patterns related to architectural distortion in mammograms.[12,13] Noise and neighboring structures could adversely affect the detection process; they may lead to the detection of spurious or ambiguously oriented structures or other unrelated intersecting patterns in the image. Characterization of the angular spread has been shown to be effective in the detection of architectural distortion.[13,26,28] In this context, the present study is directed toward the development of CAD techniques for the detection of architectural distortion in prior mammograms of interval-cancer cases through characterization and analysis of the angular spread of the magnitude and angle responses of Gabor filters, coherence, orientation strength, and power in the frequency domain. Quantification of angular spread is performed using higher-order Rényi entropy[26,29] and Tsallis entropy[26,30] along with Shannon's entropy.[26,28]

1.2 Experimental Setup and Database

A total of 158 mammographic images, including 52 images of 13 normal individuals and 106 prior mammographic images of 56 individuals diagnosed with breast cancer, were obtained from a database of 1,745 digitized mammograms of 170 subjects from Screen Test: Alberta Program for the Early Detection of Breast Cancer.[31,32] Ethics approval for the study was obtained from the Conjoint Health Research Ethics Board, Office of

Medical Bioethics, University of Calgary, and the Calgary Regional Health Authority. The film mammograms were digitized at the spatial resolution of 50 μm and grayscale resolution of 12 bits per pixel using the Lumiscan 85 laser scanner (Lumisys, Sunnyvale, CA).[31]

Mammograms acquired in the last scheduled visit to the screening program prior to the detection of cancer were included in the dataset, and labeled as "prior mammograms of interval-cancer cases."[12] The mammograms on which cancer was detected (i.e., "diagnostic mammograms") were not available for the present study. In consultation with the radiologist, all of the prior mammograms of interval-cancer cases available in the database have been included in the study, except six images in which no suspicious parts could be identified. The 106 prior mammograms of interval-cancer cases were reviewed independently by a radiologist specializing in screening mammography (J.E.L.D.).

The radiologist (J.E.L.D.) who analyzed and annotated the images used in the present study has more than 40 years of experience in mammography, of which more than 20 years is in screening for breast cancer; he was also a member of the team of radiologists in the Screen Test Program and interpreted the mammograms at the original instances of screening. All cases of interval cancer were reviewed by a panel of five experienced radiologists in the screening program as part of the standard protocol. The laterality, location, and nature of architectural distortion and/or other signs of breast cancer were determined by the radiologists and pathologists involved in the diagnostic imaging and other investigations.

Regions related to or suspected to contain architectural distortion were marked using rectangular boxes based on the reports available on subsequent imaging or biopsy, or by detailed inspection of the prior mammograms. All but two of the 106 prior mammograms had been declared to be free of any sign of breast cancer at the time of their original acquisition and interpretation in the screening program; the other two mammograms had been referred for biopsy although no signs of malignancy were present. The time interval between the diagnostic mammograms (not available) and prior mammograms ranged from 1.5 months to 24.5 months, with an average of 15.5 months and standard deviation of 7 months. Each image contained a single site of architectural distortion as identified by the rectangular box drawn by the radiologist. The average width, height, and area of the 106 suspicious parts of images marked by the radiologist are 56 mm, 39 mm, and 2274 mm^2, with standard deviation of 11.8 mm, 11.6 mm, and 1073.9 mm^2, respectively.

In addition to the above, all normal cases in the database with at least two visits to the screening program were identified. The mammograms of the penultimate screening visits of the normal cases at the time of preparation of the database were obtained and included in the present study as

mammograms of normal cases. In this manner, 52 mammographic images of 13 normal control cases were obtained for the study.

1.3 Methods

The application of Gabor filters and linear phase portrait analysis leads to the automatic detection of the locations of node-like intersecting or spiculating patterns, including potential sites of architectural distortion; the procedure also results in the detection of a number of false-positive (FP) sites. The number of FPs is reduced through the characterization and analysis of angular spread. The flowchart shown in Fig. 1.1 gives an overview of the procedure for the detection of architectural distortion.

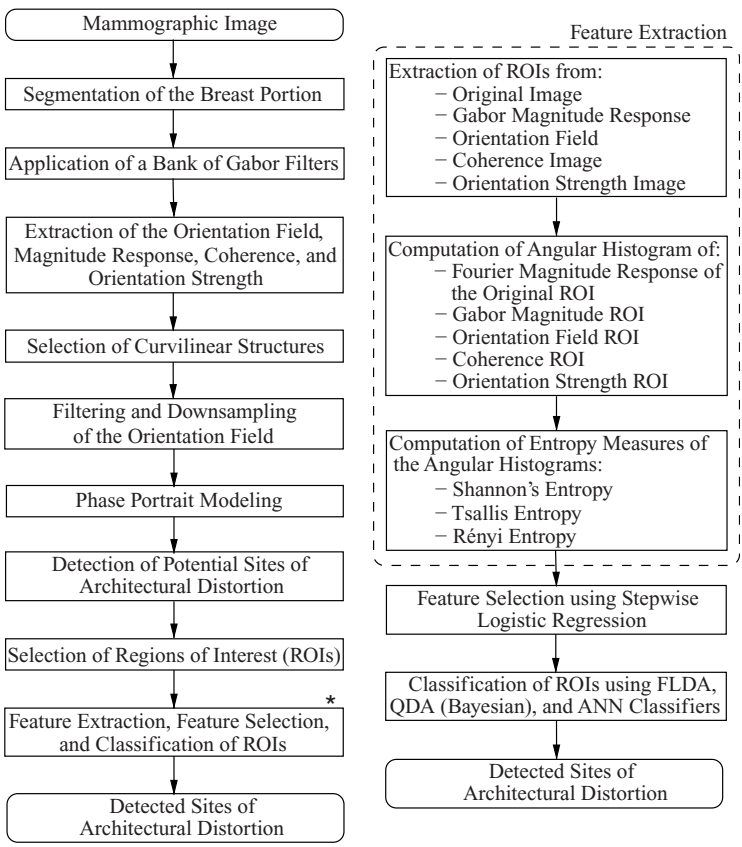

Figure 1.1 Flowchart of the procedures used to detect architectural distortion in prior mammograms. The steps in the box indicated with an asterisk (*) on the left side are shown in detail on the right side. ANN: artificial neural network; FLDA: Fisher-linear discriminant analysis; QDA: quadratic discriminant analysis; ROIs: regions of interest. (Reproduced, with kind permission from Springer Science+Business Media, from Ref. 26. © 2012 Springer.)

1.3.1 Detection of potential sites of architectural distortion

Each mammographic image was filtered and downsampled to 200 μm/pixel and 8 bits/pixel. Potential sites of architectural distortion in the prior mammograms were detected initially by the analysis of oriented texture with the application of a bank of Gabor filters and constrained linear phase portrait models.[22] The methods include steps for approximate segmentation of the breast portion in the mammographic image using Otsu's thresholding method and the morphological opening filter, as well as the use of a bank of 180 real Gabor filters with angles spaced evenly over the range $[-\pi/2, \pi/2]$ to obtain the magnitude response and orientation field.

Gabor filters are a category of filters obtained by the modulation of a Gaussian envelope by a sinusoidal function (real or complex).[33] The real Gabor filter kernel oriented at $-\pi/2$ is given as[34,35]

$$g(x, y) = \frac{1}{2\pi\sigma_x\sigma_y} \exp\left[-\frac{1}{2}\left(\frac{x^2}{\sigma_x^2} + \frac{y^2}{\sigma_y^2}\right)\right] \cos(2\pi f_o x), \qquad (1.1)$$

where σ_x and σ_y are the standard deviation values in the x and y directions, and f_o is the frequency of the modulating sinusoid. Kernels at other angles can be obtained by rotating this kernel over the range $[-\pi/2, \pi/2]$ by using coordinate transformation.[34,35] The parameters in Eq. (1.1) were derived by taking into account the size of the lines or curvilinear structures (CLSs) to be detected, as follows:[34]

- Let τ be the full-width at half-maximum of the Gaussian term in Eq. (1.1) along the x axis. Then, $\sigma_x = \tau/(2\sqrt{2\ln 2}) = \tau/2.35$.
- Let the period of the cosine term be τ; then, $f_0 = 1/\tau$.
- The value of σ_y is defined as $\sigma_y = l\sigma_x$, where l determines the elongation of the Gabor filter in the y direction, as compared to the extent of the filter in the x direction.
- The parameter τ controls the scale of the filter. In the present work, for the detection of architectural distortion, $\tau = 4$ pixels (corresponding to a thickness of 0.8 mm at the pixel size of 200 μm) and $l = 8$ were used. These values were determined empirically, by observing the typical spicule width and length in mammograms with architectural distortion.[34]

The Gabor filter provides the best compromise between spatial localization and frequency localization, as represented by the product between the spatial extent and the frequency bandwidth of the filter.[33,36–38] In the present work, a bank of 180 real Gabor filters was used to detect features with positive contrast; the filtering operation was implemented in the frequency domain. Figure 1.2 demonstrates the use of Gabor filters for the detection of oriented patterns in two directions. The test image used

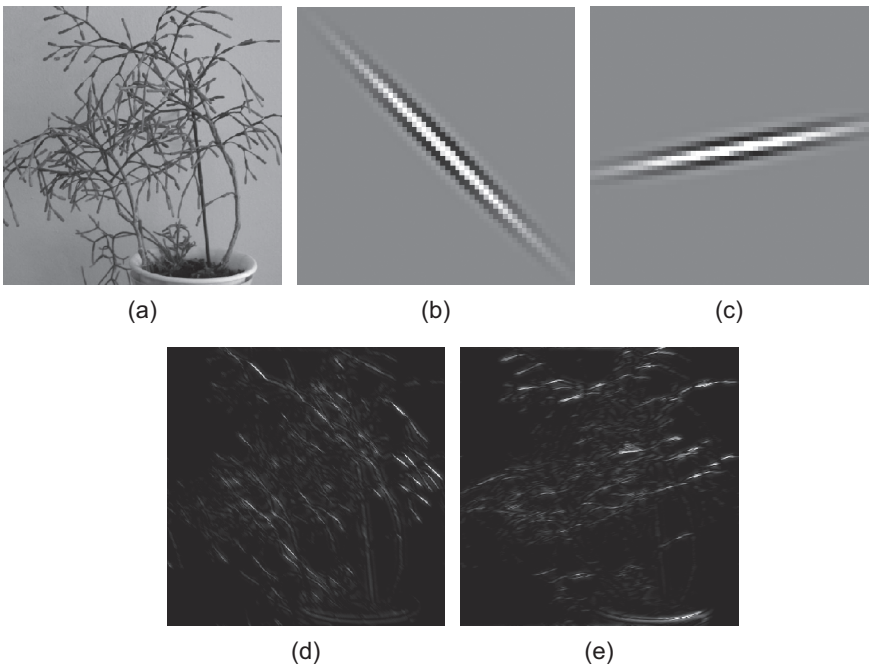

Figure 1.2 Use of Gabor filters for the detection of oriented patterns. (a) A test image of size 601 × 601 pixels. (b) Impulse response of a Gabor filter oriented at 135 deg; $\tau = 1$, $l = 15$ pixels. (c) Impulse response of a Gabor filter oriented at 10 deg. (d) Gabor magnitude response of the image shown in part (a) after filtering with the impulse response shown in part (b). (e) Gabor magnitude response of the image shown in part (a) after filtering with the impulse response shown in part (c). The images of the impulse responses are not to the same scale as the other images.

contains patterns oriented at many directions; the use of a Gabor filter oriented at a particular direction extracts only those components of the image that are oriented at the particular direction chosen.

The output of the bank of 180 real Gabor filters was used to derive the magnitude response, orientation field, coherence, and orientation strength images. The magnitude response and angle of the Gabor filter with the highest output for each pixel were used to construct the magnitude response and orientation field images. Subsequent procedures include the selection of the CLSs of interest (i.e., spicules and fibroglandular tissue), filtering and downsampling of the core CLS pixels, and application of the linear phase portrait modeling procedure with specific conditions applied to the filtered orientation field to yield node maps.[22]

Phase portrait modeling[39,40] is a method for the analysis of oriented texture that relies on the association of an image presenting an oriented textural pattern with the appearance of a phase portrait diagram and the corresponding parameters of a system of differential equations. When a

system of two linear, first-order, differential equations is linear and affine, it assumes the form

$$\begin{pmatrix} \dot{p}(t) \\ \dot{q}(t) \end{pmatrix} = \mathbf{A} \begin{pmatrix} p(t) \\ q(t) \end{pmatrix} + \mathbf{b}, \tag{1.2}$$

where $\dot{p}(t)$ and $\dot{q}(t)$ indicate the first-order derivatives with respect to time of the functions $p(t)$ and $q(t)$, respectively, $\mathbf{A}$ is a 2×2 matrix, and $\mathbf{b}$ is a 2×1 column matrix (a vector). The center (p_0, q_0) of the phase portrait is given by the fixed point of Eq. (1.2):

$$\begin{pmatrix} \dot{p}(t) \\ \dot{q}(t) \end{pmatrix} = 0 \Rightarrow \begin{pmatrix} p_0 \\ q_0 \end{pmatrix} = -\mathbf{A}^{-1}\mathbf{b}. \tag{1.3}$$

Solving Eq. (1.2) yields a linear combination of complex exponentials for $p(t)$ and $q(t)$, whose exponents are given by the eigenvalues of $\mathbf{A}$ multiplied by the time variable t. In this case, there are only three types of phase portraits: node, saddle, and spiral.[41] The type of phase portrait can be determined from the nature of the eigenvalues of $\mathbf{A}$[22,34,39,40] as given by

$$\lambda_1 = \frac{tr(\mathbf{A})}{2} + \frac{\sqrt{[tr(\mathbf{A})]^2 - 4\,det(\mathbf{A})}}{2} \tag{1.4}$$

and

$$\lambda_2 = \frac{tr(\mathbf{A})}{2} - \frac{\sqrt{[tr(\mathbf{A})]^2 - 4\,det(\mathbf{A})}}{2}, \tag{1.5}$$

where $tr(\mathbf{A})$ is the trace of matrix $\mathbf{A}$, and $det(\mathbf{A})$ is the determinant of $\mathbf{A}$.

Large orientation fields, such as those of mammograms, may contain complex patterns that are formed by superpositions of several patterns or overlapping structures; this may result in the presence of multiple focal points in the analysis of phase portraits. To perform the analysis of large orientation fields through phase portrait modeling, the analysis should be performed at multiple locations (within a small window), and the information so acquired should be accumulated in a form that permits the identification of the various significant patterns or structures present in the overall orientation field.

Rao and Jain[40] proposed the following method for the analysis of large orientation fields:

1. Create three images, referred to as *phase portrait maps*, of the same size as that of the image or orientation field under analysis. Initialize the phase portrait maps to zero.
2. Perform analysis by moving a sliding window throughout the orientation field. For every position of the analysis window, perform the following steps:
   (a) Use the local analysis procedure described above to find the optimal parameters $\mathbf{A}_{opt}$ and $\mathbf{b}_{opt}$ that best describe the orientation field within the analysis window.
   (b) Determine the type of phase portrait and the fixed-point location associated with the orientation field within the analysis window from $\mathbf{A}_{opt}$ and $\mathbf{b}_{opt}$.
   (c) Select the phase portrait map corresponding to the phase portrait type determined above and increment the value present at the pixel nearest to the fixed-point location. This procedure is referred to as *vote casting*.

When all votes are cast, the phase portrait maps could be analyzed to detect the presence of patterns in the given image or orientation field. If a part of the orientation field is composed of oriented segments radiating from a central point, in a manner similar to a node pattern, it is expected that the node map will contain a large number of accumulated votes close to the geometrical focus of the observed pattern. Spiral and saddle patterns were found to be not related with the patterns of architectural distortion; therefore, they were discarded through constrained linear phase portrait analysis with additional conditions.[14,22,34,42]

The peaks in the node map are expected to indicate potential sites of architectural distortion. Hence, the node map was analyzed by rank-ordering the peaks in the node map to detect peaks related to the sites of architectural distortion; however, the procedure also resulted in the detection of a number of FP sites.[12–14] For each peak in the node map, a square region of interest (ROI) of size 128×128 pixels at 200 μm/pixel (except at the edges of the images) was automatically obtained; the center of the node peak was taken as the center of the corresponding ROI. The ROIs were labeled at the locations indicated by the peaks in the node map, in decreasing order of the node value of the peak, with up to a maximum of 30 ROIs per mammogram.[12–14] The automatically detected ROIs that had their centers within the rectangular parts of architectural distortion marked by the radiologist were manually identified as true-positive (TP) ROIs; the others were labeled as FP ROIs. Phase portrait analysis did not detect any TP ROI in one prior mammogram of an interval-cancer case; the

radiologist had indicated that the corresponding image had no clearly evident architectural distortion.

The results of application of the methods described above are illustrated in Fig. 1.3 for a prior mammogram of an interval-cancer case. In Fig. 1.3(a), the rectangle shows the area of architectural distortion marked by the radiologist (J.E.L.D.). The magnitude image and the orientation field resulting from the Gabor filters are shown in parts (b) and (c), respectively. The node map is shown in part (d) of the same figure; the most dominant peak is evident within the site of architectural distortion. Figure 1.3(e) shows all of the automatically detected ROIs obtained by the methods described above.

From the 158 mammograms in the study, a total of 4224 ROIs (2821 from the 106 prior mammograms of interval-cancer cases with 301 related to the parts with architectural distortion, and 1403 from the 52 normal mammograms) of size 128 × 128 pixels at 200 μm/pixel (except at the edges of the images) were automatically obtained. The number of FP sites was reduced through characterization and analysis of the angular spread of the magnitude and angle responses of Gabor filters, coherence, orientation strength, and power in the frequency domain, as discussed in the subsequent sections.

1.3.2 Analysis of angular spread

In preliminary studies related to the present work, characterization of the angular spread of power in the frequency domain was found to be useful in the detection of architectural distortion.[13,28] In this context, it is hypothesized that analysis of the angular histograms of the Gabor magnitude response, orientation field (angle response), coherence, and orientation strength could reveal important information regarding the presence of architectural distortion. It should be noted that only the Gabor orientation field is used in the initial step of phase portrait analysis; the Gabor magnitude response could also aid in the detection of architectural distortion, as demonstrated in the following sections.

1.3.2.1 Angular spread of power in the frequency domain

The Fourier spectrum of an image with oriented texture contains directional spectral characteristics that may be used for the extraction of important information regarding the objects and patterns present in the image.[36] The derivation of measures of angular spread, coherence, and orientation strength is described in the following sections.

In order to perform analysis in the frequency domain, the 2D Fourier power spectrum of the ROI being processed was obtained with the application of a radial von Hann (also known as Hanning) window[18] and zero padding to the size of 256 × 256 pixels. The 2D power spectrum $S(u, v)$ in the Cartesian coordinates (u, v) was mapped to the polar coordinates (f, θ) to obtain $S(f, \theta)$, by resampling and computing a weighted average

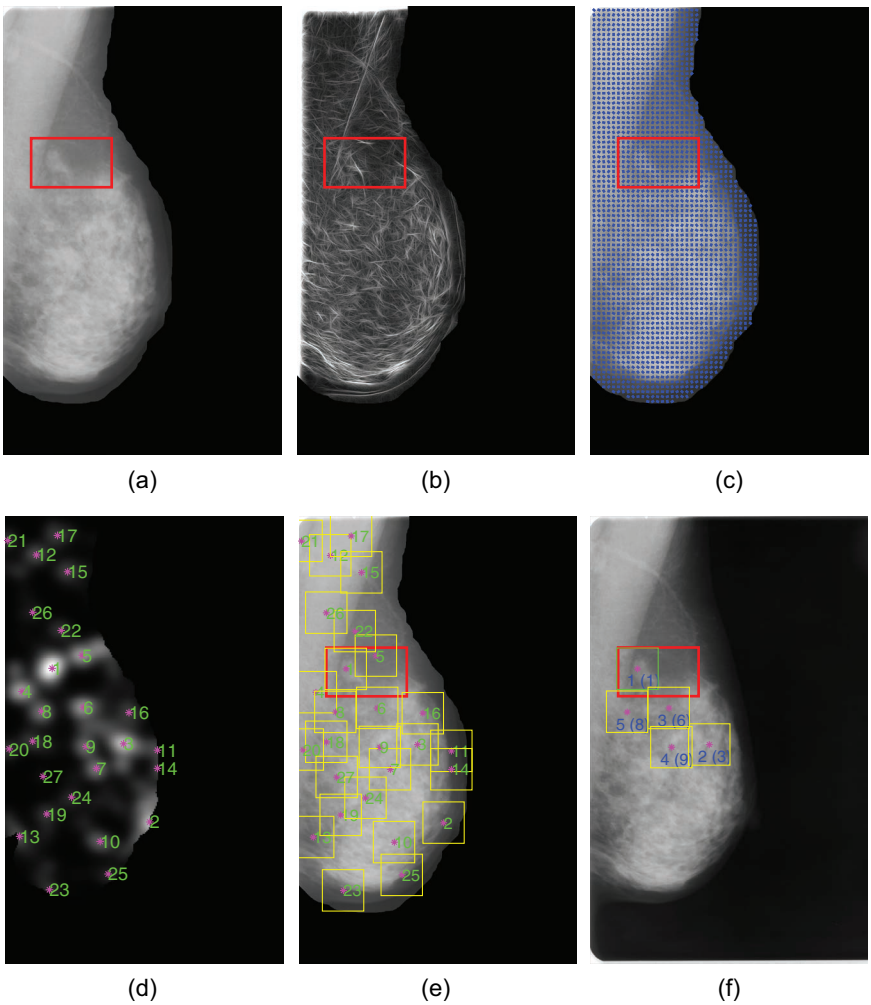

Figure 1.3 (a) The prior mammogram of an interval-cancer case. The rectangle is of size 49.4 mm $\times$ 29.9 mm and indicates the region of architectural distortion identified by a radiologist. Image size 1370 $\times$ 850 pixels at 200 μm/pixel. (b) Magnitude response obtained using a bank of 180 real Gabor filters. (c) Orientation field angle superimposed on the mammographic image; needles are drawn for every 15th pixel. (d) The node map at 800 μm/pixel. Each asterisk (*) corresponds to a peak position detected automatically in the node map. The numbers next to the asterisk marks indicate the peaks in descending order of magnitude. (e) The 27 ROIs obtained automatically using the peaks detected in the node map. The size of each ROI is 128 $\times$ 128 pixels at 200 μm per pixel (except at the edges). (f) Reduction of FPs for the image shown in part (e) using the selected features and the Bayesian classifier with the leave-one-patient-out method; only the top five ROIs on the image based on the discriminant values are shown, with the associated average sensitivity of 0.8 at 5.4 FP/patient. The numbers outside the parentheses represent the ranking based on the discriminant values obtained by the Bayesian classifier, and the numbers within the parentheses represent the earlier ranking based on the node value. (Reproduced with permission from Ref. 28.)

of the four neighbors of each pixel for radial distance f ranging from zero to half the sampling frequency and over the range of angle $\theta = [0, 179]$ deg. Although the power spectra of ROIs are transformed from rectangular to polar coordinates, the results are presented and processed further in rectangular arrays for ease of computation and representation.

The center (DC frequency) of $S(u, v)$ corresponds to pixel (129, 129). Therefore, for a pixel (f_k, θ_k) in $S(f, \theta)$, $u_k = f_k \cos\theta_k + 129$, and $v_k = 129 - f_k \sin\theta_k$, where (u_k, v_k) are the coordinates of a pixel in $S(u, v)$; see the schematic diagram in Fig. 1.4 (a). The value of $S(f_k, \theta_k)$ was computed by taking the weighted average of the values of the four neighboring pixels. Defining $u_1 = floor(u_k)$, $u_2 = ceil(u_k)$, $v_1 = floor(v_k)$, and $v_2 = ceil(v_k)$, we have

$$S(f_k, \theta_k) = \frac{1}{(d_1 + d_2 + d_3 + d_4)}[d_1 S(u_1, v_1) + d_2 S(u_1, v_2) + d_3 S(u_2, v_1) + d_4 S(u_2, v_2)], \tag{1.6}$$

where

$$\begin{aligned} d_1 &= \sqrt{2} - ED11, \quad ED11 = \sqrt{[u_k - u_1]^2 + [v_k - v_1]^2}, \\ d_2 &= \sqrt{2} - ED12, \quad ED12 = \sqrt{[u_k - u_1]^2 + [v_k - v_2]^2}, \\ d_3 &= \sqrt{2} - ED21, \quad ED21 = \sqrt{[u_k - u_2]^2 + [v_k - v_1]^2}, \\ d_4 &= \sqrt{2} - ED22, \quad ED22 = \sqrt{[u_k - u_2]^2 + [v_k - v_2]^2}; \end{aligned} \tag{1.7}$$

see the schematic diagram in Fig. 1.4(b). The weights are important to maintain homogeneity and continuity for continuous-to-discrete transformation (i.e., to reduce the estimation error) and also to account for border pixels. Although the Hankel transform[43] and the Fourier transform in polar coordinates have

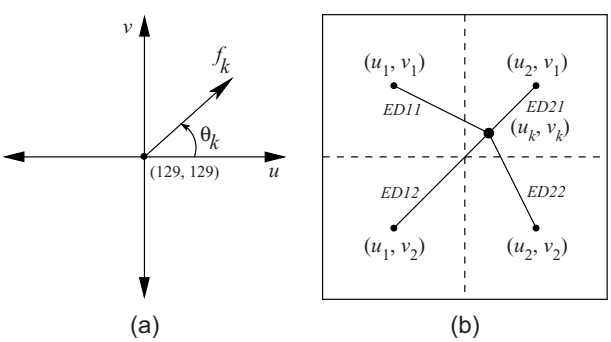

Figure 1.4 Schematic representations of (a) coordinate transformation and (b) computation of the weighted average of the transformed pixel.

been used for texture analysis and pattern recognition,[44] the method described in the present chapter to characterize the angular spread of power is novel and is shown to be effective for the analysis of oriented texture.

To obtain the angular spread of power in the frequency domain, the geometrically transformed 2D Fourier power spectrum $S(f, \theta)$, was transformed into a 1D function $S(\theta)$, by integrating as a function of the angle θ (for the range [0, 179] deg) from the zero-frequency point over radial distance $f = [6, 96]$ pixels. Selected low- and high-frequency regions were excluded so as to remove the effects of the low-frequency components related to the overall appearance of the image and the large structures present in the image, as well as to prevent the effects of high-frequency noise. The band of frequencies to be excluded (i.e., the nonlinear portion) was selected based on experimentation.[13]

1.3.2.2 Coherence

In the method for the computation of coherence, the orientation information at each pixel is represented by a pair of magnitude and orientation values. The method is based on a pixel's neighborhood that provides the dominant orientation in an average sense and the degree of alignment of the orientation information for each pixel in the neighborhood with respect to the dominant orientation.[39,45] The dominant orientation can be computed as the orientation that maximizes the coherence.

Let $G(m, n)$ and $\theta(m, n)$ denote the magnitude and orientation at the point (m, n) in an image, respectively, and $P \times P$ be the size of the neighborhood around (p, q) used for computing the dominant orientation, $\psi(p, q)$. In the present work, $G(m, n)$ and $\theta(m, n)$ are obtained from the Gabor magnitude and phase response. The projection of $G(m, n)$ onto the orientation vector at (p, q) with angle $\theta(p, q)$ is given by $G(m, n) \cos[\theta(m, n) - \theta(p, q)]$.

The sum-of-squares S_G of the projection of the Gabor response computed at each pixel of the neighborhood with respect to the dominant orientation specified by Θ is given as

$$S_G = \sum_{m=1}^{P} \sum_{n=1}^{P} G^2(m, n) \cos^2[\theta(m, n) - \Theta]. \tag{1.8}$$

The sum-of-squares S_G varies as the reference orientation Θ is varied and attains its maximum when Θ is perpendicular to the dominant orientation that corresponds to the underlying texture in the given neighborhood.[39] Differentiating S_G with respect to Θ yields

$$\frac{dS_G}{d\Theta} = 2 \sum_{m=1}^{P} \sum_{n=1}^{P} G^2(m, n) \cos[\theta(m, n) - \Theta] \sin[\theta(m, n) - \Theta]. \tag{1.9}$$

By setting $\frac{dS_G}{d\Theta} = 0$ and further simplifying the result, the solution for $\Theta = \Theta(p, q)$ that maximizes S_G at the point (p, q) in the image is given by[39]

$$\Theta(p, q) = \frac{1}{2}\tan^{-1}\left(\frac{\sum_{m=1}^{P}\sum_{n=1}^{P} G^2(m, n)\sin[2\theta(m, n)]}{\sum_{m=1}^{P}\sum_{n=1}^{P} G^2(m, n)\cos[2\theta(m, n)]}\right). \quad (1.10)$$

The second derivative $\frac{d^2S_G}{d\Theta^2}$ is given as

$$\frac{d^2S_G}{d\Theta^2} = -2\sum_{m=1}^{P}\sum_{n=1}^{P} G^2(m, n)\cos[2\theta(m, n) - 2\Theta]. \quad (1.11)$$

Setting Eq. (1.11) to zero and solving the resulting equation yields the estimated dominant angle of the texture $\psi(p, q)$ at (p, q) in the image to be

$$\psi(p, q) = \Theta(p, q) + \pi/2. \quad (1.12)$$

The coherence $\gamma(p, q)$ at a pixel (p, q) is given by the cumulative sum of the projections of the Gabor magnitude responses for the pixels in a window of size $P \times P$, in the direction of the dominant orientation at the point (p, q) under consideration,[39,45] as

$$\gamma(p, q) = G(p, q)\frac{\sum_{m=1}^{P}\sum_{n=1}^{P}\left|G(m, n)\cos[\theta(m, n) - \psi(p, q)]\right|}{\sum_{m=1}^{P}\sum_{n=1}^{P} G(m, n)}; \quad (1.13)$$

in the present work $P = 15$, with (p, q) being located at the center of the $P \times P$ window.

1.3.2.3 Orientation strength

For computation of the orientation strength, it is assumed that, rather than being a single value, the orientation information at a pixel is represented by a function $G(\theta)$ that provides the strength of orientation (at the pixel location) in the underlying image for each angle θ. The measure of orientation strength at each pixel is computed, in the present work, as a weighted average of the Gabor magnitude responses $G_k(m, n)$ for all directions of the filters used, θ_k, $k = 0, 1, 2, \ldots, 179$, as

$$\alpha(m, n) = \sqrt{\frac{\left[\sum_{k=0}^{179} G_k(m, n)\cos(2\theta_k)\right]^2 + \left[\sum_{k=0}^{179} G_k(m, n)\sin(2\theta_k)\right]^2}{\left[\sum_{k=0}^{179} G_k(m, n)\right]^2}}. \quad (1.14)$$

This measure may also be termed as "alignment energy."

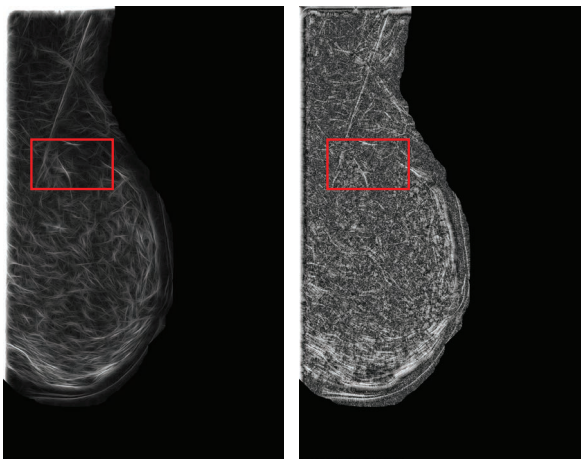

(a) (b)

Figure 1.5 (a) Coherence and (b) orientation strength images for the mammogram shown in Fig. 3(a). (Reproduced with permission from Ref. 28.)

The results of application of the methods for computing the coherence and orientation strength are illustrated in Fig. 1.5 for the mammographic image shown in Fig. 1.3(a). It can be seen that the coherence and orientation strength images appear similar to the Gabor magnitude response images: both images have high responses for oriented structures. However, coherence represents an average measure of alignment with reference to a specified angle over a neighborhood; on the other hand, the orientation strength takes into account the possibility of the presence of multiple structures oriented in several directions intersecting at the pixel considered.

1.3.3 Characterization of angular spread

Three angular histograms or rose diagrams with 60 bins equally spaced over the angular range of [−89, 90] deg were generated using the Gabor magnitude response, coherence, and orientation strength for each ROI based on the orientation field angle at each pixel. Another rose diagram was obtained using only the orientation field angle. To quantify the distribution based on the magnitude response, orientation field angle, coherence, and orientation strength, three entropy measures (Shannon's entropy, Tsallis entropy, and Rényi entropy) of each rose diagram, $F(\theta)$, were computed, after being normalized to have unit sum.

The angular spread of power in the frequency domain, $S(\theta)$, as obtained by the procedure described in the Section 1.3.2.1, was also included in the analysis,[13,28] and the three measures of entropy as above were computed.

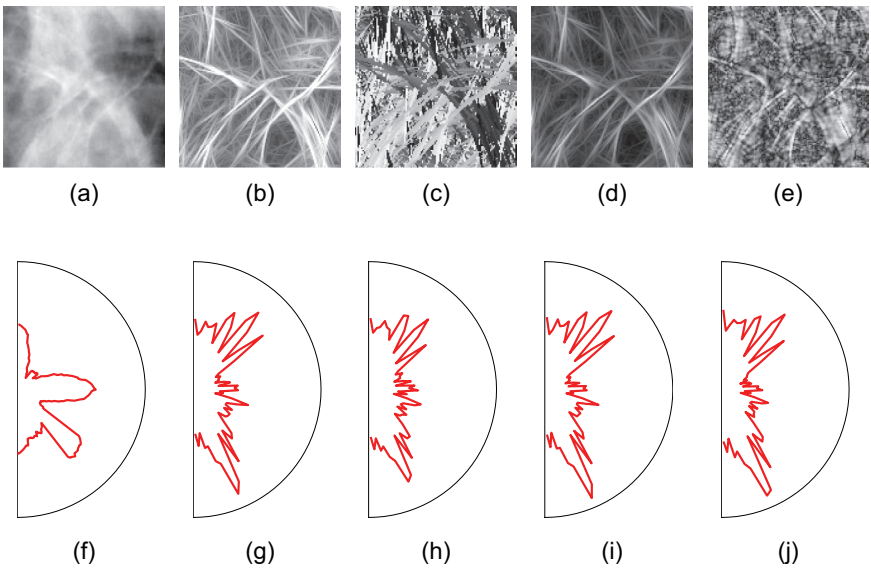

Figure 1.6 (a) A 128 × 128-pixel mammographic TP ROI with architectural distortion. (b) Gabor magnitude response. (c) Orientation field with angles in the range [–π/2, π/2] mapped to the grayscale range [0, 255]. (d) Coherence. (e) Orientation strength. (f) Angular histogram of power based on the Fourier spectrum of the image in (a). (g)–(j) Angular histograms of (b)–(e). Shannon's entropy (H_S), Tsallis entropy (H_T) of order two, and Rényi entropy (H_R) of order eight, respectively, are: (f) 7.3940, 0.9930, 6.6152; (g) 5.7950, 0.9807, 5.2649; (h) 5.8266, 0.9814, 5.4102; (i) 5.7812, 0.9803, 5.2173; and (j) 5.7756, 0.9802, 5.2218. Note: $H_{S\,\max}$ = 7.49, $H_{T\,\max}$ = 0.9944, $H_{R\,\max}$ = 7.49 for rose diagrams of type (f) with 180 bins, and 5.91, 0.9833, and 5.91, respectively, for the types in (g)–(j) with 60 bins. The rose diagram in (f) has been rotated by –90 deg to match the rose diagrams in (g)–(j). (Reproduced with permission from Ref. 28.)

Figures 1.6 and 1.7 illustrate the angular distributions (i.e., rose diagrams) obtained as above for the characterization of the angular spread of a TP ROI and an FP ROI, respectively. TP ROIs typically have patterns oriented in multiple directions, and the corresponding rose diagrams are expected to contain a wide distribution of power spread over several angular bands. On the contrary, FP ROIs are not expected to have patterns oriented in multiple directions, and the related rose diagrams should contain a narrower distribution of power over fewer angular bands. The quantification of angular histograms is discussed in detail in the subsequent sections.

1.3.4 Measures of angular spread

Entropy is a measure of information (in terms of order, disorder, or probability of occurrence) in a given set of data. Because texture can be

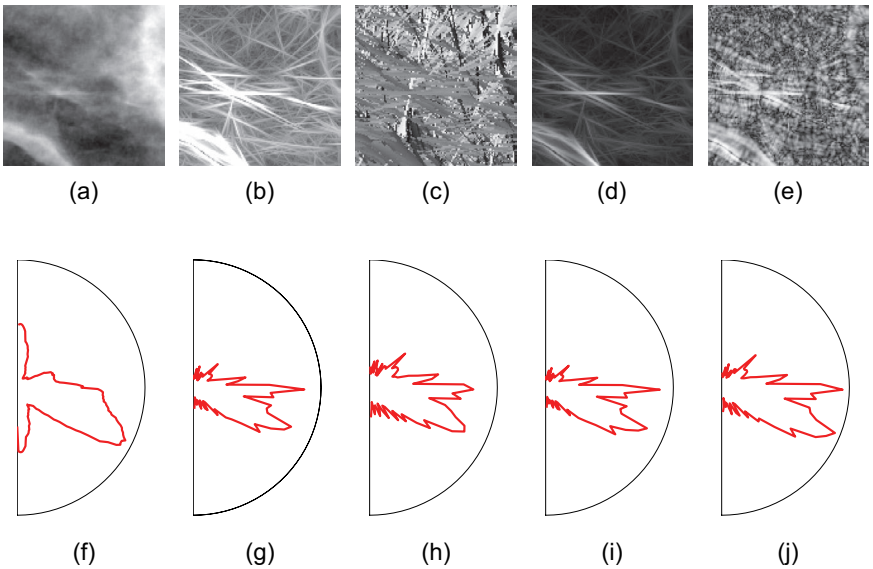

Figure 1.7 (a) A 128 × 128-pixel mammographic ROI; the ROI represents an FP detection due to overlapping or intersecting normal structures. (b) Gabor magnitude response. (c) Orientation field with angles in the range [–π/2, π/2] mapped to the grayscale range [0, 255]. (d) Coherence. (e) Orientation strength. (f) Angular histogram of power based on the Fourier spectrum of the image in (a). (g)–(j) Angular histograms of (b)–(e). Shannon's entropy (H_S), Tsallis entropy (H_T) of order two, and Rényi entropy (H_R) of order eight, respectively, are: (f) 7.2101, 0.9919, 6.4858; (g) 5.5173, 0.9731, 4.6310; (h) 5.6554, 0.9769, 4.9137; (i) 5.4814, 0.9721, 4.5846; and (j) 5.5454, 0.9739, 4.7111. Note: $H_{S\,\max} = 7.49$, $H_{T\,\max} = 0.9944$, $H_{R\,\max} = 7.49$ for rose diagrams of type (f) with 180 bins, and 5.91, 0.9833, 5.91, respectively, for the types in (g)–(j) with 60 bins. The rose diagram in (f) has been rotated by –90 deg to match the rose diagrams in (g)–(j). (Reproduced with permission from Ref. 28.)

considered as a representation of the surfaces of objects and surfaces are often composed of features with multiple orientations, analysis of the entropy of a given image may be a useful approach to the problem of texture classification.[12,13,28–30,36,46]

1.3.4.1 Shannon's entropy

The most commonly used measure of order in a dynamical system is Shannon's (or Boltzmann–Gibbs) entropy.[47,48] Shannon's entropy is defined as

$$H_S = -\sum_i p_i \log_2 p_i, \tag{1.15}$$

where p_i is the probability of occurrence of an event i, or the value of bin i is a normalized rose diagram. The measure has its maximal value when all

events are equally likely ($p_i = 1/N$, with N being the number of events or bins). H_S has the additivity (extensivity) property as

$$H_S(A \cup B) = H_S(A) + H_S(B), \tag{1.16}$$

where A and B are two independent subsystems with $p(A \cup B) = p(A)p(B)$.

However, Shannon's entropy may not be able to characterize systems with long-range interactions, long-term memory effects, or abrupt changes.[49] In this context, the use of higher-order entropy, such as Tsallis entropy and Rényi entropy,[48,50] which are generalized forms of Boltzmann's or Gibbs' traditional entropy, could be used as alternatives of the typical entropy measures. Tsallis and Rényi entropies are both appropriate choices for a system with q-exponential behavior (an identity in the variable q that provides a known result in the limit, as $q \to 1$ for an exponential function).[50]

1.3.4.2 Tsallis entropy

Tsallis entropy, a generalized form of Boltzmann–Gibbs entropy, is defined as[50–52]

$$H_T(q) = \frac{1 - \sum_i p_i^q}{(q-1)}, \tag{1.17}$$

where q is the moment order. Tsallis entropy is a generalized form of Shannon's traditional entropy[49–51] and is a nonextensive (scale-invariant) quantity for statistically independent subsystems. The parameter q measures the degree of nonextensivity. When $q \to 1$, Tsallis entropy recovers the definition of Shannon's entropy as follows:[49–51]

$$\begin{aligned} H_T(q) &= \frac{1 - \sum_i p_i^q}{(q-1)} \\ &= \sum_i p_i \frac{p_i^{q-1} - 1}{1-q} \\ &= \sum_i p_i \frac{2^{(q-1)\log_2 pi} - 1}{1-q} \\ &\approx \sum_i p_i \frac{[1 + (q-1)\log_2 p_i] - 1}{1-q} \\ &= -\sum_i p_i \log_2 p_i. \end{aligned} \tag{1.18}$$

Tsallis entropy reaches its maximum when the probability of occurrence is the same for all events ($p_i = 1/N$, N is the number of events or bins); the maximum value of Tsallis entropy is given by[49,51,52]

$$H_{T\max} = \frac{N^{1-q} - 1}{1 - q}. \tag{1.19}$$

In the limit $q \to 1$, $H_{T\max} = \ln N$.

Tsallis entropy has found applications in physics, thermodynamics, and biomedical engineering.[49,53,54] It should be noted that the parameter q measures the degree of nonextensivity. The pseudo-additivity rule, in this case, is

$$H_T(A \bigcup B) = H_T(A) + H_T(B) + (1-q)\, H_T(A)\, H_T(B), \tag{1.20}$$

where $q < 1$, $q = 1$, and $q > 1$ correspond to superextensive, extensive, and subextensive statistics, respectively.[49,55] The parameter q plays an important role in the result of computation of H_T for a given N. However, there has been no established rule for optimizing the value of q other than through experimentation based on some predefined criteria and their characteristics.[49,56] In order to quantify the angular spread of power, Tsallis entropy was computed for the five angular distributions derived for each ROI for various values of the order q. Based on an analysis of the performance using the area under the receiver operating characteristic (ROC) curves (A_z value), Tsallis entropy of second order was selected for further use in the present work. The value of H_T decreases monotonically with the increase of q.[55] Figure 1.8(a) illustrates the variation of Tsallis entropy

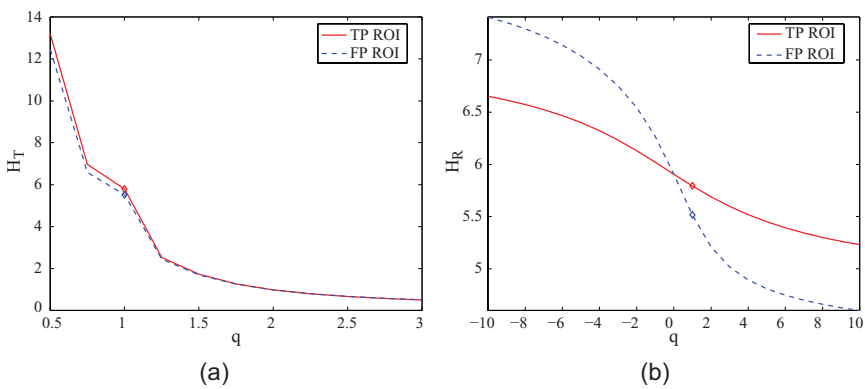

Figure 1.8 Variation of (a) Tsallis entropy and (b) Rényi entropy values with several orders q for the TP (solid line) and FP (dashed line) Gabor magnitude ROIs shown in Figs. 1.6(b) and 1.7(b), respectively. Shannon's entropy values are also shown for reference with the diamond mark.

values with several orders, $q \in [0.5, 3]$, for the TP and FP Gabor magnitude ROIs shown in Figs. 1.6(b) and 1.7(b), respectively; Shannon's entropy is also shown for reference.

1.3.4.3 Rényi entropy

Rényi entropy[48,50] is given by

$$H_R(q) = \frac{1}{(1-q)} \log_2 \left(\sum_i p_i^q \right). \tag{1.21}$$

Rényi entropy is a generalized form of Shannon's traditional entropy and is an extensive quantity for statistically independent subsystems, concave only for $0 < q < 1$. Rényi entropy tends to Shannon's entropy as a special case when $q \to 1$. Shannon's entropy is an averaged measure of information in the ordinary sense, whereas Rényi's measure represents an exponential mean over the same elementary information gains of $\log_2(1/p_i)$.[50] Rényi entropy has an additivity property similar to that of Shannon's entropy and reaches its maximum when the probability of occurrence is the same for all events ($p_i = 1/N$). The maximum value of Rényi entropy is given by[57] $\ln N$ in the limit $q \to 1$, when the probability of occurrence is the same for all events. The parameter q can be varied to make Rényi entropy more or less sensitive to the shape of probability distribution of the data being analyzed. Rényi entropy has been widely used in multifractal theory,[58] texture classification,[59] pattern recognition, and image segmentation.[60,61]

To quantify angular spread, Rényi entropy was computed for the five angular distributions derived for each ROI for various orders q. Based on an analysis of the classification performance using the A_z values, Rényi entropy of eighth order was selected for further use in the present work; other works[58] have used $-10 \le q \le 10$. Figure 1.8(a) illustrates variations of Rényi entropy values for several orders $q \in [-10, 10]$ for the TP and FP Gabor magnitude ROIs shown in Figs. 1.6(b) and 1.7(b), respectively; Shannon's entropy is also shown for reference.

For a mammographic image, it is not feasible to characterize the underlying process as an extensive or a nonextensive system. Mammograms of breasts with higher amount of fat content have been found to exhibit higher levels of nonextensiveness and fractal content.[56] The present study explores the application of entropy measures for both nonextensive and extensive systems in the form of Tsallis and Rényi entropy.

Due to the presence of spiculation radiating at several angles, TP ROIs are expected to have a wide angular spread of power.[13] On the other hand, most FP ROIs were observed to contain a few intersecting ligaments,

Table 1.1 List of features for characterization of angular spread with A_z values for the dataset of interval-cancer cases including normal control cases. H_S1–H_S5: Shannon's entropy measures; H_T1–H_T5: Tsallis entropy measures of order two; and H_R1–H_R5: Rényi entropy measures of order eight. (Reproduced, with kind permission from Springer Science+Business Media, from Ref. 26. © 2012 Springer.)

Symbol	Feature	A_z
H_S1	power in the frequency domain	0.64
H_S2	Gabor magnitude response	0.68
H_S3	Gabor angle response	0.63
H_S4	coherence	0.68
H_S5	orientation strength	0.62
H_T1	power in the frequency domain	0.64
H_T2	Gabor magnitude response	0.68
H_T3	Gabor angle response	0.64
H_T4	coherence	0.68
H_T5	orientation strength	0.63
H_R1	power in the frequency domain	0.64
H_R2	Gabor magnitude response	0.69
H_R3	Gabor angle response	0.67
H_R4	coherence	0.69
H_R5	orientation strength	0.67

ducts, or vessels with the power limited to a small number of angular bands. Figures 1.6 and 1.7 illustrate the results of the procedures for the characterization of angular distribution with a TP ROI and an FP ROI, respectively. The values of the three entropy measures are given in the captions.

Table 1.1 lists the A_z values obtained for the 15 features used in the present study. The A_z value of each of the features is presented for the full dataset of interval-cancer cases including normal control cases.

1.3.5 Feature selection and pattern classification

In performing classification tasks, numerous features may be extracted, but only a small number of them may have high discriminative capability.[62] The removal of noisy and irrelevant features can help to improve the performance of the classifier. In addition, time, labor, and expense can be saved by extracting only high-performance features. Feature selection, more precisely, feature subset selection, is the process of finding a reduced set of r features out of the given set of d features according to a given selection criterion.[62] In a classification-oriented feature selection procedure, the r selected features are expected to produce fewer classification errors.[63] In the present work, feature selection is performed using stepwise logistic regression.

Logistic classification is a widely used statistical method for feature selection and/or classification based on the probability of occurrence of an event by fitting data to a logistic regression model.[36,64] The logistic regression model is a generalized linear model used for binomial regression and is applicable to problems associated with the classification of patterns into one of two classes. Studies indicate that in the case of a binary response variable, the logistic response function is usually curvilinear and is referred to as a sigmoidal function with a typical shape of either a tilted "S" or as a reversed and tilted "S". The function can be considered to be linear except at the shoulder or toe region with asymptotes at 0 and 1. In pattern classification using logistic regression, an event is typically defined by the membership of a pattern vector in one of the two classes under consideration;[36] based on the given parameters, a response variable constrained to the range [0, 1] is computed. As a result, the variable may be considered as the probability of belonging to a class, and the probability of the pattern vector belonging to the other class can be obtained by calculating the difference between unity and the estimated value for the former class.

For ROC analysis, two classical classifiers, namely Fisher linear discriminant analysis (FLDA) and quadratic discriminant analysis (QDA) with Bayesian assumption,[65] and an artificial neural network (ANN) classifier were used in the present work. FLDA is based on a linear projection of the given M-dimensional feature data onto a line, with the expectation that such projections will be well separated by class; as such, the line is oriented to maximize class separation.

The Bayesian approach is based on quantifying the tradeoffs between various classification decisions using probability and the costs that accompany such decisions. For a binary classification problem, consider a set of observations $\mathbf{x}$, with $p(\mathbf{x}|C_1)$ and $p(\mathbf{x}|C_2)$ being both normally distributed with mean and covariance $(\boldsymbol{\mu}_1, \Sigma_1)$ and $(\boldsymbol{\mu}_2, \Sigma_2)$, respectively. Bayes' optimal solution can be obtained by classifying the component as being from class C_1 if the log-likelihood ratio is less than some threshold T,[65,66] as

$$(\mathbf{x}-\boldsymbol{\mu}_2)^T \sum_2^{-1} (\mathbf{x}-\boldsymbol{\mu}_2) + \ln\left|\sum_2\right| - (\mathbf{x}-\boldsymbol{\mu}_1)^T \sum_1^{-1} (\mathbf{x}-\mu_1) - \ln\left|\sum_1\right| + \ln\frac{P(C_1)}{P(C_2)} < T, \tag{1.22}$$

where $P(C_1)$ and $P(C_2)$ are the prior probabilities of the two classes, and T is independent of the observation $\mathbf{x}$.

Without any further assumption, the classification procedure as above is a typical QDA; with the Bayesian assumption, it is, hereafter, referred to as the Bayesian classifier.

In practical applications of pattern recognition, prior knowledge about the probabilities of an element or pattern belonging to the classes of concern could be unavailable; classical methods of pattern classification may not be applicable in such cases.[65] In this context, a classifier that can acquire and store relevant knowledge from its environment through a learning process would be more suitable. ANNs are such classifiers and could be effective in solving complex and nonlinear classification problems through adaptive learning, input-output mapping, and evidential response.[67] The ANN used in the present work consists of a single hidden layer with 10 neurons and the logistic activation function;[67] the ANN was trained and tested with the leave-one-patient-out method. The neurons in the output layer of the ANN classifier used have a pure linear activation function. The Levenberg–Marquardt algorithm[67] with an initial learning rate of 0.05 was selected for fast and robust training with the backpropagation method.

In the present work, ROC curves, A_z values, and the associated p-values of the differences of the ROC curves were obtained by using ROCKIT, a widely used software package developed at the University of Chicago (Chicago, IL).[68] ROCKIT uses maximum likelihood estimation to fit a binormal ROC curve to continuously distributed data or ordinal category data.

Free-response ROC (FROC) is a method of collecting observer performance data where the observer marks and rates suspicious regions in the images.[69–71] FROC analysis was used to assess the FP rate for a given level of sensitivity when the classification of automatically detected and segmented ROIs was placed in the context of detection of architectural distortion in the mammograms of the patient. In generating FROC curves using the leave-one-patient-out method, the TP ROI with the highest discriminant value in one of the two images (except six cases with only one image per case) was considered. The results of FROC analysis are reported in the text and tables for sensitivities of 0.8 and 0.9, unless otherwise specified. The jackknife alternative FROC (JAFROC) software package (version 4.1)[69,70] was used for statistical analysis of the FROC data. It should be noted that the results of FROC analysis in most of our previous works were reported based on the leave-one-image-out procedure.

1.4 Results

1.4.1 Analysis with various sets of features

The results of analysis of the ROC and FROC curves with various sets of selected features from the total set of 15 features obtained using several classifiers are listed in Table 1.2. Feature selection was performed with

Table 1.2 Results of ROC and FROC analysis using the selected features based on stepwise logistic regression for several types of feature sets. The dataset includes 106 prior mammograms of interval-cancer cases as well as 52 normal control mammograms. Feature selection and pattern classification were performed using the leave-one-patient-out method. FLDA: Fisher linear discriminant analysis; Bayes: Bayesian classifier; ANN: artificial neural network; H_S1–H_S5: Shannon's entropy measures; H_T1–H_T5: Tsallis entropy measures of order two; and H_R1–H_R5: Rényi entropy measures of order eight. The best ROC and FROC results are highlighted in bold. (Reproduced, with kind permission from Springer Science+Business Media, from Ref. 26. © 2012 Springer.)

Type of input features	Most frequently selected features	ROC analysis (A_z)			FROC analysis (FP/patient at the sensitivities shown)			
					Bayes		ANN	
		FLDA	Bayes	ANN	80%	90%	80%	90%
H_S1–H_S5	H_S2, H_S1, H_S3, H_S5	0.72	0.72	0.71	7.0	8.0	6.2	8.7
H_T1–H_T5	H_T2, H_T1, H_T3, H_T5	0.72	0.71	0.73	5.9	7.5	7.0	9.3
H_R1–H_R5	H_R2, H_R1, H_R3, H_R5	0.72	0.72	0.74	5.8	9.1	6.1	9.5
All	H_R2, H_R3, H_S1, H_T5, H_S3	0.73	0.73	**0.75**	**5.2**	**7.4**	6.0	8.2

stepwise logistic regression and the leave-one-patient-out method for ROC and FROC analysis. As a result, different features can be selected for each classification step; based on the histograms of the selection of features, the most frequently selected features are also shown in Table 1.2.

With the node value only, i.e., the results after the application of Gabor filters and phase portrait analysis, the A_z value obtained was 0.61; sensitivities of 0.8 and 0.9 were obtained at 8.1 and 13.9 FP/patient, respectively. The results indicate that node value alone is not adequate for accurate classification of the ROIs and detection of architectural distortion, and that more features need to be incorporated for proper characterization of architectural distortion.

1.4.2 Statistical significance of differences in ROC analysis

In ROC analysis, the results obtained using all of the features studied are better than those obtained using the individual feature sets. The results of analysis of the statistical significance of the differences between the various ROC and FROC curves obtained are presented in Tables 1.3 and 1.4, respectively. Because the ANN classifier was found to perform well in ROC analysis and the Bayesian classifier performed well in FROC analysis, the results of the ANN classifier and the Bayesian classifier were used for the analysis of the statistical significance of the differences between ROC curves and FROC curves, respectively.

Table 1.3 Analysis of the statistical significance, using the *p*-value, of the differences between the ROC curves obtained using the ANN and the leave-one-patient-out method for the selected features from the various types of feature sets. The *p*-values were estimated using ROCKIT (up to four decimal places). Values representing statistically significant differences are highlighted in bold. (Reproduced, with kind permission from Springer Science+Business Media, from Ref. 26. © 2012 Springer.)

Feature set	H_S	H_T	H_R	All
Node	**0.0000**	**0.0000**	**0.0000**	**0.0000**
H_S		0.2381	0.0825	**0.0003**
H_T			**0.0020**	**0.0291**
H_R				0.1387

Table 1.3 gives measures of the statistical significance of the differences between the ROC curves generated using the ANN classifier and the leave-one-patient-out method for the four sets of selected features as well as the node value. The results obtained using the selected features from all types of entropy measures show statistically highly significant improvement over the results obtained with the node value and Shannon entropy. The ROC performance obtained using a combination of all types of entropy measures is better, with statistical significance, than that obtained with the Tsallis entropy measures.

1.4.3 Reduction of FPs

The FROC curves obtained using the Bayesian classifier with the features selected by stepwise logistic regression are shown in Fig. 1.9 for all of the sets of features listed in Table 1.2. The FROC curves obtained using each set of features and the combination of all features indicate substantial reductions in the number of FPs/patient (above the sensitivity level of 0.7) in the detection of architectural distortion compared to the initial stage of the study, that is, node analysis.

Table 1.4 Analysis of the statistical significance, using the *p*-value, of the differences between the FROC curves obtained using the Bayesian classifier and the leave-one-patient-out method for the selected features with the various feature sets. The *p*-values were estimated using JAFROC. Values representing statistically significant differences are highlighted in bold. (Reproduced, with kind permission from Springer Science+Business Media, from Ref. 26. © 2012 Springer.)

Feature set	H_S	H_T	H_R	All
Node	**0.0193**	**0.0417**	**0.0177**	**0.0128**
H_S		0.0974	**0.0449**	0.1523
H_T			0.2590	0.4014
H_R				0.1581

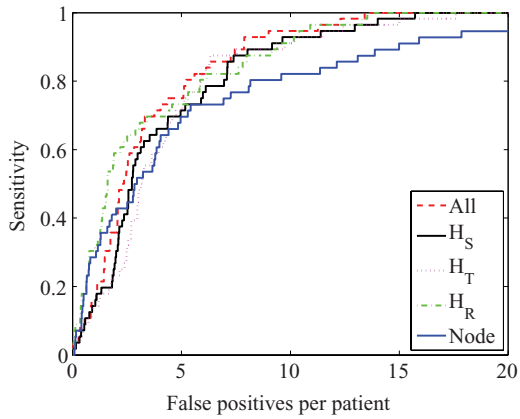

Figure 1.9 FROC curves for the dataset of 106 prior mammograms of interval-cancer cases and 52 normal control mammograms with the selected features from various sets of features using stepwise logistic regression and the Bayesian classifier with the leave-one-patient-out method. (Reproduced, with kind permission from Springer Science+Business Media, from Ref. 26. © 2012 Springer.)

The reduction of FPs in the final result is illustrated in Fig. 1.3(f) for the mammogram shown in part (e) of the same figure. The results obtained using the selected features with stepwise logistic regression and the Bayesian classifier with the leave-one-patient-out method are presented; only the top five ROIs based on the discriminant values of the features of the same image are shown; the other view of the breast is not illustrated. The numbers outside the parentheses represent the ranking based on the discriminant values obtained by the Bayesian classifier, and the numbers within the parentheses represent the earlier ranking based on the node value. From Fig. 1.3(f), it is evident that the use of the selected features has led to a substantial reduction of FPs in the detection of architectural distortion; even if only the top six ROIs per patient (5.2, on the average, to be precise) are considered, the average sensitivity remains above 80% over the entire dataset including the normal control cases.

1.4.4 Statistical significance of the differences in FROC analysis

Table 1.4 illustrates the statistical significance of the differences in FROC results, using the Bayesian classifier and the leave-one-patient-out method, for the four sets of selected features as well as the node value, obtained by comparing the discriminant values using JAFROC.[69,70] The discriminant values obtained for FROC analysis with each of the selected feature sets perform better than the node value with statistical significance. The differences between the FROC curves for the sets of the discriminant values obtained with all types of entropy measures combined and the individual types of

entropy measures are not statistically significant; therefore, any one of the sets of features H_S, H_T, or H_R may be used. However, it is evident from all of the results listed in Table 1.2 that the combination of all types of entropy measures studied in the current work could be used to facilitate efficient detection of architectural distortion in prior mammograms.

1.4.5 Effects of the initial number of ROIs selected

In the present work, the top 30 ROIs obtained from the analysis of the node map for each mammogram have been chosen for further analysis based on experimentation across several datasets (see Banik et al.[13]) for obtaining high and consistent sensitivities. The selection of the top 30 ROIs per image provided a maximum sensitivity of 99% for the dataset used in the present study. If only the top 10 or 20 ROIs were to be selected per image, the maximum sensitivities that can be obtained would be 80% and 98%, respectively, for the dataset under consideration. Table 1.5 illustrates the effects of the number of ROIs selected at the initial stage of the study; the A_z values are presented for the full dataset of interval-cancer cases including normal control cases. It is evident that our strategy of choosing up to 30 ROIs per image and allowing high sensitivity at the initial stage, even at the cost of a high FP rate, is appropriate. The subsequent steps of feature extraction and classification have significantly reduced the FP rate, as expected.

1.5 Discussion

Using all of the 15 features related to the measures of angular spread, the most frequently selected features with stepwise logistic regression and the

Table 1.5 Effects of the number of ROIs selected at the initial stage of the study. The ROC and FROC curves were obtained with the selected features from the set of all features using an ANN and the Bayesian classifier, respectively, with the leave-one-patient-out method. The maximum sensitivity achieved is reported in terms of the 106 images with architectural distortion. (Reproduced, with kind permission from Springer Science+Business Media, from Ref. 26. © 2012 Springer.)

		With node value only		With the selected features	
Initial number of ROIs/image	**Maximum sensitivity achieved**	**A_z value**	**FP/patient at 80% sensitivity**	**A_z value**	**FP/patient at 80% sensitivity**
10	80%	0.52	9.3	0.68	6.0
15	91%	0.55	8.4	0.71	5.4
20	98%	0.56	8.2	0.69	5.9
25	99%	0.59	8.1	0.73	5.7
30	99%	0.61	8.1	0.75	5.2

leave-one-patient-out method were found to be H_R2, H_R3, H_S1, H_T5, and H_S3. This selection represents a combination of all of the three types of entropy measures used, i.e., Shannon's entropy, Tsallis entropy, and Rényi entropy, and four of the five types of angular distributions proposed. The selected features resulted in the A_z value of 0.74 with the ANN classifier; a sensitivity of 0.8 was obtained at 5.2 FP/patient with the Bayesian classifier. The results indicate that the measures of angular spread have a strong capability of characterizing the oriented texture related to architectural distortion.

1.5.1 Comparative analysis with related previous works

In a related work,[28] the node value and the measures for characterization of the angular spread of power were used. For characterization of the angular spread, each ROI was represented by the Shannon entropy of the angular histogram composed with the Gabor magnitude response, angle, coherence, and orientation strength; the entropy of the angular spread of power in the Fourier spectrum was also used. An A_z value of 0.76 was obtained using an ANN based on radial basis functions (RBFs); FROC analysis indicated 82% sensitivity at 7.2 FP/image. Similar studies were conducted separately on the same dataset using Tsallis entropy[30] and Rényi entropy[29] for characterization of the angular spread of power: A_z values of 0.74 and 0.75 were obtained, respectively, using an ANN-RBF. FROC analysis indicated a sensitivity of 0.80 at 7.1 FP/image using the leave-one-image-out method with an ANN classifier for both cases.[29,30]

Characterization and analysis of the angular spread of power in the frequency domain, angular distributions of the magnitude and angle responses of Gabor filters, coherence, and orientation strength could provide important information regarding the spiculating patterns of architectural distortion. Due to the presence of spiculation radiating at several angles, TP ROIs should show a wide angular spread of power, whereas most FP ROIs should show the power limited to a small number of angular bands. The proposed entropy measures for characterization of angular distribution have shown good performance in the detection of architectural distortion.[28–30] The use of the higher-order entropy measures, namely Tsallis and Rényi entropy, along with the conventional Shannon's entropy for characterization of the angular spread has led to a reduction of FPs in the detection of architectural distortion.

In another of our related previous studies,[13] $A_z = 0.77$, and a sensitivity of 0.8 at 5.8 FP/image in FROC analysis were obtained with the same dataset and the application of Gabor filters, linear phase portrait analysis, fractal analysis, analysis of the angular spread of power in the frequency domain, structured pattern analysis using Laws' texture energy measures, and Haralick's texture features. The present work, incorporating a leave-one-patient-out approach, has led to a slightly lower value of $A_z = 0.75$

but improved results in FROC analysis, with a sensitivity of 0.8 at 5.2 FP/patient using a smaller number of features than our previous work. In the present study, the feature extraction step took about 1.2 seconds per image, and feature selection with stepwise logistic regression procedure and classification with the Bayesian (QDA) classifier took about 4 seconds per image on a Dell Precision PWS 490 workstation with Quad Intel® Xeon™ processors operating at 3.0 GHz, with 12 GB of RAM. On the other hand, the corresponding steps took approximately 40 seconds per image and 8 seconds per image, respectively, with the same computer in the previous study.[13] The preceding steps of preprocessing and detection of ROIs took about 6 minutes per image in both studies.

A combination of the several measures of angular spread proposed in the present work with other types of features could provide complementary information regarding oriented and/or spiculating texture patterns. Combining the entropy measures used in the present work with all of the features used in our previous study[13] resulted in an A_z value of 0.78 with statistically highly significant improvement (p-value = 0.0023) and a sensitivity of 0.8 at 5.2 FP/patient with statistically significant improvement (p-value = 0.0481) as compared to the results obtained in the previous study.[13] These results indicate that the features related to the angular spread of power can be used with various other types of features for improved accuracy of detection of architectural distortion.

1.5.2 Comparative analysis with other works

Various CAD techniques have been proposed for the detection of architectural distortion;[2,14,16–22] the results obtained in the present work with prior mammograms of interval-cancer cases, including normal control cases, are comparable, encouraging, and better in some aspects. Karssemeijer and te Brake[17] proposed a multiscale-based method for the detection of stellate distortion including spiculating masses and architectural distortion using the output of three directional, second-order, Gaussian derivative operators with the direction of the filters differing by $\pi/3$ in orientation, and obtained a sensitivity of about 90% at the rate of one FP/image. Matsubara et al.[2,72] used morphological image processing techniques along with a concentration index to detect architectural distortion around the skin line and within the mammary gland; the sensitivity obtained was 94% with 2.3 FP/image, and 84% with 2.4 FP/image, respectively. Guo et al.[20] used five different methods to estimate the fractal dimension (FD) and a support vector machine to differentiate masses and architectural distortion from normal parenchyma; using FD and lacunarity, the best result obtained for architectural distortion in terms of A_z value was 0.875 ± 0.055. Nemoto et al.[16] developed a method to detect architectural distortion with radiating spiculation on 25 digital mammograms and

obtained a sensitivity of 80.0% at 0.80 FP/image. Nakayama et al.[21] proposed a technique for the detection of architectural distortion using multiresolution analysis and obtained a sensitivity of 71.3% at 3.01 FP/image.

All of the works cited above, however, included clearly evident architectural distortion with pronounced radiating spiculation. The automatic detection of architectural distortion in prior mammograms of interval-cancer cases is a more difficult problem due to the subtle and irregular appearance of the associated patterns. The dataset used in the present work includes mammograms containing hard-to-detect patterns of architectural distortion that had been missed by two radiologists reviewing the mammograms at the time of the original screening and interpretation.[13] Detailed comparative analysis is not possible because of the variability of the size and types of the datasets used in the studies cited above. It should be noted that the publicly available databases of mammograms, such as the Digital Database for Screening Mammography (DDSM)[73] and the Mammographic Image Analysis Society (MIAS) database,[74] do not contain prior mammograms.

Baker et al.[9] studied the performance of two commercial CAD systems in the detection of architectural distortion; less than 50% of the 45 cases of architectural distortion were detected, with a lower image-based sensitivity of 38% (30 out of 80 images), at 0.7 FP/image. Burhenne et al.[75] evaluated the performance of a commercially available CAD system for mammography and reported a sensitivity of 75% in the detection of masses and architectural distortion at one FP/image. Birdwell et al.[76] studied the performance of a commercial CAD system used for marking the signs of cancer that were overlooked or missed by radiologists; the system was able to detect five out of six cases of architectural distortion, and 77% of the previously missed lesions, at 2.9 FP/image. Contrary to the state of the art in the detection of masses and calcifications, the results obtained in the present work indicate that the methods presented are not applicable for clinical use at the current stage; nonetheless, the present study on the detection of architectural distortion in prior mammograms of interval-cancer cases provided encouraging results that are better than those reported in studies on the detection of architectural distortion with commercially available CAD systems.[9,75,76]

1.5.3 Limitations

Selecting the appropriate orders for Tsallis entropy and Rényi entropy is challenging; in the present study, the orders were selected based on experimentation with ROC analysis. Selection of the appropriate range of frequencies for characterization of angular spread in the frequency domain is critical and could affect the results; care should be exercised in the selection of the proper frequency range.

One of the limitations of the present work is that uncertainty measures related to the FROC curves, the number of FPs reported at a given sensitivity, and the A_z values reported have not been derived. The confidence bounds of ROC and FROC curves can be obtained through resampling methods including the bootstrap, jackknife, and permutation tests.[77] ROCKIT and JAFROC can also be used to provide confidence bounds for the ROC and FROC curves, respectively.

1.6 Conclusion

The detection of architectural distortion in prior mammograms is an important yet difficult problem. The approach of simultaneous analysis of current and prior mammograms, as recommended for use by radiologists in the screening and diagnosis of breast cancer, could be used to enhance the performance of CAD systems. Limitations exist in the present work in terms of the types or patterns of architectural distortion detected by the constrained models used. Regardless, the results are promising and indicate that the proposed methods can detect architectural distortion in prior mammograms taken 15 months (on average) before clinical diagnosis of breast cancer, with a sensitivity of 0.8 at 5.2 FP/patient. The results are difficult to compare with those provided by the existing CAD systems and techniques because of their dependence on the specific database used and the unavailability of public databases with prior mammograms. The development of additional features related to the subtle patterns of architectural distortion is in progress.

The results obtained in the present work with prior mammograms of interval-cancer cases including a number of normal control cases are important and encouraging, and indicate that the proposed methods have the potential to achieve early detection of subtle signs of breast cancer in mammograms, specifically, architectural distortion.

Acknowledgments

This work was supported by the Collaborative Research and Training Experience Programme (CREATE) and the Natural Sciences and Engineering Research Council (NSERC) of Canada.

References

1. A. M. Knutzen and J. J. Gisvold, “Likelihood of malignant disease for various categories of mammographically detected, nonpalpable breast lesions,” *Mayo Clinic Proc.* **68**, 454–460 (1993).
2. T. Matsubara, T. Ichikawa, T. Hara, H. Fujita, S. Kasai, T. Endo, and T. Iwase, “Novel method for detecting mammographic architectural

distortion based on concentration of mammary gland, *Proc. of the 18th International Congress and Exhibition on Computer Assisted Radiology and Surgery (CARS2004) International Congress Series* **1268**, 867–871, Elsevier B.V. (2004).

3. B. C. Yankaskas, M. J. Schell, R. E. Bird, and D. A. Desrochers, "Reassessment of breast cancers missed during routine screening mammography: A community based study, *Am. J. Roentgenol.* **177**, 535–541 (2001).
4. H. Burrell, A. Evans, A. Wilson, and S. Pinder, "False-negative breast screening assessment: What lessons we can learn? *Clinical Radiol.* **56**, 385–388 (2001).
5. M. A. Schneider, "Better detection: Improving our chances," M. J. Yaffe, Ed., *Digital Mammography: 5th International Workshop on Digital Mammography*, Toronto, ON, Canada, Medical Physics Publishing, Madison, WI, pp. 3–6 (2001).
6. J. Tang, R. M. Rangayyan, J. Xu, I. E. Naqa, and Y. Yang, "Computer-aided detection and diagnosis of breast cancer with mammography: Recent advances," *IEEE Trans. Inf. Technol. Biomed.* **13**(2), 236–251 (2009).
7. K. Doi, "Diagnostic imaging over the last 50 years: Research and development in medical imaging science and technology," *Phys. Med. Biol.* **51**, R5–R27 (2006).
8. K. Doi, "Computer-aided diagnosis in medical imaging: Historical review, current status and future potential," *Comput. Med. Imaging Graph*. **31**, 198–211 (2007).
9. J. A. Baker, E. L. Rosen, J. Y. Lo, E. I. Gimenez, R. Walsh, and M. S. Soo, " Computer-aided detection (CAD) in screening mammography: Sensitivity of commercial CAD systems for detecting architectural distortion," *Am. J. Roentgenol.* **181**, 1083–1088 (2003).
10. J. A. A. M. van Dijck, A. L. M. Verbeek, J. H. C. L. Hendriks, and R. Holland, "The current detectability of breast cancer in a mammographic screening program," *Cancer* **72**(6), 1933–1938 (1993).
11. M. Sameti, R. K. Ward, J. Morgan-Parkes, and B. Palcic, "Image feature extraction in the last screening mammograms prior to detection of breast cancer," *IEEE J. Sel. Topics Signal Process.* **3**(1), 46–52 (2009).
12. R. M. Rangayyan, S. Banik, and J. E. L. Desautels "Computer-aided detection of architectural distortion in prior mammograms of interval cancer," *J. Digital Imaging* **23**(5), 611–631 (2010).
13. S. Banik, R. M. Rangayyan, and J. E. L. Desautels, "Detection of architectural distortion in prior mammograms," *IEEE Trans. Med. Imaging* **30**(2), 279–294 (2011).

14. R. M. Rangayyan, S. Prajna, F. J. Ayres, and J. E. L. Desautels, "Detection of architectural distortion in mammograms acquired prior to the detection of breast cancer using Gabor filters, phase portraits, fractal dimension, and texture analysis," *Int. J. Comput. Assist. Radiol. Surg.* **2**(6), 347–361 (2008).
15. M. J. M. Broeders, N. C. Onland-Moret, H. J. T. M. Rijken, J. H. C. L. Hendriks, A. L. M. Verbeek, and R. Holland, "Use of previous screening mammograms to identify features indicating cases that would have a possible gain in prognosis following earlier detection," *Eur. J. Cancer* **39**, 1770–1775 (2003).
16. M. Nemoto, S. Honmura, A. Shimizu, D. Furukawa, H. Kobatake, and S. Nawano, "A pilot study of architectural distortion detection in mammograms based on characteristics of line shadows," *Inter. J. Comp. Assist. Radiol. Surg.* **4**(1), 27–36 (2009).
17. N. Karssemeijer and G. M. te Brake, "Detection of stellate distortions in mammograms," *IEEE Trans. Med. Imaging* **15**(5), 611–619 (1996).
18. G. D. Tourassi, D. M. Delong, and C. E. Floyd, Jr., "A study on the computerized fractal analysis of architectural distortion in screening mammograms," *Phys. Med. Biol.* **51**(5), 1299–1312 (2006).
19. M. P. Sampat, M. K. Markey, and A. C. Bovik, "Measurement and detection of speculated lesions," *IEEE Southwest Symposium on Image Analysis and Interpretation*, IEEE Computer Society, pp. 105–109, (2006).
20. Q. Guo, J. Shao, and V. F. Ruiz, "Characterization and classification of tumor lesions using computerized fractal-based texture analysis and support vector machines in digital mammograms," *Inter. J. Comp. Assist. Radiol. Surg.* **4**(1), 11–25 (2009).
21. R. Nakayama, R. Watanabe, T. Kawamura, T. Takada, K. Yamamoto, and K. Takeda, "Computer-aided diagnosis scheme for detection of architectural distortion on mammograms using multiresolution analysis," *Proceedings of the 22nd International Congress and Exhibitionon Computer Assisted Radiology and Surgery (CARS 2008)* **3**(1), S418–S419, Barcelona, Spain (2008).
22. F. J. Ayres and R. M. Rangayyan, "Reduction of false positives in the detection of architectural distortion in mammograms by using a geometrically constrained phase portrait model," *Int. J. Comp. Assist. Radiol. Surg.* **1**, 361–369 (2007).
23. J. H. Sumkin, B. L. Holbert, J. S. Herrmann, C. A. Hakim, M. A. Ganott, W. R. Poller, R. Shah, L. A. Hardesty, and D. Gur, "Optimal reference

mammography: A comparison of mammograms obtained one and two years before the present examination," *Am. J. Roentgenol.* **180**, 343–346 (2003).

24. C. Varela, N. Karssemeijer, J. H. C. L. Hendriks, and R. Holland, "Use of prior mammograms in the classification of benign and malignant masses," *Eur. J. Radiol.* **56**, 248–255 (2005).
25. A. S. Majid, E. S. de Paredes, R. D. Doherty, N. R. Sharma, and X. Salvador, "Missed breast carcinoma: Pitfalls and pearls," *Radiographics* **23**, 881–895 (2003).
26. S. Banik, R. M. Rangayyan, and J. E. L. Desautels, "Measures of angular spread and entropy for the detection of architectural distortion in prior mammograms, " *Inter. J. Comp. Assist. Radiol. Surg.* **8**(1), 121–134 (2013).
27. American College of Radiology (ACR), *Illustrated Breast Imaging Reporting and Data System (BI-RADS®)*, 3rd edition, American College of Radiology, Reston, VA (1998).
28. R. M. Rangayyan, S. Banik, and J. E. L. Desautels, "Detection of architectural distortion in prior mammograms using measures of angular distribution," *Proc. SPIE* **7963**, 796308:1–9 (2011) [doi: 10.1117/12.877587].
29. S. Banik, R. M. Rangayyan, and J. E. L. Desautels, "Rényi entropy of angular spread for detection of architectural distortion in prior mammograms," *Proc. of the 2011 IEEE International Symposium on Medical Measurements and Applications (MeMeA)*, pp. 609–612, Bari, Italy (2011).
30. S. Banik, R. M. Rangayyan, and J. E. L. Desautels, "Detection of architectural distortion in prior mammograms of interval cancer using measures of angular spread and Tsallis entropy," *Proc. of the 25th International Congress and Exhibition: Computer Assisted Radiology and Surgery* **6**, pp. S188–S189, Berlin, Germany (2011).
31. H. Alto, R. M. Rangayyan, R. B. Paranjape, J. E. L. Desautels, and H. Bryant, "An indexed atlas of digital mammograms for computer-aided diagnosis of breast cancer," *Annales des Télécommunications* **58**(5–6), 820–835 (2003).
32. Alberta Cancer Board, www.cancerboard.ab.ca/screentest, Alberta, Canada. *Screen Test: Alberta Program for the Early Detection of Breast Cancer – 2001/03 Biennial Report* (2004).
33. D. Gabor, "Theory of communication," *J. Inst. Electric. Eng.* **93**, 429–457 (1946).
34. R. M. Rangayyan and F. J. Ayres, "Gabor filters and phase portraits for the detection of architectural distortion in mammograms," *Med. Biol. Engin. Computing* **44**, 883–894 (2006).

35. F. J. Ayres and R. M. Rangayyan, "Design and performance analysis of oriented feature detectors," *J. Electron. Imaging* **16**(2), 023007 (2007) [doi: 10.1117/1.2728751].
36. R. M. Rangayyan, *Biomedical Image Analysis*, CRC Press, Boca Raton, FL (2005).
37. C. K. Chui, *An Introduction to Wavelets*, Vol. 1 of *Wavelet Analysis and its Applications*, Academic Press, San Diego (1992).
38. B. S. Manjunath and W. Y. Ma, "Texture features for browsing and retrieval of image data," *IEEE Trans. Pattern Anal. Mach. Intell.* **18**(8), 837–842 (1996).
39. A. R. Rao, *A Taxonomy for Texture Description and Identification*, Springer-Verlag, New York (1990).
40. A. R. Rao and R. C. Jain, "Computerized flow field analysis: Oriented texture fields," *IEEE Trans. Pattern Anal. Mach. Intell.* **14**(7), 693–709 (1992).
41. C. R. Wylie and L. C. Barrett, *Advanced Engineering Mathematics*, 6th edition, McGraw-Hill, New York (1995).
42. F. J. Ayres and R. M. Rangayyan, "Characterization of architectural distortion in mammograms," *IEEE Eng. Med. Biol. Mag.* **24**(1), 59–67 (2005).
43. H. H. Barrett and K. J. Myers, *Foundations of Image Science*, Wiley, Hoboken, NJ (2004).
44. P. Campisi and G. Scarano, "A multiresolution approach for texture synthesis using the circular harmonic functions," *IEEE Trans. Image Process.* **11**(1), 37–51(2002).
45. N. R. Mudigonda, R. M. Rangayyan, and J. E. L. Desautels, "Detection of breast masses in mammograms by density slicing and texture flow-field analysis," *IEEE Trans. Med. Imaging* **20**(12), 1215–1227 (2001).
46. R. M. Haralick, K. Shanmugam, and I. Dinstein, "Textural features for image classification," *IEEE Trans. Systems Man. Cybern.* **3**(6), 610–622 (1973).
47. C. E. Shannon, "A mathematical theory of communication," *Bell System Tech. J.* **27**, 379–423, 623–656 (1948).
48. A. Rényi, "On measures of entropy and information," *Proc. of the 4th Berkeley Symposium on Mathematics*, *Statistics and Probability* **1**, 547–561, Berkeley, CA, University of California Press (1961).
49. D. Zhang, X. Jia, H. Ding, D. Ye, and N. V. Thakor, "Application of Tsallis entropy to EEG: Quantifying the presence of burst suppression after asphyxial cardiac arrest in rats," *IEEE Trans. Biomed. Eng.* **57**(4), 867–874 (2010).

50. M. Masi, "A step beyond Tsallis and Rényi entropies," *Phys. Lett. A* **338**(3–5), 217–224 (2005).

51. C. Tsallis, "Possible generalization of Boltzmann-Gibbs statistics," *J. Statist. Phys.* **52**(1), 479–487 (1988).

52. R. S. Johal and U. Tirnakli, "Tsallis versus Renyi entropic form for systems with q-exponential behaviour: The case of dissipative maps," *Physica A* **331**(3–4), 487–496 (2004).

53. P. S. Rodrigues, G. A. Giraldi, R.-F. Chang, and J. S. Suri, "Non-extensive entropy for CAD systems of breast cancer images," *19th Brazilian Symposium on Computer Graphics and Image Processing*, pp. 121–128 (2006).

54. P. S. Rodrigues and G. A. Giraldi, "Computing the q-index for Tsallis nonextensive image segmentation," *Brazilian Symposium on Computer Graphics and Image Processing*, pp. 232–237 (2009).

55. C. Tsallis, "Nonextensive statistics: Theoretical, experimental and computational evidences and connections," *Brazil. J. Phys.* **29**(1), 1–35 (1999).

56. J. Mohanalin, P. K. Kalra, and N. Kumar, "Extraction of micro calcification using non extensive property of mammograms," *Proc. of the 2009 IEEE International Advance Computing Conference (IACC 2009)*, pp. 636–641, Patiala, India (2009).

57. T. Maszczyk and W. Duch, "Comparison of Shannon, Renyi and Tsallis entropy used in decision trees," *Proc. of the 9th International Conference on Artificial Intelligence and Soft Computing*, ICAISC '08, Springer-Verlag, Berlin, Heidelberg, pp. 643–651 (2008).

58. W. Kinsner, "A unified approach to fractal dimensions," *Proc. of the Fourth IEEE International Conference on Cognitive Informatics (ICCI)*, pp. 58–72, Irvine, CA, IEEE Computer Society (2005).

59. S. Gabarda and G. Cristóbal, "Discrimination of isotrigon textures using the Rényi entropy of Allan variances," *J. Optic. Soc. Am. A* **25**(9), 2309–2319 (2008).

60. Y. Li, X. Fan, and G. Li, "Image segmentation based on Tsallis-entropy and Renyi-entropy and their comparison," *IEEE International Conference on Industrial Informatics*, pp. 943–948, Singapore (2006).

61. P. Sahoo, C. Wilkins, and J. Yeager, "Threshold selection using Renyi's entropy," *Pattern Recog.* **30**(1), 71–84 (1997).

62. L. Wang, "Feature selection with kernel class separability," *IEEE Trans. Pattern Anal. Mach. Intell.* **30**(9), 1534–1546 (2008).

63. K. Fukunaga, *Introduction to Statistical Pattern Recognition*, 2nd edition, Academic Press Professional, Inc., San Diego (1990).

64. F. L. Ramsey and D. W. Schafer, *The Statistical Sleuth: A Course in Methods of Data Analysis*, Duxbury Press, Belmont, CA (1997).
65. R. O. Duda, P. E. Hart, and D. G. Stork, *Pattern Classification*, 2nd edition, Wiley-Interscience, New York (2001).
66. R. Schalkoff, *Pattern Recognition: Statistical*, *Structural and Neural Approaches*, Wiley, New York (1992).
67. S. Haykin, *Neural Networks: A Comprehensive Foundation*, 2nd edition, Prentice Hall, Englewood Cliffs, NJ (1999).
68. ROCKIT, Kurt Rossmann Laboratories for Radiologic Image Research, ROC Software, http://www-radiology.uchicago.edu/krl/roc_soft6.htm, accessed on March 15, 2012.
69. D. P. Chakraborty, "Statistical power in observer-performance studies: Comparison of the receiver operating characteristic and free-response methods in tasks involving localization," *Acad. Radiol.* **9**(2), 147–156 (2002).
70. D. P. Chakraborty, "Validation and statistical power comparison of methods for analyzing free response observer performance studies," *Acad. Radiol.* **15**(12), 1554–1566 (2008).
71. D. P. Chakraborty, "Analysis of location specific observer performance data: Validated extensions of the jackknife free-response (JAFROC) method," *Acad. Radiol.* **13**(10), 1187–1193 (2006).
72. T. Matsubara, T. Ichikawa, T. Hara, H. Fujita, S. Kasai, T. Endo, and T. Iwase, "Automated detection methods for architectural distortions around skinline and within mammary gland on mammograms," H. U. Lemke, M. W. Vannier, K. Inamura, A. G. Farman, K. Doi, and J. H. C. Reiber, Eds., *International Congress Series: Proceedings of the 17th International Congress and Exhibition on Computer Assisted Radiology and Surgery*, pp. 950–955, London, UK, Elsevier (2003).
73. M. Heath, K. Bowyer, D. Kopans, R. Moore, and W. P. Kegelmeyer, "The Digital Database for Screening Mammography," M. J. Yaffe, Ed., *Proc. of the Fifth International Workshop on Digital Mammography*, Medical Physics Publishing, Madison, WI, pp. 212–218 (2001).
74. J. Suckling, J. Parker, D. R. Dance, S. Astley, I. Hutt, C. R. M. Boggis, I. Ricketts, E. Stamakis, N. Cerneaz, S.-L. Kok, P. Taylor, D. Betal, and J. Savage, "The Mammographic Image Analysis Society Digital Mammogram Database," A. G. Gale, S. M. Astley, D. D. Dance, and A. Y. Cairns, Eds., *Digital Mammography: Proceedings of the 2nd International Workshop on Digital Mammography*, pp. 375–378, York, UK, Elsevier (1994).
75. L. J. W. Burhenne, S. A. Wood, C. J. D'Orsi, S. A. Feig, D. B. Kopans, K. F. O'Shaughnessy, E. A. Sickles, L. Tabar, C. J. Vyborny, and

R. A. Castellino, "Potential contribution of computer-aided detection to the sensitivity of screening mammography," *Radiol.* **215**(2), 554–562 (2000).

76. R. L. Birdwell, D. M. Ikeda, K. F. O'Shaughnessy, and E. A. Sickles, "Mammographic characteristics of 115 missed cancers later detected with screening mammography and the potential utility of computer-aided detection," *Radiol.* **219**(1), 192–202 (2001).
77. F. W. Samuelson, N. Petrick, and S. Paquerault, "Advantages and examples of resampling for CAD evaluation," *4th IEEE International Symposium on Biomedical Imaging: From Nano to Macro (ISBI 2007)*, pp. 492–495, Arlington, VA (2007).

Rangaraj M. Rangayyan is a Professor with the Department of Electrical and Computer Engineering, and an Adjunct Professor of Surgery and Radiology, at the University of Calgary, Calgary, Alberta, Canada. He received the Bachelor of Engineering degree in Electronics and Communication in 1976 from the University of Mysore at the People's Education Society College of Engineering, Mandya, Karnataka, India, and the Ph.D. degree in Electrical Engineering from the Indian Institute of Science, Bangalore, Karnataka, India, in 1980. His research interests are in the areas of digital signal and image processing, biomedical signal analysis, biomedical image analysis, and computer-aided diagnosis. He has published more than 140 papers in journals and 240 papers in proceedings of conferences. His research productivity was recognized with the 1997 and 2001 Research Excellence Awards of the Department of Electrical and Computer Engineering, the 1997 Research Award of the Faculty of Engineering, and by appointment as a "University Professor" in 2003 at the University of Calgary. He is the author of two textbooks: *Biomedical Signal Analysis* (IEEE/Wiley, 2002) and *Biomedical Image Analysis* (CRC, 2005); he has coauthored and coedited several other books. He was recognized by the IEEE with the award of the Third Millennium Medal in 2000, and was elected as a Fellow of the IEEE in 2001, Fellow of the Engineering Institute of Canada in 2002, Fellow of the American Institute for Medical and Biological Engineering in 2003, Fellow of SPIE in 2003, Fellow of the Society for Imaging Informatics in Medicine in 2007, Fellow of the Canadian Medical and Biological Engineering Society in 2007, and Fellow of the Canadian Academy of Engineering in 2009. He has been awarded the Killam Resident Fellowship thrice (1998, 2002, and 2007) in support of his book-writing projects.

Shantanu Banik received his Ph.D. degree in 2011 and M.Sc. degree in 2008 from the Department of Electrical and Computer Engineering, University of Calgary, Calgary, Alberta, Canada, and his B.Sc. degree in 2005 in Electrical and Electronic Engineering from the Bangladesh University of Engineering and Technology (BUET), Dhaka, Bangladesh. His research interests include medical signal and image processing and analysis, development of computer-aided diagnosis techniques for the detection of cancer, landmarking and segmentation of medical images, pattern recognition and classification, radiology, medical imaging, and automatic segmentation and analysis of tumors. He has coauthored several journal papers, a number of conference papers, several book chapters, and a book titled *Landmarking and Segmentation of 3D CT Images* (Morgan & Claypool, 2009).

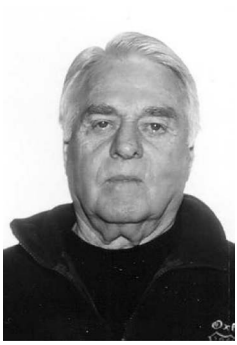

J. E. Leo Desautels obtained his M.D. from the University of Ottawa in 1955 and completed post-graduate training in radiology at the Henry Ford Hospital, Detroit, MI. He was a Staff Radiologist at the Foothills Hospital and a Clinical Professor with the Faculty of Medicine, the University of Calgary, Calgary, AB, Canada, from 1970 to 1994. He served as a Reference Radiologist to the Alberta Program for the Early Detection of Breast Cancer until 2007. He is an Adjunct Professor of Electrical and Computer Engineering at the University of Calgary. He is interested in computer applications in mammography.

Chapter 2
Texture-based Automated Detection of Breast Cancer Using Digitized Mammograms: A Comparative Study

U. Rajendra Acharya
Department of Electronics and Computer Engineering, Ngee Ann Polytechnic, Singapore and Department of Biomedical Engineering, University of Malaya, Malaysia

E. Y. K. Ng
School of Mechanical and Aerospace Engineering, College of Engineering, Nanyang Technological University, Singapore

Jen-Hong Tan
Department of Electronics and Computer Engineering, Ngee Ann Polytechnic, Singapore

S. Vinitha Sree
Global Biomedical Technologies, Roseville, California, USA

Jasjit S. Suri
Fellow AIMBE, Global Biomedical Technologies, Roseville, California, USA and Affiliated Research Professor, Biomedical Engineering Department, Idaho State University (Aff.), Idaho, USA

2.1 Introduction

Breast cancer is the second leading cause of cancer death in women today. It was estimated that 207,090 women would be diagnosed with cancer and 39,480 women would die of breast cancer in 2010 in the United States.[1] For better survival odds and less use of the treatments and therapies and, therefore, fewer side-effects, many imaging systems are continually being developed to diagnose this disease as early as possible. Even though breast self-examinations (BSEs) and clinical breast examinations (CBEs) are affordable options to women, there is a lack of education regarding these methods, and these methods are not capable of detecting the cancer at its earliest stages.

Mammography, which is the most popular technique for breast cancer detection, uses low-dose x-ray, high-contrast, high-resolution detectors, and an x-ray system designed specifically for imaging the breasts. Mammography has found its application in both screening and diagnosis of breast cancer. In the case of screen-film mammography (SFM), the end-recording device is a film screen. Full-field digital mammography (FFDM), on the other hand, uses digital detectors as the recording media. The digital images provided by FFDM offer many advantages over their film counterpart. In FFDM, image enhancement to accentuate pathology is possible (postprocessing) and, because of the acquisition of digital images, CAD software can be used to highlight and detect suspicious areas in the mammograms. In the Digital Mammographic Imaging Screening Trial (DMIST),[2] 49,528 asymptomatic women were evaluated by both SFM and FFDM. Results reported a significantly better detection by FFDM in women of age 50 or younger, premenopausal women, or women with dense breasts.[3] This better detection can be attributed to the improved contrast resolution of digital mammography. An update on digital mammography techniques can be found in Ref. 4. In spite of the use of ionizing radiation that may be potentially harmful on repeated use and its lower sensitivity in

detecting cancers in dense breasts, mammography is still the most recommended examination for breast cancer screening and detection.[5,6] Studies show that mammography can be used for early detection and treatment of breast lesions.[7–9] However, interpretation of mammograms is a subjective process; hence, interobserver variability is common. Therefore, CAD tools are being developed and studied in order to assist radiologists in relatively better objective interpretation of mammograms.

CAD systems combine a variety of techniques from the fields of artificial intelligence and digital image processing along with the domain knowledge from the medical experts to support cancer detection. CAD software helps radiologists better detect masses and microcalcifications in mammograms. Microcalcifications have small size (0.1–1 mm), low contrast, and various shapes and sizes, and are quite similar to the surrounding tissues. Masses are quite subtle, often occur in dense areas of the breast, and have smoother boundaries than microcalcifications, various shapes (circumscribed, speculated, lobulated, or ill-defined), and similar density to that of normal tissue. Detection and classification of microcalcifications and masses using CAD tools can improve the accuracy of mammography and also reduce the subjectivity associated with the manual interpretation process. In CAD software, the mammograms are first enhanced using standard image-enhancement methods mainly to sharpen the boundaries of the ROI and to increase the contrast between the ROI and the nearby normal tissue. The ROIs are then segmented through common statistical, region-based, or morphological approaches, and significant features are extracted for subsequent clustering or classification. Reviews on CAD tools and techniques for microcalcification and mass detection can be found in Refs. 10–12.

In 2009, Sadaf et al.[13] studied the performance of FFDM augmented with CAD tools. The study showed that CAD combined with mammography presented 100% sensitivity in identifying cancers manifesting as microcalcifications only, and 86% sensitivity for other mammographic appearances of cancer. In another recent study by Karssemeijer et al.,[14] FFDM using CAD was compared with SFM in a population-based breast cancer screening program. They found that the detection rate with FFDM-CAD was as good as that with SFM, with FFDM-CAD providing better detection of ductal carcinoma *in situ* and microcalcification clusters. They also found that the recall rate of FFDM-CAD was higher. Thus, CAD in mammography shows great promise in being used as an adjunct tool for early breast cancer detection.

In the proposed work, we extracted seven texture parameters from the mammogram images and fed them into six classifiers, namely, support

vector machine (SVM), Gaussian mixture model (GMM), fuzzy, *k*-nearest neighbor (*k*-NN), probabilistic neural network (PNN), and decision tree (DeTr). To compare the performance of these classifiers, we used the area-under-the-ROC curves (AUC), sensitivity, specificity, accuracy, and positive predictive value as measures. The layout of the chapter is as follows: Section 2.2 presents the details about the studied mammogram images and the preprocessing steps followed. The feature extraction techniques used are described in Section 2.3. Section 2.4 describes the classifiers used. Section 2.5 presents the results obtained in this work. A review of relevant literature on the use of texture features in CAD tools for mammography and a discussion on the obtained results are given in Section 2.6. Finally, the chapter concludes in Section 2.7.

2.2 Data Acquisition and Preprocessing

300 mammograms from the Digital Database for Screening Mammography (DDSM)[15,16] were used for evaluating the proposed CAD-based system. The DDSM database contains approximately 2620 mammogram images of normal, benign, and malignant classes in 43 volumes. Four medical institutions from the U.S. contributed to the DDSM database: Massachusetts General Hospital (MGH), Wake Forest University School of Medicine (WFUSM), Sacred Heart Hospital (SHH), and Washington University in St. Louis (WU). Along with the digitized mammograms, the DDSM contains "boundary" files of the abnormalities. The outlines (thumbnails) of the abnormalities as indicated by a radiologist are stored in "chain code" in these files. Using this chain code, borders of the abnormalities can be reconstructed. In this work, we have used 100 normal and 100 malignant images from MGH and 100 benign images from SHH. The original image file is very large because the films were manually scanned with a resolution between 42 and 100 μm. These images were cropped to leave out any dark space and to extract only the breast area, then resized to 300×100 pixels. Since the aspect ratio (ratio of the width to the height of the image) of the resized image was kept the same as that of the original image, the quality of the resized image is comparable to that of the original image. After resizing every image, we extracted the texture features of all of the images of three classes on a different scale (multiplying by a fraction). Hence, there is no effect on the texture feature extraction,[17,18] and thus, no bearing on the classification efficiency. The resized grayscale images were subjected to histogram equalization in order to improve image contrast. Sample mammograms taken from normal, benign, and cancerous breasts are depicted in Fig. 2.1.

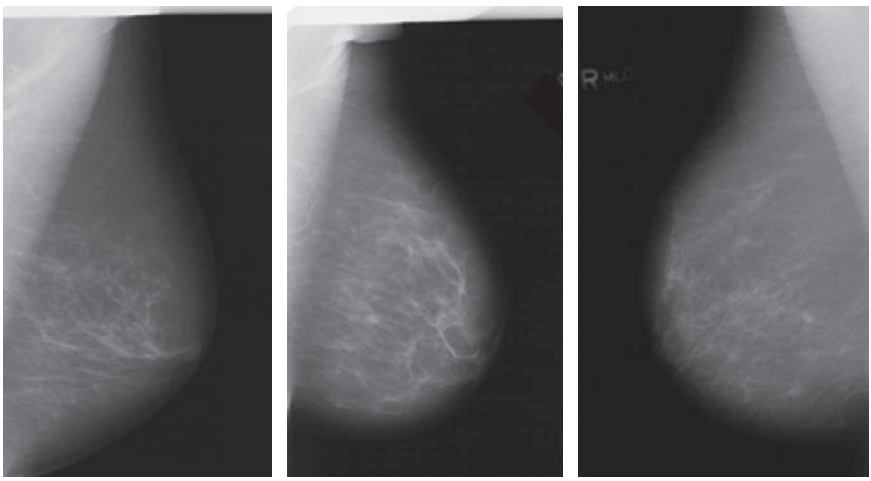

(a) (b) (c)

Figure 2.1 Sample mammograms: (a) normal, (b) benign, and (c) cancerous.

2.3 Feature Extraction

Feature extraction is one of the most important steps in an automated CAD system. In this step, relevant representative features that describe the image are extracted from the preprocessed image. Texture features were extracted in this work. Texture features measure the smoothness, coarseness, and regularity of pixels in an image. These features describe a mutual relationship among intensity values of neighboring pixels repeated over an area larger than the size of the relationship.[17,19] There are two common approaches to texture analysis: statistical analysis and structural analysis. In the statistical approach, scalar measurements of the textures are obtained. This approach characterizes the textures as smooth, coarse, grainy, etc. These methods are based on the distribution and relationships between intensity values of pixels. Measures include entropy, contrast, and correlation based on the gray-level co-occurrence matrix (GLCM). Structural texture analysis is complex compared to the statistical approach.[17] It presents detailed symbolic descriptions of the image. Parameters that are extracted using the statistical approach are more suitable for image analysis than are those obtained using the structural method.[20] In this section, the statistical parameters extracted from the mammograms are briefly described.

2.3.1 Gray-level co-occurrence matrix

Texture characteristics were computed from the GLCM. Our image has 256 discrete gray levels. Hence, we define the spatial gray-level

dependency matrix $P(i, j)$ of size 256×256 for each i and j. It is given by

$$\text{spatial gray-level dependency matrix} = \begin{pmatrix} p_{00} & p_{01} & \cdot & \cdot & p_{0,N-1} \\ p_{10} & p_{11} & \cdot & \cdot & p_{1,N-1} \\ \cdot & \cdot & \cdot & \cdot & \cdot \\ \cdot & \cdot & \cdot & \cdot & \cdot \\ p_{N-1,0} & p_{N-1,1} & \cdot & \cdot & p_{N-1,N-1} \end{pmatrix}, \tag{2.1}$$

where $P_{i,j} = \dfrac{\text{number of pixel pairs with intensity } (i, j)}{\text{total number of pairs considered}}$.

The term p_{ij} is defined as the relative number of times the gray-level pair (i, j) occurs when pixels are separated by the distance $(i, j) = (1, 0)$ (Fig. 2.2). Then, each element is normalized by dividing by the total number of occurrences resulting in the co-occurrence matrix P.

The GLCM of an $m \times n$ image can also be defined[18] by

$$C_d(i, j) = |\{(p, q), (p + \Delta x, q + \Delta y): I(p, q) = i, I(p + \Delta x, q + \Delta y) = j\}|, \tag{2.2}$$

where $(p, q), (p + \Delta x, q + \Delta y) \in M \times N$, $d = (\Delta x, \Delta y)$, and $|\cdot|$ denotes the cardinality of a set. The probability of a pixel with a gray-level value i having a pixel with a gray-level value j at a $(\Delta x, \Delta y)$ distance away in an image is

$$P_d(i, j) = \frac{C_d(i, j)}{\sum_i \sum_j C_d(i, j)}. \tag{2.3}$$

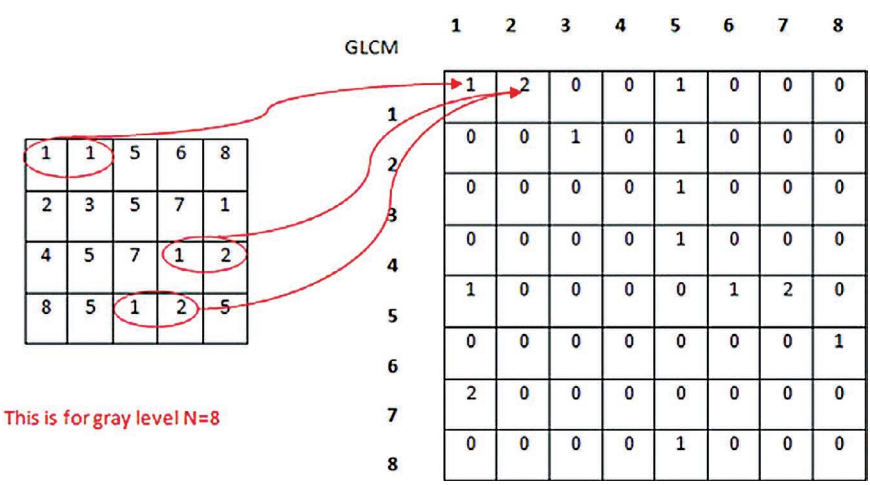

Figure 2.2 Calculation of the GLCM for eight discrete gray levels ($N = 8$).

Based on Eq. (2.3) we obtain the following features:

Energy: $$E = \sum_i \sum_j [P_d(i, j)]^2 \tag{2.4}$$

Contrast: $$Co = \sum_i \sum_j (i - j)^2 P_d(i, j) \tag{2.5}$$

Homogeneity: $$H = \sum_i \sum_j \frac{P_d(i, j)}{1 + (i - j)^2} \tag{2.6}$$

Entropy: $$En = -\sum_i \sum_j P_d(i, j) \cdot \ln P_d(i, j) \tag{2.7}$$

Moments m_1, m_2, m_3 and m_4: $m_g = \sum_i \sum_j (i - j)^g P_d(i, j)$ (2.8)

The similarity between two pixels that are (Δx, Δy) apart is measured by the homogeneity feature. On the contrary, the local variation between those two pixels is captured by the contrast feature. The denseness and the degree of disorder in an image are measured by energy and entropy features. The entropy feature has a maximum value when all elements of the co-occurrence matrix are the same.

Difference statistics is defined as "the distribution of the probability that the gray-level difference is k between the points separated by δ in an image."[21] The difference statistics vector, being a subset of the co-occurrence matrix, can be obtained from GLCM as[21]

$$P_\delta(k) = \sum_i \sum_{\substack{j \\ |i-j|=k}} P_d(i, j), \tag{2.9}$$

where $k = 0, 1, \ldots, n - 1$, n is the number of the grayscale level,[22] and δ is $d = (\Delta x, \Delta y)$. Based on the acquired vector, we obtain the following properties:[23]

Angular second moment: $$\sum_{k=0}^{n-1} P_\delta(k)^2 \tag{2.10}$$

Mean: $$\sum_{k=0}^{n-1} k P_\delta(k) \tag{2.11}$$

2.3.2 Run length matrix

The run length matrix $P_\theta(i,j)$ consists of the number of elements where the gray-level value i has a run length j continuous in the direction θ.[24] Often the direction θ is set as 0, 45, 90, and 135 deg,[25] and the features listed below are calculated for analysis and classification:

$$\text{Short-run emphasis: } \sum_i \sum_j \frac{P_\theta(i,j)}{j^2} \Big/ \sum_i \sum_j P_\theta(i,j) \tag{2.12}$$

$$\text{Long-run emphasis: } \sum_i \sum_j j^2 P_\theta(i,j) \Big/ \sum_i \sum_j P_\theta(i,j) \tag{2.13}$$

$$\text{Gray-level nonuniformity: } \sum_i \left\{ \sum_j P_\theta(i,j) \right\}^2 \Big/ \sum_i \sum_j P_\theta(i,j) \tag{2.14}$$

$$\text{Run-length nonuniformity: } \sum_j \left\{ \sum_i P_\theta(i,j) \right\}^2 \Big/ \sum_i \sum_j P_\theta(i,j) \tag{2.15}$$

$$\text{Run percentage: } \sum_i \sum_j P_\theta(i,j) \Big/ A, \tag{2.16}$$

where A is the area of the image of interest. The software MATLAB®[26] was used to write the code to extract the texture features described in this section from the digital mammogram images.

2.4 Classifiers

The classifiers used in this work are briefly described in this section.

2.4.1 Support vector machine

The support vector machine (SVM) classifier has demonstrated excellent performance in a large number of pattern recognition problems.[27–29] SVM is a supervised learning method that aims to determine a separating hyperplane that maximizes the margin between the input data classes that are viewed in an n-dimensional space (n is the number of features used as inputs). To calculate the margin, two parallel hyperplanes are constructed, one on each side of the separating hyperplane. These two hyperplanes are computed directly using the training set. The input data is often transformed to a high-dimensional feature space with the use of nonlinear kernel functions so that the transformed data becomes more separable than the original input data. The methodology is described in detail by Vapnik[29] and in the tutorial by Burges.[27]

2.4.2 Gaussian mixture model

A Gaussian mixture model (GMM) is a parametric model used to estimate a continuous probability density function from a set of multidimensional feature observations. The Gaussian mixture distribution can be written as a linear superposition of K Gaussian components:

$$p(x) = \sum_{k=1}^{K} \pi_k N(x|\mu_k, \Sigma_k), \tag{2.17}$$

where π_k, μ_k, Σ_k are mixing coefficients, mean, and covariance, respectively.

The probability density of a single Gaussian component of D dimensions is given by

$$g\left(x\middle|\mu_i, \sum_i\right) = \frac{1}{\sqrt{(2\pi)^D \left|\sum_i\right|}} \exp\left(-\frac{1}{2}(x-\mu_i)' \sum_i^{-1} (x-\mu_i)\right), \tag{2.18}$$

where $(.)'$ denotes the vector transpose. The solution for determining the parameters of the GMM uses the maximum likelihood (ML) parameter estimation criterion. The model parameters are estimated through training such that they maximize the likelihood of the observations using the expectation-maximization (E-M) algorithm.[30–32] In this work, the initial estimates of the parameters were obtained from training data using the K-means algorithm. The algorithm starts with randomly chosen initial means and assumed unit variances for the covariance matrix. We have used the diagonal covariance matrix as it is computationally more efficient and performs better than the full covariance matrix.[30,31]

2.4.3 Fuzzy Sugeno classifier

In fuzzy classification, the pattern space is divided into many subspaces. For each subspace, the relationships between the target patterns and their corresponding classes are indicated by if–then-type fuzzy rules.[33] Nonlinear classification boundaries can be easily implemented in this type of classifier. The fuzzy inference classifier classifies the unknown patterns by fuzzy inference; patterns of unknown class, which are not considered by learning, are rejected. A fuzzy classifier using subtractive clustering and the Sugeno fuzzy inference system[34] was used as the classifier in this work.

2.4.4 *k*-nearest neighbor

k-NN is a very simple classifier that uses the minimum distance from the query instance to the training samples to determine the *k* nearest neighbors.

After gathering *k* nearest neighbors, a majority of these *k* nearest neighbors are used for the prediction of the class of the new sample. A detailed explanation of *k*-NN can be found in Ref. 35.

2.4.5 Probabilistic neural network

PNN is a type of radial basis network used for classification. It has four layers. The first layer of PNN is the *input layer* wherein the features are fed to the neurons. The next layer is the *hidden layer*. In this layer, there is one neuron for each training data set. The neuron stores the values of the features along with the target value. This hidden neuron computes the Euclidean distance of the test case from the neuron's center point and then applies the radial basis function (RBF) kernel function using the sigma values. The resulting value is passed to the neurons in the pattern layer. In the pattern (summation) layer, there is one pattern neuron for each class of the target variable. The actual target class of each training case is stored in each hidden neuron; the weighted value coming out of a hidden neuron is fed only to the pattern neuron that corresponds to the hidden neuron's category. The pattern neurons add the values for the class that they represent (hence, it is a weighted vote for that category). The final layer is the *decision layer*, which compares the weighted votes for each of the target classes accumulated in the pattern layer and uses the largest vote to predict the target category. More details about this classifier can be found in an excellent tutorial in Ref. 36.

2.4.6 Decision tree

A DeTr classifier generates a tree and a set of rules to represent the model in order to identify different classes from a given data. This decision tree produces a series of rules that can be used to recognize the unknown data. Larose[37] presents the methodology of the DeTr classifier in detail.

2.5 Results

2.5.1 Performance measures

Several parameters can be used to describe the quality and usefulness of a diagnostic test. Among those, the most commonly used parameters for clinical trial results analysis are sensitivity, specificity, accuracy, and positive predictive value. Sensitivity is the probability that a test will produce a positive result when used on diseased population. Specificity is the probability that a test will produce a negative result when used on disease-free population. Accuracy is the ratio of the number of correctly classified samples to the total number of samples. The positive predictive value is the proportion of patients with positive test results who are correctly

Table 2.1 Definition of performance measures.

	Actual disease status	
Test result	**Malignant**	**Benign**
Positive	True Positive (TP)	False Positive (FP)
Negative	False Negative (FN)	True Negative (TN)
	Performance measures	
Sensitivity	TP/(TP+FN)	
Specificity	TN/(TN+FP)	
Accuracy	(TP+TN)/(TP+TN+FP+FN)	
Positive predictive value	TP/(TP+FP)	

TP: Number of diseased patients for whom the test results were positive.
TN: Number of disease-free patients for whom the test results were negative.
FP: Number of disease-free patients for whom the test results were positive.
FN: Number of diseased patients for whom the test results were negative.

diagnosed. The formulae to calculate these parameters are shown in the contingency table (Table 2.1).

2.5.2 Receiver operating characteristics

An ROC curve is obtained by calculating the sensitivity and specificity of a diagnostic test at different threshold values and plotting sensitivity versus (1 – specificity).[38] A test that perfectly discriminates between the two groups (benign and malignant) would yield a curve that coincides with the left and top sides of the plot. This means that sensitivity is high and the FP rate is low. It indicates that the diagnostic test has small FP and FN rates across a reasonable range of threshold values. Generally, the soundness of a diagnostic test is assessed by determining the AUC, which can vary between 0.5 and 1. In practice, the closer the area is to 1.0, the better the test is, and the closer the area is to 0.5, the worse the test is. To evaluate the efficiency of the classifiers, the ROC analysis of the respective results was performed using MedCalc® software.[39]

2.5.3 Classification results

The texture features that were extracted from the mammograms using codes written in MATLAB were subjected to the analysis of variance (ANOVA) test. ANOVA uses variances to decide whether the *means* are different. In the present study, this test was used to compute the variation between features within a class and between classes. When the variation between classes was seen to be relatively high compared to the variation within the class, the test was considered to be statistically significant (low value of p). In this work, seven features resulted in a p-value less than 0.0001. Hence,

Table 2.2 Range of texture features.

Texture parameters	Normal	Benign	Malignant	p-value
Homogeneity	62.569 ± 4.71	66.889 ± 7.51	70.262 ± 8.70	<0.0001
Energy	1.451E+05 ± 1.004E+05	1.372E+05 ± 9.302E+04	3.363E+05 ± 3.783E+05	<0.0001
Contrast	311.63 ± 48.1	346.51 ± 66.3	328.34 ± 67.7	<0.0001
Moment 2	388.9 ± 3.198E+03	7044.8 ± 5.738E+03	6442.3 ± 4.543E+03	<0.0001
Short-run emphasis	0.784 ± 2.642E-02	0.792 ± 2.671E-02	0.812 ± 3.176E-02	<0.0001
Long-run emphasis	11.742 ± 9.32	36.435 ± 26.9	109.47 ± 150.0	<0.0001
Run percentage	1.451 ± 0.171	1.398 ± 1.31	0.939 ± 0.189	<0.0001

these features are clinically significant. The values (mean ± standard deviation) of the seven features extracted from the three classes (normal, benign, and malignant) of mammograms are listed in Table 2.2. The seven features are homogeneity, energy, contrast, moment 2, short-run emphasis, long-run emphasis, and run percentage. It can be seen from the table that homogeneity, energy, short-run emphasis, and long-run emphasis are higher for malignant and lower for normal cases.

Ten-fold stratified cross-validation method was used to test all classifiers. The whole dataset was split into ten equal parts (30 images in each of the ten sets). Nine parts of the data (training set) were used for classifier development, and the built classifier was evaluated using the remaining one part (test set) (i.e. 270 images were used for training and 30 images for testing each time). This procedure was repeated ten times using a different part as the test set in each case. Finally, the average of the accuracy, sensitivity, specificity, positive predictive accuracy, and AUC obtained over the ten evaluations were taken as the overall performance measures.

Table 2.3 shows the results of SVM, GMM, fuzzy, *k*-NN, PNN, and DeTr classifiers. It can be seen from this table that the fuzzy classifier is able to identify the unknown class with an accuracy of more than 93.3%. Table 2.4 shows the sensitivity, specificity, positive predictive accuracy, and AUC values obtained using these classifiers. The fuzzy classifier resulted in higher sensitivity (92.38%), specificity (87.56%), positive predictive accuracy (93%), and AUC value (0.925) compared to the other classifiers. Figure 2.3 presents the ROC curves of the six classifiers.

Table 2.3 Results of classification using classifiers: SVM, GMM, fuzzy, *k*-NN, PNN, and DeTr.

Classes	No. of images used for training	No. of images used for testing	No. of correctly classified images					
			SVM	GMM	Fuzzy classifier	k-NN	PNN	DeTr
Normal	90	10	9	10	9	8	8	8
Benign	90	10	6	5	9	6	6	6
Malignant	90	10	7	9	10	7	7	9
Overall accuracy			**73.3%**	**80%**	**93.3%**	**70%**	**70%**	**76.7%**

Table 2.4 Sensitivity, specificity, positive predictive accuracy, and AUC for SVM, GMM, fuzzy, *k*-NN, PNN, and DeTr classifiers.

Classifier	Average No. TNs	Average No. TPs	Average No. FPs	Average No. n FNs	Average sensitivity	Average specificity	Average positive predictive accuracy	AUC
SVM	10	14	6	0	95.75%	61.21%	76.99%	0.850
GMM	10	14	6	0	97.97%	66.57%	72%	0.850
Fuzzy	**9**	**19**	**1**	**1**	**92.38%**	**87.56%**	**93%**	**0.925**
K-NN	8	18	2	2	78.95%	89.17%	89%	0.850
PNN	8	18	2	2	90.73%	80.87%	90%	0.850
DeTr	8	17	3	2	88.825%	75.143%	86%	0.825

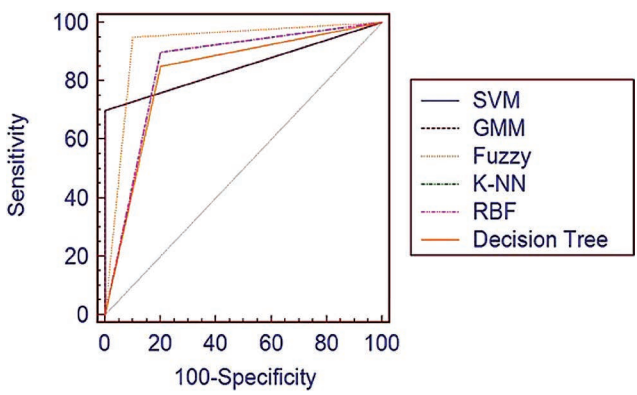

Figure 2.3 ROC curves showing the performance of the SVM, GMM, fuzzy, *k*-NN, PNN, and DeTr classifiers.

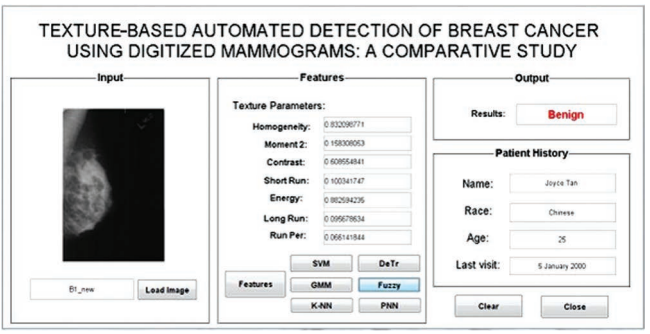

Figure 2.4 GUI of the proposed system.

2.5.4 Graphical user interface

A graphical user interface (GUI) was developed for ease of use of the proposed system (Fig. 2.4). The entire GUI was divided into three sections: input, features, and output. To upload a mammogram image, the user clicks the *Load Image* push button. In the illustration, the uploaded image is 'B1_new'. Once the image is selected, it is displayed in the input section. When the *Features* push button is pressed, the seven features corresponding to the loaded image are displayed in the features section of the GUI. The six push buttons named *SVM, GMM, Fuzzy, K-NN, PNN,* and *DeTr* allow the user to choose one of the six classifiers. When the classifier is selected, the classification result is subsequently displayed in the output section. In this illustration, the result is 'benign'. When the image is uploaded, the name, race, age, and date of the last visit of the patient are automatically displayed in the output section.

2.6 Discussion

In this section, we present the results of some of the related studies that evaluated CAD tools using texture features for mammogram analysis, and compare these results with the results obtained in our work. In the study in Ref. 40, the mean and the first three central moments were extracted from the mammograms and fed into an RBF neural network. The proposed system detected 16 out of the studied 22 abnormal mammograms and 42 out of the 54 normal mammograms. The overall accuracy was around 75.2%. The same four features that were used in the study in Ref. 40 were also used in another study[41] to evaluate the performance of an association rule mining classifier. Results of evaluation of the classifier with 322 images belonging to two classes—normal and abnormal—showed that the classifier had an accuracy of

around 80%. A neuro-fuzzy classifier was evaluated using nine texture features derived from GLCM matrices at various spatial orientations.[42] Only 22 images were tested, and classification accuracies of 100% and 80% were reported for abnormal and normal mammograms, respectively. An automated technique for the quantitative assessment of breast density from digitized mammograms using image processing and data mining techniques was studied.[43] Three features (area, homogeneity, and microcalcification) were extracted using image processing techniques from the raw mammograms. These features were fed to feedforward neural network and GMM classifiers for automated detection of breast abnormalities. The classifiers were able to identify the abnormalities with a sensitivity and specificity of more than 90%.

A new texture shape feature coding (TSFC)-based CAD method was proposed in Ref. 44. The authors converted the texture shape features determined from mammogram masses into texture feature numbers, the histogram of which was then used to determine seven texture descriptors. These descriptors were then fed into an SVM classifier, and a good accuracy of over 86% was obtained. However, this technique was used to classify only the fatty and dense masses in mammograms into benign and malignant classes. In another study, the contours of a set of 108 regions on mammograms related to breast masses were manually delineated, and ribbons of pixels were extracted around the boundaries.[45] Three shape factors and 14 texture features based on GLCMs of the pixels in the ribbons were computed and fed into the perceptron algorithm. It was reported that using only shape features presented an AUC of 0.99, while using only texture features resulted in an AUC of only 0.63. In a subsequent study by the same group,[46] apart from the above indicated 17 features, an additional three measures of edge-sharpness-related features were also studied in a set of 111 regions from mammograms. Several feature subsets were evaluated using perceptron classifiers of varying topology and training procedures. AUC values of up to 0.99 were reported in feature subsets that had at least one shape factor as a feature. In another more-recent study,[47] two more shape factors were included as features. Feature selection was performed by a genetic algorithm, and several linear and kernel-based classifiers were evaluated. The kernel-based nonlinear classifiers presented an AUC of around 0.95.

A novel method for an automatic detection of mammographic masses was presented in Ref. 48. The method consists of an enhancement algorithm for image contrast improvement, a segmentation technique that uses thresholding at multiple levels, and a region-ranking system to identify the regions that most-likely represent abnormalities based on the computed features. The method was evaluated using 57 mammographic images of masses, and a sensitivity of 80% at 2.3 FPs per image was reported. Local

binary patterns (LBPs) were used for representing the textural properties of the mammogram masses.[49] The basic LBP histogram descriptor was extended into a spatially enhanced histogram that encodes both the local region appearance and the spatial structure of the masses. An SVM classifier was used to differentiate masses from normal breast parenchyma. The study concluded that the LBPs are effective and efficient descriptors for mammographic masses.

An SVM-based CAD system for the characterization of clustered microcalcifications (MCCs) in digitized mammograms was proposed.[50] After the ROI in the mammogram was enhanced using morphological techniques, the potential MCC regions were segmented using edge detection and morphological methods. Subsequently, features based on shape, texture, and statistical properties were extracted from each region and fed to an SVM classifier. The SVM classifier with an RBF kernel presented 97% accuracy, and that with a polynomial kernel provided 95% accuracy. Again, this technique deals particularly with MCC cluster classification into benign and malignant. Another CAD system for automatic detection of clustered MCs in digitized mammograms was proposed.[51] The proposed system had two key steps. First, potential MCC pixels in the mammograms were detected and grouped into MCC objects using a multilayer feed-forward neural network classifier. Next, 17 statistical features were extracted from the MCC objects and fed to an AdaBoost algorithm with an SVM-based component classifier. An 89.55% mean TP detection rate was achieved at the cost of 0.921 FP per image.

The studies in Refs. 40–43 evaluated CAD tools for the classification of benign and malignant mammograms. The studies in Refs. 44–49, on the other hand, employed CAD techniques to extract masses from mammograms and to classify these masses into benign and malignant classes. Similar work was performed with respect to MCC analysis.[50,51] There is a dirth of studies on the use of texture features to classify the entire set of mammogram images into three categories (normal, benign, and malignant). Therefore, in this work, we extracted seven texture features from the raw mammogram images (without using segmentation algorithms to determine ROIs) and fed them to the six classifiers: SVM, GMM, fuzzy, *k*-NN, PNN, and DeTr. On evaluation of the proposed system using 300 mammograms, we found that the fuzzy classifier presented an accuracy of more than 93%, and sensitivity and specificity of around 93% and 88%, respectively. In comparison with the other studies described in this section, our method has demonstrated the ability to classify a significant number of mammograms (300 images) with a high degree of clinically acceptable accuracy. Due to the absence of segmentation steps in the proposed technique, the computational load as well as the time required for the analysis is minimized.

Compared to the other classifiers, the fuzzy classifier showed higher accuracy in detection of the normal, benign, and malignant classes. The fuzzy classifier mimics human decision making and can handle vague, imprecise, nonlinear texture features. It dynamically constructs the input and output membership functions based on the nonlinear nature of texture features. These texture features are able to capture the subtle variations in the pixels of the image. Our fuzzy logic algorithm has the ability to describe these subtle variations of texture features in a descriptive human-like manner in the form of simple fuzzy rules. Sometimes, there may be many fuzzy rules. Hence, a clustering algorithm is used to reduce the number of fuzzy rules and improve the system interpretability. Therefore, this technique improves the accuracy of classification and reduces the complexity of the problem. Additionally, fuzzy classifiers take less computational time due to their intrinsic parallel-processing nature.

The key features of the proposed work are summarized below:

- The feature set consisting of seven features is powerful enough to effectively classify normal, benign, and malignant classes with good accuracy of 93.3%. The texture features were found to be significantly different, as indicated by their p-value in Table 2.2. Therefore, on using them in the fuzzy classifier, good accuracy was obtained. We observed that our fuzzy logic algorithm has the ability to describe these subtle variations of texture features in a descriptive human-like manner in the form of simple fuzzy rules.
- We evaluated the technique using a large database consisting of 300 images belonging to the three classes (normal, benign, and malignant). In order to obtain a robust system, we trained and built the fuzzy classifier using a ten-fold cross-validation data-resampling technique. No other past studies have obtained such a close-to-theoretical accuracy using such a balanced dataset.
- The proposed CAD framework is very simple to use and can be extended to study other medical images. It can also be used to diagnose the efficacy of the drugs during the treatment of breast cancer.

2.7 Conclusion

We have proposed a system for the automated detection of normal, benign, and cancerous breasts using texture features extracted from digitized mammograms and data mining techniques. These texture parameters capture the subtle variation in the pixel intensities and contours in the images and serve as good features for classification. SVM, GMM, fuzzy, *k*-NN, PNN and DeTr classifiers were used to aid the physician in

automatic detection of the breast cancer. We used AUC, sensitivity, specificity, accuracy, and positive predictive value to evaluate the performance of the classifiers used. The novelty of this work is to automatically classify the mammogram in to normal, benign, and malignant classes using the *texture features alone* with an efficiency of 93.3%, sensitivity of 92.3%, specificity of 87.56%, and AUC of 0.925. A user-friendly GUI was created to visualize the unknown class immediately even by a nurse's untrained eye. However, the performance can be further improved by increasing the size and quality of the training data and the rigor of the training imparted, as well as the parameters used.

Acknowledgments

The authors thank Ms. Hui Ping and Ms. Lyna Wong Wen Cui for their help in the development of software.

References

1. S. F. Altekruse, C. L. Kosary, M. Krapcho, N. Neyman, R. Aminou, W. Waldron, J. Ruhl, N. Howlader, Z. Tatalovich, H. Cho, A. Mariotto, M. P. Eisner, D. R. Lewis, K. Cronin, H. S. Chen E. J. Feuer, D. G. Stinchcomb, and B. K. Edwards, Eds, *SEER Cancer Statistics Review, 1975–2007*, National Cancer Institute, Bethesda, MD, http://seer.cancer.gov/csr/1975_2007/, based on November 2009 SEER data submission, posted to the SEER web site 2010.
2. E. D. Pisano, C. Gatsonis, E. Hendrick, et al., "Diagnostic performance of digital versus film mammography for breast-cancer screening," *New Engl. J. Med.* **353**, 1773–1783 (2005).
3. E. D. Pisano, R. E. Hendrick, M. J. Yaffe, et al., "Diagnostic accuracy of digital versus film mammography: Exploratory analysis of selected population subgroups in DMIST," *Radiol.* **246**, 376–383 (2008).
4. R. Schulz-Wendtland, M. Fuchsjägerb, T. Wackerc, and K.-P. Hermannd, "Digital mammography: An update," *Eur. J. Radiol.* **72**, 258–265 (2009).
5. J. G. Gilmore, K. Armstrong, C. D. Lehman, and S. W. Fletcher, "Screening for breast cancer," *JAMA* **293**, 1245–1256 (2005).
6. A. J. Kearney and M. Murray, "Breast cancer screening recommendations: Is mammography the only answer?," *J. Midwifery Womens Health* **54**, 393–400 (2009).
7. J. S. Suri, R. M. Rangayyan, and S. Laxminarayan, *Emerging Technologies in Breast Imaging*, American Scientific Publishers, Valencia, CA (2006).

8. J. S. Suri and R. M. Rangayyan, Eds., *Recent Advances in Breast Imaging, Mammography, and Computer-Aided Diagnosis of Breast Cancer*, SPIE Press, Bellingham, WA (2006) [doi: 10.1117/3.651880].
9. X. Wang, L. Chao, L. Chen, G. Ma, G. Jin, M. Hua, and G. Zhou, "The mammographic correlations with basal-like phenotype of invasive breast cancer," *Acad. Radiol.* **17**, 333–339 (2010).
10. H. D. Cheng, X. Cai, X. Chen, L. Hu, and X. Lou, "Computer-aided detection and classification of microcalcifications in mammograms: A survey," *Pattern Recog.* **36**, 2967–2991 (2003).
11. H. D. Cheng, X. J. Shi, R. Min, L. M. Hu, X. P. Cai, and H. N. Du, "Approaches for automated detection and classification of masses in mammograms," *Pattern Recog.* **39**, 646–668 (2006).
12. M. Elter and A. Horsch, "CADx of mammographic masses and clustered microcalcifications: A review," *Med. Phys.* **36**, 2052–2068 (2009).
13. A. Sadaf, P. Crystal, A. Scaranelo, and T. Helbich, "Performance of computer-aided detection applied to full-field digital mammography in detection of breast cancers," *Eur. J. Radiol.* **77**(3), 457–61 (2011).
14. N. Karssemeijer, A. M. Bluekens, D. Beijerinck, J. J. Deurenberg, M. Beekman, R. Visser, R. van Engen, A. Bartels-Kortland, and M. J. Broeders, "Breast cancer screening results 5 years after introduction of digital mammography in a population-based screening program," *Radiol.* **253**, 353–358 (2009).
15. M. Heath, K. Bowyer, D. Kopans, R. Moore, and W. P. Kegelmeyer, "The Digital Database for Screening Mammography," *Proc. of the 5th International Workshop on Digital Mammography*, M. J. Yaffe., Ed., 212–218, Medical Physics Publishing (2001).
16. University of South Florida Digital Mammography Home Page: DDSM: Digital Database for Screening Mammography. URL: http://marathon.csee.usf.edu/Mammography/Database.html (Last accessed in July 2011).
17. S. B. Park, J. W. Lee, and S. K. Kim, "Content-based classification using a neural network," *Pattern Recog. Lett*. **25**(3), 287–300 (2004).
18. J. H. Tan, E. Y. K. Ng, and U. R. Acharya, "Study of normal ocular thermogram using textural parameters," *Infrared Phys. Tech.* **53**, 120–126 (2009).
19. C. Gonzalez and R. E. Woods, *Digital Image Processing*, 2nd edition," Prentice Hall , Upper Saddle River, NJ (2001).
20. M. Mirmehdi, X. Xie, and J. S. Suri, *Handbook of Texture Analysis*, Imperial College Press, London (2008).

21. G. Castellano, L. Bonilha, L. M. Li and F. Cendes, "Texture analysis of medical images," *Clinical Radiol.* **59**, 1061–1069 (2004).
22. F. Tomita and S. Tsuji, *Computer Analysis of Visual Textures*, Kluwer Academic Publishers, Boston (1990).
23. J. S. Weszka and A. Rosenfield, "An application of texture analysis to material inspection," *Pattern Recog.* **8**, 195–200 (1976).
24. K. V. Ramana and B. Ramamoorthy, "Statistical methods to compare the texture features of machined surfaces," *Pattern Recog.* **29**, 1447–1459 (1996).
25. M. M. Galloway, "Texture analysis using gray level run lengths," *Comp. Graphics Image Process.* **4**, 172–179 (1975).
26. MATLAB: http://www.mathworks.com/products/matlab/ (Last accessed in July 2011).
27. C. J. C. Burgess, "A tutorial on support vector machines for pattern recognition,"*Data Mining & Knowledge Discovery* **2**, 1–47 (1998).
28. V. David and A. Sanchez, "Advanced support vector machines and kernel methods," *Neurocomputing* **55**(1–2), 5–20 (2003).
29. V. Vapnik, *Statistical Learning Theory*, Wiley, New York (1998).
30. J. A. Bilmes, *A Gentle Tutorial of the EM Algorithm and its Application to Parameter Estimation for Gaussian Mixture and Hidden Markov Models*, International Computer Science Institute (1998).
31. F. V. Nelwamondo and T. Marwala, "Fault detection using Gaussian mixture models, mel-frequency cepstral coefficients, and kurtosis," *IEEE Trans. Syst. Man. Cybern.*, **1**, 290–295 (2006).
32. D. A. Reynolds, T. Quatieri, and R. Dunn, "Speaker verification using adapted Gaussian mixture models," *Digital Signal Process.* **10**, 19–41 (2000).
33. I. T. Nozaki, "Selecting fuzzy if-then rules with forgetting in fuzzy classification systems," *J. Japan Society for Fuzzy Theory and Systems* **6**, 585-602 (1994).
34. G. J. Klir and Bo Yuan, *Fuzzy Sets and Fuzzy logic: Theory and Applications*, Prentice Hall, Upper Saddle River, NJ (1995).
35. D. T. Larose, "k-Nearest Neighbor," Chapter 5 in *Discovering Knowledge in Data: An Introduction to Data Mining*, Wiley Interscience, Hoboken, NJ (2004).
36. V. Cheung and K. Cannons, "An Introduction to Probabilistic Neural Networks," URL: http://www.psi.toronto.edu/~vincent/research/presentations/PNN.pdf (Last accessed in July 2011).

37. D. T. Larose, "Decision Trees," Chapter 6 in *Discovering Knowledge in Data: An Introduction to Data Mining*, Wiley Interscience, Hoboken, NJ (2004).
38. N. A. Obuchowski, "Receiver operating characteristic curves and their use in radiology," *Radiol.* **229**, 3–8 (2003).
39. MedCalc software, URL: http://www.medcalc.org/ (Last accessed in July 2011).
40. I. Christoyianni, E. Dermatas, and G. Kokkinakis, "Fast detection of masses in computer-aided mammography," *IEEE Signal Process. Magazine* **17**, 54–64 (2000).
41. O. R. Zaıane, M. L. Antonie, and A. Coman, "Mammography classification by an association rule-based classifier," *MDM/KDD 2002: International Workshop on Multimedia Data Mining (with ACM SIGKDD)*, 62–69 (2002).
42. N. Youssry, F. E. Z. Abou-Chadi, and A. M. El-Sayad, "Early detection of masses in digitized mammograms using texture features and neuro-fuzzy model," *4th Intl. IEEE EMBS Special Topic Conf. on Inf. Tech. Appl. in Biomedicine*, 226–229 (2003).
43. U. R. Acharya, E. Y. K. Ng, Y. Hong, Y. Jie, and G. J. L. Kaw, "Automatic identification of breast cancer using mammogram," *J. Med. Syst.* **32**, 499–507 (2008).
44. Y. Chen and C. I. Chang, "New texture shape feature coding-based computer aided diagnostic methods for classification of masses on mammograms," *Conf. Proc. IEEE Eng. Med. Biol. Soc.* **2**, 1275–1278 (2004).
45. T. C. S. S. Andre and R. M. Rangayyan, "Classification of tumors and masses in mammograms using neural networks with shape and texture features," *Proc. 25th Ann. Intl. Conf. IEEE EMBS* **3**, 2261–2264 (2003).
46. T. C. S. S. Andre and R. M. Rangayyan, "Classification of breast masses in mammograms using neural networks with shape, edge sharpness, and texture features," *J. Electronic Imaging* **15**, 678–688 (2006) [doi: 10.1117/1.2178271].
47. T. Mu, A. K. Nandi, and R. M. Rangayyan, "Classification of breast masses using selected shape, edge-sharpness, and texture features with linear and kernel-based classifiers," *J. Digit. Imaging* **21**, 153–169 (2008).
48. A. R. Domínguez and A. K. Nandi, "Detection of masses in mammograms via statistically based enhancement, multilevel-thresholding

segmentation, and region selection," *Comput. Med. Imaging Graphics* **32**, 304–315 (2008).

49. X. Lladó, A. Oliver, J. Freixenet, R. Martí, and J. Martí, "A textural approach for mass false positive reduction in mammography," *Computerized Medical Imaging and Graphics* **33**, 415–422 (2009).
50. S. Singh, V. Kumar, H. K. Verma, and D. Singh, "SVM based system for classification of microcalcifications in digital mammograms," *Conf. Proc. IEEE Eng. Med. Biol. Soc.* **1**, 4747–4750 (2006).
51. F. Dehghan, H. Abrishami-Moghaddam, and M. Giti, "Automatic detection of clustered microcalcifications in digital mammograms: Study on applying adaboost with SVM-based component classifiers," *Conf. Proc. IEEE Eng. Med. Biol. Soc.* 4789–4792 (2008).

U. Rajendra Acharya is a visiting faculty member at Ngee Ann Polytechnic, Singapore. He is also (i) Adjunct professor at University of Malaya, Malaysia, (ii) Adjunct faculty member at Singapore Institute of Technology – University of Glasgow, Singapore, (iii) Associate faculty at SIM University, Singapore, and (iv) Adjunct faculty member at Manipal Institute of Technology, Manipal, India. He received his Ph.D. from National Institute of Technology Karnataka, Surathkal, India and D.Engg. from Chiba University, Japan. He has published more than 275 papers in refereed international SCI-IF journals (176), international conference proceedings (48), textbook chapters (62), books (13, including in Press) with h-index of 22. He has worked on various funded projects with grants worth more than 2 million SGD. He is on the editorial board of many journals and served as Guest Editor for many journals. His major interests are in biomedical signal processing, bio-imaging, data mining, visualization and biophysics for better healthcare design, delivery, and therapy.

Eddie Y. K. Ng received the Ph.D. at Cambridge University, UK. His main interest is thermal imaging and physiology, breast cancer detection, biomedical engineering; computational turbomachinery aerodynamics, and, CFD-CHT. He is Associate Professor at NTU and has published more than 300 technical articles and ten books. He is an Editor for eight international journals: *JMMB*, *JBiSE*, *OMIJ*, *CMJ*, *CFDJ*, *IJRM, JHE*, and *ONMJ*.

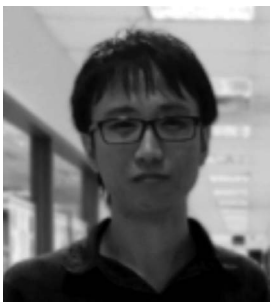

Jen Hong Tan earned his Ph.D. degree from Nanyang Technological University, Singapore. His principal research activity involves the advancement of computer-assisted tools for physicians in their daily clinical session, with a primary focus on the diagnostics of medical images. This activity can be divided into two focuses: first, to propose novel computer methods that could achieve accurate, efficient, and quantitative diagnosis; second, to develop user-centered, intuitive medical algorithms, interfaces, or applications/apps to ease doctor's workload. (Note: he has never considered Ctrl-Alt-Del to be intuitive). Additionally, using computer methods, he also attempts to unveil and explain the underlying physiologies or pathologies in the disease of interest. Hitherto, he has drafted two research fund proposals, one to SATA CommHealth Singapore and another to Singapore MOE Innovation Fund. Both proposals were awarded. Also, he has co-edited a book entitled *Human Eye Imaging and Modeling*, published by CRC Press in 2012.

S. Vinitha Sree received her Ph.D. from Nanyang Technological University, Singapore, in 2010. Her areas of interest include medical data mining, computer-aided diagnosis, breast imaging systems, and healthcare systems and management. She has published 53 papers, and is an associate editor *for J. Medical Imaging* and *Health Informatics* and a reviewer for *J. of Mechanics in Medicine and Biology*.

Jasjit S. Suri, an innovator, visionary, scientist, and an internationally known world leader in biomedical engineering, has spent over 25 years in the field of biomedical engineering/sciences and its management, where he has championed the field of imaging sciences. Dr. Suri has written over 350 peer-reviewed technical publications. He received his Master's degree from University of Illinois, Chicago, Doctorate from University of Washington, Seattle, and Executive Management degree from Weatherhead School of Management (CWRU), Cleveland, Ohio. Dr. Suri is a committee member of several journals and companies. He was was awarded the President's Gold medal in 1980 by India's Directorate General National Cadet Corps and was elected as a Fellow of the American Institute for Medical and Biological Engineering (AIMBE) by the National Academy of Sciences, Washington, DC, in 2004. Dr. Suri has been the chairman of IEEE Denver section and has won more than 50 awards during his career.

Chapter 3
Case-based Clinical Decision Support for Breast Magnetic Resonance Imaging

Ye Xu
Department of Clinical Informatics, Interventional, and Translational Solutions, Philips Research, NY, USA

Hiroyuki Abe
Department of Radiology, The University of Chicago Medicine, Chicago, Illinois, USA

3.1 Introduction

Breast cancer is the most common cancer (excluding skin cancer) and the second most frequent cause of cancer death among women in the United States.[1,2] Dynamic contrast-enhanced MRI (DCE-MRI) screening is recommended as an adjunct for mammography for high-risk women and is increasingly used as a key staging tool for newly diagnosed breast cancer.[1,2]

Case-based clinical decision support (CDS) methods mimic natural physicians' reasoning for diagnosis by reading similar cases that have been previously reviewed and diagnosed. A case-based CDS for breast lesion diagnosis may help physicians to decide whether a queried case is likely

to be malignant or benign, thus avoiding misinterpretation and preventing unnecessary biopsies.

Most of the case-based approaches in the published literature focus on breast cancer diagnosis based on mammogram and ultrasound images.[3–5] Extending the case-based approach to DCE-MRI may improve the sensitivity and specificity. The challenge is to design an algorithm by taking more computer-calculated features into account to capture characteristics of malignant lesions. Additionally, there is also a challenge in obtaining the similarity relationship among cases for a case-based CDS system.

As described in BIRADS® (Breast Imaging Reporting and Data System)[6] for MRI and other imaging modality studies, morphologic descriptors (such as shape or margin) are crucial for determining the diagnosis of a breast lesion. For example, as we know from experienced physicians, a smaller, close to round or elliptical shaped lesion with a smooth lesion boundary margin tends to be a benign lesion, while a bigger, more irregularly shaped lesion with a spiculated margin is more likely to be a malignant lesion (see Fig. 3.1).

In addition, DCE-MRI internal enhancement patterns are also important characteristics in determining the malignancy of a breast lesion. There are four types of internal enhancements, as shown in Fig. 3.2. If the enhancement of the lesion is uniform, it tends to be more homogeneous; if the enhancement is nonuniform, it is heterogeneous.[6,7] The benign cases tend to have a homogeneous texture inside the lesions. Rim enhancement of breast lesions in MRI is due to a combination of angiogenesis and the distribution and degree of fibrosis.[7–9] A lesion with rim enhancement shows a cluster of "black holes" of dead tissue.[9] The thicker the rim (the white area of the lesion) is, the more likely the lesion is malignant. The appearance of rim enhancement is statistically significantly associated with malignant

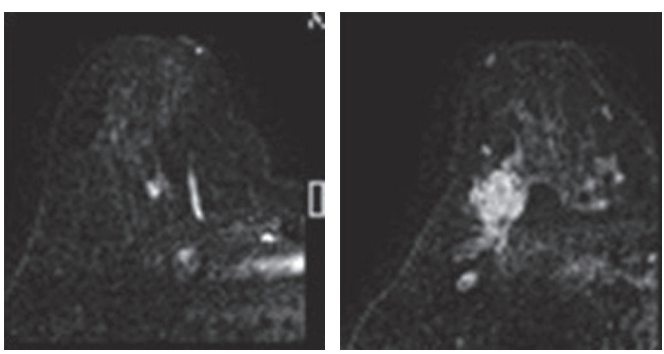

(a) (b)

Figure 3.1 (a) A benign lesion. (b) A malignant lesion. (Derived from the DCE-MRI database provided by University of Chicago Medical Center.)

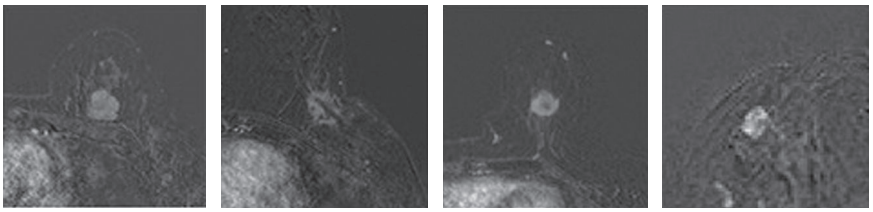

Figure 3.2 Four types of enhancement: homogeneous, heterogeneous, rim enhancement, and dark internal septation. (Derived from the DCE-MRI database provided by University of Chicago Medical Center.)

lesions and is a useful indicator or malignancy of the lesions.[8–10] Dark internal septation refers to nonenhancing septation in an enhancing mass and tends to manifest as crossing lines in the lesion.[11] These characteristics are typical for fibroadenomas, and the presence of dark internal septation is found to be highly predictive of benignity.[7]

Currently, researchers have developed computer algorithms that quantify image characteristics of lesions, such as texture, margin, and shape features to help characterize lesions.[3,12–20] However, most of the developed image algorithms use texture features to characterize homogeneous and heterogeneous enhancement, and there are no computer calculated features available for characterizing lesions with special enhancement characteristics, such as rim enhancement and dark internal septation. We sought to provide similar cases with these additional special characteristics (e.g., dark internal or rim enhancement) since these characteristics can be crucial for diagnosis.

In order to obtain a similarity relationship among cases, most of current researchers use pair-wise comparisons of images to acquire similarity information among images.[4,5,21–24] Muramatsu et al.[4] worked on 50 ROIs (25 benign and 25 malignant) that had unknown diagnoses in their centers. They compared these ROIs with the ROIs of 6 known cases. Ten radiologists independently provided the subjective similarity ratings for 300 pairs of masses with a rating scale between 0 and 1. Nishikawa et al.[22] worked on 30 pairs of mammograms showing clustered calcification using a rating on a 5-point scale of their similarity. All possible combinations of pairs ($n = 435$) were shown to the 4 readers, and each reader selected which pair was most similar. The experiment was repeated by the observers with at least a week between reading sessions. Rogowitz et al.[23] selected 97 digitalized photographic images, and each image was compared with 8 randomly picked images. Fifteen observers were involved in the experiment.

The collection of similarity relationships among cases is very important for the case-based approach, since future similar cases will be presented to

users based on the similarity information. However, a pair-wise approach might lose global similar information since it can only compare a given case with a limited number of cases (4–8 cases) and because it is time consuming to go through different combinations of cases. Additionally, the rating score, having large interobserver variance, is very subjective.

In this chapter, a "similarity experiment" that determines the similarity relationship among cases will be described. Clinical similarity for mass lesions was established by four expert radiologists who systematically sorted lesions visualized by DCE-MRI into similarity clusters using a proprietary software tool. The main purpose of these experiments was to extract image characteristics of breast lesions on DCE-MRI and develop a CDS system to assist radiologists using DCE-MRI for breast cancer diagnosis. The results of these experiments will be used to develop a case-based reasoning system that relies on presenting prior similar cases with known diagnosis from a database to aid decision making.

This chapter proposes a case-based CDS system using a similarity metric combining clinical data with morphological, kinetic features and internal enhancement features extracted from DCE-MRI studies. Results are presented that demonstrate a high sensitivity and specificity achieved by this system.

3.2 Methodologies

3.2.1 Data preparation

Data were collected from 220 patients (241 mass lesions, average age 55 years) scanned using DCE-MRI at the University of Chicago Medical Center between 2001 and 2003 [slice thickness ranging from 2 to 3.5 mm, spacing between slicing ranging from 1 to 3 mm; scanners included Philips Healthcare Intera 1.5T and Achieva 1.5T MR scanners (scanned at axial view), GE Medical Systems Genesis Signa (scanned at coronal view) and GE Signa Excite (scanned at axial view)]. The similarity experiment included 241 mass lesions; 15 lesions were removed that could not be recognized by experts either because of the poor image quality or the insufficient lesion size. Three lesions were also removed because of bad segmentation. Finally, 223 mass lesions (124 malignant, 99 benign) from 203 patients with different types of shape, margin, and enhancement remained for further experimentation. Ground truth diagnosis of malignancy for each lesion was established by histopathological analysis of biopsy samples.

Each set of DCE-MRI images contains several images at different time series, as shown in Fig. 3.3. In order to make a lesion and its boundary more visible, we worked on the subtraction image, which was generated from the image T1-Gd at second phase minus the T1-weighted precontrast image. Then we calculated features on the segmented lesion

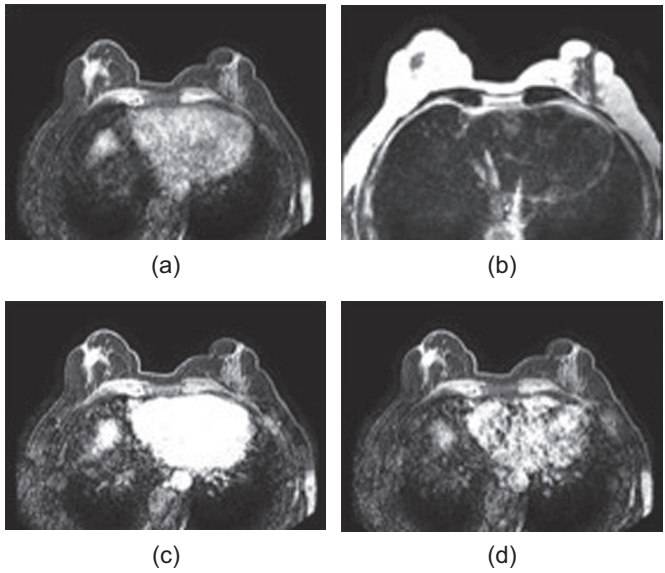

Figure 3.3 DCE-MRI images in different time series: (a) precontrast, (b) T2-weighted, (c) multiple postcontrast, and (d) T1-weighted images.

on the substation image. Figure 3.4 shows an example of preprocessing images and the segmented mass.

3.2.2 Block diagram of our case-based approach

Figure 3.5 showed the block diagram of our proposed system. The main steps are as follows:

1. Store features of the training data in the database.
2. Compare them with the features of the queried case.
3. Calculate and rank the distances between the queried case and the cases in the database.
4. Present the most similar cases.

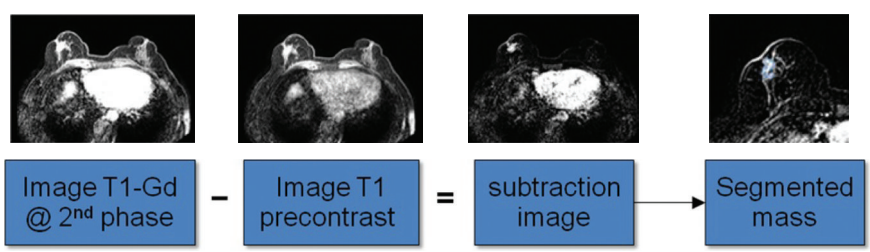

Figure 3.4 Preprocessing of the images and the segmented mass.

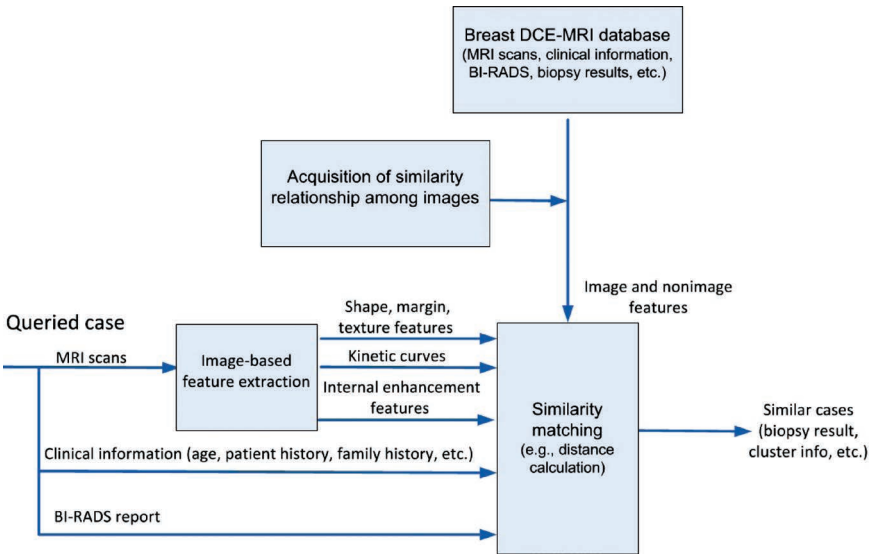

Figure 3.5 Block diagram of the case-based approach.

We used four categories of features (25 features) to represent each case: morphological, kinetic curve, and clinical information, and four new features of internal enhancement. We had described some of the features in the previous research.[20,25–27] Morphological features capture shape or margin characteristics of lesions. Kinetic features[28] show the intensity change of the lesion through different time series of the image, as shown in Fig. 3.6. The kinetic curve includes initial (curve pattern from the first two time

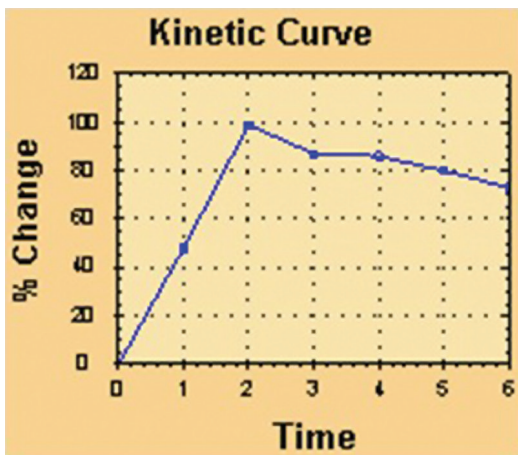

Figure 3.6 Kinetic curve presentation.

periods, including slow, medium, and rapid) and delay (curve pattern after the second time period, including persistent, plateau, and washout). Clinical information includes age and the physicians' impression of the lesion according to BIRADS for MRI (BIRADS-MRI). The approach consists of following steps:

1. Calculate image features to describe the segmented lesion; morphological, kinetic curve, and internal enhancement features are computed by segmenting the lesion on a subtraction image (second postcontrast minus precontrast[29] (see Section 3.2.3 for more details of those features).
2. Calculate the Euclidean distances between the queried case and the cases in the database from input information and calculated features. We converted non-numeric data to digital values (for details of the conversion, see Table 3.3).
3. Sort the cases according to the distances.

In order to ensure that the presenting similar cases fit the point of view of similarity from the experts, we asked the experts to perform the similarity experiment in order to explore the similarity among cases according to their experience.

Figure 3.7 provides an example of how to use a case-based CDS system for CAD of breast cancer. Figure 3.7(a) shows a queried case—a case with unknown diagnosis for which a physician would like to use a

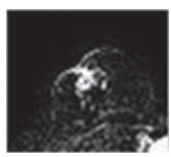

Queried case

ID: 123 Age: 62
Shape: round Margin: irregular
Inter Enhancement: heterogeneous

(a)

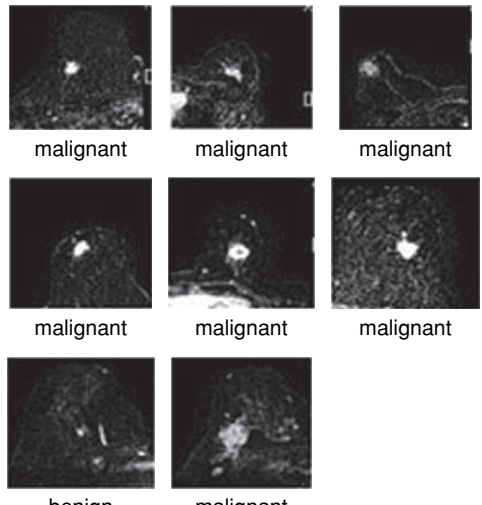

(b)

Figure 3.7 Example of how to use a case-based CDS system: (a) a queried case; (b) the top eight retrieved cases.

case-based system to aid in the final diagnosis. Figure 3.7(b) shows the eight most-similar cases that match the queried case in the order of the rank of similarity. The retrieved cases were selected through a series of processes, as shown in Fig. 3.5, which includes calculation of features and similarity matching (Euclidian distance). From the eight cases with known prior diagnosis (either through biopsy results or follow up) in Fig. 3.7(b), we can see 7 out of 8 cases are malignant, and only 1 out of 8 is benign. Therefore, the current queried case is more likely to be a malignant lesion (the probability is 7/8 = 87.5%). The final decision depends on physicians' detailed analysis of the presenting cases. For instance, the physician can click on each of the eight cases, and look at the images at different series in detail, e.g., precontrast image, post–T1-weighted images at the first time phase, post–T1-weighted images at the second time phase, subtraction image, and post–T2-weighted image.

3.2.3 Features to calculate on breast MRI images

We used four types of features to represent each case: morphological, kinetic curve, clinical information, and four internal enhancement features with a total of 25 features,[20,25–27] as shown in Table 3.1. Morphological, kinetic, and internal enhancement features were computed by segmenting the lesion on a subtraction image (second postcontrast minus precontrast), and then calculating image features to describe the segmented lesion. Clinical information includes age and the physicians' impression (shape, margin, and enhancement) of the lesion according to BIRADS-MRI.

In our previous research on computed tomography (CT),[26,27] we developed 3D texture-based features to characterize heterogeneous and homogeneous gray-level distribution in lesions. Those features were used to assist in predicting the malignancy of lung lesions on CT images based on the well-known co-occurrence matrices. We applied a similar algorithm for calculating 3D texture-based features in MRI images.

We implemented four new 2D image-based features of internal enhancement in order to characterize the four types of enhancement: homogeneous, heterogeneous, the rim enhancement, and dark internal septation for breast cancer in MRI. The approach consists of following steps:

1. Locate the lesion boundary on the cross-sectional slice with the largest area of the lesion after segmentation.[30]
2. Identify heterogeneous regions (dark regions) inside the lesion (an iterative method is used to find a threshold to separate white and black region).
3. Search for the largest isolated heterogeneous region, which shows as "a black hole" of dead tissue.

Table 3.1 Type and definition of the features in the case-based CDS system.

Feature type	Definition	Number of features
3D morphology		**10**
Shape: eccentricity	Measure of how much the shape deviates from an ellipse	
Shape: ellipse/irregularity	1 minus the ratio of the number of voxels around the fitted ellipse to the total voxel number on the object boundary	
Shape: flatness	Ratio of element 1 to element 2 in the eigenvalue matrix	
Shape: enlongation	Ratio of element 3 to element 2 in the eigenvalue matrix	
Shape: sphericity	Ratio between the volume of the structure within a volume-equivalent sphere centered at the centroid of the object and the whole volume	
Contrast	Ratio between the mean gray values inside and in a shell surrounding the object	
Gradient	Ratio of the value of the gradient magnitude that is less than threshold to the value of the surface	
Fractal	Fractal feature around the border of the object	
Edge gradient	Edge gradient standard deviation	
Kurtosis histogram	Kurtosis of gray values in a cube centered in the volume of interest (VOI)	
3D texture		**5**
GLCM entropy inside	GLCM entropy of inside region	
GLCM correlation	GLCM correlation of inside region	
GLCM inertia inside	GLCM inertia of inside region	
GLCM entropy outside	GLCM entropy of outside region	
GLCM inertia outside	GLCM inertia of outside region	
Kinetic curve		**2**
Initial	Intensity change from the first two time periods	
Delayed	Intensity change after the second time period	
BIRADS physician's impression	Shape, margin, and enhancement	**3**
Age		**1**
Internal enhancement		**4**
Ratio of dark to white	Ratio of the mean intensity of dark regions to white regions	
Heterogeneous regions	Total number of heterogeneous regions	
Max_rim	Maximum thickness of the rim	
Mean_rim	Mean thickness of the rim	

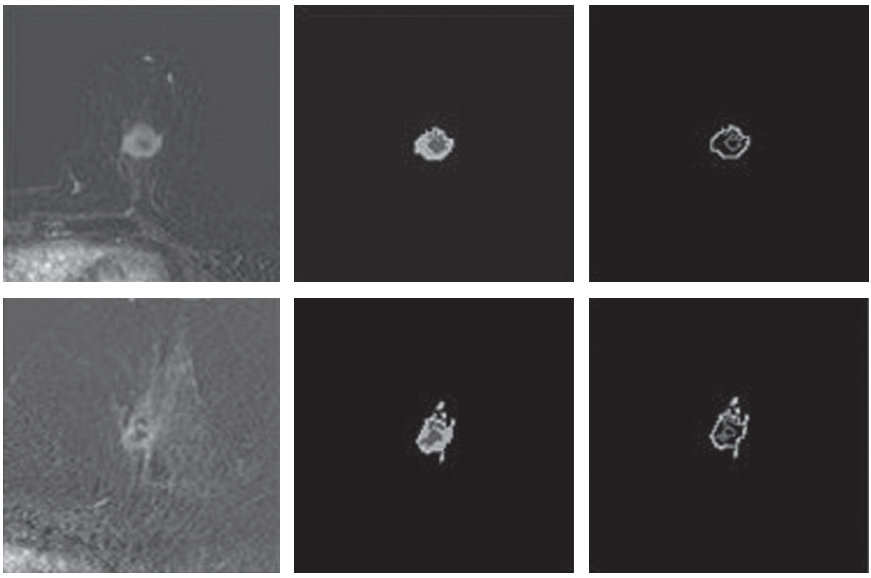

(a) (b) (c)

Figure 3.8 Image processing for the two cases with rim enhancement: (a) original VOI images; (b) image after finding the inner "black holes." The rim is the white area inside the lesion; (c) gray edge showing the boundary of the "black hole," with the white edge showing the lesion boundary. (Derived from the DCE-MRI database provided by University of Chicago Medical Center.)

4. Identify the edge and rim of this dark region. The rim is defined as the area covered by the lesion minus the largest dark region and appears as the white area of the lesion. Figure 3.8 shows the result of image processing of two lesions with rim enhancement.
5. Calculate four new 2D features after the above image processing: (1) the ratio of the mean intensity of dark regions and white regions; (2) the total number of heterogeneous regions; (3) the maximum and (4) mean thickness of the rim.

After learning from the similarity experiment, we assigned digital values for each category of BIRADS and kinetic curve features (see Table 3.3 for more details). Once the imaging, age, and BIRADS-MRI features of a queried case were sent into the system, we normalized each feature value using standard scores (Z values, $z = (x\text{-}\mu)/\sigma$). Then the Euclidean distances between the queried case and the cases in the database were calculated, and cases in the database were sorted according to the distances (the Euclidian distance was calculated from the feature vector of the queried case to the feature vector of a case in the database). Each feature was weighted equally.

3.2.4 Collections for ground truth of similarity from data

In order to obtain the ground truth of the similarity among images, a similarity experiment was performed. We first asked four radiologists to independently participate in the experiment, shown in Fig. 3.9. Experts clicked the snap shots to view all of the detailed images, and then dragged the snap shots into the clusters on the right. Users can also add notes at the bottom of each cluster.

We helped experts to analyze the data by providing them statistical information on their agreement. Based on the agreement (majority voting), they had a discussion, and then made a consensus on the number of the clusters, the name of each cluster, and one representative case for each cluster. After that, they were ready to drag cases into different clusters. Following the experiment, we interviewed each expert, requesting them to describe and draw the main characteristics of each cluster, find one representative case for each cluster, and tell us the significant characteristics for malignant lesions.

3.2.5 Evaluation

We evaluated our system by using the Euclidean distance metric in a k-NN classifier, which provides an estimate of the posterior probability that a query case belongs to the class of malignant samples.[7] Based on the k most-similar retrieved cases with shortest distances (most similar), this probability is estimated by the number of malignant cases in the k most-similar cases divided by k. In order to evaluate the results, we used 0.5 as a probability threshold such that probabilities exceeding the threshold would be classified as malignant and probabilities below the threshold would be classified as benign, even though in practice the radiologist, not the CDS system, would make this decision. We used a leave-one-out cross-validation method and

(a) (b)

Figure 3.9 Screenshots to establish clinical similarity: (a) snap shots of all images; (b) several clusters.

calculated the area under the ROC curve (AUC), accuracy, sensitivity, and specificity for different values of *k*.

3.3 Results and Discussion

For the independent study of the similarity experiment by four experts, the unanimous consensus is only 20%, and the majority agreement is around 60%. Then, the four experts came to a census. After consensus, experts made 16 clusters, each including two main characteristics of shape, margin, or internal enhancement. For example, the first cluster is round/oval and homogeneous, and the second cluster is irregular, homogeneous. Table 3.2 lists the number of cases in each cluster, the rank of the cluster based on number of cases in that cluster, and the number of malignant cases in each cluster.

From Table 3.2, we can conclude that the most popular group of cases is irregular, homogeneous (cluster 2), followed by lobular, homogeneous (cluster 7), round, homogeneous (cluster 1), irregular, heterogeneous (cluster 4), and spiculated, heterogeneous (cluster 3). For most of the cases in cluster 16, the image quality was not very good. Since experts had difficulty recognizing lesion characteristics, they labeled these cases as *cannot recognize*. Cluster 12 was labeled *focus* since experts found them too small. We are not very interested in those two groups, so we removed those cases from our list. Additionally, we can see that all of

Table 3.2 16 clusters resulting from the similarity experiment.

Cluster number	Cluster characteristics	Total number	Popularity ranking number	No. of malignant cases
1	Round/oval, homogeneous	35	3	7/35
2	Irregular, homogeneous	66	1	35/66
3	Spiculated, heterogeneous	12	5	12/12
4	Irregular, heterogeneous	25	4	18/25
5	Spiculated, homogeneous	10	7	10/10
6	Lobular, heterogeneous	7	8	2/7
7	Lobular, homogeneous	48	2	21/48
8	Round/oval, heterogeneous	2	15	1/2
9	Lobular, rim	4	9	3/4
10	Spiculated, rim	4	9	4/4
11	Round/oval, dark internal septations	2	15	1/1
12	Focus	11	6	
13	Irregular, rim	3	14	2/3
14	Round/oval, rim	4	9	1/4
15	Lobular, dark int. septations	4	9	3/4
16	Unrecognizable	4	9	

the cases that are spiculated, heterogeneous (cluster 3) are malignant. Almost all of the cases of spiculated, rim (cluster 10) or irregular, rim (cluster 13) are malignant (6/7). Spiculated is an important characteristic for classification of malignant lesions. Most of the cases that are round, homogeneous (cluster 1) are benign (28/35). For some clusters, such as cluster 2, since irregular shape might be a sign for a malignant lesion, while homogeneous might be a sign for a benign lesion, the group is a mixture of both malignant and benign lesions.

After learning from the similarity experiment, we assigned digital values for each category of BIRADS and kinetic curve features based on interviews and experiments, where a lower value indicates a lower risk for malignancy and a higher value indicates a higher risk or weight for malignancy. The digital value is not evenly distributed, and the distance between two values is based on their category similarity. For example, the distance between round and oval is 0.25 since round and oval are similar, while the distance between round and irregular is 1.5 because there is much difference between them as shown in Table 3.3. Since we normalized those digital values to Z values later, it is reasonable to use them in the distance calculation.

As a final step, we evaluated our proposed system. The AUC, accuracy, sensitivity, and specificity with values for the parameter k (the number of nearest neighbors) are as shown in Fig. 3.10. Because the performance declined significantly at large values of k, we only display the results for

Table 3.3 Feature values assigned for narrative value based on feature similarity.

Shape	Round	0.5
	Oval	0.75
	Lobular	1.25
	Irregular	2
Margin	Smooth	0.5
	Irregular	1.5
	Spiculated	3
Enhancement	Homogenous	0.5
	Dark internal enhancement	1
	Heterogeneous	2
	Rim enhancement	3
Kinetic curve initial	Slow	0.5
	Medium	0.75
	Rapid	1
Kinetic curve delay	Plateau	1
	Persistent	2
	Washout	3

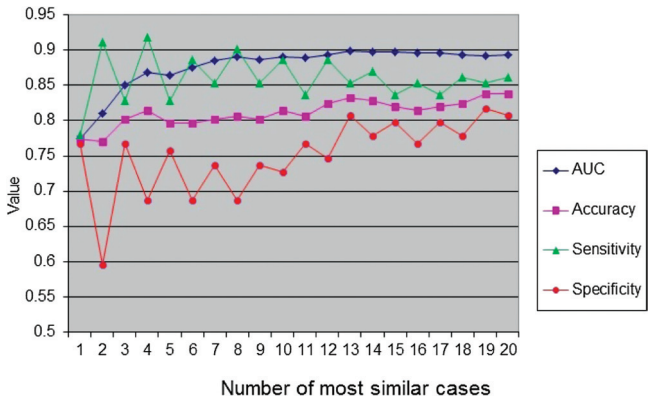

Figure 3.10 AUC, accuracy, sensitivity, and specificity with varying values of k (number of most similar cases considered).

k from 1 through 20 (it showed gradual decline after $k = 20$). The decline in performance at high k is due to the influence of very distant (nonsimilar) cases in the likelihood estimation. In practice, a cutoff k may need to be defined. The results show that the AUC, accuracy and sensitivity are almost maximized when we selected the top thirteen similar cases ($k = 13$). The performance measured at this point was AUC = 0.90, accuracy = 0.83, sensitivity = 0.88, and specificity = 0.81. Furthermore, the results were stable, yielding similarly high-performance characteristics for other nearby values of k.

We can see that after $k = 13$, the four curves are more stable. The curves of sensitivity and specificity show zigzags at the beginning because the effective threshold for malignancy is greater than 0.5 when k is an odd number. The higher the effective threshold for malignancy, the lower the sensitivity, and the higher the specificity. Thus, we see that the sensitivity dropped at odd numbers, while the specificity rose at odd numbers. For example, when $k = 3$, the effective threshold for malignancy is $2/3 = 0.67$; when $k = 5$, it is $3/5 = 0.60$, while for $k = 2$ or $k = 4$, the threshold is 0.5.

As a single feature, the mean thickness of the rim and the maximum thickness of the rim can achieve AUC at 0.774 and 0.768, respectively, for CAD of malignancy, as shown in Fig. 3.11. (These values are comparable to published optimal individual features.[19]) Two other features, the ratio of the mean intensity of dark regions and white regions and the total number of heterogeneous regions reached AUC = 0.704 and 0.708, respectively. These four features can be used in future work for malignancy prediction or other related work needing quantified image values.

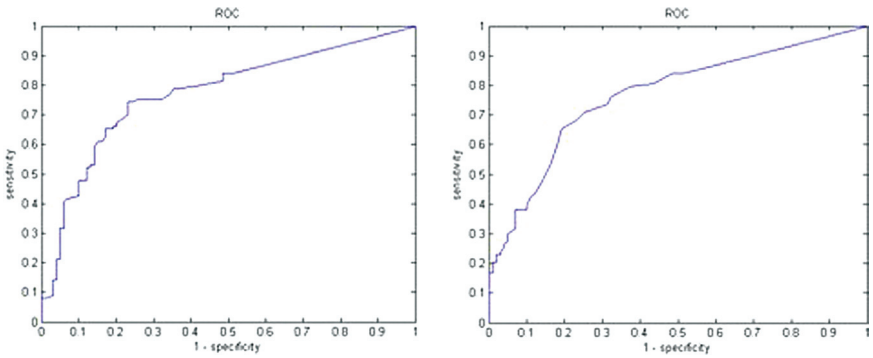

(a) (b)

Figure 3.11 ROC curves for the two best features for predicting the malignancy of breast lesions: (a) mean thickness of the rim; (b) maximum thickness of the rim.

The results show our extended system with four times as many cases as in the previous research;[20] yet, despite the increase in data, the system demonstrates robust performance, which might suggest that the proposed case-based CDS could be used for a reference of diagnosis for physicians. It shows a high sensitivity and specificity, which means that physicians can rely on and have confidence in this CDS system, avoid misinterpretation of results, and reach the most patients requiring biopsy, while preventing unnecessary biopsies.

In our CDS system, instead of presenting only cases with known diagnosis, we also provide cluster names that experts have assigned from the similarity experiment. By presenting this information to users, users will more readily decide which cluster group the queried case belongs to. If most of the cases (majority voting) are from one particular cluster group, then the algorithm is more reliable, and vice versa.

We include multiple lesions for some patients (10–20 patients) in our analysis. However, since we use *age* as only one of the clinical features, this should not bias the results. In our system, we used both BIRADS reports of physician's impression and computer-calculated features to enhance performance. However, if the computer-calculated features are more robust and precise enough with current computer technology, we might use only computer-calculated features in the future.

Currently, we have used some of what we have learned from the similarity experiment, such as assigning reasonable digital value for category inputs and presenting cluster information to improve the confidence level of users. In the future, we will add a weighting factor to each feature in the algorithm.

3.4 Conclusions

We have proposed a case-based CDS system for breast cancer using a similarity metric combining clinical data with morphological, kinetic, and internal enhancement features extracted from DCE-MRI studies. We have also provided cluster information collected through a similarity experiment for each case. Leave-one-out cross-validation suggests that the proposed system can retrieve prior cases with the same diagnosis and similar imaging and clinical characteristics as the queried case. Further research will consider feature selection and weighting in order to optimize the system for diagnostic decision making.

References

1. American Cancer Society, "Cancer Facts & Figures 2010," American Cancer Society, Atlanta, GA (2010).
2. R. M. Mann, C. K. Kuhl, K. Kinkel, C. and Boetes. "Breast MRI: Guidelines from the European Society of Breast Imaging," *Eur. Radiol.*, **18**(7), 1307–18 (2008).
3. K. Horsch, M. L. Giger, C. J. Vyborny, L. Lan, E. B. Mendelson, and R. E. Hendrick, "Classification of breast lesions with multimodality computer-aided diagnosis: Observer study results on an independent clinical data set," *Radiol.* **240**(2), 357–68 (2006).
4. C. Muramatsu, Q. Li, R. A. Schmidt, J. Shiraishi, K. Suzuki, G. M. Newstead, and K. Doi, "Determination of subjective and objective similarity for pairs of masses on mammograms for selection of similar images," *Prog. Biomed. Optics Imaging* **6514**(1l), 1–9 (2007).
5. I. E. Naqa, Y. Yang, N. P. Galatsanos, R. M. Nishikawa, and M. N. Wernick, "A similarity learning approach to content-based image retrieval: Application to digital mammography," *IEEE Trans. Med. Imaging* **23**(10), 1233–44 (2004).
6. C. J. Orsi, *BI-RADS®, Breast Imaging Reporting and Data System*, 4th, edition, American College of Radiology, Reston, VA (2003).
7. BI-RADS® Atlas 2010, Access Date: 01/20/2010; Available from: http://www.acr.org/SecondaryMainMenuCategories/quality_safety/BIRADSAtlas.aspx.
8. G. Agrawal, M. Y. Su, O. Nalcioglu, S. A. Feig, and J. H. Chen, "Significance of breast lesion descriptors in the ACR BI-RADS MRI lexicon," *Cancer* **115**(7) 1363–1380 (2009).

9. R. Matsubayashi, Y. Matsuo, G. Edakuni, T. Satoh, O. Tokunaga, and S. Kudo, "Breast masses with peripheral rim enhancement on dynamic contrast-enhanced MR images: Correlation of MR findings with histologic features and expression of growth factors," *Radiol.* **217**, 841–848 (2010).
10. M. Tozaki and K. Fukuda, "High-spatial-resolution MRI of non-mass like breast lesions: Interpretation model based on BI-RADS MRI descriptors," *Am. J. Roentgenol.* **187**, 330–337 (2006).
11. M. Tozaki, "Interpretation of breast MRI: correlation of kinetic and morphological parameters with pathological findings," *Magn. Reson. Med. Sci.* **3**(4) 189–197 (2004).
12. N. Bhooshan, M. L. Giger, S. A. Jansen, H. Li, L. Lan, and G. M. Newstead, "Cancerous breast lesions on dynamic contrast-enhanced MR images: Computerized characterization for image-based prognostic markers," *Radiol.* **254**(3), 680–90 (2010).
13. K. Drukker, N. P. Gruszauskas, C. A. Sennett, and M. L. Giger, "Breast US computer-aided diagnosis workstation: Performance with a large clinical diagnostic population," *Radiol.* **248**(2), 392–397 (2008).
14. M. Elter and E. Hasslmeyer, "A knowledge-based approach to the CADx of mammographic masses," *Proc. SPIE* **6915**, 69150L (2008) [doi: 10.1117/12.770135].
15. M. Elter, T. Wittenberg, R. Schulz-Wendtland, and T. M. Deserno, "A multi-image approach to CADx of breast cancer with integration into PACS," *Proc. SPIE* **7264**, 72640X (2009) [doi: 10.1117/12.810983].
16. M. L. Giger, Z. Huo, L. Lan, and C. J. Vyborny, "Intelligent search workstation for computer-aided diagnosis," *Proc. Computer Assisted Radiology and Surgery (CARS 2000)*, 822–827 (2000).
17. K. G. Gilhuijs, M. L. Giger, and U. Bick, "Computerized analysis of breast lesions in three dimensions using dynamic magnetic-resonance imaging," *Med. Phys.* **25**(9), 1647–54 (1998).
18. C. D. Lehman, C. Gatsonis, and K. C. Kuhl, "MRI evaluation of the contralateral breast in women with recently diagnosed breast cancer," *N. Engl. J. Med.* **356**, 1295–303 (2007).
19. K. Nie, J. H. Chen, H. J. Yu, Y. Chu, O. Nalcioglu, and M. Y. Su, "Quantitative analysis of lesion morphology and texture features for diagnostic prediction in breast MRI," *Acad. Radiol.* **15**(12), 1513–1525 (2008).
20. Y. Xu, L. Boroczky, J. Drysdale, M. C. Lee, T. Buelow, and A. Meinel "Case-based clinical decision support for breast cancer diagnosis

using dynamic contrast-enhanced MRI images," *Int. J. Comp. Assist. Radiol. Surg*. **4**(1), 175–176 (2009).

21. C. Muramatsu, Q. Li, R. A. Schmidt, et al., "Determination of subjective similarity for pairs of masses and pairs of clustered microcalcifications on mammograms: Comparison of similarity ranking scores and absolute similarity ratings," *Med. Phys.* **34**(7), 2890–5 (2007).
22. R. M. Nishikawa, Y. Yang, D. Huo, M. Wernick, C. A. Sennett, J. Papaioannou, W. and Wei, "Observers' ability to judge the similarity of clustered calcifications on mammograms," *Med. Imaging: Image Perception, Observer Performance, and Tech Asses.* **5372**, 192–198 (2004).
23. B. E. Rogowitz, T. Frese, J. R. Smith, C. A. Boumanz, and E. Kaliny, "Perceptual image similarity experiments," *Proc. SPIE* **3299**, 576–590 (1998).
24. S. Santini and R. Jain, "The 'El Nino' image database system," *in IEEE International Conference on Multimedia Computing and Systems* **1**, 524–529 (1999).
25. L. Boroczky, M. C. Lee, L. Agnihotri, et al., "Computer-aided diagnosis for lung cancer using a classifier ensemble," *Int. J. Comp. Assist. Radiol. Surg.* (**2**)1, S362–S364 (2007).
26. L. Boroczky, L. Zhao, and K. P. Lee, "Feature subset selection for improving the performance of false positive reduction in lung nodule CAD," *IEEE Trans. Inf. Technol. Biomed.* **10**(3), 504–511 (2006).
27. L. Zhao, L. Boroczky, J. Drysdale, L. Agnihotria, and M. C. Lee, "False positive reduction for lung nodule CAD," *Proc. SPIE* **6514**, 65143F (2007) [doi: 10.1117/12.708291].
28. W. Chen, M. L. Giger, U. Bick, et al., "Automatic identification and classification of characteristic kinetic curves of breast lesions on DCE-MRI," *Med. Phys.* **33**(8), 2878–87 (2006).
29. T. Bülow, R. Wiemker, L. A. Meinel, H. Buurman, U. Kose, and G. Newstead, "Temporal variations in apparent breast lesion volume in dynamic contrast enhanced breast MR imaging," *Proc. SPIE* **7260**, 726029 (2009) [doi: 10.1117/.12.812220].
30. T. Bülow, L. A. Meinel, R. Wiemker, U. Kose, A. Shimauchi, and G. Newstead, "Segmentation of suspicious lesions in dynamic contrast-enhanced breast MR images," *Proc. SPIE* **6514**, 65140T (2007) [doi: 10.1117/12.706537].

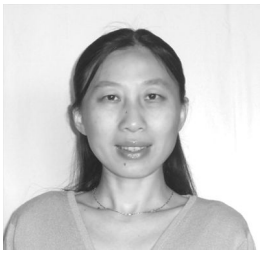

Ye Xu obtained her Ph.D. in Computer Science (2007), and M.C.S. (2001) at the University of Iowa, where she started her research on computer-aided diagnosis with medical images. In 2007 she joined Philips North America as a senior research scientist, where she worked on multiple projects related to CDS systems, including diagnosis of lung nodules, case-based breast cancer CDS systems, etc. Recently, she has also been involved in multiple CDS projects in other related fields, such as neurology and endoscopy. She actively participates in multiple prestigious conferences and has been a reviewer for many journals of medical imaging, clinical informatics, health informatics, machine learning, and pattern recognition.

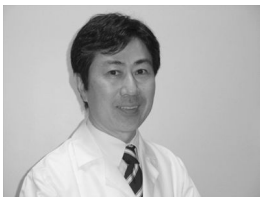

Hiroyuki Abe, M.D., Ph.D. is a radiologist, currently practicing as an Assistant Professor in the Section of Breast Imaging, Department of Radiology, at The University of Chicago Medicine. He graduated from Tohoku University, School of Medicine in 1987, finished his residency training at National Cancer Center in Tokyo, Japan, and had fellowship training at the University of Chicago from 2003 to 2005. He spent a dedicated research period between 2000 and 2003 at The University of Chicago for the study of CAD. His publications include multiple studies related to artificial neural network and observer performance tests.

Chapter 4
Registration, Lesion Detection, and Discrimination for Breast Dynamic Contrast-Enhanced Magnetic Resonance Imaging

Valentina Giannini
Department of Radiology, IRCC—Institute for Cancer Research and Treatment, Torino, Italy and Electronics Department, Politecnico di Torino, Italy

Anna Vignati and Massimo De Luca,
Department of Radiology, IRCC—Institute for Cancer Research and Treatment, Torino, Italy

Silvano Agliozzo, Alberto Bert, Lia Morra, and Diego Persano
im3D S.p.A., Medical Imaging Lab, Torino, Italy

Filippo Molinari
Electronics Department, Politecnico di Torino, Italy

Daniele Regge
Department of Radiology, IRCC—Institute for Cancer Research and Treatment, Torino, Italy

4.1 Introduction

Breast cancer is the second most common malignancy after lung cancer, and the most common cancer in women.[1,2] Dynamic contrast-enhanced (DCE) breast MRI, in which the breast is imaged before (unenhanced image), during, and after (enhanced images) the administration of a contrast agent, provides a noninvasive assessment of the microcirculatory characteristics of tissues in addition to traditional anatomical structure information.[3]

DCE-MRI shows promise in detecting both invasive and ductal carcinoma *in situ* cancers, gives information on the biological aggressiveness of tumors, and may be used to evaluate the response to neoadjuvant chemotherapy[4–7] and is therefore increasingly used in breast cancer diagnosis as an adjunct to conventional imaging techniques.[8,9] Furthermore, DCE-MRI is highly sensitive, allowing detection of malignancy that is occult on physical examination, mammography, and sonography. However, despite its high sensitivity, several factors have precluded more widespread use of this technique. Current challenges include the lack of standardized acquisition protocols, time required for image processing and interpretation, and variable specificity of this imaging tool. In addition, the particular combinations of morphologic and kinetic features that best discriminate benign from malignant lesions have yet to be fully defined.[10]

In recent years, CAD systems have been introduced to overcome these obstacles. CAD systems aid in the visualization of kinetic information by providing color mapping, facilitating analysis through graphical and quantitative representations, and providing an index of suspicion. In order to compute morphological features and kinetic curves for use in predicting pathology probability (discrimination step), a typical CAD system also includes (1) a procedure of motion compensation between unenhanced and enhanced images (registration) and (2) a procedure of lesion identification (lesion detection). In this chapter a specific approach is chosen and described for each step of a CAD system: im3D's research version of a system called CAD-BREAST MRI.

4.2 Registration

This step is aimed at correcting possible misalignment in the dynamic sequence due to patient motion. It was performed by registering all of the contrast-enhanced images with reference to the unenhanced sequence.

4.2.1 Method

The registration method, illustrated in Fig. 4.1, is based on the method proposed by Rueckert[11] and was implemented using the Insight Toolkit (ITK).[12] To reduce the computational burden, the registration is performed at a minimal predefined resolution in each axis direction. Therefore, if the frames of the dynamic series present a lower resolution in any of the directions, the images are downsampled to the predefined minimal resolution. Otherwise, registration is performed at the original resolution. In addition, the registration is performed within a rectangular ROI that contains the relevant part of the scans for the diagnosis (i.e., breasts and axillae). The ROI is automatically determined based on the maximum and minimum points of the breast (as defined in Section 4.3.1.1).

The registration itself consists of two main steps. First, the global misalignment is compensated by using a translation and a rigid-body transformation. Subsequently, local motion is corrected by a free-form deformation model based on B-splines.[11] In all cases, mutual information is used as an image similarity function; in particular, the method specified by Mattes et al. was developed.[13] Optimization is carried out by means of a gradient descent optimizer for the rigid registrations, and of the L-BFGS-B (limited-memory Broyden–Fletcher–Goldfarb–Shanno for bound constrained optimization) optimizer for the nonrigid substep.[14] If the contrast-enhanced frames were downsampled before the registration, the respective

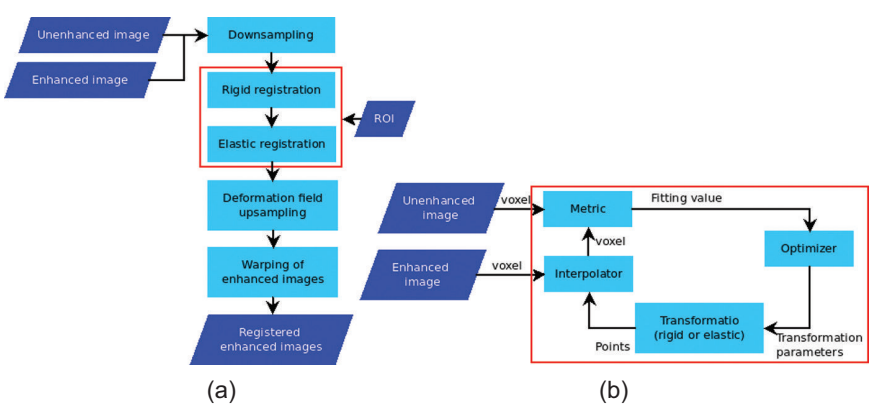

Figure 4.1 (a) Scheme of the registration method. (b) Basic components of the ITK registration framework used for the rigid and nonrigid registration steps.

deformation fields are up-sampled to the original resolution. Finally, the original contrast-enhanced frames are warped to obtain the transformed (aligned) contrast-enhanced frames by applying the respective deformation field. In the warping, B-spline interpolation is used to minimize the introduction of sampling artifacts.

4.2.2 Results

The dataset used to test the registration method was composed of images acquired on a 1.5T scanner using a 3D axial FLASH sequence.[15,16] A total of 24 patients (mean age 55 years, range 37–79 years) were included; 16 were randomly selected, while the remaining 8 were added, as they presented relevant artifacts due to patient movement.

The registration method was applied to the enhanced sequences with reference to the unenhanced sequence. Registered (REG) and nonregistered (N-REG) axial images and maximum-intensity projections (MIPs) of the first enhanced subtracted frame were randomized and blindly evaluated by two radiologists separately by scrolling the axial images and rotating the MIPs, with free windowing. Image quality was assessed for both axial images and MIPs. Readers were asked to define equivalence or superiority of one of the two datasets of each patient, simultaneously presented. Finally, the im3D CAD-BREAST MRI system (research version) identified suspicious enhancements (prompts) for REG and N-REG images. A radiologist excluded prompts related to real findings; the remaining false prompts and their volume were obtained for both REG and N-REG images. Sign test, weighted κ, and Wilcoxon exact test were used.[17]

Image quality of REG MIPs was found to be significantly superior to that of N-REG MIPs for both readers (p-value < 0.001) with quite a good inter-rater agreement ($\kappa = 0.5$). Image quality of REG axial images was found to be slightly better than that of N-REG axial images by both readers without significant difference. The mean number of false prompts per patient was 29.4 ± 17.7 on N-REG and 25.0 ± 16.5 for REG (p-value = 0.041). Excluding one patient with wrong segmentation of the heart, the mean volume of false prompts was $13{,}000 \pm 11{,}641$ mm^3 for N-REG and only $4{,}345 \pm 4{,}274$ mm^3 for REG (p-value < 0.001). Examples of how registration was able to compensate for motion artifacts are shown in Figs. 4.2 and 4.3.

4.3 Lesion Detection

As DCE-MRI data analysis is time consuming, lesions may be isolated by segmentation to reduce reporting time. This image processing procedure is preliminary to the extraction of quantitative information on lesion

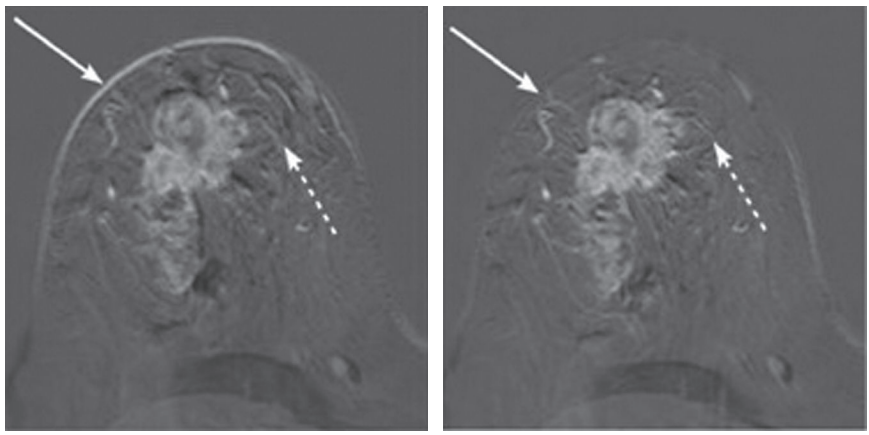

(a) (b)

Figure 4.2 Comparison between subtracted images with and without registration. (a) Subtraction artifacts due to patient movement are visible along the breast profile (plain arrow), in the breast parenchyma (dotted arrow), at lesion and vessel borders, as well as at the borders of fat lobules. These artifacts may introduce spurious enhancing voxels, thus increasing the number of false-positive (FP) findings at segmentation. (b) Subtraction artifacts are dramatically reduced when elastic registration is used.

morphology, kinetics, and volume, and to distinguish viable from nonviable tissue.[18] Most segmentation methods are manual or semi-automatic and, therefore, may be affected by high inter- and intra-observer variability.[19–21] On the contrary, a fully automatic lesion segmentation process has the potential to reduce reading time and provide more-reproducible results.

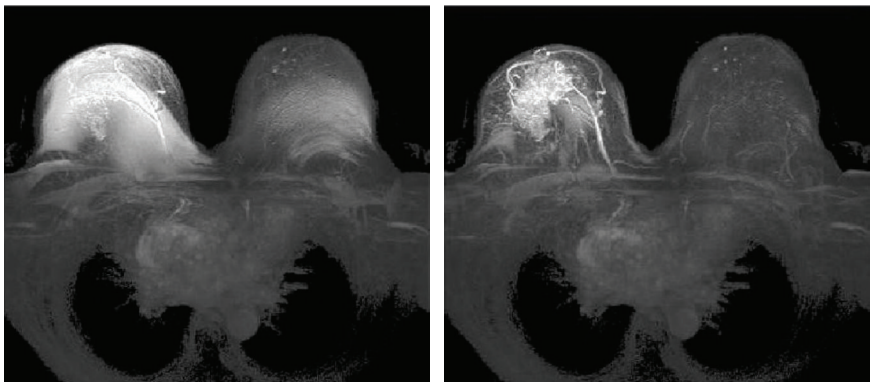

(a) (b)

Figure 4.3 Comparison of (a) nonregistered and (b) registered MIPs. The image quality is significantly superior in registered images (in N-REG images the motion artifacts introduce spurious enhancing voxels).

Unfortunately, few papers have addressed automatic lesion detection and segmentation techniques for breast DCE-MRI.[22–24] Furthermore, to our knowledge, these methods have been tested only on non–fat-saturated (fat-sat) contrast-enhanced images. Fat saturation allows enhancement of the contrast between the lesion and surrounding tissue[6] but introduces additional challenges for lesion segmentation, such as artifacts from inhomogeneous signal saturation and a lower contrast-to-noise-ratio between enhanced lesions and surrounding parenchyma.[25]

A new, fully automatic algorithm for breast lesion detection is presented.[26] The method has been conceived to run on both fat-sat and non–fat-sat DCE-MRI datasets obtained from different MR scanners.

4.3.1 Method

The detection pipeline of the CAD-BREAST MRI research-version system consists of three main processing steps, none of which requires user interaction:

(1) breast segmentation to automatically identify the breast and axillary regions;
(2) lesion detection to extract suspicious contrast-enhanced areas; and
(3) FP reduction to identify and discard regions incorrectly extracted.

4.3.1.1 Breast segmentation

The breast segmentation itself is preceded by a process of identifying the approximate breast size and location. A rough estimate of breast location is obtained by identifying the maximum point, defined as the most anterior point reached by the breasts, and the minimum point, which is the deepest point within the concavity between the breasts (Fig. 4.4).

These measures were obtained following a rough segmentation of the patient's body, based on Otsu's thresholding algorithm.[27] The central line, defined as the line running along the concavity between the breasts, was computed by exploiting image symmetry and by searching for the skin voxel around the center of each slice.

Once the central line has been obtained, two different procedures for breast segmentation are performed. If fat-sat is not used, the breasts can be easily identified based on the high signal intensity of fat tissue. Similarly to the technique used by Twellmann et al.,[24] a satisfactory segmentation can be obtained by combining morphological operations and Otsu's thresholding.[28] On the contrary, if fat-sat is used, intensity alone is not sufficient to obtain a reliable segmentation. In this case, an *a priori* knowledge of the main anatomical structures in the field of view was exploited, using an atlas-based segmentation scheme. A simplified atlas was used in which the breasts, heart, chest wall, and lungs have been previously

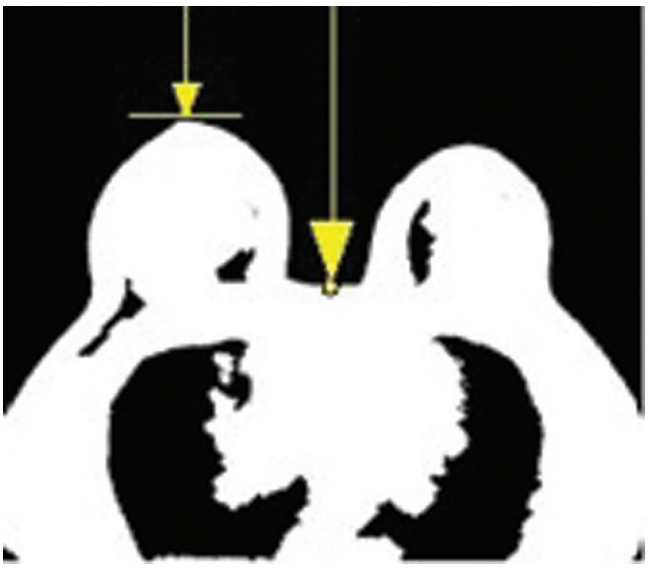

Figure 4.4 Arrows point to the maximum (left arrow) and minimum (right arrow) points.

manually segmented and color coded. Because breast size and shape may vary considerably across subjects, three different atlases were generated for large, medium, and small breasts. The most appropriate model was automatically selected for each patient according to breast size, measured as the distance between the maximum point and the minimum point along the central line.

The patient's body was identified by the abovementioned Otsu's thresholding method, and the image was first downsampled to a predefined resolution to reduce the computational burden, then it was registered to the appropriate breast atlas. Two examples of breast segmentation results are shown in Fig. 4.5.

The two methodologies yield slightly different results in the axillary area, but this is not compromising for lesion detection. Axillae, supraclavicular fossae, chest wall, and anterior mediastinum can be assessed by breast MRI (e.g., to search for enlarged lymph nodes), but their evaluation can be omitted, as there is no evidence of its diagnostic value.[25]

4.3.1.2 Lesion detection

Differences in vascular permeability[29,30] and other technical and physiological parameters, including type and dose of contrast material,[31,32] cause large physiologic variations in the contrast enhancement of breast lesions. Differences may depend on lesion histology, on the timing of imaging, or on inhomogeneities within the lesions, such as those observed in necrotic

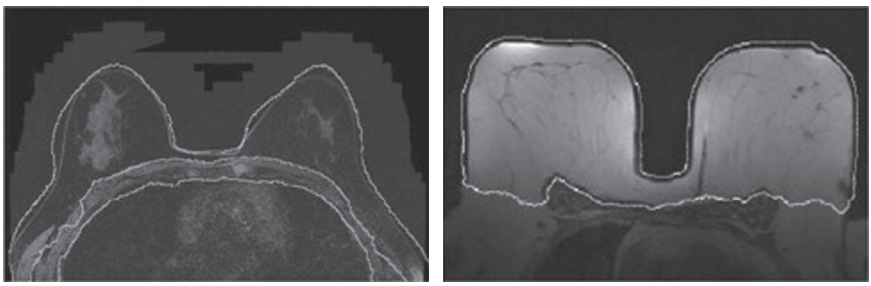

(a) (b)

Figure 4.5 (a) Example of breast segmentation for a study acquired with fat-sat. The breast mask extends farther than in non–fat-sat sequences, as defined by the breast atlas. (b) Example of breast segmentation for a study acquired without fat-sat.

areas or in fibrosis. The proposed approach used the subtracted mean intensity projection image over time (mIPT) in order to consider the nonuniform uptake of contrast, reducing at the same time the computational burden associated with processing all of the contrast-enhanced registered frames. The dynamic sequence is a 4D image ($x \times y \times z \times t$), where t is time, and the mIPT is the 3D image ($x \times y \times z$) formed by averaging along the t axis each voxel of each registered enhanced frame. In order to neglect the contribution of regions that do not show contrast enhancement, subtraction of the unenhanced frame was performed.

Different scanners, coils, acquisition modalities, types and amounts of contrast agent injected, and patient physiologies, along with other external factors, result in significant variations of image intensities among images acquired in different hospitals, in different patients, or even among different examinations from the same patient.[31,32] The subtracted mIPT was normalized by contrast enhancement of the mammary vessels to compensate for these effects.

In the first-dynamic-phase images, it is possible to obtain the best "angiographic effect" for both arteries and veins because in the subsequent acquisitions a more pronounced distribution of contrast material in the interstitial space reduces the vascular enhancement.[33] Therefore, the mammary vessels were automatically segmented on the first subtracted contrast-enhanced frame. Referring to the position of the central line, a suitable ROI was automatically selected by placing a rectangle of a fixed size in each slice. The mammary vessels were then identified by applying to the ROI the multiscale 3D Sato's vessel-enhancement filter, which is based on the eigenvalues of the Hessian matrix.[34,35]

Sato's vessel-enhancement filter considers the mutual magnitude of the eigenvalues as indicative of the shape of the underlying object; isotropic

structures are associated with eigenvalues that have a similar nonzero magnitude, while vessels present one negligible and two similar nonzero eigenvalues. Let the eigenvalues of the Hessian matrix be λ_1, λ_2, λ_3 (with $\lambda_1 > \lambda_2 > \lambda_3$). On a given scale, vesselness is thus defined as

$$V_\sigma = \begin{cases} \exp\left(\dfrac{\lambda_1^2}{2(\alpha_1\lambda_c)^2}\right) & \lambda_1 \le 0, \lambda_c \neq 0 \\ \exp\left(\dfrac{\lambda_1^2}{2(\alpha_2\lambda_c)^2}\right) & \lambda_1 > 0, \lambda_c \neq 0, \\ 0 & \lambda_c = 0 \end{cases} \tag{4.1}$$

where $\lambda_c = \min(\lambda_2, \lambda_3)$, and α_1 and α_2 are set to 0.5. The σ subscript in V_σ indicates that the vesselness is computed on a smoothed version of the image and is therefore representative of the variations of image intensity on the σ spatial scale. As vessels in the breasts can have different diameters, the vesselness is evaluated on a range of spatial scales, and the highest response is selected for each voxel. Specifically, the vesselness response is computed at 6 exponentially distributed scales between the maximum and minimum scales $\sigma_{min} = 0.5$ and $\sigma_{max} = 1.0$.

A threshold equal to one-half of the maximum vesselness value observed in the ROI identified as described above was then applied to select the most vessel-like voxels. Figure 4.6 shows an example of mammary vessels.

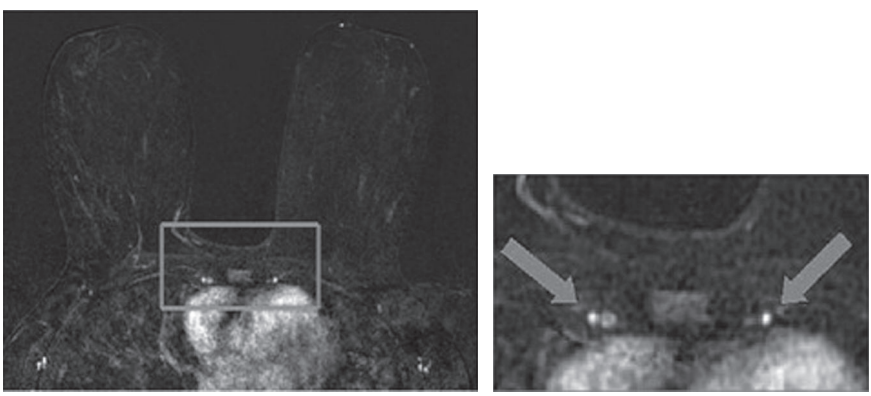

(a) (b)

Figure 4.6 (a) First subtracted contrast-enhanced frame with the region where the mammary vessels are located in the rectangle. (b) Zoom of the region in the rectangle highlighted in (a). Arrows point to mammary arteries that will be segmented by the system.

The mean contrast enhancement of the mammary vessel voxels in the first contrast-enhanced frame was considered as a normalization factor. After normalizing the subtracted mean intensity projection, regions showing contrast enhancement were extracted. Even if the contrast-enhanced frames were normalized, a fixed threshold was not found to be suitable to successfully segment lesions on all scans. As a consequence, a global threshold T_I was empirically determined as

$$T_I = mean_I + \frac{max_I}{3}, \tag{4.2}$$

where $mean_I$ is the mean value of the normalized intensity histogram of the breast and axillary region, and max_I is the highest intensity value observed in the same region.

Lesions and connected feeding vessels are often segmented together, leading to lesion oversegmentation, which can reduce the diagnostic quality of the segmentation and limit the performance of segmentation-based CAD applications. To avoid this risk, the eigenvalues of the covariance matrix were extracted for each voxel, and the ratio between the highest and medium eigenvalues was used as a vesselness measure. Voxels with a ratio larger than a fixed threshold T_v were labeled as vessels and excluded from lesion detection. Connected components were then extracted from the resulting mask.

4.3.1.3 False-positive reduction

The method based on the covariance matrix eigenvalues, described above, does not completely discard all vessels; therefore, together with motion artifacts and noise, the remaining vessels contribute to the number of FPs.

A few heuristic criteria were applied in our algorithm to exclude regions showing contrast enhancement that were different from lesions. First, regions with a volume of less than 20 mm^3 were excluded. Taking into account image resolution and possible lesion undersegmentation, this roughly corresponded to a lesion of 5 mm in diameter, which is the cutoff between foci and lesions.[36]

Contrast enhancement kinetics can be classified as curves I, II, and III with an increasing probability of malignancy (6%, 64%, and 87%, respectively).[37] However, these curves are commonly referred to individual voxels or to a set of several contiguous voxels within a plane belonging to a single portion of tissue that has uniform vascular characteristics and therefore has homogeneous contrast enhancement. The average intensity curve calculated over the entire lesion (typically without homogeneous vascular characteristics) is generally more similar to the average signal intensity curves shown in Fig. 4.7. Thus, the aim

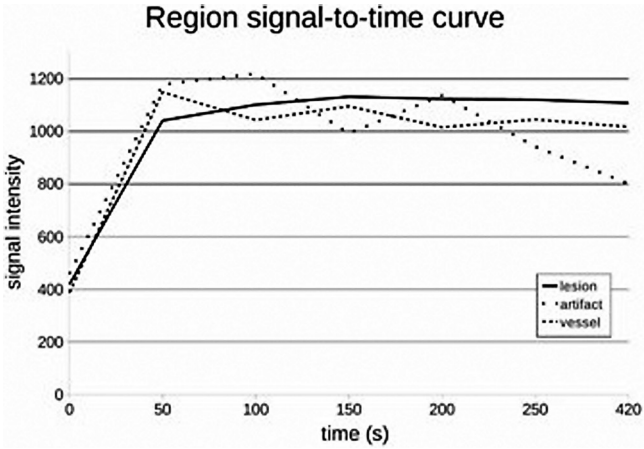

Figure 4.7 Signal intensity curves calculated over an entire connected component in the case of a lesion, a vessel and an artifact.

was to identify trends that are indicative of structures other than benign and malignant lesions, such as noise, artifacts, or vessels. Empirically, some simple kinetic features were found to identify trends that are rather typical of vessels or artifacts, as shown in Fig. 4.7. For instance, artifacts due to noise and patient motion are usually characterized by high signal variations; hence, regions with standard deviation greater than a specific value, or with a higher-than-10% decrease or increase in signal intensity in the last frame, with respect to the second-to-last frame, were discarded. Furthermore, regions with mean intensity decreasing from the first to the second enhanced frame were discarded, as this pattern is found in vessels but not in lesions.

4.3.2 Results

4.3.2.1 Subjects and MRI protocols

Algorithm performance was evaluated on a dataset of 48 DCE-MRI studies (mean patient age 51 years, range 31–79 years) performed on women with suspicion of breast cancer based on conventional imaging.[26]

Nineteen (group A) of the 48 studies were acquired on a 1.5T scanner, using a fat-sat 3D axial fast spoiled-gradient-echo sequence and administering gadopentetate dimeglumine, for a total of 7 scans for each study (1 baseline, 5 contrast-enhanced frames with 50-s time resolution, and one delayed frame acquired 7 min after contrast injection).

The remaining 29 studies (group B) were acquired on a different 1.5T scanner, using a dynamic 3D axial spoiled fast low-angle-shot sequence and administering Gd-BOPTA, for a total of 6 scans for each

study (1 baseline, 5 contrast-enhanced frames taken 118 s apart). Fat-sat sequences were not performed in group B patients.

The entire dataset included 12 benign and 53 malignant lesions. The median of the largest diameter of benign and malignant lesions was, respectively, 6 mm (range, 5–15 mm) and 26 mm (range, 5–75 mm). Overall, there were 16 lesions sized 10 mm or less, 15 lesions between 11 and 20 mm, and 34 lesions sized larger than 20 mm.

4.3.2.2 Statistical analysis

A radiologist with more than four years of experience in breast MRI labeled a finding as a TP if the lesion was confirmed at histology or at follow up, otherwise it was defined as a FP.

Detection rate was calculated as the number of TPs (both malignant and benign) over the total number of lesions as defined at the reference standard, whereas sensitivity was calculated as the number of malignant lesions detected by the system over the total number of malignant lesions.

Lesions were grouped according to size (see Table 4.1), and detection rate and sensitivity were calculated for each group. Sensitivity and detection rate values are presented with 95% confidence intervals (CIs) using the Wilson method for single proportions. Detection rate and sensitivity were also separately calculated for fat-sat and non–fat-sat exams, and the χ^2 test was used to assess differences between the two subgroups. Detection rate was analyzed separately for satellite lesions for which a lesion-by-lesion pathological analysis was not reported by the radiologist.

FP findings were recognized by the radiologist according to the position (mammary or extramammary) and the type (vessels, image artifacts, lymph nodes, normal gland, or other findings). The FP median, 1st, and 3rd quartiles were calculated for the entire testing set, and for the fat-sat and non–fat-sat subgroups. A two-sided Kruskal–Wallis test was applied to test for differences between the medians of the total number of

Table 4.1 Number of lesions and performance for each dimension group. Lesions were grouped according to the National Cancer Institute. Detection rate and sensitivity were calculated with a 95% CI.

Lesion dimension (mm)	Number malignant	Number benign	Number total	Detection rate (upper–lower limit; 95% CI)	Sensitivity (upper–lower limit; 95% CI)
5–10	6	10	16	69% (44–86%)	100% (61–100%)
11–20	13	2	15	87% (62–96%)	92% (67–99%)
> 20	34	0	34	100% (90–100%)	100% (90–99%)
Total	**53**	**12**	**65**	**89% (79–95%)**	**98% (90–99%)**

FPs/patient. A p-value of less than 0.05 was considered to be statistically significant.

4.3.2.3 Results

The automatic algorithm detected 58 of the 65 lesions (89% detection rate; 95% CI 79–95%), including 52 of the 53 malignant lesions (98% sensitivity; 95% CI 90%–99%). Detection rate and sensitivity according to lesion size are shown in Table 4.1.

In the fat-sat subgroup, 20 of the 25 lesions (80% detection rate; 95% CI 61%–91%) were detected, including 19 of the 20 malignant lesions (95% sensitivity; 95% CI 76%–99%). In the non-fat-sat subgroup, 38 of the 40 lesions (95% detection rate; 95% CI 84%–99%) were detected, including all 33 malignant lesions (100% sensitivity; 95% CI 90%–100%). Differences in sensitivity and detection rate between the two groups were not statistically significant (p-value = 0.798 and p-value = 0.137, respectively).

A total of 7 lesions with an average size of 7 ± 3 mm [mean ± standard deviation (std)] were missed by the algorithm, including 6 benign and 1 malignant nodules. Five of the undetected lesions were in dataset A, including: 2 fibroadenomas, 2 small enhancements with a negative MRI follow up of 5 mm and 7 mm in size, respectively, and a 12-mm invasive ductal carcinoma. Missed lesions in dataset B were two 5-mm small enhancements unchanged at MRI follow up. Examples of lesions detected and missed by the system are shown in Fig 4.8.

In addition to malignant lesions histologically confirmed as a result of a lesion-by-lesion analysis in the pathological report, 17 lesions satellite to malignant index lesions, with a median diameter of 7 mm (range, 5–20 mm) were detected by two radiologists. Sixteen of them (94%) were detected by the system.

Median mammary FPs per breast were 4 (1st–3rd quartiles 3–7.25), while median extramammary FPs per study were 2 (1st–3rd quartiles 1–5). Table 4.2 shows the distribution of FP findings according to the type. For the fat-sat subgroup, median mammary FPs per breast were 4 (1st–3rd quartiles 2–7.25); median extramammary FPs per study were also 4 (1st–3rd quartiles 3–6). In the non–fat-sat group, median mammary FPs per breast were 4.5 (1st–3rd quartiles 3.5–7), while median extramammary FPs per study were 1 (1st–3rd quartiles 1–2). No statistical significant differences were detected between the two subgroups (p-value = 0.72).

4.4 Lesion Discrimination

Lesion discrimination is a diagnostic stage in the CAD pipeline dedicated to recognizing the level of malignancy of previously detected lesions.

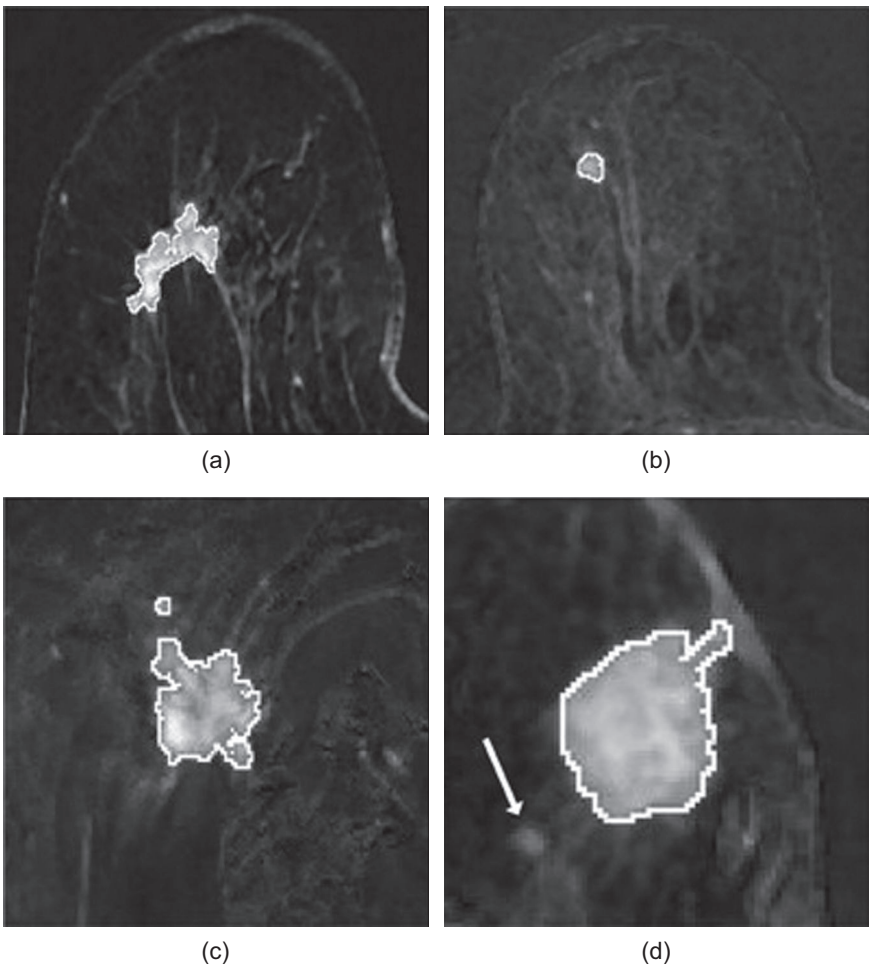

Figure 4.8 Examples of segmentation results superimposed on the normalized and subtracted mean projection over time: (a) a 33-mm invasive ductal carcinoma (fat-sat image) correctly segmented; (b) a 7-mm invasive ductal carcinoma (fat-sat image) correctly segmented; (c) a 26-mm invasive ductal carcinoma (non–fat-sat image) correctly segmented; (d) a 25-mm invasive ductal carcinoma (fat-sat image) correctly segmented; here a 5-mm satellite lesion (arrow) was missed by the system.

Breast DCE-MRI allows depiction of differences between malignant and benign lesions according to morphological and contrast-enhancement kinetic features of lesions.

Morphological attributes such as irregular or spiculated margins, irregular shapes, and heterogeneous and peripheral internal contrast enhancement are important indicators of malignancy.[38] Signal-to-time curves with a rapid decrease of signal intensity after peak enhancement,

Table 4.2 Classification of FP findings according to type.

FP findings		
Type	**Number**	**Percentage**
Vessels	267	54
Artifacts*	113	23
Glands	80	16
Lymph nodes	2	0.4
Other**	32	6

*e.g., chemical shift, skin, patient movement
**i.e., nipple, pectoral muscle

reached approximately 2 or 3 min after contrast injection, are more frequently found in malignant lesions, whereas benign lesions have typically slow, persistent enhancement increase.[38] Figure 4.9(a) shows an example of a malignant lesion with irregular margins and heterogeneous internal enhancement, and Fig. 4.9(b) shows a benign lesion with regular margins and homogeneous internal enhancement.

Clinical interpretation of the kinetic and morphological properties is subjective and qualitative; therefore, several studies have proposed computer-assisted approaches. Gihuijs et al.[39,40] extracted morphological and kinetic features from lesions segmented manually or semi-automatically after manual indication of a seed point and used linear discriminant analysis and step-wise selection to select the best subset of features. Gibbs et al.[41] applied texture analysis based on Haralick features and used logistic regression analysis with a backward elimination method to select the most

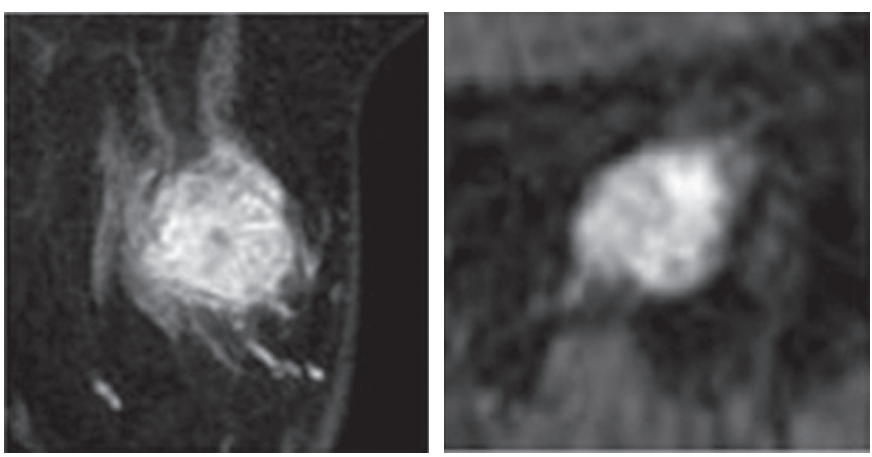

(a) (b)

Figure 4.9 Examples of invasive ductal carcinoma (a) and benign fibroadenoma (b) breast lesions.

discriminating subset of texture features. Gal et al.[42] compared different classifiers (logistic regression, linear discriminant analysis, Bayesian, and SVM), combining kinetic and morphological features, and using an exhaustive search to select the best features.

In the following section, a multiparametric model is presented that combines a selection of morphological and kinetic features for discriminating malignant from benign mass-like breast lesions in DCE-MRI.[43] Original features are introduced and combined with features already presented in literature, with the aim of trying a different approach. Model selection is performed by a genetic search[44] and a wrapper approach[45] using a support vector regressor.

4.4.1 Method

To validate the method, 73 mass-like lesions were retrospectively used. Lesions were detected in 51 exams acquired in two centers at 1.5T with the MRI protocols described in Section 4.3.2.1 and confirmed by histopathology (54 malignant and 19 benign). Lesions were automatically segmented after image normalization and elastic registration of contrast-enhanced frames, as described in the previous steps, and then selected by two experienced radiologists in order to exclude non–mass-like lesions or blood vessels.

Lesion size was 13 ± 8.4 mm (mean ± std) for benign lesions and 16.1 ± 14.7 mm for malignant lesions, with lesion size determined as the longest diameter measured by radiologists. Thirty-three lesions had a size smaller than 10 mm (22 malignant, 11 benign), whereas 40 lesions had a size larger than 10 mm (32 malignant, 8 benign). Table 4.3 summaries the lesion histology.

For each lesion, a set of 19 features was automatically extracted: 10 morphological features related to shape, margins, and internal contrast-enhancement distribution, and 9 kinetic features computed from

Table 4.3 Histological types of the 73 lesions included in the study.

Tumor types	Number
Malignant lesions	54
Invasive ductal carcinoma	36
Invasive lobular carcinoma	4
Ductal carcinoma *in situ*	4
Mixed invasive carcinoma	10
Benign lesions	19
Fibroadenoma	9
Papilloma	4
Other benign lesions	6

signal-to-time intensity curves. Two morphological features related to the lesion shape are calculated on the binary mask: circularity[39] and convex index.[46]

Three features are used to describe the margin of the lesion: irregularity,[39] mean and standard deviation of angles between surface normals [(mean(ABSN) and std(ABSN), respectively].[47] Five other features characterizing the internal enhancement pattern are extracted: the autocorrelation function (evaluated at 2-mm displacement), two features related to the peripheral uptake, and one feature related to the mean and one to the standard deviation of the shape index (SI)[48] computed inside the segmented mass.

Enhancement kinetic features are used to characterize the time course of signal intensity through the contrast enhancement defined as

$$C(\mathbf{r},i) = \frac{S(r,i) \quad S(r,0)}{S(r,0)} \quad i = 1, \ldots, N(N = 5/6), \tag{4.3}$$

where $S(\mathbf{r}, i)$ is the intensity at voxel location r at time frame i, and it is normalized to the contrast enhancement of mammary vessels. Two types of features are derived from the contrast enhancement. The first type is related to the fitting of the contrast enhancement to the following analytical exponential function:

$$C(t) = Ate^{-t^D}, \tag{4.4}$$

where the coefficients A and D control the function amplitude and decay, respectively. These coefficients therefore characterize the contrast uptake and washout inside the lesion. The lesion uptake and washout of contrast material were characterized by fitting the contrast enhancement $C(\mathbf{r}, i)$ with an analytical function rather than using a two-compartmental pharmacokinetic model.[49] The use of a pharmacokinetic model implies strict constraints in the acquisition protocol[50] that were not fulfilled in the acquisition of many clinical datasets. Although the analytical function proposed [Eq. (4.4)] cannot physiologically model the lesion, its simple form allows for relaxing constraints on the acquisition protocols still characterizing the kinetic behavior of the lesion.

The second type of feature computes the area under the contrast enhancement curve $C(\mathbf{r}, i)$ (AUCEC). This feature is related to the total amount of contrast material in the lesion tissue. The mean, standard deviation, and entropy were computed in the lesion segmented volume, yielding a total of nine contrast-enhancement kinetic features.

A SVM was trained with feature subsets selected by a genetic search. The best subsets were composed of the features most frequently selected

by majority rule. The performance was measured by ROC analysis with the 10-fold cross-validation method that prevents optimistically biased evaluations due to overfitting. The bootstrap technique was used in order to estimate the confidence interval of the AUC and to compare the classification performances of the different feature subsets. A Wilcoxon matched-pairs one-tailed test was also performed to determine the significance level of the performance improvement.

4.4.2 Results

Figure 4.10 shows the mean ROC curves related to the feature subsets selected in separate genetic searches for each class of features and to the feature subset selected by the genetic search using both classes of features.

Mean(ABSN), std(ABSN), and peripheral uptake were selected for the morphological subset, while mean(D), entropy(D), and entropy(A) were selected for the kinetic subset. From the combination of the morphological and kinetic features, the mean(ABSN), std(SI), mean(D), and mean(AUCEC)] were selected.

The AUC obtained in the three genetic searches were 0.90 ± 0.06 (mean ± std) for the morphological features subset, 0.87 ± 0.06 for the kinetic features subset, and 0.94 ± 0.03 for the combined feature subset. The AUC resulting from the combined feature subset was significantly

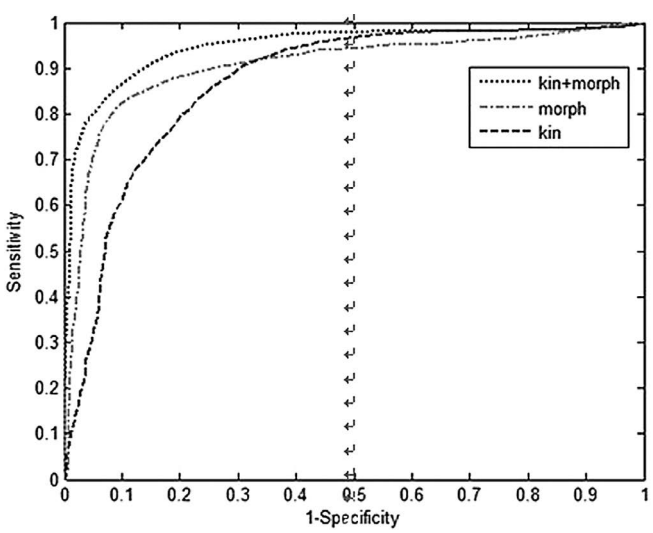

Figure 4.10 ROC curves associated with the feature subsets selected in separate genetic searches for each class of features and with the feature subset selected by the genetic search using both classes of features.

higher (p-value < 0.01) than those obtained with the other feature subsets, showing that the combination of features increases the classification performances.

4.5 Discussion and Conclusions

The CAD system (im3D's research version of CADBREAST MRI) presented here achieves good performance in detecting and discriminating breast lesions in a fully automatic manner, thus having the potential of reducing inter- and intra-observer variability and reading time.[19,21]

The lesion-detection step achieved a sensitivity of 98%, with an acceptable number of FP findings. Moreover, the good performance obtained in detecting satellite lesions (16 of 17 were identified) highlights the system's potential to aid in the detection of multifocal and multicentric breast cancers.

The widespread use of the DCE-MRI in clinical practice is hindered by the lack of automatic methods to make its analysis less time consuming and independent of the expertise of the radiologist. Few methods have been developed to detect and characterize breast lesions automatically with DCE-MRI. Ertas et al. developed an automatic algorithm for the detection of breast lesions based on cellular neural network segmentation and 3D template matching,[22] but their dataset was composed only of non–fat-sat images, and they applied a fixed threshold to extract suspicious areas, limiting the applicability to studies acquired with different protocols. They assessed the performance of the system on a dataset of 39 lesions (19 benign and 20 malignant), obtaining a detection rate of 100% with less than one FP per study. An automatic lesion-detection method based on the SVM, proposed by Twellmann et al. also showed promising results, yielding an AUC of 0.98. However, the algorithm was tested on a limited dataset of 12 patients and only on non–fat-sat images.[24]

The innovation of the proposed lesion-detection method relies on the possibility of being used with both fat-sat and non–fat-sat images since the normalization is not performed by dividing each enhanced image by an unenhanced image, but by using an intrinsic value of the image related to contrast agent administration. The normalization process used in literature, in fact, yields very noisy images if fat-sat is applied, as most of the breast signal is suppressed in the unenhanced frame. On the other hand, the proposed normalization requires that the mammary vessels be included in the field of view with an adequate spatial resolution; therefore, DCE-MRI should be performed on the axial plane.

A second innovation relies on the use of the mIPT instead of the commonly used MIPT (maximum-intensity projection over time). The MIPT is very sensitive to artifacts and noise, and, due to the "blooming sign"

effect,[51–53] the lesion size can be overestimated. Vice versa, the use of the mIPT can produce an underestimation of the lesion size by averaging over time but allows more reliable segmentations, as it is less sensitive to noise and thus produces a lower number of FPs.

The higher number of FPs compared to other commercial and academic software[54] is a limitation of the proposed method. As most of the FPs are vessels, mainly tortuous vessels or bifurcations with low vesselness values,[55,56] research on fully automatic blood vessel detection is ongoing, aiming to dramatically decrease the number of FPs. Moreover, improving the accuracy of the breast-segmentation step, especially around the ribcage area, could lead to an increase in the specificity of the lesion-detection step.

In the proposed method the detected lesions were analyzed and discriminated by a classifier based on the SVM. For this step a more accurate identification of lesion boundary and morphology could be useful, and further refinement of the lesion segmentation may become necessary, even if the results obtained during the lesion-discrimination step are satisfactory.

The classifier proposed here is able to discriminate malignant from benign breast mass-like lesions using two groups of features (morphological and kinetic), and obtaining an AUC of 0.94 ± 0.03. The AUC for the feature selection (FS) resulting from the combination of both feature groups was significantly higher than that the AUCs obtained with all other selected FSs, showing that the combination of features increases the classification performance.

A genetic algorithm was used for selecting feature subsets in order to prevent unnecessary computation and overfitting, and to ensure a reliable classifier. The main limitation of the discrimination step is the limited number of lesions. This can produce overfitting of the training data, leading to an overestimate of the classifier's performance. In order to reduce these effects, the total number of features was limited to 19, and the selected feature subsets were composed only of 3 to 4 features. Moreover, classification performances were evaluated with a stratified 10-fold cross-validation method to reduce the classification bias.

Another limitation is the unbalanced dataset. The number of malignant lesions is higher than the number of benign lesions, leading to a possible bias in the discrimination of malignancy. This problem was partially reduced by presenting at training the same number of malignant and benign lesions using copies of benign lesions. Nevertheless, the benign class might be poorly described in the feature space.

In conclusion, the proposed CAD system was tested on MR datasets obtained from different scanners, with a variable temporal and spatial resolution and on both fat-sat and non–fat-sat images, and has shown promising results. This type of system could potentially be used for early diagnosis and staging of breast cancer to reduce reading time and to improve

detection, especially of the smaller satellite nodules. Further refinements are ongoing to improve vessel detection and breast segmentation, and to validate these conclusions on a larger dataset.

References

1. M. C. Mahoney, T. Bevers, E. Linos, and W. C. Willett, "Opportunities and strategies for breast cancer prevention through risk reduction," *CA Cancer J. Clin.* **58**, 347–371 (2008).
2. P. Boyle and J. Ferlay, "Cancer incidence and mortality in Europe, 2004," *Ann. Oncol.* **16**, 481–488 (2005).
3. Q. Wu and M. K. Markey, "Computer-Aided Diagnosis of Breast Cancer on MR Imaging," Chapter 22 in *Recent Advances in Breast Imaging, Mammography, and Computer-Aided Diagnosis of Breast Cancer,* J. S. Suri and R. M. Rangayyan, Eds., SPIE Press, Bellingham, WA (2006) [doi: 10.1117.3.651880].
4. K. Chakraborti, P. Bahl, M. Sahoo, S. Ganguly, and C. Oberoi, "Magnetic resonance imaging of breast masses: Comparison with mammography," *Indian J. Radiol. Imaging* **15**, 381–387 (2005).
5. F. Montemurro, L. Martincich, I. Sarotto, et al., "Relationship between DCE-MRI morphological and functional features and histopathological characteristics of breast cancer," *Eur. Radiol.* **17**, 1490–1497 (2007).
6. C. K. Kuhl, "The current status of breast MR imaging. Part I. Choice of technique, image interpretation, diagnostic accuracy, and transfer to clinical practice," *Radiol.* **244**, 356–378 (2007).
7. C. K. Kuhl, "Current status of breast MR imaging. Part 2. Clinical applications," *Radiol.* **244**, 672–691 (2007).
8. F. Sardanelli, G. M. Giuseppetti, G. Canavese, et al., "Indications for breast magnetic resonance imaging. Consensus document, "Attualita in senologia," Florence 2007," *Radiol. Med.* **113**, 1085–1095 (2008).
9. F. Sardanelli, C. Boetes, B. Borisch, et al., "Magnetic resonance imaging of the breast: recommendations from the EUSOMA working group," *Eur. J. Cancer* **46**, 1296–1316 (2010).
10. L. C. Wang, W. B. De Martini, S. C. Partridge, S. Peacock, and C. D. Lehman, "MRI-detected suspicious breast lesions: Predictive values of kinetic features measured by computer-aided evaluation," *Am. J. Roentgenol*. **193**(3), 826–831 (2009).
11. D. Rueckert, L. I. Sonoda, C. Hayes, D. L. Hill, M. O. Leach, and D. J. Hawkes, "Nonrigid registration using free-form deformations:

Application to breast MR images," *IEEE Trans. Med. Imaging* **18**, 712–721 (1999).

12. L. Ibàñez, W. Schroeder, L. Ng, and J. Cates, *The ITK Software Guide,* 1st edition, Kitware Inc. (2005).
13. D. Mattes, D. Haynor, H. Vesselle, T. W. E. Lewellyn, and W. Eubank "Nonrigid multimodality image registration," *Proc. SPIE* **4322**, 1609–1620 (2001) [doi: 10.1117/12.431046].
14. C. Broyden, "The convergence of a class of double-rank minimization algorithms 1. General considerations," *IMA J. Appl. Math.* **6**, 76–90 (1970).
15. L. A. Carbonaro, D. Persano, S. Delsanto, D. Brizzi, A. Vignati, V. Giannini, L. Morra, A. Bert, and F. Sardanelli, "Non-rigid registration of contrast-enhanced (CE) MR images of the breast," *Proc. European Congress of Radiology*, 4–8 March 2010, Vienna, Austria (2001).
16. L. Carbonaro, D. Persano, S. Delsanto, D. Brizzi, A. Vignati, V. Giannini, A. Bert, and F. Sardanelli, "Evaluation of non-rigid registration method for MR with contrast agent injection images applied to the breast," *Proc. National Conference of Senology*, Ancona, Italy, 18–20 June (2009).
17. J. D. Gibbons, *Nonparametric Statistical Inference*, 2nd edition, Marcel Dekker (1985).
18. I. Bankman, T. Nizialek, I. Simon, O. Gatewood, I. Weinberg, and W. Brody, "Algorithms for segmenting small-low contrast objects in images," Chapter 21 in *Recent Advances in Breast Imaging, Mammography, and Computer-Aided Diagnosis of Breast Cancer,* J. S. Suri and R. M. Rangayyan, Eds., SPIE Press, Bellingham, WA (2006) [doi: 10.1117.3.651880].
19. S. Mussurakis, D. L. Buckley, and A. Horsman, "Dynamic MRI of invasive breast cancer: Assessment of three region-of-interest analysis methods," *J. Comput. Assist. Tomogr.* **21**, 431–438 (1997).
20. G. P. Liney, P. Gibbs, C. Hayes, M. O. Leach, and L. W. Turnbull, "Dynamic contrast-enhanced MRI in the differentiation of breast tumors: User-defined versus semi-automated region-of-interest analysis," *J. Magn. Reson. Imaging* **10**, 945–949 (1999).
21. T. Niemeyer, C. Wood, K. Stegbauer, and J. Smith, "Comparison of automatic time curve selection methods for breast MR CAD," *Proc. SPIE* **5370**, 785–790 (2004) [doi: 10.1117/12.535992].
22. G. Ertas, H. O. Gulcur, O. Osman, O. N. Ucan, M. Tunaci, and M. Dursun, "Breast MR segmentation and lesion detection with cellular neural networks and 3D template matching," *Comput. Biol. Med.* **38**, 116–126 (2008).

23. B. J. Woods, B. D. Clymer, T. Kurc, et al., "Malignant-lesion segmentation using 4D co-occurrence texture analysis applied to dynamic contrast-enhanced magnetic resonance breast image data," *J. Magn. Res. Imaging* **25**, 495–501 (2007).
24. T. Twellmann, A. Saalbach, C. Muller, T. W. Nattkemper, and A. Wismuller, "Detection of suspicious lesions in dynamic contrast enhanced MRI data," *Proc. IEEE Eng. Med. Biol. Soc.* **1**, 454–457 (2004).
25. R. M. Mann, C. K. Kuhl, K. Kinkel, and C. Boetes, "Breast MRI: Guidelines from the European Society of Breast Imaging," *Eur. Radiol*. **18**, 1307–1318 (2008).
26. A. Vignati, V. Giannini, M. De Luca, et al. "Performance of a fully automatic lesion detection system for breast DCE-MRI," *J. Magn. Res. Imaging* **34**(6), 1341–1351 (2011).
27. N. Otsu, "A threshold selection method from gray-level histograms," *IEEE Trans. Syst. Man. Cybern. B* **9**, 62–66 (1979).
28. V. Giannini, A. Vignati, L. Morra, D. Persano, D. Brizzi, L. Carbonaro, A. Bert, F. Sardanelli, and D. Regge, "A fully automatic algorithm for segmentation of the breasts in DCE-MR images," *Conf. Proc. IEEE Eng. Med. Biol. Soc*. **2010**, 3146–3149 (2010).
29. I. Gribbestad, K. Gjesdal, G. Nilsen, S. Lundgren, M. Hjelstuen, and A. Jackson, "An introduction to dynamic contrast-enhanced MRI in oncology," *Dynamic Contrast-enhanced Magnetic Resonance Imaging in Oncology*, A. Jackson, D. Buckley, and G. J. M. Parker, Eds., pp. 3–20, Springer Verlag, Heidelberg (2005).
30. S. H. Heywang-Kobrunner and R. Beck, *Contrast-Enhanced MRI of the Breast,* pp. 229, Springer, New York (1996).
31. L. A. Carbonaro, N. Verardi, G. Di Leo, and F. Sardanelli, "Handling a high relaxivity contrast material for dynamic breast MR imaging using higher thresholds for the initial enhancement," *Invest. Radiol.* **45**, 114–120 (2010).
32. F. Sardanelli, A. Fausto, A. Esseridou, G. Di Leo, and M. A. Kirchin, "Gadobenate dimeglumine as a contrast agent for dynamic breast magnetic resonance imaging: Effect of higher initial enhancement thresholds on diagnostic performance," *Invest. Radiol.* **43**, 236–242 (2008).
33. F. Sardanelli, A. Iozzelli, A. Fausto, A. Carriero, and M. A. Kirchin, "Gadobenate dimeglumine-enhanced MR Imaging breast vascular maps: Association between invasive cancer and ipsilateral increased vascularity," *Radiol.* **235**, 791–797 (2005).
34. L. Antiga, "Generalizing vesselness with respect to dimensionality and shape," *The Insight Journal*, July–December (2007). Available at: http://hdl.handle.net/1926/576. Accessed September 2011.

35. Y. Sato, S. Nakajima, N. Shiraga, et al., "Three-dimensional multi scale line filter for segmentation and visualization of curvilinear structures in medical images," *Med. Image Anal.* **2**, 143–168 (1998).
36. ACR Practice guideline for the performance of contrast-enhanced magnetic resonance imaging (MRI) of the breast. 2008. Available at: http://www.acr.org/secondarymainmenucategories/quality_safety/guidelines/breast/mri_breast.aspx. Accessed September 2011.
37. C. K. Kuhl, P. Mielcareck, S. Klaschik, et al., "Dynamic breast MR imaging: Are signal intensity time course data useful for differential diagnosis of enhancing lesions?" *Radiol.* **211**, 101–110 (1999).
38. Breast Imaging Reporting and Data System (BIRADS) 2003. Available at: http://www.acr.org/SecondaryMainMenuCategories/quality_safety/BIRADSAtlas/BIRADSAtlasexcerptedtext/BIRADSMRIFirstEdition.aspx Accessed September 2011.
39. K. G. Gilhuijs, M. L. Giger, and U. Bick. "Computerized analysis of breast lesions in three dimensions using dynamic magnetic-resonance imaging" *Med. Phys.* **9**, 1647–1654 (1998).
40. K. G. Gilhuijs, E. Deurloo, S. H. Muller, J. L. Peterse, and L. J. Schultze Kool, "Breast MR imaging in women at increased lifetime risk of breast cancer: Clinical system for computerized assessment of breast lesions," *Radiol.* **225**, 907–916 (2002).
41. P. Gibbs and L. Turnbull, "Textural analysis of contrast-enhanced images of the breast," *Magn. Reson. Med.* **50**, 92–98 (2003).
42. Y. Gal, A. Mehnert, A. Bradley, et al., "Feature and classifier selection for automatic classification of lesions in dynamic contrast-enhanced MRI of the breast," *Proc. Digital Image Computing: Techniques and Applications (DICTA)*, 132–139 (2009).
43. S. Agliozzo, M. De Luca, L. Martincich, et al., "A multiparametric model combining a selection of morphological, kinetic, and spatio-temporal features of mass-like lesions at breast MRI*," Proc. RSNA Annual Meeting*, November 28–December 3, Chicago IL (2010). Available at: http://rsna2010.rsna.org/search/search.cfm?action=add&filter=Author&value=89595
44. L. J. Eshelman, "The CHC Adaptive Search Algorithm," in *Foundations of Genetic Algorithms*, G. J. E. Rawlins, Ed., Morgan Kaufmann Publishers, San Mateo, CA (1991) .
45. R. Kohavi and G. John, "Wrappers for feature subset selection," *Artif. Intell*. **97**, 273–324 (1997).
46. C. B. Barber, D. P. Dobkin, and H. T. Huhdanpaa, "The Quickhull algorithm for convex hulls," *ACM Trans. Math. Software* **22**, 469–483 (1996).

47. T. Zhang and G. Nagy, "Surface turtuosity and its application to analyzing cracks in concrete," *Proc. IAPR International Conference on Pattern Recognition*, 851–854 (2004).
48. J. Koenderink, *Solid Shape*, MIT Press, Cambridge, MA (1990).
49. P. Tofts "Modelling tracer kinetics in dynamic Gd-DTPA MR imaging," *J. Magn. Res. Imaging* **7**, 91–101 (1997).
50. E. Henderson, B. K. Rutt, and T. Y. Lee, "Temporal sampling requirements for the tracer kinetics modeling of breast disease," *Magn. Reson. Imaging* **16**, 1057–1073 (1998).
51. M. Dietzel, P. A. Baltzer, T. Vag, et al., "Differential diagnosis of breast lesions 5 mm or less: Is there a role for magnetic resonance imaging?," *J. Comput. Assist. Tomogr*. **34**(3), 456–464 (2010).
52. A. Penn, S. Thompson, R. Brem, et al., "Morphologic blooming in breast MRI as a characterization of margin for discriminating benign from malignant lesions," *Acad. Radiol*. **13**(11), 1344–1354 (2006).
53. D. R. Fischer, S. Wurdinger, J. Boettcher, A. Malich, and W. A. Kaiser, "Further signs in the evaluation of magnetic resonance mammography: A retrospective study," *Invest. Radiol*. **40**(7), 430–435 (2005).
54. K.D. Kurz, D. Steirthaus, V. Klar, et al., "Assessment of three different software systems in the evaluation of dynamic MRI of the breast," *Eur. J. Radiol.* **69**(2), 300–307 (2009).
55. C. Kirbas and F. Quek, "A review of vessel extraction techniques and algorithms," *ACM Comput. Surveys* **36**(2), 81–121 (2004).
56. M. Freiman, L. Joskowicz, and J. Sosna, "A variational method for vessel segmentation: Algorithm and application to liver vessels visualization," *Proc. SPIE* **7261**, 72610H (2009) [doi: 10.1117/12.810611].

Valentina Giannini received her M.Sc. degree in Biomedical Engineering in 2007 and the High Qualification Ph.D. in Biomedical Engineering offered by the "Scuola Interpolitecnica" at the Politecnico di Torino, Torino, Italy. During her Ph.D. program she spent six months studying at the Radiological Science Lab. of Stanford University. She is presently a researcher at the Institute for Cancer Research and Treatment (IRCC), Candiolo, Torino, Italy. Her current research area is biomedical image processing, especially on MR images.

Anna Vignati received her M.Sc. degree in Physics in 2006 and her Ph.D. degree in Complex Systems of Post-genomic Biology in 2010 from the University of Torino, Torino, Italy. She is presently a researcher at the Institute for Cancer Research and Treatment (IRCC), Candiolo, Torino, Italy. Her current research area is biomedical image processing, especially on MR images.

Massimo De Luca received his M.Sc. degree in Telecommunications Engineering in 2001 and his Ph.D. degree in Bioengineering in 2008 from the University of Padova, Italy. He is presently a researcher at the Institute for Cancer Research and Treatment (IRCC), Candiolo, Torino, Italy. His current research area is biomedical image processing, especially on MR images.

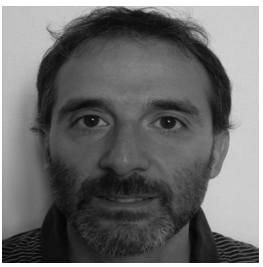

Silvano Agliozzo received his M.Sc. degree from the University of Torino, Torino, Italy, in 1998, and his Ph.D. from Joseph Fourier University, Grenoble, France, in 2002, both in Physics. From 2002 to 2004, he was a researcher collaborating with the ISI Foundation, Institute for Scientific Interchange, Torino, Italy. Currently, he is a researcher at im3D S.p.A., Medical Imaging Laboratory, Torino, Italy. His research interests include medical decision support systems, CAD applied to virtual colonoscopy, breast dynamic contrast-enhancement MRI, and breast digital tomosynthesis.

Alberto Bert received his M.Sc. in Chemistry in 2001 and his Ph.D. degree in 2006 from the University of Torino, Torino, Italy. After a postdoctorate at the University of California, Los Angeles, he is currently the Head of Research at im3D S.p.A. and teaches the course “Analysis of Biomedical Images and Signals” at the University of Turin. His main research interests are image analisys and CAD systems.

Lia Morra received her M. Sc. degree in Computer Engineering in 2002 and her Ph.D. degree in Computer Engineering from the Politecnico di Torino in 2006. Since 2006 she has been a researcher at im3D S.p.A., Medical Imaging Lab. Her current research area focuses on CAD and diagnosis systems, with special emphasis on the detection of breast and colon cancer.

Diego Persano received his M.S. degree in Industrial Engineering from the National University of General Sarmiento, Buenos Aires, Argentina, in 2003, and a second M.S. degree in modeling and simulation of complex realities from the International Centre for Theoretical Physics, Trieste, Italy, in 2005. He is currently an employee of im3D S.p.A., Torino, Italy. His research interests include medical image processing and CAD systems for early detection and prevention of cancer.

Filippo Molinari is Assistant Professor of Biomedical Engineering at the Department of Electronics of the Politecnico di Torino, Torino, Italy. His main research interests include biomedical signal processing and medical imaging. He is an expert in automated techniques for aiding the diagnostic process in ultrasound imaging. Vascular sonography, atherosclerosis, and tumor detection are Dr. Molinari's main research topics. He has published more than 80 peer-reviewed articles and 3 collaborative books. Dr. Molinari is a member of the IEEE EMBS, the European Society for Molecular Imaging (ESMI), and of the American Institute of Ultrasounds in Medicine (AIUM). He is Regional Associate Editor for Europe of the *Journal of Medical Imaging and Health Informatics* and is on the Editorial Board of five other international journals.

Daniele Regge received his M.D. degree from University of Torino, Faculty of Medicine in 1984. He proceeded with a specialization in Radiology, at the Institute of Radiology, University of Torino, in 1988. Since 1997, he has been Director of the Radiology Department of the Institute for Cancer Research and Treatment (IRCC), Candiolo, Italy. He is a member of the Scientific Editorial Board for *European Radiology*. His research interest areas are diagnostic colon, breast, and prostate imaging and development of CAD systems.

Chapter 5
Advanced Modality Imaging of the Systemic Spread of Breast Cancer

Cher Heng Tan
Department of Diagnostic Radiology, Tan Tock Seng Hospital, Singapore

5.1 Staging Evaluation of Breast Cancer

In this section we highlight a few of the international consensus guidelines on the use of imaging in staging assessment of breast cancer (BC). The role of imaging in the screening of breast cancer is an entirely different subject and beyond the scope of current discussion.

Based on the 7th edition of the American Joint Committee on Cancer (AJCC), BC is staged according to the TNM classification, as with other common solid adult tumors. The T-stage (primary tumor) is dependent on tumor size, invasion of chest wall (importantly, deep

to the pectoralis muscles) and skin, and presence of an inflammatory component.[1] The N-stage (nodal) is determined by the presence and numbers of involved nodes based on location; involvement of supraclavicular, infraclavicular, and internal mammary lymph nodes confer a higher nodal stage than do axillary lymph nodes, in that order. Presence of microscopic foci of tumor cells in circulating blood, bone marrow, or nonregional nodal tissue in asymptomatic patients constitutes M0 (i+) disease, while macroscopic deposits in distant organs constitutes M1 disease.

Recommendations from the National Institute for Health and Clinical Excellence (NICE) of the United Kingdom are as follows: For early and locally advanced breast cancer, pretreatment ultrasound (US) evaluation of the axillae should be performed for all patients being investigated for early invasive breast cancer, and, if morphologically abnormal lymph nodes are identified, US-guided needle sampling should be offered. For advanced breast cancer, one should assess the presence and extent of visceral metastases using a combination of chest radiography (CXR), US, computed tomography (CT) scans, and MRI. To assess the presence and extent of metastases in the bones of the axial skeleton, bone windows on a CT scan or MRI or bone scintigraphy (BS) should be employed. The proximal limb bones should be assessed for the risk of pathological fracture in patients with evidence of bone metastases elsewhere, using BS and/or CXR. MRI should be employed to assess bony metastases if other imaging is equivocal for metastatic disease or if more information is needed (for example, if lytic metastases are encroaching on the spinal canal). Positron emission tomography fused with computed tomography (PET-CT) should only be used to make a new diagnosis of metastases for patients with breast cancer whose imaging is suspicious but not diagnostic of metastatic disease.[2] In the ensuing sections of this chapter, the use of PET-CT considers only the use of F^{18}-deoxyglucose; use of other novel tracers will be discussed in a separate chapter.

The American College of Radiology (ACR) has issued a limited set of Appropriateness Criteria® guidelines for BC. In asymptomatic stage 1 BC disease, imaging for detection of metastases is generally not recommended.[3] This is echoed by a more detailed set of guidelines issued by the Breast Cancer Disease Site Group (BCDSG, Ontario) concerning imaging for BC.[4] The evidence for the BCDSG guidelines is modality specific as well as organ-system specific. The recommendations also take into account the incidence of metastatic disease in BC.

Based on the review of the literature by BCDSG, it was concluded that incidence of skeletal metastases detected on BS increased with tumor stage (in 0.5% of women with stage I disease, in 2.4% with stage II, and in 8.3% with stage III). The incidence of metastases detected by liver US also

increased with tumor stage (in no patients with stage I disease, in 0.4% with stage II, and in 2.0% with stage III). Similar findings for lung metastases were detected on CXR (in 0.1% of stage I patients, in 0.2% of stage II, and in 1.7% of stage III). Variably high false-positive (FP) rates were encountered for each of the abovementioned imaging modalities (10% to 22% for bone scanning, 33% to 66% for liver US, and 0 to 23% for CXR). Hence, use of imaging for BC staging evaluation should be prudent and performed in tandem with tumor stage.

According to the BCDSG guidelines, for asymptomatic patients who have undergone surgery for their BC and where the treatment options are restricted to tamoxifen or no further treatment because of age or other factors, the use of routine staging should be discouraged. Women who have stage II disease should undergo routine BS for detection of bone metastases. US of the liver and CXR are not routinely indicated in this group. In women with pathological stage III tumors, routine bone scan, liver US and CXR should be performed postoperatively.

5.2 Nodal Disease

The axillary lymph nodes are divided into three levels based on their position relative to the pectoralis minor muscle.[5] Level 1 nodes lie lateral to the lateral border of the pectoralis minor, level 2 nodes lie between the medial and lateral borders of the pectoralis minor, and level 3 nodes lie medial to the medial border of the pectoralis minor (Fig. 5.1).

Axillary lymph node involvement is one of the most important prognostic factors in BC. For detection of axillary lymph node metastases, more invasive methods such as sentinel lymph node biopsy (SNLB) or four-node

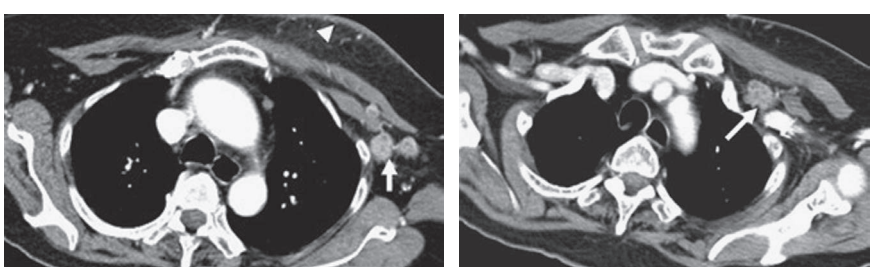

(a) (b)

Figure 5.1 (a) Axial contrast enhanced CT (CECT) image shows metastatic level 1 axillary lymph nodes (arrow). Note changes of skin thickening (arrowhead), consistent with inflammatory breast cancer, a subtype that confers poorer prognosis. (b) Axial CECT image shows metastatic level 3 axillary lymph node (medial to the medial border of the pectoralis minor muscle) (arrow). This implies deeper lymphatic dissemination and is associated with poorer prognosis.

sampling are most accurate and considered to be the reference standards. SLNB is based on the drainage pathway of BC; if the first draining lymph node in the axilla is free from tumors, no future dissection is performed, and the extent of surgery can also be reduced using breast-conserving surgical techniques.[6]

In an Asian series published by Tan et al.,[7] 35% of patients with early BC were found to have nodal metastases. The four independent predictors of node positivity were tumor size, lymphovascular invasion, histology other than invasive ductal or lobular carcinoma, and presence of progesterone receptors.

A recent study by Valente et al.[8] on 244 patients showed that physical examination and multimodal imaging with mammography, US, and MRI can be useful for treatment planning but remain inadequate predictors of axillary lymph node involvement, with a false negative (FN) rate of 14%. Although imaging remains limited for nodal status evaluation, continued improvements in accuracy have been made in the recent years through research.

5.2.1 Axillary nodes

US of the axillary lymph nodes is usually performed using high-frequency linear transducers that afford high spatial resolution. This is particularly important in the assessment of the level 1 nodes, given their superficial location (Fig. 5.2). In contrast, CT, MRI, and scintigraphic techniques play an important role in assessment of deep nodes such as those in the internal mammary chain, given the limited penetration of US across the bony chest wall.

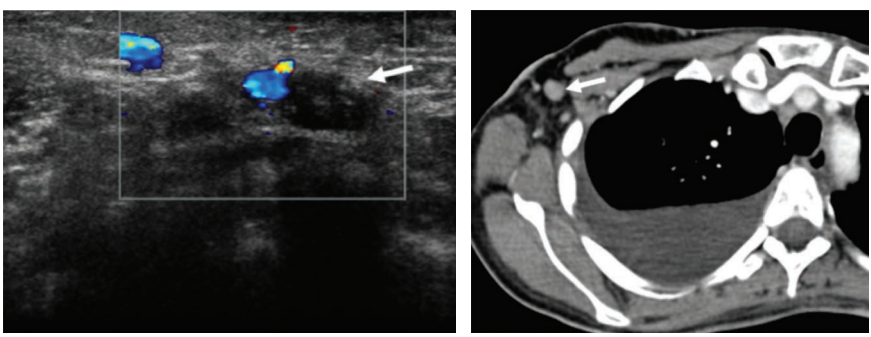

(a) (b)

Figure 5.2 (a) Duplex sonography image shows a suspicious right axillary lymph node (arrow) with increased color flow. The node is highly irregular and markedly hypoechoic. This was proven to be metastatic by biopsy. (b) Axial CECT image shows the same lymph node (arrow) to be round and borderline enlarged (10 mm). The morphologic characteristics of the node are better depicted on US than on CT.

Bedi et al.[9] showed that there can be up to 88% interobserver agreement for differentiating between benign and malignant nodes, with sensitivity and specificity of 77% and 80% respectively. In that study, it was shown that predominantly hyperechoic lymph nodes can be considered benign, while the presence of asymmetric focal hypoechoic cortical lobulation or a completely hypoechoic node should prompt further evaluation with needle biopsy (Fig. 5.2). Some authors advocate size measurement; Cho et al.[10] showed a cutoff of 2.5 mm for cortical thickness of a node with an AUC of 0.861 (95% CI: 0.796%–0.926%).

Increasingly, needle aspiration biopsy combined with US is being used to improve the accuracy of nodal status determination. The FN error can be reduced with the use of a modified 14-gauge core needle biopsy technique that can be successfully performed without major complications.[11] The study by Garcia-Ortega et al.[12] showed a sensitivity and specificity of US of 63% and 89% respectively, and of core biopsy of 67% and 100%, respectively. This allowed for avoidance of SLNB in 33% of patients. In the study by Moore et al.,[13] assessment of sonographic characteristics of axillary nodes, combined with needle biopsy, achieves high accuracy in staging and has been advocated as potentially replacing SLNB. Similar findings have been echoed in a study by van Rijk et al.[14] In that study, which looked at 726 patients, combined US and fine-needle aspiration cytology (FNAC) carried a sensitivity of 21% and avoided SLNB in 8% of patients. Finally, the meta-analysis by Houssami[15] showed that US combined with biopsy is accurate and carries a pooled sensitivity and specificity of 80% and 98%, particularly in patients with average or high underlying risk of nodal metastases.

CT has poor sensitivity of only 50–60% and does not currently play any role in routine preoperative staging assessment for axillary nodal involvement[16,17] (Fig. 5.2). Its use is reserved for locally advanced tumors where the suspicion for occult metastatic disease is high. Some authors have reported improved accuracy with thin section CT scanning in the prone position, but this can be technically more challenging.[18]

MRI confers great soft tissue contrast resolution and allows for more than morphologic assessment. Increased T2-signal, lack of uptake of ultrasmall superparamagnetic iron oxide (USPIO) contrast agents that are preferentially taken up by normal lymph nodes and altered contrast perfusion, metabolic profile, and water diffusion characteristics have all been advocated for the diagnosis of nodal disease. Luciani et al.[19] showed that morphologic assessment of nodes on MRI can discriminate between benign and malignant nodes. The findings that were most significant include irregular contours, high signal intensity on T2-weighted imaging, marked gadolinium enhancement, and round hila with abnormal cortices.

Among the various functional imaging techniques for nodal assessment, USPIO imaging has been best studied. Memarsadeghi et al.[20] showed that USPIO-MRI is superior to nonenhanced imaging and carried a sensitivity, specificity, and accuracy rate of 100%, 98%, and 98%, respectively. Additionally, Harada et al.[21] showed that use of USPIO imaging improved sensitivity and specificity of MRI over morphologic assessment. With morphologic assessment only, the sensitivity and specificity were 36% and 94%, respectively; with USPIO imaging, the sensitivity and specificity were 85% and 98%, respectively. Similar findings were demonstrated by Michel et al., who showed that USPIO imaging carried a sensitivity of 82% and specificity of 100%;[22] Motomura et al.[23] evaluated the use of USPIO-MRI for sentinel node involvement and found a sensitivity, specificity, and accuracy rate of 84%, 91% and 89%, respectively. The meta-analysis by Cooper et al.[24] showed that among other imaging modalities, USPIO-MRI showed a lower specificity at 73%, but a higher sensitivity at 88% than PET-CT, which yielded sensitivity and specificity rates of 56% and 96%, respectively. Furthermore, the diagnostic accuracy of USPIO-MRI appears to be superior to that of DCE-MRI. In a more general meta-analysis by Wu et al.[25] on USPIO-enhanced MRI for lymph node metastases in different body regions, use of USPIO-MRI offers significantly higher diagnostic performance than conventional MRI. These having been said, routine clinical use of USPIO agents have been hampered by frequent side effects (back pain, anaphylaxis), cumbersome administration protocols, and lack of commercial availability.

DCE-MRI assesses the perfusion characteristics of lesions. It is assumed that the concentration of gadolinium is proportional to the vascularity of lesions. This can be more simply assessed by plotting a concentration–time curve, also known as a contrast-enhancement kinetics curve. Malignant lesions tend to show rapid uptake and washout of contrast compared to normal soft tissue. More-complicated methods of analysis have also been used; some of these are now commercially available. Among them, the Tofts' model is one of the most frequently used methods of quantitative analysis of various perfusion parameters, including blood flow and vascular permeability.[26] Kvistad et al.[27] showed that the sensitivity, specificity, and accuracy of DCE-MRI (using a 100% increase in signal intensity as a marker for node-positive disease) was 83%, 90%, and 88%, respectively. The meta-analysis by Klerkx et al.[28] showed that the weighted estimated sensitivity and specificity of DCE-MRI (for all 43 papers studied) was 0.72 and 0.87, respectively. Sensitivity was increased to 0.84 without significant reduction in specificity (0.82) for subgroup analysis reviewing studies that incorporated contrast enhancement.

Diffusion-weighted (DW) MRI assesses for free diffusion of water molecules and has shown promise for assessment of tumor involvement. The advantages of this technique are rapid acquisition (approximately 3 min for

one station or body part) and no need for intravenous contrast administration. Heusner et al.[29] showed that whole-body (WB) DW MRI might be sensitive but at present is not specific enough for the detection of locoregional or metastatic BC. In that study, the sensitivity and specificity of PET-CT was 94% and 98%, respectively, while that of DW MRI was 91% and 72%, respectively.

MR spectroscopy (MRS) assesses the metabolic profile of lesions. This can be performed using either single-voxel (for small lesions such as lymph nodes) or multivoxel techniques. The main limitations of MRS in practice are that technical competency is necessary (to avoid artifacts such as fat contamination) and that it is prone to artifacts (noise) and long acquisition times (10–30 mins). Yeung et al.[30] showed that sensitivity, specificity, and accuracy of MRS was 81%, 100%, and 90%, respectively, with choline being consistently detected in invasive ductal carcinoma. Asiago et al.[31] showed that a combination of nuclear MR and 2D gas chromatography-mass spectrometry to profile the metabolites of samples yielded a sensitivity of 86% and specificity of 84%.

5.2.2 Other draining nodes

The other draining nodes in BC include the internal mammary (IM) and mediastinal lymph nodes. According to early studies of patients who underwent extended radical mastectomy, metastasis to IM nodes occurs in close to 20% of women with stage II and stage III BC.[32,33] The study of patients with early BC by Byrd et al.[34] revealed that the overall prevalence of metastatic IM nodes was 17%. IM node drainage was significantly less frequent when tumors were located in the upper outer quadrant of the breast (10%) than when tumors were located in the other three quadrants or the subareolar portion (17%–29%). Metastasis to the IM and axillary nodes usually occurs synchronously; however, it can be infrequently isolated to the IM chain in 4%–6% of cases.[35] Furthermore, the prognosis of patients with IM and axillary node metastases is significantly worse than that of patients with only axillary node disease, suggesting that the IM nodal chain may be a conduit for more-widespread dissemination of disease.[36]

Unlike axillary nodes, IM nodes are not routinely biopsied as part of an individual patient's staging workup, and their status is generally unknown. CT has been the main modality used to evaluate mediastinal nodes in oncologic patients, but this technique, which uses size as the main criterion to assess nodal status, is limited by poor sensitivity and specificity. At present, PET-CT appears superior to other imaging modalities for detection of nodal disease. In a preliminary analysis of 73 patients with recurrent or metastatic BC, the prevalence of suspected disease in mediastinal and IM nodes on fluorodeoxyglucose (^{18}F or FDG) PET was significantly higher than the prevalence on CT (40% versus 23%).[37] Uematsu et al.[38]

showed that while PET is not a breast imaging modality for evaluating the local tumor extent compared to MRI (accuracy for PET is 43.5% and for MRI is 91%), it is useful for predicting the prognoses of patients who are candidates for breast-conservation therapy (BTC) because it showed an accuracy of 87% for nodal status evaluation.

5.3 Distant Metastases

The retrospective review study by Whitlock et al.[39] showed that the most common sites of metastatic disease was the skeleton (67%) as detected on BS, liver (32%) as detected on US, and lungs (42%) as detected on CXR. The study by Mvere et al.[40] showed that metastases were more common in patients with the inflammatory subtype of BC (26% compared to 10% in the noninflammatory subtype). With the inflammatory subtype, the lungs and pleura were the most common sites of metastases.

Imaging assessment for metastatic disease is typically performed using a combination of "conventional" imaging techniques: BS, CXR, or CT of the lungs, and US, CT, or MRI of the liver. More recently, the advent of PET-CT has altered the imaging algorithm for staging evaluation of BC patients. Dose-Schwarz et al.[41] showed that the sensitivity and specificity of PET was 93% and 77%, respectively, compared to 61% and 87% for conventional imaging, which included CXR, US of the liver, and BS. PET-CT is more sensitive than conventional imaging procedures for detection of distant BC metastases and should be considered for additional staging, especially in patients with high-risk primary BC. Meta-analysis by Brennan et al.[42] showed that conventional imaging studies, which included CXR, US, BS and CT, yielded lower sensitivity and specificity than PET-CT (sensitivity/specificity: combined conventional imaging 78.0%/91.4%; BS 98.0%/93.5%; CXR 100%/97.9%; liver US 100%/96.7%; CT chest/abdomen 100%/93.1%; and FDG-PET 100.0%/96.5%). Interestingly, the recent meta-analysis by Pan et al.[43] showed that MRI was the most useful imaging technique to assess patients for suspected recurrent or metastatic disease (followed by PET-CT), when compared to other imaging modalities such as US, CT, and scintimammography (AUCs of 0.9718, 0.9604, 0.9251, 0.8596, 0.9386, respectively).

On the whole, MRI may appear to be more cost effective than either PET alone or PET-CT as a diagnostic tool to replace the more-invasive reference methods. However, in a direct comparison between WB MRI and PET-CT in 33 patients, Schmidt et al.[44] found that while both modalities are useful for detection of tumor recurrence at follow up, WB MRI is more sensitive to distant metastases (PET-CT 86%, WB MRI 93%), while PET-CT is more sensitive in detecting nodal disease. Extensive discussion on the role of PET-CT will appear in a separate chapter. In the ensuing

sections, we focus more on the use of the imaging modalities, particularly ultrasound, CT, and MRI.

5.3.1 Pulmonary metastases

Complete resection of pulmonary metastases in selected cases can lead to improved disease-free survival, with low morbidity.[45] The study by Ludwig et al.[46] showed that a disease-free interval of more than two years influenced the mean disease-free survival rate (36.1 months). Those in whom the disease-free interval was less than two years had a mean disease-free survival rate of 8.5 months. Patients with solitary metastases also tended to survive longer, compared to those with multiple metastases (28.8 months versus 13.1 months). Eubank et al.[37] showed that patients with mediastinal or IM node disease on PET had a significantly greater likelihood of developing ipsilateral pleural or lung parenchymal metastasis than did patients without mediastinal or IM node disease on PET. The characteristic pattern of the spread of disease to the pleura, mediastinum, and lung as well as isolated sternal metastases has been described in patients with IM node metastases.[47] In the study by Mahner et al.,[48] the sensitivity and specificity of CXR, CT, and PET-CT were 28% and 100%, 65% and 97%, as well as 75% and 97%, respectively. PET also identified bone metastases with higher accuracy compared with BS. On the other hand, CT had distinct advantages in the identification of both small lung and liver metastases (Fig. 5.3).

MRI has been considered as an alternative to CT for detecting pulmonary metastases, primarily because exposure to ionizing radiation is avoided, an

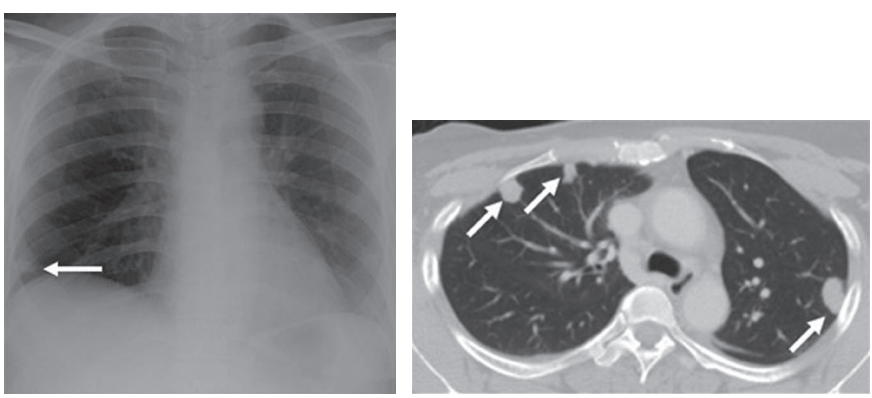

(a) (b)

Figure 5.3 (a) CXR shows faint ill-defined opacity (arrow) in the lower zone of the right lung that was confirmed to represent a metastasis on CT. (b) Axial CT image of the upper lungs show multiple metastases (arrows) that were not well depicted on CXR. This clearly illustrates the higher sensitivity of CT over CXR in the detection of pulmonary metastases.

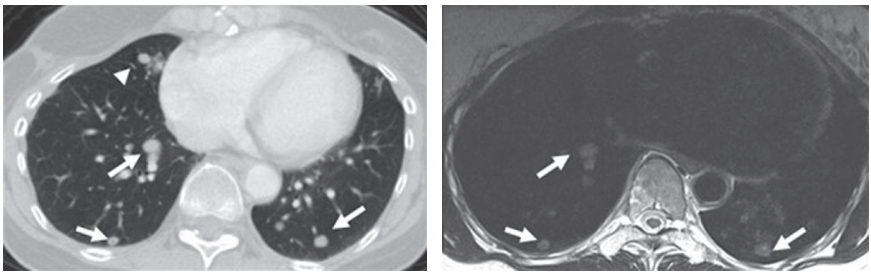

(a) (b)

Figure 5.4 (a) Axial CT image shows multiple pulmonary metastases in bilateral lower lobes (arrows) and the middle lobe (arrowhead). (b) Axial T2-weighted MR image shows the same bilateral pulmonary metastases (arrows). However, the middle lobe metastasis is not depicted as a result of respiratory and cardiac motion artifacts.

issue of particular concern with younger patients undergoing multiple follow-up examinations. However, motion-related artifacts, a lower spatial resolution than CT, and an inability to detect calcification within lesions all represent limitations of MRI (Fig. 5.4). Therefore, it is generally accepted that MRI does not currently have a role in screening of patients for pulmonary metastases.

The study by Kersjes et al.,[49] which evaluated turbo-spin echo MRI using CT as the reference standard, demonstrated a lower sensitivity for MRI in detecting pulmonary metastases; for 340 metastases identified on CT, the overall sensitivity of MRI was 84%, but for nodules <5 mm in diameter, sensitivity was only 36%. A more recent study comparing the nodule (greater than 5 mm) detection accuracy of various MRI sequences supports these results. The optimal sequence [short tau inversion recovery (STIR)] had a 72% sensitivity for nodule detection.[50]

5.3.2 Bone metastases

Bone metastases are one of the most common forms of BC dissemination. The incidence of bone metastases is dependent on the stage and histology of the primary tumor. Patients with more-advanced disease tend to have a higher incidence of bone metastases. In the study by Koizumi et al.,[51] patients diagnosed with disease at or above stage IIIA had incidence of more than 3% per person-year, while those with stage 1 disease had incidence of <1% per person-year. Traditionally, BS with Tc-99m chelates (commonly methylene disphosphonate, MDP) has been used to evaluate for osseous metastases. This is based on the fact that tumor incites bone reaction in the form of increased osteoblastic activity.

The ACR Appropriateness Criteria[52] on metastatic bone disease recommends that in stage 1 breast carcinoma where BS is usually negative, routine baseline and follow-up bone scans are probably unwarranted because

of the very low true-positive (TP) yield. Hence, no imaging studies of the skeleton are required in asymptomatic patients with stage 1 carcinoma of the breast at presentation. BS and PET-CT have been shown to be useful in the preoperative staging and postoperative followup of stages 2, 3, and 4 breast carcinoma. In a symptomatic patient with stage 2 breast carcinoma, radiography of the back and hip and radionuclide bone scan are warranted. In the setting of "hot" lesions on BS, if radiography is negative, single-photon emission computed tomography (SPECT) and MRI may be recommended. On MRI, use of a dual echo T1-weighted (also referred to as in- and out of phase) sequence may best assess for marrow replacement by tumor. CT may be performed for localization before needle biopsy.

PET is more sensitive than BS for detection of lytic metastases or lesions predominantly involving the bone marrow, accounting for cases that are positive on PET and negative on bone scanning; BS is more sensitive than PET for detection of osteoblastic metastases, accounting for cases that are positive on bone scanning and negative on PET.[53] In the study by Hahn et al.[54] on a per lesion basis, PET-CT was more sensitive and showed no significant difference in specificity compared to BS; the sensitivity and specificity of BS and PET-CT were 76%/95% and 96%/92%, respectively.

MRI is a highly sensitive imaging modality for detection and characterization of osseous metastases, in part due to the high soft-tissue contrast resolution achieved between tumor and normal fat-containing marrow (Fig. 5.5). The main limitations of MRI are the long scanning times required to obtain a WB scan and the related high costs of the procedure. With the advent of newer WB imaging techniques that utilize parallel imaging, imaging times are now significantly reduced. A typical WB MRI scan to look for osseous metastases now takes approximately 30 min. This is not significantly different from the scan time of BS.

Nakanishi et al.[55] directly compared WB MRI to BS and showed that there was an 81% concordance between the modalities, and that MRI is considered to be an excellent screening modality for bone metastases, especially in the vertebral body. Schmidt et al.[56] showed that WB MRI carries a sensitivity of 94%, while PET-CT achieved 78% for detection of osseous metastases. Grankvist et al.[57] showed that using PET-CT as the reference standard, MRI carried a sensitivity of 98%, and combining findings from T1-weighted imaging (STIR and DW MRI), the specificity was 95%. Houssami et al.[58] performed a systemic review on 16 studies and found that PET-CT and MRI may provide small increments to the accuracy of BS for detecting bone metastases; at this point, there is insufficient evidence to support the use of SPECT and WB MRI as first-line imaging modalities. Engelhard et al.[59] showed that using a moving table technique, WB MRI was superior in detection of metastases with sensitivity, specificity, and accuracy rates of 92%, 90%, and 91%, respectively, as compared

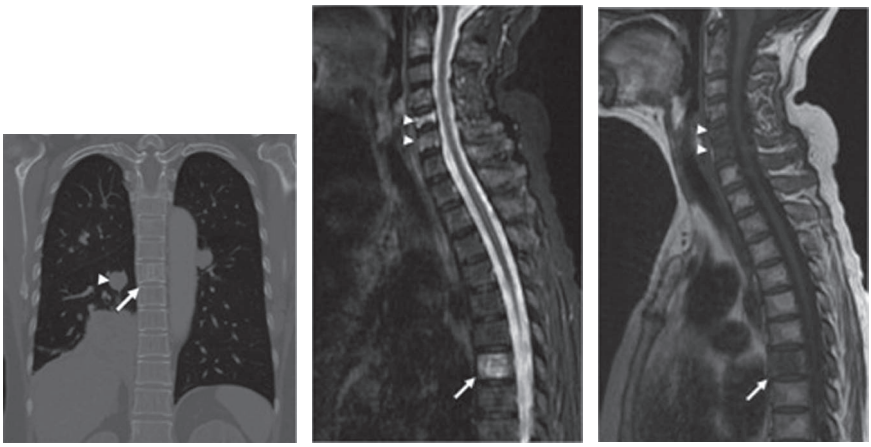

(a) (b) (c)

Figure 5.5 (a) Coronal reformat CT image shows subtle heterogeneity of the T7 vertebral body (arrow). A pulmonary metastasis (arrowhead) is also present in the right lower lobe. (b) Sagittal STIR image of the cervical and upper thoracic spine shows multiple areas of increased T2 signal (cervical vertebrae: arrowheads; T2 vertebra: arrow), consistent with metastases. These are much better depicted on MRI than on CT. (c) Corresponding sagittal T1-weighted image shows metastases as hypointense lesions (cervical vertebrae: arrowheads; T2 vertebra: arrow) as a result of replacement of fatty marrow. The lesions showed corresponding enhancement with gadolinium (not shown), in keeping with active metastases.

to BS with sensitivity, specificity, and accuracy rates of 83%, 80%, 82%, respectively. Furthermore, MRI showed metastases of the lung and liver, which BS failed to demonstrate. Wu et al.[60] showed that WB MRI had pooled sensitivity and specificity of 0.899 and 0.918, respectively. DW MRI appeared to reduce overall specificity (0.961 without DW MRI). Yilmaz et al.[61] directly compared MRI to BS and found greater sensitivity and specificity (95%, 100%) in MRI than in BS (70%, 94%) in detecting bone metastases (Fig. 5.6).

5.3.3 Liver metastases

Liver metastases generally occur later than locoregional recurrences and are associated with a much worse prognosis.[62] Patients with estrogen receptor (ER)–negative primary tumors have an increased risk of liver metastases compared with patients with ER-positive tumors.[63] The predominant mode of metastasis to the liver is hematogenous; however, lymphatic spread from IM nodes to pericardial nodes and below the diaphragm to nodes in the porta hepatis and finally the hepatic parenchyma has been described.[64] Detection of liver metastases can be important for curative treatment. In a small series by Selzner et al.,[65]

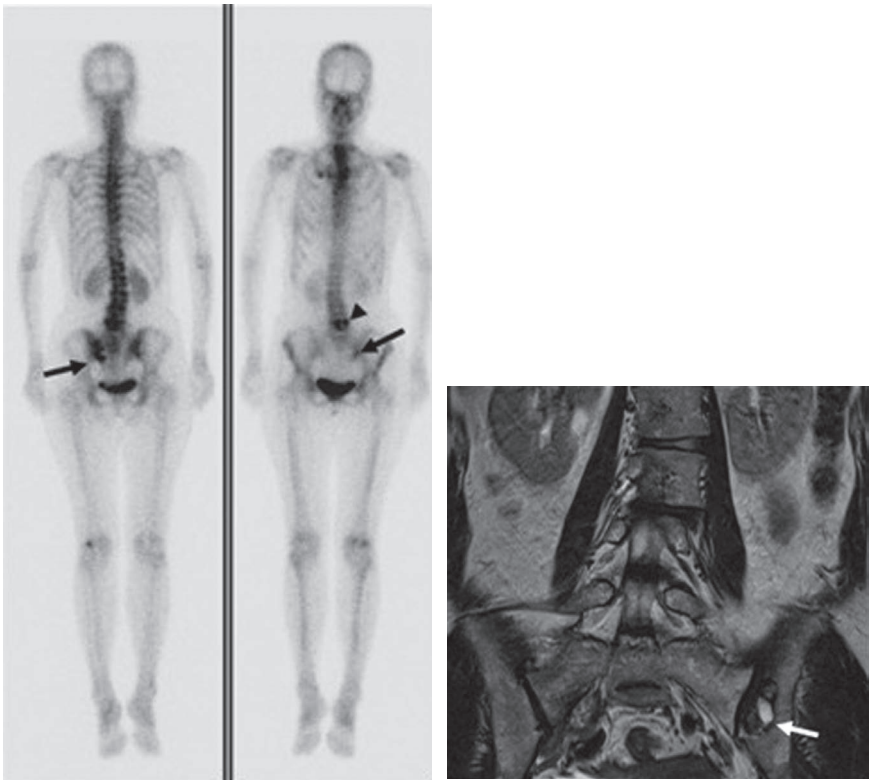

(a) (b)

Figure 5.6 (a) Bone scintigraphy image shows foci of increased osteoblastic activity in the medial left iliac bone (arrows) and L5 vertebral body (arrowhead), consistent with metastases. (b) Coronal T2-weighted MR image shows a heterogeneously hyperintense lesion (arrow) in the medial left iliac bone, consistent with a partially sclerotic metastasis.

BC in patients undergoing liver metastectomy, a long-term survival of 22% was demonstrated.

In the study by Mahner et al.,[48] the sensitivity and specificity of US, CT, and PET-CT was 100% and 67%, 40% and 92%, and 19% and 76%, respectively. In the study by Ravaioli et al.,[66] the TP rate for liver metastases was 0.8%, and the FP rate was 0.4%. Furthermore, the detection (TP rate) was 0% for stage 1 BC, 0.5% for stage 2 with < 4 nodes involved, 2.1% in stage 2 with >3 nodes involved (now considered stage 3), and 2.9% in stage 3 patients. The specificity of US was 62%, sensitivity 99%, positive predictive value 67%, and negative predictive value 99%, using distant metastases confirmed by CT or MRI during the six-month followup as the reference standard.

A commonly encountered problem with the use of CT staging evaluation of BC is the identification of incidentally detected small hypodensities. These have become even more common with the advent of multidetector row CTs that allow for higher spatial and temporal resolution imaging. The study by Khalil et al.[67] showed that among 1012 women who underwent CT of the liver, at least one indeterminate lesion [too small to characterize (TSTC)] was found in 29% of patients. Using best- and worst-case scenario analyses, the lesions were shown to be benign in 97% and 93% of patients, respectively.

BC liver metastasis is most commonly present as hypervascular hepatic metastases, which may develop early enhancement with variable degrees of washout and peripheral rim enhancement[68] (Fig. 5.7).

A more generalized study on patients with metastatic liver disease from various primary diseases, by Hagspiel et al.,[69] showed that USPIO-MRI

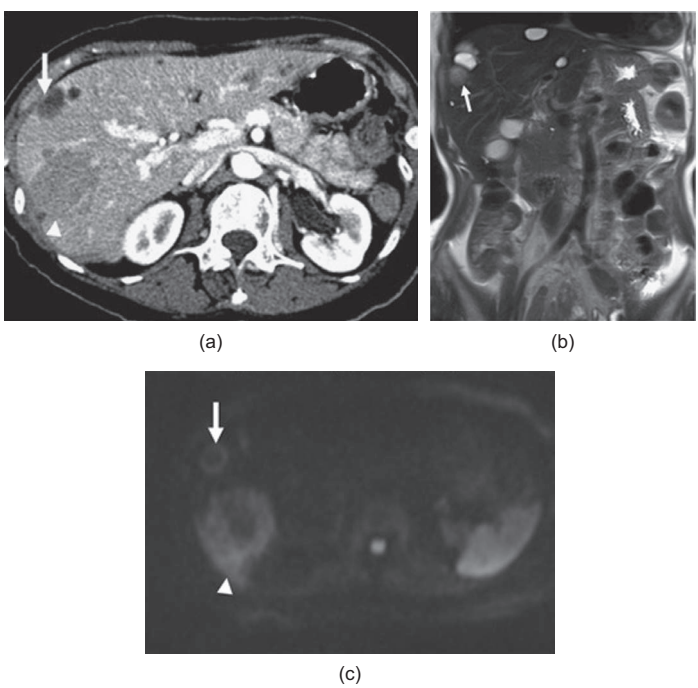

Figure 5.7 (a) Axial CECT image shows hypoattenuating lesion (arrow) in the anterior right hepatic lobe, indeterminate for a metastasis. The larger lesion in the posterior right lobe (arrowhead) is consistent with a metastasis. (b) Coronal single shot fast spin echo image of the lesions shows a mildly T2 hyperintense lesion (arrow) that lies adjacent to a cyst, in keeping with a metastasis. (c) Axial DW MRI image (b = 100 sec/mm^2) shows a rim of restricted diffusion in both lesions (anterior: arrow; posterior: arrowhead). DW MRI can be useful to increase sensitivity of MRI for metastases.

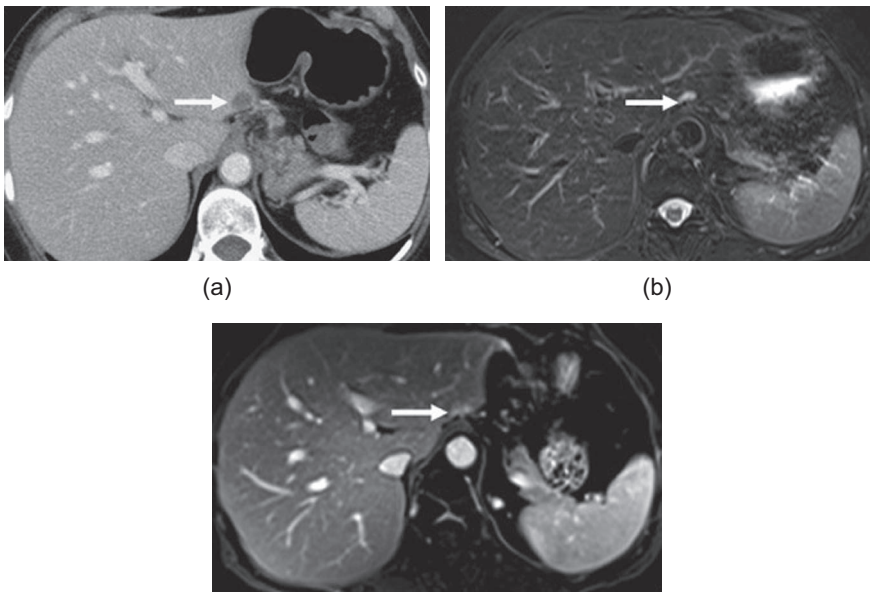

Figure 5.8 (a) Axial CECT image in a patient with known BC shows an indeterminate hypoattenuating lesion (arrow) in the posterior lateral left hepatic lobe. (b) Axial T2-weighted MR image at the same level shows the signal within the lesion (arrow) to approach that of fluid. (c) Axial T1-weighted contrast-enhanced MR image of the same lesion (arrow) in the late hepatic arterial phase demonstrates a nodular pattern of enhancement. The MRI features are more in keeping with a haemangioma. This case illustrates that MRI is superior to CT in characterizing focal liver lesions.

was the most sensitive imaging method, when compared to preoperative CT and preoperative US. On a per lesion analysis, USPIO was less sensitive than intraoperative ultrasonography (IOUS) (56% versus 80%). The study by Patterson et al.[70] on TSTC liver lesions that underwent further evaluation with MRI showed that immediate further evaluation of these lesions with MRI offers marginal benefit over CT, and among patients studied, only 5% were found to subsequently represent metastases (Fig. 5.8).

Given the minimal complication rate of liver biopsy, the authors suggest that liver biopsy should still be performed in the types of cases studied here, despite the finding that the vast majority of biopsies produced the expected result and presumably did not change patient management.

5.3.4 Brain metastases

Gonzalez-Angulo et al.[71] reviewed 668 BC patients treated with multimodality therapy and found that 8% of patients developed brain metastases

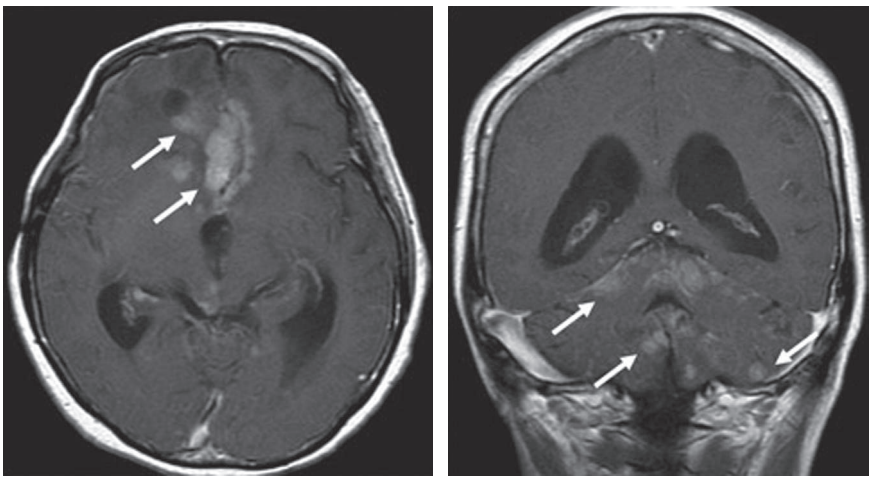

(a) (b)

Figure 5.9 (a) Axial T1-weighted contrast-enhanced MR image shows multiple nodular enhancing metastases (arrows) in the frontal lobes. (b) Coronal T1-weighted contrast-enhanced MR image shows many more metastases (arrows) in the cerebellar hemispheres. The high soft-tissue contrast resolution of MRI makes it superior to CT in the detection of intracranial metastases.

at a median follow-up duration of 9.5 years. Brain metastases represented the first site of recurrence for 63% of the affected patients. Characteristics associated with the development of central nervous system (CNS) metastases over time included negative hormone receptor status, grade 3 disease, and larger tumor size. MRI is currently regarded to be the most appropriate test for detection of brain metastases (Fig. 5.9).

The use of PET-CT for brain metastases is hampered by the inherent high background activity of normal brain parenchyma, while the sensitivity of CT can be reduced by its relatively poorer soft-tissue contrast resolution, in which case iodinated contrast administration is considered mandatory (Fig. 5.10).

5.4 Treatment Response Evaluation: Response Evaluation Criteria in Solid Tumors (RECIST)

In 1979, the World Health Organization (WHO) issued its first version of tumor response criteria based on assessment of tumor burden. This was calculated by summing the products of 2D lesion measurements. Baseline lesion measurements were then compared with follow-up measurements assessed for change.[72] In 2000, the WHO, the United States National Cancer Institute (US NCI) and the European Organization for Research and Treatment of Cancer (EORTC) adopted a new set of tumor response criteria, the Response Evaluation Criteria In Solid Tumors (RECIST, version 1.0).[73]

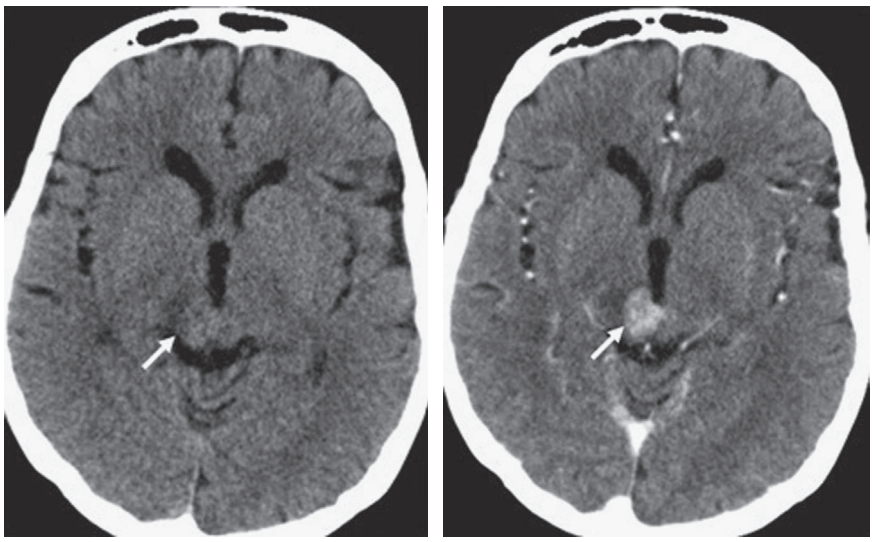

(a) (b)

Figure 5.10 (a) Axial noncontrast-enhanced CT image shows subtle hypoattenuation (arrow) in the posterior medial right thalamus. (b) Axial CECT image at the same level shows avid contrast enhancement in the metastasis (arrow) to the right thalamus. Iodinated contrast enhancement is important for increasing the sensitivity of CT for intracranial metastases, particularly in the leptomeninges.

RECIST was initially based on a 1D lesion measurement criterion instead of the 2D criterion used in the initial WHO guidelines.

With the advent of PET-CT and its increasing use in oncologic imaging, the RECIST working group published a revised version of the guidelines (RECIST, version 1.1) in 2009, drawing on data analysis of more than 6500 patients and more than 18000 target lesions.[74] Based on the new guidelines, size measurement of five target lesions, with a maximum of two per organ, is recommended. The key points (revisions) to the updated RECIST criteria (version 1.1) are as follows:

- Complete response (CR): disappearance of all target lesions, plus reduction in short-axis diameter of pathologic lymph nodes to < 10 mm;
- Partial response (PR): ≥30% decrease in the sum of the longest diameters of target lesions;
- Progressive disease (PD): >20% increase (5-mm absolute increase) in the sum of the longest diameters in comparison with the small sum of the longest diameters recorded since treatment started;
- Stable disease (SD): neither PR nor PD;
- Lymph nodes that possess a short axis diameter of at least 10 mm are considered normal, while those with short axis of 10–15 mm are nontarget lesions, and those with >15 mm in short axis diameter are considered

to be target lesions. Bone metastases are now considered target lesions if they are either lytic or mixed lytic/blastic, with a soft tissue component that is measureable; however, these should be assessed with either CT or MRI.

- Nontarget lesion status may reduce overall response; e.g., for a nonprogressive disease in a nontarget lesion with CR in the target lesion, the treatment is considered to have achieved only PR.

Accordingly, disease progression is defined in part by an absolute increase of 5 mm or more in the sum of the longest dimensions of the target lesions, and in part by an increase of 20% or more in the sum of the longest diameters of target lesions.

Even with the revised criteria, a few limitations to RECIST persist. This includes the assumption that all lesions are spherical (allowing for single 2D measurement) and that those that respond to treatment will decrease uniformly in size. In addition, newer imaging modalities (such as DCE-MRI to assess tumor vascularity and DW MRI as a marker of lesion cellularity) are not used for assessment of tumor response. Finally, detection of new lesions is used for defining progressive disease. However, bone metastases may heal and become sclerotic and thereafter mistakenly be attributed to disease progression.

Given that RECIST is based entirely on size measurement to determine tumor burden, US, which is operator dependent and may therefore lead to subjective measurements, is not considered an acceptable imaging modality for treatment response assessment under the RECIST guidelines. Similarly, PET and other functional imaging techniques are currently not sufficiently standardized to merit substitution for anatomical assessment described in RECIST. A series of prospectively conducted multicenter clinical trials to validate PET-CT as an appropriate end-point is desired.[75] With more correlation between volumetric tumor measurements and results of molecular and functional imaging, further updates to the RECIST criteria can be anticipated.

5.5 Surveillance: To Do or Not To Do?

The Canadian Breast Cancer Initiative issued a set of Clinical practice guidelines for the care and treatment of BC as well as followup after treatment for BC, updated in 2005. Based on the recommendations, routine laboratory and radiographic investigations should not be carried out for the purpose of detecting distant metastases[76] (Fig. 5.11). This is based on the rationale that in the absence of evidence that early treatment of metastatic disease will prolong life, one should avoid the inconvenience and expense of carrying out routine tests to detect it.

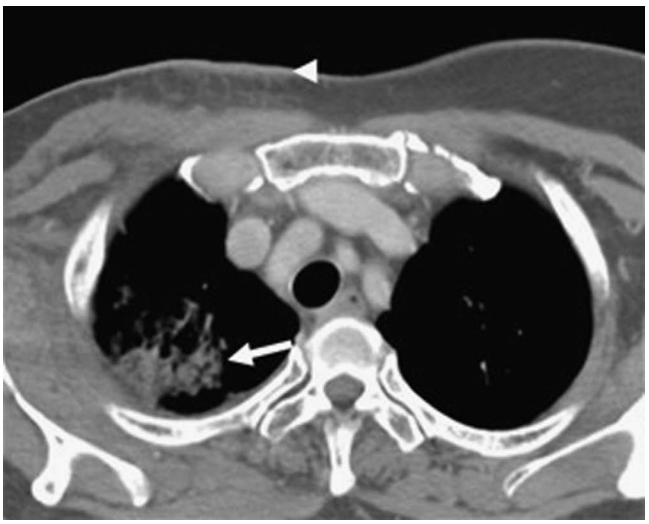

Figure 5.11 Axial CECT of the upper lungs shows post-treatment changes in the form of cutaneous thickening (arrowhead) and a focus of consolidation in the right upper lobe (arrow) in a patient who completed radiotherapy for right BC. These are common findings that should not be mistaken for residual or recurrent disease.

In one trial, 655 patients who were randomly assigned to receive intensive surveillance consisting of physician visits, bone scanning, liver US examination, CXR, and laboratory tests had a survival rate that was almost identical to that of a control group of 665 women who received only tests that were clinically indicated.[77] In another randomized trial of similar size and duration, CXR and bone scans obtained every 6 months had no influence on mortality at 5 years. This has been verified in a recent meta-analysis by Rojas et al.[78] Hence, it is believed that except for mammographic examination, scientific evidence does not support the routine use of any other instrumental or laboratory test, including biologic markers as follow-up treatment for BC.[79–82] Radiographic disease stability may represent either beneficial effect of treatment or indolent disease; patients with stable disease show survival equal to that of patients with tumor regression on radiographic assessment; hence, therapy is continued as long as toxicity is acceptable and there is no evidence of disease progression.

Among laboratory-based markers, circulating tumor cells hold promise and have been shown to be an independent predictor of progression-free survival and overall survival in patients with metastatic BC.[83] Budd et al.[84] showed that the use of circulating tumor cells conferred less inter-reader variability (1%) compared with radiographic assessment using the WHO criteria of 15% to determine disease progression. Further validation of circulating tumor cells as a marker of disease burden is required.

5.6 Locoregional Recurrence

Goerres et al.[85] demonstrated in 32 patients with BC and suspected recurrence that, while PET had greater specificity, MRI showed greater sensitivity for the presence of locoregional recurrence. As MRI is limited by its small field of view, PET was able to detect five additional metastases beyond those detected by MRI. Hathaway et al.[86] showed that, while PET was effectively able to identify the presence of recurrence disease, MRI plays an important role in determining the relationship of the metastatic tumor to the axillary and supraclavicular neurovascular structures. Hence, both imaging modalities play a complementary role.

Gallowitsch et al.[87] looked at 62 patients with surgically resected BC with a mean follow-up period of 2 years. On a per lesion basis, PET-CT showed a sensitivity, specificity, positive predictive value (PPV), negative predictive value (NPV), and accuracy for detecting local recurrence or distant metastases of 97%, 82%, 87%, 96%, and 90%, respectively, compared with 84%, 60%, 73%, 75%, and 74%, respectively, with conventional techniques including mammography, CT, MRI, CXR and BS (Fig. 5.12).

5.7 Summary

Imaging plays a pivotal role in the evaluation of metastatic spread of disease in BC. For early BC, the routine use of advanced imaging modalities needs to be weighed against increased costs and potential for exposure to ionizing radiation (CXR, BS, CT, PET-CT). For regional nodal involvement, US with needle biopsy is increasingly preferred in select patients. In advanced BC where there is strong clinical suspicion for metastatic

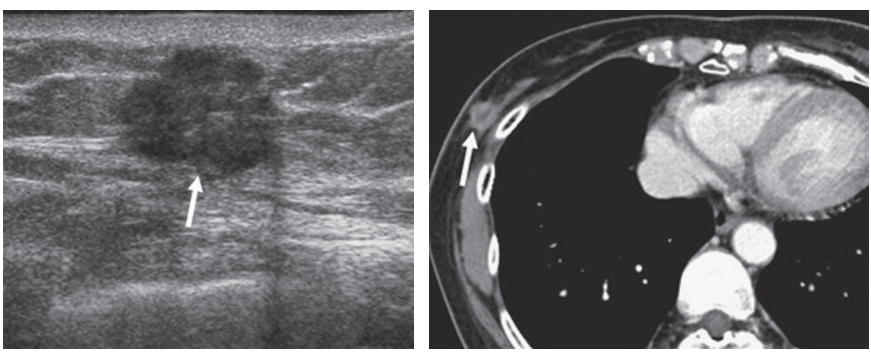

(a) (b)

Figure 5.12 (a) Grayscale sonographic image of the right anterior chest wall post-wide local excision shows a lobulated hypoechoic mass (arrow) in the subcutaneous tissues. (b) Axial CECT shows the same lesion as a peripherally enhancing nodule (arrow), in keeping with recurrence disease.

disease, MRI and PET-CT now show great promise for accurate noninvasive diagnosis, while possessing WB-imaging capabilities. While routine imaging surveillance for recurrent metastatic disease is not advocated due to lack of evidence for increased long-term survival, the correct approach should be tailored to a case-by-case basis by taking into account the underlying tumor biology (e.g., aggressive subtypes such as triple-negative disease) and the stage of the disease at presentation.

References

1. S. Edge, *AJCC Cancer Staging Manual*, 7th edition, Springer, New York, pp. 347–376 (2010).
2. National Collaborating Centre for Cancer, "Advanced breast cancer: diagnosis and treatment," National Institute for Health and Clinical Excellence (NICE), London (2009).
3. American College of Radiology, "ACR Appropriateness Criteria®: Breast Imaging: Stage 1 Breast Carcinoma," available at http://www.acr.org/SecondaryMainMenuCategories/quality_safety/app_criteria/pdf/ExpertPanelonWomensImagingBreastWorkGroup/StageIBreastCarcinomaDoc4.aspx. Accessed 2 Feb 2012.
4. R. E. Myers, M. Johnston, K. Pritchard, M. Levine, and T. Oliver, "Breast Cancer Disease Site Group of the Cancer Care Ontario Practice Guidelines I. Baseline staging tests in primary breast cancer: a practice guideline," *Can. Med. Assoc. J.* **164**(10), 1439–1444 (2001).
5. F. L. Greene, D. L. Page, I. D. Fleming, et al., Eds., *AJCC Cancer Staging Manual*, 6th edition, Springer-Verlag, New York, pp. 91–241 (2002).
6. P. J. Borgstein, S. Meijer, R. J. Pijpers, and P. J. van Diest, "Functional lymphatic anatomy for sentinel node biopsy in breast cancer: echoes from the past and the periareolar blue method," *Ann Surg.* **232**(1), 81–89 (2000).
7. L. G. Tan, Y. Y. Tan, D. Heng, and M. Y. Chan, "Predictors of axillary lymph node metastases in women with early breast cancer in Singapore," *Singapore Med. J.* **46**(12), 693–697 (2005).
8. S. A. Valente, G. M. Levine, M. J. Silverstein, et al., "Accuracy of predicting axillary lymph node positivity by physical examination, mammography, ultrasonography, and magnetic resonance imaging," *Ann. Surg. Oncol.* **19**(6), 1825–30 (2012).
9. D. G. Bedi, R. Krishnamurthy, S. Krishnamurthy, et al., "Cortical morphologic features of axillary lymph nodes as a predictor of

metastasis in breast cancer: In vitro sonographic study," *Am. J. Roentgenol.* **191**(3), 646–652 (2008).

10. N. Cho, W. K. Moon, W. Han, I. A. Park, J. Cho, and D. Y. Noh, "Preoperative sonographic classification of axillary lymph nodes in patients with breast cancer: Node-to-node correlation with surgical histology and sentinel node biopsy results," *Am. J. Roentgenol.* **193**(6), 1731–1737 (2009).
11. H. Abe, R. A. Schmidt, K. Kulkarni, C. A. Sennett, J. S. Mueller, and G. M. Newstead, "Axillary lymph nodes suspicious for breast cancer metastasis: Sampling with US-guided 14-gauge core-needle biopsy—Clinical experience in 100 patients, *Radiol.* **250**(1), 41–49 (2009).
12. M. J. Garcia-Ortega, M. A. Benito, E. F. Vahamonde, P. R. Torres, A. B. Velasco, and M. M. Paredes, "Pretreatment axillary ultrasonography and core biopsy in patients with suspected breast cancer: Diagnostic accuracy and impact on management, *Eur. J. Radiol.* **79**(1), 64–72 (2011).
13. A. Moore, M. Hester, M. W. Nam, et al., "Distinct lymph nodal sonographic characteristics in breast cancer patients at high risk for axillary metastases correlate with the final axillary stage, *Brit. J. Radiol.* **81**(968), 630–636 (2008).
14. M. C. van Rijk, E. E. Deurloo, O. E. Nieweg, et al., "Ultrasonography and fine-needle aspiration cytology can spare breast cancer patients unnecessary sentinel lymph node biopsy, *Ann. Surg. Oncol.* **13**(1), 31–35 (2006).
15. N. Houssami, S. Ciatto, R. M. Turner, H. S. Cody III, and P. Macaskill, "Preoperative ultrasound-guided needle biopsy of axillary nodes in invasive breast cancer: Meta-analysis of its accuracy and utility in staging the axilla, *Ann. Surg.* **254**(2), 243–251 (2011).
16. M. Miyauchi, N. Yamamoto, N. Imanaka, and M. Matsumoto, "Computed tomography for preoperative evaluation of axillary nodal status in breast cancer, *Breast Cancer* **6**(3), 243–248 (1999).
17. D. E. March, R. J. Wechsler, A. B. Kurtz, A. L. Rosenberg, and L. Needleman, "CT-pathologic correlation of axillary lymph nodes in breast carcinoma," *J. Comput. Assist. Tomogr.* **15**(3), 440–444 (1991).
18. Y. Hata, Y. Ogawa, A. Nishioka, T. Inomata, and S. Yoshida, "Thin section computed tomography in the prone position for detection of axillary lymph node metastases in breast cancer, *Oncol. Rep.* **5**(6), 1403–1406 (1998).
19. A. Luciani, T. H. Dao, M. Lapeyre, et al., "Simultaneous bilateral breast and high-resolution axillary MRI of patients with breast cancer: Preliminary results, *Am. J. Roentgenol.* **182**(4), 1059–1067 (2004).

20. M. Memarsadeghi, C. C. Riedl, A. Kaneider, et al., "Axillary lymph node metastases in patients with breast carcinomas: assessment with nonenhanced versus uspio-enhanced MR imaging, *Radiol.* **241**(2), 367–377 (2006).
21. T. Harada, N. Tanigawa, M. Matsuki, T. Nohara, and I. Narabayashi, "Evaluation of lymph node metastases of breast cancer using ultrasmall superparamagnetic iron oxide-enhanced magnetic resonance imaging," *Eur. J. Radiol.* **63**(3), 401–407 (2007).
22. S. C. Michel, T. M. Keller, J. M. Fröhlich, D. Fink, R. Caduff, B. Seifert, B. Marincek, and R. A. Kubik-Huch, "Preoperative breast cancer staging: MR imaging of the axilla with ultrasmall superparamagnetic iron oxide enhancement," *Radiol.* **225**(2), 527–36 (2002).
23. K. Motomura, M. Ishitobi, Y. Komoike, et al., "SPIO-enhanced magnetic resonance imaging for the detection of metastases in sentinel nodes localized by computed tomography lymphography in patients with breast cancer, *Ann. Surg. Oncol.* **18**(12), 3422–3429 (2011).
24. K. L. Cooper, Y. Meng, S. Harnan, et al., "Positron emission tomography (PET) and magnetic resonance imaging (MRI) for the assessment of axillary lymph node metastases in early breast cancer: Systematic review and economic evaluation," *Health Technol. Assess.* **15**(4)iii–iv, 1–134 (2011).
25. L. Wu, Y. Cao, C. Liao, J. Huang, and F. Gao, "Diagnostic performance of USPIO-enhanced MRI for lymph-node metastases in different body regions: A meta-analysis," *Eur. J. Radiol.* **80**(2), 582–589 (2011).
26. P. S. Tofts, G. Brix, D. L. Buckley, et al., "Estimating kinetic parameters from dynamic contrast-enhanced T(1)-weighted MRI of a diffusable tracer: Standardized quantities and symbols," *J. Magn. Reson. Imaging* **10**(3), 223–232 (1999).
27. K. A. Kvistad, J. Rydland, H. B. Smethurst, S. Lundgren, H. E. Fjosne, and O. Haraldseth, "Axillary lymph node metastases in breast cancer: Preoperative detection with dynamic contrast-enhanced MRI," *Eur. Radiol.* **10**(9), 1464–1471 (2000).
28. W. M. Klerkx, L. Bax, W. B. Veldhuis, et al., "Detection of lymph node metastases by gadolinium-enhanced magnetic resonance imaging: Systematic review and meta-analysis," *J. Natl. Cancer Inst.* **102**(4), 244–253 (2010).
29. T. A. Heusner, S. Kuemmel, A. Koeninger, et al., "Diagnostic value of diffusion-weighted magnetic resonance imaging (DWI) compared to FDG PET/CT for whole-body breast cancer staging," *Eur. J. Nucl. Med. Mol. Imaging* **37**(6), 1077–1086 (2010).

30. D. K. Yeung, W. T. Yang, and G. M. Tse, "Breast cancer: In vivo proton MR spectroscopy in the characterization of histopathologic subtypes and preliminary observations in axillary node metastases," *Radiol.* **225**(1), 190–197 (2002).

31. V. M. Asiago, L. Z. Alvarado, N. Shanaiah, et al., "Early detection of recurrent breast cancer using metabolite profiling," *Cancer Res.* **70**(21), 8309–8318 (2010).

32. U. Veronesi, N. Cascinelli, M. Greco, et al., "Prognosis of breast cancer patients after mastectomy and dissection of internal mammary nodes," *Ann. Surg.* **202**(6), 702–707 (1985).

33. J. Lacour, M. Le, E. Caceres, T. Koszarowski, U. Veronesi, and C. Hill, "Radical mastectomy versus radical mastectomy plus internal mammary dissection: Ten year results of an international cooperative trial in breast cancer," *Cancer* **51**(10), 1941–1943 (1983).

34. D. R. Byrd, L. K. Dunnwald, D. A. Mankoff, et al., "Internal mammary lymph node drainage patterns in patients with breast cancer documented by breast lymphoscintigraphy," *Ann. Surg. Oncol.* **8**(3), 234–240 (2001).

35. M. Noguchi, N. Ohta, M. Thomas, H. Kitagawa, and I. Miyazaki, "Risk of internal mammary lymph node metastases and its prognostic value in breast cancer patients," *J. Surg. Oncol.* **52**(1), 26–30 (1993).

36. H. S. Cody III and J. A. Urban, "Internal mammary node status: A major prognosticator in axillary node-negative breast cancer, *Ann. Surg. Oncol.* **2**(1), 32–37 (1995).

37. W. B. Eubank, D. A. Mankoff, J. Takasugi, et al., "18fluorodeoxyglucose positron emission tomography to detect mediastinal or internal mammary metastases in breast cancer," *J. Clin. Oncol.* **19**(15), 3516–3523 (2001).

38. T. Uematsu, M. Kasami, and S. Yuen, "Comparison of FDG PET and MRI for evaluating the tumor extent of breast cancer and the impact of FDG PET on the systemic staging and prognosis of patients who are candidates for breast-conserving therapy," *Breast Cancer* **16**(2), 97–104 (2009).

39. J. P. Whitlock, A. J. Evans, L. Jackson, S. Y. Chan, and F. J. Robertson, "Imaging of metastatic breast cancer: Distribution and radiological assessment at presentation, *Clin. Oncol. (R. Coll. Radiol).* **13**(3), 181–186 (2001).

40. M. Z. Mvere, J. J. James, E. J. Cornford, et al., "Frequency and patterns of metastatic disease in locally advanced inflammatory and

non-inflammatory breast cancer, *Clin. Oncol. (R. Coll. Radiol)*. **23**(9), 608–612 (2011).

41. J. Dose-Schwarz, S. Mahner, S. Schirrmacher, et al., "Detection of metastases in breast cancer patients: Comparison of FDG PET with chest X-ray, bone scintigraphy and ultrasound of the abdomen," *Nuklearmedizin.* **47**(3), 97–103 (2008).
42. M. E. Brennan and N. Houssami, "Evaluation of the evidence on staging imaging for detection of asymptomatic distant metastases in newly diagnosed breast cancer," *Breast* **21**(2), 112–23 (2012).
43. L. Pan, Y. Han, X. Sun, J. Liu, and H. Gang, "FDG-PET and other imaging modalities for the evaluation of breast cancer recurrence and metastases: A meta-analysis. *J. Cancer Res. Clin. Oncol.* **136**(7), 1007–1022 (2010).
44. G. P. Schmidt, A. Baur-Melnyk, P. Herzog, et al., "High-resolution whole-body magnetic resonance image tumor staging with the use of parallel imaging versus dual-modality positron emission tomography-computed tomography: Experience on a 32-channel system," *Invest. Radiol.* **40**(12), 743–753 (2005).
45. G. Friedel, U. Pastorino, R. J. Ginsberg, et al., "Results of lung metastasectomy from breast cancer: Prognostic criteria on the basis of 467 cases of the International Registry of Lung Metastases," *Eur. J. Cardiothorac. Surg.* **22**(3), 335–344 (2002).
46. C. Ludwig, E. Stoelben, and J. Hasse, "Disease-free survival after resection of lung metastases in patients with breast cancer," *Eur. J. Surg. Oncol.* **29**(6), 532–535 (2003).
47. A. K. Banerjee, I. Willetts, J. F. Robertson, and R. W. Blamey, "Pleural effusion in breast cancer: A review of the Nottingham experience," *Eur. J. Surg. Oncol.* **20**(1), 33–36 (1994).
48. S. Mahner, S. Schirrmacher, W. Brenner, et al., "Comparison between positron emission tomography using 2-[fluorine-18]fluoro-2-deoxy-D-glucose, conventional imaging and computed tomography for staging of breast cancer," *Ann. Oncol.* **19**(7), 1249–1254 (2008).
49. W. Kersjes, E. Mayer, M. Buchenroth, K. Schunk, N. Fouda, and H. Cagil, "Diagnosis of pulmonary metastases with turbo-SE MR imaging," *Eur. Radiol.* **7**(8), 1190–1194 (1997).
50. T. H. Mohammed, A. Chowdhry, G. P. Reddy, J. K. Amoroso, K. Brown, D. S. Dyer, M. E. Ginsburg, D. E. Heitkamp, J. Jeudy, J. Kirsch, H. MacMahon, J. A. Parker, J. G. Ravenel, A. G. Saleh, and

R. D. Shah, Expert Panel on Thoracic Imaging, "ACR Appropriateness Criteria® screening for pulmonary metastases," online publication, American College of Radiology, Reston,VA (2010).

51. M. Koizumi, S. Takahashi, and E. Ogata, "Bone metabolic markers in bisphosphonate therapy for skeletal metastases in patients with breast cancer," *Breast Cancer* **10**(1), 21–7 (2003).
52. C. C. Roberts, R. H. Daffner, B. N. Weissman, L. Bancroft, D. L. Bennett, J. S. Blebea, M. A. Bruno, I. B. Fries, I. Germano, L. Holly, J. A. Jacobson, J. S. Luchs, W. B. Morrison, J. J. Olson, W. K. Payne, C. S. Resnik, M. E. Schweitzer, L. L. Seeger, M. Taljanovic, J. N. Wise, and S. T. Lutz, Expert Panel on Musculoskeletal Imaging, "ACR Appropriateness Criteria® Metastatic Bone Disease, online publication, American College of Radiology Reston, VA (2009).
53. G. J. Cook, S. Houston, R. Rubens, M. N. Maisey, and I. Fogelman, "Detection of bone metastases in breast cancer by 18FDG PET: Differing metabolic activity in osteoblastic and osteolytic lesions, *J. Clin. Oncol.* **16**(10), 3375–3379 (1998).
54. S. Hahn, T. Heusner, S. Kummel, et al., "Comparison of FDG-PET/CT and bone scintigraphy for detection of bone metastases in breast cancer," *Acta Radiol.* **52**(9), 1009–1014 (2011).
55. K. Nakanishi, M. Kobayashi, S. Takahashi, et al., "Whole body MRI for detecting metastatic bone tumor: comparison with bone scintigrams, *Magn. Reson. Med. Sci.* **4**(1), 11–17 (2005).
56. G. P. Schmidt, S. O. Schoenberg, R. Schmid, et al., "Screening for bone metastases: Whole-body MRI using a 32-channel system versus dual-modality PET-CT," *Eur. Radiol.* **17**(4), 939–949 (2007).
57. J. Grankvist, R. Fisker, V. Iyer V, et al., "MRI and PET/CT of patients with bone metastases from breast carcinoma," *Eur. J. Radiol.* **81**(1), e13–8 (2011).
58. N. Houssami and C. M. Costelloe, "Imaging bone metastases in breast cancer: Evidence on comparative test accuracy," *Ann. Oncol.* **23**(4), 834–843 (2012).
59. K. Engelhard, H. P. Hollenbach, K. Wohlfart, E. von Imhoff, and F. A. Fellner, "Comparison of whole-body MRI with automatic moving table technique and bone scintigraphy for screening for bone metastases in patients with breast cancer," *Eur. Radiol.* **14**(1), 99–105 (2004).
60. L. M. Wu, H. Y. Gu, J. Zheng, et al., "Diagnostic value of whole-body magnetic resonance imaging for bone metastases: A systematic

review and meta-analysis," *J. Magn. Reson. Imaging* **34**(1) 128–135 (2011).

61. M. H. Yilmaz, M. Ozguroglu, D. Mert, et al., "Diagnostic value of magnetic resonance imaging and scintigraphy in patients with metastatic breast cancer of the axial skeleton: A comparative study," *Med. Oncol.* **25**(3), 257–263 (2008).
62. C. Kamby, I. Vejborg, B. Kristensen, L. O. Olsen, and H. T. Mouridsen, "Metastatic pattern in recurrent breast cancer: Special reference to intrathoracic recurrences, *Cancer* **62**(10), 2226–2233 (1988).
63. C. Kamby, J. Andersen, B. Ejlertsen, et al., "Histological grade and steroid receptor content of primary breast cancer: Impact on prognosis and possible modes of action," *Brit. J. Cancer* **58**(4), 480–486 (1988).
64. C. Haagensen, "Anatomy of the Mammary Glands," in *Diseases of the Breast*, 3rd edition, C. Haagensen, Ed., Saunders, Philadelphia (1986).
65. M. Selzner, M. A. Morse, J. J. Vredenburgh, W. C. Meyers, and P. A. Clavien, "Liver metastases from breast cancer: Long-term survival after curative resection, *Surgery* **127**(4), 383–389 (2000).
66. A. Ravaioli, G. Pasini, A. Polselli, et al., "Staging of breast cancer: New recommended standard procedure," *Breast Cancer Res. Treat.* **72**(1), 53–60 (2002).
67. H. I. Khalil, A. S. Patterson, and D. M. Panicek, "Hepatic lesions deemed too small to characterize at CT: Prevalence and importance in women with breast cancer," *Radiol.* **235**(3), 872–878 (2005).
68. S. Namasivayam, D. R. Martin, and S. Saini, "Imaging of liver metastases: MRI," *Cancer Imaging* **7**, 2–9 (2007).
69. K. D. Hagspiel, K. F. Neidl, A. C. Eichenberger, W. Weder, and B. Marincek, "Detection of liver metastases: comparison of superparamagnetic iron oxide-enhanced and unenhanced MR imaging at 1.5 T with dynamic CT, intraoperative US, and percutaneous US," *Radiol.* **196**(2), 471–478 (1995).
70. S. A. Patterson, H. I. Khalil, and D. M. Panicek, "MRI evaluation of small hepatic lesions in women with breast cancer, *Am. J. Roentgenol.* **187**(2), 307–312 (2006).
71. A. M. Gonzalez-Angulo, M. Cristofanilli, E. A. Strom, et al., "Central nervous system metastases in patients with high-risk breast carcinoma after multimodality treatment," *Cancer* **101**(8), 1760–1766 (2004).

72. A. B. Miller, B. Googstraten, M. Staquet, and A. Winkler, "Reporting results of cancer treatment," *Cancer* **47**(1), 207–214 (1981).

73. P. Therasse, S. G. Arbuck, E. A. Eisenhauer, et al., "New guidelines to evaluate the response to treatment in solid tumors, European Organization for Research and Treatment of Cancer, National Cancer Institute of the United States, National Cancer Institute of Canada," *J. Natl. Cancer Inst.* **92**(3), 205–216 (2000).

74. E. A. Eisenhauer, P. Therasse, J. Bogaerts, et al., "New response evaluation criteria in solid tumours: Revised RECIST guideline (version 1.1)," *Eur. J. Cancer* **45**(2), 228–247 (2009).

75. D. J. Sargent, L. Rubinstein, L. Schwartz, et al., "Validation of novel imaging methodologies for use as cancer clinical trial end-points," *Eur. J. Cancer* **45**(2) 290–299 (2009).

76. E. Grunfeld, S. Dhesy-Thind, and M. Levine, "Clinical practice guidelines for the care and treatment of breast cancer: Follow-up after treatment for breast cancer (summary of the 2005 update)," *Can. Med. Assoc. J.* **172**(10), 1319–1320 (2005).

77. P. Ghezzi, S. Magnanini, M. Rinaldini, et al. (the GIVIO investigators), "Impact of follow-up testing on survival and health-related quality of life in breast cancer patients: A multicenter randomized controlled trial," *J. Am. Med. Assoc.* **271**(20), 1587–1592 (1994).

78. M. P. Rojas, E. Telaro, A. Russo, et al., "Follow-up strategies for women treated for early breast cancer, *Cochrane Database Syst Rev.* **1**, CD001768 (2005).

79. J. Dewar, "Follow up in breast cancer," *Brit. Med. J.* **310**(6981), 685–686 (1995).

80. American Society of Clinical Oncology, "Clinical practice guidelines for the use of tumor markers in breast and colorectal cancer," Adopted on May 17, 1996 by the American Society of Clinical Oncology, *J. Clin. Oncol.* **14**(10), 2843–2877 (1996).

81. L. D. Wagman, R. D. Sanders, J. J. Terz, J. D. Beatty, W. A. Kokal, and D. U. Riihimaki, "The value of symptom directed evaluation in the surveillance for recurrence of carcinoma of the breast," *Surg. Gynecol. Obstet.* **172**(3), 191–196 (1991).

82. R. C. Bast, Jr., P. Ravdin, D. F. Hayes, et al., "2000 update of recommendations for the use of tumor markers in breast and colorectal cancer: clinical practice guidelines of the American Society of Clinical Oncology," *J. Clin. Oncol.* **19**(6), 1865–1878 (2001).

83. M. Cristofanilli, G. T. Budd, M. J. Ellis, et al., "Circulating tumor cells, disease progression, and survival in metastatic breast cancer," *N. Engl. J. Med.* **351**(8), 781–791 (2004).

84. G. T. Budd, M. Cristofanilli, M. J. Ellis, et al., "Circulating tumor cells versus imaging: Predicting overall survival in metastatic breast cancer," *Clin. Cancer Res.* **12**(21), 6403–6409 (2006).

85. G. W. Goerres, S. C. Michel, M. K. Fehr, et al., "Follow-up of women with breast cancer: Comparison between MRI and FDG PET," *Eur. Radiol.* **13**(7), 1635–1644 (2003).

86. P. B. Hathaway, D. A. Mankoff, K. R. Maravilla, et al., "Value of combined FDG PET and MR imaging in the evaluation of suspected recurrent local-regional breast cancer: Preliminary experience," *Radiol.* **210**(3), 807–814 (1999).

87. H. J. Gallowitsch, E. Kresnik, J. Gasser, et al., "F-18fluorodeoxyglucose positron-emission tomography in the diagnosis of tumor recurrence and metastases in the follow-up of patients with breast carcinoma: A comparison to conventional imaging, *Invest. Radiol.* **38**(5), 250–256 (2003).

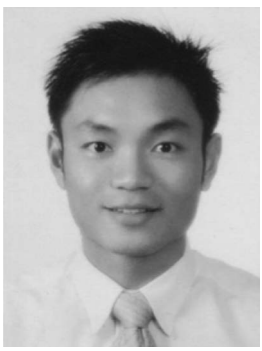

Cher Heng Tan, M.D. obtained his medical degree from the National University of Singapore (NUS) in 2001 and completed his training in diagnostic radiology in 2009. He is presently a consultant with the Department of Diagnostic Radiology at Tan Tock Seng Hospital. His subspecialty interests are in oncologic imaging and abdominal MRI, for which he completed a clinical fellowship at MD Anderson Cancer Center, Houston, Texas, USA in 2009. He now serves as Chairman of the Abdominal Radiology Subsection of the Singapore Radiological Society. As a clinical core faculty member of the NHG-AHPL Diagnostic Radiology Residency Program, Cher Heng is involved with training of radiology residents. He is also a clinical tutor for medical students with Yong Loo Lin School of Medicine, NUS. Cher Heng is currently involved, with various NTU scientists, in a number of funded research projects primarily related to MRI. He has been appointed Specialty Editor for the *Singapore Medical Journal*.

Chapter 6
Nuclear Imaging with PET CT and PET Mammography

Andrew Eik Hock Tan
Department of Radiology, Raffles Hospital, Singapore

Wanying Xie
Department of Nuclear Medicine and PET, Singapore General Hospital, Singapore

6.1 Introduction

This chapter reviews the state of molecular imaging in breast cancer, specifically the various indications for PET and the supportive evidence behind such clinical use, with a brief discussion into the molecular genetics of breast tumors and its relation to molecular imaging.

Medical imaging plays an integral role in the management of breast cancers, allowing for noninvasive staging, prognostication, and response evaluations of patients. Advanced cross-sectional imaging modalities such as computed tomography (CT) and magnetic resonance imaging (MRI) are routinely used in the assessment of such patients.

Molecular imaging techniques such as positron emission tomography (PET) have only been used more recently than CT and MRI but are quickly gaining acceptance in clinical practice. The basis of molecular imaging lies with the detection of specific cell processes or targets, allowing for a precise and more specific identification of target tissue.

The most commonly used radiotracer in PET imaging is fluorodeoxyglucose (FDG or ^{18}F). Generally, malignant tissues tend to demonstrate significantly increased metabolism and glucose uptake compared to normal tissue, and FDG can be used as a substrate to identify such tissue.[1] The molecular basis of such increased glucose usage in tumor cells appears related to a multitude of factors, but two major factors have been implicated. Firstly, tumor cells have been found to overexpress glucose transporters (predominantly GLUT 1, 3 and 5), which actively drive glucose into the cells, and secondly, there is an overexpression of hexokinase enzymes that increase glucose metabolism.[2–4]

It is justifiable to claim that it was the success of FDG PET imaging that led to the explosive growth of molecular and functional imaging. Since the United States (US) Food and Drug Administration (FDA) approval of FDG as a radiopharmaceutical in 1997, advances and adoption by clinical medicine has been encouraging, and this trend has been accelerated by developments in imaging technologies, especially hybrid PET/CT scanners.

The overall use of FDG PET in oncology is established with consistent clinical impact across a range of tumors,[5] and, pertinent to this chapter, breast cancers included. We now discuss the specific uses of PET in breast cancer and touch briefly on the molecular pathology and how this relates to our current understanding of molecular imaging.

6.2 Breast Cancer Molecular Pathology and PET

Breast cancer is the most commonly diagnosed cancer in women, accounting for approximately 30% of all cancers occurring in women with an estimated lifetime risk of 6.1%.[6] Established risk factors for this disease include age, family history, late first pregnancy, and obesity.[7]

Treatment options can be divided into locoregional (mastectomy, breast conservation surgery, radiotherapy) and systemic (chemotherapy, endocrine treatment, biological therapies) treatments, the use of which is dependent on various factors such as the underlying genetic risks, disease burden at presentation, risk of spread and recurrence, patient functional status, and social factors.

Breast cancers arise from the epithelial cells of the breast ducts, and the most important histological feature is the presence of tumor invasion through the ductal architecture, which divides the tumor into noninvasive and invasive subtypes. Other important features include the architectural pattern (ductal, lobular, or mixed), histological grading, and presence of lymphovascular invasion.[8]

The changes in metabolism in malignant cells cannot be explained by a single factor but is rather a complex interaction of various mechanisms that results in the increased glycolysis.[4,9] Reported biological and genetic

changes in breast cancer that influence the degree of FDG uptake include factors such as microvascular changes resulting in increased blood flow, increased expression of glucose transporters (GLUT-1, predominantly) resulting in increased glucose uptake by the cells, upregulated hexokinase enzyme activity that metabolizes and traps the FDG glucose analogue, tumor cellular proliferation (ki-67), and associated inflammatory changes.

Because of this complex interaction between the tumor microenvironment and intrinsic cellular energy demands, FDG PET cannot be reliably used to determine specific biological characteristics of the tumor such as proliferation, differentiation, or histopathological grading.

However, general differences in such biological changes can be characterized using FDG PET. For example, in the context of breast cancers, there are distinct biological differences between ductal and lobular carcinoma subtypes, in which lobular histological subtypes have a lower level of glucose transporter expression, decreased proliferation rates, and lower tumor density compared to ductal histological subtypes. This is translated into generally lower FDG uptake in lobular cancers in comparison to ductal carcinomas.[10,11]

Recently, there has been expanded use of molecular genetic profiling to identify patients at risk of local or regional recurrence. A commonly used classification scheme uses a six-marker immunohistochemistry panel that includes estrogen receptor (ER), progesterone receptor (PR), human epidermal growth factor receptor (HER2 or Neu), epidermal growth factor receptor (EGFR) expression, cytokeratin 5 and 6 (CK 5/6), and presence and degree of proliferation based on the Ki-67 index. This classification scheme divides breast tumors into six specific subtypes (Table 6.1), in which the cellular phenotype lies in a range between that of ductal epithelial cells (termed luminal) and the outer myoepithelial cell layer (termed basal).

Table 6.1 Immunohistochemistry criteria for defining breast cancer subtypes.

Subtype	ER	PR	HER2	EGFR	CK5/6	Ki-67
Luminal A	Either positive		Negative	+/–	+/–	Negative
Luminal B	Either positive		Negative	+/–	+/–	Positive
Luminal HER2	Either positive		Positive	+/–	+/–	+/–
HER2 enriched	Negative	Negative	Positive	+/–	+/–	+/–
Basal	Negative	Negative	Negative	Either positive		+/–
Trip negative nonbasal	Negative	Negative	Negative	Negative	Negative	+/–

Abbreviations: ER: estrogen receptor; PR: progesterone receptor; HER2: human epidermal growth factor receptor 2; EGFR: epidermal growth factor receptor (HER1); CK: cytokeratin.

Luminal A–type tumors are generally associated with a low risk of local or regional recurrence, whereas other subtypes such as basal (triple negative) and HER2-enriched tumor types impose a significance risk of recurrence,[12] suggesting that additional (adjuvant) treatments might be indicated to address the possibility of such increased risk.

Of interest, correlations between the degree of FDG uptake and the presence or absence of markers such as ERs, PRs, and HER2 has been shown, and this is of possible significance in disease prognostication.[13]

The discovery of BRCA-1 and BRCA-2 tumor suppressor gene mutations in the germ cell lines shed some light on the mechanism of breast cancer inheritance, with patients with such mutations at markedly increased risk of breast and ovarian cancers.[14–16] Data regarding the use of PET imaging in such patients is scarce, but there are arguable indications for the use of FDG-dedicated PET mammography in screening such high-risk patients.[17]

In looking at specific biological changes or factors in the tumor, more specialized radiotracers have been and are being investigated. The ability to target and specifically image the tumor receptor and proteins such as ERs and HER2 is of clinical relevance in breast cancers, as they allow the identification of therapy targets such as for hormonal and biological therapies.

The gold standard evaluation of ER status is performed by immunohistochemical staining of the tumor. However, the technique is influenced by interobserver variations and the type of antibody used, and this can lead to inaccurate assessments.[18] In terms of clinical impact, the absence of ER expression on immunohistochemistry staining has a strong negative predictive value (NPV) for response to antihormonal treatment,[19] but poor positive predictive value (PPV) in predicting response.[20]

The use of imaging has several advantages over histological sampling. Firstly, it allows the assessment of the entire tumor burden and limits the possibility of sampling errors, as hormonal expression is often heterogeneous.[21] In breast cancer patients, discordant ER expression between the primary tumor and metastatic lesions has been reported in 18–55% of patients, and loss of ER expression in distant metastasis was a predictor of poor response to hormonal treatment.[22–24] Secondly, molecular imaging allows the "sampling" of tumors that might be difficult to target and allows repeated noninvasive assessment of such receptor expression that might not be feasible with direct sampling.

The use of steroid-radiolabelled tracers such as ^{18}fluorine fluoro-17β-estradiol (^{18}F-FES) has allowed for the PET imaging of ER expression, and several studies have shown that such FES PET assessment of ER expression correlates well with immunohistochemical scoring for ER.[25–27] Clinically, FES uptake in breast tumors has been shown to be able to predict response to tamoxifen therapy in patients with advanced ER expressing tumors,[28] with one study reporting that treatment selection using FES

PET would have increased the rate of response from 23 to 34% overall, and up to 46% if the tumors did not overexpress HER2/Neu.[29]

HER2 expression in breast tumors is an important prognostic factor and is an increasingly important target for treatment.[30] HER2 belongs to the family of tyrosine-specific protein kinases, which act primarily as growth factor receptors and regulate downstream growth factor pathways. Such pathways are often dysregulated in human cancers, resulting in uncontrolled proliferation of cells, making such receptors an attractive target for anticancer treatment.[31]

Several groups have developed radioligands for the *in vivo* imaging of HER2 expression, using a variety of ligands and tracers. These include iodine-124–labeled divalent HER2 antibody fragment,[32] yttrium-86– and indium-111–labeled trastuzumab,[33] ^{18}F affibody molecules,[34] and gallium-68–labeled affibody molecules.[35] Most of the studies have been preclinical animal studies with few early human trials conducted, but these results have been promising and have shown the feasibility of PET characterization and semiquantification of HER2 receptor expression.

Cellular proliferation is a fundamental property of cancers, and thymidine analogues radiolabelled with ^{18}F have been developed that allow *in vivo* PET imaging of tumor proliferation, with such radiotracer uptake significantly correlating with cellular proliferation as measured by the Ki-67 labeling index.[36] Of significance, early studies have shown the promise of such proliferation imaging in the early prediction of tumor therapy response, and have shown that such studies can be performed with high reproducibility in patients with breast cancer.[37]

Overall, an understanding of the molecular pathogenesis and genetics of breast cancers and its influence on management is needed before appropriate utilization of medical imaging can be effectively applied.

6.3 Diagnosis of Primary Breast Cancers

Currently, most primary breast cancers are detected through self-breast examinations or during screening with mammography or ultrasound, with breast MRI emerging as a screening tool for high-risk patients.[37]

Current whole body (WB) PET/CT scanners have an average of 4- to 6-mm spatial resolution, although there are claims of up to 2-mm resolution. This generally means that the sensitivity of current general PET/CT machines for lesions less than 1 cm is limited; this sensitivity has been corroborated by several published reports detailing the accuracy of WB PET/CT devices in the primary diagnosis or characterization of breast tumors.

Initial studies in clinical trials with qualitative analysis consider visually conspicuous foci with increased FDG accumulation above that of background at the site of the lesion as positive. These yielded sensitivity

rates of 80–86%.[39] More-recent studies employ quantitative FDG uptake, measuring the ratio of maximum FDG uptake [the maximum standardized uptake value (SUVmax) of the lesion in question] to the SUVmean of the background tissue. The authors found that a lesion-to-background (LTB) ratio of 2.0 with focal localization is considered a sound indicator of malignancy. Burg et al.[40] stressed the importance of interpreting positron emission mammography (PEM) images with mammographic correlation, as they found that a mismatch between mammographic and PET findings, such as expected focal radiotracer activity based on mammographic tissue distribution, was highly predictive of malignancy. In their study, three false positives on PEM imaging could be reduced with correlative mammography, as these lesions were clearly identified as benign on mammography.

A concern in regard to breast imaging is the temporal related change that occurs in breast parenchyma, in relation to the hormonal status of the patient. For FDG PET imaging, the generally low background breast tissue FDG uptake, even in dense breast parenchyma, is unlikely to affect the ability of PET to discriminate between benign and malignant findings.[41] This is in contrast to conventional mammograms whereby imaging sensitivities are known to decrease with increasing breast densities.[42]

Overall, reported WB FDG PET sensitivity in the detection of primary breast cancer is 64–96%, specificity is 73–100%, PPV is 81–100%, and NPV is 52–89%,[43] with the main limitations being partial volume effects and variable activity.[44]

Prompted by the generally poor sensitivities of WB PET in the identification of small (pT1a and pT1b) lesions, high-resolution dedicated PET imaging for the breast, also known as PEM, was designed to improve detection of early primary breast carcinomas.

Several factors contribute to the improved results of PEM compared to WB PET. Reduced detector size, diminished interdetector distances, and advances in camera technologies with increased count rates all contribute to improved tumor contrast and SNRs. Reported PEM spatial resolutions have been in the region of 1–2 mm, in contrast to the typical values of 4–6 mm of WB scanners.

Preliminary results with PEM have been promising, with pilot studies showing sensitivities of 80–91% and overall accuracies of 89%.[45,46] In a series of 77 patients, Burg et al.[40] reported an overall specificity of 86%, which was increased to 93% if diabetic patients and those with lesions clearly benign on conventional imaging were excluded. Higher sensitivity rates approaching 93% have been reported in more-recent studies, demonstrating figures comparable with that of MRI.[47] In addition, the value of PEM in evaluating for multifocal disease was shown in these studies.

Surgeons typically plan their surgeries based on available imaging devices of mammogram, US, and MRI. In a pilot clinical trial of 44

patients where 19 were planned for breast conservation surgery, the surgeons in this trial were blinded to the results of PEM, employing conventional imaging to determine resection margins. PEM accurately predicted 6 of 8 patients (75%) with positive margins and 11 of 11 patients (100%) with negative margins. PEM showed effectiveness in defining local disease extent and was shown to illustrate clinically relevant lesions that were occult by conventional imaging. The authors postulated that with data from PEM imaging, clinicians would be able to determine whether breast conservation would be successful in achieving clear margins. Sequentially, more-precise surgical planning with reduction in the numbers of re-excision will be possible.[48]

Hence, with the advent of a high-resolution dedicated breast imaging system, functioning imaging has shown its potential in detection of small (<1.0 cm) and nonpalpable breast lesions that were previously not reliably demonstrated with WB PET scanners. PEM should not be viewed as a competitive tool to replace conventional imaging. Rather, the integration of metabolic (PEM) and anatomic (mammography and US) imaging should offer higher sensitivity and specificity rates than with either alone. This has generated interest in applying PEM as an instrument for local staging and detection of multifocal disease (see Fig. 6.1), as a problem solving tool, for tumor response assessment, and, finally, as an adjunct to screening. Pertinent disadvantages of PEM such as radiation dose, cost, and ability to image posterior lesions should be addressed before adopting it in larger clinical trials to establish the role of PEM in clinical management.

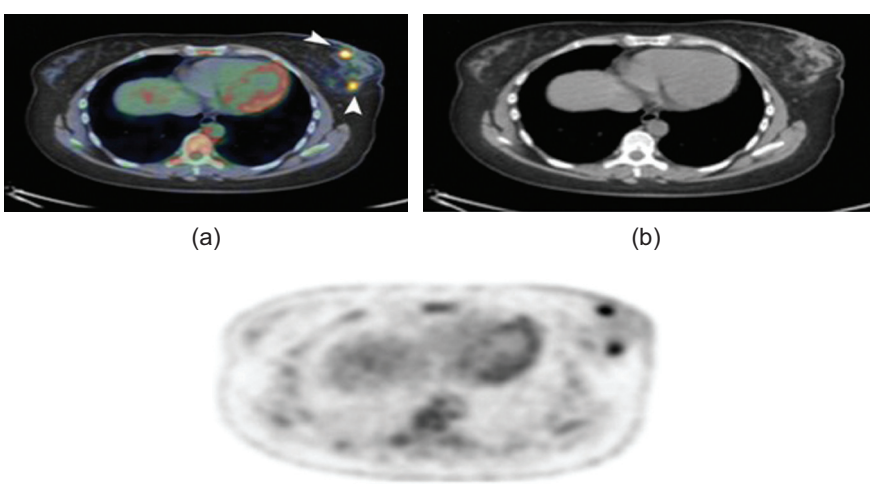

Figure 6.1 Multifocal breast cancer.

6.4 Staging of Breast Cancers

FDG PET is commonly used in breast cancer to determine disease spread, which can be divided into axillary nodal, mediastinal nodal, and distant metastasis assessment.

6.4.1 Axillary nodal evaluation

The presence of axillary nodal disease in breast cancer is an important factor in prognostic evaluation and determining management, and patients with invasive breast tumors typically undergo sentinel lymph node evaluation as part of the initial staging.

Several of the early studies evaluating the use of FDG PET in breast cancer looked into its utility in axillary node staging. Published reports were mixed, with several groups publishing very promising results, and others showing PET sensitivities as low as 20–30%.[49,50]

A review of studies evaluating the utility of FDG PET in assessing axillary nodal disease using axillary nodal dissection as the gold standard shows a wide variation in reported accuracies, with a sensitivity range of 46 to 95%, specificities ranging from 66 and 100%, PPVs of 62–100%, and NPVs of 60–99%.[51]

The largest study[52] was a prospective multicenter trial involving 360 women with newly diagnosed invasive breast cancer. The objective was to determine the accuracy of FDG PET in the assessment of axillary nodal metastasis using axillary nodal dissection as the gold standard. Sensitivities of 61%, specificities of 80%, PPVs of 62%, and NPVs of 79% were reported. The authors[52] further found that false-negative axilla had significantly smaller and fewer tumor positive nodes, but that FDG PET may be highly predictive for axillary nodal disease when multiple intense foci of uptake are seen (see Fig. 6.2). These findings are not surprising and are in fact expected with current WB PET devices, in which current resolution capabilities are unlikely to detect small-volume metastatic disease in the axillary nodes.

Of further interest, the histology of the primary tumor is of importance as lobular-type carcinomas were found to have significantly lower FDG uptake compared to ductal-type carcinomas; this translates into substantially lower sensitivities of 12.5–37.5% in the detection of lobular-type nodal metastasis. These lower sensitivities are consistent with previous reports of ductal breast cancers having significantly higher FDG avidity compared with lobular type cancers,[10] and correlate without previous discussion in regard to the biological differences between ductal and lobular histological subtypes.

A further review in which FDG PET was evaluated against sentinel lymph node biopsies as a gold standard found even lower sensitivities,

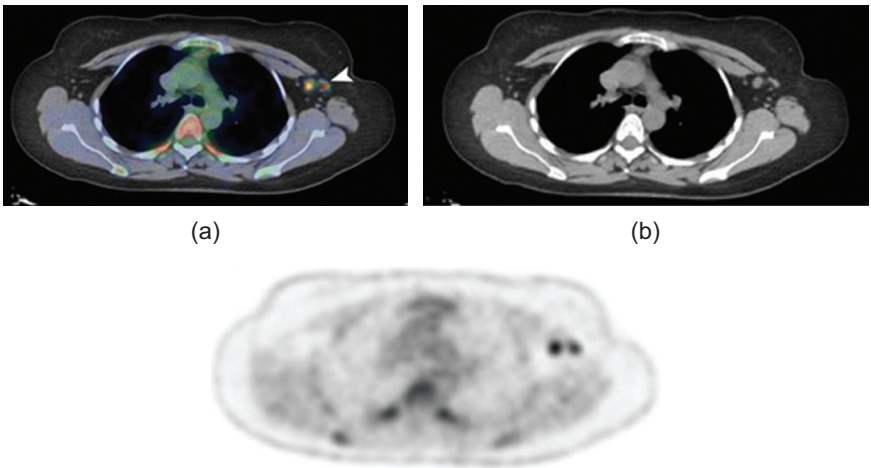

(a) (b)

(c)

Figure 6.2 Axillary nodal metastasis.

ranging from 15 to 47%.[53–55] Postulated reasons include the fact that sentinel lymph node histological assessments with its more detailed examination of a small number of nodes is more likely to detect foci of micrometastasis that cannot be identified with current PET detector sensitivities.

Overall, FDG PET is currently unable to replace sentinel lymph node biopsies in patients with early-stage breast cancer but may have a role in the evaluation of patients with locally advanced primary disease in which the risk of nodal metastasis is high, and the use of FDG PET might avoid the necessity of a sentinel lymph node biopsy if the results are unequivocally positive. In addition, caution in the interpretation of negative FDG PET results in primary lobular breast cancers is advised due to the generally lower FDG avidity.

6.4.2 Mediastinal and internal mammary nodal evaluation

The presence of mediastinal or internal mammary nodal metastasis in patients with breast cancers has important implications in management and is generally associated with poorer prognosis.[56,57] In contrast to the equivocal findings in axillary nodal assessment, there have been consistently encouraging results regarding the use of FDG PET in the detection of mediastinal and axillary nodal disease.

A retrospective review of 73 patients using FDG PET and CT data reported PET sensitivities, specificities, and accuracies of 85%, 90% and 88%, respectively, in the assessment for mediastinal or internal mammary nodal disease, in contrast to 54%, 85% and 73% for CT evaluation.[58] The recognition of disease in the internal mammary or mediastinal regions (see Fig. 6.3) has prognostic implications, as metastasis to the internal

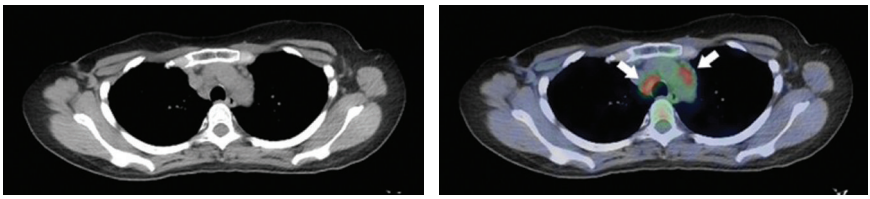

(a) (b)

Figure 6.3 Mediastinal nodal metastasis.

mammary nodal chain has been reported to occur in a substantial portion of patients, up to 25% as reported in some studies, and is associated with a poorer prognosis.[59–60] Further reports have suggested that the presence of internal mammary nodal disease as evidenced by FDG uptake is predictive of failure patterns consistent with such involvement.[61] In addition, the identification of such disease sites has therapeutic implications, as changes to locoregional treatment such as extensions of radiotherapy fields, or more aggressive systemic therapies may be performed depending on findings.

6.4.3 Distant metastasis and overall staging impact of FDG PET

The use of FDG PET in the evaluation of distant metastasis and its general utility as a single tool staging modality is very promising, with several studies demonstrating the increased sensitivity and utility of FDG PET over current conventional techniques.

In one of the earlier studies[62] using FDG PET in staging for breast cancers, WB PET imaging was performed on 57 patients with suspected recurrent or metastatic disease. Encouraging findings were reported: 93% sensitivity, 79% specificity, 82% PPV and 92% NPV of FDG PET in detecting recurrent or metastatic disease.

Heusner et al.[63] from the University Hospital Essen, Germany, demonstrated the technical feasibility and utility of a dedicated PET/CT protocol in breast cancers in which a general WB PET/CT scanner is utilized to perform PET/CT mammography. In a follow-up study, [64] the same authors evaluated the diagnostic accuracy of an all-in-one protocol of WB FDG PET/CT and integrated FDG PET/CT mammography, and compared it to the diagnostic accuracy of a multimodality algorithm for initial breast cancer staging. Forty women with suspected breast cancers were evaluated, and the combination FDG PET/CT protocol was able to demonstrate good accuracies in local disease (95%), nodal disease (80%), and distant metastasis (100%) assessment. Of interest, FDG PET/CT was reported to have greater accuracy in detecting lesion focality compared to MRI, and

there was an overall 12.5% change in patient management with FDG PET/CT imaging.

A study evaluating the effect of adding FDG PET to conventional screening in patients with locally advanced breast cancer was performed by van der Hoeven et al.[65] Forty-eight patients were evaluated with PET, and in 8% of the patients, FDG PET correctly detected distant metastasis not seen with routine evaluations. The authors concluded that the addition of FDG PET to standard work-ups for patients with locally invasive breast cancers may lead to the detection of unsuspected distant metastasis and could contribute to a more accurate staging and stratification of patients.

Similar findings were reported by the group from Hospital Clinic of Barcelona, in which a prospective study involving 60 consecutive patients with large (>3 cm) primary breast cancer was imaged using WB FDG PET/CT and compared to typical conventional investigations.[66] The reported sensitivities and specificities for lymph node assessment was 70% and 100%, respectively, and for distant metastasis it was 100% and 98%, respectively. In contrast, the detection of distant metastasis with conventional imaging was reported with 60% sensitivity and 83% specificity, and FDG PET resulted in a change in the initial staging in 42% of patients.

Mahner et al.[67] evaluated 119 consecutive patients with newly diagnosed locally advanced breast cancer or patients with suspected recurrent metastatic disease (see Fig. 6.4), and imaging was correlated with histopathology and clinical followup. Reported FDG PET sensitivities and specificities were 87% and 83%, respectively, in the detection of distant

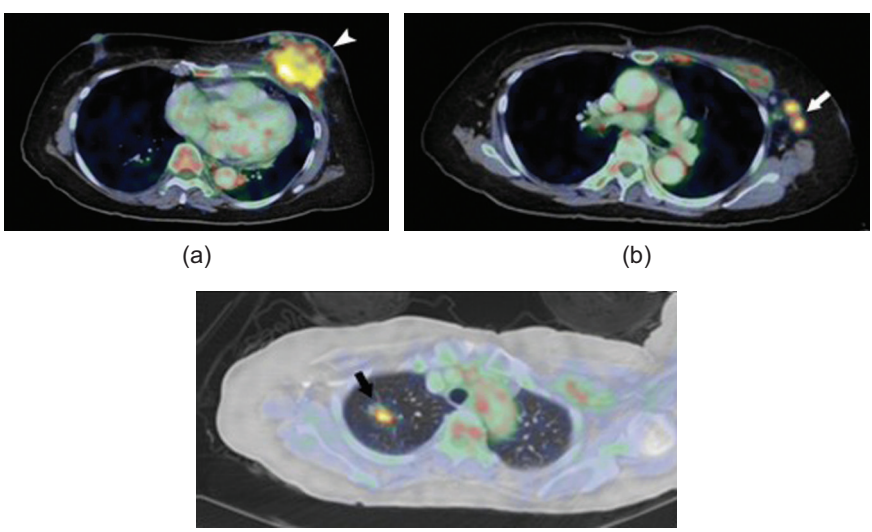

(a) (b)

(c)

Figure 6.4 Metastatic breast cancer.

metastasis, compared to conventional imaging modality sensitivity of 43% and specificity of 98%.

The overall impact of FDG PET on clinical management is significant. An interesting study investigating the impact of FDG PET from the referring physician's perspective concluded that there was a major impact on the management of breast cancer patients, influencing both clinical staging and management in more than 30% of cases.[68]

6.5 Response Assessment

Imaging plays an important role in determining the response of tumors to systemic or locoregional treatments, predominantly in the settings of neoadjuvant treatment and metastatic disease. Prior to the advent of functional imaging, morphologic or size-based criteria have been traditionally used to measure response, but there were several limitations that include delays in significant size changes, reproducibility of measurements, and lack of correlation to clinical endpoints such as overall survival and time to tumor progression. These potentially may be addressed with functional imaging.

Approximately 10–15% of patients present with locally advanced breast cancer,[69] and neoadjuvant treatment (see Fig. 6.5) is becoming standard treatment for such patients to both improve surgical options and to provide prognostic information.[70] Patients with complete response or minimal residual disease typically have longer disease-free and overall survival rates.[71] Techniques that allow prediction of therapeutic response at early time points could potentially halt ineffective treatments early.

Typical morphological approaches to neoadjuvant treatment response evaluation have limitations, and it is often difficult to determine or stratify the response. In 1989, the use of the FDG radiotracer in breast cancer was

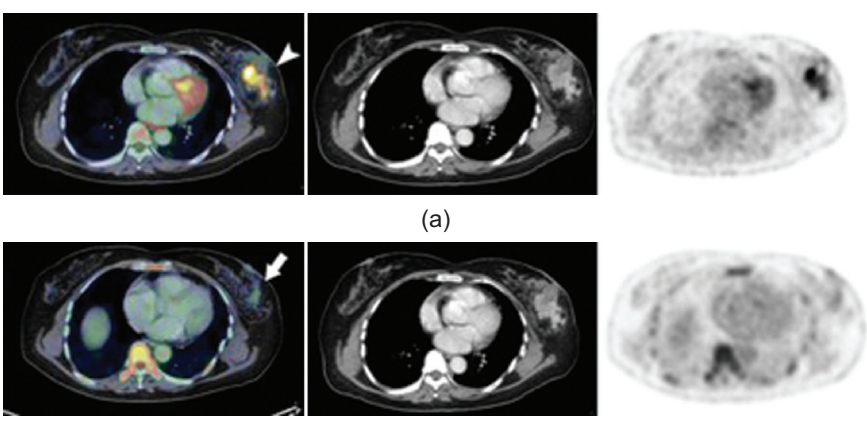

Figure 6.5 Neoadjuvant breast cancer therapy.

performed by Minn et al.,[72] in which a gamma camera was used to image breast cancer patients injected with FDG. Even then with basic equipment, the lesions could be clearly visualized, and changes in FDG uptake could be observed following treatment. One of the earliest studies on neoadjuvant response[73] evaluated the use of sequential FDG PET in monitoring neoadjuvant chemotherapy response in a group of 11 patients with locally advanced breast cancer. Responding tumors demonstrated fast and significant decreases in FDG uptake, and these metabolic changes preceded size changes. Nonresponding tumors did not show any significant decreases in FDG uptake.

Smith et al.[74] investigated 30 patients with noninflammatory locally advanced breast cancers receiving neoadjuvant chemotherapy. Using a 20% cut-off value in assessing changes in SUV, PET imaging was able to predict complete pathological response with a sensitivity and specificity of 90% and 74%, respectively.

Similarly, a pilot study of 22 patients with locally advanced breast tumors reported an accuracy of 88% and 91% in predicting histopathological response after the first and second cycles of neoadjuvant chemotherapy, respectively.[75]

Rousseau et al.[76] prospectively evaluated 64 patients with stage II and III breast cancers undergoing neoadjuvant chemotherapy, and found that FDG PET could predict pathologic response accurately after 2 courses of chemotherapy, with a sensitivity of 89%, specificity of 95%, and NPV of 85%. Another similar study[77] evaluating 47 women went one step further in concluding that FDG PET is able to predict pathological response with neoadjuvant chemotherapy after 1 cycle of treatment.

A large prospective multicenter trial evaluating the use of FDG PET in predicting response during neoadjuvant treatments of locally advanced breast cancers concluded similar findings.[78] One-hundred four patients were recruited, with 272 FDG PET scans performed at base line and after the first and second chemotherapy cycles. All patients underwent surgery after neoadjuvant therapy, and histopathological evaluation was used as the gold standard. Histological nonresponders could be identified with an NPV of 90%, and relative drops in SUV values after each chemotherapy cycle were strong predictors of response.

In regard to metastatic disease, the reported utility of FDG PET in response assessment was similar to neoadjuvant response assessment. In a small study of 11 patients with 26 metastatic lesions, Schwarz et al.[79] found significant differences in SUV changes between nonresponders and responders, and concluded that sequential FDG PET was able to predict response after the first cycle of chemotherapy.

For bone metastasis, FDG PET imaging is more reflective of tumor viability and activity, compared to conventional imaging in which morphological changes can widely vary. In addition, FDG PET findings were

correlated with survival, in which the prognosis for patients with persistently FDG avid bone lesions was poorer.[80]

The correlation between FDG PET findings and clinical outcomes of survival was further substantiated by a study by Cachin et al,[81] in which 47 patients with metastatic breast cancer were treated with 3 cycles of high-dose chemotherapy and autologous stem cell transplant. The response assessment was performed with FDG PET and conventional imaging after the last chemotherapy cycle. Significant differences were found in complete response rates, with 37% based on conventional imaging and 72% with FDG PET. Of significance, FDG PET was found to be the most powerful and independent predictor of survival.

6.6 Conclusion

The role of PET is established in the practice of oncology, and advances in functional and molecular imaging techniques have allowed increased accuracies and confidence in the diagnostic evaluation of breast cancers.

References

1. S. S. Gambhir, J. Czernin, J. Schwimmer, D. H. Silverman, R. E. Coleman, and M. E. Phelps, "A tabulated summary of the FDG PET literature," *J. Nucl. Med*. **42**(5), 1S–93S (2001).
2. E. K. Pauwels, E. J. Sturm, E. Bombardieri, F. J. Cleton, and M. P. Stokkel, "Positron-emission tomography with [18F]fluorodeoxyglucose. Part I. Biochemical uptake mechanism and its implication for clinical studies," *J. Cancer Res. Clin. Oncol*. **126**, 549–559 (2000).
3. S, Zhao, Y. Kuge, T. Mochizuki, et al., "Biologic correlates of intratumoral heterogeneity in 18F-FDG distribution with regional expression of glucose transporters and hexokinase-II in experimental tumor," *J. Nucl. Med*. **46**, 675–682 (2005).
4. R. Bos, J. J. van Der Hoeven, E. van Der Wall, et al., "Biologic correlates of 18 fluorodeoxyglucose uptake in human breast cancer measured by positron emission tomography," *J. Clin. Oncol*. **20**, 379–387 (2002).
5. B. E. Hillner, B. A Siegel, R. E. Coleman, et al., "Relationship between cancer type and impact of PET and PET/CT on intended management: Findings of the national oncology PET registry," *J. Nucl. Med*. **49**, 1928–1935 (2008).
6. Singapore Cancer Registry, Updated Sept. 2011.
7. F. Salehi, M. C. Turner, K. J. Aronson, et al., "Review of the etiology of breast cancer with special attention to organochlorines as

potential endocrine disruptors," *J. Toxicol. Environ. Health* **11**, 276–300 (2008).

8. S. J. Schnitt, "Traditional and newer pathologic factors," *J. Natl. Cancer Inst. Monogr*. **30**, 22–26 (2001).
9. N. Avril, M. Menzel, J. Dose, M. Schelling, W. Weber, F. Jänicke, W. Nathrath, and M. Schwaiger, "Glucose metabolism of breast cancer assessed by 18F-FDG PET: Histologic and immunohisto-chemical tissue analysis," *J. Nucl. Med*. **42**, 9–16 (2001).
10. A. Buck, H. Schirrmeister, T. Kuhn, C. Shen, T. Kalker, J. Kotzerke, A. Dankerl, G. Glatting, S. Reske, and T. Mattfeldt, "FDG uptake in breast cancer: Correlation with biological and clinical prognostic parameters," *Eur. J. Nucl. Med. Mol. Imaging* **29**, 1317–1323 (2002).
11. A. K. Buck, H. Schirrmeister, T. Mattfeldt, and S. N. Reske, "Biological characterisation of breast cancer by means of PET, "*Eur. J. Nucl. Med. Mol. Imaging* **31**(1), S80–S87 (2004).
12. K. D. Voduc, M. C. Cheang, S. Tyldesley, et al., "Breast cancer subtypes and the risk of local and regional relapse," *J. Clin. Oncol*. **28**, 1684–1691 (2010).
13. A. Mavi, T. F. Cermik, M. Urhan, et al., "The effects of estrogen, progesterone, and C-erbB-2 receptor states on 18F FDG uptake of primary breast cancer lesions," *J. Nucl. Med*. **48**, 1266–1272 (2007).
14. M. C. King, J. H. Marks, and J. B. Mandell, "New York Breast Cancer Study Group. Breast and ovarian cancer risks due to inherited mutations in BRCA1 and BRCA2," *Science* **302**, 643–646 (2003).
15. D. Thompson, D. F. Easton, and the Breast Cancer Linkage Consortium, "Cancer incidence in BRCA1 mutation carriers," *J. Natl. Cancer Inst*. **94**, 1358–65 (2002).
16. D. F. Easton and the Breast Cancer Linkage Consortium, "Cancer risks in BRCA2 mutations carriers," *J. Natl. Cancer Inst*. **91**, 1310–6 (1999).
17. E. E. Sapir and M. Inbar, "PET in women with high risk for breast or ovarian cancer," *Lancet Oncol*. **11**(9), 899–905 (2010).
18. M. E. Hammond, D. F. Hayes, M. Dowsett, et al., "American Society of Clinical Oncology/College of American Pathologists guideline recommendations for immunohistochemical testing of estrogen and progesterone receptors in breast cancer," *J. Clin. Oncol*. **28**, 2784–2795 (2010).
19. C. Davies, J. Godwin, and the Early Breast Cancer Trialists' Collaborative Group (EBCTCG), "Relevance of breast cancer hormone

receptors and other factors to the efficacy of adjuvant tamoxifen: Patient-level meta-analysis of randomised trials," *Lancet* **378**, 771–784 (2011).

20. E. R. DeSombre, S. M. Thorpe, C. Rose, et al., "Prognostic usefulness of estrogen receptor immunocytochemical assays for human breast cancer," *Cancer Res*. **46**, 4256s–4264s (1986).
21. G. G. Chung, M. P. Zerkowski, S. Ghosh, R. L. Camp, and D. L. Rimm, "Quantitative analysis of estrogen receptor heterogeneity in breast cancer," *Lab. Invest*. **87**, 662– 669 (2007).
22. E. Amir, M. Clemons, O. C. Freedman, et al., "Tissue confirmation of disease recurrence in patients with breast cancer: Pooled analysis of two large prospective studies," *J. Clin. Oncol*. **28**, 15s, abstract 1007 (2010).
23. C. Simmons, N. Miller, W. Geddie W, et al., "Does confirmatory tumor biopsy alter the management of breast cancer patients with distant metastases?" *Ann. Oncol*. **20**, 1499–1504 (2009).
24. E. Karlsson, L. S. Lindstrom, U. Wilking, L. Skoog, U. Johansson, and J. Bergh, "Discordance in hormone receptor status in breast cancer during tumor progression," *J. Clin. Oncol*. **28**, abstract 1009 (2010).
25. M. A. Mintun, M. J. Welch, B. A. Siegel, et al., "Breast cancer: PET imaging of estrogen receptors," *Radiol*. **169**, 45–48 (1988).
26. A. H. McGuire, F. Dehdashti, B. A. Siegel, et al., "Positron tomographic assessment of 16 alpha-[18F] fluoro-17 beta-estradiol uptake in metastatic breast carcinoma," *J. Nucl. Med*. **32**, 1526–1531 (1991).
27. L. M. Peterson, D. A. Mankoff , T. Lawton, et al., "Quantitative imaging of estrogen receptor expression in breast cancer with PET and 18F-fluoroestradiol," *J. Nucl. Med*. **49**, 367–374 (2008).
28. J. E. Mortimer, F. Dehdashti, B. A. Siegel, et al., "Metabolic flare: Indicator of hormone responsiveness in advanced breast cancer," *J. Clin. Oncol*. **19**, 2797–2803 (2001).
29. H. M. Linden, S. A. Stekhova, J. M Link, et al., "Quantitative fluoestradil positron emission tomography imaging predicts response to endocrine treatment in breast cancer," *J. Clin. Oncol*. **24**, 2793–2799 (2006).
30. L. Harris, H. Fritsche, R. Mennel, et al., "American Society of Clinical Oncology 2007 update of recommendations for the use of tumor markers in breast cancer," *J. Clin. Oncol*. **25**, 5287–5312 (2007).
31. D. S. Krause, "Tyrosine kinases as targets for cancer therapy," *N. Engl. J. Med*. **353**, 172–87 (2005).
32. M. K. Robinson, M. Doss, C. Shaller, et al., "Quantitative immuno positron emission tomography imaging of HER2-positive tumor

xenografts with an iodine-124 labeled anti-HER2 diabody," *Cancer Res*. **65**, 1471–1478 (2005).

33. K. Garmestani, D. E. Milenic, P. S. Plascjak, and M. W. Brechbiel, "A new and convenient method for purification of 86Y using a Sr(II) selective resin and comparison of biodistribution of 86Y and 111In labeled Herceptin," *Nucl. Med. Biol*. **29**, 599–606 (2002).
34. G. Kramer-Marek, D. O. Kiesewetter, and J. Capala, "Changes in HER2 expression in breast cancer xenografts after therapy can be quantified using PET and 18F-labelled affibody molecules," *J. Nucl. Med*. **50**, 1131–1139 (2009).
35. R. P. Baum, V. Prasad, D. Müller, et al., "Molecular imaging of HER2 expressing malignant tumors in breast cancer patients using synthetic 111IN or 68Ga labeled affibody molecules," *J. Nucl. Med*. **51**, 892–897 (2010).
36. L. M. Kenny, D. M. Vigushin, A. Al-Nahhas, S. Osman, S. K. Luthra, S. Shousha, R. C. Coombes, and E. O. Aboagye, "Quantification of cellular proliferation in tumor and normal tissues of patients with breast cancer by [18F] fluorothymidine-positron emission tomography imaging: Evaluation of analytical methods," *Cancer Res*. **65**, 10104–12 (2005).
37. L. Kenny, R. C. Coombes, D. M. Vigushin, A. Al-Nahhas, S. Shousha, and E. O. Aboagye, "Imaging early changes in proliferation at 1 week post chemotherapy: a pilot study in breast cancer patients with 3'-deoxy-3'-[18F]fluorothymidine positron emission tomography," *Eur. J. Nucl. Med. Mol. Imaging* **34**, 1339–1347 (2007).
38. D. Saslow, C. Boetes, W. Burke, et al. "American Cancer Society guidelines for breast screening with MRI as an adjunct to mammography," *CA Cancer. J. Clin*. **57**, 75–89 (2007).
39. K. Murthy, M. Aznar, A. M. Bergman, et al., "Positron emission mammographic instrument: Initial results," *Radiol*. **215**, 280–285 (2000).
40. W. A. Berg, I. N. Weinberg, D. Narayanan, et al., "High resolution fluorodeoxyglucose positron emission tomography with compression (positron emission mammography) is highly accurate in depicting primary breast cancer," *The Breast J*. **12**(4), 309–323 (2006).
41. D. Vranjesevic, C. Schiepers, D. H. Silverman, et al., "Relationship between 18F-FDG uptake and breast density in women with normal breast tissue," *J. Nucl. Med*. **44**, 1238–1242 (2003).
42. M. T. Mandelson, N. Oestreicher, P. L. Porter, et al., "Breast density as a predictor of mammographic detection: Comparison of interval- and screen-detected cancers," *J. Natl. Cancer Inst*. **92**, 1081–1087 (2000).

43. K. Scheidhauer, C. Walter, and M. D. Seemann, "FDG PET and other imaging modalities in the primary diagnosis of suspicious breast lesions," *Eur. J. Nucl. Med. Mol. Imaging* **31**(1), S70–S79 (2004).

44. N. Avril, C. A. Rosé, M. Schelling, et al., "Breast imaging with positron emission tomography and fluorine-18 fluorodeoxyglucose: Use and limitations," *J. Clin. Oncol*. **18**, 3495–3502 (2000).

45. E. L. Rosen, T. G. Turkington, M. S. Soo, J. A. Baker, and R. E. Coleman, "Detection of primary breast carcinoma with a dedicated large field of view FDG PET mammography device: Initial experience," *Radiol*. **234**, 527–534 (2005).

46. E. A. Levine, R. I. Freimanis, N. D. Perrier, et al., "Positron emission mammography: Initial clinical results," *Annals Surg. Oncol*. **10**(1), 86–91 (2003).

47. K. Schilling, D. Narayanan, J. E. Kalinyak, et al., "Positron emission mammography in breast cancer presurgical planning: Comparison with magnetic resonance imaging," *Eur. J. Nucl. Med. Mol. Imaging* **38**, 23–36 (2011).

48. L. Tafra, Z. Cheng, J. Uddo, et al., "Pilot clinical trial of 18F-fluorodeoxyglucose positron emission mammography in the surgical management of breast cancer," *Am. J. Surg*. **190**, 628–632 (2005).

49. F. Crippa, A. Gerali, A. Alessi, R. Agresti, and E. Bombardieri, "FDG-PET for axillary lymph node staging in primary breast cancer," *Eur. J. Nucl. Med. Mol. Imaging* **31** (suppl 1), S97–S102 (2004).

50. E. L. Rosen, W. B. Eubank, and D. A. Mankoff, "FDG PET, PET/CT, and breast cancer imaging," *Radiographics* **27**(suppl 1), S215–S229 (2007).

51. A. Quon and S. S. Gambhir, "FDG-PET and beyond: Molecular breast cancer imaging," *J. Clin. Oncol*. **23**, 1664–1673 (2005).

52. R. L.Wahl, B. A. Siegel, R. E. Coleman, et al., "Prospective multicenter study of axillary nodal staging by positron emission tomography in breast cancer: A report of the staging breast cancer with PET study group," *J. Clin. Oncol*. **22**, 277–285 (2004).

53. U. Guller, E. U. Nitzsche, and U. Schirp, "Selective axillary surgery in breast cancer patients based on positron emission tomography with 18F- fluoro-2-deoxy-D-glucose: Not yet!" *Breast Cancer Res. Treat*. **71**, 171–173 (2002).

54. J. J. Van der Hoeven, O. S. Hoekstra, E. F. Comans, et al., "Determinants of diagnostic performance of [F-18]fluorodeoxyglucose positron emission tomography for axillary staging in breast cancer," *Ann. Surg*. **236**, 619–624 (2002).

55. P. Lovrics, V. Chen, G. Coates, et al., "A prospective comparison of positron emission tomography scanning, sentinel lymph node biopsy and axillary dissection in staging patients with early stage breast cancer," *Breast Cancer Res. Treat*. **76**, S129 (2002).

56. S. L. Sugg, D. J. Ferguson, M. C. Posner, et al., "Should internal mammary nodes be sampled in the sentinel lymph node era?" *Ann. Surg. Oncol*. **7**, 188–192 (2000).

57. U. Veronesi, N. Cascinelli, and M. Greco, "Prognosis of breast cancer patients after mastectomy and dissection of internal mammary nodes," *Ann. Surg*. **202**, 702–707 (1985).

58. W. B. Eubank, D. A. Mankoff, J. Takasugi, et al., "18fluorodeoxyglucose positron emission tomography to detect mediastinal or internal mammary metastases in breast cancer," *J. Clin. Oncol*. **19**, 3516–3523 (2001).

59. A. Tran, B. S. Pio, B. Khatibi, J. Czernin, M. E. Phelps, and D. H. Silverman, "18F-FDG PET for staging breast cancer in patients with inner-quadrant versus outer-quadrant tumors: comparison with long-term clinical outcome," *J. Nucl. Med*. **46**, 1455–1459 (2005).

60. D. N. Danforth, Jr., L. Aloj, J. A. Carrasquillo, et al., "The role of 18F-FDG-PET in the local/regional evaluation of women with breast cancer," *Breast Cancer Res. Treat*. **75**, 135–146 (2002).

61. J. R. Bellon, R. B. Livingston, W. B. Eubank, et al., "Evaluation of the internal mammary lymph nodes by FDG-PET in locally advanced breast cancer (LABC)," *Am. J. Clin. Oncol*. **27**, 407–410 (2004).

62. D. H. Moon, J. Maddahi, D. H. Silverman, J. A. Glaspy, M. E. Phelps, and C. K. Hoh, "Accuracy of whole-body fluorine-18-FDG PET for the detection of recurrent or metastatic breast carcinoma," *J. Nucl. Med*. **39**, 431–435 (1998).

63. T. A. Heusner, L. S. Freudenberg, H. Kuelh, et al., "Whole body PET/CT mammography for staging breast cancer: Initial results," *Br. J. Radiol*. **81**(969), 743–748 (2008).

64. T. A. Heusner, S. Kuemmel, L. Umutl, et al., "Breast cancer staging in a single session: Whole-body PET/CT mammography," *J. Nucl. Med*. **49**, 1215–1222 (2008).

65. J. J. M. van der Hoeven, N. C. Krak, O. S. Hoekstra, et al., "18F-2-fluoro-2-deoxy-D-glucose positron emission tomography in staging of locally advanced breast cancer," *J. Clin. Oncol*. **22**, 1253–1259 (2004).

66. D. Fuster, J. Duch, P. Paredes, et al., "Preoperative staging of large primary breast cancer with [18F]fluorodeoxyglucose positron

emission tomography/computed tomography compared with conventional imaging procedures," *J. Clin. Oncol*. **26**, 4746–4751 (2008).

67. S. Mahner, S. Schirrmacher, W. Brenner, et al., "Comparison between positron emission tomography using 2-[fluorine-18]fluoro-2-deoxy-D-glucose, conventional imaging and computed tomography for staging of breast cancer," *Ann. Oncol*. **19**, 1249–1254 (2008).
68. C. S. Yap, M. A. Seltzer, C. Schiepers, et al., "Impact of whole body 18F FDG PET on staging and managing patients with breast cancer: The referring physician's perspective," *J. Nucl. Med*. **42**, 1334–1337 (2001).
69. S. H. Giordano, "Update on locally advanced breast cancer," *Oncologist* **8**, 521–530 (2003).
70. S. Chia, S. M. Swain, D. R. Byrd, and D. A. Mankoff "Locally advanced and inflammatory breast cancer," *J. Clin. Oncol*. **26**, 786–790 (2008).
71. E. R. Fisher, J. Wang, J. Bryant, et al., "Pathobiology of preoperative chemotherapy: Findings from the National Surgical Adjuvant Breast and Bowel (NSABP) Protocol B-18," *Cancer* **95**, 681–695 (2002).
72. H. Minn and I Soini, "18F fluorodeoxyglucose scintigraphy in diagnosis and follow up of treatment in advanced breast cancer," *Eur. J. Nucl. Med*. **15**, 61–66 (1989).
73. R. L. Wahl, K. Zasadny, M. Helvie, et al., "Metabolic monitoring of breast cancer chemohormonotherapy using positron emission tomography: Initial evaluation," *J. Clin. Oncol*. **11**(1), 2101–11 (1993).
74. I. C. Smith, A. E. Welch, A. W. Hutcheon, et al., "Positron emission tomography using [18F]-fluorodeoxy-D-glucose to predict the pathological response of breast cancer to primary chemotherapy," *J. Clin. Oncol*. **18**(8), 1676–1688 (2000).
75. M. Schelling, N. Avril, J. Nährig, et al., "Positron emission tomography using [18F]fluorodeoxyglucose for monitoring primary chemotherapy in breast cancer," *J. Clin. Oncol*. **18**(8), 1689–1695 (2000).
76. C. Rousseau, A. Devillers, C. Sagan, et al., "Monitoring of early response to neoadjuvant chemotherapy in stage II and III breast cancer by [18F]fluorodeoxyglucose positron emission tomography," *J. Clin. Oncol*. **24**, 5366–5372 (2006).
77. A. Berriolo-Riedinger, C. Touzery, J. M. Riedinger, et al., "[18F] FDG-PET predicts complete pathological response of breast cancer to neoadjuvant chemotherapy," *Eur. J. Nucl. Med. Mol. Imaging* **34**, 1915–1924 (2007).

78. J. Schwarz-Dose, M. Untch, R. Tiling, et al., "Monitoring primary systemic therapy of large and locally advanced breast cancer by using sequential positron emission tomography imaging with [18F]fluorodeoxyglucose," *J. Clin. Oncol*. **27**, 535–541 (2008).

79. J. Schwarz-Dose, M. Bader, L. Jenicke, et al., "Early prediction of response to chemotherapy in metastatic breast cancer using sequential 18F-FDG PET," *J. Nucl. Med*. **46**, 1144–1150 (2005).

80. Y. Du, I. Cullum, T. M. Illidge, and P. J. Ell, "Fusion of metabolic function and morphology: Sequential [18F]fluorodeoxyglucose positron emission tomography/computed tomography studies yield new insights into the natural history of bone metastases in breast cancer," *J. Clin. Oncol*. **25**, 440–3447 (2007).

81. F. Cachin, H. M. Prince, A. Hogg, R. E. Ware, and R. J. Hicks, "Powerful prognostic stratification by [18F]fluorodeoxyglucose positron emission tomography in patients with metastatic breast cancer treated with high-dose chemotherapy," *J. Clin. Oncol*. **24**, 3026–3031 (2006).

Andrew Eik Hock Tan received his MBBS from the National University of Singapore School of Medicine in 2001. He was admitted as a Fellow of the Royal College of Radiologists, UK, in 2008 and the Academy of Medicine of Singapore in 2009, and was awarded a diploma in Nuclear Cardiology from the Certification Council in Nuclear Cardiology, USA, in 2011. Dr. Tan holds clinical faculty appointments in the Singapore General Hospital Diagnostic Radiology residency program and in the Nanyang Polytechnic School of Health Sciences, and is currently practicing as a consultant nuclear physician in Raffles Hospital, Singapore. His research interest is in molecular oncologic imaging, with a focus on the research and clinical implementation of novel imaging and diagnostic techniques.

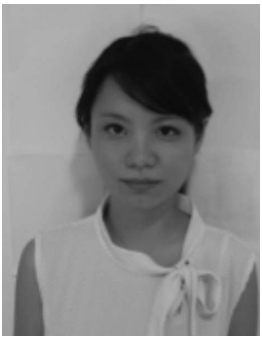

Wanying Xie received her MBBS from the National University of Singapore School of Medicine in 2005. She was admitted as a Fellow of the Royal College of Radiologists, UK, in 2011 and as a Master of Medicine of Singapore in 2011. Dr. Xie is currently practicing as a nuclear medicine physician registrar in Singapore General Hospital, Singapore. Her main interest lies in diagnostic oncologic imaging, with emphasis on the use of novel radiotracers in molecular PET/CT imaging.

Chapter 7
3D Whole-Breast Ultrasonography

Ruey-Feng Chang and Yi-Wei Shen
Department of Computer Science and Information Engineering, National Taiwan University, Taipei, Taiwan

7.1 Introduction

3D whole-breast ultrasonography (US) has become a popular subject of research and an important screening technique in recent years. The benefits of 3D whole-breast US over 2D US are operator independence,[1,2] time efficiency, reproducibility, improved visualization of the breast anatomy, and high resolution for tumor detection.[3,4] In the traditional 2D US examination, the results of breast cancer detection and diagnosis are highly dependent on the operator. It is possible that some difficult-to-detect tumors will not be identified by an inexperienced operator. The examination times can vary according to the size of the breast and the experience of the operator. Patients usually need to have follow-up examinations, but 2D US cannot provide full-field images for reproducibility.

The 3D whole-breast US examination procedure is usually semi-automatic or automatic. The procedure is simple to use and consistent from operator to operator. Inexperienced operators need but a small amount of time for training, and the time required for examination by different operators is not significantly different.[4] As for reproducibility, 3D whole-breast US can provide full-field images for follow-up examinations, and the reconstructed coronal view can provide potential information of the breast lesion. Due to the benefits of 3D whole-breast US, many 3D whole-breast

US machines have been proposed and used in clinical studies. The following section introduces several 3D whole-breast US machines.

7.2 3D Whole-Breast Ultrasonography Machines

Prosound-II SSD-5500 (Hitachi Aloka Medical, Ltd., Tokyo, Japan) with the ASU-1004 scanner is a whole-breast US machine. The ASU-1004 scanner is composed of a water tank and a 6-cm linear transducer with a frequency range of 5–10 MHz, as shown in Fig. 7.1(a). The resolution is 0.23 mm/pixel at axial plane, and the slice interval is between 0.25 mm and 2 mm. For scanning, the patient lies prone to the water tank, and the transducer moves automatically to scan the breast. Because the width of the transducer is too short to cover the entire breast in one scanning pass, three scanning passes are needed to cover the whole breast. In the procedure, a 1-cm overlapping width exists between the adjacent passes, as shown in Fig. 7.1(b). Because three passes are needed, an image-stitching procedure[5,6] is used for reconstructing the whole breast; stitching results are shown in Fig. 7.2(b). After reconstruction, the entire scanning area is 16×16 cm^2.

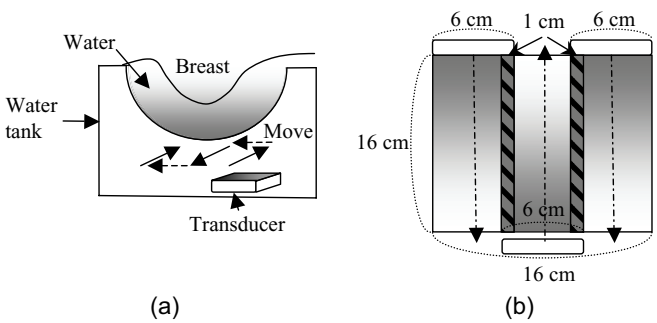

Figure 7.1 (a) The ASU-1004 scanner consists of a water tank and a transducer. (b) Three passes are needed to cover the entire breast.

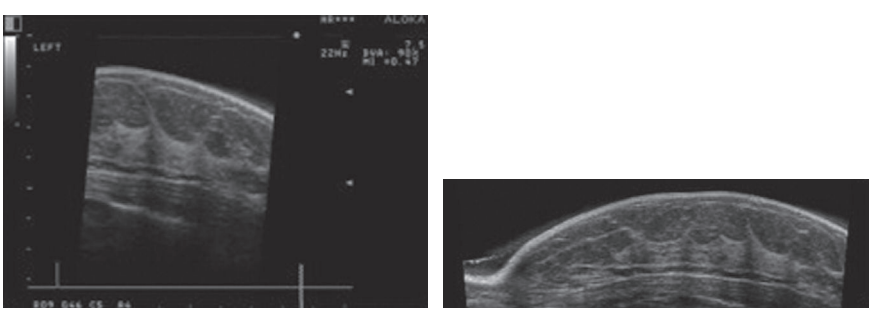

Figure 7.2 (a) One pass of a whole-breast US image. (b) Stitched whole-breast image.

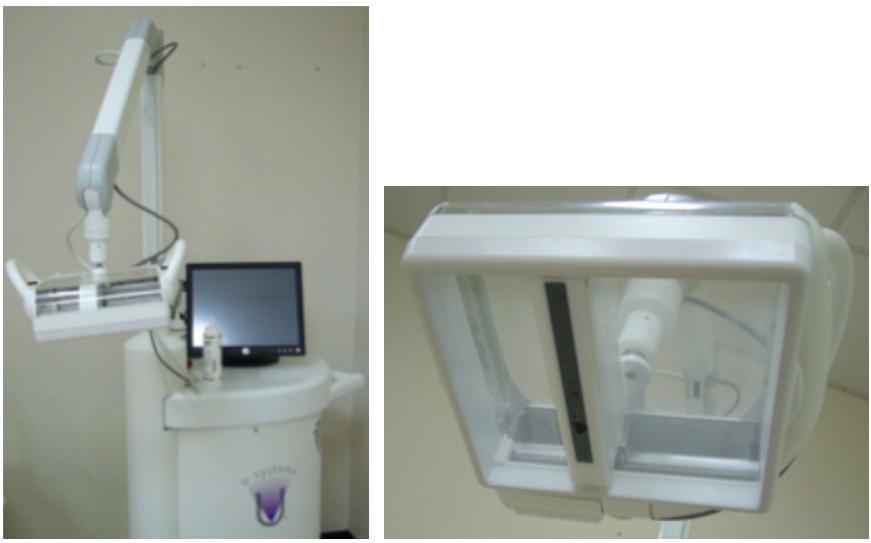

(a) (b)

Figure 7.3 (a) The SomoVu scan station. (b) The scanner with a 15.4-cm linear transducer.

The SomoVu™ Automated Breast Ultrasound (ABUS) (U-systems Inc., San Jose, CA, USA) consists of a scan station and a view station, as shown in Fig. 7.3(a). During the breast US examination, the scanner, with a 15.4-cm linear transducer as shown in Fig. 7.3(b), automatically scans the patient's breast in the supine position, and the view station reviews and manipulates the acquired data. Although the transducer is wider than other 3D transducers, more than one pass is still needed to cover the entire breast. The scanning volume of one pass is $15.4 \times 17 \times 5$ cm^3. The SomoVu station provides several functions for breast tumor detection. The physician can switch to six view options (wide field of view, coronal view, multislice view, transverse view, sagittal view, radial view, and antiradial view) for tumor detection and diagnosis. Figure 7.4 shows images that have been processed in three of these views.

The Automated Breast Volume Scanner (ABVS) (Siemens, Munich, Germany) (Fig. 7.5) can acquire full-field volumes of the breast automatically. The data acquisition procedure is similar to that of the SomoVu station. The frequency bandwidth of the transducer is 5 to 14 MHz, the width of the transducer is 15.4 cm, and the resolution is 0.09 mm in the axial direction, 0.16 mm in the lateral direction, and 0.44 mm in the sagittal direction.

The Orison Corporation has developed the Embrace 3D™ US system (Orison, Bristol, TN, USA) with an automatic scanning concave transducer.

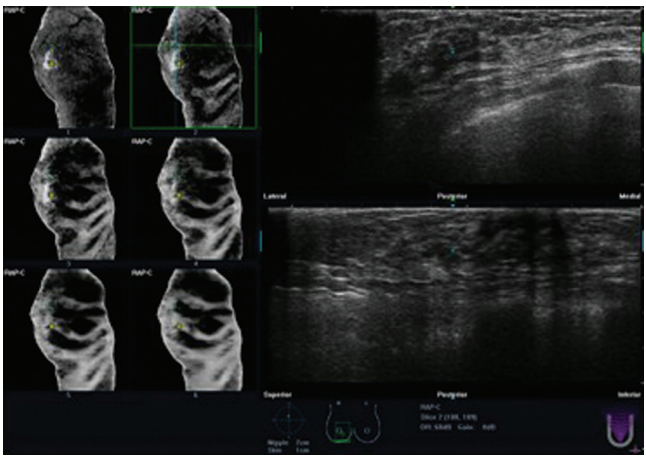

Figure 7.4 The six small images on the left were processed by maximum-intensity projection (MIP) in the coronal view; the upper right image is in the transverse view, and the lower right image is in the sagittal view.

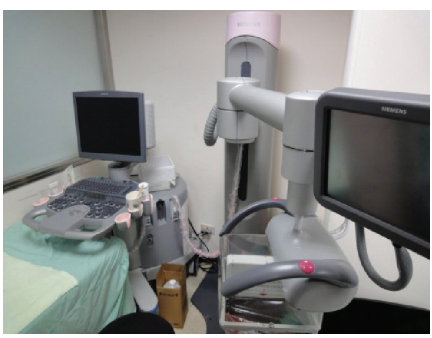

(a)

(b)

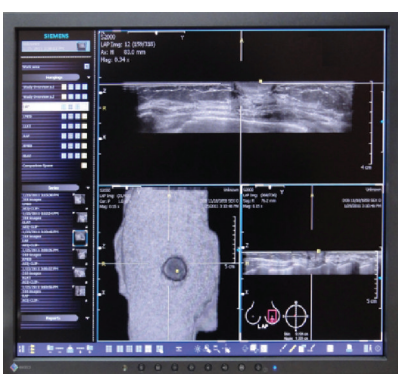

(c)

Figure 7.5 (a) The ABVS system. (b) The transducer of the ABVS system. (c) A screenshot from the ABVS system.

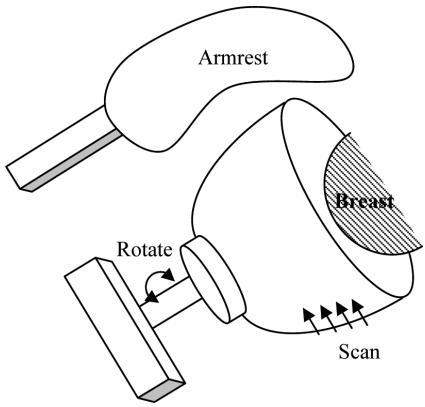

Figure 7.6 The Embrace 3D™ US system.

A rotating concave transducer, as shown in Fig. 7.6, is used for obtaining 3D US images. The patient leans against the armrest, and the breast is placed tightly into the fluid-filled vessel. The hemisphere-shaped transducer scans the breast, and the hemisphere 3D images are reconstructed by visualization software. The operator can detect or diagnose tumors with the multiplanar view.

The Sofia™ automated whole-breast US system has been developed by iVu Imaging (iVu Imaging Corp., Grapevine, TX, USA). While the patient is in a prone position, the transducer scans the breast, which is in a fluid-filled constraining cone, as shown in Fig. 7.7. The acquired images are 120 slices in the 360-deg scanning procedure, and the scanning time is 3 min.

The SonoCiné system (SonoCiné, Inc., Reno, NV, USA) uses a computer-guided arm to move the traditional 2D probe and generate the image sequences. The generated image sequences are usually 2000 to 5000 slices and are stored in the computer for radiologist review. Kelly et al.[7] compared the SonoCiné system to mammography, and the experimental results showed that 3D whole-breast US performed well in tumor detection.

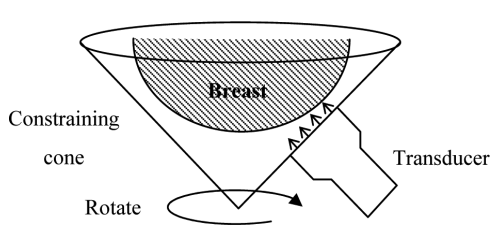

Figure 7.7 The scanning procedure of the Sofia™ system.

In 3D whole-breast US scanning, the patients are in a prone or supine position. For prone scanning, a fluid-filled container is needed to hold the breast. The whole-breast image can be easily reconstructed, which is helpful for whole-breast density analysis. However, the US image quality might be reduced because the probe does not directly contact the skin. On the other hand, with supine scanning, the US image quality might be better due to the probe being in direct contact with the skin. The reduced thickness of the breast in the supine position could improve sound penetration and reduce the acoustic shadows due to refraction effects.[8]

Another advantage is that the patient is in the same position as she would be during breast surgery. Thus, supine scanning can help to locate lesions for biopsy and surgery.[8] However, the whole-breast image is not easily reconstructed, even using several passes to cover the whole breast, because the breast shape cannot be preserved during US scanning. Also, some regions might be not be scanned if the operator does not place the probe in the correct position. Some 3D whole-breast US machines use a conventional or dedicated probe, which is short in length and can only cover a small region. Hence, a longer dedicated probe is used for scanning a large region. Most of the automated 3D whole-breast US machines use a longer dedicated probe.

Most of the probes are linear, like the probe used in the conventional 2D breast US machines. Only Orison's Embrace 3D uses a concave probe to fit the breast shape. In most of the 3D whole-breast US machines, the probe is moved automatically by a scanning apparatus. The probe of only the SonoCiné machine is moved by hand. The probe movement of 3D whole-breast US machines can be linear or rotary, and most of the machines need several passes to cover the whole breast. Only Orison's Embrace 3D uses a concave rotary probe and can scan the whole breast in a single pass. For rotary scanning, a more complicated algorithm is needed to reconstruct the whole-breast image. A comparison of various 3D whole-breast US machines is provided in Table 7.1.

7.3 Related Studies of 3D Whole-Breast Ultrasonography

Several studies have explored 3D whole-breast US. In a study by Tozaki et al.,[4] 61 lesions were used for comparing tumor detection performance between 3D whole-breast US and handheld US. The results show that all of the lesions detected by handheld US were also detected by 3D whole-breast US. The scanning time among different examiners was also not of significant difference. In a study by Kelly et al.,[7] tumor detection improved significantly with a combination of 3D whole-breast US and mammography, compared to detection with mammography alone.

Table 7.1 Comparison of various 3D whole-breast US machines.

	Aloka ASU-1004	U-systems ABUS	Siemens ABVS	Orison Embrace 3D	iVu Sofia	Sono-Ciné
Patient position	Prone	Supine	Supine	Prone	Prone	Supine
Probe length	Middle	Long	Long	Long	Short	Short
Probe type	Linear	Linear	Linear	Concave	Linear	Linear
Scanning method	Automated	Automated	Automated	Automated	Automated	Manual
Contacting skin	No	Yes	Yes	No	No	Yes
Image quality	Average	High	High	Average	Average	High
Probe position	Automated	Manual	Manual	Automated	Automated	Manual
Probe movement	Linear	Linear	Linear	Rotation	Rotation	—
Scanning passes	3	3–5	3–5	1	≥3	—
Breast shape	Preserved	Not preserved	Not preserved	Preserved	Preserved	Not preserved

Breast density is an important factor for estimating breast cancer risk with mammography.[9,10] However, the use of 2D mammography to estimate breast density has some flaws. Breast density estimation using mammography is affected by variations in the position, the degree of compression, and the thickness of the compressed breast.[11] Recently, MRI has been used to estimate breast density because it can provide 3D information of the breast. However, MRI has some drawbacks such as high cost, high noise volume, and image distortion caused by the slightest movement. In a study by Chen et al.,[12] 3D whole-breast US images scanned by the ASU-1004 were used to classify the BIRADS® density grades. In their experiments, the density grades from the proposed method were compared with the ground-standard BIRADS density grades assigned by a majority voting of three experienced breast radiologists. The results showed that density analysis of the 3D whole-breast US could be a reference and provide consistent quantification for radiologists. In the study of Moon et al.,[13] 3D whole-breast US and MRI were used to compare the measurements of breast density. The results showed that the correlations of breast density and breast volume between 3D whole-breast US and MRI were high.

Although there are many advantages to using 3D whole-breast US, reviewing and diagnosing 3D US images requires a lot of physician time, and misdiagnosis can occur due to the fatigue of the physician. Therefore,

a computer-aided detection (CADe) system has been proposed to assist the physician in making diagnoses.[14,15] Ikedo et al.[5] proposed a CADe system 3D whole-breast US. Two features based on edge direction and density difference were adopted in their study. The tumor detection accuracy was 80.6% with 3.8 FPs per whole-breast image. Chang et al.[6] also proposed a CADe system for 3D whole-breast US. Seven features were used in the system, which had a sensitivity of 92.3% with 1.76 FPs per case. In order to segment the lesion boundary for diagnosis, Sahiner et al.[16] proposed a 2D/3D active-contour model for automated lesion segmentation. In their experiments, features, including texture and morphology, were extracted according to the segmented lesions, and classification of the benign and malignant lesions was performed. For comparison with the system classification result, four experienced breast radiologists also diagnosed these lesions. The results showed that the AUC value of the automated system was significantly higher than the AUC values that resulted from three of the four radiologists. In a computer-aided diagnosis (CADx) system, Moon et al.[17] proposed a diagnostic method using ellipsoid-fitting features and shape features. The performances had 85.0% accuracy, 84.5% sensitivity, 85.5% specificity, and an AUC value of 0.9466.

7.4 Conclusion

3D whole-breast US provides the entire breast anatomy for later review. The physician can review the acquired data from different orientations, so lesions can be more easily identified than with the traditional 2D US. The 3D whole-breast US procedure and required training time are simpler and shorter than for 2D US. It also provides interoperator consistency, and its reproducibility is better for follow-up studies. However, the large images can increase the interpreting time and reduce the diagnosis accuracy for the physician. Hence, developing CADe and CADx systems for 3D whole-breast US will be necessary in the future.

References

1. W. A. Berg, J. D. Blume, J. B. Cormack, et al., "Operator dependence of physician-performed whole-Breast US: Lesion detection and characterization," *Radiol.* **241**(2), 355–365 (2006).
2. A. M. Bosch, A. G. H. Kessels, G. L. Beets, et al., "Interexamination variation of whole breast ultrasound," *Brit. J. Radiol.* **76**(905), 328–331 (2003).
3. Y.-H. Chou, C.-M. Tiu, J. Chen, et al., "Automated full-field breast ultrasonography: The past and the present," *J. Med. Ultrasound* **15**(1), 31–44 (2007).

4. M. Tozaki, S. Isobe, M. Yamaguchi, et al., "Optimal scanning technique to cover the whole breast using an automated breast volume scanner," *Jap. J. Radiol.* **28**(4), 325–328 (2010).
5. Y. Ikedo, D. Fukuoka, T. Hara et al., "Development of a fully automatic scheme for detection of masses in whole breast ultrasound images," *Med. Phys.* **34**(11), 4378–88 (2007).
6. R. F. Chang, K. C. Chang-Chien, E. Takada, et al., "Rapid image stitching and computer-aided detection for multipass automated breast ultrasound," *Med. Phys.* **37**(5), 2063–73 (2010).
7. K. Kelly, J. Dean, W. Comulada, et al., "Breast cancer detection using automated whole breast ultrasound and mammography in radiographically dense breasts," *Eur. Radiol.* **20**(3), 734–742 (2010).
8. H. Madjar and E. B. Mendelson, *The Practice of Breast Ultrasound: Techniques, Findings, Differential Diagnosis*, Thieme Medical Publishers, New York (2008).
9. N. F. Boyd, G. S. Dite, J. Stone, et al., "Heritability of mammographic density: A risk factor for breast cancer," *New Engl. J. Med.* **347**(12), 886–894 (2002).
10. N. F. Boyd, H. Guo, L. J. Martin, et al., "Mammographic density and the risk and detection of breast cancer," *New Engl. J. Med.* **356**(3), 227–236 (2007).
11. D. B. Kopans, "Basic physics and doubts about relationship between mammographically determined tissue density and breast cancer risk," *Radiol.* **246**(2), 348–353 (2008).
12. J.-H. Chen, C.-S. Huang, K.-C. C. Chien, et al., "Breast density analysis for whole breast ultrasound images," *Med. Phys.* **36**(11), 4933–4943 (2009).
13. W. K. Moon, Y.-W. Shen, C.-S. Huang, et al., "Comparative study of density analysis using automated whole breast ultrasound and MRI," *Med. Phys.* **38**(1), 382–389 (2011).
14. M. A. Helvie, L. Hadjiiski, E. Makariou, et al., "Sensitivity of noncommercial computer-aided detection system for mammographic breast cancer detection: Pilot clinical trial," *Radiol.* **231**(1), 208–14 (2004).
15. L. A. Khoo, P. Taylor, and R. M. Given-Wilson, "Computer-aided detection in the United Kingdom National Breast Screening Programme: Prospective study," *Radiol.* **237**(2), 444–9 (2005).
16. B. Sahiner, H. P. Chan, M. A. Roubidoux, et al., "Computerized characterization of breast masses on three-dimensional ultrasound volumes," *Med. Phys.* **31**(4), 744–54 (2004).

17. W. K. Moon, Y. W. Shen, C. S. Huang, et al., "Computer-aided diagnosis for the classification of breast masses in automated whole breast ultrasound images," *Ultrasound Med. Biol.* **37**(4), 539–48 (2011).

Ruey-Feng Chang received his B.S. degree in Electrical Engineering from National Cheng Kung University, Tainan, Taiwan, in 1984, and his M.S. degree in Computer and Decision Sciences and Ph.D. degree in Computer Science from National Tsing Hua University, Hsinchu, Taiwan, in 1988 and 1992, respectively. Since 2006, he has been a professor in the Department of Computer Science and Information Engineering, National Taiwan University, Taipei, Taiwan. He was a professor from 1992 to 2006 and served as the Chairman from 2003 to 2006 at the Department of Computer Science and Information Engineering, National Chung Cheng University, Chiayi, Taiwan. His research interests include medical computer-aided diagnosis systems, image/video processing and retrieval, and multimedia systems and communication. Dr. Chang is a senior member of IEEE and a member of AAPM and Phi Tau Phi. He received the Distinguished Research Award from the National Science Council of Taiwan in 2004 and Distinguished Scholar Research Project Award in 2009.

Yi-Wei Shen received his B.S. degree in Electronic Engineering from National Taipei University of Technology, Taipei, Taiwan, in 2004, and his M.S. degree in Computer Science and Information Engineering from National Chung Cheng University, Chiayi, Taiwan, in 2006. He is a Ph.D. student in Computer Science and Information Engineering at National Taiwan University, Taipei, Taiwan. His research interest areas include medical image processing, machine learning, and computer vision.

Chapter 8
Diagnosis of Breast Cancer Using Ultrasound

Chui-Mei Tiu and Yi-Hong Chou
Department of Radiology, Taipei Veterans General Hospital, Taipei, Taiwan and National Yang-Ming University, Taipei, Taiwan

Chung-Ming Chen and Jie-Zhi Cheng
Institute of Biomedical Engineering, College of Medicine and College of Engineering, National Taiwan University, Taipei, Taiwan

8.1 Introduction

Improvements in technology over the past 20 years have made real-time ultrasonography (US) an important imaging modality for evaluation of breast lumps and detection of breast cancer. Considerable advancements in US image quality and ultrasonic tissue characterization have taken place due to improvements in the resolution of high-frequency transducers, and

development of color Doppler US (CDU) technology, tissue harmonic imaging, and various image processing techniques.[1–5]

The use of hand-held high-resolution real-time scanners operating at frequencies of 7.5–15 MHz (or even higher) with a penetrating depth of about 6 cm has become fairly standard among practitioners. State-of-the-art scanners with advanced US technology have significantly contributed to the improvements in spatial and contrast resolution. Physicians who are facing an increasing incidence of breast cancer in Asia and even in western countries are now becoming aware of the usefulness of breast US. Familiarity with the diagnostic accuracy and commonly used lexicon in breast US is helpful for physicians during communication with diagnostic imaging experts, breast surgeons, and patients.

8.2 Instrument Requirements

8.2.1 Equipment and transducer

Breast US requires the use of hand-held, high-frequency, linear-array transducers. These should be able to be focused in the near field and have a capacity for variable focus, e.g., adjustable focal zone, or multifocal or dynamic focal zone, so that the sound beam can be focused at the level of interest in the breast. Transducer frequency should be at least 7.5 MHz. Transducers with a higher frequency may improve spatial resolution. However, with increasing frequency, the ability of the sound beam to penetrate tissue decreases. Therefore, very high-frequency transducers (e.g., 16–18 MHz) may not be able to fully penetrate large breasts. The state-of-the-art scanner may utilize broadband technology to provide both high resolution and adequate penetration. For breast imaging, a transducer with a properly wide aperture (e.g., 4.5 cm or more) is preferred to increase the field of view. The transducers are designed to have a variable focus that is electronically controlled. Depending on the timing of excitation of various elements in the transducer, the focus can be altered to a variety of distances from the transducer surface. Electronic focusing technology makes it possible to focus the sound beam during transmission (i.e., multiple transmit focusing) and during reception (i.e., dynamic focusing). Improvement of lateral resolution over a wide range of distances from the transducer surface is made possible. Further improvement in focusing is possible by electronically adjusting the aperture. While dynamic focusing capability improves resolution simultaneously at various depths, multiple transmit focusing may decrease the frame rate. Therefore, in some equipment, when dynamic evaluation (graded compression) of the lesion is applied, image quality

may be degraged to a certain degree. If such multifocal capability is not desirable and not chosen, the examiner must adjust the depth of focus to the depth of the region in question. Dynamic focusing is always active during reception, and no control element is necessary.[6–8]

8.2.2 Image quality and equipment quality control

The image quality of a breast US unit is generally determined by the following factors: spatial and contrast resolutions, image quality in the near field, and slice thickness. The *axial resolution* is determined by the spatial length of an US pulse, which is usually two wavelengths. The minimum axial resolution is half of this value. The *lateral resolution* is determined by the size of transducer element, the frequency, and the focal zone. The *contrast resolution* depends on the transducer and signal processing inside the US unit. The recently developed technology of tissue harmonic imaging (THI) has further improved US image quality. Because the thickness of most breasts is only few centimeters on US, many lesions lie close to the transducer. High image quality in the near field is essential for an accurate assessment of these relatively superficial lesions. Occasionally, a stand-off pad can be used between the transducer and the breast to achieve good images of the skin, and subcutaneous and superficial breast tissues. *Slice thickness* is a function of transducer design. When purchasing US equipment, slice thickness should be evaluated by checking the ability of the transducer to demonstrate small pure cysts, which should appear echo free. If the slice thickness is too thick, pure cysts will become atypical on US because of the inclusion of adjacent echogenic soft tissue within the slice. *Equipment quality control* is indispensable to ensure a high-quality breast US study. Each US machine should have a quality control program to maximize the quality of US imaging and other functions. Ongoing monitoring and evaluation of equipment should be a part of this program. A routine preventive maintenance program is desirable, and records should be kept to document this program. Efforts undertaken to improve quality of care should also be documented for the breast US team.[1,6]

8.3 Examination Technique

8.3.1 Patient positioning

The patient is generally studied in a supine or slightly oblique position, with the ipsilateral arm comfortably elevated. For relatively large or pendulous breasts, the women should be positioned obliquely toward the contralateral side to allow the breast to lie flat on the chest wall.[6]

8.3.2 Scanning technique

The breast can be studied in an infinite number of planes. Standardization of the examination and appropriate labeling of images are necessary to make these studies interpretable by those who have not performed them and also makes them reproducible.[1,6]

The transducer should be held firmly with gentle pressure applied on the breast. An adequate amount of coupling gel should be used to avoid interference of the interposed air. Imaging the nipple–areola complex requires special maneuvers. The fibrous elements within the nipple and the abrupt edges between nipple and the areola may cause distal acoustic shadowing. If the image is not diagnostic with the transducer directly contacting the nipple–areola complex, the transducer should be placed adjacent to the nipple with the sound beam angled into the retro-areolar area. A number of scanning maneuvers have been suggested, e.g., sagittal, transverse, radial/antiradial. Using a sagittal scan to examine the whole breast is the most convenient and time-saving way for a complete US scanning coverage of the breast. However, we prefer to image the breast in the radial and antiradial planes (planes corresponding to a clock surface extending from the nipple and at right angle to these axes, respectively). The radial plane corresponds to the normal pattern of the duct anatomy of the breast. The labeling of lesions at o'clock axes is also more accurate than labeling with quadrant location. When needed, imaging in additional planes with appropriate annotation on the images can be performed. Imaging in at least two orthogonal planes usually makes it possible to differentiate real lesions from normal breast anatomy such as fat lobules. Dynamic imaging with graded compression of a suspected lesion is also helpful to evaluate the elasticity and mobility of a lesion.[9] Fibroadenomas are typically extremely mobile. When compressibility of a lesion suggests that it is soft, often a cyst or other benign lesion is considered. If these features cannot be shown, malignancy should be suspected, even in the case of completely well-circumscribed lesions with homogeneous echogenicity.[1,9]

8.3.3 Doppler imaging and contrast-enhanced US

It has been suggested that breast cancers tend to show more vascularity than benign breast tumors. A malignant tumor is usually associated with vessels arising along the edge of the mass and extending into its center. These vessels are often branching and irregular. Smooth vessels paralleling the periphery of a mass are more characteristic of benign lesions, such as fibroadenomas. However, both patterns can be seen in benign and malignant processes. In addition, benign lesions can be hypervascular and malignant lesions hypo- or avascular (e.g., scirrhous-type

carcinomas). For this reason, the use of Doppler or power Doppler interrogation of breast masses has not been found to be useful by most experts in determining which lesions require biopsy and which are benign.[10,11] However, the additional color Doppler information may increase diagnostic confidence; for example, a typical ovoid, sharply demarcated solid lesion presenting with only parallel marginal vessels is most likely a benign lesion and often a fibroadenoma. A small (e.g., <0.7 cm) relatively round hypoechoic nodule presenting with positive color flow signals in the peripheral or central zone is most likely a solid tumor and most often a papilloma or another cellular tumor. The use of microbubble contrast agents has also been described in several studies that attempt to better define vascular patterns within lesions, and to distinguish benign from malignant masses. The results are promising. Some studied showed that sentinel node identification can be effectively achieved by using microbubbles and contrast-enhanced US.[12–16]

8.3.4 Elastography

Elastography provides a measure of the stiffness of a lesion and is an option available on most standard US equipment. In the study conducted by Itoh et al.,[17] conventional US and real-time US elastography with the combined autocorrelation method (CAM) were performed on 111 women with breast lesions (59 benign and 52 malignant cases). The researchers used an elasticity score (1–5) to represent the stiffness (from soft to hard) of tumors and found that malignant lesions were harder (mean: 4.2 ± 0.9) and benign lesions were softer (mean: 2.1 ± 1.0) ($P < 0.001$). US elastography (cutoff points of 3 and 4) showed a sensitivity of 86.5%, specificity of 89.8%, and accuracy of 88.3%, while conventional US (cutoff points of BIRADS 4 and 5) showed a sensitivity of 71.2%, specificity of 96.6%, and accuracy of 84.7%. Elastography had a higher sensitivity than conventional US ($P < 0.05$), and the specificity of elastography was not inferior to that of conventional US. The accuracy of elastography was equivalent to that of conventional US.[17]

Benign breast masses tend to appear similar in size or slightly smaller on elastography than on conventional imaging; on the contrary, malignant masses have the converse appearance, appearing larger on an elastogram than on conventional US. It is hypothesized that the larger size depicted on the elastogram is due to the infiltrative nature of the cancers. On conventional imaging, cancers appear smaller than on elastography because the infiltrative portions are not well visualized.[18] Many new techniques using relevant strain imaging or acoustic radiation force imaging have been introduced in the past nine years. Compression elastography is an evolving technology, and different methods and algorithms are used by different manufacturers. With shear-wave elastography, low-frequency

shear waves are propagated in tissue, and the elasticity of the tissue is quantitatively and reproducibly assessed.[19] Elastography is now considered to be an important adjunct to conventional and Doppler US.

8.3.5 Image labeling

Precise labeling of images is necessary so that US examinations are reproducible and lesions can be demonstrated on a repeat study. Labeling of US studies of the breast should include: (1) patient identification, including name and identifying number such as medical record number, birth date or age; (2) examination date; (3) breast laterality (right or left); (4) scanning locations, including (a) axis, indicated by o'clock designation, (b) distance of the lesion from the nipple, and (c) an indication whether the lesion is palpable; and (5) identification of the physician or technologist performing the study.

8.4 Grayscale Ultrasonic Criteria of Breast Disease

8.4.1 General criteria of interpretation

Identification of a focal area with different echogenicity in the background of (relatively hyperechoic) breast stroma remains the most important point in US interpretation. The primary characteristics of breast masses include shape and margins of a mass, boundary echoes, internal echotexture, and alternation of sonic transmission.[1,20,23]

8.4.2 Diagnosing cysts

Simple cysts are epithelium-lined, fluid-filled, round or oval structures that are thought to occur secondary to obstructed ducts. US allows high confidence in the diagnosis of a simple cyst. Diagnosing cysts is one of the most important contributions of US to breast imaging. The diagnosis of a simple cyst makes it possible to assure that a mass is benign and that it requires no additional workup for definitive diagnosis. US is essentially 100% accurate in this diagnosis. Therefore, US is useful in the workup of any palpable or nonpalpable lesions that could be due to a simple cyst.[1,2,21,22]

8.4.3 Differentiating solid lesions

US is a very helpful adjunct to mammography in assessing the internal texture and shape of the margins of masses that are partially or completely obscured by dense tissue on mammography. Palpable or nonpalpable lesions that are located in dense tissue and cannot be clearly or completely visualized on mammography can often be further characterized by US.[23,24]

Imaging characteristics of benign and malignant solid nodules have been reviewed by several authors and proven useful in the differentiation between

benign and malignant solid nodules. Generally speaking, the borders of benign nodules are sharply demarcated; they displace rather than invade surrounding tissue. Benign masses are round, oval, or minimally (gently) lobulated in shape. Their boundary echoes are relatively strong. Benign lesions contain relatively homogeneous internal echoes, which are usually low level but may vary from very low to intermediate level. Sonic transmission in benign solid nodules is relatively stronger than that in malignant ones.[23,25–29] During interpretation of a focal breast lesion, the ACR BIRADS® lexicon is generally recommended.[30]

8.4.4 Diagnosing carcinoma

The anterior boundary echogenicity of malignant nodules varies from weak to strong. The posterior boundary echoes are usually weak or absent in larger tumors, due to some degree of desmoplasia in carcinomas. However, certain malignancies with homogeneous cellular arrangement liquid contents may show good sonic transmission as noted in benign lesions. The internal echoes of a nodule depend on the histology of the lesion. Although many carcinomas are seen sonographically as hypoechoic masses, the echogenicity of carcinomas is variable. Some carcinomas are isoechoic or even hyperechoic with respect to the subcutaneous fat. Circumscribed carcinomas are usually very hypoechoic (or nearly anechoic) lesions, containing few low-level echoes in a relatively nonuniform distribution and sometimes containing microcalcification. During the interpretation of a noncystic focal mass using US, the through transmission, coexisted ductal changes, and the associated cystic components should be also evaluated[31] (see Tables 8.1–8.3). The sonographic visibility of carcinomas also depends on the surrounding tissue.

Table 8.1 Differential diagnoses of breast nodules based on through transmission.

1. **Mass with distal sound attenuation**
(a) Scirrhous types of ductal carcinoma
(b) Hyalinized or calcified fibroadenoma
(c) Cyst containing (echogenic) materials
(d) Sclerosing adenosis
(e) Surgical scar/radiating scar
2. **Mass with distal enhancement**
(a) Cyst
(b) Complicated cyst or cystic tumor
(c) Fibroadenoma/phylloid tumor
(d) Circumscribed carcinoma
3. **Mass with intermediate trans-sonicity**
(a) Relatively small cyst containing echogenic materials
(b) Papilloma
(c) Fibroadenoma
(d) Circumcribed carcinoma
(e) Sclerosing adenosis/focal fibrosis

Table 8.2 Differential diagnosis of intracystic tumors.

(a) Intracystic (intraductal) papillomas
(b) Intracystic (intraductal) carcinoma
(c) Invasive ductal carcinoma with necrosis

Since fat has a lower level of echogenicity compared to the glandular tissue, hypoechoic carcinomas may be missed sonographically within fatty tissue. Intramammary fat lobules may, furthermore, mimic malignancy. Because of these factors, some cancers will not be seen with US, although they may be easily found on mammography in fatty breasts.[25–29,32]

8.4.5 Secondary signs of malignancy

During the evaluation of breast nodules, some secondary signs of malignancy are also important in distinguishing benign from malignant lesions, namely, disruption of breast architecture, skin distortion or thickening, breast contour changes, thickening of Cooper's ligaments, alteration of subcutaneous fat layer, reactive changes surrounding a mass, interruption of the retromammary space and/or pectoralis muscles, and presence of axillary adenopathy. When secondary signs are present, the lesions in the breast are usually clinically obvious; however, when lesions are relatively small, the reactive changes surrounding the tumor may be extremely helpful in differentiating benign from malignant lesions.[1,25–27]

8.4.6 Evaluation of breast calcifications

Breast calcifications may be associated with inflammatory, degenerative, and toxic metabolic processes. They may also result from inspissated secretions in ducts, acini, cysts, or malignancies such as cribiform carcinoma, or from deposition of calcium salts in necrotic tissue (e.g., in comedocarcinoma or fat necrosis). Some of these calcifications may be quite large and obvious (e.g., in degenerative fibroadenomas), and some may be very tiny (e.g., microcalcifications, usually <0.25–0.5 mm). State-of-the-art US scanners may depict calcifications larger than 0.5–1 mm without apparent difficulty, particularly when there is a relatively homogeneous hypoechoic background. Acoustic shadows are frequently present in denser

Table 8.3 Differential diagnosis of dilated duct with or without internal echoes.

(a) Intraductal carcinoma
(b) Intraductal papilloma
(c) Epithelial hyperplasia
(d) Other fibrocystic changes
(e) Thick milk, inspissated secretion or calcific plug in dilated duct

calcifications. However, without a relatively homogeneous (hypoechoic) background, tiny calcifications may be hardly seen and therefore difficult to demonstrate. Malignancy with calcium deposits or microcalcifications may present on US as (1) a circumscribed solid tumor with microcalcifications: most easily identified; (2) ductal dilatation with intraductal echoes and microcalcifications: better delineated when ductal dilatation is apparent (e.g., >2 mm); (3) clustered microcalcifications in a poorly defined hypoechoic background, representing carcinoma *in situ* or minimally invasive pathology: often not easy to identify, but now relatively frequently identifiable on state-of-the-art high-resolution US scanners; (4) clustered microcalcification without apparent ductal dilation or hypoechoic background, representing carcinoma *in situ* or comedocarcinoma: most difficult to identify but occasionally appreciated with recently developed technologies.

Some benign pathologies such as cystic breast diseases, duct ectasia, or scar tissues with microcalcification may also present with microcalcifications on US. When a cystic lesion or dilated duct is appreciated by US, the tiny calcium deposit or milk of calcium may be identified inside the fluid spaces, as in cyst or duct, and can be differentiated from microcalcification in carcinoma. However, lesions such as microcystic adenosis, sclerosing adenosis, or radiating scar with microcalcification may be difficult to distinguish from malignancy, and demonstration of microcalcifications is not easy.[33,34]

8.5 Considerations in Interpreting US Examination Results

Certain considerations should be taken into account when interpreting US examination results:

- If a lesion is not a simple cyst and a mammogram has not been performed, a mammogram should be taken to further characterize the mass on the basis of echotexture, contour, borders, and the possible diagnostic patterns of calcifications.
- Benign US findings in the presence of suspicious mammographic findings do not exclude malignancy.
- A mass that cannot be seen on US should be considered not to be a cyst and therefore solid. This implies that these lesions may also be caused by a carcinoma.
- If there are any doubts about the benignity of a lesion after a complete imaging assessment, further diagnostic procedures (short-term followup or biopsy) are indicated.
- Some cancers will not be seen with US, although they may be easily found with mammography. This pitfall may occur in any type of breast

tissue but is more frequent within fatty breast tissue than in mixed breast tissue or dense hyperechoic glandular tissue.

Knowledge of some common pathologies and their US presentations is essential in interpretation of an US examination result.

8.6 Ultrasonography of Malignant Tumors

8.6.1 Invasive ductal carcinoma

Invasive ductal carcinoma (IDC) is the most common type of breast malignancy, accounting for around 80% of all breast carcinomas.[35] IDC is the most common malignancy in women throughout the Western world and ranks first or second in the Eastern world.[36] The lifetime risk of developing breast carcinoma is 1 in 9 in the United States and 1 in 12 in the UK,[37] with an incidence that rises progressively with age.[4] Environmental influences, such as diet, genetic factors, and endocrine factors, have been suggested as risk factors. The effect of estrogens is well documented to be related to the predisposition of breast cancer.[38,39] Postmenopausal hormone replacement therapy (HRT) is suggested to be associated with a minimally increased risk, but its risk remains controversial.[40]

The most common presentation of breast cancer is a solitary hard mass, often associated with irregular contour. The fixation within the breast tissues to subcutaneous fat, skin, or the pectoralis muscle is a suggestive sign of a carcinoma. Pain or tenderness, although generally considered a sign of benign lesions, can be encountered in about 15% of carcinomas.

Clinical signs of breast carcinomas include flattening or dimpling of the overlying skin, flattening or retraction of the nipple, and nipple discharge, which are related to fibrotic stromal reaction, shortening of the Cooper's ligaments, and involvement of the duct systems. Skin and subcutaneous edema can be seen in patients with inflammatory carcinoma.

IDCs have a variable appearance and may even show significant histological and cytological heterogeneity within the same lesion. Most IDCs are hard with an irregular stellate outline (scirrhous type), while the others may be softer and circumscribed on macroscopic examination. On microscopic study, the tumor cells are usually arranged in nests or cords, often with a variable amount of tubule formation. Scirrhous tumors contain abundant stroma with a large amount of collagen and, frequently, significant quantities of elastin. The tumor cells are usually uniform in size, shape, and staining intensity, and occasionally show marked pleomorphism. Some large and cellular tumors may present with necrosis, especially in densely cellular lesions. Microcalcification (usually composed of hydroxyapatite) within the tumor nest and stroma is a common feature.

8.6.1.1 Sonographic findings

An IDC typically presents as a mass on US.[41] For lesions that do not produce mass effect, the secondary signs related to the surrounding tissue changes should be carefully evaluated. To detect a focal pathology, searching for a mass (primary feature) or surrounding tissue changes (secondary features) is very important.

8.6.1.1.1 Primary features

The US features of breast carcinoma are variable (Figs. 8.1–8.11). The ultrasonographically identifiable mass is typically less reflective (hypoechoic) than the surrounding glandular tissue and is usually also less reflective than the subcutaneous fat layer. Tumors that are highly

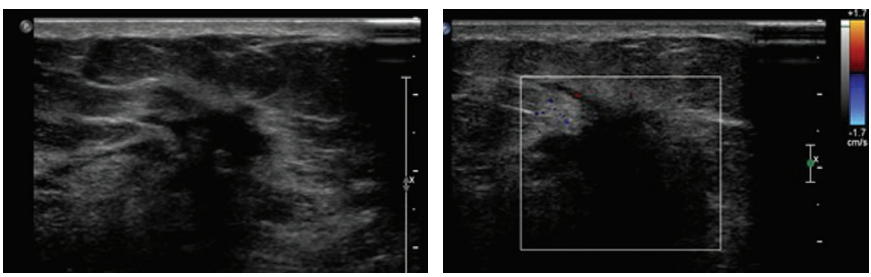

(a) (b)

Figure 8.1 A 51-year-old female presenting with a palpable mass on the right breast: IDC. (a) US: a hypoechoic tumor with irregular margins, speculation, angulation, and an echogenic halo are noted. (b) CDU: only minimal marginal color flow signals are evident.

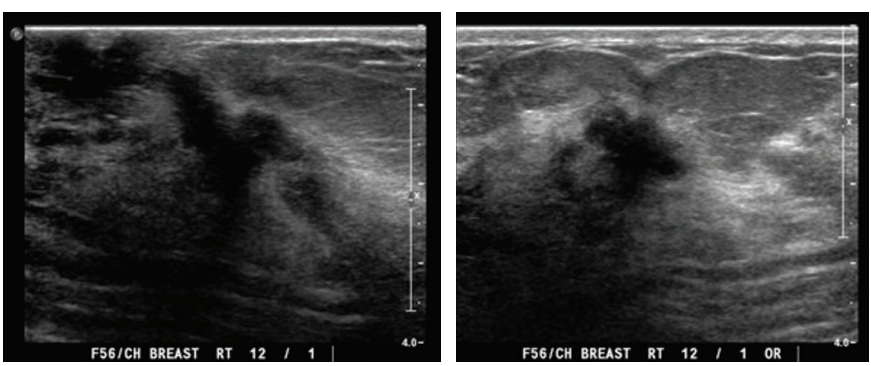

(a) (b)

Figure 8.2 A 56-year-old female presenting with bloody nipple discharge: IDC. (a) US: A very hypoechoic lesion with irregular margins and extending to the nipple, representing ductal extension. (b) US: orthogonal view.

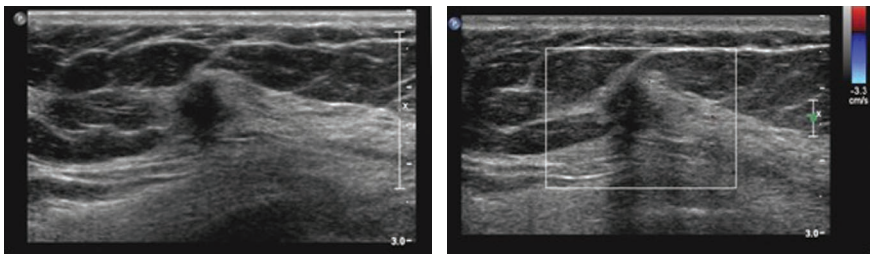

(a) (b)

Figure 8.3 A 53-year-old female presenting with a suspicious breast nodule: IDC (a) US: a 1-cm hypoechoic nodule with vertical orientation and distal sound attenuation. (b) CDU: No significant color flows are noted.

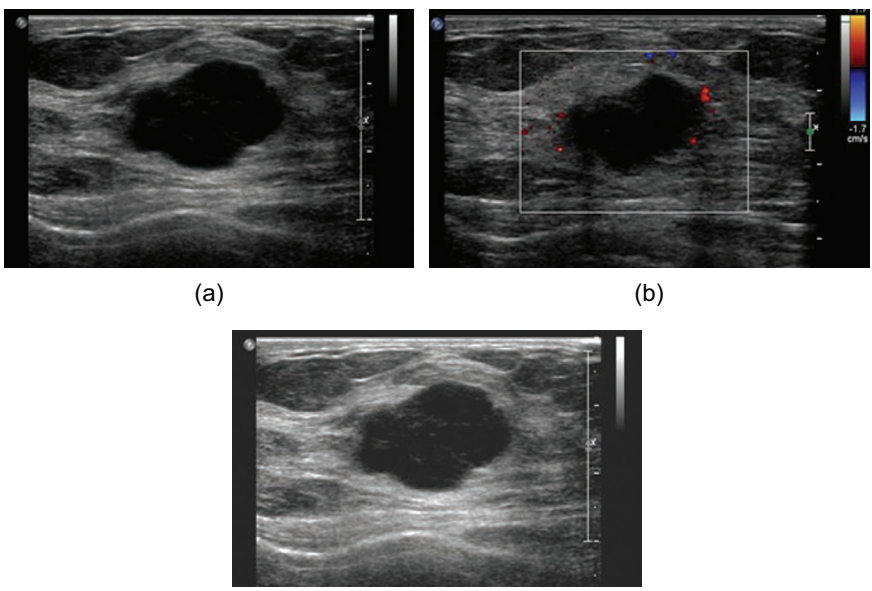

(a) (b)

(c)

Figure 8.4 A 42-year-old female presenting with palpable left breast mass: IDC. (a) US: A very hypoechoic mass is noted, showing lobulated margins and distal enhancement. (b) CDU: Only marginal color flow signals are demonstrated. (c) US: Increased gain setting may demonstrate weak internal echoes and prevent a misinterpretation as a cystic lesion.

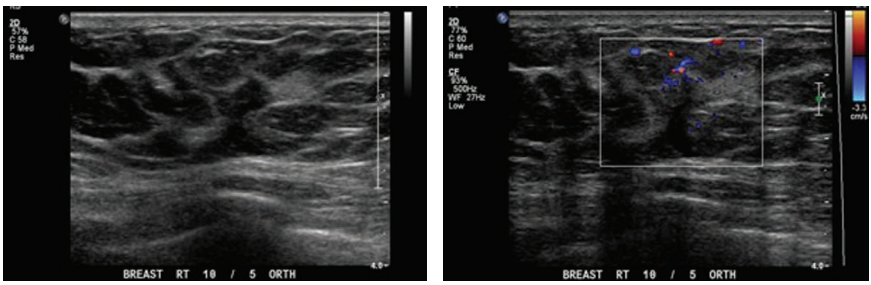

(a) (b)

Figure 8.5 A 55-year-old female without clinically palpable breast mass: IDC. (a) US: An isoechoic lesion is suspected in the center of the image, about 1.1 cm in size. (b) CDU: Increased marginal and peripheral color flow signals are suggestive of a relatively hypervascular tumor.

calcified are a rare exception: they may be more reflective than breast parenchyma. The nidus usually has a heterogeneous texture (Figs. 8.1–8.4), perhaps due to the irregular alignment of the tumor cells or to necrosis. Microcalcification may add to the heterogeneous texture. Occasionally, cystic change may be apparent; it is more common with larger tumors and is probably due to necrosis or hemorrhaging. Carcinomas can be multifocal, multicentric, or bilateral, and can be occult, hidden in breast stroma (Figs. 8.12–8.18).

IDC tends to be hypo- or very hypoechoic on US (Fig. 8.4); only occasionally is it isoechoic (Fig. 8.5). Mucinous carcinoma may sometimes be hyperechoic. IDC is usually irregular in shape. Orientation of the tumor is usually nonparallel, with the depth-to-width ratio (D:W or AP/L) often exceeding 0.7–0.8.[35]

The borders of IDCs are irregular and usually appear ill defined or fuzzy because of their invading margins and desmoplastic reaction, particularly in the scirrhous type of tumor. The desmoplastic reaction is seen on US as an echogenic halo, usually thicker than 3 mm, surrounding the hypoechoic nidus. This hyperechoic halo sign is important in distinguishing IDCs from fibroadenomas, which are typically encapsulated by a thin and smooth hyperechoic line. Posterior shadowing is a classical appearance in IDCs, typically seen in scirrhous-type tumors (Figs. 8.1, 8.2, and 8.16) but not in circumscribed-type tumors (Figs. 8.4, 8.8, and 8.19).

8.6.1.1.2 Secondary features

Carcinomas often break through normal structures and not uncommonly cause distortion of the surrounding breast stroma (Fig. 8.17). The US signs of invasion are particularly useful when a carcinoma is superficially located and may be apparent even with small tumors when the glandular tissue is

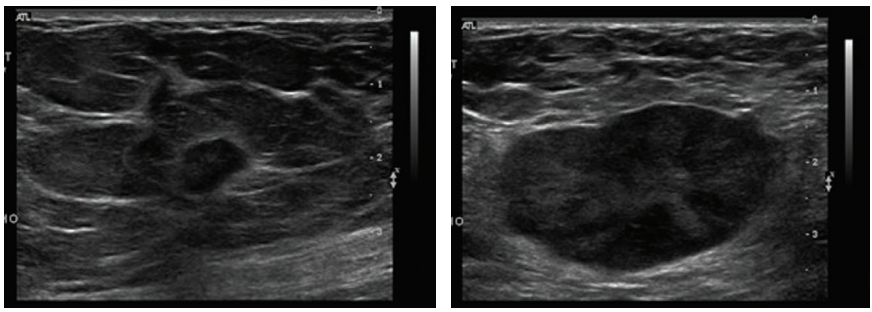

(a) (b)

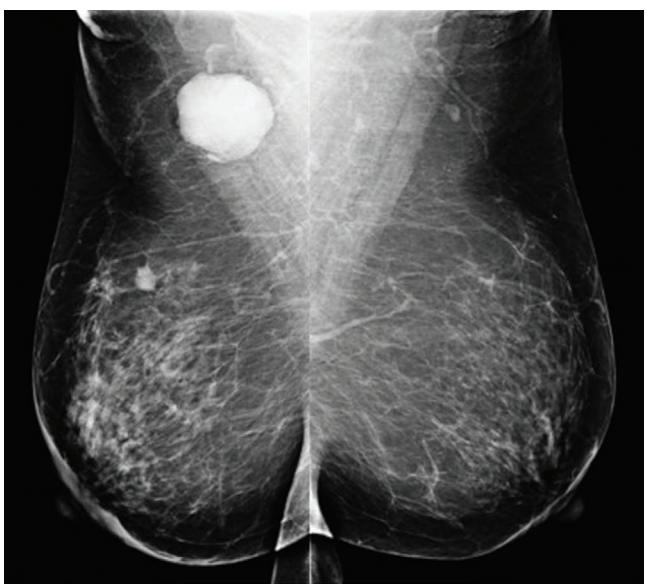

(c)

Figure 8.6 A 49-year-old female presenting with a palpable right axillary mass: Occult IDC with axillary and intramammary lymph node metastases. (a) US: An ovoid hypoechoic nodule in the center of the image is actually an intramammary lymph node with metastasis; the primary breast lesion is occult and small, located superficially, vertical in orientation, measuring 0.5×0.8 cm. (b) US: The apparently enlarged lymph node is the only metastasized lymph node in the axillary region. (c) Mammography: The enlarged axillary lymph node, intramammary node, and the small superficially located tumor are seen on the right breast (mediolateral oblique view).

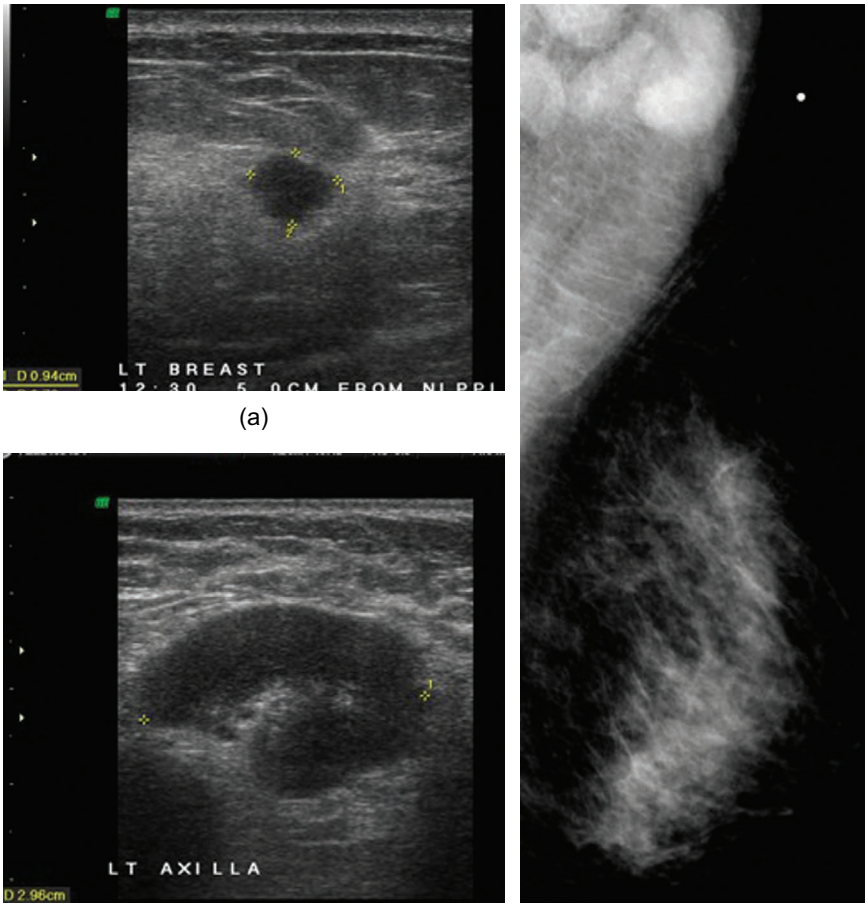

Figure 8.7 A 47-year-old female presenting with palpable left axillary mass: nonpalpable IDC with axillary lymph nodes metastasis. (a) US: A 0.9-cm round hypoechoic nodular in a dense breast, associated with relatively poorly defined boundary, and with no significant change of sonic transmission. (b) US: Multiple enlarged axillary lymph nodes are shown. (c) Mammography: No focal mass can be identified in the relatively dense breast. Multiple large and dense axillary lymph nodes are noted.

atrophic. When the primary feature of a lesion cannot be well appreciated on US, the US sign of invasion or the secondary sign can be the major feature. Invasion of a carcinoma may develop along Cooper's ligaments, into the skin, between the dermis and subcutaneous fat, or into the underlying muscle. These changes may cause skin thickening, skin dimpling, stellate and speculation patterns, and interruption of the subcutaneous fat or underlying muscle fascia.

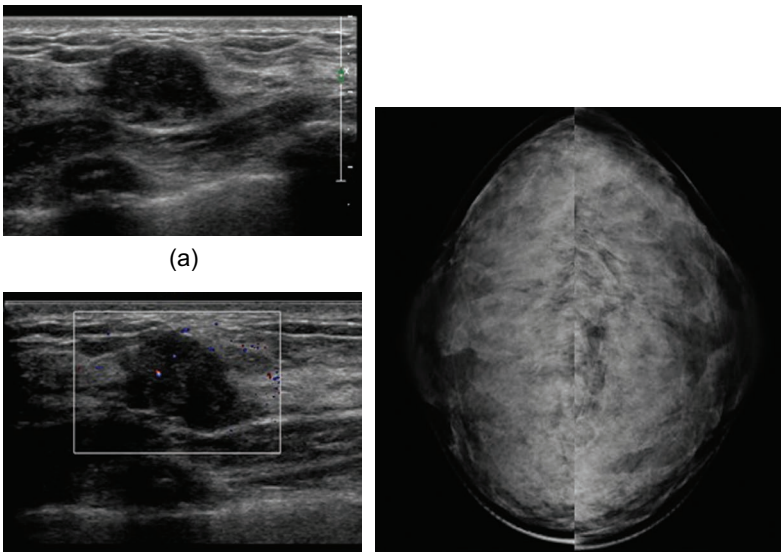

(a) (b) (c)

Figure 8.8 A 25-year-old female presenting with a palpable, movable left breast lump: IDC. (a) US: A hypoechoic mass (1.7 cm), heterogeneous in echopattern and associated with microlobulated margins showing minimal distal enhancement. (b) CDU: Minimal intratumoral color flows are evident. (c) Mammography: No demonstrable mass in the left breast.

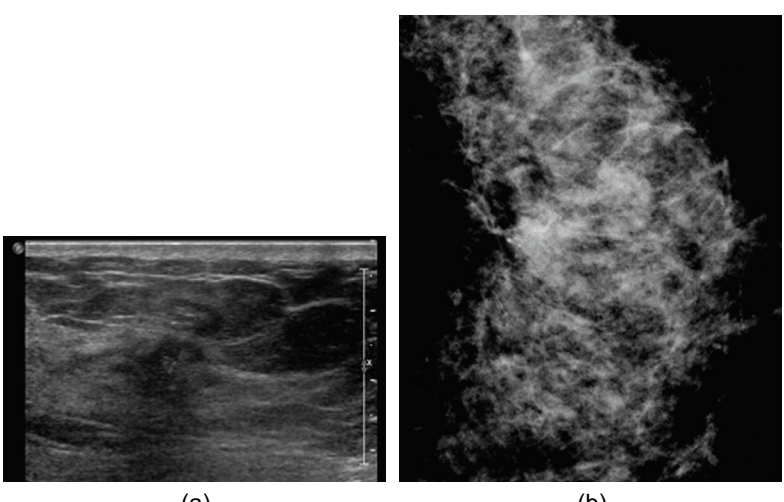

(a) (b)

Figure 8.9 A 57-year-old female presenting with a palpable breast mass: IDC. (a) US: A hypoechoic mass with irregular margins and distal sound attenuation is seen. There are some tiny punctuate calcifications (microcalcifications) in the lesion. (b) Mammography: A small relatively dense area with poorly defined margins and some punctuate calcifications is noted in the central deep portion.

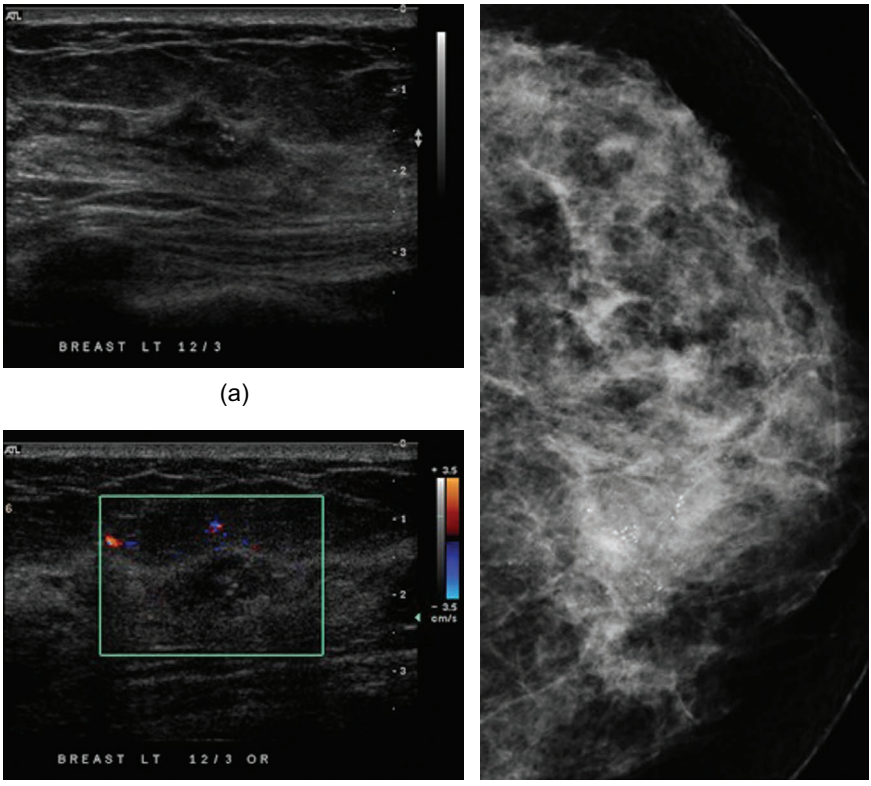

(a) (b) (c)

Figure 8.10 A 59-year-old female suspected to have a left-breast lump on physical examination: IDC. (a) US: A hypoechoic mass lesion with irregular margins, minimal distal sound attenuation, and microcalcifications. The lesion is horizontal in orientation. (b) CDU: No significant color flow signal is demonstrated. (c) Mammography: A relatively dense area with microcalcification is noted in the medial aspect of the left breast.

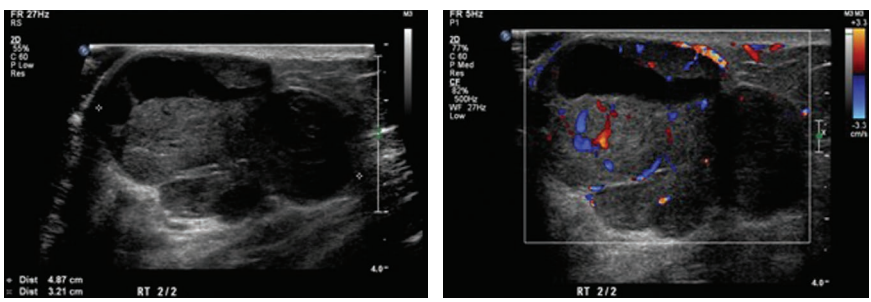

(a) (b)

Figure 8.11 A 62-year-old female with a history of palpable right breast mass for five months: IDC. (a) US: A large (4.9-cm) lobulated mass lesion with fluid spaces is seen. (b) CDU: some peripheral, marginal, and penetrating vessels are demonstrated in the solid part of the lesion.

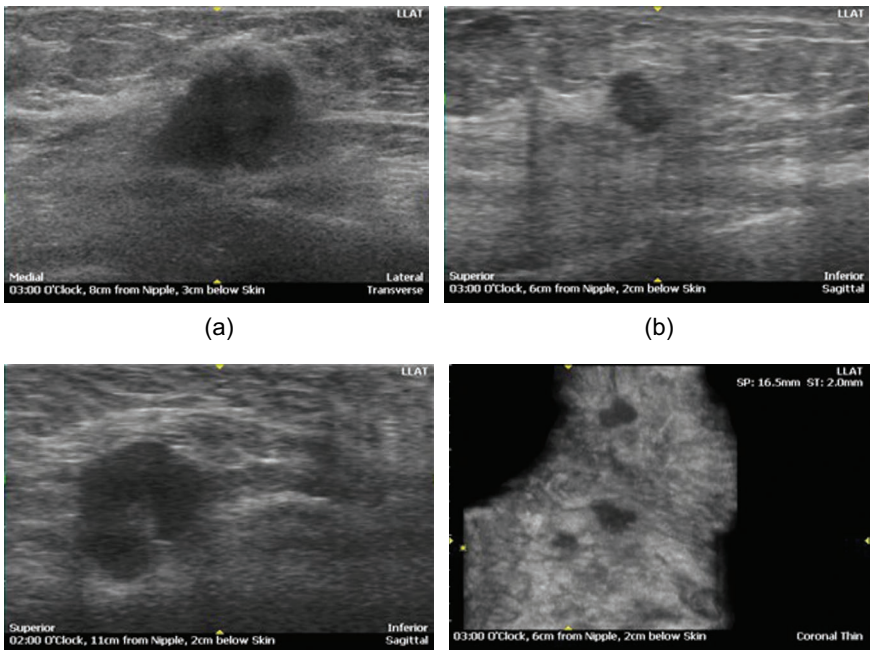

(a) (b)

(c) (d)

Figure 8.12 A 70-year-old female presenting with a palpable mass in the axillary region: multifocal IDC. (a) US: 2.0-cm hypoechoic mass is noted in the region of the tail of Spence, showing irregular margins, and poorly defined boundary. (b) US: Another 0.7-cm hypoechoic nodule is also noted medial to larger mass, vertical in orientation, with no change in sound transmission. (c) US: An enlarged axillary lymph node. (d) Automated whole-breast US: Three lesions are demonstrated, including the diseased axillary lymph node, the larger cancer, and the small cancer.

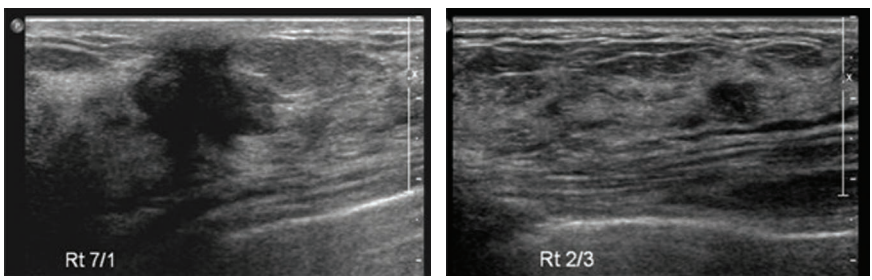

(a) (b)

Figure 8.13 A 47-year-old female presenting with a palpable lump on the right breast: multicentric IDC. (a) US: A very hypoechoic mass is seen in the right outer lower quadrant, associated with irregular margins, focal distal acoustic shadows, corresponding to the physical examination. (b) US: Another nodule is depicted in the right inner upper quadrant of right breast.

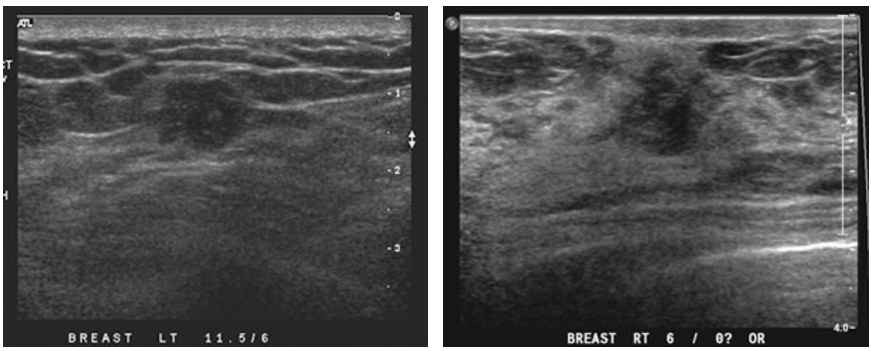

(a) (b)

Figure 8.14 A female presenting with metachronous bilateral IDC. (a) US: A hypoechoic mass is noted in the left breast, showing heterogeneous echopattern and irregular margins. (b) US: Two years after surgery of the left breast, another cancer is demonstrated in the right breast, showing similar US findings.

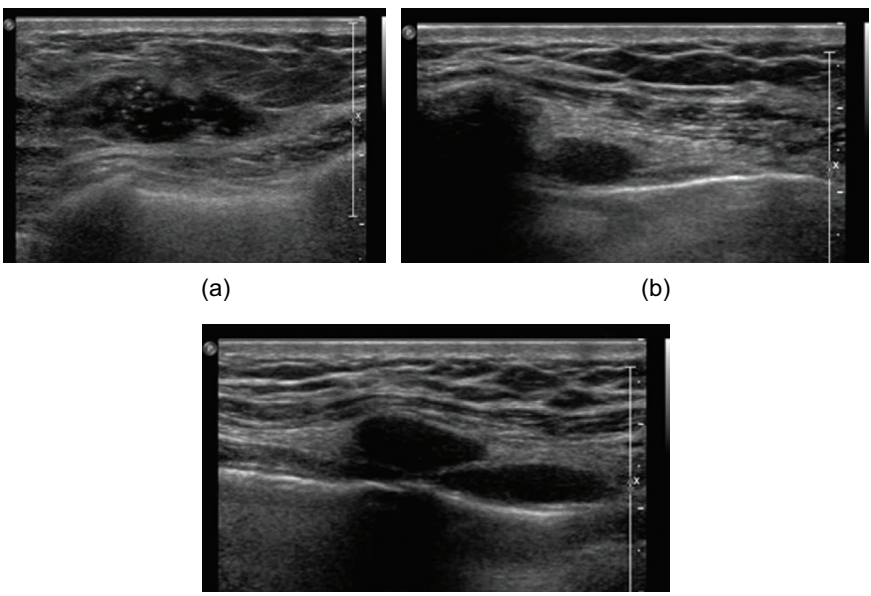

(a) (b)

(c)

Figure 8.15 IDC of the left breast over the central upper part: left internal mammary lymph node metastasis. (a) US: The primary breast tumor is a horizontally oriented, mildly irregular, hypoechoic mass, associated with microcalcifications. (b) US: transverse and (c) sagittal scans of the left parasternal region demonstrate the ovoid hypoechoic mass posteroinferior to the cartilagenous part of the left second rib, representing the metastasized internal mammary lymph node.

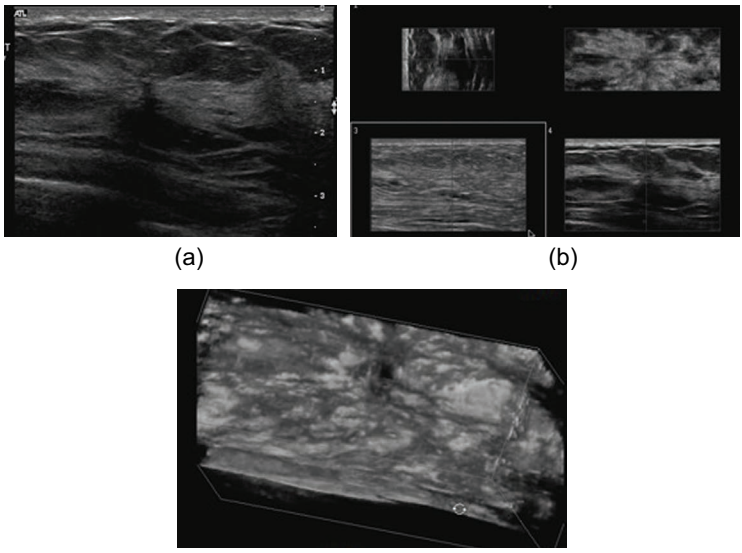

(a) (b)

(c)

Figure 8.16 Screening US study of a 42-year-old female: IDC. (a) US: A small hypoechoic zone in the left breast is depicted (0.5×0.4 cm). The focal lesion is associated with acoustic shadows and irregular margins. (b) 3D US: The lesion shows speculation on the C plane (right upper image), typical of invasive carcinoma. (c) 3D US: Volume image shows architectural distortion.

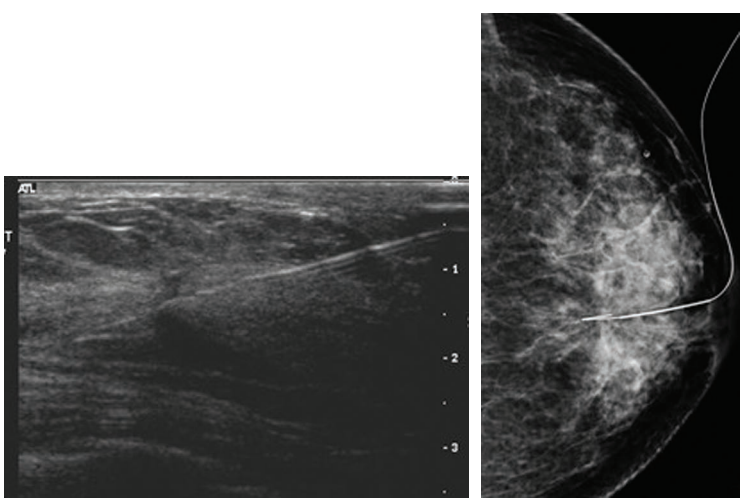

(a) (b)

Figure 8.17 Same patient as in Fig. 8.16. (a) US-guided-wire localization: A hook wire is inserted through the lesion under US guidance with the hook opened. (b) Mammography: After the localization procedure, the mammography demonstrates the location of the hook wire. Minimal tissue changes are evident in the region where the hook is located.

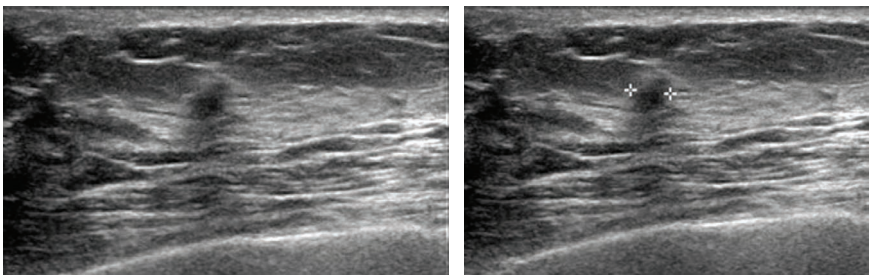

(a) (b)

Figure 8.18 Screening breast US in a 43-year-old female depicts (a) a nonpalpable solid nodule: IDC. (b) The hypoechoic lesion measures 0.5 × 0.4 mm in size, showing relatively irregular margins and indistinct boundary.

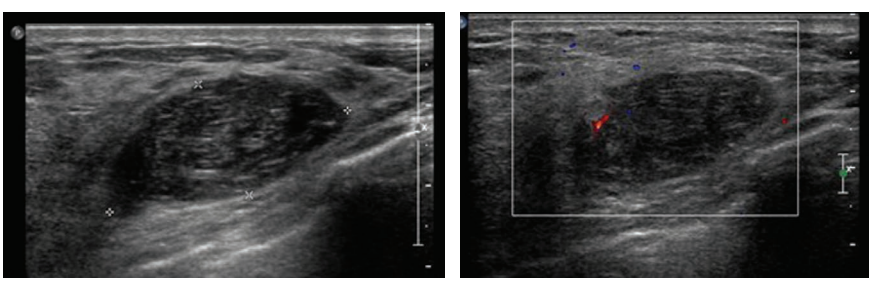

(a) (b)

Figure 8.19 A 53-year-old female presenting with palpable mass on the left breast: mucinous carcinoma. (a) US: A 3-cm ovoid hypoechoic lesion with heterogeneous echopattern, lobulated margins, and minimal distal enhancement. Part of the tumor margin is not very sharp. (b) CDU: Only minimal marginal color flows are shown.

8.6.1.1.3 Color or power Doppler ultrasound

Doppler flow signals on color Doppler ultrasound (CDU) or power Doppler ultrasound (PDU) due to increased vascularity are usually demonstrable within and at the margins of malignant tumors[3,5,10] (Figs. 8.20 and 8.21). Increased vascularity in a well-circumscribed mass is a suspicious feature, especially when found in postmenopausal women. Spectral Doppler US of malignant tumors shows relatively higher resistivity index (RI) of the feeding arteries, frequently higher than 0.7–0.75 (Fig. 8.22). A knot of abnormal vessels may be a clue to the presence of a mass that is difficult to detect on grayscale imaging (Fig. 8.23).

8.6.1.1.4 Elastography

Compression elastography is an evolving technology, and different methods and algorithms are used by different manufacturers. Many

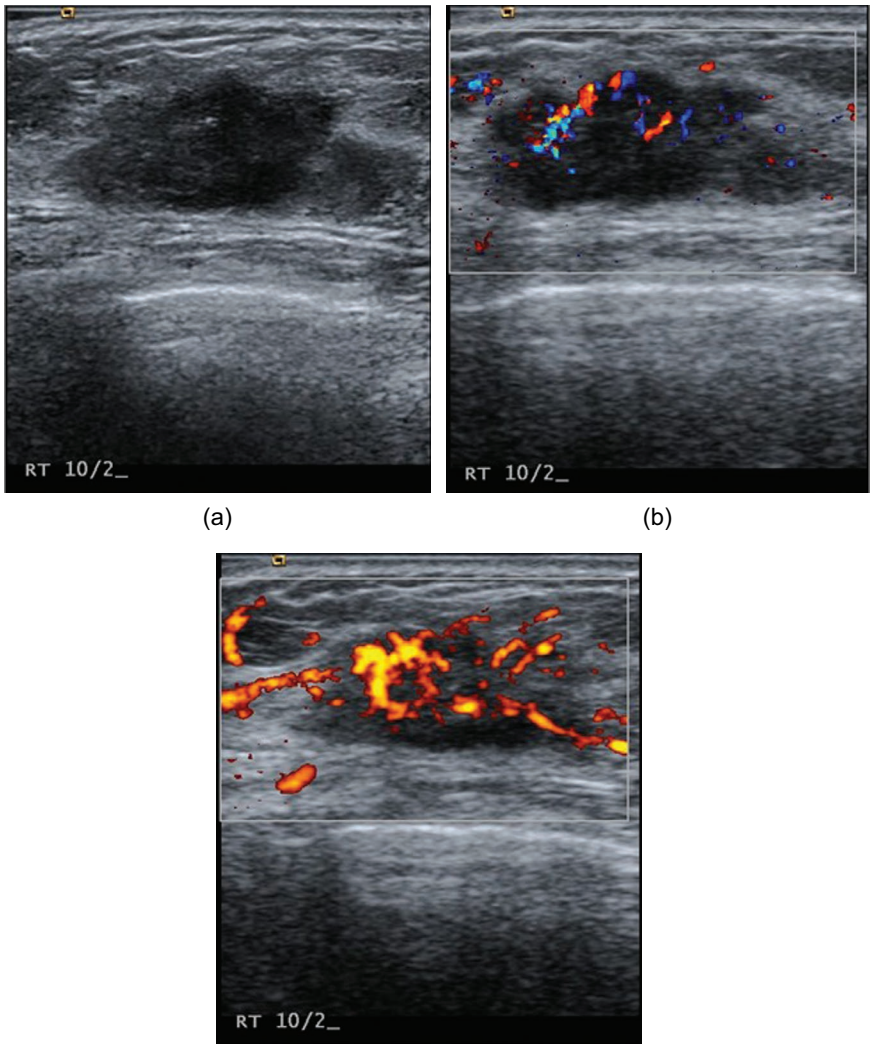

(a) (b)

(c)

Figure 8.20 CDU and PDU imaging of an IDC. (a) US: A hypoechoic mass is demonstrated and is associated with irregular margins and parallel orientation. Slightly heterogeneous echotexture is seen, with minimal distal enhancement and a tendency of halo formation. (b) CDU and (c) PDU imaging show increased vascularity of the tumor; a more-profuse color flow signal wall is depicted using PDU [in (c)].

new techniques using relevant strain imaging or acoustic radiation force imaging have been introduced in recent years. There are different formats for display of elasticity data (either color or black & white format, or quantitative elastography). In general, malignant lesions are harder, and benign lesions are softer[42,43] (Figs. 8.24–8.27).

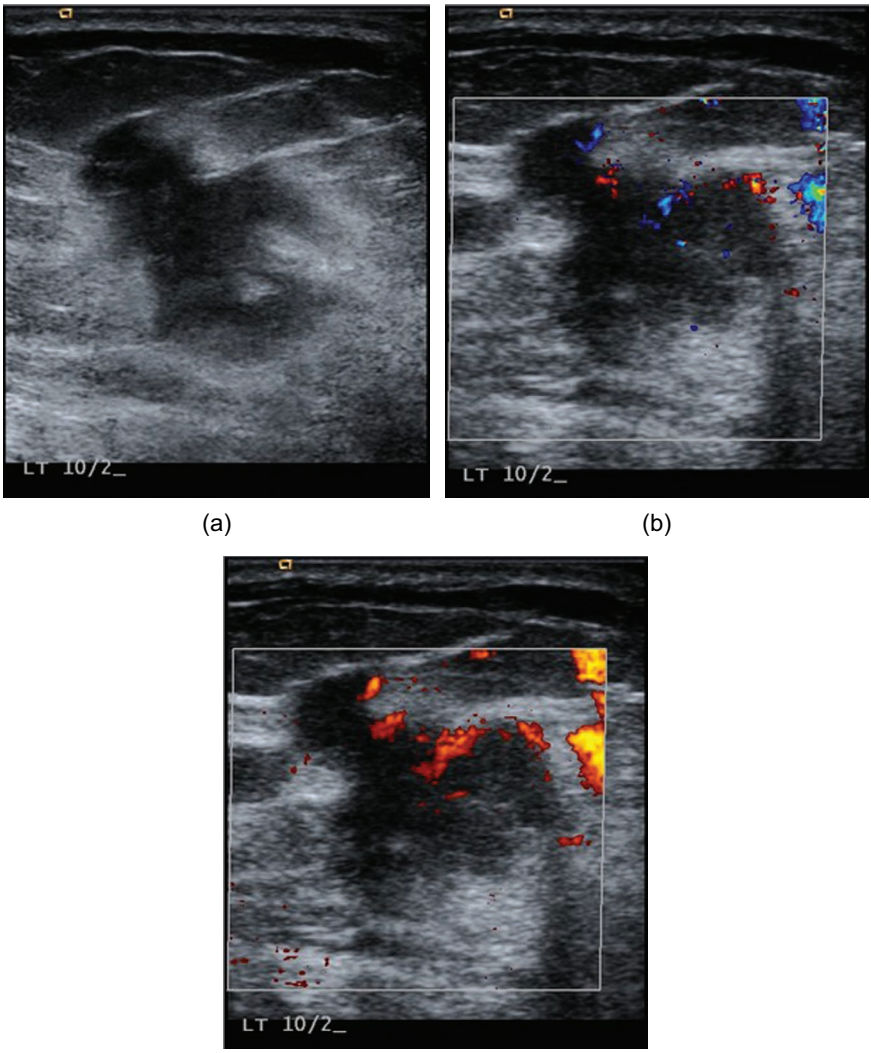

(a) (b)

(c)

Figure 8.21 CDU and PDU imaging of an IDC. (a) US: An irregular hypoechoic mass is identified, associated with a hyperechoic halo or speculation, nonparallel orientation, and no significant change in through transmission. (b) CDU and (c) PDU. Both techniques demonstrate increased vascularity of the tumor. Vascularity is shown using PDU [in (c)].

8.6.2 Mucinous carcinoma

Mucinous carcinoma, also known as colloid carcinoma, mucoid, or gelatinous carcinoma, is a rare variety with an incidence of less than 5% of all infiltrating carcinomas. It tends to occur in older women. Mucinous carcinomas are well circumscribed and often large. They are composed of nests,

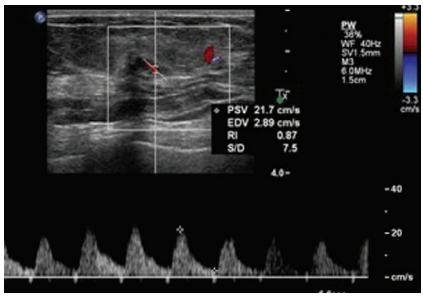

(a)

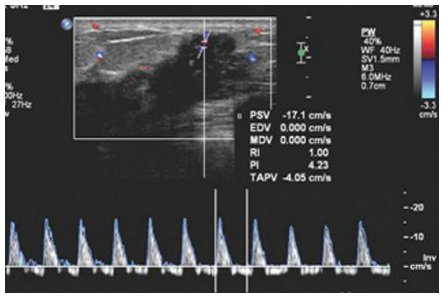

(b)

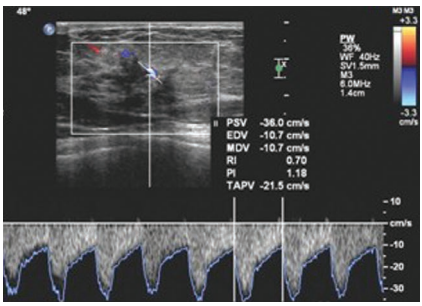

(c)

Figure 8.22 Spectral Doppler US of three IDCs. (a) A relatively small (1.3-cm) tumor with high resistivity index (RI = 0.87).(b) A large (0.3-cm) tumor with very high RI (>1.0). (c) A 2.5-cm tumor with intermediate RI (0.7).

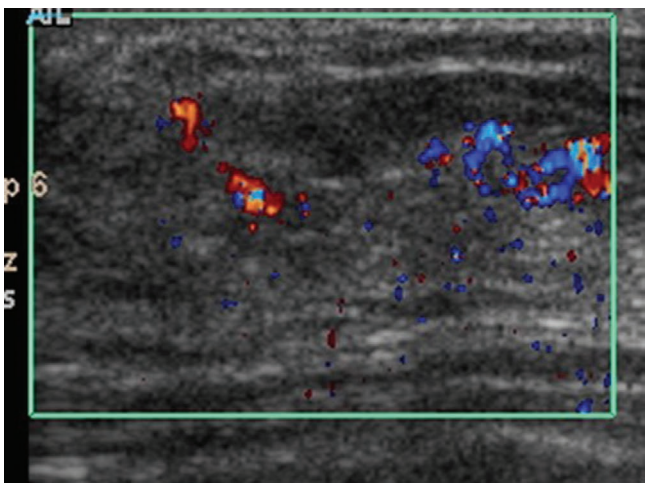

Figure 8.23 Color Doppler US of a microinvasive *in situ* carcinoma. CDU shows a poorly defined, heterogeneously hyperechoic zone (as compared to the subcutaneous fat) with increased color flow signals, suggestive of ductal carcinoma *in situ* (DCIS).

cords, and even isolated cells lying in lakes of extracellular mucin separated by a small amount of fibrous stroma.[44] Mucinous carcinomas have relatively well-defined margins and lobulated contours. The echo-intensity of the tumor tends to be isoechoic or even hyperechoic with respect to subcutaneous fat tissue. Mucinous carcinoma is not uncommonly misinterpreted as a fibroadenoma, which may also have relatively strong internal echoes and be well circumscribed. The internal echoes of mucinous carcinomas tend to be more heterogeneous, and the distal echoes may be enhanced. Mucinous carcinomas are harder and less compressible than fibroadenomas (Figs 8.19 and 8.28).

8.6.3 Medullary carcinoma

Less than 5% of all breast carcinomas are diagnosed as medullary carcinoma.[45,46] Pathologically medullary carcinomas are well delineated from

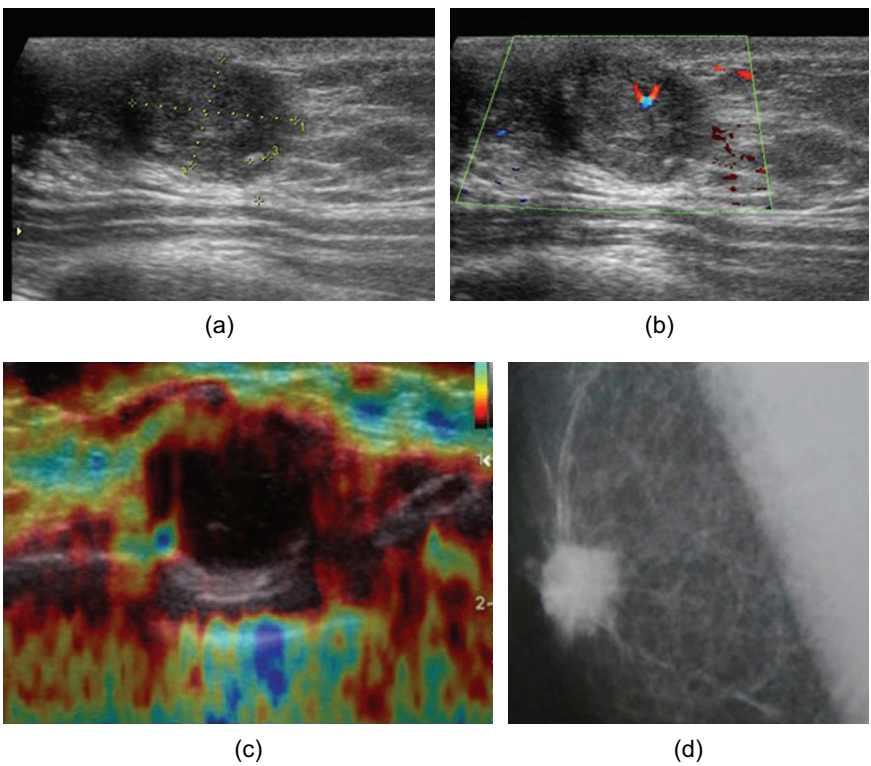

Figure 8.24 A 57-year-old female presenting with a palpable mass on the right breast: IDC. (a) US and (b) CDU show a heterogeneous hypoechoic mass. The lesion is associated with poorly defined margins [shown in (a)] and positive color flow signals [shown in (b)]. (c) Elastography demonstrates a hard mass (note the elasticity scale on the right margin of the image) [Image (c) courtesy of Samsung Medison.] (d) Mammography shows a round, speculated mass.

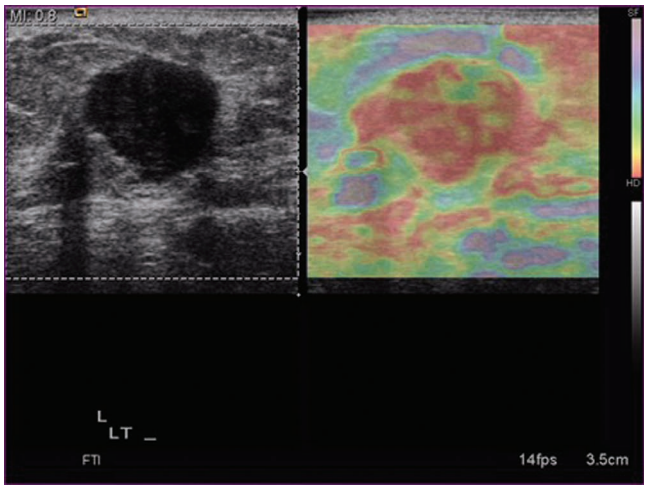

(a) (b)

Figure 8.25 A 52-year-old female presenting with an IDC. (a) US: Grayscale image shows a round hypoechoic mass with mildly irregular margins and asymmetric critical-angle artifacts. (b) Elastography: Generally reddish color in the mass on color format is indicative of a hard lesion, with a larger area of hard pathological tissue than that on the US image. [Image (b) courtesy of Siemens.]

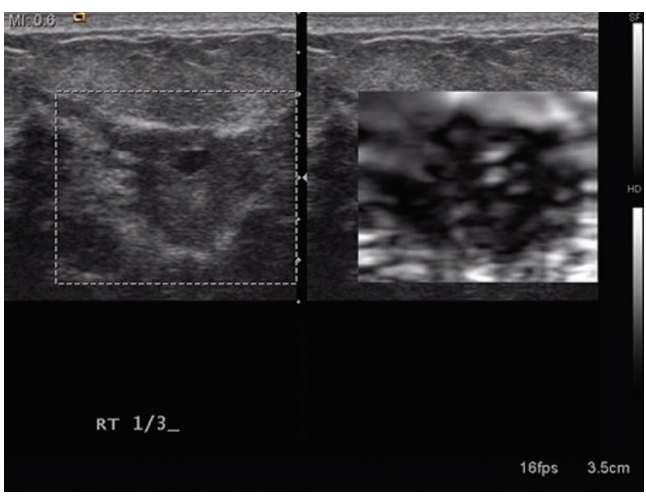

(a) (b)

Figure 8.26 IDC in a 56-year-old female. (a) US: A hypoechoic tumor with a central cystic zone, speculated margins, and an echogenic halo is shown. (b) Elastography: The elastographic appearance shows a larger area with hard pathology (darker on black-and-white format). [Image (b) courtesy of Siemens.]

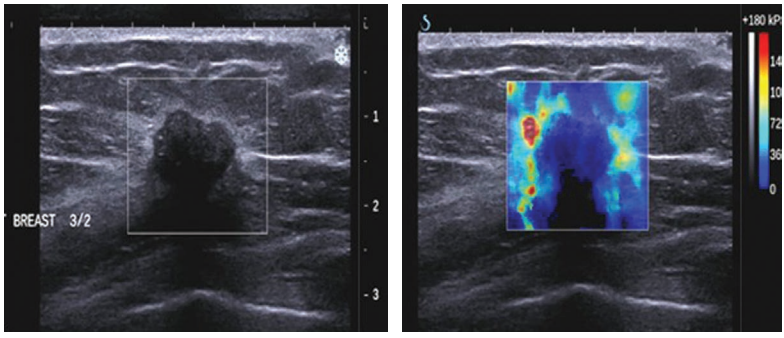

(a) (b)

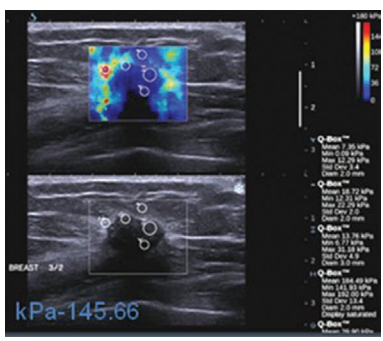

(c)

Figure 8.27 Invansive lobular carcinoma in a 53-year-old female. (a) US: A round hypoechoic tumor with acoustic shadows, microlobulated margins, and a hyperechoic halo. (b) Shear wave US elastography: A "ring of fire" pattern is demonstrated. [Image (b) courtesy of SuperSonic Imagine.] (c) Quantitative shear wave elastography: The value of elasticity is obtained by measuring the region of interest within the tumor. In this example, the mean value is 145.66 kPa, indicating a very hard tumor (a cutoff value of 55 kPa is used).

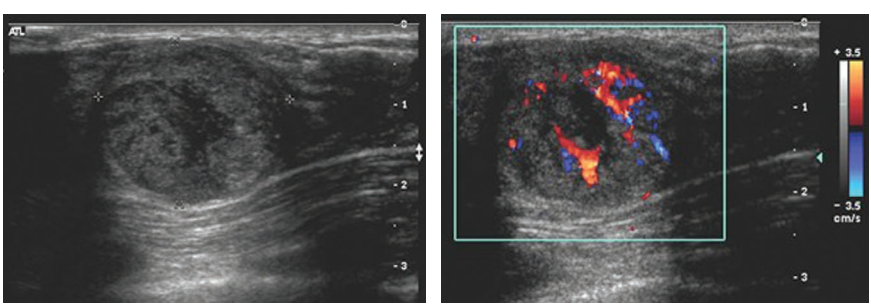

(a) (b)

Figure 8.28 A 59-year-old female presenting with a palpable left breast mass: Mucinous carcinoma. (a) US: A 2.3-cm round hyperechoic lesion with a heterogeneous echopattern and distal enhancement. The margin is generally smooth. There is a central nearly anechoic zone, representing mucin accumulation. (b) CDU: The tumor is hypervascular with profuse color flow signals.

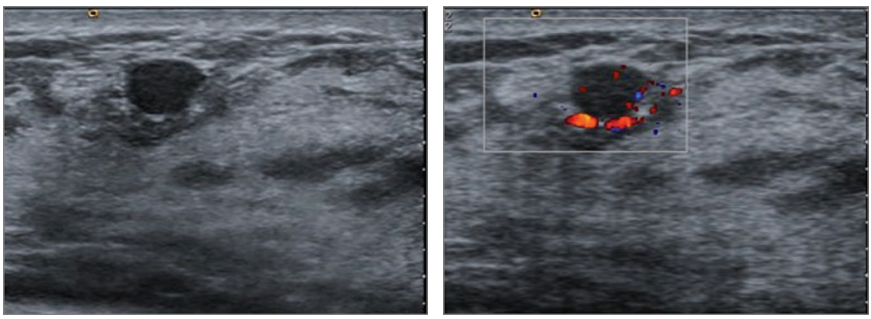

(a) (b)

Figure 8.29 A 51-year-old female presenting with a small palpable nodule in the right breast: Medullary carcinoma. (a) US: The round hypoechoic lesion, measuring 0.7 cm in size, shows relatively sharp and smooth margins, with no significant change in through transmission. The echopattern is quite similar to some fibroadenomas. (b) CDU: Increased color flow signals in the lesion, suggestive of a hypervascular tumor.

the surrounding breast. Medullary carcinomas are circumscribed, cellular carcinomas.[47,48] They are rounded or lobulated in shape. The margins are well defined and generally smooth. The internal echoes are very weak and slightly heterogeneous (Fig. 8.29). Calcification is not common. The posterior acoustic enhancement is often marked.[49]

8.6.4 Invasive lobular carcinoma

Invasive lobular carcinoma is the second most-common breast malignancy, making up some 10% of cancers.[50–52] The tumor shows a high incidence of bilaterality and multicentricity.[52,53] Invasive lobular carcinomas may be difficult to detect on mammography. The first and second most-common mammographic features are asymmetric density without a definable mass, and dense mass with speculation, respectively.[54]

8.6.4.1 Ultrasound features

The US features of invasive lobular carcinoma are similar to those of IDC, particularly of the scirrhous type (Fig. 8.30). Invasive lobular carcinomas tend to be highly infiltrative and sometimes do not have a distinct nidus; in some cases only focal heterogeneous tissue with sound attenuation or architectural distortion can be demonstrated.

8.6.5 Ductal carcinoma *in situ*

Before use of screening mammography became prevalent, less than 5% of all breast malignancies were classified as ductal carcinoma *in situ* (DCIS). During the past 10 years, however, DCIS constitutes 20% to 40% of all

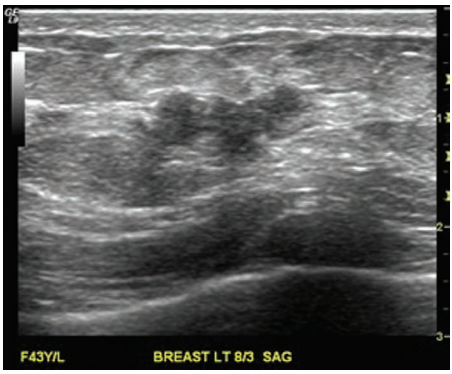

(a)

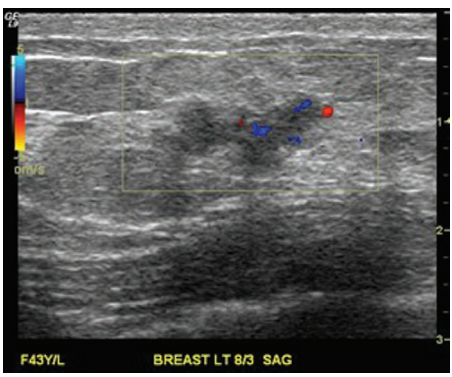

(b)

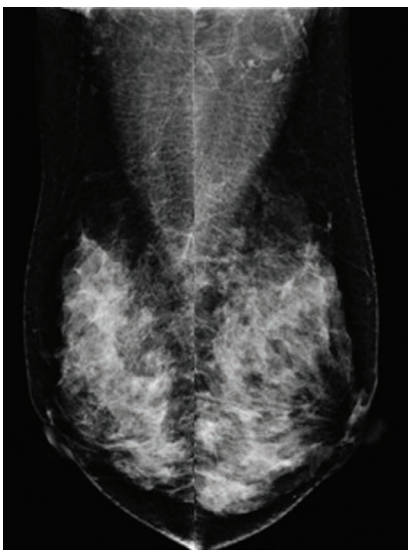

(c)

Figure 8.30 A 43-year-old female presenting with a palpable mass in the left breast: Invasive lobular carcinoma. (a) US: A 1.8 × 0.7-cm lobulated hypoechoic mass is noted. The margins are mildly irregular in some parts. (b) CDU: The lesion shows increased color flow signals in some parts. (d) Mammography: Increased density in the lower part of the left breast.

breast malignancies because it is detected during routine mammographic screening.

DCIS represents a spectrum of noninvasive neoplasms. The classification of the various types of DCIS is somewhat controversial. Traditionally, DCIS has been subdivided into comedo necrosis and noncomedo necrosis groups. Noncomedo DCIS is further subdivided into micropapillary, cribriform, and solid types. Solid-type DCIS is most frequently associated with comedo necrosis. Each type of DCIS is further subdivided into nuclear grade groups: low nuclear grade (LNG), intermediate nuclear grade (ING), or high nuclear grade (HNG). Comedo necrosis occurs most frequently in HNG DCIS.

The prognosis of DCIS may be related to the nuclear grade and necrosis. HNG DCIS and lesions with necrosis are the most aggressive, are the

more likely to demonstrate micro-invasion, and more likely to progress to invasive carcinoma in a shorter time. They are more likely to recur early after wide excision and have a 1–2% positive axillary node rate compared to cases of LNG DCIS without necrosis.

Based on different recurrent rates, the Van Nuys classification system for DCIS identifies three different groups. Group 1 is non-HNG DCIS without comedo necrosis (recurrent rate: 3.8%). Group 2 includes non-HNG DCIS with comedo necrosis (recurrent rate: 11.1%). Group 3 includes HNG DCIS with or without comedo necrosis (recurrent rate: 26.5%). HNG DCIS more frequently presents with a palpable soft-tissue mass on imaging than does LNG DCIS because it more grossly distends ducts (filled with tumor cells or necrotic debris) and it incites periductal inflammation and fibrosis.

8.6.5.1 Sonographic findings

Mammography is generally more accurate than US for detection of DCIS because of its effectiveness in demonstrating and characterizing microcalcifications with which DCIS presents in most cases. Patients with calcifications are usually referred for stereotactically mammography-guided needle or wire localization and surgical biopsy, and do not undergo diagnostic breast US. However, US may be helpful in the evaluation of patients with DCIS in certain aspects, including: (1) evaluation of the 10% of patients with soft-tissue densities without calcifications, (2) evaluation of patients with palpable abnormalities and negative or nonspecific mammograms, and (3) evaluation of patients with nipple discharge and guiding aspiration and core needle biopsy of intracystic papillary DCIS, (4) evaluation of the size of the lesion in cases of noncomedo DCIS in which the extent of calcifications on mammography is likely to underestimate the size of the lesion, (5) identification of invasive components of carcinoma when calcifications suggest pure DCIS, (6) assessment of regional lymph nodes in large, HNG DCIS, (7) guidance of needle localization of calcifications, (8) guidance of ductography or needle localization of intraductal papillary lesions, and (9) guidance of core needle biopsy in the rare cases in which stereotactic biopsy is not possible.

Normal ducts and TDLUs can be demonstrated on high-resolution US. It is also known that abnormally distended ducts and TDLUs in patients with DCIS are demonstrable sonographically. The DCIS distended ducts are easily appreciated in a plane that is parallel to the long axis of the ducts, i.e., the radial plane. The long axis of the dilated ducts documented with relative effectiveness of long-axis and short-axis scanning of mammary ducts as opposed to random longitudinal and transverse scan planes.[55–58]

Duct extension and branch pattern are suggestive signs of DCIS or DCIS components of disease, signs that indicate the presence of tumor-enlarging

ducts. Microlobulations can be seen with either invasive and intraductal tumors but more frequently represent tumor-filled ducts or TDLUs. Microcalcifications representing the necrotic debris in the center of the lumen of involved ducts or ductules are also important findings that suggest that DCIS can be associated with any of the other abovementioned findings. The calcifications within DCIS can be large enough (e.g., 0.3–0.7 mm) to cause punctate, bright echoes without shadowing. DCIS can also be identified as amorphous sheets of isoechoic tissue (Figs. 8.31–8.37). Intracystic papilloma may be associated with *in situ* carcinoma, or a frank DCIS may be located in a cystically dilated duct that attains a size sufficient to produce a macroscopic nodule or mass in a cystic lesion.[59,60]

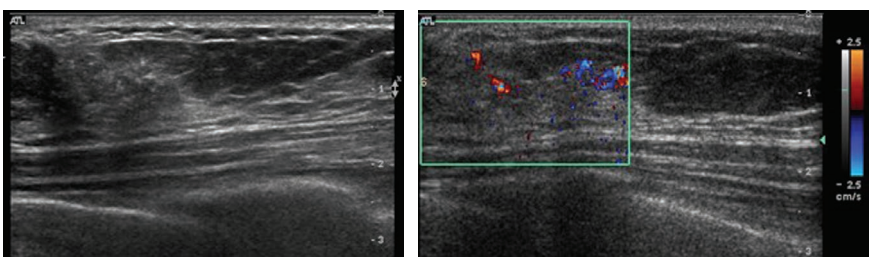

(a) (b)

Figure 8.31 A 48-year-old referred for breast US examination because of right breast pain: Ductal carcinoma *in situ* with micro-invasion. (a) US: A relatively hyperechoic area (with respect to the subcutaneous fat) occurs in the subareolar region of the left breast. Some tiny echogenic spots are indicative of microcalcifications. Physical examination revealed a relatively thick breast tissue. (b) CDU: Increased color flow signals in the region of suspicion.

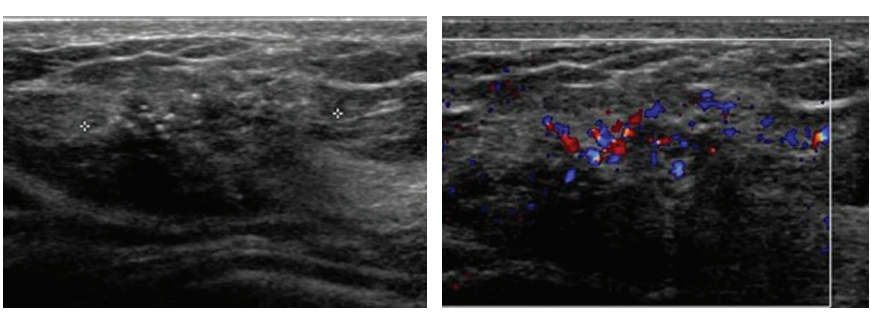

(a) (b)

Figure 8.32 A 34-year-old female presenting with clinically suspicious abnormal finding in the left breast: Ductal carcinoma with micro-invasion. (a) US: A 2.5-cm hypoechoic zone in the left breast with microcalcifications. The lesion is associated with poorly defined margins and distal sound attenuation. (b) CDU: Increased color flow signals in the lesion.

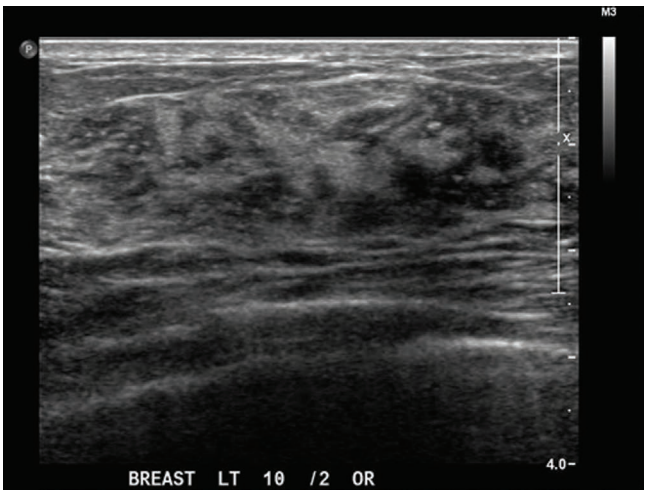

Figure 8.33 A 39-year-ole female presenting with left breast lump: Comedocarcinoma, invasive. US shows a heterogeneous region with punctuate hyperechoic spots, suggestive of microcalcifications. Some microcalcifications are located in the distended ducts (left-hand aspect). An irregular hypoechoic zone in the right-hand aspect is compatible with the invasive component of the carcinoma.

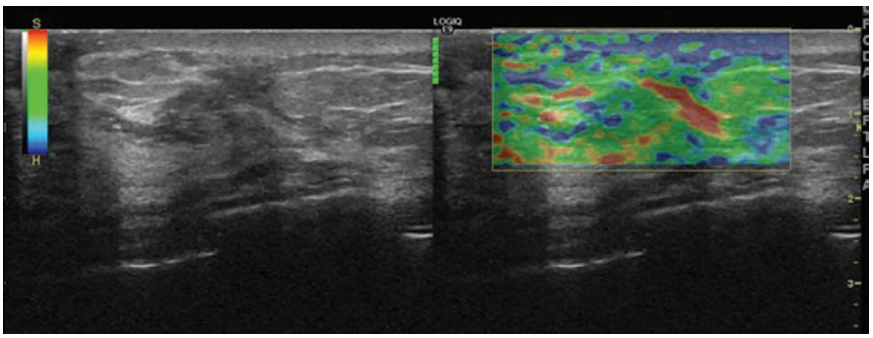

(a) (b)

Figure 8.34 A 53-year-old female presenting with a palpable mass in the right breast: IDC with ductal invasion. (a) US: The hypoechoic lesion shows irregular margins and microcalcifications. The adjacent duct is dilated and filled with hypoechoic material and punctate spots, representing duct invasion and microcalcifications. (b) Elastography: Heterogeneous elasticity in territory of the lesion is demonstrated.

8.6.6 Lobular carcinoma *in situ*

Most lesions of lobular carcinoma *in situ* (LCIS) are of microscopic size and are consequently asymptomatic and nonpalpable; they are incidental findings in biopsy specimens. The clinical importance of LCIS is the

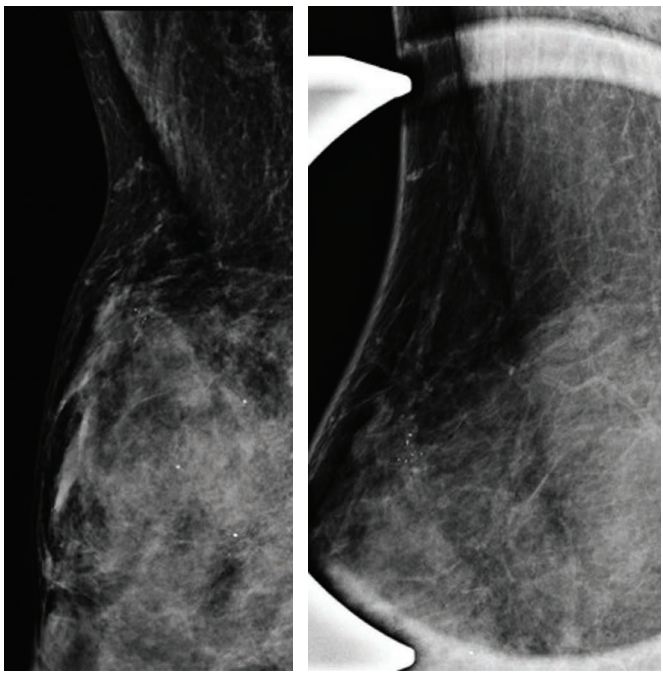

(a) (b)

Figure 8.35 The same patient as Fig. 8.34: mammography of the right breast, mediolateral oblique view. (a) Some microcalcifications are shown in the margins of the breast stroma near the breast tail. (b) Ancillary view, compression: The microcalcifications are better shown.

high incidence of multicentricity and bilaterality. The incidence depends on the thoroughness of sampling; multicentricity is reported as 70% in mastectomy specimens, and bilaterality in biopsy specimens of the contralateral breast as 30%. Histologically, LCIS causes a lesser degree of distension of the involved terminal duct lobular unit, and therefore the disease is of microscopic size. The growth pattern of LCIS is typically solid, and necrosis is absent. Extension into interlobular ducts can occur but shows a lesser degree of the ductal enlargement seen in DCIS[61] (Fig. 8.38).

8.6.7 Inflammatory carcinoma

The diagnosis of inflammatory carcinoma is based on the clinical findings of tenderness, pain, and firm enlargement of the breast, together with reddening and edema of the skin affecting more than one-third of the breast. Flattening or retraction of the nipple is a frequent finding, and most patients have axillary lymph node metastases by the time of presentation.

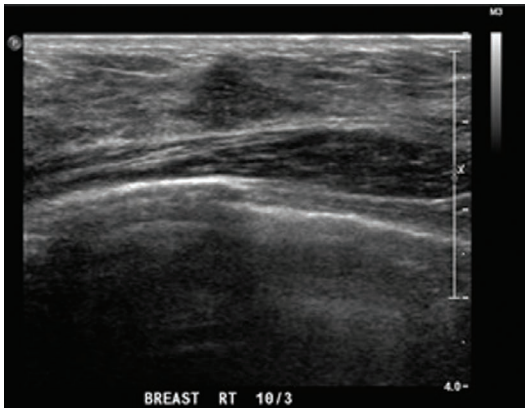

(a)

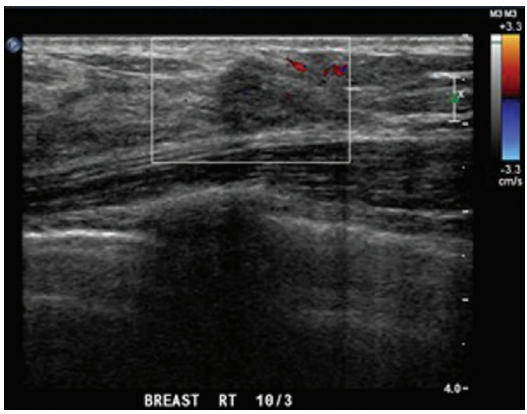

(b)

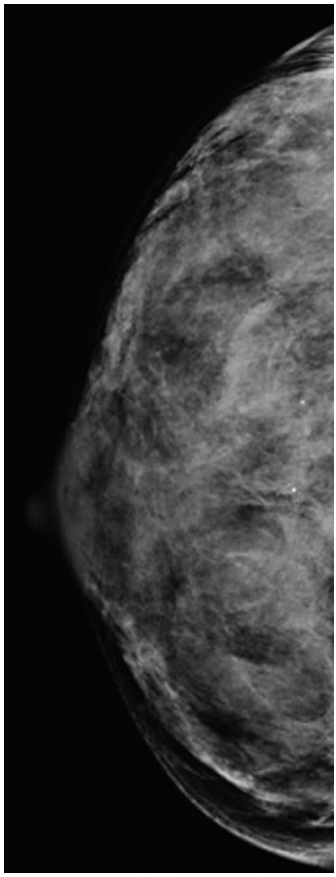

(c)

Figure 8.36 A 45-year-old female presenting with a small palpable nodule in the right breast: DCIS. (a) US: A hypoechoic lesion in the right upper outer quadrant, with suspicious microcalcifications. The tumor margins are irregular, with no change of the through transmission. (b) CDU: Only minimal color flow signals are noted on the margins of the lesion. (c) Mammography, craniocaudal view: Some tiny calcifications of intermediate suspicion are seen. No definite focal mass is depicted.

Skin thickening is of various degrees. With progressive edema, the echogenicity of the skin decreases. The echogenicity of the subcutaneous fatty tissue may be diffusely increased (Fig. 8.39).

The tumor itself cannot always be demonstrated. If depicted, it may show an appearance as an infiltrative ductal carcinoma, a textural distortion of the glandular tissue, or a significant attenuation arising from the thickened heterogeneous diseased breast tissue. Axillary lymphadenopathy is a common finding.[62]

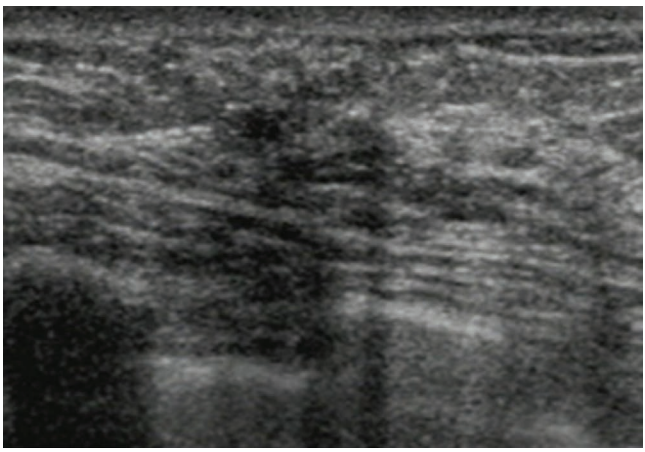

Figure 8.37 A 43-year-old female presenting with palpable breast nodules: DCIS. US of bilateral breasts shows cysts of variable sizes (0.3–0.9 cm). However, a focal nonpalpable pathology is depicted at US, measuring 0.8 × 0.7 cm. The lesion is associated with microcalcifications.

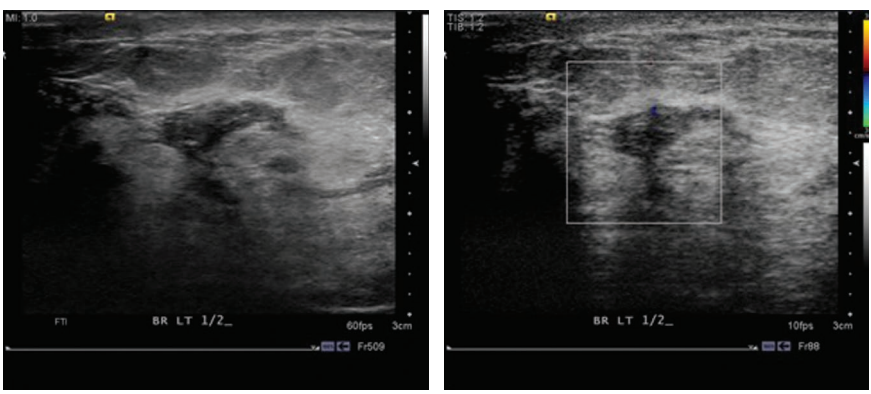

(a) (b)

Figure 8.38 A 54-year-old female was found to have bilateral breast lumps on physical examination: Lobular carcinoma *in situ* (LCIS). (a) US: The hypoechoic area in the center of the image is of indeterminate nature. (b) CDU: No demonstrated color flow signals. LCIS was confirmed by using wire-localization surgical excision biopsy.

8.6.8 Lymphoma and metastases of the breast

Although breast involvement by metastases is uncommon, in females with a known history of malignancy, metastases should be always included in the differential diagnoses when dealing with patients with palpable breast lumps or solid breast masses on US. These lumps and masses can be metastases from a carcinoma in the opposite breast, metastasis from extramam-

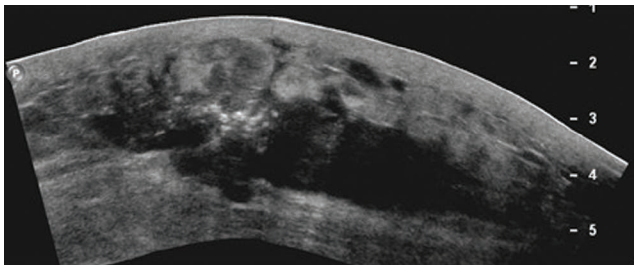

(a)

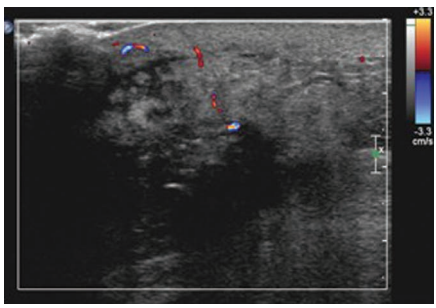

(b)

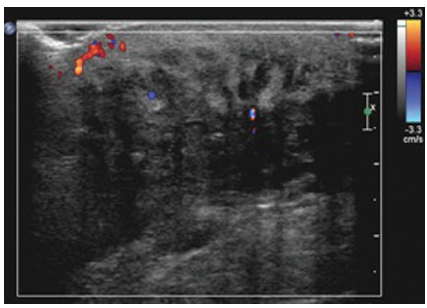

(c)

Figure 8.39 A 59-year-old female presenting with inflammatory carcinoma. (a) US: Panoramic view of the right breast shows diffuse thickening of the skin (up to 0.6 cm) and subcutaneous fat, which shows increased echogenicity. An extensive irregular hypoechoic mass with hyperechoic areas is noted. The hyperechoic structures are most likely due to thickly clumped microcalcifications. (b) and (c) CDU: Minimally increased color flow signals are evident on the skin, in the subcutaneous fat, and on part of the tumor.

mary primary malignancies, or breast involvement in hematological malignancies. Among these, lymphoma involving the breast is the most common. Lymphoma occasionally originates primarily in the breast, but in most cases distinguishing primary from secondary involvement is difficult. Metastasis to the opposite breast usually occurs via lymphatics across the anterior chest wall, and usually the primary lesion is already far advanced. A multicentric origin is believed to be more common than intramammary spread; however, only a histological study can confirm its nature. Metastases can be from bronchogenic carcinoma, melanoma, ovarian carcinoma, renal cell carcinoma, colon carcinoma, or sarcoma.[63] Discrete nodules are more common than diffuse involvement at first presentation.[64]

8.6.8.1 Sonographic features

The metastatic nodules within the breast are usually hypoechoic with relatively poorly defined margins. Small metastases are relatively round, and larger lesions are ovoid. The echopattern is heterogeneous. These

findings are related to minimal local reactive changes or signs of invasion in the surrounding tissues. A metastasis cannot be differentiated from a well-circumscribed breast carcinoma, although multiplicity may be suggestive of metastasis. Lymphoma can present as discrete nodules, solitary, or multiple. Because of their uniform cellularity, the internal echoes are extremely low with strong enhancement and can be misdiagnosed as cysts. Occasionally, lymphoma may present as diffuse thickening of the glandular tissue and a generalized decrease of echogenicity with preservation of the structure of the glandular tissue (Figs. 8.40–8.42).

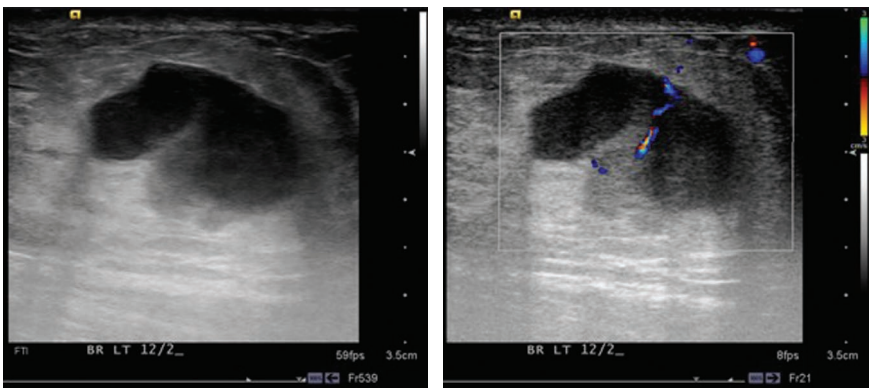

(a) (b)

Figure 8.40 Lymphoma involving the intramammary lymph node. (a) US: The enlarged intramammary lymph node is very hypoechoic and is associated with distal enhancement. The hilum is preserved. (b) CDU: Positive color flow signals adjacent to and in the hilum.

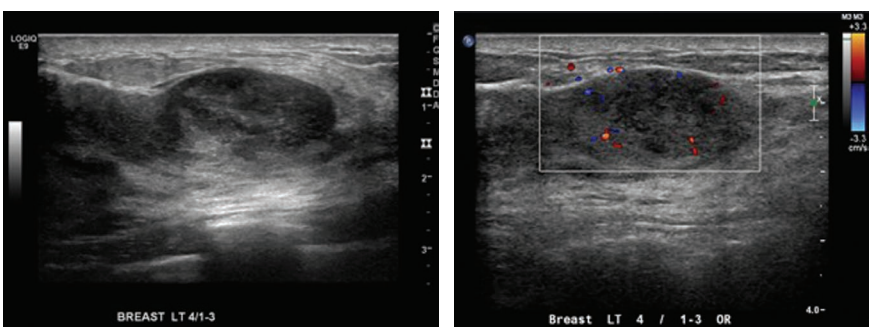

(a) (b)

Figure 8.41 A 55-year-old female presenting with palpable left breast mass: lymphoma.(a) US: A focal heterogeneously hypoechoic mass is noted in the left lower outer quadrant. Distal enhancement is present. (b) CDU: Color flow signals are demonstrated in the lesion.

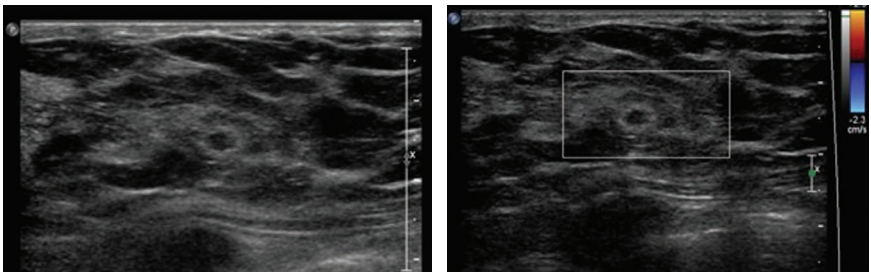

(a) (b)

Figure 8.42 A 61-year-old female with a history of colon cancer. Status four years after surgery: Metastasis from colon cancer. (a) US: A 0.4-cm isoechoic nodule is depicted in the upper outer quadrant of the left breast. The nodule is surrounded by an echogenic halo. (b) CDU: No color flow signals can be demonstrated.

8.7 Fibrocystic Changes and Breast Cysts

8.7.1 Fibrocystic changes and benign proliterative disorders

Fibrocystic change (FCC) is often used as a collective term for a wide spectrum of non-neoplastic structural changes in the breast glandular tissue. FCC refers to hormonally induced transformations of the breast parenchyma. This very common benign condition usually involves the entirety of both breasts and is often found in premenopausal women. Histologically, FCC presents with interlobular and intralobular fibrosis, acinolobular hyperplasias with cysts and ductal ectasia, and ductal epithelial proliferation. Nearly all women over the age of 30 have small breast cysts that can be detected by US. The cysts usually appear between 30 and 50 years of age and are rare before age 20 and after age 60. Breast cysts noted in FCC range from a few millimeters to 6 cm in size. The cysts occurring in FCC may have a great variety of presentation on US. A typical cyst on US has acoustic properties that differentiate it from a solid lesion; i.e., anechoic, smooth, thin, and hyperechoic border, well-defined boundary, parallel in orientation (elliptical), posterior acoustic enhancement (enhanced sound transmission), bilateral edge shadows (lateral shadows), readily compressible, and no architectural change (Fig. 8.43).

However, cysts can be atypical because of their content, anatomic variation, background, age of the cysts, and the associated changes developed in the cysts. The atypical cysts may be multilocular, septated, clustered, or echogenic (Fig. 8.44). Echoes can appear within a cyst due to hemorrhage, mucinous secretion, infection, inspissated milk, oil droplets, crystals, etc. Whenever intracystic solid structures are detected, histological confirmation should be performed to exclude intracystic neoplasm (e.g., papilloma or carcinoma). The risk posed by FCC are two-fold: certain types of FCC

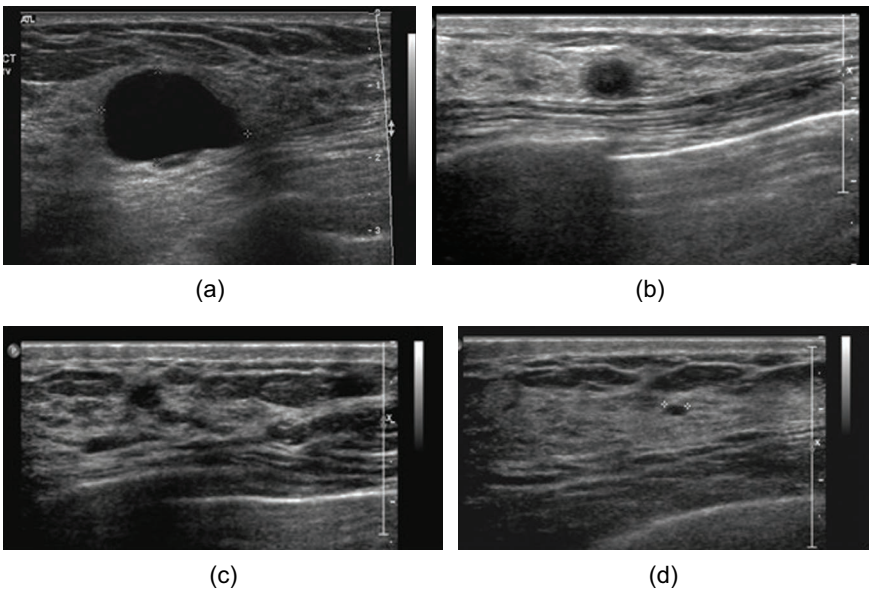

(a) (b)

(c) (d)

Figure 8.43 Variable patterns of breast cysts: (a) A typical simple cyst with a clear-cut boundary, a thin and smooth wall, distal enhancement, and critical-angle artifacts. (b) A cyst with weak internal echoes and a relatively thick wall. (c) A cyst with adjacent fibrosis. (d) A tiny cyst (2–3 mm).

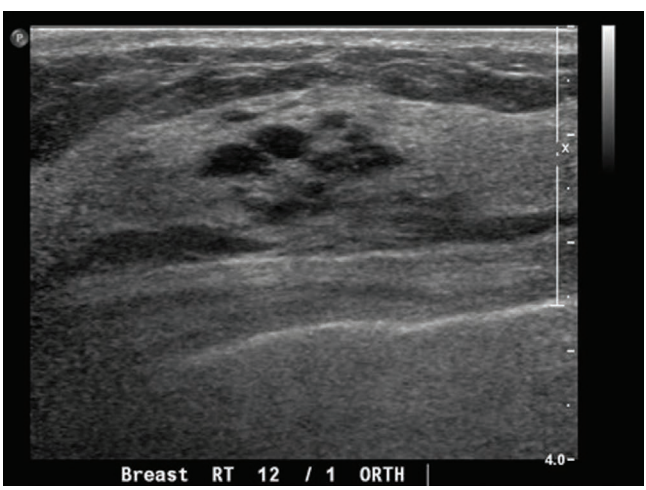

Figure 8.44 A nodular structure in the upper part of the right breast: Clustered microcysts. US shows multiple small cysts of variable sizes. Most of the cysts are less than 2–3 mm, and two are about 4–5 mm.

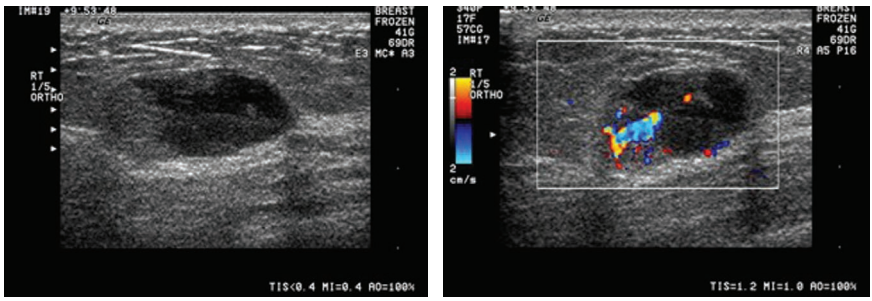

(a) (b)

Figure 8.45 An atypical or complex cystic lesion: Intracystic papillary cancer. (a) US: An ovoid cystic lesion is seen. Weak internal echoes are present with sedimentation, suggestive of debris or hemorrhage. A solid part is noted in the left-hand side of the lesion. (b) CDU: Color flow signals are demonstrated in the solid part, indicating a mural tumor.

increase the risk of developing breast cancer, and features of FCC on US can mimic the appearance of malignancy[65–68] (Fig. 8.45).

8.7.1.1 Benign proliferative disorders in fibrocystic changes

Fibrocystic changes may be associated with various types of proliferative disorders such as epithelial hyperplasia and adenosis. Atypia can be found in some cases of epithelial hyperplasia or adenosis. (Fig. 8.46). Adenosis is hyperplasia of the intralobular ductules that leads to enlargement of lobules and an increase in the number of lobules. When adenosis becomes extensive enough, the enlarged and more numerous lobules can coalesce into a solid mass termed tumoral adenosis. Tumoral adenosis is distinguished from adenosis or sclerosing adenosis only in extent.

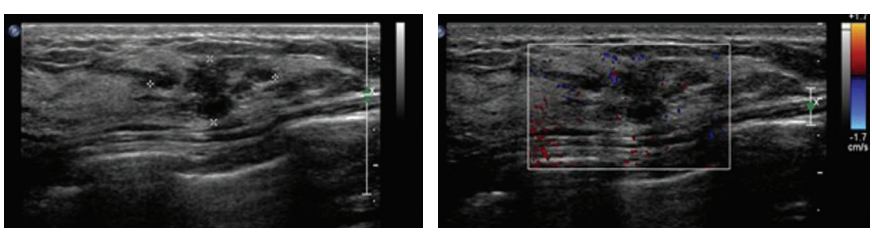

(a) (b)

Figure 8.46 A case with fibrocystic changes and a focal lesion confirmed to be epithelial hyperplasia and atypia. (a) US: Multiple small hypoechoic zones represent coalescent lobular changes that contain epithelial hyperplasia and fibrosis. Foci of atypia are revealed on histological specimens. (b) CDU: Only minimal color flow signals are demonstrated.

8.7.1.2 Sonographic findings

8.7.1.2.1 Sclerosing adenosis

Sclerosing adenosis has a variety of sonographic appearances. It can present as a microlobulated solid nodule with a central echogenic focus representing the sclerosis. If the sclerosis is severe, the small nodule formed may be angular or frankly speculated. The calcifications in adenosis may be large enough to cause punctate internal echoes but only occasionally present as sonographic microcalcifications (Fig. 8.47).

8.7.1.2.2 Tumoral adenosis

Tumoral adenosis is a more extensive and confluent focal involvement with adenosis or sclerosing adenosis. US may show large isoechoic masses that are difficult to distinguish from DCIS or invasive carcinoma. Unlike DCIS or invasive carcinoma, tumoral adenosis may contain well circumscribed and thinly encapsulated simple cysts (Fig. 8.48).

8.7.2 Fibroadenomas

Fibroadenomas are the most common benign tumors in premenopausal women. The tumors occur in a wide age range that spans from adolescents to octogenarians. The tumor arises from the terminal ductolobular unit (TDLU) and contains variable amounts of stromal and epithelial elements. The stroma can be highly cellular or paucicellular and can also undergo myxoid change, sclerosis, hyalinization, and calcification. Fibroadenomas are usually encapsulated by a pseudo-capsule of compressed breast tissue. They may regress spontaneously, or grow rapidly but usually do not become larger than 3.5 cm. However, *giant fibroadenomas* and *juvenile fibroadenomas* often grow rapidly larger than 3 cm and sometimes even up to 6 to 10 cm, at which point they are usually termed fibroadenomas with highly cellular stroma. The histologic distinction of fibroadenomas with

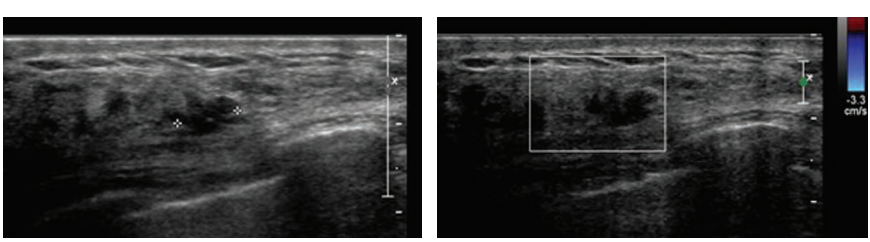

(a) (b)

Figure 8.47 Sclerosing adenosis with calcification. (a) US and (b) CDU: A hypoechoic nodule with irregular margins and a central hypoechoic spot represents a focal fibrotic lesion with a focally dilated acinus containing a tiny calcification. No color flow signal can be seen on CDU.

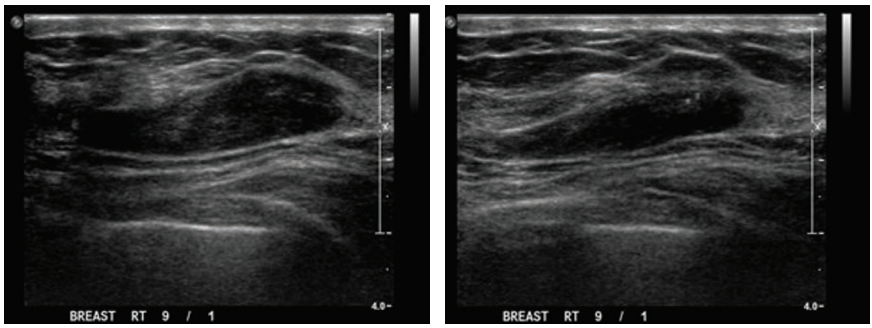

(a) (b)

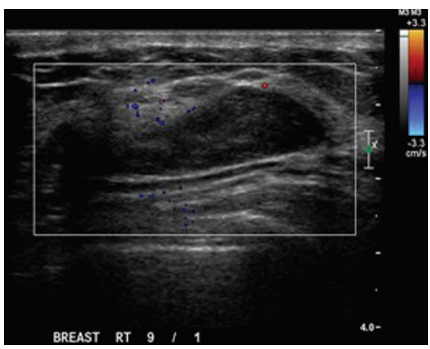

(c)

Figure 8.48 Tumoral adenosis in a 42-year-old female. (a) and (b) US: An ovoid hypoechoic lesion with essentially sharp margins is shown, mimicking a fibroadenoma on US. (c) CDU: No significant color flow is seen in the lesion.

cellular stroma from benign phyllodes tumor can be difficult. Fibroadenomas rarely undergo malignant change (about 1 in 1,000).

8.7.2.1 Sonographic findings

The sonographic findings for fibroadenomas are usually sharply demarcated from surrounding tissue and often encapsulated, suggestive of benign lesions, but may not always be classic (Figs. 8.49 and 8.50). Giant fibroadenomas and juvenile fibroadenomas often grow larger than 3 cm but retain the classic sonomorphology of a fibroadenoma (Fig. 8.51). Nonclassic findings tend to require exclusion of the lesion from BIRADS category 3 or, occasionally, BIRADS 4. The classic sonographic findings of fibroadenomas include: (1) elliptical (parallel in orientation) or gently lobulated shape, (2) isoechoic or mildly hypoechoic echotexture, (3) a thin echogenic capsule, (4) increased or no significant change in through transmission, (5) thin lateral shadows (critical-angle artifacts), (6) slight compressibility on dynamic study, and (7) mobility during compression or palpation.

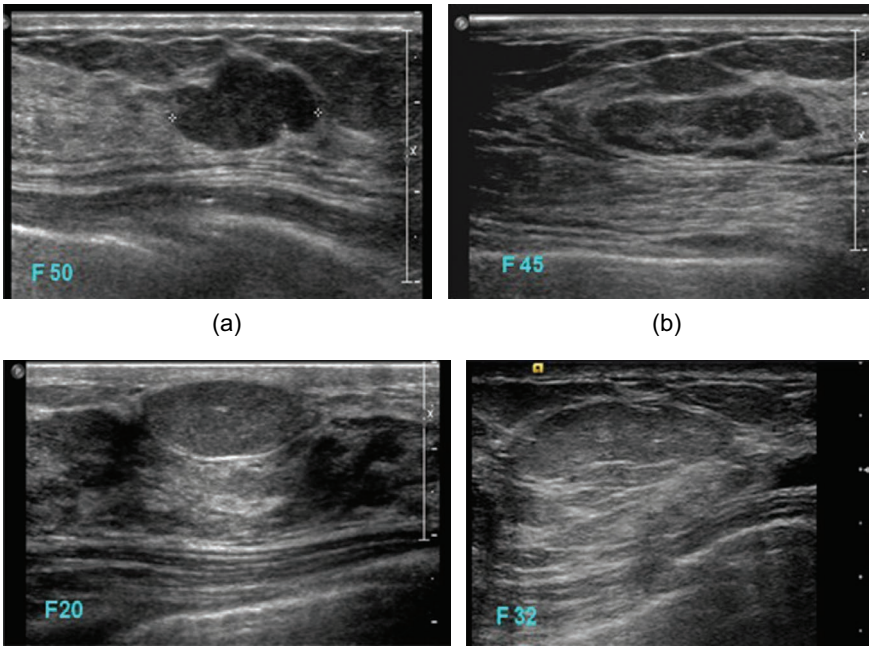

(a) (b)

(c) (d)

Figure 8.49 Variable echopatterns of fibroadenomas in females of different age groups. (a) A lobulated hypoechoic nodule with mild heterogeneous pattern and minimal distal enhancement. (b) A flat ovoid isoechoic tumor with mildly heterogeneous pattern and septation. (c) An ovoid nearly isoechoic nodule with a homogeneous pattern and sharp, smooth margins, distal enhancement, and critical-angle artifacts. (d) An ovoid, slightly lobulated, homogeneously hyperechoic tumor with septation and distal enhancement.

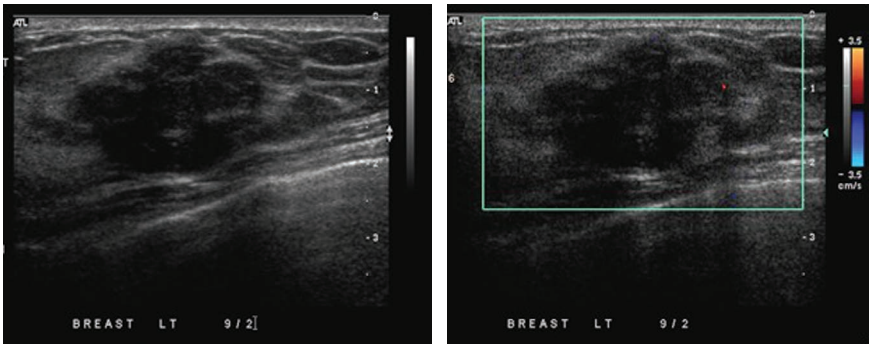

(a) (b)

Figure 8.50 A 47-year-old female presenting with a relatively round lobulated hypoechoic mass with a mild heterogeneous echopattern and septation. The mass is a hyalinized fibroadenoma. Heterogeneous distal sound attenuation is evident. (a) US: The lesion shows a relatively thick hyperechoic zone surrounding the hypoechoic nidus. (b) CDU: Only minimal color flow signals on the margins.

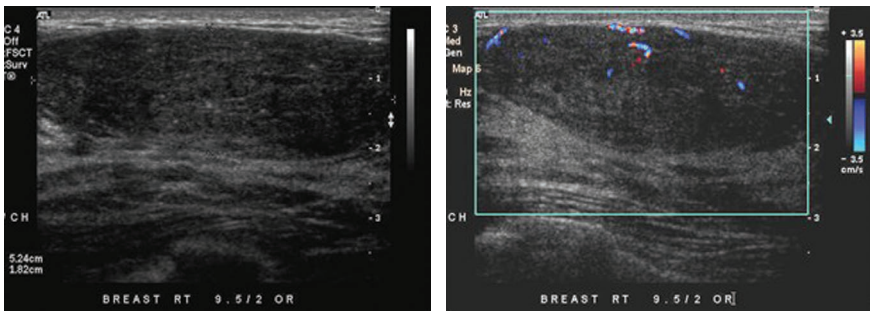

(a) (b)

Figure 8.51 A 17-year-old female presenting with a large palpable mass on the right breast: Juvenile fibroadenoma. (a) US: A large smoothly marginated hypoechoic tumor is demonstrated (5.2 × 1.8 cm). The echopattern is similar to usual fibroadenoma.(b) CDU: Relatively increased color flow signals in the tumor.

As fibroadenomas become larger (e.g., >2–3 cm), they are less likely to remain elliptically shaped and are more likely to develop more than three lobulations or microlobulations in some parts, features that currently still require BIRADS 3 and, occasionally, BIRADS 4 classification. On color Doppler US, a fibroadenoma frequently shows smooth vessels paralleling the periphery, a sign more characteristic of benign lesions. Penetrating vessels may be seen in some cases, especially in younger females (e.g., younger than 25–30 years)[69–72] (Fig. 8.52).

8.7.3 Fibroadenoma variants

8.7.3.1 Complex fibroadenomas

Fibroadenomas are composed of a variable mixture of stromal and epithelial elements. The epithelial elements within the fibroadenoma may undergo proliferative changes that include cyst formation, apocrine metaplasia, epithelial hyperplasia with epithelial-type calcifications, and sclerosing adenosis. Fibroadenomas that contain these epithelial changes are termed as complex lesions. The presence of histologic changes suggesting the presence of a complex rather than a simple fibroadenoma might precipitate biopsy rather than followup.

8.7.3.2 Sonographic findings

Epithelial calcifications within complex fibroadenomas appear as small, punctate hyperechoic structures. They are usually too small to cause acoustic shadowing. Sclerosing adenosis within a complex fibroadenoma in the periphery may result in angular margins. Other sonographic findings include heterogeneous internal texture, internal cysts, and internal foci of hyperechogenicity (Figs. 8.50, 8.53, and 8.54). When a fibroadenoma

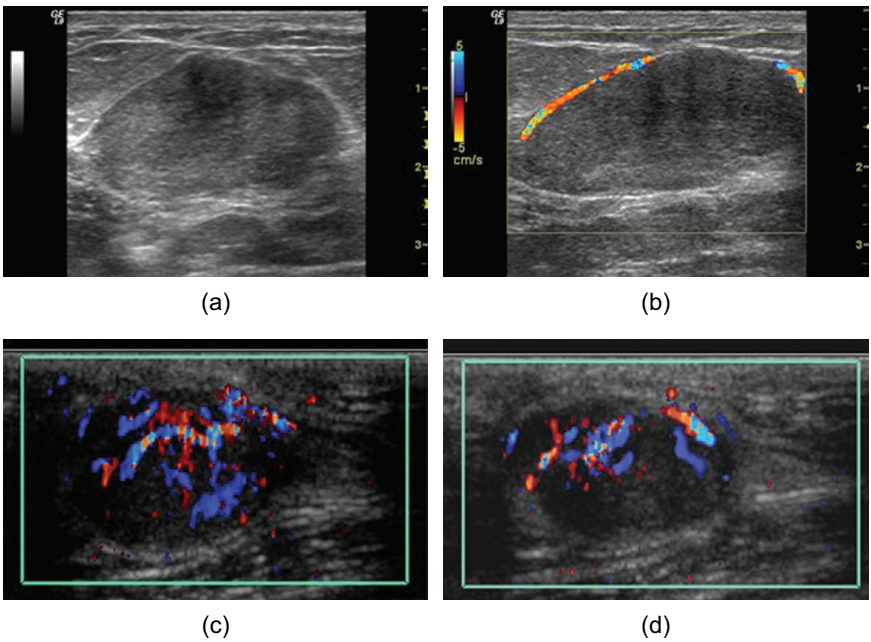

Figure 8.52 Fibroadenomas from two female patients of different ages. (a) and (b) A 48-year-old female. (a) A smoothly marginated ovoid hypoechoic lesion is seen on US. (b) Smooth vessels paralleling the periphery are demonstrated on CDU. (c) and (d) A 28-year-old female for which CDU of the typical ovoid fibroadenoma shows profuse vascularity. (c) CDU study three days before menstruation. (d) CDU study four days after menstruation shows minimally decreased vascularity, suggesting the physiological change of vascularity responding to the estrogen effect.

undergoes malignant change, color Doppler US may demonstrate focally increased color flow signals in the focus with malignancy.[73]

8.7.4 Tubular adenomas and lactating adenomas

Tubular and lactating adenomas represent an almost pure form of epithelial growth, with a very small stromal component.

8.7.4.1 Sonographic findings

Tubular adenomas tend to be elliptical and parallel in orientation. They may be gently lobulated or may appear fusiform in shape and pointed on the lateral margins. Enhanced through transmission is more common because of the predominance of epithelial elements. Tubular adenomas that have undergone infarction can demonstrate acoustic shadowing. *Lactating adenomas* are minimally hypoechoic and commonly microlobulated, and demonstrate enhanced through transmission. The pattern may occasionally be characterized as BIRADS 3 or even 4, especially in tumors seen during the third trimester of pregnancy or during lactation. The microlobulated contour may

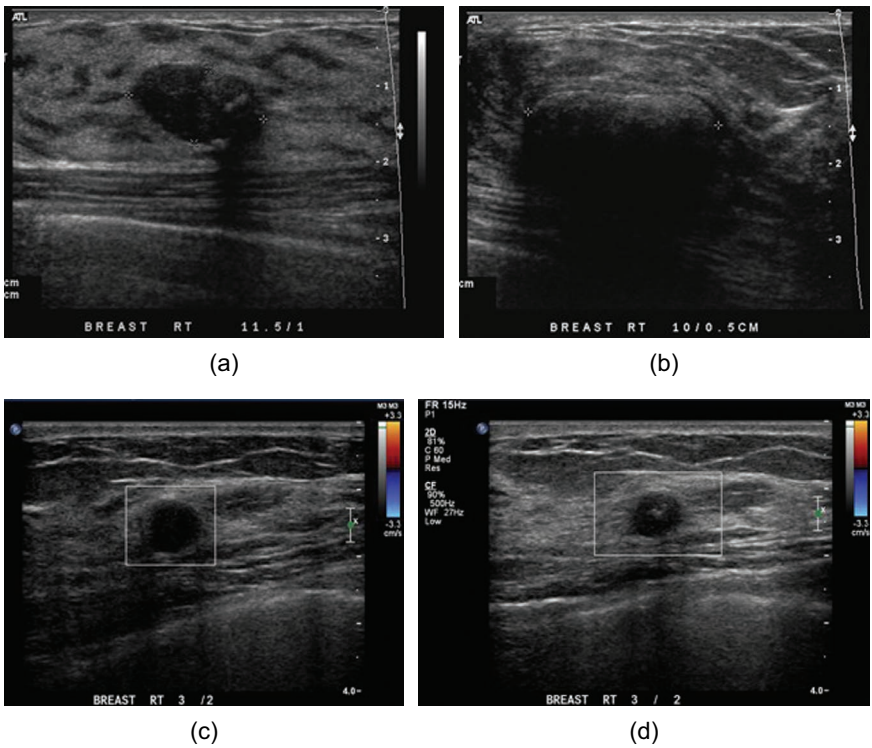

Figure 8.53 Fibroadenomas with calcifications. (a) Calcifications in part of the tumor, casting acoustic shadows. (b) Diffuse thick calcification in the tumor with strong acoustic shadows. (c) Initial US of the fibroadenoma shows a homogeneous hypoechoic nodule with smooth sharp margins. (d) Three years later the tumor becomes calcified in the center.

be related to the secretion-distended acini. Multiple small cystic spaces representing lactational lobules can be occasionally demonstrated (Fig. 8.55). Most lactating adenomas are hypoechoic and heterogeneous in texture. However, with inspissated milk or secretions within the dilated acini, they can become hyperechoic. Lactating adenomas can be hypervascular (more vascularity than the usual adenomas) with intratumoral vessels, but the smooth vessels paralleling the periphery of the mass are frequently preserved.

8.7.5 Papilloma

Intraductal papillomas are a relatively common benign tumor of the breast. They are more commonly incidentally found in surgical or biopsy specimens than they are detected at imaging studies. In patients with clinical signs of nipple discharge, either bloody or serous, the possibility of intraductal papilloma should be suspected first. The incidence of US-detected papillomas in nipple discharge can be about 11%.[74] Most intraductal papillomas are

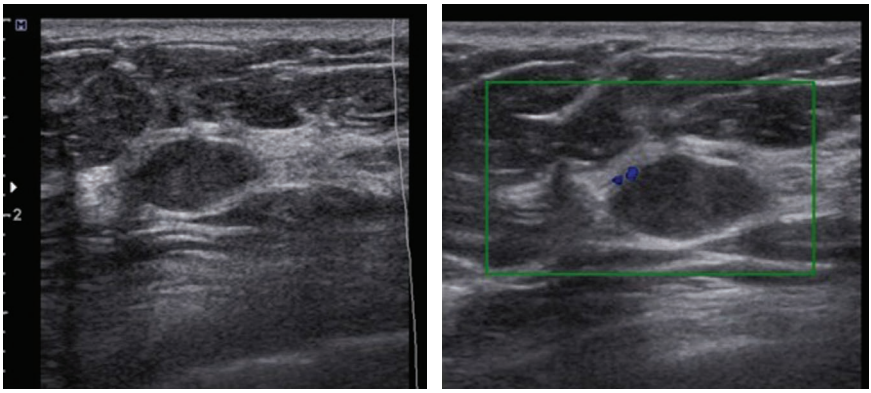

(a) (b)

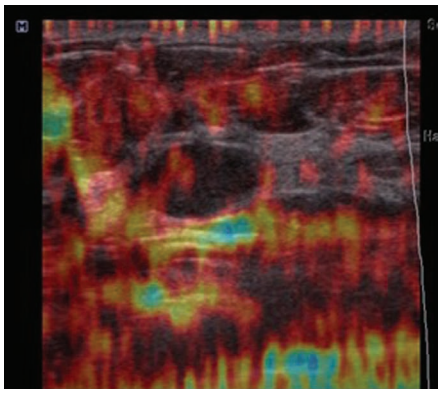

(c)

Figure 8.54 A 43-year-old female presenting with a palpable mass on the left breast: Fibroadenoma. (a) US and (b) CDU show a well-defined isoechoic ovoid mass, with only minimal marginal color flow signals shown in (b). (c) Elastography shows a mosaic pattern within the mass, suggesting a relatively soft lesion or fibroadenoma. [Image (c) courtesy of Samsung Medison.]

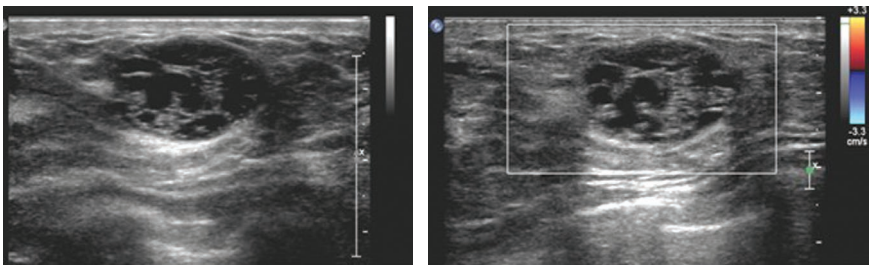

(a) (b)

Figure 8.55 A lactating adenoma with cystic changes. (a) US and (b) CDU demonstrating multiple small cystic spaces representing lactational lobules in the sharply marginated tumor. No demonstrable color flow is noted on CDU in this case.

located in the subareolar region when present with nipple discharge. However, in quite a number of cases, small papillomas can be detected peripherally. On microscopic study, a papilloma typically shows an arborescent growth pattern with branching fibrovascular cores of myoepithelial and epithelial cells.

8.7.5.1 Sonographic findings

A large papilloma growing along a duct is frequently elongated (especially in the subareolar region) and occasionally round in shape. When the lesion is located within a focally dilated duct, the term *intracystic papilloma* is often used and the lesion presents sonographically as a solid nodule growing on the wall of a thin-walled cyst. Tumors in the cystic structures can be round, ovoid, or flat, attaching on the wall. In larger lesions the surface may be rough, showing a frond-like pattern. A fluid-sediment level in the cystic lesion is a common feature that represents intracystic bleeding and arouses a strong suspicion of mural tumor in the cystic structure, especially intraductal papillary carcinoma (Fig. 8.45). Differentiation between intraductal papilloma and papillary carcinoma is difficult on the basis of sonographic pattern alone. A lesion of larger size (>2.0 cm) carries a higher risk of malignancy. An intraductal papilloma is typically associated with dilated ducts and intraductal solid component. When there are symptoms such as nipple disease, the findings of dilated a duct with a solid component deserves US-guided biopsy.[75–78]

A single dilated duct in the breast should be carefully traced along the duct so that any fixed intraductal nodules can be detected and biopsied. Inspissated material or calcified nodules inside the dilated duct (or ectatic duct) should be cautiously evaluated so as not to miss the intraductal tumors. Color Doppler US usually demonstrates color flow signals in the tumor, especially in larger tumors (e.g., >1 cm) (Figs. 8.56–8.59).

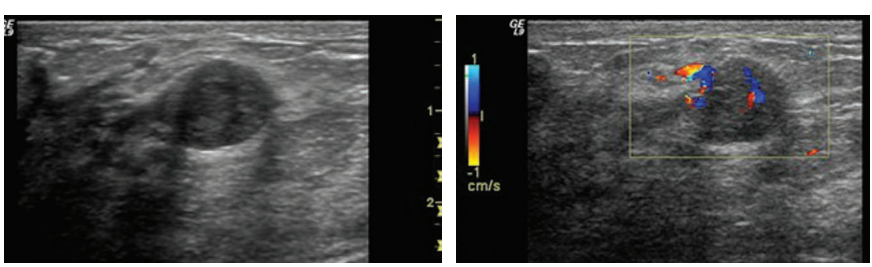

(a) (b)

Figure 8.56 A 51-year-old female presenting with bloody nipple discharge and a palpable nodule about 2 cm from the nipple: Papilloma. (a) US: A hypoechoic nodule is noted in the subareolar region, showing a relatively homogeneous echotexture, a clear-cut boundary, distal enhancement, and bilateral thin critical-angle artifacts. The adjacent duct is minimally dilated. (b) CDU: Color flow signals are demonstrated on the margins and in the periphery and center of the tumor.

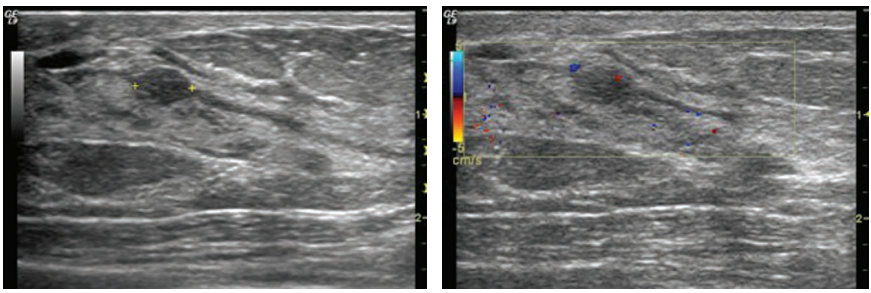

(a) (b)

Figure 8.57 Screening breast US of a 47-year-old female: Papilloma. (a) US: A small (0.6-cm) hypoechoic nodule is depicted in the subareolar region, in continuation with the minimally prominent duct, suggesting an intraductal tumor. (b) CDU: Minimal color flow signals are seen in the tumor and on the tumor margins.

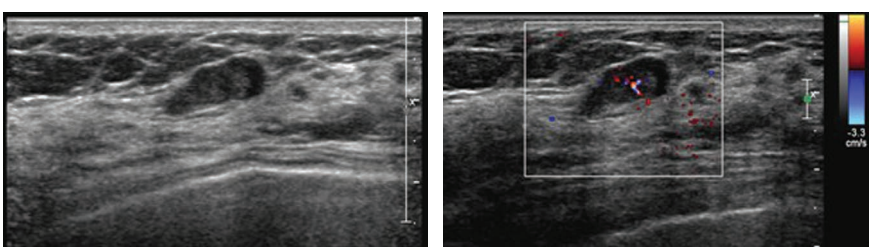

(a) (b)

Figure 8.58 A 75-year-old female presenting with a small palpable nodule in the left breast: Papilloma. (a) US: An ovoid isoechoic nodule (1.1 × 0.6-cm) located in the periphery of the breast, partially surrounded by a crescent-shaped fluid space, indicating an intraducal papilloma.(b) CDU: Increased color flow signals in the tumor are demonstrated, suggesting a hypervascular tumor.

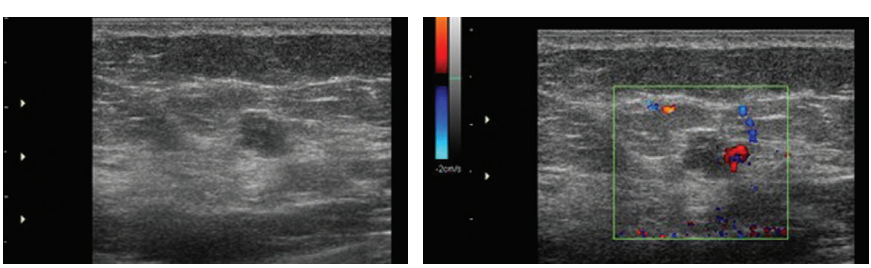

(a) (b)

Figure 8.59 An asymptomatic 43-year-old female: Papilloma. (a) US: A small (0.7 × 0.5-cm) round hypoechoic nodule is depicted in the periphery of the breast, showing lobulated margins, a partially poorly defined boundary, and minimal distal enhancement. (b) CDU: Color flow signals are shown on the margins.

8.7.6 Intramammary lymph nodes

Intramammary lymph nodes are almost always an incidental finding on mammograms and also frequently at US. The lymph nodes are generally located in the upper outer quadrants of the breast, embedded in the breast tissue. They usually are of little clinical significance.[79]

8.7.6.1 Sonographic findings

The lymph nodes typically appear as ovoid hypoechoic structures with an echogenic fibrofatty hilum. Like the axillary lymph nodes, an intramammary lymph node typically shows a smooth and sharp boundary. The intramammary lymph node is usually less than 1.5 cm, generally smaller than the axillary lymph node. They can be better appreciated if the parenchymal thickness is greater than 2 mm, and more confidently diagnosed in the scanning plane through the nodule at the echogenic hilum (Fig. 8.60). On color Doppler US, an intramammary lymph node frequently shows (hilar) vessels running through the hyperechoic zone or notch (representing the hilum), as is more characteristic of intramammary lymph nodes than of axillary lymph nodes. Metastasis or involvement of lymphoma in the intramammary lymph node may show thickened parenchyma and distorted or obliterated hila (Figs 8.6 and 8.40).

8.7.7 Hamartomas

Breast hamartomas, similar to fibroadenomas, occur in a wide age range of 15–88 years but are most common during the reproductive years, especially the early 40s. They are localized overgrowth of fibrous, epithelial, and fatty elements. Other terms that are used to describe a breast hamartoma are adenolipofibroma, lipofibroadenoma, and fibroadenolipoma, depending on the major component of the overgrowth. When there are

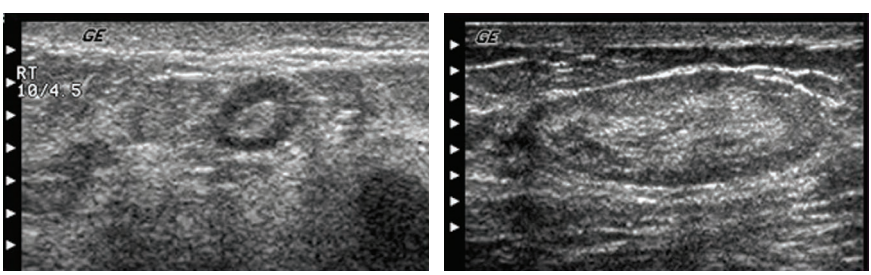

(a) (b)

Figure 8.60 (a) A small intramammary lymph node in the right upper outer quadrant (0.8 cm). (b) A large intramammary lymph node (3.0 cm) with a prominent echogenic hilum, mimicking a hematoma.

primarily glandular and fatty elements without an associated fibrous element, the term adenolipoma is preferred.

8.7.7.1 Sonographic findings

Because of their relatively low prevalence, hamartomas have been underdiagnosed and inaccurately interpreted as normal breast tissue on breast imaging. The composition can be minimally heterogeneous, especially in small lesions that show no significant mass effect on the background breast tissue. These lesions, like normal intramammary lymph nodes, are definitely benign (BIRADS 2) based on the typical mammographic findings alone and do not require biopsy or special followup. The sonographic findings of hamartomas are variable but tend to be ovoid in shape and very heterogeneous, composed of a variable mixture of nearly isoechoic fatty or lobular elements and hyperechoic fibrous elements. The proportions of each echotexture reflect the underlying histologic constituents. A flattened target-like or multilaminated pattern with an isoechoic center is rather typical, reflecting a mixture of fatty, glandular, and fibrous elements and a central lobular tissue (Figs. 8.61 and 8.62). A thin echogenic rim of fibrous tissue is a common finding. The adenomatous elements of hamartomas can undergo fibrocystic or benign proliferative changes; it is rare that a malignant change develops in these tumors. Color Doppler US reveals no or only minimal vessels in the heterogeneous zone.

8.7.8 Lipomas

Lipomas arise from adipose tissue and are contained within a well-defined capsule. Breast lipomas do not differ from lipomas found elsewhere in the body and are actually subcutaneous lesions rather than breast lesions. Many patients with breast lipomas have lipomas elsewhere in the body.

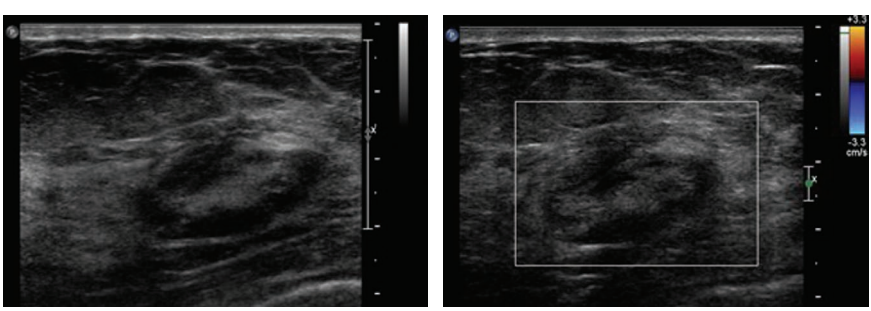

(a) (b)

Figure 8.61 A 47-year-old female presenting without significant clinical symptoms. (a) US: A heterogeneously hypoechoic mass with a central hyperechoic zone is noted. (b) CDU: No significant color flow signal is evident in the tumor.

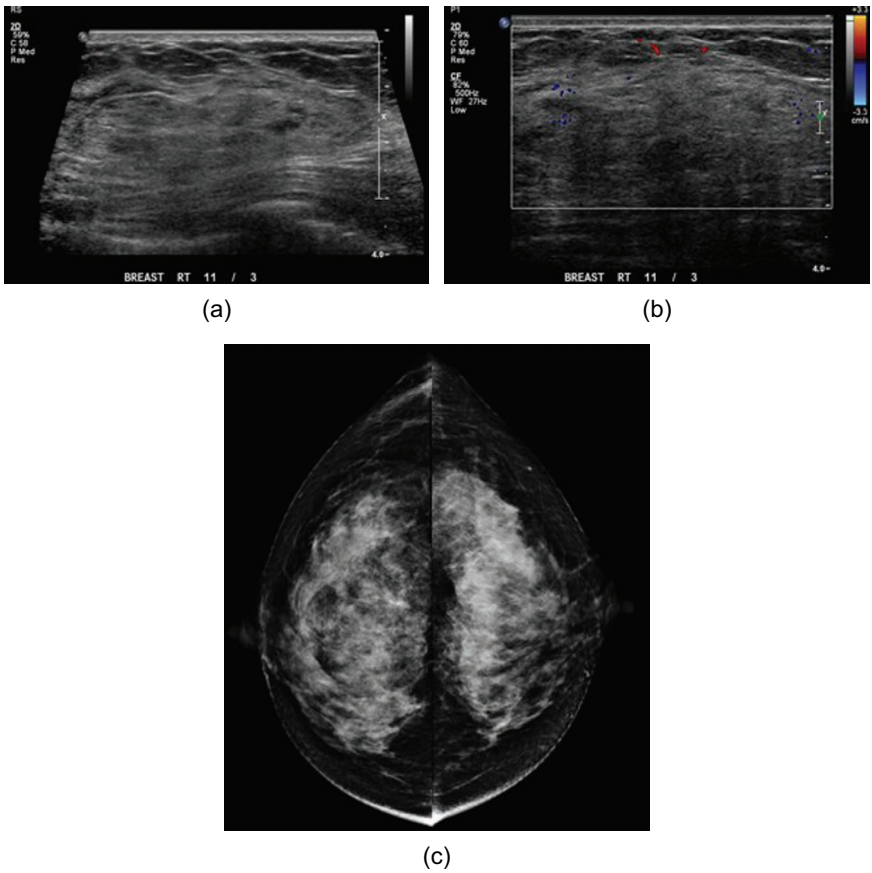

(a) (b)

(c)

Figure 8.62 A 44-year-old female presenting with a suspicious lump on the right breast: Hamartoma. (a) US: A large heterogeneously hyperechoic mass with laminated pattern and small central hypoechoic areas. (b) CDU: Only minimal marginal color flows are demonstrated. (c) Mammography shows a large heterogeneously hypodense zone in the center, compatible with a fat-containing tumor with variable proportions of different components.

Lipomas are probably variants of hamartomas that contain only fat. Most lipomas arise within the subcutaneous fat layer, but some may be also embedded within the retromammary fat or within involuted fatty lobules within the native mammary zone. Lipomas occasionally arise within or adjacent to the chest wall muscles.[80]

8.7.8.1 Sonographic findings

Sonography is usually performed on lipomas presenting as palpable abnormalities associated with negative or nonspecific mammographic findings (Fig. 8.63). Lipomas can typically appear as one of the following three features: (1) completely isoechoic with other nearby normal breast fat

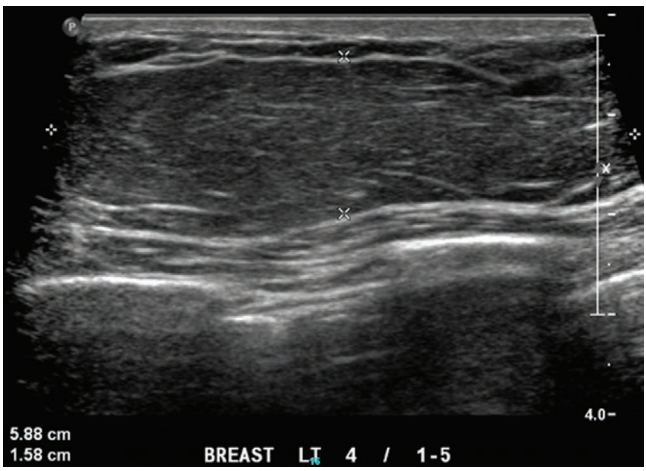

Figure 8.63 A lipoma in a 43-year-old female. US shows a minimally hyperechoic lesion (with respect to the subcutaneous fat) in the left breast, measuring 5.9 × 1.6 cm. The lesion is associated with some echogenic streaks, compatible with fibrous septa.

lobules, (2) mildly hyperechoic with respect to other adjacent normal breast fat lobules, or (3) isoechoic with adjacent fat lobules, but having numerous thin, internal echogenic septa that course parallel to the skin line. In addition to the sonographic appearance, demonstration of softness is key to sonographic diagnosis. Hyperechoic lipomas tend to be somewhat less compressible than the isoechoic variety, possibly because of edema or increased fibrous elements within the lipoma. Calcifications may only occasionally occur within lipomas. The fatty lesions that are difficult to distinguish from each other sonographically are all definitively benign (BIRADS 2), obviating additional evaluation and the need for followup. Like lipomas, normal fat lobules occasionally cause palpable breast abnormalities. Color Doppler US of a lipoma shows virtually no vessels in the lesion.

8.7.9 Pseudo-angiomatous stromal hyperplasia

Pseudo-angiomatous stromal hyperplasia (PASH) is a benign focal overgrowth of stromal tissue, presenting as nonpalpable, mammographically detected nodules or clinically nontender mobile nodules. This condition occurs primarily in premenopausal women or in postmenopausal women under combined estrogen–progesterone hormone replacement therapy.

8.7.9.1 Sonographic findings

About half of the nodules of PASH are ovoid and well circumscribed. The nodules are surrounded by a thin, echogenic pseudo-capsule, and

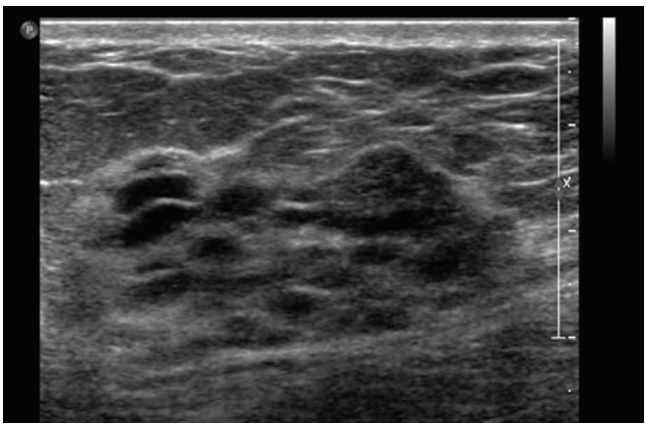

Figure 8.64 A 40-year-old female presenting with a palpable lump on the right breast: pseudo-angiomatous stromal hyperplasia (PASH). US shows a focal hypoechoic area with lobulated margins, mixed with cystic structures. The pattern is indistinguishable from a fibroadenoma or fibrosis adjacent to small cysts. The diagnosis of PASH was surgically proved.

the US pattern is indistinguishable from a fibroadenoma. Similar to complex fibroadenomas, some PASH nodules contain cysts (Fig. 8.64). Sound transmission is usually not changed, or is slightly enhanced or decreased. Nodules with acoustic shadowing, together with ill-defined, angular, and microlobulated margins, have been reported in a few cases.[81,82] According to Stavros et al., a little more than half of PASH nodules that undergo biopsy are not encapsulated and have angular or microlobulated margins or other suspicious features that prevent them from being characterized as BIRADS 3.

8.7.10 Hemangiomas

Hemangiomas, especially small, microscopically detectable perilobular hemangiomas, are usually clinically unrecognized and incidental findings at histology. They are generally only 2–4 mm in size. However, larger hemangiomas may present as nonpalpable mammographic nodules with a size of 4 mm–2 cm. Histologically, the tumors can be classified as cavernous or capillary, depending on the size of the vessels contained within them. Cavernous hemangiomas are the most common type and may contain phleboliths.

8.7.10.1 Sonographic findings

Microscopic perilobular hemangiomas are rarely (or almost impossible to be) demonstrated on US. The sonographic appearance of macroscopic hemangiomas depends on the size of the vascular spaces and the presence or absence

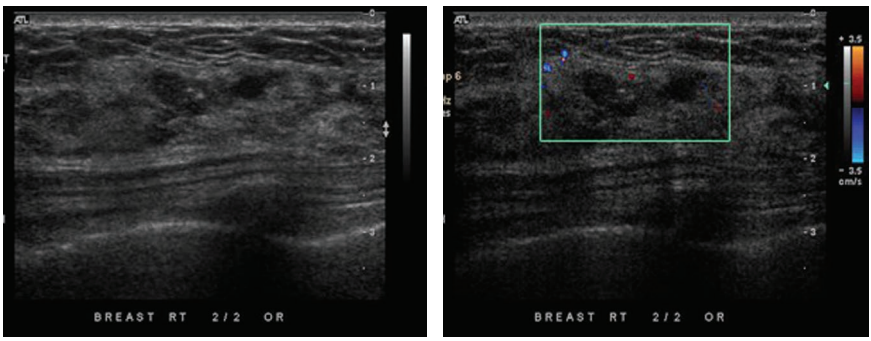

(a) (b)

Figure 8.65 An intramammary hemangioma. (a) US: A horizontally oriented hypoechoic lesion with lobulated margins and 1–2 mm calcification. (b) CDU: Only minimal marginal color flows are evident.

of fibrosis, scarring, thrombosis, or phleboliths. Cavernous hemangiomas are usually superficially located and ovoid in shape; they are commonly hypoechoic and only occasionally isoechoic or mildly hyperechoic.[83,84] Phleboliths, when present, appear as punctate areas of strong echogenicity that may cause acoustic shadowing if the diameter of the calcification is larger than 1.5–2.0 mm (Fig. 8.65).

8.7.11 Phyllodes tumors

Phyllodes tumors, also known as cystosarcoma phyllodes, are a rare breast tumor that constitutes 0.3–1.0% of mammary tumors and 2–3% of fibroepithelial neoplasms of the breast. Similar to fibroadenomas, phyllodes tumors consist of epithelial elements and a cellular, spindle cell stroma. The stroma of the phyllodes tumor has a greater cellular activity and cellular content than fibroadenoma has. The tumor is characterized by the formation of leaf-like processes protruding into cystic spaces. Determination of the benign, malignant, and border forms of the phyllodes tumor are based on microscopic findings. The malignant characteristics of the lesions are based on the stromal features. Phyllodes tumors resemble giant fibroadenomas concerning their clinical, radiologic, and histopathologic appearance, whereas phyllodes tumors differ by the type of surgical management and variable prognosis.[85,86]

8.7.11.1 Sonographic findings

About 75% of tumors were seen on US as well-defined masses, round or lobulated in shape with a heterogeneous, hypoechoic echopattern. Cystic areas (3–10 mm) were found in 58% of tumors. All lesions showed posterior acoustic enhancement, but 25% of them also presented areas of

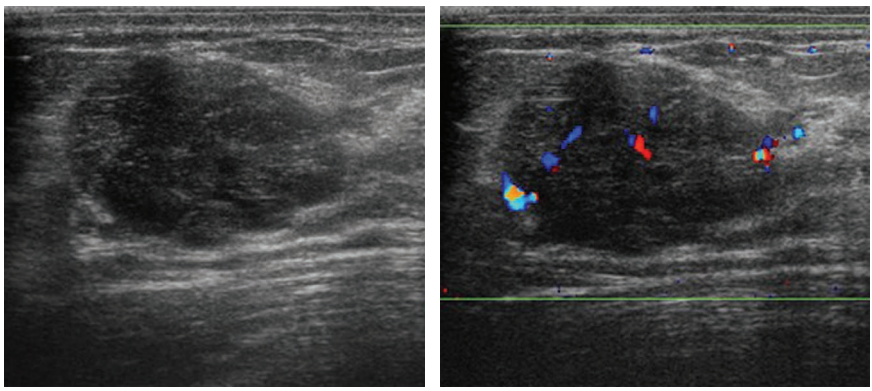

(a) (b)

Figure 8.66 A 45-year-old female presenting with a palpable lump on the right breast: Phyllodes tumor. (a) US: A large well-circumscribed hypoechoic mass (3 cm) with a slightly heterogeneous internal echotexture, lobulated margins, and posterior enhancement. No identifiable fluid-filled spaces in the mass. The sonographic appearances are almost identical to those of large fibroadenomas. (b) CDU: Some color flow signals are showing, indicating a relatively hypervascular tumor.

acoustic shadowing.[86] The major US features in phyllodes tumors are shape and posterior acoustic phenomena (Figs. 8.66 and 8.67). Although the findings can be clues for differentiation between phyllodes tumors and fibroadenomas, there is a substantial overlap between many imaging appearances of phyllodes tumors and large-sized fibroadenomas. Therefore, in suspicious masses, a biopsy should be performed for a definitive diagnosis.

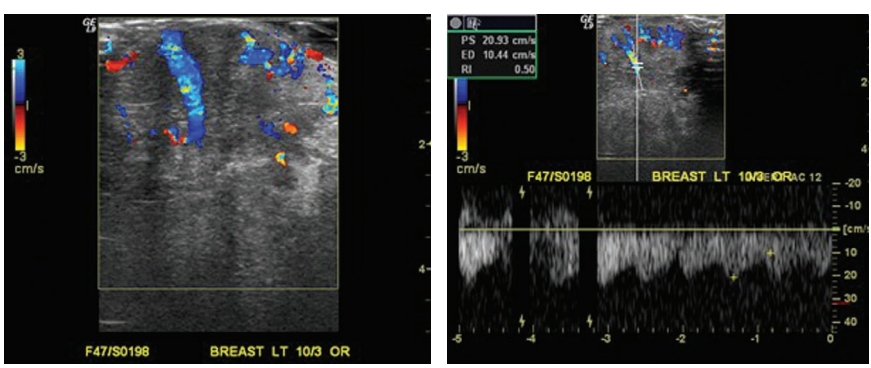

(a) (b)

Figure 8.67 A 58-year-old female presenting with a large hard mass on the left breast: Malignant phyllodes tumor. (a) CDU: Hypervascularity is demonstrated in the tumor. (b) Spectral Doppler US: The feeding artery shows relatively low resistivity index (RI = 0.50).

8.7.12 Focal fibrosis

The term *focal breast fibrosis* is commonly used in some cases to describe histologic findings in patients with a palpable or ultrasonographic or mammographic mass, although no features are specific for this diagnosis.[89] Lesions composed of only fibrous stroma may be encountered in breast US imaging. Some other terms such as *breast fibrosis*, *breast sclerosis*, and *fibrous mastopathy* are used interchangeably by pathologists and do not reflect distinct histologic entities. *Focal fibrosis* is used by some pathologists to describe lesions with less collagen deposition than lesions of fibrous mastopathy. Histologically, breast fibrosis is defined as proliferation of the stroma with obliteration of the lobular-ductal elements.[88] *Sclerosis* is descriptive of fibrosis with little cellularity. Septal fibrosis found in diabetic patients and patients with renal failure is known as diabetic mastopathy.[94] The pathogenesis of breast fibrosis is controversial. Proliferation of the fibrous tissue can be the result of hormonal stimulation,[88] or a condition of normal breast involution,[89] and some may be the end result of an inflammatory process.[91] Focal fibrosis alone is a common histologic finding in normal breast parenchyma and can be noticed as a finding in parenchyma surrounding a lesion. The mammographic appearance of breast fibrosis has been emphasized when it presents as architectural distortion or a spiculated mass. The pattern often overlaps in appearance with that of carcinoma.[91,92]

8.7.12.1 Sonographic findings

The sonographic appearance of breast fibrosis has received little attention and has been limited to descriptions of acoustic shadowing[91] and hyperechoic lesions.[92] However, breast fibrosis presenting as noncalcified lesions due to perilobular collagen deposition (or fibrosis) may result in masses with iso- or hypoechoic, well circumscribed, partially obscured, or (occasionally) ill-defined margins (Fig. 8.68), and abuts adipose tissue. Careful histologic review of adequate core tissue samples can confirm the diagnosis of focal fibrosis. While in lesions containing microcalcifications on mammography, very careful histologic imaging correlation should be performed. Histologic-radiologic concordance and adequate lesion sampling are easier to assess when the targeted lesion contains microcalcifications. If the histologic diagnosis of focal fibrosis on a core biopsy is discordant with marginal speculation or areas of architectural distortion on US studies, excisional biopsy is necessary so as not to misdiagnose a malignant lesion.[87,93] Histologic overlap in the appearance of fibroadenomas and focal fibrosis may be encountered, especially in a core needle biopsy specimen. Needle sampling of a large fibrotic fibroadenoma can easily miss the characteristic lobulated architecture and contain only fibrotic stroma, resulting in a diagnosis of fibrosis. In contrast, periductal fibrosis occurring in a large lobular unit

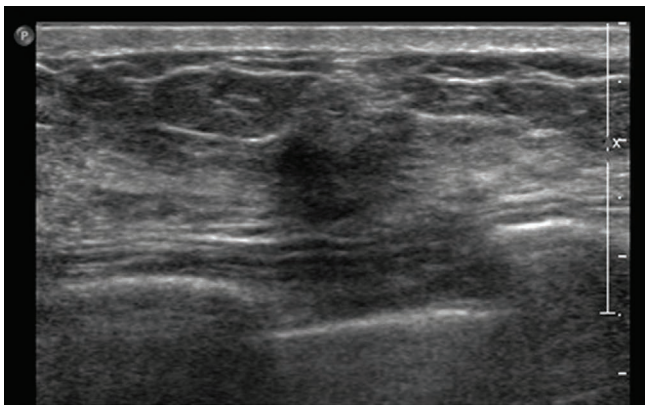

Figure 8.68 A focal fibrosis: US study shows a focal hypoechoic zone with irregular margins and an ill-defined boundary. No apparent change in the through transmission is observed.

displays a lobulated pattern that may closely resemble a small hyalinized fibroadenoma. Thus, the overlap in the sonographic (and mammographic) appearances of focal fibrosis is explained by the histologic overlap between these two entities. Whenever possible, a mammogram should be reviewed so as not to miss the microcalcification, which can only be deprecated on mammography.

8.7.13 Diabetic mastopathy

Diabetic mastopathy, also known as diabetic fibrosis, is typically a disease process of multifocal, multicentric, and bilateral involvement of the breast. It usually presents in premenopausal diabetic patients about 20 years after onset of diabetes. Most of these patients had onset of type I diabetes before the age of 20 years. Only a few cases had type II diabetes. The condition is thought to result from disorders in collagen metabolism related to diabetes and is considered an inflammatory condition in which lymphocystic infiltration is noted surrounding the small vessels. Histologically, the mass is composed of denser collagenous stroma containing more histologically normal fibroblasts compared to usual fibroglandular tissue.

8.7.13.1 Sonographic findings

Diabetic mastopathy of larger volume can present with hard lumps and almost invariably has a central hypoechoic focus that has many suspicious features on US. It is ill-defined, angular, and microlobulated and may be nonparallel in orientation, sonomorphologically indistinguishable from those of malignant lesions (BIRADS 4), and may mimic low-grade invasive ductal or lobular carcinoma, and tubular carcinoma. (Fig. 8.69).

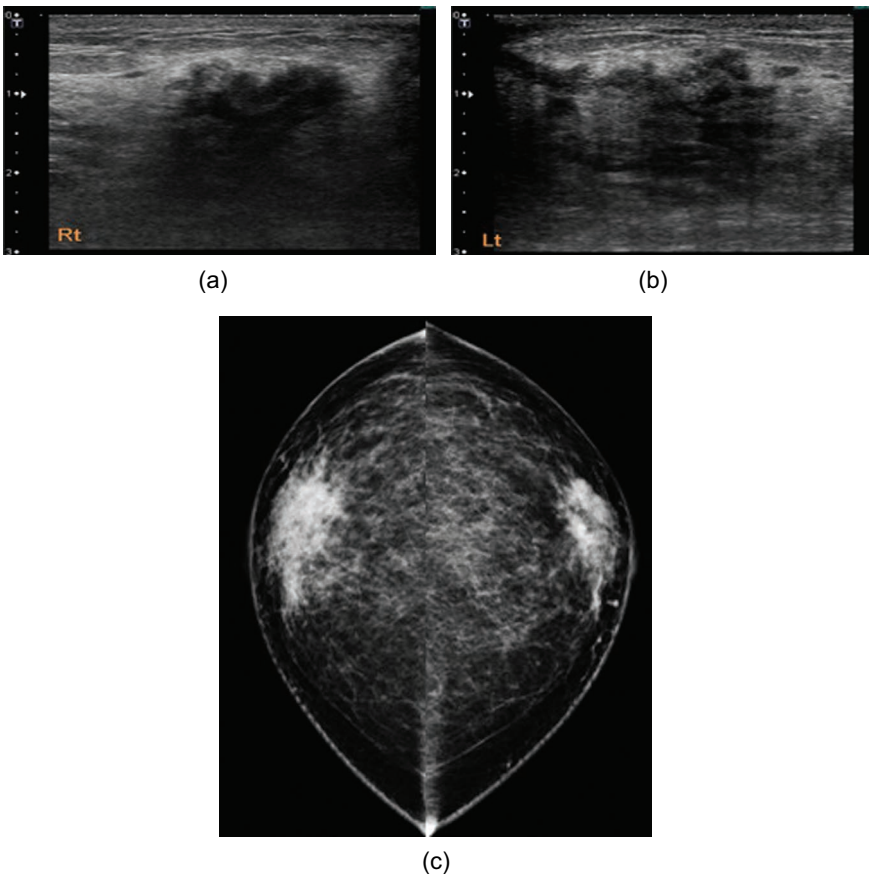

(a) (b)

(c)

Figure 8.69 A 48-year-old female with a known history of diabetes for 15 years. (a) and (b) US: (a) Right and (b) left breasts show large hypoechoic zones with distal sound attenuation or acoustic shadows. The pattern is compatible with dense fibrous tissue.(c) Mammography: The dense subareolar tissue is highly suggestive of thick fibrous tissue.

8.7.14 Infections and abscesses of the breast

Infections of the breast are relatively uncommon except during the postpartum period. These include mastitis (lactating mastitis), infected sebaceous cyst, abscess, and other relatively rare infections, e.g., tuberculosis, syphilis, and fungal or viral infections. Breast abscess is the second most-common infectious disease of the breast after mastitis.[95] Abscesses have been reported to develop in 5–11% of lactating women with infectious mastitis.[96] They occur most commonly during lactation as a result of a rupture of overfilled lactiferous ducts and frequently develop following lactational mastitis. However, this common disease entity can also occur in nonlactating women of all ages.[97] In a study of 136 patients (ranged in age

from 18 to 75 years, mean: 32 years) with specific aspiration and/or biopsy/histopathological results, 59 patients (43%) were lactating at the time of US examination; the other 77 (57%) were not lactating. Microscopically, an abscess consists of a cavity filled with necrotic debris and white blood cells (chiefly neutrophils). The adjacent parenchyma undergoes acute and chronic inflammatory change. The surrounding tissue changes may progress to granulation and fibrosis if the disease process is prolonged.[95]

The diagnosis of a breast abscess can usually be easily made based on the clinical presentation related to the infectious nature such as local heat, swelling, pain, and redness of the overlying skin, and occasionally systemic infectious signs. Although typical abscesses on US are rarely misinterpreted, a considerable overlap of the imaging appearances between abscess and malignancy has been reported.[98,99]

8.7.14.1 Sonographic findings

The typical US features of an abscess are the following: a hypoechoic lesion with an irregularly shaped contour, relatively ill-defined wall, and containing low-level or medium-level internal echoes representing necrotic debris. Because in the acute phase of inflammation (e.g. acute mastitis) the parenchymal edema causes a decrease of echogenicity and architectural disturbances and ductal dilatation may develop, an acute abscess can be appreciated only by demonstration of an ill-defined anechoic or hypoechoic fluid space.[100] The breast parenchymal surrounding the abscess may show poorly defined hypoechoic areas (26%) or hypoechoic interstitial streaks (7%). The poorly defined hypoechoic areas are correlated with edema and inflammatory cell infiltration. The interstitial streaks may be related to thickened and edematous fibrous septa or Cooper's ligaments. These surrounding parenchymal changes may provide sufficient information of the infectious nature (33%) and should be kept in mind during evaluation.[101]

High-resolution US has significantly improved the visualization of the superficial anatomic structures such as the skin, subcutaneous fat, lactiferous ducts, and even dilated lymphatic ducts. Skin thickening and increased echogenicity of the subcutaneous fat are frequently seen.[102] A hypoechoic rim (13%, 18/136) can be demonstrated on US, corresponding to the inflammatory tissue seen on histopathological study. A relatively thick hypoechoic rim surrounding the nearly anechoic fluid space is usually more vascular and more fibrous than the breast stroma peripheral to the hypoechoic rim. The hypoechoic rim represents a relatively thick layer of granulation tissue that contains fluid, fibroblasts, inflammatory cells, and vessels. An inflammatory tumor usually presents as a hypoechoic mass with relatively poorly defined margins and poor sound penetration[103] (Figs. 8.70–8.72).

The common US features of the tissue reactions in a relatively chronic abscess include: skin thickening, increased echogenicity of the subcutaneous

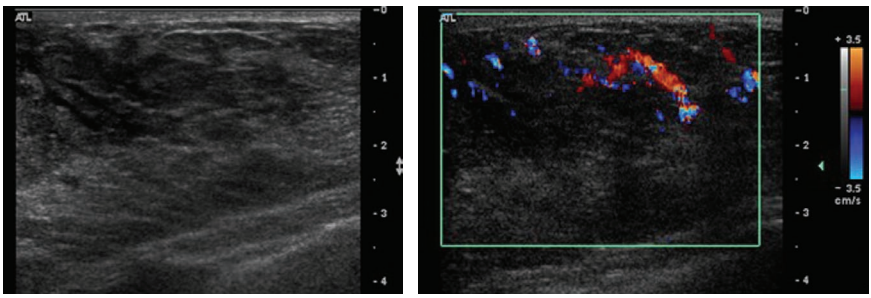

(a) (b)

Figure 8.70 A 33-year-old female presenting with left breast pain: Acute mastitis. (a) US: Decreased echogenicity of the left breast stroma with slightly increased echogenicity of the subcutaneous fat, compatible with edema of the breast stroma and subcutaneous fat. (b) CDU: Increased color flow signals in the region with edema, consistent with hyperemic reaction.

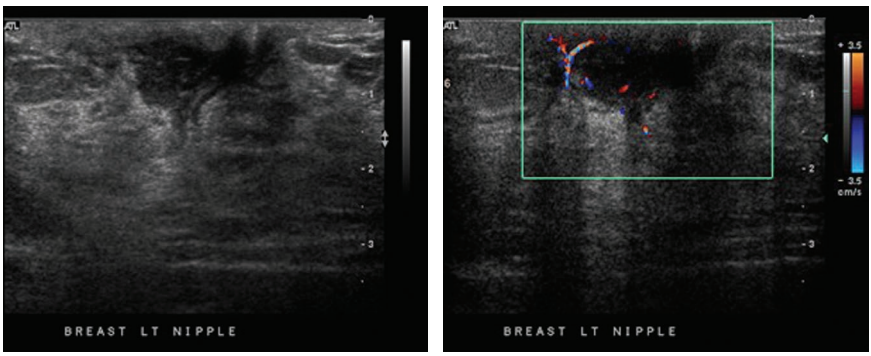

(a) (b)

Figure 8.71 A 47-year-old female presenting with a painful nodule in the areola region: Breast abscess. (a) US: A hypoechoic lesion is noted, associated with irregular margins and distal enhancement. (b) CDU: Marginal color flow signals are noted, indicating hyperemic reaction, compatible with abscess.

fat, and decreased echogenicity of the originally relatively hyperechoic breast stroma in acute phase or surrounding hyperechoic zone.[98,104–106] Hypoechoic or nearly anechoic streaks representing interstitial edema may be encountered in acute phase.

8.8 Clinical Usefulness of US-Guided Aspiration and Biopsy

Breast lesions detected by imaging modalities such as mammography and US may not be palpable on physical examination. These lesions may be

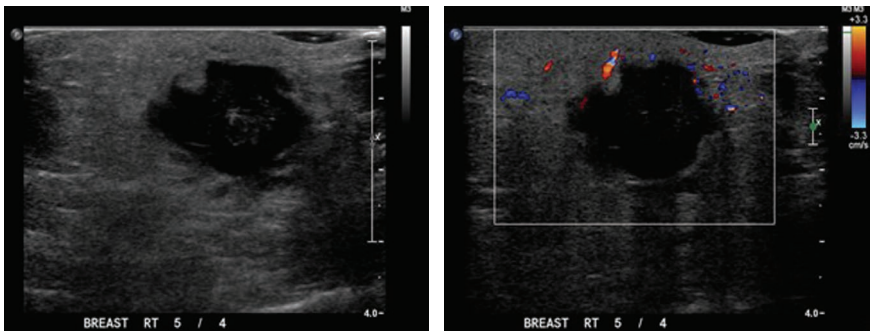

(a) (b)

Figure 8.72 A 63-year-old female presenting with a tender lump and reddish skin in the right breast: Breast abscess. (a) US: A nearly anechoic lesion is demonstrated, associated with skin thickening, increased echogenicity of the surrounding tissue and the subcutaneous fat, in favor of abscess formation. (b) CDU: Minimally increased color flow signals on the margins, suggestive of a relatively chronic inflammatory process.

either small in size, deeply located, or confined in the ducts or lobules. Even with the knowledge of the findings on mammography or US, most of them are still nonpalpable. Mammography is the most important screening modality of breast cancer. However, in many patients, this technique has limitations, especially in dense breast tissue, which is a common breast pattern in Asian women. US and MRI are important adjuncts to mammography. Lesions not identified on mammography may be detected by US or MRI. Because US is readily available and more cost effective than MRI and mammography, more and more lesions are being detected by US, and US-guided aspiration/biopsy for cytological and/or histological evaluation are frequently performed to achieve a definite diagnosis.

8.8.1 Ultrasound-guided breast aspiration

During US-guided breast aspiration, the patient is in a supine or oblique position so that she is comfortable and the region of interest is easily accessible to the radiologist for biopsy. Placing the patient in a semi-oblique position with a cushion behind her back is helpful for posterior lesions or for lesions located in the periphery of the breast. The transducer should be rotated over the lesion to create the best access for the operator to place the needle into the breast. The distances from the skin to the middle of the lesion and from the skin to the chest wall are determined. The needle tip will be visible within the lesion when the needle has been inserted at the proper depth and angle. Fine-needle aspiration cytology (FNAC) is usually performed with a free-hand puncture under US guidance (Fig. 8.73). Full retraction of a 10-ml syringe provides an adequate vacuum

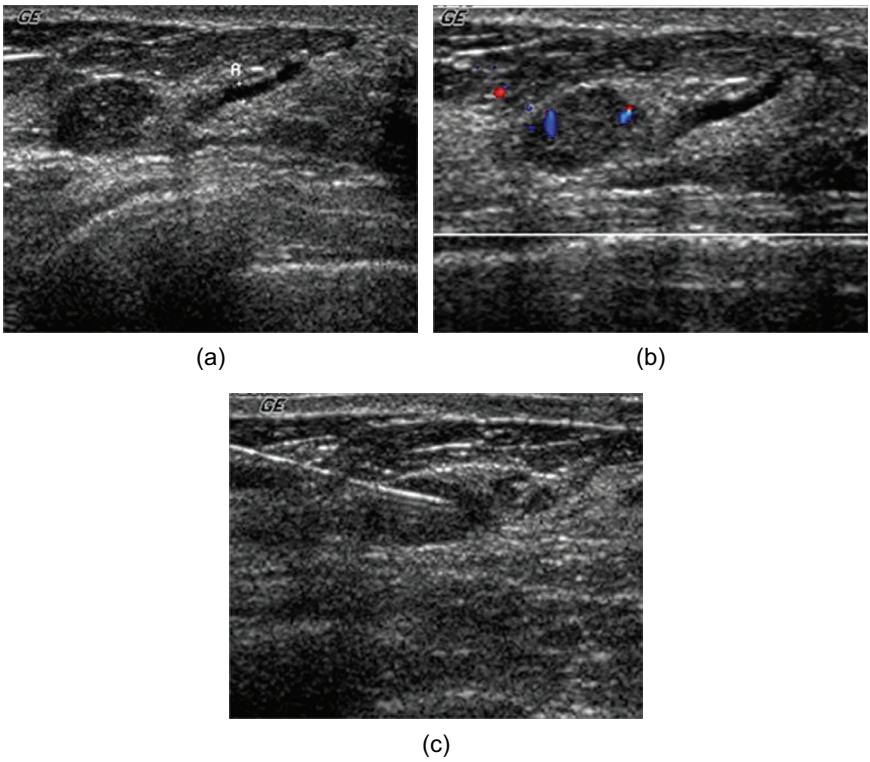

Figure 8.73 Needle aspiration cytology. (a) US: A hypoechoic nodule with an adjacent dilated duct. (b) CDU: The nodule shows positive color flow. (c) A needle (bright linear echoes) is inserted into the nodule. Aspiration cytology shows papillary neoplasm.

for aspiration of cell clusters using a fine needle (a 22- or 23-gauge needle is preferred). Local anesthesia is not recommended in the FNAC procedure. Although US is almost always (96–100%) accurate in the diagnosis of cysts, difficulties may still be encountered in lesions without all of the US characteristics for a typical cyst. Lack of distal acoustic enhancement, presence of internal echoes, wall irregularity, or solid projections into the cyst may indicate intracystic pathologies or tumors. Aspiration in these patients with equivocal US findings is usually very helpful or diagnostic.

Accuracies of FNAC in different series vary from 72 to 94%. The results depend on several factors, such as the histological nature of the lesion, the background of the breast stroma, the skill of the operator, and the experience of the cytologist.[107–113]

8.8.2 Ultrasound-guided breast biopsy

Although a needle guide attachment can be used for needle localization or cyst aspiration, a freehand approach is essential for core-needle biopsy.

For core biopsy, a horizontal or parallel-to-the-chest-wall approach is required to avoid pnuemothorax. A needle guide does not permit this type of approach. For a histological core biopsy, 1–2% lidocaine is administered for local anesthesia before puncture of a 18- to 14-gauge cutting-edge needle. A variety of biopsy guns with different advantages are currently used. Routine US is used to visualize a mass that has been identified on previous US or mammography to determine whether it is visible sonographically and is applicable for US-guided biopsy. US guidance for percutaneous biopsy is required for those lesions seen only on US, and it is best for those lesions that are more clearly seen on US than on mammography (Fig. 8.74).

US guidance is also advantageous for the following cases: biopsy of pregnant patients, patients who are more comfortable in a supine position, very obese patients whose weight exceeds the prone stereotactic table weight limit, and patients with implants. If there are more than two adjacent lesions on mammography, US guidance is best for definitive biopsies of the suggestive

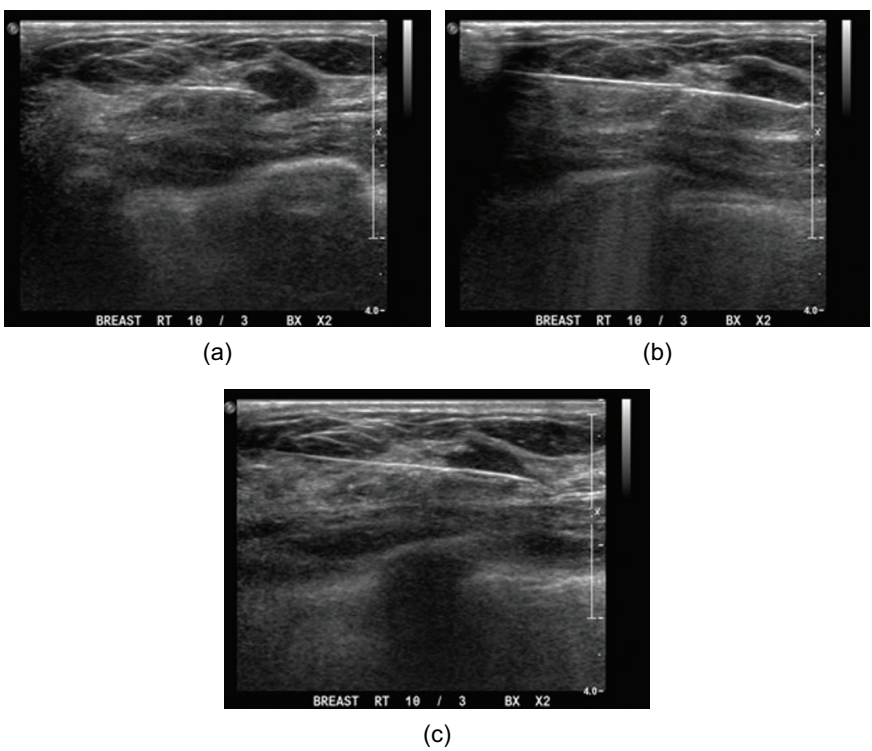

(a) (b)

(c)

Figure 8.74 Core needle biopsy: Fibroadenoma. (a) Insertion of the needle with the tip lined up with the edge of the hypoechoic tumor. (b) Advancing the inner needle through the tumor with the trough facing upward. (c) Firing to advance the outer sheath of the biopsy needle.

or more aggressive lesion. Because it is necessary to mark the exact center of a lesion on both stereotactic images for stereotactically guided breast biopsy, there is greater likelihood of observer error in stereotactically targeting larger lesions. US guidance certainly requires greater operator skill in the performance of the procedure in comparison with stereotaxis. Moreover, because the breast is not fixed by a compression device and the needle is not fixed by needle guides, there is a potential risk of pneumothorax. Histological core biopsy has several advantages: it can provide adequate material for a definite diagnosis, and the result is more representative for a focal lesion. However, it has certain disadvantages: compared to US-guided breast aspiration, it is more traumatic, and a specimen takes longer to process (therefore causing more anxiety for the patient). It is also more painful and can have delayed complications. The accuracy of biopsy may reach 90%.[75,114–116]

8.8.3 Vacuum-assisted biopsy

Vacuum-assisted biopsy (VAB) is fast and simple to perform, with a very low complication rate. For accurate lesion sampling, conventional core biopsy requires the lesion to be at the 'line of fire'; thus, pin-point accuracy is mandatory. VAB, on the other hand, is a directional device, so it does not require the lesion to be lying along the path of the needle. Instead, it is better positioned next to the lesion so that the sampling chamber can be placed toward the direction of the lesion.[117,118] The use of the VAB device may have a role in patients with US evidence of microcalcification where 14-gauge core biopsy does not provide a definitive diagnosis. It can provide a high-quality specimen with accurate diagnosis.[119,120] Its versatility enables its use in challenging cases such as in deep lesions near the chest wall. VAB can reduce the overall costs of breast disease diagnosis when compared to open-surgical biopsy and spares the patients from surgical removal of benign tumors such as fibroadenomas (Figs. 8.73–8.75). It has been reported that lesions <1.5–2 cm can be completely excised.[121,122]

8.9 Conclusion

During a fifty-year period of continuous improvement, medical US has proved very useful in the evaluation of breast disease. State-of-the-art high-resolution US can detect tiny breast lesions as small as 1–2 mm in size, and sometimes microcalcifications even less than 0.5 mm, or small carcinomas 3–6 mm in diameter. Although highly sensitive in detecting space-occupying lesions in the breast stroma, high-resolution US has limited specificity in the differentiation of malignant and benign lesions smaller than 0.5–1.0 cm. US-guided fine-needle aspiration cytology and core needle biopsy may provide highly accurate diagnostic yield. The use

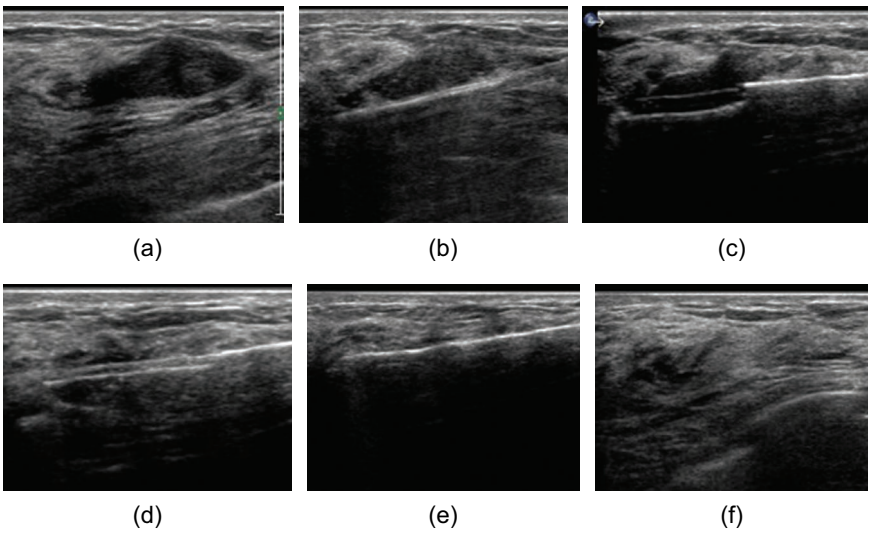

Figure 8.75 Removal of a benign tumor (fibroadenoma) by using a vaccum-assisted biopsy (9-gauge) needle. (a) US shows an ovoid hypoechoic tumor. (b) Insertion of the needle underneath the tumor with the sampling chamber facing upward. (c) After three 'bites' the opened sampling chamber is demonstrated with the posterior aspect of the tumor sucked into the chamber. (d) and (e) Throughout the procedure, the tumor samples are withdrawn piece by piece and the tumor size is decreased, and finally, (f) the tumor is totally removed.

of vacuum-assisted biopsy may have a role in patients with US evidence of microcalcification to obtain enough representative samples and also provide a possibility of minimally invasive removal of benign tumors. US-guided preoperative wire localization can provide an accurate guidance for removal of nonpalpable breast nodules in patients who refuse to have a fine-needle aspiration cytology or biopsy.

Spectral Doppler US, color and power Doppler US, or the newer strain or elasticity imaging techniques by which the vascularity and stiffness of the focal breast lesion can be evaluated, may offer certain advantages in the diagnosis of breast cancer; however, these techniques have limited usefulness in smaller lesions (e.g., <0.6 cm). Ultrasound contrast agents have proved to be useful in the differentiation of nonpalpable breast nodules. A malignant nodule tends to be more vascular than a benign nodule. Sophisticated computer techniques are being applied to the interpretation of US images with ever-increasing success. Artificial neural networks (ANNs) may be able to speed up interpretation of US evaluation of breast tumors. Computer-aided diagnosis (CAD) that has been developed using echotexture or contour analysis on breast lesions is similar to CAD for mammography. The results from the most recent articles show that the ANN

demonstrated high accuracy (96.47%), sensitivity (97.22%), specificity (96.35%), and negative predictive value (99.3%). The positive predictive value was 81.40%. This result is very encouraging.[123–127]

High-resolution US is an indispensible imaging modality in the diagnosis of breast disease, but the goal of replacing mammography in screening breast cancer is not yet realized.

References

1. E. Tohno, D. O. Cosgrove, and J. P. Sloane, *Ultrasound Diagnosis of Breast Diseases*, Churchill Livingstone, London (1994).
2. V. P. Jackson, "The role of US in breast imaging," *Radiol*. **177**, 305–311 (1990).
3. D. O. Cosgrove, J. C. Bamber, J. B. Davey, J. A. McKinna, and H. D. Sinnett, "Color Doppler signals from breast tumours," *Radiol*. **176**, 176–180 (1990).
4. M. M. McNicholoas, P. M. Mercer, J. C. Miller, E. W. M. Mcdermott, N. J. O'Higgins, and D. P. MacErlean, "Color Doppler sonography in the evaluation of palpable breast masses," *Am. J. Roentgenol.* **161**, 765–769 (1993).
5. R. P. Kedar, D. O. Cosgrove, J. C. Bamber, J. B. Davey, J. A. McKinna, and I. E. Smith, "Color Doppler in the differential diagnosis of breast diseases," *Radiol.* **189**, 99–104 (1993).
6. D. Leucht and H. Madjar, *Lehratlas der Mammasonographie*, 2nd edition, Thieme, Stuttgart (1995).
7. C. S. Chapman and J. C. Lazenby, "Ultrasound imaging system employing phase inversion subtraction to enhance the image," U.S. patent No. 5, 632, 277 (1997).
8. R. Haerten, C. Lowery, G. Becker, M. Gebel, S. Rosenthal, and E. Sauerbrei, "Ensemble TM tissue harmonic imaging: The technology and clinical utility," *Electromedica* **67**, 50–56 (1999).
9. E. Ueno, E. Tohno, S. Soeda, Y. Asaoka, J. C. Bamber, M. Blaszczyk, J. Davey, and J. A. Mckinna, "Dynamic tests in real-time breast echography," *Ultrasound Med. Biol.* **14**, 53–57 (1988).
10. D. O. Cosgrove, R. P. Kedar, J. C. Bamber, B. Al-Murrani, J. B. Davey, C. Fisher, J. A. McKinna, W. E. Svensson, E. Tohno, and E. Vagios, "Breast diseases: Color Doppler sonography in differential diagnosis," *Radiol.* **189**, 99–105 (1993).
11. S. Raza and J. K. Baum, "Solid breast lesions: Evaluation with power Doppler US," *Radiol.* **203**, 164–170 (1997).

12. P. G. Sorelli, D. O. Cosgrove, W. E. Svensson, N. Zaman, K. Satchithananda, N. K. Barrett, and A. K. Lim, "Can contrast-enhanced sonography distinguish benign from malignant breast masses?" *J. Clin. Ultrasound* **38**(4), 177–81 (2010).
13. N. Caproni, F. Marchisio, A. Pecchi, B. Canossi, R. Battista, P. D'Alimonte, and P. Torricelli, "Contrast-enhanced ultrasound in the characterisation of breast masses: Utility of quantitative analysis in comparison with MRI," *Eur. Radiol.* **20**(6), 1384–95 (2010).
14. K. Hoyt, J. M. Warram, H. Umphrey, L. Belt, M. E. Lockhart, M. L. Robbin, and K. R. Zinn, "Determination of breast cancer response to bevacizumab therapy using contrast-enhanced ultrasound and artificial neural networks," *J. Ultrasound Med.* **29**(4), 577–85 (2010).
15. A. R. Sever, P. Mills, S. E. Jones, W. Mali, and P. A. Jones, "Sentinel node identification using microbubbles and contrast-enhanced ultrasonography," *Clin. Radiol.* **67**(7), 687–94 (2012).
16. A. Sever, S. Jones, K. Cox, J. Weeks, P. Mills, and P. Jones, "Preoperative localization of sentinel lymph nodes using intradermal microbubbles and contrast-enhanced ultrasonography in patients with breast cancer," *Br. J. Surg.* **96**(11), 1295–99 (2009).
17. A. Itoh, E. Ueno, E. Tohno, H. Kamma, H. Takahashi, T. Shiina, M. Yamakawa, and T. Matsumura, "Breast disease: Clinical application of US elastography for diagnosis," *Radiol.* **239**(2), 341–50 (2006).
18. T. J. Hall, Y. Zhu, and C. S. Spalding, "In vivo real-time freehand palpation imaging," *Ultrasound Med. Biol.* **29**, 427–435 (2003).
19. A. Evans, P. Whelehan, K. Thomson, D. McLean, K. Brauer, C. Purdie, L. Jordan, L. Baker, and A. Thompson, "Quantitative shear wave ultrasound elastography: Initial experience in solid breast masses," *Breast Cancer Res.* **12**(6), R104–114 (2010).
20. L. W. Bassett, "Imaging of breast masses," *Radiol. Clin. North Am.* **38**(4), 669–91 (2000).
21. W. A. Berg, A. G. Sechtin, H. Marques, and Z. Zhang, "Cystic breast masses and the ACRIN 6666 experience," *Radiol. Clin. North Am.* **48**(5), 931–987 (2010).
22. W. A. Berg, C. I. Campassi, and O. B. Ioffe, "Cystic lesions of the breast: Sonographic-pathologic correlation," *Radiol.* **227**, 183–91 (2003).
23. A. T. Stavors, D. Thickman, C. L. Rapp, M. A. Dennis, S. H. Parker, and G. A. Sisney, "Solid breast nodules: Use of sonography to

distinguish between benign and malignant lesions," *Radiol.* **196**, 123–134 (1995).

24. S. R. Benson, J. Blue, K. Judd, and J. E. Harman, "Ultrasound is now better than mammography for the detection of invasive breast cancer," *Am. J. Surg.* **213**, 889–894 (2004).
25. D. D. Adier, D. L. Hyde, and D. M. Ikeda, "Quantitative sonographic parameters as a means of distinguishing breast cancers from benign solid breast masses," *J. Ultrasound Med.* **10**, 505–508 (1991).
26. I. Blickstein, R. Goldchmit, S. D. Strano, R. D. Goldman, and N. Barzili, "Echogenicity of fibroadenoma and carcinoma of the breast. Quantitative comparison using gain-assisted densitometric evaluation of sonograms," *J. Ultrasound Med.* **l4**, 661–664 (1995).
27. S. A. Feig, "Breast masses. Mammographic and sonographic evaluation," *Radiol. Clin. North Am*. **30**, 67–92 (1992).
28. P. Skaane and K. Engedal, "Analysis of sonographic features in the differentiation of fibroadenoma and invasive ductal carcinoma," *Am. J. Roentgenol.* **170**, 109–114 (1998).
29. A. T. Stavros, D. Thickman, C. L. Rapp, M. A. Dennis, S. H. Parker, and G. A. Sisney, "Solid breast nodules: Use of sonography to distinguish between benign and malignant lesions," *Radiol.* **196**, 123–134 (1995).
30. E. B. Mendelson, J. K. Baum, and W. A. Berg, "Breast imaging reporting and data system, BI-RADS: ultrasound," 1st edition, American College of Radiology, Reston, VA (2003).
31. M. L. Framarino dei Malatesta, M. G. Piccioni, A. Felici, A. Paolucci, A. Triglia, and G. Galati, "Intracystic carcinoma of the breast. Our experience," *Eur. J. Gynaecol. Oncol.* **13**(1 Suppl), 40–4 (1992).
32. A. S. Hong, E. L. Rosen, M. S. Soo, and J. A. Baker, "BI-RADS for sonography: Positive and negative predictive values of sonographic features," *Am. J. Roentgenol.* **184**(4), 1260–5 (2005).
33. C. Balu-Maestro, J. N. Bruneton, P. Melia, P. Chauvel , and A. Aviotti-Casperoni, "High frequency ultrasound detection of breast calcification," *Eur. J. Ultrasound*. **3**, 247–254 (1994).
34. S. Y. Chiou, Y. H. Chou, H. J. Chiou, H. K. Wang, C. M. Tiu, L. M. Tseng, and C. Y. Chang, "Sonographic features of nonpalpable breast cancer: A study based on ultrasound-guided wire-localized surgical biopsies," *Ultrasound Med. Biol.* **32**, 1299–1306 (2006).
35. R. W. McDivitt, F. W. Stewart, and J. W. Berg, *Tumors of the Breast*, Armed Forces Institute of Pathology, Washington, D.C. (1968).

36. E. Silverberg, C. C. Boring, and T. S. Squires, "Cancer statistics, 1990" *CA Cancer J. Clin.* **40**(1), 9–26 (1990).
37. Medical Research Council Annual Report 1988/1989, Medical Research Council Headquarters Office, London, pp. 31–32 (1989).
38. D. Trichopoulos, B. MacMahon, and P. Cole, "Menopause and breast cancer risk," *J. Natl. Cancer Inst.* **48**, 605–613 (1972).
39. UK National Case Control Study Group, "Oral contraceptive use and breast cancer risk in younger women," *Lancet* **1**, 973–982 (1989).
40. K. Hunt, M. Vessey, K. McPherson, and M. Coleman, "Long-term surveillance of mortality of cancer incidence in women receiving hormone replacement therapy," *Br. J. Obstet. Gynaecol.* **94**, 620–635 (1987).
41. C. Cole-Beuglet, R. Z. Soriano, A. B. Kurtz, and B. B. Goldberg, "Ultrasound analysis of 104 primary breast carcinomas classified according to histologic type," *Radiol.* **147**, 191–196 (1983).
42. R. G. Barr, "Real-time ultrasound elasticity of the breast: Initial clinical results," *Ultrasound Q.* **26**(2), 61–6 (2010).
43. D. T. Ginat, S. V. Destounis, R. G. Barr, B. Castaneda, J. G. Strang, and D. J. Rubens, "US elastography of breast and prostate lesions," *Radiographics* **29**(7), 2007–2016 (2009).
44. A. Memis, N. Ozdemir, M. Parildar, M. M. Ustun, and Y. Erhan, "Mucinous (colloid) breast cancer: Mammographic and US features with histologic correlation," *Eur. J. Radiol.* **35**(1), 39–43 (2000).
45. R. W. McDivitt, F. W. Stewart, and J. W. Berg, *Tumors of the Breast*, Armed Forces Institute of Pathology, Washington, D.C. (1968).
46. H. J. G. Bloom, W. A. V. Richardson, and J. R. Field, "Host resistance and survival in carcinoma of the breast: A study of 104 cases of medullary carcinoma in a series of 1411 cases of breast cancer followed for 20 years," *Br. Med. J.* **3**, 181–188 (1970).
47. F. Kasumi, A. Fukami, K. Kuno, and T. Kajitani, "Characteristic echographic features of circumscribed cancer," *Ultrasound Med. Biol.* **8**, 369–375 (1982).
48. C. Cole-Beuglet, "Sonographic manifestations of malignant breast disease," *Semin. Ultrasound.* **3**, 51–57 (1982).
49. J. E. Meyer, E. Amin, K. K. Lindfors, J. C. Lipman, P. C. Stomper, and D. Genest, "Medullary carcinoma of the breast: Mammographic and US appearance," *Radiol.* **170**, 79–82 (1989).
50. J. G. Azzopardi, *In Situ and Invasive Lobular Carcinoma of the Breast: New Frontiers in Mammary Pathology*, K. H. Hollmann and J. M. Verley, Eds., Plenum Press, New York, pp. 127–145 (1983).

51. J. M. Dixon, T. J. Anderson, D. L. Page, D. Lee, S. W. Duffy, and H. J. Stewart, "Infiltrating lobular carcinoma of the breast: An evaluation of the incidence and consequences of bilateral disease," *Br. J. Surg.* **70**, 513–516 (1983).

52. M. L. Lesser, P. P. Rosen, and D. W. Kinne, "Multicentricity and bilaterality in invasive breast carcinoma," *Surgery* **91**, 234–240 (1982).

53. R. W. McDivitt, F. W. Stewart, and J. W. Berg, *Tumors of the Breast*, Armed Forces Institute of Pathology, Washington, D.C. (1968).

54. M. Bazzocchi, I. Facecchia, C. Zuiani, F. Puglisi, C. Di Loreto, and S. Smania, "Diagnostic imaging of lobular carcinoma of the breast: Mammographic, ultrasonographic, and MR findings," *Radiol. Med. (Torino)* **100**(6), 436–443 (2000).

55. H. Gufler, C. H. Buitrago-Téllez, H. Madjar, K. H. Allmann, M. Uhl, and A. Rohr-Reyes, "Ultrasound demonstration of mammographically detected microcalcifications," *Acta Radiol.* **41**(3), 217–221 (2000).

56. B. E. Hashimoto, D. J. Kramer, and V. J. Picozzi, "High detection rate of breast ductal carcinoma in situ calcifications on mammographically directed high-resolution sonography," *J. Ultrasound Med.* **20**(5), 501–508 (2001).

57. W. J. Lennington, R. A. Jensen, L. W. Dalton, and D. L. Page, "Ductal carcinoma in situ of the breast: Heterogeneity of individual lesions," *Cancer* **73**(1), 118–124 (1994).

58. J. M. Schoonjans and R. F. Brem, "Sonographic appearance of ductal carcinoma in situ diagnosed with ultrasonographically guided large core needle biopsy: Correlation with mammographic and pathologic findings," *J. Ultrasound Med.* **19**(7), 449–57 (2000).

59. R. Sakr, R. Rouzier, C. Salem, M. Antoine, J. Chopier, E. Daraï, and S. Uzan, "Risk of breast cancer associated with papilloma," *Eur. J. Surg. Oncol.* **34**(12), 1304–8 (2008).

60. T. B. Sheridan, W. A. Berg, and J. K. Warner, "Papillary lesions diagnosed by core needle biopsy of the breast: Diagnostic pitfalls and management update," Paper presented at USCAP 2008; Denver, CO, March 4 (2008).

61. D. Georgian-Smith and T. Lawton, "Calcifications of lobular carcinoma in situ of the breast: Radiologic-pathologic correlation," *Am. J. Roentgenol.* **176**, 1255–1259 (2001).

62. D. D. Dershaw, M. P. Moore, L. Liberman, and B. M. Deutch, "Inflammatory breast carcinoma: Mammographic findings," *Radiol.* **190**(3), 831–834 (1994).

63. D. D. Paulus and H. I. Libshitz, "Metastasis to the breast," *Radiol. Clin. North Am.* **20**, 561–568 (1982).
64. B. D. Toombs and L. Kalisher, "Metastatic disease to the breast: Clinical, pathologic, radiologic features," *Am. J. Roentgenol.* **129**, 673–676 (1977).
65. W. A. Berg, "Sonographically depicted breast clustered microcysts: Is follow-up appropriate?" *Am. J. Roentgenol.* **185**(4), 952–959 (2005).
66. W. Berg, C. Campassi, and O. Ioffe, "Cystic lesions of the breast: Sonographic-pathologic correlation," *Radiol.* **227**, 183–191 (2003).
67. C. P. Daly, J. E. Bailey, K. A. Klein, and M. A. Helvie, "Complicated breast cysts on sonography: Is aspiration necessary to exclude malignancy?" *Acad. Radiol.* **15**(5), 610–617 (2008).
68. Y. W. Chang, K. H. Kwon, D. E. Goo, D. L. Choi, H. K. Lee, and S. B. Yang," Sonographic differentiation of benign and malignant cystic lesions of the breast," *J. Ultrasound Med.* **26**(1), 47–53 (2007).
69. K. S. Baker, B. S. Maonsees, N. M. Diaz, J. M. Destouet, and R. W. McDivitt, "Carcinoma within fibroadenomas: Mammographic features," *Radiol.* **176**(2), 371–374 (1990).
70. I. Blickstein , R. Goldchmit, S. D. Strano, R. D. Goldman, and N. Barzili, "Echogenicity of fibroadenoma and carcinoma of the breast: Quantitative comparison using gain-assisted densitometric evaluation of sonograms," *J. Ultrasound Med.* **14**(9), 661–664 (1995).
71. B. D. Fornage, J. G. Lorigan, and E. Andry, "Fibroadenoma of the breast: Sonographic appearance," *Radiol.* **172**(3), 671–5 (1989).
72. M. Leonardi, G. Pedretti, E. Caprioli, and G. Bellicini, "The value of ultrasonography in benign breast diseases," *Minerva Ginecol.* **45**(3), 113–6 (1993).
73. C. M. Tiu, Y. H. Chou, S. Y. Chiou, C. Y. Hsu, S. P. Chen, H. R. Chiang, C. R. Lai, L. M. Tseng, H. K. Wang, and H. J. Chiou, "Development of a carcinoma in situ in a fibroadenoma: Color Doppler sonographic demonstration," *J. Ultrasound Med.* **25**, 1335–1338 (2006).
74. C. M. Tiu, S. Y. Chiou, Y. H. Chou, C. Y. Hsu, C. H. Lai, H. J. Chiou, H. R. Chiang, S. P. Chen, H. K. Wang, C. S. Yen, and C. Y. Chang, "Clinical significance of ductal dilatation on breast ultrasonogram," *J. Med. Ultrasound.* **13**, 127–134 (2005).
75. L. Liberman, C. Tornos, R. Huzjan, L. Bartella, E. A. Morris, and D. D. Dershaw, "Is surgical excision warranted after benign, concordant diagnosis of papilloma at percutaneous breast biopsy?" *Am. J. Roentgenol.* **186**(5), 1328–1334 (2006).

76. C. L. Mercado, D. Hamele-Bena, S. M. Oken, C. I. Singer, and J. Cangiarella, "Papillary lesions of the breast at percutaneous core needle biopsy," *Radiol.* **238**(3), 801–808 (2006).

77. R. Sakr, R. Rouzier, C. Salem, M. Antoine, J. Chopier, E. Daraï, and S. Uzan, "Risk of breast cancer associated with papilloma," *Eur. J. Surg. Oncol.* **34**(12), 1304–1308. (2008).

78. T. B. Sheridan, W. A. Berg, and J. K. Warner, "Papillary lesions diagnosed by core needle biopsy of the breast: Diagnostic pitfalls and management update," Paper presented at USCAP 2008; Denver, CO, March 4 (2008).

79. D. D. Dershaw, M. P. Moore, L. Liberman, and B. M. Deutch, "Inflammatory breast carcinoma: Mammographic findings," *Radiol.* **190**(3), 831–834 (1994).

80. F. M. Solvetti, M. F. Thorel, and F. Marandino, "Breast lipomas in echography. A discussion of 3 cases and review of the literature," *Radiol. Med.* **99**, 281–284 (2000).

81. M. A. Cohen, E. A. Morris, P. P. Rosen, D. D. Dershaw, L. Liberman, and A. F. Abramson, "Pseudoangiomatous stromal hyperplasia: Mammographic, sonographic, and clinical patterns," *Radiol.* **198**(1), 117–20 (1996).

82. D. Cyriak and P. M. Carpenter, "Breast imaging case of the day. Pseudoangiomatous stromal hyperplasia," *Radiographics* **19**(4), 1086–1088 (1999).

83. C. Carreira, C. Romano, R. Rodriguez, J. Martin de Francisco, M. Urbasos, and J. Pinto, "A cavernous haemangioma of breast in male: Radiological-pathologic correlation," *Eur. Radial.* **11**(2), 292–294 (2001).

84. C. Dener, N. Sengul, S. Tez, and M. Caydere, "Haemangiomas of the breast," *Eur. J. Surg.* **166**, 977–979 (2000).

85. W. Buchberger, K. Strasser, K. Heim, E. Müller, and H. Schröcksnadel, "Phyllodes tumor: Findings on mammography, sonography, and aspiration cytology in 10 cases," *Am. J. Roentgenol.* **157**, 715–719 (1991).

86. L. Liberman, E. Bonaccio, D. Hamele-Bena, A. F. Abramson, M. A. Cohen, and D. D. Dershaw, "Benign and malignant phyllodes tumors: Mammographic and sonographic findings," *Radiol.* **198**, 121–124 (1996).

87. D. D. Dershaw, E. A. Morris, L. Liberman, and A. F. Abramson, "Nondiagnostic stereotaxic core breast biopsy: Result of rebiopsy," *Radiol.* **198**, 323–325 (1996).

88. C. D. Haagensen, "Fibrous Disease of the Breast," in *Diseases of the Breast*, 2nd edition, C. D. Haagensen, Ed., Saunders, Philadelphia, pp. 185–189 (1971).

89. J. G. Azzopardi, *Problems in Breast Pathology*, Saunders, Philadelphia, pp. 89–90 (1979).

90. V. P. Jackson, R. Jahan, and Y. S. Fu, "Benign Breast Lesions," in *Diagnosis of Diseases of the Breast*, L. W. Bassett, V. P. Jackson, R. Jahan, Y. S. Fu, and R. H. Gold, Eds., Saunders, Philadelphia, pp. 411–412 (1997).

91. W. P. Evans, "Breast masses," *Radiol. Clin. North Am.* **33**, 1080–1085 (1995).

92. G. Hermann and I. S. Schwartz, "Focal fibrous disease of the breast: Mammographic detection of an unappreciated condition," *Am. J. Roentgenol.* **140**, 1245–1246 (1983).

93. L. Liberman, D. D. Dershaw, J. R. Glassman, A. F. Abramson, E. A. Morris, L. R. LaTrenta, and P. P. Rosen, "Analysis of cancers not diagnosed at stereotactic core breast biopsy," *Radiol.* **203**, 151–157 (1997).

94. S. Minkowitz, H. Hedayati, S. Miller, and B. Gardner, "Fibrous mastopathy: A clinical histopathologic study," *Cancer* **32**, 913–916 (1973).

95. V. Bychkov, "Pathology of the Breast," in *Textbook of Breast Disease*, J. H. Isaacs, Ed., Mosby Year Book, St. Louis, pp. 155–78 (1992).

96. F. A. Tavassoli, "Miscellaneous lesions," in *Pathology of the Breast*, F. A. Tavassoli, Ed., Appleton & Lange, Norwalk, pp. 609–623 (1992).

97. D. A. Ekland and M. G. Zeigler, "Abscess in the non-lactating breast," *Arch. Surg.* **107**, 398–401 (1973).

98. R. Hayes, M. Michell, and H. B. Nunnerley, "Acute inflammation of the breast-the role of breast ultrasound in diagnosis and management," *Clin. Radiol.* **44**, 253–256 (1991).

99. S. H. Heywang, E. R. Lipsit, L. M. Glassman, and M. A. Thomas, "Specificity of ultrasonography in the diagnosis of benign breast masses," *J. Ultrasound Med.* **3**, 453–61 (1984).

100. R. Chersevani and G. Rizzatto, "Acute breast inflammation and sonography," in *Breast Ultrasound Update*, H. Madjar, J. Teuberner, and B.-J. Hackeloer, Eds., Darger, Basel, pp. 214–9 (1994).

101. C. M. Tiu, H. J. Chou, Y. H. Chou, C. C. Hsu, K. J. Lin, C. M. Chen, J. S. C. Ko, L. M. Tseng, C. R. Lai, and W. Y. Lui, "Sonography

features of breast abscesses with emphasis on 'hypoechoic rim' sign," *Chin. Med. J.* **64**, 153–160 (2001).

102. G. Rizzatto, R. Chersevani, and L. Solbiati, "High resolution ultrasound assists in breast diagnosis," *Diagn. Imaging Int.* **9**, 42–45 (1993).
103. L. Nguyen, A. J. Doyle, and P. J. Symmans, "Interstitial fluid and hypoechoic wall: Two sonographic signs of breast abscess," *J. Clin. Ultrasound* **28**, 319–324 (2000).
104. M. H. Lequin, J. Van Spengler, and R. Van Pel, "Mammographic and sonographic spectrum of non-puerperal mastitis," *Eur. J. Radiol.* **21**, 138–142 (1995).
105. D. J. Crowe, M. A. Helvie, and T. E. Wilson, "Breast infection: Mammographic and sonographic findings with clinical correlation," *Invest. Radiol.* **30**, 582–7 (1995).
106. M. Muttarak, "Abscess in the non-lactating breast: Radiodiagnostic aspects," *Australas. Radiol.* **40**, 223–5 (1996).
107. B. H. Drukker, "Breast cysts and solid lesions: The role of fine-needle aspiration," *Curr. Opin. Obstet. Gynecol.* **6**(6), 492–494 (1994).
108. T. Franquet, R. Cozcolluela , and C. De Miguel, "Stereotaxic fine-needle aspiration of low-suspicion, nonpalpable breast nodules: Valid alternative to follow-up mammography," *Radiol.* **183**(3), 635–7 (1992).
109. J. P. Hogg, K. M. Harris, and M. L. Skolnick, "The role of ultrasound-guided needle aspiration of breast masses," *Ultrasound Med. Biol.* **14**(Suppl 1), 13–21 (1988).
110. V. P. Jackson, "The current role of ultrasonography in breast imaging," *Radiol. Clin. North Am*. **33**, 1161–1170 (1995).
111. L. Liberman, T. L. Feng, and B. Susnik, "Case 35: Intracystic papillary carcinoma with invasion," *Radiol.* **219**, 781–784 (2001).
112. G. Rotili, A. Bigerna, G. Fabbri , L. Perugini, S. Boni, and L. Volterrani, "The percutaneous treatment of breast cysts. A proposed new method," *Radiol Med (Torino)* **88**(3), 225–227 (1994).
113. E. E. Sterns, "The natural history of macroscopic cysts in the breast," *Surg. Gynecol. Obstet.* **174**(1), 36–40 (1992).
114. R. J. Jackman, F. Burbank, S. H. Parker, W. P. Evans III, M. C. Lechner, T. R. Richardson, A. A. Smid, H. B. Borofsky, C. H. Lee, H. M. Goldstein, K. J. Schilling, A. B. Wray, R. F. Brem, T. H. Helbich, D. E. Lehrer, and S. J. Adler, "Stereotactic breast biopsy of nonpalpable lesions: Determinants of ductal carcinoma in situ underestimate rates," *Radiol.* **218**, 497–502 (2001).

115. W. A. Berg, "Image-guided breast biopsy and management of high-risk lesions," *Radiol. Clin. North Am.* **42**(5), 935–46 (2004).

116. T. W. Jacobs, J. L. Connolly, and S. J. Schnitt, "Nonmalignant lesions in breast core needle biopsies: To excise or not to excise?" *Am. J. Surg. Pathol.* **26**(9), 1095–110 (2002).

117. R. J. Jackman, F. A. Marzoni, Jr., and J. Rosenberg, "False-negative diagnoses at stereotactic vacuum-assisted needle breast biopsy: Long-term follow-up of 1280 lesions and review of the literature," *Am. J. Roentgenol.* **192**, 341–351 (2009).

118. U. Kettritz, K. Rotter, I. Schreer, M. Murauer, R. Schulz-Wendtland, D. Peter, and S. H. Heywang-Köbrunner, "Stereotactic vacuum-assisted breast biopsy in 2847 patients: A multicenter study," *Cancer* **100**, 245–251 (2004).

119. A. Sie, D. C. Bryan, V. Gaines, L. K. Killebrew, C. H. Kim, C. C. Morrison, W. R. Poller, A. P. Romilly, K. Schilling, and J. H. Sung, "Multicenter evaluation of the breast lesion excision system: A percutaeneous, vacuum-assisted, intact-specimen breast biopsy device," *Cancer* **107**(5), 945–949 (2006).

120. C. Y. Lui and H. S. Lan, "Ultrasound guided vacuum assisted breast biopsy: Techniques and applications," *J. Med. Ultrasound.* **18**(1), 1–10 (2010).

121. F. Sperber, A. Blank, U. Metser, G. Flusser, J. M. Klausner, and D. Lev-Chelouche, "Diagnosis and treatment of breast fibroadenomas by ultrasound-guided vacuum-assisted biopsy," *Arch. Surgery* **138**(7), 796–800 (2003).

122. E. Baez, A. Huber, M. Vetter, and B. J. Hackeloer, "Minimally invasive complete excision of benign breast tumors using a three-dimensional ultrasound guided mammotome vacuum device," *Ultrasound Obst. Gynecol.* **21**(3), 267–272 (2003).

123. D. R. Chen, R. F. Chang, and Y. L. Huang, "Computer-aided diagnosis applied to US of solid breast nodules by using neural networks," *Radiol.* **213**, 407–412 (1999).

124. Y. H. Chou, C. M. Tiu, G. S. Hung, S. C. Wu, T. Y. Chang, and H. H. K. Chang, "Stepwise logistic regression analysis of tumor contour features for breast ultrasound diagnosis," *Ultrasound Med. Biol.* **27**, 1493–1498 (2001).

125. J. Z. Cheng, Y. H. Chou, and C. M. Chen, "Computer-aided diagnosis of breast lesions on sonograms: Automatic boundary delineation and nearly setting-independent morphological features," in *Performance Evaluation of Breast Cancer Screening, Diagnosis*

and Treatment, E. Y. K. Ng, R. Acharya, and J. S. Suri, Eds., American Scientific Publishers, Stevenson Ranch, CA, pp. 67–76 (2010).

126. W. C. Shen, R. F. Chang, W. K. Moon, Y. H. Chou, and C. S. Huang, "Breast ultrasound computer-aided diagnosis using BI-RADS features," *Acad. Radiol.* **14**, 928–939 (2007).
127. J. Z. Cheng, Y. H. Chou, C. S. Huang, Y. C. Chang, C. M. Tiu, K. W. Chen, and C. M. Chen, "Computer-aided US diagnosis of breast lesions by using cell-based contour grouping," *Radiol.* **255**, 746–754 (2010).

Chui-Mei Tiu is a clinical professor at the National Defense University and associate professor at the National Yang Ming University of Taiwan, R.O.C. She received her medical degree from the National Taiwan University, College of Medicine in 1976. She has published more than 200 papers, 3 books, and 15 book chapters, and has been an invited speaker for numerous international meetings. She is also on the administrative boards for the Radiological and Ultrasound Societies in Taiwan. Her major research interests are general diagnostic imaging, especially for breast, pediatrics, and oncology. She is now the chief of Pediatric Radiology in the Taipei Veterans General Hospital.

Yi-Hong Chou is Chief of the Ultrasound Section and Breast Imaging at Taipei Veterans General Hospital and professor of radiology at National Yang Ming University School of Medicine, Taipei, Taiwan. He is the former president of the Society of Ultrasound in Medicine, ROC (SUMROC) (1995–1998), currently is the Secretary General of the Asian Federation of Societies for Ultrasound in Medicine and Biology (AFSUMB) and SUMROC, is President of the Asian Breast Diseases Association (ABDA, 2011–), Congress President of AOCR 2010, Treasurer of the Asian Society of Radiology (AOSR), and President Elect of the Asian Society of Abdominal Radiology (ASAR). He is the Editor-in-Chief of the *Journal of Medical Ultrasound* (*JMU*, the official journal of the AFSUMB), and is Associate Editor of *Ultrasound in Medicine and Biology* (the official journal of the World Federation of Ultrasound in Medicine and Biology, WFUMB). Dr. Chou has been active in international scientific and education programs and has organized a number of international

congresses (e.g., AFSUMB 1998, AOCR 2010), workshops, and symposia, particularly on ultrasound, radiology, and breast imaging. Dr. Chou has published more than 330 articles and book chapters and has co-edited two books on abdominal and breast imaging. His current research includes clinical and experimental studies on various aspects of tumor vascularity with regard to color Doppler techniques and microbubble contrast agents, and interventional techniques in tumor ablation.

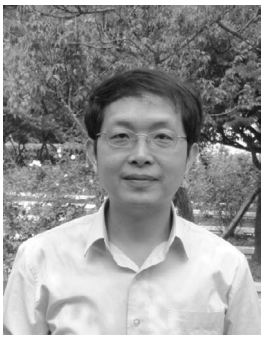

Chung-Ming Chen received his Ph.D. degree in electrical engineering from Cornell University, Ithaca, New York, USA. He subsequently joined the Center for Biomedical Engineering, National Taiwan University, Taiwan, where he served as a research assistant professor. He is currently a professor at the Institute of Biomedical Engineering, National Taiwan University, Taiwan. He is also the Associate Director of the Molecular Imaging Center, National Taiwan University. His research interests are in medical image analysis, bioinformatics, and computer-aided diagnosis. He has published more than 66 journal papers and 90 conference papers. He is a member of the IEEE and is Associate Editor of *Biomedical Engineering—Applications, Basis, and Communication*.

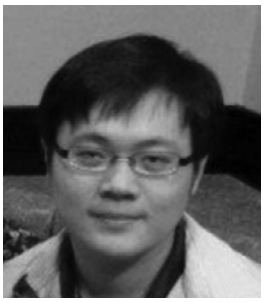

Jie-Zhi Cheng was born and raised in Taichung City, Taiwan, R.O.C. He received his Bachelor's degree from National Taiwan University with a major in computer science in 2002. After military service, he earned his Master's degree in biomedical engineering from National Taiwan University in 2007. After two years of research in medical imaging at Siemens Corporate Research and Biomedical Research Imaging Center, University of North Carolina at Chapel Hill, he is currently pursuing a Ph.D. degree at National Taiwan University. His research interests range from computer-aided diagnosis, intervention, and surgery, to computer vision and machine learning.

Chapter 9
Abnormal Lesion Detection from Breast Thermal Images Using Chaos with Lyapunov Exponents

Mahnaz Etahadtavakol
Medical Image and Signal Processing Research Center, Isfahan University of Medical Sciences, Isfahan, Iran

E. Y. K. Ng
School of Mechanical and Aerospace Engineering, Nanyang Technological University, Singapore

Caro Lucas
Electrical and Computer Engineering Department, University of Tehran, Tehran, Iran

Mohammad Ataei
Department of Electrical Engineering, University of Isfahan, Isfahan, Iran

9.1 Introduction

Breast cancer is the second most common cancer in women, and incidences of it continue to rise. The cure rate is increasing for breast cancer that is diagnosed in its early stages. That is why the value of breast health care is so important. Malignant breast tumor detection is extremely important for the physician. Generally, this task has been performed based on the experience and knowledge of the radiologists by analyzing the visual characteristics of the structures that appear in mammograms. The irregularity that exists in the edge of the typical cell that forms part of the tumor and tumoral structures (angiogenesis) is one of the major characteristics.[1] Particularly, some malignant tumors involve a more irregular boundary edge, as compared to the benign ones.[2] Speculating this feature by means of evaluating the irregularities can help support the diagnosis of malignancy. Hence, study of chaotic time series (CTS) can afford the tools necessary to generate the procedures to speculate the irregularities in the edges, through the use of the concept of fractal dimension (FD), which can produce the parameters to describe and categorize the structures under study. To detect the tumors and generate the time series (TS) characterizing the edge, techniques of digital image processing are applied over breast thermal images. Ahmed concluded that tumor growth, argued as a dynamical system, is chaotic. Proposed chaotic models fit the observations well. Some of these models treat the tumor as a fractal.[1]

In this chapter, Lyapunov exponents (LEs) are computed from CTS based on the Jacobian approach by using polynomial models. The chapter is organized as follows: the CTS is introduced in Section 9.2, the time-delay embedding (TDE) method is described in Section 9.3, followed by an explanation of LEs in 9.4. In Section 9.5, a method that is used to calculate the LEs is presented. The outline of the method to generate the TS of the edge is explained in Section 9.6, and Section 9.7 presents the results produced by using this process on the different types of tumors under study. Finally, the findings are concluded in Section 9.8.

9.2 Time Series

A nonlinear dynamical system that is hard to capture using conventional tools such as Fourier analysis is represented by TS. If the signal is generated by a linear source, a regular Fourier spectrum provides useful information. For signals generated by a nonlinear source, an alternative characterization of such TS is desired. The reason for choosing CTS analysis is that an unknown complex system can be described by a strange attractor in its phase space (PS), and it is crucial to reconstruct the system state-space starting from the observed TS. The observed TS can be observed as the output of an unknown system corrupted by noise. A trajectory is constituted of the time evolution of these observables in the state-space.

Full knowledge of the system dynamics is not available because access to all measurements for each possible variable in the system is not possible. However, practically, only one TS measurement is available. In such a case, although the exact PS of the system cannot be found, a pseudo PS (equivalent to the original PS in terms of the system invariants) may still be constructed. This pseudo PS is called the reconstructed phase space (RPS).[3] Nevertheless, generating RPS is a crucial task on CTS analysis. The PS is reconstructed with a time-delay embedding (TDE) method in this work.

9.3 Time-Delay Embedding

The most intelligible method of embedding scalar data is the method of delays. Suppose that $\{x_i\}$ represents the CTS. With an embedding dimension m and a time delay τ, $\{x_i\}$ can be embedded into an RPS. When applying the TDE method, two parameters: (1) the embedding dimension m and (2) the time delay τ need to be determined.[4] Parameter m can be obtained by several methods, and parameter τ can be selected arbitrarily by Takens' theorem.

Estimating the LEs and the efficiency of modeling is significantly affected by the optimality of the embedding dimension. Equation (9.1) represents one RPS matrix that is generated by sliding a window of length m through the data to form a series of vectors, stacked row-wise in the matrix. Each row of the matrix represents a point in the RPS:

$$\begin{bmatrix} x_0 & x_\tau & \cdots & x_{(m-1)\tau} \\ x_1 & x_{1+\tau} & \cdots & x_{1+(m-1)\tau} \\ x_2 & x_{2+\tau} & \cdots & x_{2+(m-1)\tau} \\ \vdots & \vdots & \vdots & \vdots \end{bmatrix} \tag{9.1}$$

Suppose that d is the inherent system dimension. From information regarding the system dimension, an upper bound on the dimension of the RPS can be obtained. The Takens' theorem states that, by embedding with a dimension m greater than $2d + 1$, an RPS can be constructed that is equivalent to the original PS.[5] In spite of the fact that this theorem provides a theoretically sufficient bound, practically, such a bound is not necessary. Accordingly, most systems can be embedded in much lower-dimensional spaces. Several methods such as false nearest neighbor (FNN), time delay, and singular value decomposition (SVD) can attain embedding.[6]

9.4 Lyapunov Exponents

Lyapunov exponents are quantities that characterize the averaged rate of divergence or convergence of two neighboring trajectories in the PS. It can measure the sensitive dependency on the initial conditions.

The long-term evolution of an infinitesimal n sphere initial condition can be monitored with a continuous dynamical system in an n-dimensional PS. Parameter n is the number of equations (or equivalently, the number of state variables) used to describe the system. The sphere evolves into an ellipsoid whose principle axes expand (or contract) at rates given by the LEs as time t progresses.

Error amplification during the course of the iteration to $E_1, E_2, \ldots$ can be recorded by comparing an orbit belonging to some initial conditions with an orbit for an initial condition that carries an error E_0. The error amplification factor can be obtained as telescope product E_n / E_0:

$$\frac{E_n}{E_0} = \left|\frac{E_n}{E_{n-1}}\right|\left|\frac{E_{n-1}}{E_{n-2}}\right| \ldots \left|\frac{E_1}{E_0}\right|. \tag{9.2}$$

LEs characterize the average logarithmic growth of the relative error per iteration. We let the size of the initial error go to zero to arrive at a well-defined exponent.

Practically, in each iteration, the size of the error can be renormalized to some convenient number ε. This arrives at an LE λ that characterizes for a given orbit how fast the nearby orbits are growing closer or moving away. By way of explanation, in each iteration, a small error in an initial point is scaled by the factor of e^{λ} (on average). Hence, a negative exponent means that the nearby orbits are attracted, while a positive exponent implies that the nearby orbits move away, which is expected for a chaotic attractor.

Suppose that the original separation is $|\delta x(0)|$, and the separation to time t is $|\delta x(t)|$, and assume that the rate of growth (or decay) of the separation between the trajectories is exponential in time. Hence, if the function of $\lim_{t\to\infty}|\delta x(t)| = e^{\lambda t}|\delta x(0)|$ holds in the lim $t\to\infty$, then the LE is defined as λ.

The LEs associated with a trajectory provide us with a measure of average rates of divergence or convergence of the surrounding trajectories. These are speculated to be a crucial invariant characterization of the dynamical system. Additionally, LEs are good quantities for categorizing fixed points and periodic, quasi-periodic, and chaotic motions.[7]

For a multidimensional system, there are as many LEs as there are dimension of the system. They may be positive, or negative, or zero. The sum of all LEs should be less than or equal to zero for a dynamical system with a bounded attractor. The positive LEs indicate that the system is chaotic, while negative LEs characterize a system's tendency to pull an evolving trajectory toward the basin of attraction. In addition, zero exponents suggest that the system is in some sort of steady state mode.

9.5 Computation of the Lyapunov Exponents

Geometrical and Jacobian approaches are two general methods for computing LEs from TS output. In geometrical approaches, the long-term evolution of an infinitesimal sphere of initial conditions is considered. This method suffers from a significant drawback: a huge number of data points is required; hence, it is time consuming.[8]

Assuming the discrete time dynamical system expressed by Eq. (9.3), the adaptive LE estimation based on the Jacobian approach is given by

$$X_{k+1} = F(X_k) \qquad k = 0, 1, \ldots, \tag{9.3}$$

where X_k is the state vector, and $F(\cdot)$ is a continuously differentiable nonlinear function. We are interested to see what goes to X_1 with a small change in X_0. We can find this by iteration of the tangent space as given by the Jacobian matrix. The approach is implemented by first linearizing the system for a small change around the operational trajectory in the PS, and then decomposing the system using a Taylor series, by neglecting the higher-order terms yields:

$$\delta X_{k+1} \cong J_k \delta X_k \qquad k = 0, 1, \ldots, \tag{9.4}$$

where $J_k = \partial F / \partial X \,|_{X_k}$ is its Jacobian matrix of partial derivatives in point k, and δX_k is the change in X_k. Let $\{X_0, X_1, \ldots, X_{k-1}\}$ be the sequence generated by successive iterations of the initial condition X_0. We introduce the matrix defined by Eq. (9.5) as

$$Y^k = J(X_{k-1})J(X_{k-2}) \ldots J(X_1)J(X_0) \tag{9.5}$$

for this sequence. Consequently, the matrix defined by Eq. (9.6) is

$$\Lambda = \lim_{k \to \infty} \left[(Y^k)^T Y^k \right]^{\frac{1}{2k}}. \tag{9.6}$$

Hence, LEs are the logarithms of the eigenvalues of Λ.

There are some problems with computation of the LEs using Eq. (9.6). One of the problems is that for large values of k, the calculation of Λ may not be possible since the fundamental solution Y^k may be very large. In addition, the linear independence of the columns must be guaranteed in order to evaluate Y^k. Otherwise, only the largest LEs will be obtained. In order to overcome these limitations, the *QR* factorization algorithm, which decomposes the matrix into an orthogonal and an upper triangular matrix, is

applied to approximate the LEs.[9–12] The following steps are involved in this method:

1. Orthogonal Q_0 is given such that
2. $Q_0^T \cdot Q_0 = I$.
3. $Z_{k+1} = J_k \cdot Q_k$, $k = 0, 1, \ldots$ is solved, and $Z_{k+1} = Q_{k+1} \cdot R_{k+1}$ is obtained, where Q_k is an orthogonal matrix, and R_{k+1} is an upper triangular matrix with positive diagonal elements.
4. By using Eq. (9.7), the LEs are calculated as

$$\begin{aligned} \lambda_j &= \lim_{k\to\infty} \frac{1}{k} \log[(R_k)_{jj} \quad (R_1)_{jj}] \\ &= \lim_{k\to\infty} \frac{1}{k} \sum_{i=1}^{k} \log[(R_i)_{jj}] \quad j = 1, \quad , m \end{aligned} \tag{9.7}$$

9.5.1 Polynomial model

The nonlinear difference equation expressed in Eq. (9.7) represents the dynamical behavior of the system

$$y(k+1) = f(x_k), \tag{9.8}$$

where $f(\cdot)$ is a continuously differentiable function, in which x_k is a state vector. Supposing that Eq. (9.9) represents the output data of the dynamical system available in TS,

$$y(t + t_s), y(t + 2t_s), ..., y(t + Nt_s), \tag{9.9}$$

where t_s is the sampling time, and N is the total number of measurements. The structure of the underlying dynamical system that generates the data is unknown in this situation. Accordingly, an arbitrary polynomial is selected to fit the output data:

$$\begin{aligned} y(k+1) = \theta_0 &+ \sum_{i=0}^{d-1} \theta_{1i} y(k-i) + \sum_{i=0}^{d-1} \sum_{j=1}^{d-1} \theta_{2ij} y(k-i) y(k-j) \\ &+ \cdots + \sum_{i=0}^{d-1} \sum_{j=1}^{d-1} \cdots \sum_{v=u}^{d-1} \theta_{nijp} y(k-i) y(k-j) \cdots y(k-u) y(k-v) \end{aligned} \tag{9.10}$$

Equation (9.11) defines the number of parameters in vector θ that should be estimated to identify the underlying model:

$$n_{\theta} = \frac{(d+n)!}{d!n!}, \tag{9.11}$$

where d is the model order, and n is the degree of nonlinearity. Then, this identification can be obtained by using a least-squares method.

9.6 Generating the Time Series

In this work, we represent a region by TS to generate a 1D signal that allows the application of estimating the embedding dimension. Using this estimated dimension is helpful in reconstructing the PS with a TDE method and allows LEs of the TS to be estimated. Figure 9.1 shows a sample contour and the distances (in blue) between some of the boundary contour points and the center of mass.

Considering that cancer is often characterized as a chaotic, poorly regulated growth of tumor boundaries,[2] the algorithm for extracting a scalar signal from the 2D breast thermal images is proposed as follows. By using a fuzzy c-means algorithm, the breast thermal images are segmented.[13,14] The number of clusters depends on the number of camera palette colors:

1. Based on the color related to the maximal temperature, the first hottest regions are identified. Consequently, the axilla and close sternal boundaries are removed.
2. The distance between each of the subsequent boundary contour points and the center of the mass of the first hottest region in terms of the sequence of the former is estimated. This can be done by starting from an initial point of the contour and traversing in either a clockwise or

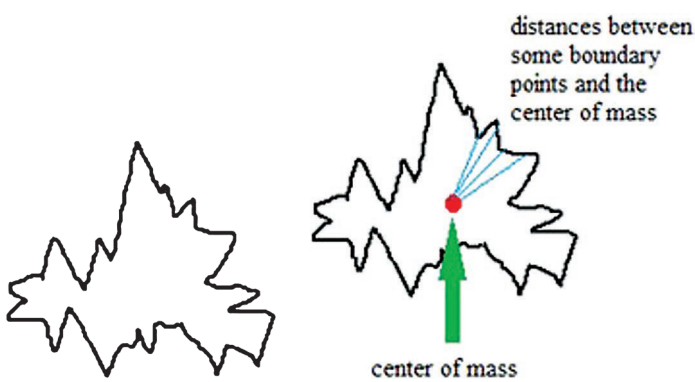

Figure 9.1 (a) A sample contour. (b) Four boundary contour points, center of mass, and the distances between the boundary points and the center of mass.

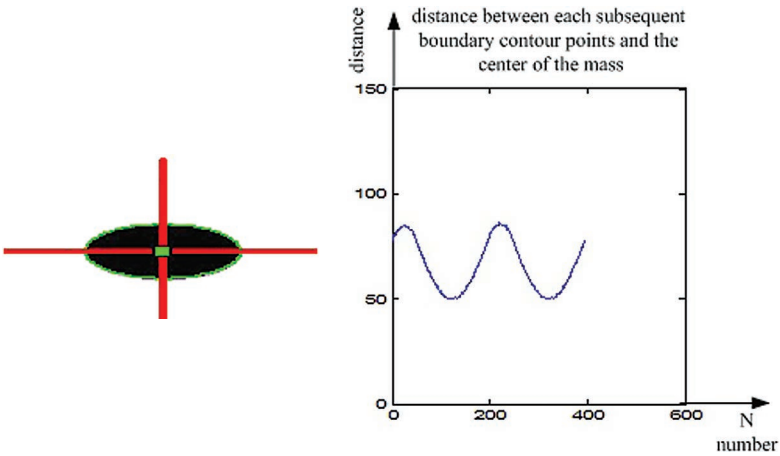

Figure 9.2 (a) An ellipse and (b) its corresponding generated 1D time series. (Reprinted from Ref. 14 with permission. © 2012 Elsevier.)

counterclockwise direction. According to the geometrical shape and size of the region, the number of sample points in the sequence is different.

3. If the first hottest region is composed of several separated regions, one 1D signal composed of the separated corresponding 1D signals would be generated.

For example, the implementation of the algorithm for an ellipse is shown in Fig. 9.2(a). Its center of mass is marked with a green square, and the boundary contour points as green points. The corresponding 1D time series is shown in Fig. 9.2(b).

9.7 Experimental Results and Discussion

In this work, two groups of images—synthetic images and real-world thermal images—were studied.

9.7.1 Fractal images

Some common fractal images that are produced by mathematical models as well as some sample contours with different irregularities were investigated in this section. The Koch snowflake is an example of a fractal image that is a mathematical curve based on the Koch curve as depicted in Fig. 9.3(a). Another example is the Mandelbrot set, which is a set of points in the complex plane, the boundary of which forms a fractal. A Mandelbrot set is depicted in Fig. 9.4(a). A fern and one chaos image are the next two examples, which are demonstrated in Figs. 9.5(a) and 9.6(a), respectively. In addition, four different sample contours are presented in Figs 9.7(a), 9.8(a), 9.9(a), and 9.10(a). The corresponding generated 1D TSs for Figs. 9.3(a)–9.10(a) are shown in Figs. 9.3(b)–9.10(b).

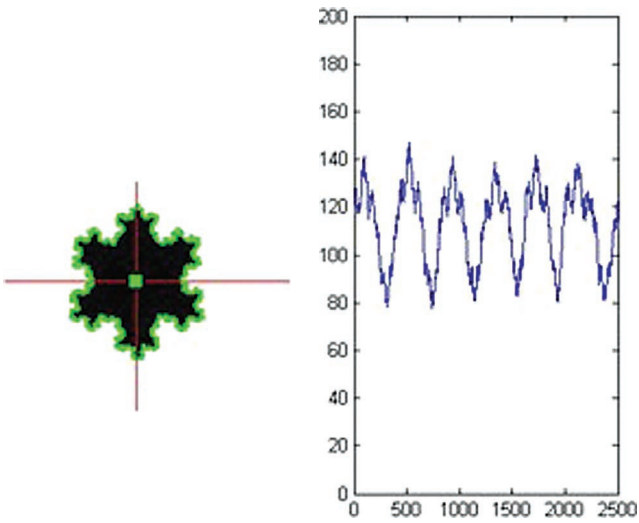

Figure 9.3 (a) A Koch snowflake image and (b) its corresponding generated 1D TS. (Reprinted from Ref. 14 with permission. © 2012 Elsevier.)

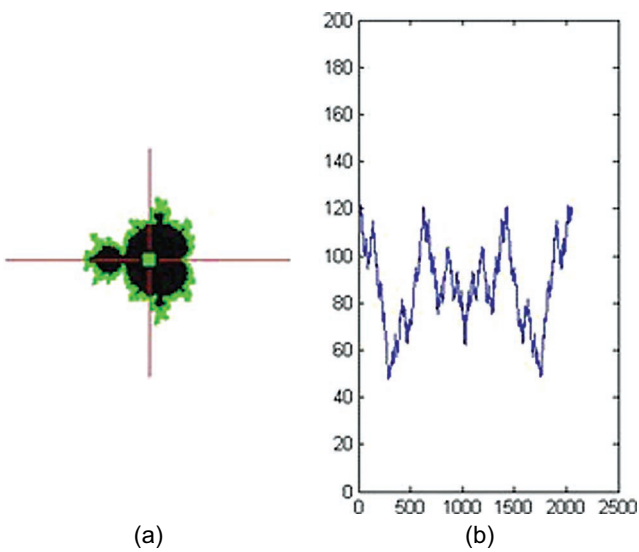

Figure 9.4 (a) A Mandelbrot image and (b) its corresponding generated 1D TS. (Reprinted from Ref. 14 with permission. © 2012 Elsevier.)

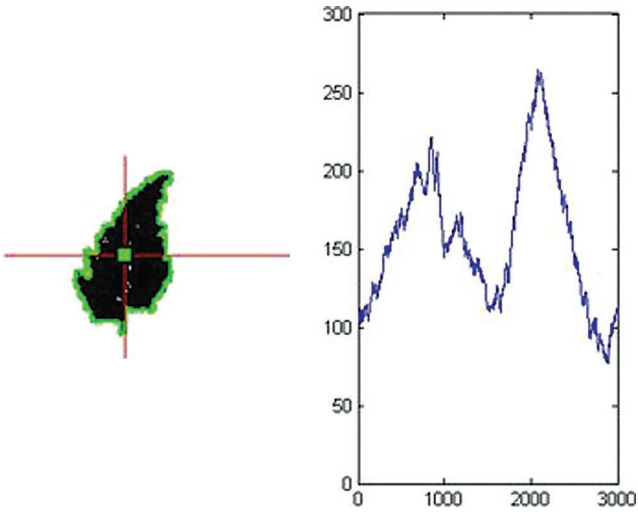

(a) (b)

Figure 9.5 (a) A fern image and (b) its corresponding generated 1D TS. (Reprinted from Ref. 14 with permission. © 2012 Elsevier.)

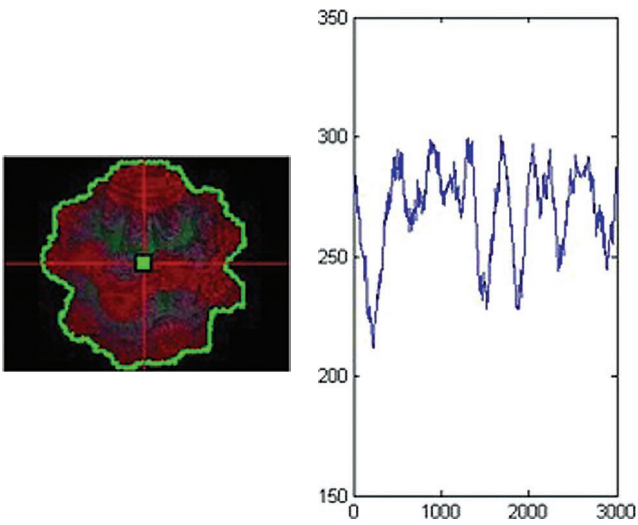

(a) (b)

Figure 9.6 (a) A chaos image and (b) its corresponding generated 1D TS. (Reprinted from Ref. 14 with permission. © 2012 Elsevier.)

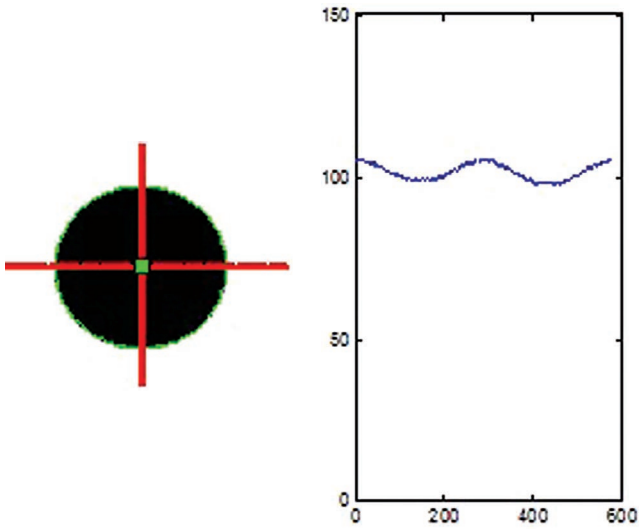

Figure 9.7 (a) First contour (a circle) and (b) its corresponding generated 1D TS. (Reprinted from Ref. 14 with permission. © 2012 Elsevier.)

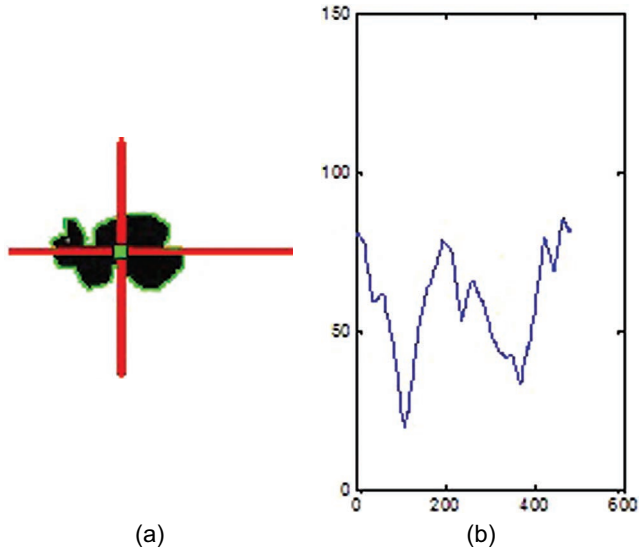

Figure 9.8 (a) Second contour and (b) its corresponding generated 1D TS. (Reprinted from Ref. 14 with permission. © 2012 Elsevier.)

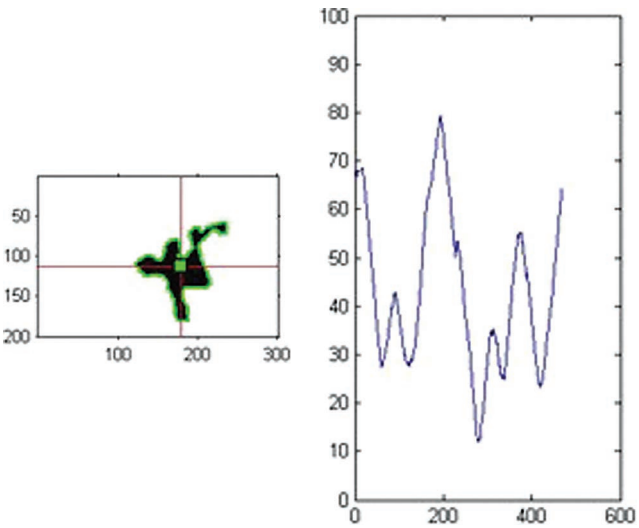

(a) (b)

Figure 9.9 (a) Third contour and (b) its corresponding generated 1D TS.

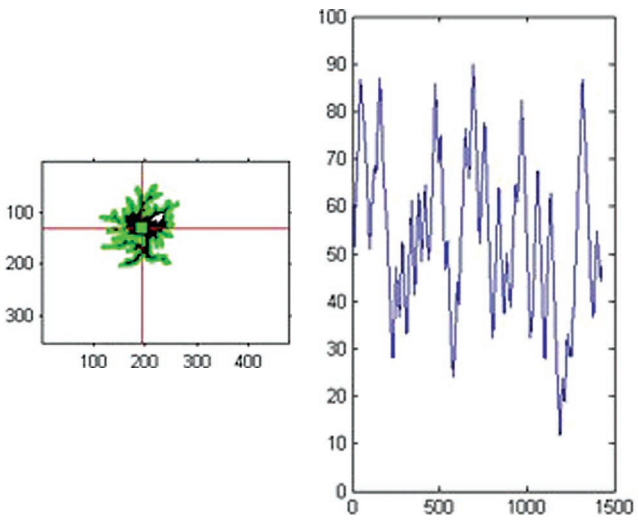

(a) (b)

Figure 9.10 (a) Forth contour and (b) its corresponding generated 1D TS.

Table 9.1 Calculated LEs for eight selected synthetic images.

Images	Polynomial degrees (*m*)	Lyapunov exponents
Koch snowflake		0.0526, –0.0612, –0.1660, –0.3668, –0.7678
Mandelbrot	5	0.1077, –0.0388, –0.1433, –0.3384, –0.8055
	4	0.1429, –0.0548, –0.2614, –0.7413
Fern	4	0.0716, –0.1125, –0.3241, –0.7751
	5	0.0462, –0.0803, –0.1869, –0.3574, –0.7749
Chaos (Fig. 9.6)	4	0.3869, 0.1134, –0.1032, –0.7119
Circle [Fig. 9.7(a)]	5	–0.0077, –0.1891, –0.3406, –0.4775, –1.0653
	4	0.0074, –0.2241, –0.3840, –.7416
Fig. 9.8(a)	5	0.1113, –0.0275, –0.2997, –0.4377, –0.7181
	4	0.0074, –0.2241, –-0.3840, –0.7416
Fig. 9.9(a)	5	0.3540, 0.0530, –0.0976, –0.2890, –0.7572
	4	0.4182, 0.0034, –0.2411, –0.8235
Fig. 9.10(a)	5	0.7868, 0.2778, 0.0512, –0.1673, –0.7394
	4	0.8143, 0.2185, –0.0757, –0.6372

Their LEs for eight of these synthetic images are calculated for two polynomial degrees ($m = 4$ and $m = 5$), and the results are included in Table 9.1.

Several studies have been performed using the LEs computed from a CTS. In this study, the LEs were computed from a CTS based on a Jacobian approach by applying polynomial modeling. Normally, *a priori* knowledge concerning the dimension of a system does not exist, so it was imperative that our method was evaluated for different embedding dimensions.

For different embedding dimensions and different polynomial degrees, the LEs for all cases of the first group were computed. Results were included in Table 9.1. It was apparent that satisfactory results were obtained when m was below the Takens' criterion. The results for parameter $m = 4$ and 5 are also demonstrated in Table 9.1.

In summary, our desired application is real-world breast thermal images, and analysis of the first two groups reconfirms the results for the real-world cases.

9.7.2 Real-world IR images

Our algorithm was implemented for several real-world breast thermal images, images from the second group in this study. One typical malignant case is shown in Fig. 9.11. The original image, the corresponding hottest regions, its boundaries, and the center of mass as well as its corresponding generated 1D time series are demonstrated in Figs. 9.11(a)–(d), respectively.

In addition, the second malignant case (M2) and one benign case (B1) are depicted in Figs. 9.12 and 9.13, respectively.

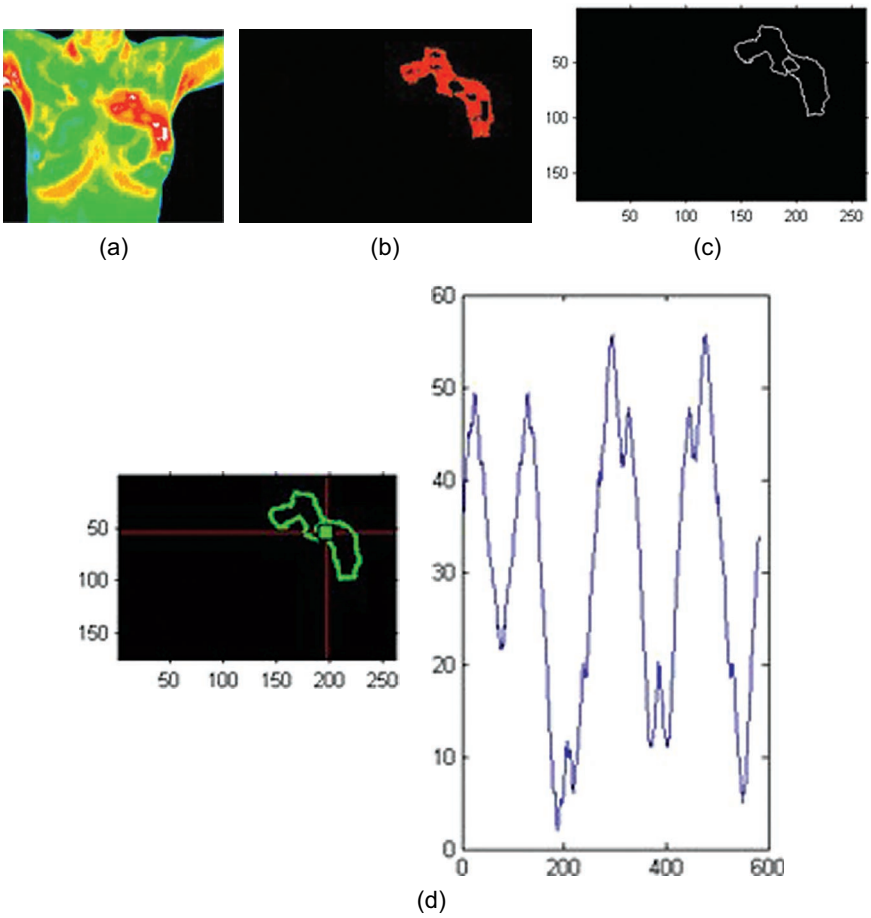

Figure 9.11 (a) Malignant case 1 (M1). (b) The first hottest regions for M1. (c) Boundaries of the first hottest regions for M1. (d) Boundaries and the center of mass of the first hottest regions for M1 (left) and corresponding generated 1D TS (right).

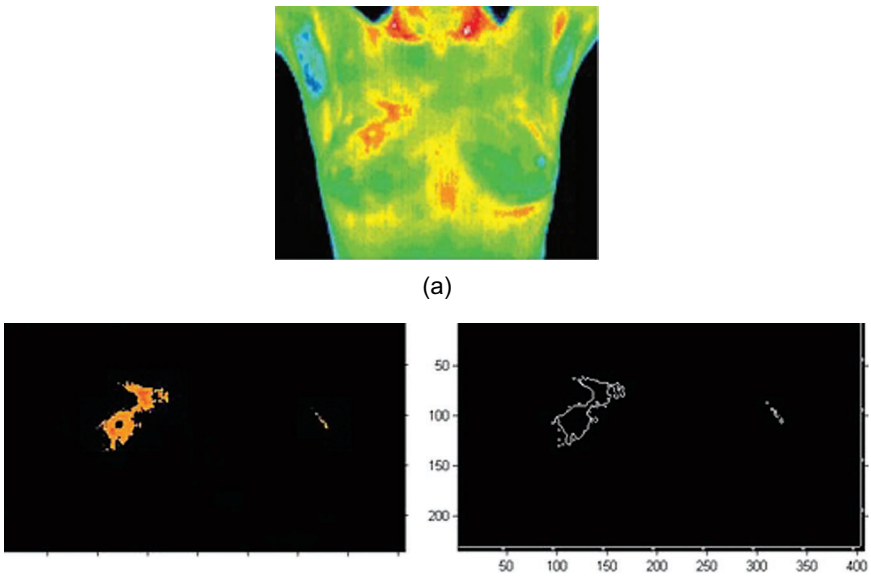

(a)

(b) (c)

Figure 9.12 (a) The second malignant case (M2). (b) The first hottest region of M2 (left) and the its boundaries (right).

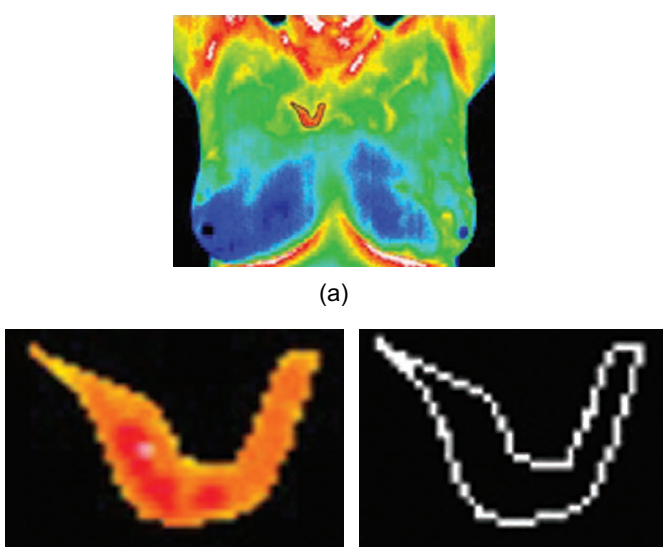

(a)

(b)

Figure 9.13 (a) Benign case 1 (B1). (Reprinted from Ref. 14 with permission. © 2012 Elsevier.) (b) The first hottest region of B1 and its boundaries (right).

Table 9.2 Calculated LEs for the two typical malignant cancer cases and one benign case.

Images	*m*	Lyapunov exponents (LEs)
M1	5	0.9209, 0.2859, 0.0338, –0.1632, –0.7875
	4	0.8244, 0.2522, –0.0882, –0.6269
M2	5	0.4810, 0.2385, –0.0087, –0.1579, –0.6613
	4	0.6071, 0.2013, –0.1601, –0.6767
B1	5	0.0995, –0.0399, –0.2756, –0.4369, –0.7814
	4	0.1698, –0.0523, –0.4580, –1.1290

LEs were calculated for the two typical malignant cases and the one benign case. Parameter *m* (polynomial degrees) was chosen as 4 and 5. The calculated LEs are shown in Table 9.2.

From a mathematical point of view, the TS of the circle indicated in Fig. 9.7(b) is expected to be a straight line, but, instead, the generated sequence is periodic with very small magnitude. Moreover, a circle has a nonchaotic contour and is expected to have only negative LEs. However, the results in Table 1 show three negative LEs and one small positive LE. These errors are related to the pixel errors that are due to the difference between the original analog data and the approximate discrete data.

Similarly, for Figs. 9.8(a)–9.10(a), we expected their generated TSs to be nonperiodic and hence their LEs to be positive. Additionally, as their contours become more complex, their LEs become more positive.

The malignant case M1 indicated in Fig. 9.11 has three positive LEs for polynomials of degree 5, and two LEs for polynomials of degree 4. In addition, the malignant case M2 (Fig. 9.12) has two positive LEs for both polynomials of degrees 5 and 4. This fact thus indicates chaos in the boundaries of the first hottest regions of the images. As we expected theoretically, it is observable from the obtained LEs that the rate of chaos for the benign case B1 is much less than that for the two other malignant cases M1 and M2. By way of explanation, the boundaries of the benign case are smoother than those of the malignant case.

9.8 Conclusion

This is a preliminary study that aims to explore the possibility of differentiating between malignant cases and benign cases with experiments on nonlinear analysis of breast thermograms using LEs. Our approach is to check the differences between the TSs generated from the first hottest regions of the malignant case and those of the benign case.

The described model confirmed the research questions that systems science, complexity, and chaos theory can be applied to biologic entities. Cancer is often characterized as a chaotic, poorly regulated growth. Cancerous cells, tumors, and vasculature have irregular shapes that have the potential to be described by a nonlinear dynamical system. Chaotic time series (CTS) can provide the tools necessary to generate the procedures for evaluating the nonlinear system. Computation of LEs is a powerful means of quantifying the degree of the chaos.

Moreover, the largest LEs can indicate the rate of chaos. We analyzed two groups of images: mathematical and synthetic images in the first group, and real-world breast thermal images in the second group. It is shown that our algorithm is potentially capable of differentiating between different patterns with different boundary irregularities.

In addition, the study indicates some errors in the estimated LEs due to pixel errors. Although our desired cases are real-world breast thermal images, inspecting our first group helps to confirm the results of the real-world cases. This study presents a novel approach for nonlinear analysis of breast thermograms to identify abnormal lesions. The application of Lyapunov exponents for breast thermograms is new. This work can be extended for classifying different stages of breast cancer; the authors are currently working toward this objective.

References

1. E. Ahmed, "Fractals and chaos in cancer models," *Int. J. Theoret. Phys. A* **32**(2), 353–355 (2004).
2. J. W. Baish and R. K. Jain, "Fractals and cancer," *Cancer Res.* **60**, 3683–3688 (2000).
3. A. H. Nayfeh and B. Balachandran, *Applied Nonlinear Dynamics*, *Wiley Interscience*, New York (1995).
4. A. G. Darbyshire and D. S. Broomhead, "Robust estimation of tangent maps and Liapunov spectra," *Physica D* **89**, 287–305 (1996).
5. F. Takens, "Detecting strange attractors in turbulence," in *Notes in Mathematics* **898**, D. A. Rand and L. S. Young, Eds., Springer, Berlin, 366–381 (1981).
6. A. I. Mees, P. E. Rapp, and L. S. Jenning, "Singular value decomposition and embedding dimension," *Phys. Rev. A* **36**(1), 340–346 (1987).
7. S. Strogatz, *Nonlinear Dynamics and Chaos,* Perseus Publishing (2000).
8. T. Kambe, *Geometrical Theory of Dynamical System and Fluid Flows*, World Scientific Publishing Co., Pte. Ltd., Singapore (2004).

9. J. P. Eckmann, S. O. Kamphorst, D. Ruelle, and S. Ciliberto, "Lyapunov exponents from time series," *Phys. Rev. A* **34**(6), 4971–4979 (1986).
10. R. Brown, P. Bryant, and H. D. I. Abarbanel, "Computing the Lyapunov spectrum of a dynamical system from an observed time series" *Phys. Rev. A* **43**(6), 2787–2806 (1991).
11. N. Oiwa and N. Fiedler-Ferrara, "A fast algorithm for estimating Lyapunov exponents from time series," *Phys. Let. A* **246**, 117–121 (1998).
12. L. Diect, R. D. Russell, and E. S. Van Vleck, "On the computation of Lyapunov exponents from continuous dynamical systems," *SIAM J. Numer. Anal.* **34**(1), 402–423 (1997).
13. M. EtehadTavakol, S. Sadri, and E. Y. K. Ng, "Application of K- and fuzzy c-beans for color segmentation of thermal infrared breast images," *J. Med. Systems* **34**(1), 35–42 (2010).
14. M. Etehad Tavakol, E.Y. K. Ng, C. Lucas, S. Sadri, and M. Ataei, "Nonlinear analysis using Lyapunov exponents in breast thermal images to identify abnormal lesions," *Infrared Phys. Technol*. **55**(4), 345–352 (2012).

Mahnaz Etahadtavakol received both her B.S. in Electrical Engineering and her M.S. in Applied Mathematics from at Purdue University, West Lafayette, Indiana, in 1987 and 1989, respectively. She was a Ph.D. candidate in Electrical Engineering at University of Texas at Arlington from 2006 to 2007. She continued her doctorate program at Isfahan University of Technology, Iran, obtaining her Ph.D. in April 2011. She is currently working in the Medical Image and Signal Processing Research Center of Isfahan University of Medical Sciences, Isfahan, Iran. Her main areas of research are breast thermal infrared imaging and biomedical engineering.

E. Y. K. Ng received his Ph.D. at Cambridge University, UK. His research is in thermal imaging, biomedical engineering, and computational methods of heat transfer (CHT) and fluid dynamics (CFD). He is a professor at the Nanyang Technological University. He has published many papers in SCI journals (173), conference proceedings (50), and textbook chapters (74), has coauthored 9 books, and has given more than 10 keynote speeches. Ng is Editor-

in-Chief for both the *Journal of Mechanics in Medicine & Biology* and the *Journal of Medical Imaging & Health Informatics*, and is Associate Editor-in-Chief for *World Journal of Clinical Oncology.*

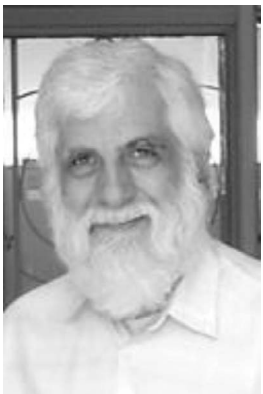

Caro Lucas (1949–2010) received his M.S. degree in Electrical Engineering from the University of Tehran in 1973 and his Ph.D. in Electrical Engineering and Computer Sciences from University of California Berkeley in 1976, majoring in Control Systems Engineering. He lectured/conducted research at several universities including UCLA, UC Berkeley, and University of Toronto, and was a full-time tenured Professor at University of Tehran. Professor Lucas was the author of 8 books/edited volumes, 40 chapters/articles in books/edited volumes, 342 journal papers, and 835 conference papers. He delivered more than 190 invited talks, organized more than 100 conferences, and served on the editorial/advisory boards of 27 journals. He was the founder and director/chair of the Intelligent Systems Research Faculty of the Institute for Studies in Theoretical Physics and Mathematics (IPM), Tehran,Iran; IEEE, Iran Section; and the Center of Excellence for Control and Intelligent Processing (CIPSE), Tehran, Iran. His interests included emotion modeling, hazard prediction, intelligent control, biomotivated computing, data mining, business intelligence, socioeconomic systems, and research-centric education.

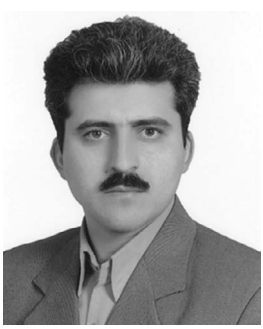

Mohammad Ataei received his B.S. degree from the Isfahan University of Technology, Isfahan, Iran, in 1994, his M.S. degree from the Iran University of Science & Technology, Tehran, Iran, in 1997, and Ph.D. degree from K. N. Toosi University of Technology, Tehran, Iran, in 2004, all in Electrical Engineering. He performed his Ph.D. project jointly with the University of Bremen in Germany from 2001 to 2003. Since 2004, he has been with the Department of Electrical Engineering at the University of Isfahan, Iran. He has worked on time series analysis of chaotic systems, and control theory and applications. His main areas of research are chaos control and synchronization, and nonlinear control.

Chapter 10
Intelligent Rule-based Classification of Image Features for Breast Thermogram Analysis

Gerald Schaefer
Department of Computer Science, Loughborough University, Loughborough, United Kingdom

10.1 Introduction

Breast cancer is the most commonly diagnosed form of cancer in women, accounting for about 30% of all cases.[1] Despite earlier, less encouraging studies, which were based on low-capability and poorly calibrated equipment, thermal infrared imaging has been shown to be well suited for the task of detecting breast cancer, in particular when the tumor is in its early stages or in dense tissue.[2,3] Early detection is important as it provides significantly higher chances of survival,[4] and in this respect, infrared imaging[5] outperforms the standard method of mammography. While mammography can detect tumors only once they exceed a certain size, even small

tumors can be identified using thermography[6] due to the high metabolic activity of cancer cells that leads to an increase in local temperature that can be picked up in the infrared.

In this chapter, we derive a number of image features from breast thermograms. These features are designed to describe the bilateral differences between regions of interest of the left and right breast. We then use these features in a pattern classification process to discriminate malignant cases from benign ones. Our pattern classification systems are based on rules, and we employ two different approaches to generate rule bases. The first utilizes fuzzy if-then rules and applies a genetic algorithm to optimize the rule base,[7] while the second uses an ant colony optimization classification algorithm.[8] Both approaches are shown to provide good classification accuracy.

10.2 Image Features

As has been shown, an effective approach to automatically detect cancer cases based on breast thermograms is to study the symmetry between the left and right breast.[7,9] A tumor will recruit blood vessels, resulting in hot spots and a change in vascular pattern and hence an asymmetry between the temperature distributions of the two breasts. On the other hand, symmetry typically identifies healthy subjects. We follow this approach and segment the areas corresponding to the left and right breast from the thermograms. Once segmented, we convert the breast regions to a polar coordinate representation, which simplifies the calculation of several of the features that we employ. A series of statistical features is then calculated to provide indications of symmetry between the regions of interest (i.e., the two breasts).[7]

Clearly, the simplest feature to describe a temperature distribution such as those encountered in thermograms is found by calculating its statistical mean. As we are interested in symmetry features, we calculate the mean for both breasts and use the absolute value of the difference of the two. Similarly, we calculate the standard temperature deviation and use the absolute difference as a feature. Furthermore, we employ the absolute differences of the median temperature and the 90-percentile as further descriptors.

We further utilize moments of order 1, which essentially describe the center of gravity of the breast regions, as well as the distance (both in x and y direction) of the center of gravity from the geometrical center of the breast. For all four features, we calculate the absolute differences of the values between the left and right breast.

Histograms record the frequencies of certain temperature ranges of the thermograms. In our work, we construct normalized histograms for both regions of interest (i.e., left and right breast) and use the cross correlation between the two histograms as a feature. From the difference histogram

(i.e., the difference between the two histograms), we compute the absolute value of its maximum, the number of bins exceeding a certain threshold, the number of zero crossings, the energy, and the difference of the positive and negative parts of the histogram.

Co-occurrence matrices have been widely used in texture recognition tasks[10] and, applied to thermograms, record the joint probabilities of pixel (i.e., temperature) values a certain distance away from each other. In order to arrive at an indication of asymmetry between the two sides, we use the cross co-occurrence matrix[11] where one pixel value is extracted from the left breast and the other from the right. From this matrix, we extract some statistical features, namely homogeneity, energy, contrast, and symmetry,[10] and the first four moments of the matrix.

The mutual information between two distributions can be calculated from the joint entropy of the distributions and is employed as a further descriptor. As final feature descriptors, we calculate the Fourier spectrum and use the difference of absolute values of the ROI spectra. The features we adopt are the difference maximum and the distance of this maximum from the center.

In summary, each breast thermogram is thus described by the following set of features: four basic statistical features, four moment features, eight histogram features, eight cross co-occurrence features, mutual information, and two Fourier descriptors. We further apply a Laplacian filter to enhance the contrast and calculate another subset of features (the eight cross co-occurrence features together with mutual information and the two Fourier descriptors) from the resulting images. In total, we hence end up with 38 descriptors per breast thermogram that describe the asymmetry between the two sides.

10.3 Fuzzy Rule-based Classification

10.3.1 Classification algorithm

Pattern classification typically is a supervised process where, based on a set of training samples, a classifier is derived that automatically assigns unseen data samples to the predefined classes. Let us assume that our pattern classification problem is an n-dimensional problem with C classes (for the purpose of breast cancer diagnosis, $C = 2$) and m given training patterns $\mathbf{x}_p = (x_{p1}, x_{p2}, \ldots, x_{pn})$, $p = 1, 2, \ldots, m$. Without loss of generality, we assume each attribute of the given training patterns to be normalized into the unit interval [0, 1]; that is, the pattern space is an n-dimensional unit hypercube $[0, 1]^n$. We use fuzzy if-then rules of the form

$$\begin{aligned} &\text{Rule } R_j\text{: If } x_1 \text{ is } A_{j1} \text{ and } \ldots \text{ and } x_n \text{ is } A_{jn} \\ &\text{then Class } C_j \text{ with } CF_j, \quad j = 1, 2, \ldots, N, \end{aligned} \tag{10.1}$$

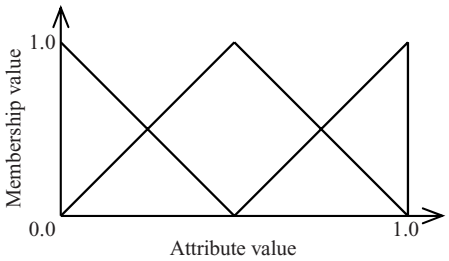

Figure 10.1 Triangular fuzzy membership partitions.

where R_j is the label of the j-th rule, $A_{j1}, \ldots, A_{jn}$ are antecedent fuzzy sets on the unit interval [0, 1], C_j is the consequent class (i.e., one of the C given classes), and CF_j is the grade of certainty. As antecedent fuzzy sets, we use triangular fuzzy sets as shown in Fig. 10.1.

Our fuzzy rule-based classification system consists of N fuzzy if-then rules. There are two steps in the generation of fuzzy if-then rules: specification of antecedent part and determination of consequent class C_j and the grade of certainty CF_j. The antecedent part of a rule is specified manually. Then, the consequent part (i.e., consequent class and grade of certainty) is determined from the given training patterns.[12] It has been shown that the use of the grade of certainty in fuzzy if-then rules allows us to generate comprehensible fuzzy rule-based classification systems with high classification performance.[13]

Let us assume that m training patterns $\mathbf{x}_p = (x_{p1}, \ldots, x_{pn})$, $p = 1, \ldots, m$, are given for an n-dimensional C-class pattern classification problem. The consequent part of the rule is determined by calculating $\beta_{\text{Class } h}(j)$ for class h as

$$\beta_{\text{Class } h}(j) = \sum_{\mathbf{x}_p \in \text{Class } h} \mu_j(\mathrm{x}_p), \tag{10.2}$$

where

$$\mu_j(\mathbf{x}_p) = \mu_{j1}(x_{p1}) \cdots \mu_{jn}(x_{pn}), \tag{10.3}$$

and $\mu_{jn}(\cdot)$ is the membership function of the fuzzy set A_{jn}.

Then, we find the class $\hat{h}$ that has the maximum value of $\beta_{\text{Class } h}(j)$:

$$\beta_{\text{Class } \hat{h}}(j) = \max_{1 \le k \le C} \{\beta_{\text{Class } k}(j)\}. \tag{10.4}$$

The grade of certainty CF_j is determined as

$$CF_j = \frac{\beta_{\text{Class } \hat{h}}(j) - \overline{\beta}}{\sum_h \beta_{\text{Class } h}(j)} \tag{10.5}$$

with

$$\overline{\beta} = \frac{\sum_{h \neq \hat{h}} \beta_{\text{Class } h}(j)}{C - 1}. \tag{10.6}$$

Using this procedure, we can generate N fuzzy if-then rules as in Eq. 10.1.[1] After both the consequent class C_j and the grade of certainty CF_j are determined for all N rules, a new pattern $\mathbf{x} = (x_1, \ldots, x_n)$ can be classified by calculating $\alpha_{\text{Class } h}(\mathbf{x})$ for Class h, $j = 1, \ldots, C$, as

$$\alpha_{\text{Class } h}(\mathbf{x}) = \max\left\{\mu_j(\mathbf{x}) \cdot CF_j | C_j = h\right\}, \tag{10.7}$$

and finding the class h' that has the maximum value of $\alpha_{\text{Class } h}(x)$:

$$\alpha_{\text{Class } h'}(\mathbf{x}) = \max_{1 \leq k \leq C}\left\{\alpha_{\text{Class } k}(\mathbf{x})\right\}. \tag{10.8}$$

It is well known that any type of rule-based system suffers from the course of dimensionality. Our fuzzy rule-based classifier is no exception, in particular, considering the variety of features we are using as input. In our approach, we therefore employ a genetic algorithm that evolves a rule base to select a fixed, small number of rules without sacrificing classification performance.[14] We also apply a cost term in the classification rules to be able to put more emphasis on correctly identifying maligant cases.[15]

10.3.2 Experimental results

For our experiments, we utilized a dataset of 146 thermograms of which 29 cases have been confirmed as malignant, whereas the other 117 cases were benign. This is the same dataset that was used in Ref. 11 and is significantly larger than those used in other studies (e.g. Ref. 9). For all thermogram pairs, we extracted the 38 features described in Section 10.2.

The best results, based on standard 10-fold cross validation (where the data are split into 10 disjoint sets and the classification performance of one such set based on training the classifier with the remaining 90% of samples is evaluated in turn for all 10 combinations), were obtained using a set of

20 rules and 12 fuzzy partitions per attribute. Using this configuration, a classification accuracy of 80.89% was achieved, which is similar to that obtained by other imaging modalities.[11]

10.4 Ant Colony Optimization Classification

10.4.1 Classification algorithm

Ant colony optimization (ACO)[16] is a relatively recent computational intelligence paradigm that is inspired by the collective behavior of natural ants. In ant colonies, each individual ant performs its own task independently, yet the various individual tasks are related, and through collaboration it is possible to solve complex problems. In particular, ants are capable of finding the shortest path between their nest and a food source based only on local information. They are furthermore capable of adapting to changes in the environment. To achieve this, ants communicate with each other by means of pheromone trails. Ants leave pheromone as they move around in the environment, while other ants can follow pheromone paths. Therefore, the more ants follow a certain trail, the more attractive this trail becomes to other ants, hence leading to the equivalent of a positive feedback loop where the probability of following a certain path is proportional to its 'quality.'

Ant colony optimization can also be employed for pattern classification as has been shown in Ref. 17 with the introduction of the Ant-Miner algorithm. The basic idea is to perform classification using a rule base and to optimize this rule base through ACO. In Ant-Miner, each path constructed by an ant represents one rule of the rule base. Each such rule has the form

```
IF <term1 AND term2 AND ...>
THEN <class>
```

with each term being defined by a triple

```
<attribute, operator, value>
```

such as <Day = Monday> and class representing the consequent class, i.e., one of a set of predefined categories.

Algorithm 1 presents a high-level overview of the Ant-Miner algorithm. Ant-Miner starts with an empty rule base and successively adds rules one by one. To construct a new rule, an ant is initialized with an empty rule (i.e., no terms in the antecedent part), and one term is added at a time to the antecedent. Terms are added until a term would cause the rule to cover fewer than a preset number of training samples, or all possible attributes have been added. Once the rule has been constructed, a pruning step is applied to remove any irrelevant terms. Then, the consequent class of the rule is determined as the most frequent class of the covered training

```
Initialize training set
Reset rule base
repeat
  Initialize all paths
  repeat
    Use ant to construct a rule
    Prune rule
    Determine consequent class of rule
    Update pheromones
  until (stopping criterion)
  Select best rule from constructed rules
  Add selected rule to rule base
  Eliminate training samples covered by selected rule
until (stopping criterion)
```

Algorithm 1 Pseudo-code of the Ant-Miner algorithm.

samples. Rule construction is continued until a predefined number of rules has been built or an already existing rule is recreated. Of the created rules, the best one is chosen based on a quality measure that is often defined as the product of sensitivity and specificity. This rule is then added to the rule base, and the process is repeated until all but a predefined number of training samples are covered by the rule base.

While Ant-Miner has been shown to provide good classification performance coupled with a compact rule base,[17] one downside of the algorithm is that it is only capable of processing nominal data, i.e., data that can be described by a finite number of nominal or discrete values. Therefore, as such, it cannot be applied to handle continuous numerical data directly. The only way to cope with continuous data is hence to discretize them in a preprocessing step, e.g., using the C4.5-Disc method.[18]

The *c*Ant-Miner algorithm[19] takes a different, integrated approach to ant-based classification. Discrete intervals are created on-the-fly, and hence no preprocessing step is required. This dynamic discretization is directly incorporated into the rule-construction stage of the Ant-Miner algorithm and consequently supports also terms that include $<$ and $\geq$ operators. The discretization itself is based on an entropy measure that describes the impurity of a collection of samples.

10.4.2 Experimental results

We utilize the same dataset as in Section 10.3.2, employing the *c*Ant-Miner algorithm and using all 38 features of each thermogram. We use 2000 ants for rule construction; the minimum number of samples covered per rule was set to 3, the maximum number of uncovered training samples to 3, and the number of rules used for testing convergence was set to 5.

The achieved classification performance, based on 10-fold cross validation, using this approach was 79.52%. Although this does not quite match the performance of the fuzzy classifier, the rule bases of the ACO approach prove to be much more compact compared to the fuzzy rule bases. On average, the ACO classifier generated a rule base of only 7 rules (each with on average only 2 attributes), compared to the 20 rules of the fuzzy classification system.

10.5 Conclusions

In this chapter, we have presented a computer-aided diagnostic (CAD) approach to the analysis of breast thermograms with the aim of identifying malignant cases. For this, we extract a number of image features from the thermograms to describe the bilateral differences of regions of interest of both breasts. These features are then used in a pattern classification stage. We have presented two different rule-based approaches for this purpose. The first employs fuzzy if-then rules coupled with genetic algorithms to generate a rule base, while the second uses an ant colony optimization algorithm to add rules to a rule base. Both approaches were shown to give good classification performance on a large dataset of breast thermograms.

Acknowledgments

The author would like to acknowledge Tomoharu Nakashima of Osaka Prefecture University and Michal Zavisek of Brno Technical University with whom much of the work presented in this chapter was conducted.

References

1. American Cancer Society, “Cancer Facts and Figures,” http://www.cancer.org/docroot/STT/stt_0.asp.
2. N. Anbar, L. Milescu, A. Naumov, C. Brown, T. Button, C. Carly, and K. AlDulaimi, “Detection of cancerous breasts by dynamic area telethermometry,” *IEEE Eng. Med. Biol. Mag*. **20**(5), 80–91 (2001).
3. J. F. Head, F. Wang, C. A. Lipari, and R. L. Elliott, “The important role of infrared imaging in breast cancer,” *IEEE Eng. Med. Biol. Mag*. **19**, 52–57 (2000).
4. M. Gautherie, “Thermobiological assessment of benign and malignant breast diseases,” *Am. J. Obstet. Gynecol*. **147**(8), 861–869 (1983).
5. B. F. Jones, “A reappraisal of infrared thermal image analysis for medicine,” *IEEE Trans. Medical Imaging* **17**(6), 1019–1027 (1998).

6. J. R. Keyserlingk, P. D. Ahlgren, E. Yu, N. Belliveau, and M. Yassa, "Functional infrared imaging of the breast," *IEEE Eng. Med. Biol. Mag*. **19**(3), 30–41 (2000).
7. G. Schaefer, M. Zavisek, and T. Nakashima, "Thermography based breast cancer analysis using statistical features and fuzzy classification," *Pattern Recog*. **42**(6), 1133–1137 (2009).
8. G. Schaefer, "Ant colony classification for analysis of image features in breast thermograms," *Proc. IPVV 2009,* 81–888 (2009).
9. H. Qi, W. E. Snyder, J. F. Head, and R. L. Elliott, "Detecting breast cancer from infrared images by asymmetry analysis," *22nd IEEE Int. Conference on Engineering in Medicine and Biology*, 1227–1228 (2000).
10. R. M. Haralick, "Statistical and structural approaches to texture," *Proc. IEEE* **67**(5), 786–804 (1979).
11. M. Zavisek and A. Drastich, "Thermogram classification in breast cancer detection," *The 3rd European Medical and Biological Engineering Conference*, 1727–1983 (2005).
12. H. Ishibuchi, K. Nozaki, and H. Tanaka, "Distributed representation of fuzzy rules and its application to pattern classification," *Fuzzy Sets and Systems* **52**(1), 21–32 (1992).
13. H. Ishibuchi and T. Nakashima, "Effect of rule weights in fuzzy rule based classification systems," *IEEE Trans. Fuzzy Systems* **9**(4), 506–515 (2001).
14. G. Schaefer, T. Nakashima, and M. Zavisek, "Analysis of breast thermograms based on statistical image features and hybrid fuzzy classification," *Int. Symposium on Visual Computing*, *Springer Lecture Notes on Computer Science* **5358**, 753–762 (2008).
15. T. Nakashima, Y. Yokota, H. Ishibuchi, G. Schaefer, A. Drastich, and M. Zavisek, "Constructing cost-sensitive fuzzy rule-based classification systems for pattern classification problems," *J. Advanced Comput. Intell. Intelligent Informatics* **11**(6), 546–553 (2007).
16. M. Dorigo and T. Stuetzle, *Ant Colony Optimization*, MIT Press, Cambridge, MA (2004).
17. R. S. Parpinelli, H. S. Lopes, and A. A. Freitas, "Data mining with an ant colony optimization algorithm," *IEEE Trans. Evolutionary Comput*. **6**(4), 321–332 (2002).
18. R. Kovahi and M. Sahami, "Error-based and entropy-based discretization of continuous features," *2nd Int. Conference on Knowledge Discovery and Data Mining*, 114–119 (1996).

19. F. E. B. Otero, A. A. Freitas, and C. G. Johnson, "cAnt-Miner: An ant colony classification algorithm to cope with continuous attributes," *ANTS '08: Proc. 6th Int. Conference on Ant Colony Optimization and Swarm Intelligence*, Springer-Verlag Berlin Heidelberg, pp. 48–59 (2008).

Gerald Schaefer gained his Ph.D. in Computer Vision from the University of East Anglia, United Kingdom. He worked at the Colour & Imaging Institute, University of Derby (1997-1999), in the School of Information Systems, University of East Anglia (2000-2001), in the School of Computing and Informatics at Nottingham Trent University (2001-2006), and in the School of Engineering and Applied Science at Aston University (2006-2009) before joining the Department of Computer Science at Loughborough University where he leads the Vision, Imaging and Autonomous Systems Research Division.

His research interests are mainly in the areas of color image analysis, image retrieval, physics-based vision, medical imaging, and computational intelligence. He has published extensively in these areas with a total publication count exceeding 300. He has been invited as keynote or tutorial speaker to numerous conferences, is the organizer of various international workshops and special sessions at conferences, and the editor of several books, conference proceedings, and special journal issues. He is a member of the editorial board of more than 10 international journals, reviews for more than 80 journals, and served on the program committee of more than 200 conferences.

Chapter 11
Infrared Imaging for Breast Cancer Detection with Proper Selection of Properties: From Acquisition Protocol to Numerical Simulation

Luciete A. Bezerra, Marília M. Oliveira, Marcus C. Araújo, Mariana J. A. Viana, Ladjane C. Santos, Francisco G. S. Santos, Tiago L. Rolim, Paulo R. M. Lyra, and Rita C. F. Lima
Mechanical Engineering Department, Federal University of Pernambuco, Pernambuco, Brazil

Tiago B. Borschartt, Roger Resmini, and Aura Conci
Computer Science Department, Fluminense Federal University, Rio de Janeiro, Brazil

11.1 Introduction

Infrared (IR) imaging has been shown to be a promising technique for the early diagnosis of breast pathologies and as a screening technique before any symptoms occur. The concept of a combined diagnostic enables a high degree of specificity and sensibility in such diagnosis. An abnormal thermogram is reported as a significant biological risk marker for the existence or development of breast diseases. Some authors state that thermography may have the potential to detect breast cancer ten years earlier than the traditional golden method: mammography. Moreover, according to some authors, whenever the breast is exposed to x-ray radiation, the risk of cancer increases by 2%.

In the last ten years, the use of IR images in medical applications and diagnosis has advanced greatly.[1] Part of this is due to infrared cameras being more accurate. On the other side, significant efforts have been made to advance the medical community's acceptance of this technology. There remain important issues, such as: standardization, wider publication, using an iterative web-based database, and acquiring and interpreting precise images, all of which should be improved in order to reach this goal.[1] In this chapter, some of these aspects are examined, and their results presented a contribution toward achieving better results in such issues. All of the 3D numerical simulations that were run aim to reach a better understanding of breast abnormalities and to learn more about how the use of IR images can validate such calculations. Finally, all of the approaches were used to perform a preliminary estimate of several physical breast and tumor parameters.

This study forms part of a research project to prove the feasibility of using IR as screening exams in a tropical country. The main purpose is to merge information from these images with other modalities of examination, such as mammograms and ultrasound, in order to improve the early detection of breast pathologies, including cancer. The images from this ongoing project are being acquired using a FLIR THERMACAM S45 at the Hospital das Clínicas of the Federal University of Pernambuco (HC-UFPE). The project was registered in the Brazilian Health Ministry (CEP/CCS/UFPE N°279/05) after being previously approved by the Ethics

Committee of UFPE. The images acquired are available (on request) on a public database at http://150.161.110.168/termo.

This chapter is organized into three further sections. Section 11.2 details the general concepts involving clinical decision support systems and computer-aided diagnosis from image acquisition to the techniques related to automatic design based on the diagnosis by image. Section 11.3 presents the several techniques that were developed for use in the numerical simulation proposed. Section 11.4 draws some conclusions and lists further studies that are in progress and are being designed.

11.2 Computer-Aided Diagnosis

Clinical decision support systems (CDSSs) have been designed to assist physicians in applying new information to patient care by analyzing their specific clinical variables.[2,3] CDSSs are computational systems designed to support high-level cognitive functions involving medical tasks.[4] According to the Agency for Healthcare Research and Quality (AHRQ), there is great potential for improving health care quality, increasing efficiency, and reducing health care costs.[5] There are pieces of evidence that suggest that CDSSs are effective in preventing medical errors. These systems may be most practical when coupled with a computerized physician order entry (CPOE) system and electronic health records (EHRs). Figure 11.1 depicts an overview of the CDSS architecture. Systems applied to classify individuals with or without disease are usually referred to as computer-aided diagnosis (CAD) systems.[6] The data that are input into CAD systems are usually medical images, e.g., magnetic resonance images (MRI), computed tomography (CT), and single-photon emission computed tomography (SPECT). This data input process involves an image segmentation algorithm to extract the features of the images, either

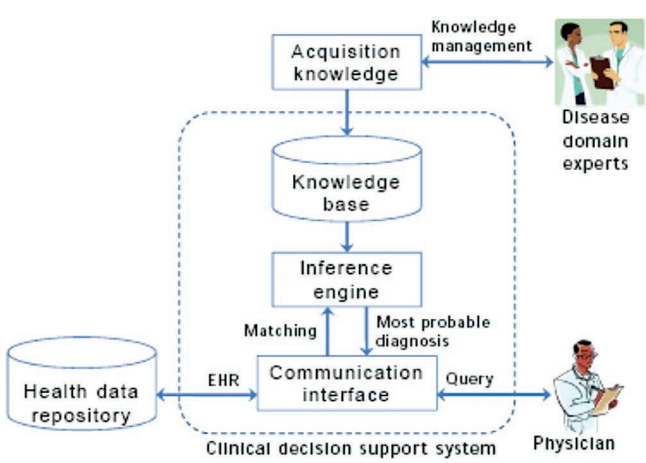

Figure 11.1 Overview of the CDSS architecture.

automatically or semi-automatically. Beyond extracting these features, some kind of artificial intelligence (AI) methodology, such as machine learning and classification algorithms, must be used to classify the patient images as normal or as presenting a specific type of disease. This section aims to discuss our proposition for a CAD using IR for the diagnosis of breast pathologies.

11.2.1 Standardization in acquiring IR breast images

For medical applications, especially when automatic analyses are considered, it is very important that well-positioned images are acquired and that a standardized protocol is used. For this purpose, an apparatus was designed and a protocol for acquisition was generated.[7] This protocol is being used in the breast thermographic exams of the Hospital das Clinicas (HC) of the Federal University of Pernambuco (UFPE), Brazil. A computer program was used to design this project, the apparatus of which is illustrated in Fig. 11.2.

11.2.1.1 The mechanical apparatus

Standardizing thermographic images during acquisition is required to obtain reliable temperature measurements. This would enable further automatic image processing and numerical simulations to be conducted. Digital images are stored in pixels, and transforming them into a reference unit of length is needed. Therefore, an additional IR image is captured using a metallic grid. From a combination of a series of such images (see Fig. 11.3), it is possible to convert pixels to a metric system and to obtain the real size of the breasts. Additionally, the patient should be located at a well-known distance from the camera. A detailed description of the images shown in Fig. 11.3 is given in the protocol description in Section 11.2.1.2.

The apparatus project took into account some features such as the distance between the IR camera and the patient, the positioning of the patient's

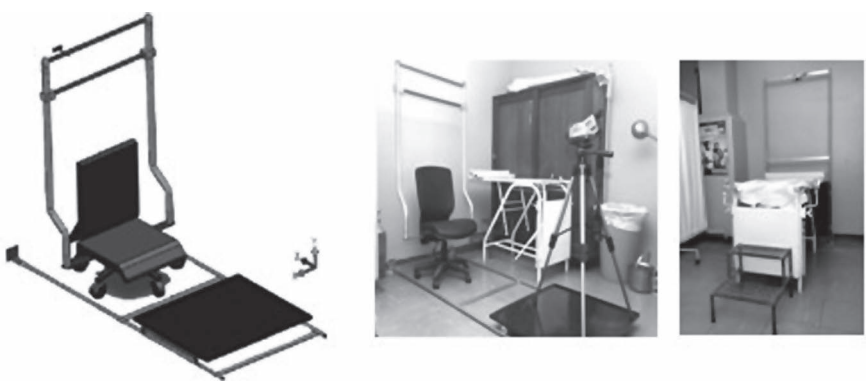

(a) (b) (c)

Figure 11.2 (a) Apparatus assembly, (b) rails on the floor (during the exams), and (c) rails folded on the wall (when no exams are being performed).

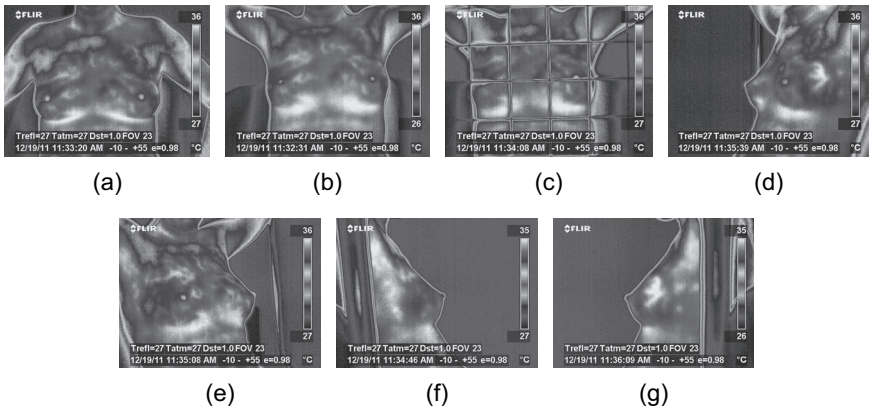

Figure 11.3 Example of D1 series images for a fixed distance of 89 cm: (a) T1, (b) T2, (c) T2 using a metallic grid, (d) LIMD, (e) LIME, (f) LEMD, and (g) LEME.

arms, and the patient being in a comfortable and ergonomic position. The size and the weight of the apparatus were analyzed so that it would fit into the space where it must be installed. This apparatus consists of two rails (see Fig. 11.2) used for the displacement of a small carriage that supports the tripod, which is attached to the IR camera. A support for the patient's arms made of steel, aluminum, and wood was fitted to a swivel chair. This support has a movable horizontal bar projected to move up and down. The bar is used to position the patient's hands and allows four different positions so as to comfortably accommodate patients of different heights. In the lower structure of this chair, two aluminum pipes were placed vertically. To prevent great interference when side-view thermograph images are to be taken, the pipes are folded backwards.

As patients have different biotypes, the camera–patient distance changes for each patient. This distance is measured with a measuring tape fixed in the chair that can be extended to the carriage, to which it can be attached using magnets. Since the movement of the camera takes place above the carriage, constancy in the distance while the image is being acquired is ensured. Moreover, the possibility of displacing the carriage allows for better agility during image acquisition. The rails were projected to allow them to be attached to the wall when they are not being used. So, when the exams are being performed, they are lowered onto the floor, as shown in Fig. 11.2(b). Due to this flexibility, the room can be freely used for other purposes.

11.2.1.2 Protocol

The protocol presented here is being used in HC/UFPE and was drawn up based on information found in the literature[1,8–18] and on the six years of experience of the Thermal Engineering Group (TEG) of UFPE.[7,19–22] It comprises three main topics that are described on the following pages.

Making the room suitable. In relation to the environment where the thermographic exams will be conducted, it is suggested that: (1) The room used should measure around 3 × 4 square meters. There must be sufficient space for the patient, the technical team, and the IR camera apparatus. (2) The people flow in and out of the room is controlled by the technical group. Only those responsible for the exam and the patient must stay in the room. (3) An air-conditioning device is responsible for the environmental conditions. (4) The room temperature and the relative humidity must be measured by a thermohygrometer. (5) In HC/UFPE, the temperature normally varies between 24 °C and 28 °C and the relative humidity ranges from 54% to 70%. (6) Fluorescent lamps are available in the room, although daylight is used whenever possible. (7) The major sources of heat inside the room are the technical team, the patient, and a multimedia projector used to explain the exam to the patient. This latter item also helps everyone in the team to support the camera operator to acquire the best possible images. (8) The room has a reserved space in which the patient dresses and undresses. This space is separated by a folding screen. (9) The mechanical apparatus used for the examination is also positioned in this section of the room. (10) The computational equipment is located in a separate part of the room.

Preparing the patient. The out-patient procedures that the patient follows before the thermographic exam require her to stay away from sunshine for at least two hours, without drinking and eating, and without taking a shower. Patients also need to sign an agreement form to participate in the research as this is required by the Ministry of Health of Brazil. During the medical appointment, the physician conducts the patient's anamnesis by asking about and recording her medical history and current complaints. The technical team keeps a copy of the anamnesis, the ultrasonography and the mammography reports, if the patient has them available.

The physician directs the patient to the thermographic examination room, where, at first, she receives explanations about the exam. The patient receives a disposable gown to be used to cover the upper body and rests for about ten minutes, without touching her breasts. This is the time interval needed for the metabolic heat emitted by the body to decrease and also for the body temperature to reach thermal equilibrium with the environment. During this time, her body temperature is measured with a clinical thermometer.

Image acquisition. The images are acquired using a FLIR THERMACAM S45, which has a field of view of 24 deg × 18 deg/0.3 m, a spatial resolution of 1.3 mrad, a detector of the focal plane array (FPA) type, an uncooled microbolometer, and 320 × 240 pixels; a spectral range of 7.5–13 μm; the temperature range was between –10 °C and +55 °C, with an accuracy of +/–1% of the reading.[23] Periodically, the thermographic camera is checked by a blackbody emitter for calibration purposes.[24] Also it is periodically calibrated by the manufacturer. Before the technical team performs the examinations, the

camera is initialized and some parameters are set. The emissivity is set to 0.98 (emissivity of the human skin[25]); the reflected temperature and the camera–patient distance is measured and updated for each patient.

Two image series[7] are performed. In the first (D1), with a fixed distance, the camera is positioned farthest from the patient. This distance will depend on the patient's anatomy and is adjusted such that frontal images of both breasts are possible. Series D1 is used for automatic image processing; standardized image acquisition is required for this series. In the second series (D2), which uses a variable distance, the camera is placed closer to the patient, and the distance used for several image acquirements can vary. The D2 series is more important for medical analysis and visualization, and for detailed analysis. Standardization is not required for this series.

In the first series with a D1 distance, seven images are taken (Fig. 11.3). One image of both breasts (T1) is taken, with the patient keeping her hands on her waist. The other images are taken with the hands on the apparatus bar. The acquired images are: a front image of both breasts (T2), the inner side of the right breast (LIMD), the inner side of the left breast (LIME), the outer side of the right breast (LEMD), the outer side of the left breast (LEME), and a T2 image with a metallic grid placed in front of the patient's breasts, without touching them. This last image is needed to calculate the approximate breast dimensions using the size of the grid and the camera-patient distance.

In the D2 series, five images are acquired, as described above. With the patient's hands put on her waist, two different images from the series D1 are taken: the image of the right breast (MD), another of the left breast (ME). Next, another T2 image is taken, with her hands on the apparatus bar, followed by other LEMD and LEME images. In both series, some extra images can be acquired for better visualization of any possible suspicious tumor and/or cyst.

After the images are acquired, they are archived in a database.[19,26] They are then ready to be interpreted by making comparisons against ultrasound and mammographic exams. Also, they are ready to be used in automatic image processing and in numerical simulations.

11.2.2 Data storage

This section introduces the database model that supports the research on breast cancer presented in this chapter. The database was designed to record the sequence of information from patients and the events necessary to obtain the thermographic images. The patient's electronic record is presented as a research application with its functionalities and modeling. One of its roles is to work as a tool for the CDSS.

11.2.2.1 Database system

A database system is basically a computerized data manager that allows users to view and, depending on their database hierarchy, to modify the

information stored.[27] Computational tools have made it possible to collect and analyze large amounts of data and have contributed to improvements in health care.[28] Large clinical databases form the basis for statistical studies such as the analysis of statistical patterns and classification rules. The main aim when developing a database system is to permanently store the maximum amount of information by grouping data used for the same purpose.

11.2.2.2 Patient's electronic record for research application

An electronic patient record stores and shares the information on a patient's health, thus speeding up clinical communication. It is a single document that systematically documents and categorizes medical information, medical images, and medical findings on a particular patient.

Today, a patient's record integrates clinical, financial, and decision support information about a patient inside a hospital.[29] As stated by the Institute of Medicine,[30] the basic functionalities of a patient medical record or patient health record are: health information and data, results management, entry order or management, decision support, electronic communication and connectivity, patient support, administrative processes, and reporting and population health management.

As a patient's medical information can be exchanged by physicians and hospitals, there was a need to create a standard to guarantee that all data transmitted could be read by any system. This is why Health Level 7 (HL7) was created. The HL7 standard is a specification for information exchange between medical applications, including a protocol for data exchange.[31] For research purposes, a patient's medical record may be simplified according to the needs of the research.

Figure 11.4 shows the database functionalities, and Fig. 11.5 shows a summarized representation of the data as a simplified entity relationship diagram of a research database. Fields were created to capture the patient's current treatment, health history (including family health history), environmental factors, and clinical examination results, as well as other image results such as mammography and ultrasound findings.

Figure 11.4 Research workflow.

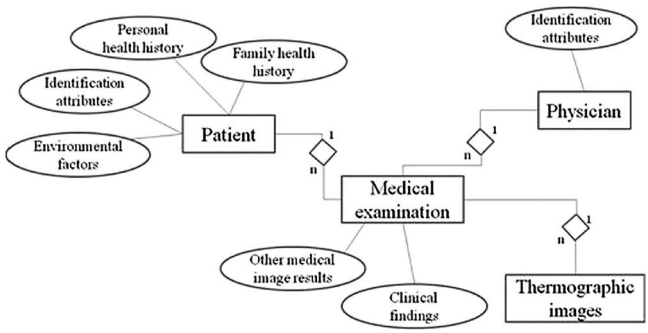

Figure 11.5 Entity relationship diagram.

11.2.2.3 Research workflow (clinical workflow)

The database was designed to accommodate the sequence of events that occurs when a patient enters the physician's office. A profile of the clinical workflow is:

(1) The physician interviews the patient and records the patient's historical data.
(2) The physician performs a clinical examination and records the findings.
(3) If are there other exam results (such as mammography and ultrasound), these are carefully annexed to the patient's data records.
(4) A technician explains the thermographic procedure, obtains a signed consent form from the patient, and takes the IR images.
(5) All data obtained are added to the database by a researcher.

11.2.2.4 Description of the database system

The system developed for this project runs on software written in PHP (hypertext preprocessor) embedded in HTML (hyper text markup language) code, connected with an Oracle database as an object-relational database (ORD).

ORDs add the advantages of both the relational-data model and the object-oriented (OO) model. This is similar to a relational-data model in which the inner structures such as relations or tables are allocated with rows and columns, but which supports custom data types and several OO structural features. This document can be split into different fields: patient identification, patient's complaint, patient's health history, environmental risks, and clinical results.

The database registers the medical conclusions, the thermographic images, the room conditions (temperature and humidity) during image acquisition, the mammographic or ultrasound findings, the patient's complaint, and other

patient medical information needed for the research. The database can be seen at http://150.161.110.168/termo (in Portuguese).

11.2.3 Breast segmentation

In image processing, segmentation is known as the separation of structures of interest from their background.[32] The segmentation of a medical image is the stage in which a large effort is made to delineate the structures and discriminate them from the background.[32] During the processing of thermal images, extracting features and mining data depend strongly on the correct segmentation of the object studied.

Many papers focus on an automatic segmentation of the breast. In mammograms, this kind of segmentation avoids human error when manual selection becomes difficult or imprecise.[33] There are several ways to perform automatic segmentation, including *edge-based* techniques, *threshold-based* techniques and *region-based* techniques.[32] Semi-automatic or manual techniques can be used when it is necessary to define the region of interest (ROI) with a physician's support and also when there is a need to obtain the whole area of the breast.

The goal is to select the full area of the breast as closely as possible to the real area, in the thermal image. Correct segmentation of the breast is extremely important for later comparison and for subsequent numerical simulation and texture mapping.

The main objective of the manual segmentation presented is, by using a simple tool, to avoid the errors that can arise due to the natural asymmetry of the human body when only automatic segmentation is used. An important aspect is the use of a temperature matrix instead of the pixel colors, as commented on in the topic that follows.

11.2.3.1 Representation of the IR image

The digital image representation of a thermogram may be defined as a 3D function $f(x, y, T)$, where x and y denote spatial (plane) coordinates and T, the temperature value at that point. Although it can be seen as an $M \times N \times 3$ array of color pixels (RGB—red, green, blue representation) by some commercial image processing software programs, it is an *indexed* image that has two components: a temperature matrix **T** and a color map matrix. This temperature matrix can be obtained by using a proprietary software of the FLIR Infrared System Company. The thermally indexed image uses the value of the temperature matrix as a pointer into the color map for each pixel in the image.[34] Therefore, the color for each pixel in the image depends on the color map applied (pallette) and on the thresholds defined by the temperature scale for each image. Thus, in IR images, the color representation can change, while the temperatures of an image remain the same. Figure 11.6 depicts a thermogram viewed by three different

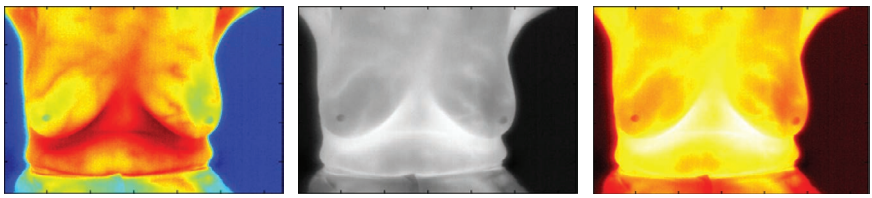

(a) (b) (c)

Figure 11.6 Different color maps of the same thermographic image on a fixed temperature scale: (a) rainbow, (b) grayscale, and (c) iron.

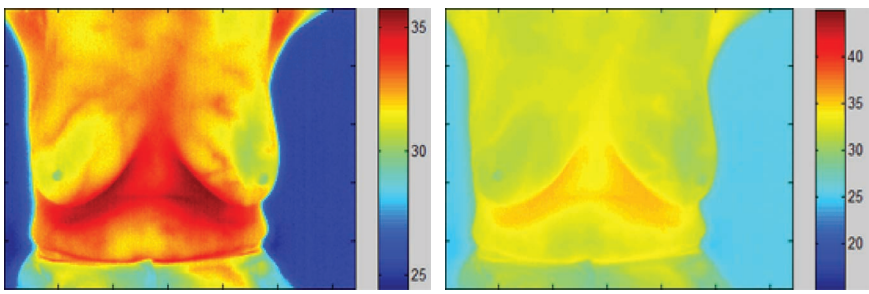

(a) (b)

Figure 11.7 Different temperature scales of the same IR image in a fixed-color map: (a) 20–38 °C and (b) 15–45 °C.

pallettes, and Fig. 11.7 shows the variation in color in the same image by varying the temperature scale. In both Figs. 11.6 and 11.7, the temperature matrix remains the same.

11.2.3.2 Manual segmentation based on a temperature matrix

The temperature matrix of the thermally indexed image can be obtained from the proprietary software ThermaCAM Quick Report and referred to and converted into a spreadsheet or a text format. Image processing based on temperature information instead of pixel intensity brings some advantages to the thermographic analysis, either for manual or automatic processing.

Based on these considerations, the process that was chosen for segmentation of the breast consists of using ellipsoidal elements for selecting the area itself. The interest was to obtain the whole area of the breasts, without including the thorax area, enabling thermography to be used for further correlation with thermal numerical simulation and other techniques such as texture mapping. To proceed with the segmentation, ellipses were adjusted to the breasts of two women, as shown in Fig. 11.8. This is done by manually adjusting the diameters of the ellipses. For this purpose, a young woman and a middle-aged woman were selected.

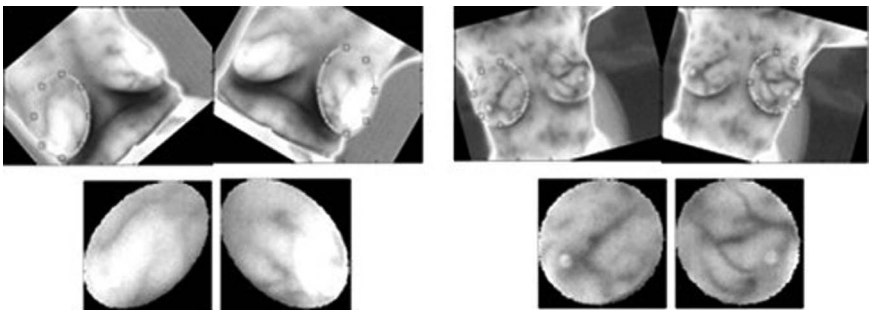

Figure 11.8 Manual segmentation of the breasts.

11.2.4 Extracting features

Texture is an important visual attribute present in an image. It enables regions to be distinguished from each other and contributes to the process of recognizing patterns, and analyzing, describing, and classifying digital images. Because of its ability to model complex elements, fractal geometry (FG) is one of the most widely used approaches in pattern recognition by texture analysis.[35]

FG had been used to link each texture to numerical measures. By having such measures, textures can be classified. In the experiments conducted using fractal features, three measures are extracted from the ROIs: the Hurst coefficient,[36] lacunarity,[37–39] and the Higuchi fractal dimension.

The Hurst coefficient is related to the density of the image, that is, how much space the image occupies in the frame. There are various applications of the Hurst coefficient, including: image classification, wear and erosion, detecting spectral bands of noise, corrosion, analyzing the diversity of the landscape, analyzing fractured surfaces, determining the roughness of a surface, determining the operational scale of natural phenomena in digital imaging, scaling applied to spatial extensions in remote sensing, distinguishing between landscape types, and analyzing the effects of converting data into geographical information systems.

The Hurst coefficient is used in two ways. Initially, the images of the right and left breast are screened (pixel by pixel for each column and row of the image) using a movable window that computes the Hurst coefficient values. Each image is characterized by various Hurst coefficient values depending on the window size w. Then, the average and standard deviation of the Hurst coefficient for each w is used for forming the first four characteristics used on our feature vector. Six different sizes of square windows ($w = 5, 7, 9, 11, 13, 15$ pixels) were used, so this first method provides 24 features. The second method employs the subtraction image of the breast. Then, the average and standard deviation of the Hurst coefficient for each window are used for

forming two other characteristics for the feature vector. Thus, the second method provides 12 features (2 features for each of 6 different windows). Therefore, the Hurst coefficient characterizes each thermal image with 36 features. Figure 11.9 summarizes the way these coefficients are used.

Lacunarity assesses the amount and distribution of gaps in an object. A high lacunarity is assigned to objects that have large gaps or holes. When the object under study is an image, greater variation in the distribution of image pixels means a high value is assigned to its lacunarity. Thus, a high value for lacunarity is associated with images that present a heterogeneous texture.[37]

A low value for lacunarity is associated with images in which the variation of the distribution of pixels is more homogeneous. Ninety seven other features were obtained from the lacunarity of the ROI. For this, the third coordinate (a temperature or grayscale) is used, and the images can be seen as a collection of voxels. Then, boxes of size s, $2 \leq s \leq 25$, are used to calculate the lacunarity; each box of size s is associated with a lacunarity value $\Lambda(s)$. Therefore, 24 lacunarity values are generated for each image (subtraction image, right breast, and left breast). The notations $\Lambda R(s)$ and $\Lambda L(s)$ are used for referring to the lacunarity values of the right and left breast, respectively. By calculating $|\Lambda R(s) - \Lambda L(s)|$, where $2 \leq s \leq 25$, 24 other features are generated. The last feature is extracted by calculating the standard deviations of $|\Lambda R(s) - \Lambda L(s)|$, where $2 \leq s \leq 25$.

Thus, this study proposes the use of the 72 features obtained from the lacunarity algorithm (24 features of each image), 24 other features obtained from $|\Lambda R(s) - \Lambda L(s)|$, where $2 \leq s \leq 25$, and another feature obtained by the standard deviation of $|\Lambda R(s) - \Lambda L(s)|$, where $2 \leq s \leq 25$. Figure 11.10 represents a scheme for lacunarity-based feature extraction.

The fractal dimension represents a measure of irregular geometries. The Higuchi form of this was used, with a view to finding some fractal pattern that describes the texture complexity of the IR thermal images.[40] The Higuchi fractal dimension[40] is used in measures of 1D signals.[41] Equation (11.1) shows how to compute the Higuchi coefficient:

$$l_m(k) = \frac{\sum_{i=1}^{\left\lfloor \frac{N-m}{k} \right\rfloor} \left| x(m+k) - x(m+(i-1)k \right| (N-1)}{\left\lfloor \frac{N-m}{k} \right\rfloor k}, \tag{11.1}$$

where k is the applied scale, N is the amount of data from x sequence, m is the sequence beginning at some k varying from 0 to –1, l_m is the sum of differences from the current data and the data from the prior k positions, and $(N-1)$ is the normalization of the sum.

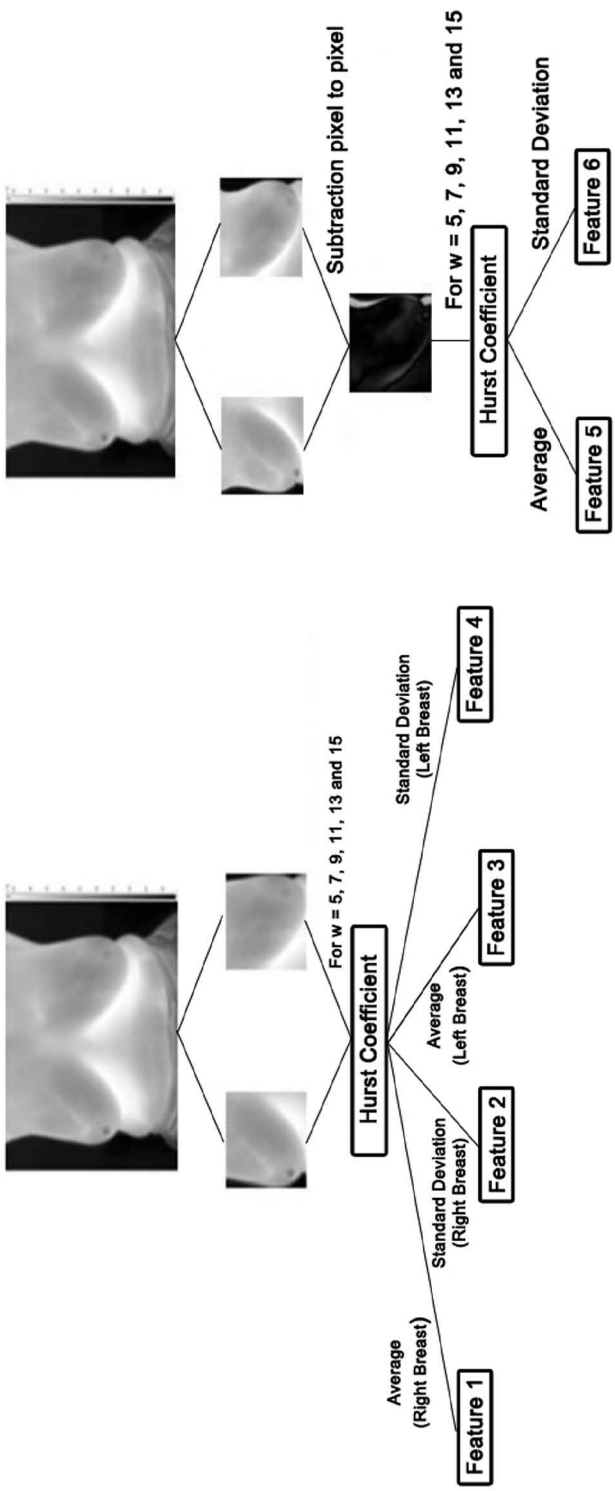

Figure 11.9 Features extracted based on the Hurst coefficient.

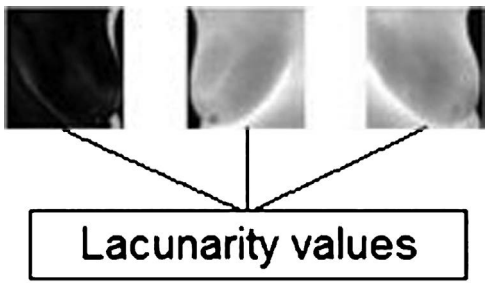

Figure 11.10 Steps of lacunarity-based feature extraction.

In the algorithm developed, the temperature matrix for each image quadrant was relocated line by line to a vector. To measure the fractal dimension, the algorithm must be run from several different image scales. Each scale represents the detail level from the analyzed signal. We applied five scales for each quadrant with the following values chosen by tests: 3, 5, 7, 9, and 11. These scale values were used for determining the window size so as to extract the fractal measurements.[41] Using this algorithm, forty features were extracted from each patient image.

Two other geostatistical features were used to extract 620 features: Moran's index and Geary's coefficient. Moran's index, [Eq. (11.2)], is a standard statistical measure to calculate spatial autocorrelation: If an event occurred in some location, it is probable that the same event will occur in neighboring regions.[42] Moran's index I is given as

$$I = \frac{N\sum_i \sum_j W_{ij}(X_i - \overline{X})(X_j - \overline{X})}{\left(\sum_i \sum_j W_{ij}\right)\sum_i (X_i - \overline{X})^2}, \tag{11.2}$$

where N is the number of occurrences (in this case N is the number of the pixels of the image), X_i and X_j are the positions of X in i and j coordinates, W is the weight of each coordinate in the image, and $\overline{X}$ is the mean value of the image.

Moran's index is not only dependent on the X values, but also on the spatial location (coordinates) of the data to be calculated for the weight W. This weight can vary between 0 and 1, and can be calculated in several ways. In this study, we calculate W using the inverse distance measure. However, Moran's index I can assume values between 1 and –1, depending on whether there is a low or high autocorrelation.

Geary's coefficient [Eq. (11.3)], is similar to Moran's index, but to calculate Geary's coefficient, it is not the standard deviation on the interaction

between i and j that is considered, but rather it is the value of each observation.[42] Geary's coefficient C gives values between 0 and 2 and is defined as

$$C = \frac{(N-1)\left[\sum_i \sum_j W_{ij}(X_i - X_j)^2\right]}{2\left(\sum_i \sum_j W_{ij}\right)\sum_i (X_i - \mathrm{X})^2}. \tag{11.3}$$

However, a value of 1 represents the case where there is no correlation among regions, and values of 0 or 2 represent cases where there is a negative or positive autocorrelation among regions, respectively. Moran's index extracts global information from the sample. On the other hand, Geary's coefficient extracts local information and perceives a larger number of small differences in the neighborhood.

Figure 11.11(a) shows an example of a pixel matrix highlighting the value named "delay" between the pixel X_i ("head") and pixel X_j ("tail"). The value of "delay" must be high or equal to 1. For this study, a total of 10 values for the "delay" variable were used. These values were defined by tests where each value was increased by 1 on each new iteration. Figure 11.11(b) shows the parameters used to calculate Geary's coefficient and Moran's index. All image pixels participate in the calculation. For each X_i, the pixels located on the "delay" parameter measurement for the iteration are counted. We chose 10 values to "delay" (from 1 to 10). There is another parameter, named "azimuth", i.e., the angle of inclination of the distance vector ("delay") in relation to the horizontal axis of the matrix. We chose four angles of "azimuth" values: 0, 45, 90, and 135 deg. These values determine the four directions to be calculated. "Delay" and "azimuth" have values of 0.45 and 22.50, respectively. Therefore, this algorithm extracts 320 features for each measurement.

Simple statistical features are considered as well. Four measures were used to extract a total of 40 features: mean, standard deviation, the quantization of

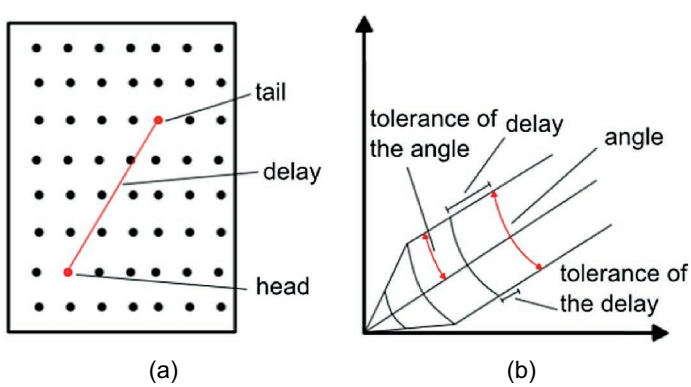

Figure 11.11 (a) Pixel matrix with (b) parameters for each pixel.

the last bin from the histogram in a posterization of 10 bins, and the range between the highest and the lowest temperature. These features are described by Borchartt et al.[43,44] Using these measurement types, eight features from each patient image were extracted.

11.2.5 Classification results

The images used in our experiments can be seen in the public database on the Visual Lab website.[45] We used two datasets: one with 28 "old" images: 24 images from patients with pathology, and 4 images from patients with no pathology; and the other with 34 "new" images: 24 images from patients with pathology, and 10 images from patients with no pathology. The images were segmented using a semi-automatic method, described in Section 11.2.3.2, in order to extract the ROI. Furthermore, the ROIs were divided into four quadrants of the same size.

As three FG measures are used in this approach, it is especially useful to verify that they are not correlated. In order to find out which features are the most suitable to describe the thermal images, the 133 features were divided into 14 groups as follows:

- Group 1: all 133 features;
- Group 2: all of the features extracted by the Hurst coefficient (36 features);
- Group 3: features $f = 1$, 2, 3, and 4 for $w = 5$, 7, 9, 11, 13, and 15 (24 features);
- Group 4: features $f = 2$ and 4 for $w = 5$, 7, 9, 11, 13, and 15 (12 features);
- Group 5: features $f = 1$ and 3 for $w = 5$, 7, 9, 11, 13, and 15 (12 features);
- Group 6: features $f = 5$ and 6 for $w = 5$, 7, 9, 11, 13, and 15 (12 features);
- Group 7: feature $f = 5$ for $w = 5$, 7, 9, 11, 13, and 15 (6 features);
- Group 8: feature $f = 6$ for $w = 5$, 7, 9, 11, 13, and 15 (6 features);
- Group 9: all of the features extracted by lacunarity (97 features);
- Group 10: $\Lambda R(s)$ and $\Lambda L(s)$ with $2 \leq s \leq 25$ (48 features);
- Group 11: $|\Lambda R(s) - \Lambda L(s)|$ with $2 \leq s \leq 25$ (24 features);
- Group 12: the standard deviation of $|\Lambda R(s) - \Lambda L(s)|$ with $2 \leq s \leq 25$ (1 feature);
- Group 13: the lacunarity $[\Lambda(s)]$ of image subtraction with $2 \leq s \leq 25$ (24 features); and
- Group 14: the features in Groups 12 and 13 (25 features).

These groups were used for classifying patients as those who were healthy and those with some possible disease. Then, machine learning techniques were used. The results obtained using the Hurst coefficient and lacunarity were evaluated using the receiver operating characteristic (ROC). Tables 11.1 and 11.2 present the best results for the groups considered.

Table 11.1 Results of Groups 1–6.

Techniques	G1	G2	G3	G4	G5	G6
Naïve Bayes simple	0.792	0.854	0.885	0.927	0.667	0.484
Classification via clustering	0.771	0.375	0.771	0.792	0.646	0.500
Naïve Bayes	0.708	0.875	0.927	0.958	0.667	0.490
Naïve Bayes updateable	0.708	0.875	0.927	0.958	0.667	0.490
Random committee	0.516	0.865	0.667	0.833	0.734	0.411
Non-nested generalized exemplars	0.500	0.500	0.479	0.458	0.750	0.500

Table 11.2 Results of Groups 7–14.

Techniques	G7	G8	G9	G10	G11	G12	G13	G14
Naïve Bayes simple	0.625	0.484	0.557	0.542	0.281	0.698	0.417	0.422
Classification via clustering	0.708	0.563	0.688	0.625	0.479	0.813	0.417	0.438
Naïve Bayes	0.594	0.438	0.490	0.488	0.313	0.625	0.443	0.453
Naïve Bayes updateable	0.594	0.438	0.490	0.488	0.313	0.625	0.443	0.453
Random committee	0.391	0.745	0.568	0.391	0.271	0.563	0.542	0.557
Non-nested generalized exemplars	0.458	0.458	0.438	0.500	0.458	0.563	0.500	0.667

Groups 6, 9, 10, 11, 13, and 14 did not show good results. However, as can be seen in the Tables 11.1 and 11.2, the proposed method did produce excellent results (ROC area = 0.958 using the features of Group 4) for other groups. The best results were obtained for Group 1 using a naïve Bayes simple classifier (0.792); for Group 2 using naïve Bayes and naïve Bayes updateable (0.875); for Group 3 using naïve Bayes and naïve Bayes updateable (0.927); for Group 4 using naïve Bayes and naïve Bayes updateable (0.958); for Group 5 using non-nested generalized exemplars (0.750); for Group 7 using classification via clustering (0.708); for Group 8 using random committee (0.745); and for Group 12 using classification via clustering (0.813). In future studies, those features presented in this study will be used as well as other fractal measures to diagnose breast diseases in early stages.

WEKA software[46] was used to perform the classification. WEKA is a well-known software program in the area of data mining that performs clusterization, classification, feature reduction, etc. The reduction of dimensionality is necessary to reduce the number of calculations (because we extracted a total of 712 features). WEKA can be used with a view to improve the accuracy of the method, choosing the best features that represent the sample.[47] In this study, this is not discussed, and only two dimensionality-reduction techniques—principal components analysis (PCA) and information gain—are conducted. We used an algorithm of support vector machines (SVM) implemented in WEKA, named LibSVM.[48,49] For the parameters of LibSVM we

Table 11.3 Results from methods used in other studies and in this study.

Authors	Accuracy (%)	Sensitivity (%)	Specificity (%)
Ng and Kee[50]	80.95	81.20	88.20
Schaefer et al.[51]	79.53	79.86	79.49
Acharya et al.[52]	88.10	85.71	90.48
Borchartt et al. approach 1[43]	85.70	95.80	25.00
Borchartt et al. approach 2[43]	60.70	66.70	25.00
Borchartt et al.[44]	92.86	95.83	25.00
Resmini et al. (old)[53]	82.14	91.70	25.00
Resmini et al. (new)[53]	88.23	80.00	91.70

chose the SVMType, nu-SVC; nu value of 0.5; and kernelType linear. Other parameters were set up with standard values. Table 11.3 shows the results achieved from these and the results for the other methods in the literature. However, it is important to note that the image samples and algorithms are different for each of the first three approaches.

The dataset deemed "old" did not achieve good results. This occurred because the sample is unbalanced: only 4 images from patients with no pathology and 24 from patients with pathology. The results achieved from this study, using the dataset deemed "new," are promising because every measure is over 80%.

When we used this dataset with only geostatistical measures, we achieved a similar outcome. But when we used this same dataset with no geostatistical measures, the outcome was inferior: 64.70% accuracy, 30.00% sensitivity, 79.20% specificity, and an AUC (area under the ROC curve) of 0.546.

This outcome encourages more research to improve our method with geostatistical measures. Furthermore, we achieved an AUC of 0.858. Serrano et al.[40] had achieved an AUC of 0.958. These two evaluations are close. However, every analyzed evaluation criterion using extracted features by geostatistical measures proves that it is a promising methodology. The information gain is shown to be better with a low rate, around 5%. This was the value used on classification that achieved the best outcomes.

11.3 Several Approaches for Improving the Numerical Simulation of Temperature Profiles

Breast modeling has been conducted by using several techniques and for different purposes, such as: epidemiological studies,[54] breast surgery procedures[55,56] temperature simulations, and so forth. In order to achieve these goals, a 3D geometry of the breast, within a shape as close as possible to that of the patient under analysis, is necessary. Surrogate geometries can be used for this purpose.

11.3.1 Surrogate geometry of the breast

Surrogate geometry is a geometry that swaps places with the patient in order to evaluate simulations. Gonzalez[57] modeled the breast as a hemisphere attached to a layer that replicates the chest wall. Bezerra[20] also used a hemisphere as a breast surrogate geometry to locate tumors inside the volume to calculate the temperature. Ng and Sudharsan[58] modeled the female breast divided into four quadrants and inner layers so that the properties of each tissue could be used. This section describes how to acquire and use surrogate geometries of external breast prostheses used by patients who have undergone complete surgical removal of the mamma.[21] The improvement of this model is due to the fact that the shape of these prostheses is quite similar to a real female breast.

11.3.1.1 Acquiring surrogate geometries

Coordinate measuring machines (CMMs) were introduced more than thirty years ago and are among the most important tools of measurement for dimensional control commercially available.[59] A CMM is able to determine dimensional parameters of an object by taking coordinate measurements of points over the surface of the object. These points are adjusted in order to build the geometry of the object by several methods; the one most used is the least-squares method (LSM).[60] Such geometries are called surrogate geometries, and their characteristics or main parameters, or even both, can be compared with the real dimensions of the object.

Seven different breast external prostheses were scanned: the model can be SG-419 or SG-420, with sizes 1, 2, 4, 6, 8, 10, and 12, manufactured by Orto Pauher, which donated all of the prostheses. The CCM CRYSTA 547 manufactured by Mitutoyo™, measured the prostheses. The pre-processor software, GAMBIT™, was used to build surrogate geometries so as to allow the correct usage of FLUENT™, a computational fluid dynamics (CFD) software program.

The CMM machine scanned the prostheses in longitudinal and latitudinal directions and obtained four lists of points. The fifth and last curve was obtained from the points at the base of the prostheses. The point coordinates in each direction were saved as text files in order to build the surrogate geometry. How the points were acquired followed the directions illustrated in Fig. 11.12(b). The upper and lower surfaces of the model were obtained, and afterwards the volume was built up. Figure 11.12(a) shows one example of a surrogate geometry.

In the sequence, the surrogate geometry was customized to each patient by inserting in it as many 3D volumes as the number of patient abnormalities. Each volume has the same dimensions as the corresponding abnormality described by the ultrasound examination. These volumes were located inside the model at the position given by the ultrasound examination.

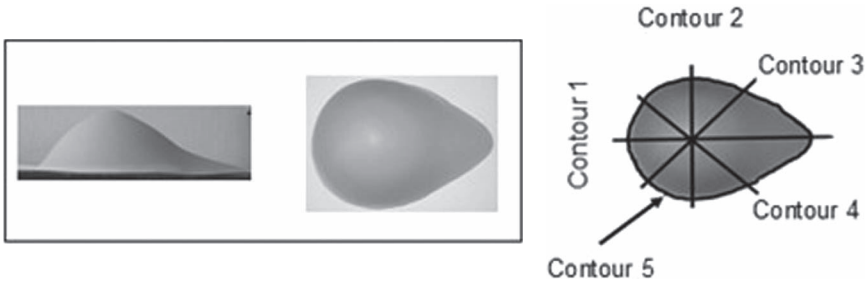

(a) (b)

Figure 11.12 (a) External breast prosthesis. (b) External breast prosthesis and the directions of the scan process.

At this point, the personalized model containing the regions of normal tissue and abnormalities tissue was meshed. The information related to the mesh was exported to the FLUENT program that uses the finite volume method (FVM) to evaluate temperature profiles.

11.3.1.2 Choice of the surrogate geometry that best fits the real breast being studied

Extracting the points of the inframammary fold from the patient's IR image is the first step. Figure 11.13 shows the points extracted from the IR image and overlapped on it. The software developed by Silva[61] was used for this. The points of the contour of the breast were cut from the body contour and joined to the point coordinates of the inframammary fold. These coordinates were saved into text files.

The points extracted from the IR image were adjusted by using the LSM. This curve was compared with the curves obtained from the base of the surrogate geometries in order to find the one that best fits the patient's breast. In order to do so, these curves must run in the same direction, and

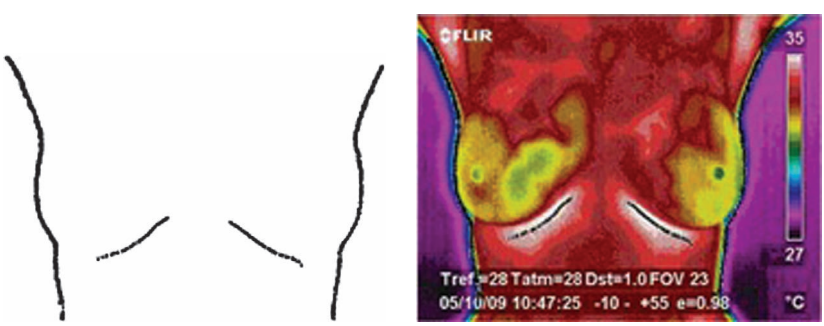

(a) (b)

Figure 11.13 (a) Points extracted from the IR image IR_0860. (b) The extracted points (black dots) overlapped on the IR image.

the origin of their coordinate system must be placed at the same point. A numerical program in the C++ language was developed for this purpose. The steps for doing so are listed below:

1. The software reads the text file that contains the coordinates of the breast contour extracted from the IR image.
2. The operator translates the origin to the middle point.
3. The operator rotates the points by the angle formed by the symmetry axis and the vertical axis *Y* using the concept of the moment of inertia in digital formulation.[62,63]
4. The operator writes the file with the new coordinates. At this point, the coordinates are referenced to the same origin, which was the middle point of the curves, and they run in the same direction, as can be seen in Fig. 11.14(a).

Finally, the best surrogate geometry can be chosen. For this purpose, another software program using the C++ language was developed. The steps for doing so are listed below:

1. The software reads the coordinate file obtained from the IR image after it has been rotated and translated to the middle point by the earlier software program.
2. The operator calculates the coefficients of the curve that fits the given points using the LSM and the Gauss method with a pivoting strategy.[64,65]
3. The operator submits the points of the base of each surrogate geometry to a curve that fits them using LSM with the same order of the curve that fits the IR image, and evaluate the errors between the coefficients of the curve of the surrogate geometry and those of the curve of the IR image.
4. The operator chooses the surrogate geometry that presents the least error.

Figure 11.14(b) shows the result of the choice of the surrogate geometry (#6) that best fits the patient shown at Fig. 11.13(b).

Figure 11.14 (a) The result of the procedure on the base curves of the surrogate geometries. (b) The overlap of the points extracted from the IR image and the base curve of the surrogate geometry #6.

11.3.2 A parametric analysis to investigate IR sensitivity

IR imaging promises to be a noninvasive and effective adjunctive modality to screen for early breast cancer, although its use is still hindered because of its poor sensitivity to deeper or smaller tumors.[66] In this section a parametric analysis is used for investigating the sensitivity of IR imaging when detecting breast cancer. Initially, an idealized tumor was set into a 3D breast surrogate geometry. During this procedure, the position and size of the idealized tumor were changed. Some results showed the influence of these variations on the profile of the breast temperature. The technique developed was also used to estimate the height of the breast abnormality which, in general, is not measured by an ultrasound exam.

11.3.2.1 The mathematical model

The physical process is assumed to be governed by the bioheat transfer equation (BHTE) [Eq. (11.4)], which is a heat conduction equation with specific terms for volumetric heat generation due to the blood perfusion Q_p and for volumetric metabolic heat generation Q_m. It is used to calculate and analyze temperature profiles. Such an equation, for a homogeneous isotropic medium, with constant properties, is given by

$$\rho c \frac{\partial T}{\partial t} = k\nabla^2 T + Q_p + Q_m, \tag{11.4}$$

where k is the thermal conductivity of the tissue, ρ is the density, c is the specific heat, T is the temperature of the local tissue, t is the time variable, and ∇^2 is the Laplacian operator.

The heat flow due to blood perfusion is given by

$$Q_p = \omega \rho_b c_b (T_a - T), \tag{11.5}$$

where ω is the blood perfusion rate [(ml/s) blood/ml tissue], ρ_b is the blood density, c_b is the blood specific heat, T_a is the temperature of the arterial blood entering the tissue, and T is the temperature of the venous blood leaving the tissue (T is assumed to be equal to the temperature of the tissue).

For the numerical simulations analyzed in this chapter, the breast was represented by two regions of different thermophysical properties: glandular tissue and tumor tissue. Currently, some structures such as breast lobules and ducts were discarded.

The boundary and initial conditions used to solve the BHTE are:

- Heat is transferred by convection between the breast surface and the external environment.

- The prescribed temperature at the chest wall is 37 °C.
- The initial temperature of the breast is considered to be 37 °C.
- The heat transfer coefficient adopted is a combination of convection, radiation, and the evaporation effects and is 13.5 W/m^2 °C.[67]

According to Gautherie,[68] Ng,[67] and Mitra,[69] tumor doubling time τ and tumor metabolic heat Q_m are related by a hyperbolic function:

$$Q_m \tau = C, \tag{11.6}$$

where C is a constant (3.27×10^6 W day/m^3), and τ is the time (in days) required for the tumor to double its volume. The diameter D (in meters) of the tumor is related to τ according to

$$D = 0.01e^{[0.002134(\tau - 50)]}. \tag{11.7}$$

Equations (11.6) and (11.7) were used to calculate Q_m for each patient, with the information supplied by the patients' exams.

When the nodule is considered as a cylinder, the volume of the cylinder is calculated; from this result it is possible to find the diameter D of a hypothetical breast nodule. For nodules with a diameter smaller than 1 cm, a metabolic heat of 65,400 W/m^3 is considered.[67]

It is assumed that the values of thermal conductivity k, density ρ, and specific heat c are constant within each region of the breast. The volumetric metabolic heat generation of the breast is considered to be 450 W/m^3.[20] The thermophysical properties adopted for the tissues analyzed are described in Table 11.4.

11.3.2.2 A parametric study using a phantom 3D geometry

As a first attempt, a 3D breast geometry obtained from a female mannequin was used as a human phantom. The CMM shown in Fig. 11.15(d) was used to acquire the point coordinates over the breast surface. Figures 11.15(a)–(c) show the steps used for the geometry reconstruction and the mesh associated with it to calculate the temperature.

A computational tool PARAMETRICA was developed on the MATLAB® platform with the objective of managing the influence of the

Table 11.4 Thermophysical properties of the breast.[20]

Tissue	k (W/m°C)	ρ (kg/m^3)	c (J/kg°C)	ω (s^{-1})
Glandular	0.48	1,080	3,000	0.00018
Malignant tumor	0.48	1,080	3,500	0.009
Fibroadenoma	0.48	1,080	3,500	0.0018
Blood	—	1,060	4,200	—

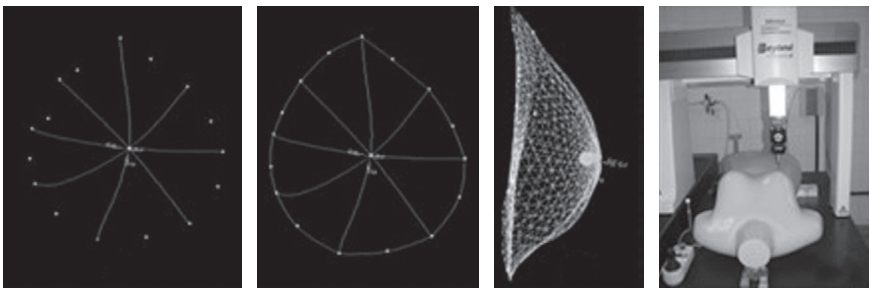

(a) (b) (c) (d)

Figure 11.15 (a) Sequence of acquiring points. (b) Building a contour line. (c) The generated mesh used for the numerical simulation. (d) Phantom at the CMM workstation.

size of a tumor and its position on the temperature profile, which is calculated automatically by the successive simulations. In each case, FLUENT calculates the profile of the temperature of the breast, and the results are then stored in a new directory named as the patient's name. How PARAMETRICA is implemented can be seen in Ref. 70. Originally, the tumor geometry was spherical. Its radius was then modified, and all of the simulations were conducted by the software program developed. The thermophysical properties used in this study are close to those of a real breast and are shown in Table 11.4.

Figure 11.16 shows one of the obtained results with which it is possible to check the reduction in temperature at a fixed position when the size of the tumor is reduced from 17 to 5 mm. For this calculation the external environment was 23.8 °C. Another result of some simulations performed

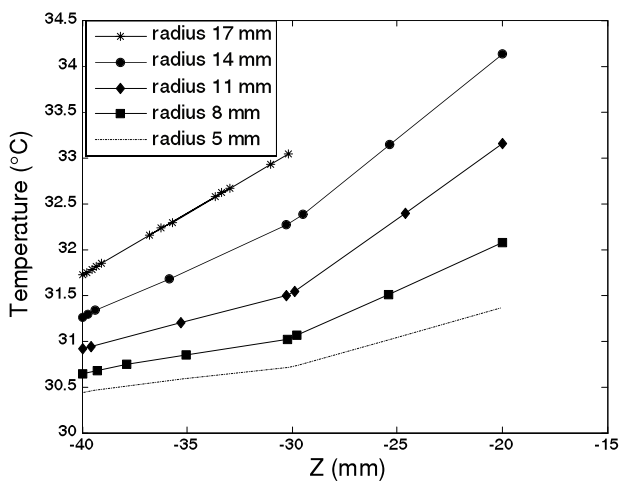

Figure 11.16 Temperature profile versus tumor position for tumors with different radii ($Z = 0$ corresponds to the nipple position).

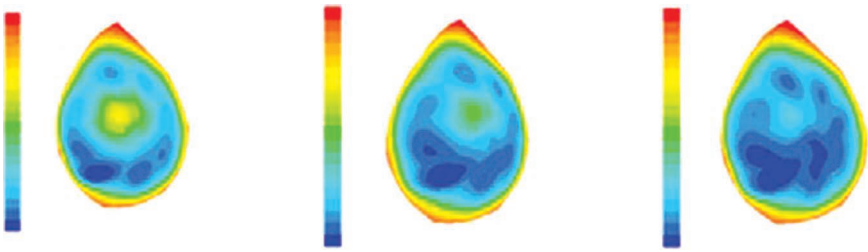

Figure 11.17 Breast temperature profiles (a) r = 20 mm; (b) r = 15 mm; (c) r = 10 mm, where r is the nodule radius.

using PARAMETRICA is shown in Fig. 11.17, where it can be seen that when the tumor size is reduced, the same occurs to its image. The present result considered a nodule with a 20-mm radius. The maximum temperature calculated was 34.6 °C [Fig. 11.17(a)]. When the radius is reduced to 15 mm [Fig. 11.17(b)], the maximum temperature was 32.7 °C. In the third case, a tumor radius of 10 mm, it can be seen that the nodule image is almost invisible, and the maximum temperature is 31.7 °C [Fig. 11.17(c)].

11.3.2.3 Calculating the temperature profile: An example of the use of breast prosthesis and parametric analysis

Generally, ultrasound examinations describe the position and size of the nodule. However, in many cases, some details are missed. A study[21,71] was undertaken to estimate the height of the nodule, using PARAMETRICA.[72] Infrared images were obtained from the database[19] (http://150.161.110.168/termo). A previously developed protocol[7] was used to acquire them. Figure 11.18 shows the patient's IR image with the region of the solid nodule highlighted. The maximum temperature measured in this region was 33.1 °C. Note that in the first image, the region near the nipple is hotter on the

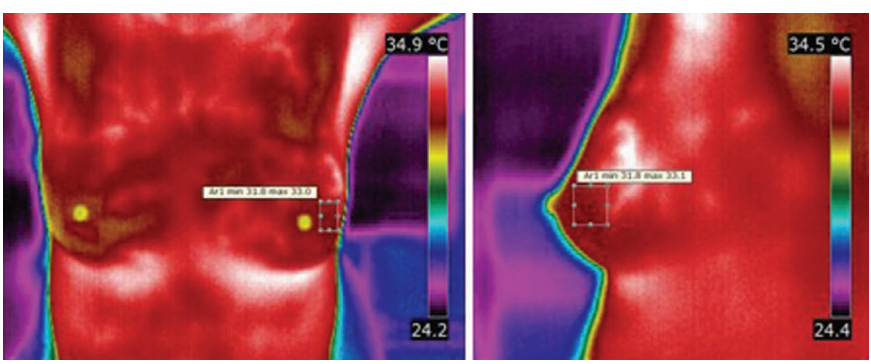

Figure 11.18 IR image with the region of the solid nodule highlighted.

left breast than on the right one. This is probably due to the presence of the tumor.

An ultrasound examination of the patient's breast indicated a solid nodule with regular contours inside the left breast, BIRADS® 3, located at 3h, i.e., located at the junction of the external lateral quadrants, 1.5 cm from the areola and 0.7 cm from the skin surface. The dimensions given were 0.6 cm × 0.4 cm. It was considered as a volume [Fig. 11.19(a)] with elliptical bases placed inside the surrogate geometry as described by the ultrasound examination. The third dimension was not measured by the ultrasound examination. PARAMETRICA[71,72] estimated the value of the height of the tumor by making several calculations using a nodule with a different height at each cycle. The initial height set was 0.1 cm, and the last one was 0.7 cm. A routine that tests this parameter before performing the temperature simulation was used to ensure that the nodule did not exceed the limits of the breast. Any nodule, the height of which lay beyond the volume of the breast, was discarded.

The surrogate geometry was acquired[21] as described in the previous topic.

The pre-processor software built the meshed geometry. One of these meshed geometries is shown in Fig. 11.19(b).

The computational program PARAMETRICA starts the CFD software to perform temperature calculations. The temperature profile on the tumor region was calculated and compared to the maximum temperature over the tumor region on the IR image. Finally, the calculated tumor height was that one whose temperature profile matched the patient's IR image with the smallest error. The graphic displayed in Fig. 11.20 compares the results of each cycle for the surrogate geometry #1. The temperatures were measured on a surface point just above the nodule.

The temperature profile that is closest to the IR temperature is shown in Fig. 11.21. The temperature reached above the nodule region was 33.18 °C.

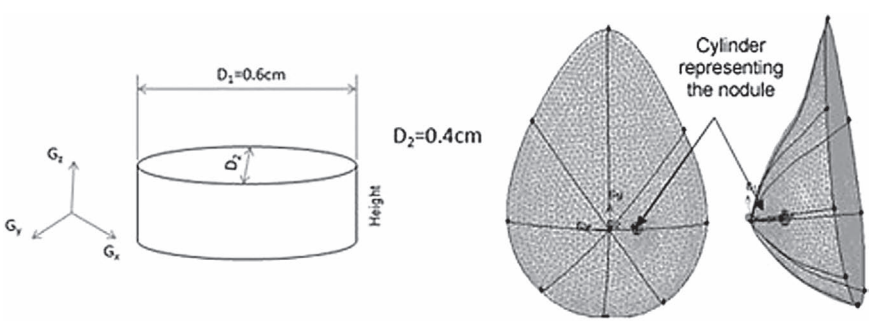

Figure 11.19 (a) Representation of the first nodule. (b) Frontal and lateral views of the 3D surrogate geometry of the patient's breast with mesh.

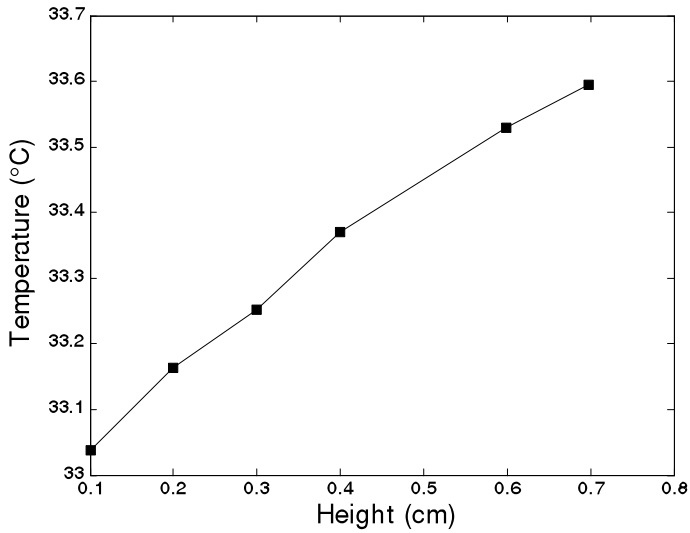

Figure 11.20 Calculated surface temperature for each tumor height.

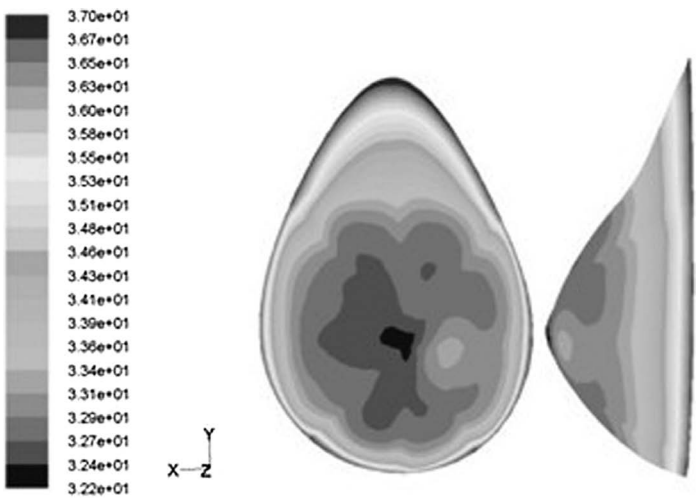

Figure 11.21 Simulated temperature profile of surrogate geometry #1.

The calculated height was 0.2 cm. The difference between the maximum temperatures of the simulated profile and the IR image was 0.08 °C, which gives a percentage error of 0.24%

11.3.3 Estimation of some breast and tumor properties

During the last thirty or so years, in many disciplines, especially in medicine, the inverse method has been used to solve the problems of heat transfer.

The breast consists of a combination of tissues and other structures. Younger women have higher levels of glandular tissue in their breasts. At the onset of menopause, the glandular tissue begins to atrophy and is progressively replaced by fatty tissue. In postmenopausal women, the breasts consist almost exclusively of fat and traces of glandular tissue.

One of the difficulties in constructing a real model of the breast is to find the thermophysical properties of the several tissues of the breast. Also, it is not easy to find accurate values of these properties for breast nodules. Thus, it is proposed to use thermography in conjunction with inverse methods to estimate these parameters, taking a simplified breast model as a homogeneous medium.

In this section, a first attempt is made to estimate the thermophysical properties of the breast and breast tumors, using the maximum superficial temperature (measured by IR images) of the breast over the tumor region. The sequential quadratic programming (SQP) method was used to solve the inverse problem and to estimate the thermal conductivity and blood perfusion of breast tissues, and FLUENT was adopted to compute the temperature profiles.

11.3.3.1 The inverse method

For the approach of the inverse heat conduction problem (IHCP) employed in this study, thermal conductivity and blood perfusion are regarded as unknowns. The inverse problem is thus solved as an optimization problem of finite dimension, in which it is sought to minimize the objective function $F(\mathbf{x})$, given by Eq. (11.8). This equation represents the mean square of the residues between the calculated temperature T_{cal} and the temperature measured experimentally by thermography T_{exp}. The numerical values for T_{cal} can be obtained from numerical solutions using a finite volume method or other methods.

Consider $\mathbf{x}$ as the vector of the design variables, in which $i = 1,\ldots, I$, and I is the total number of experimental measurements. The vector $\mathbf{x} = [k, \omega]$ represents the set of unknown parameters, the values of which it is sought to specify using the optimization process.

The formulation of the inverse problem can be described mathematically by the following expression:

$$\underset{\mathbf{x}}{Min}\, F(\mathbf{x}) = \sum_{i=1}^{I} [T_{cal_i}(\mathbf{x}) - T_{exp_i}]^2, \tag{11.8}$$

subject to

$$k^L \le k \le k^U$$

$$\omega^L \le \omega \le \omega^U,$$

where, k^L, k^U, and ω^L, ω^U are the lower and upper limit constraints of each design variable that bound the design space and so avoid optimizing algorithms that provide physically incorrect results such as negative values.

To minimize the objective function, the SQP method is used.[73–75] In this method, quadratic programming (QP) subproblems are solved at each iteration, based on a quasi-Newtonian approximation of the Hessian of the Lagrangian function, and in a search direction, with a quadratic objective function and linear constraints.[76]

The MATLAB platform has a *fmincon* function in its Optimization Toolbox™. This function implements the SQP method, in which the Hessian of the Lagrangian is calculated using the Broyden–Fletcher–Goldfarb–Shanno (BFGS) method.[77] This method searches for a local minimum of a scalar variable function, which is submitted to limit constraints. It starts from an initial estimate x_0. The entire process of the optimization consists of choosing an initial estimate for x, and conducting the optimization problem with a modification of the variables until the optimal solution is reached. The stopping criterion used for all optimization in this study is the standard criterion given as the default in the MATLAB Optimization Toolbox. The termination tolerances on x and on the function value are set as 10^{-6}. A flowchart of the method is presented in Fig. 11.22.

In order to evaluate the influence of the parameters on the distribution of breast temperature, a sensitivity analysis was conducted for each case

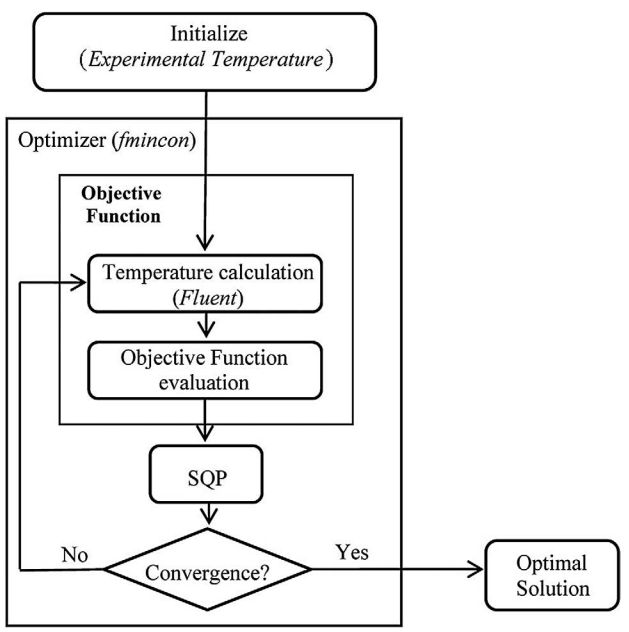

Figure 11.22 Flowchart of the optimization method.

studied. This analysis is very important in enabling an evaluation of which parameters can be estimated[78,79] and which are the most important in the process.[79] The sensitivity of the parameter to be determined must be large enough to ensure that the response of the model reflects small perturbations in these parameters.

The numerical finite difference approximation was used to analyze the sensitivity coefficients. The method modifies each design variable x_i independently, with a relatively small value. In general, the finite difference method can be expressed by

$$\frac{\partial T}{\partial x_i} \approx \frac{\Delta T}{\Delta x_i} = \frac{T(x_i + \Delta x_i) - T(x_i)}{\Delta x_i} . \tag{11.9}$$

According to Blackwell,[79,80] if the simultaneous estimation of parameters is to succeed, the coefficients must be linearly independent, and the sensitivity coefficients must also be sufficiently large.

11.3.3.2 Experimental validation of the methodology

FLUENT was used to solve the BHTE [Eq. (11.4)]. The rate of blood perfusion and the metabolic heat generation were added to the calculations by means of a user-defined function (UDF) written in the C++ language.

The manual segmentation described in Section 11.2.3 was used to select the ROI where the breast nodule is located. During this procedure, the maximum temperature measured by the IR image in that ROI was obtained.

A laboratory experiment was performed to validate this methodology. An incandescent bulb of 7 W was inserted into the right breast of the phantom described in Section 11.3.2.2. The breast was filled with silicone rubber,[81] and the lamp acted as a localized heat source. The lamp was modeled as a cylinder with a radius of 1 cm and a height of 3 cm. The lamp filament was modeled as a cylinder with a 3-mm radius and 1.5-cm height. The boundary conditions involved were: convection heat exchange between the breast surface and the environment, the temperature of which was 25.4 °C. The rear part of the breast was at a fixed temperature of 37.2 °C. The lamp had a volumetric heat generation rate equal to 1.65×10^7 W/m^3. Silicone rubber was used as breast tissue. The lamp was deemed as being filled with air, and the material used in the filament was tungsten. The geometry and unstructured tetrahedral mesh were obtained using GAMBIT®. One mesh with 6,006 nodes, 32,888 cells, and 66,726 faces was chosen after a mesh convergence study.

The thermophysical properties considered are presented in Table 11.5. Figure 11.23(a) shows the frontal thermogram of the phantom. The

Table 11.5 Thermophysical properties of the materials.[82]

Material	k (W/m°C)	ρ (kg/m³)	c (J/kg°C)
Silicone rubber	0.21	970	65.68
Air	0.0242	1,006.43	1.225
Tungsten	174	19,250	132

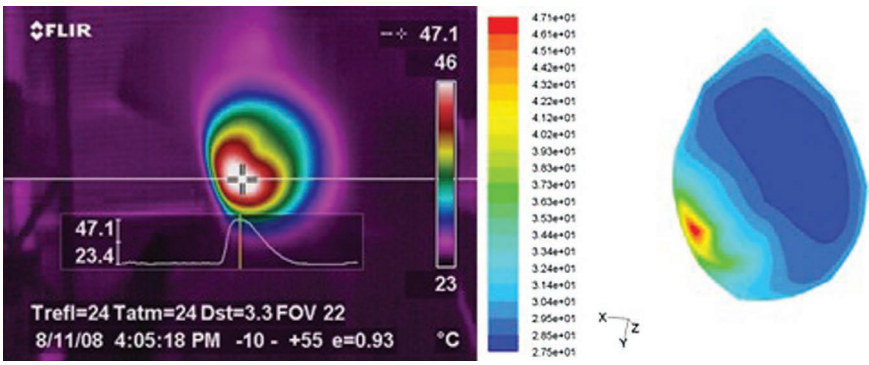

(a) (b)

Figure 11.23 (a) Thermogram of the phantom breast. (b) Calculated temperature distribution of the surface of the breast.

detailed information printed on this image was generated directly by the thermographic camera. The maximum temperature measured in the region where the lamp was located was 47.1 °C. Figure 11.23(b) shows the distribution of the surface temperature of the breast using a numerical simulation. The maximum temperature obtained using a numerical simulation was also 47.1 °C.

It is possible to estimate the thermophysical properties of the breast and the tumor using this temperature profile. Currently, only the maximum breast temperature, from the thermogram, over the region where the tumor is located is used. In the near future, the complete distribution of temperature obtained by texture mapping will be used for making estimates.

The major reason for using this phantom in order to validate the methodology was the previous knowledge of the physical properties of the materials and, mainly, because it is a simpler model with a homogeneous medium, quite unlike that of a real human breast. Also, both the position of the lamp and its geometry are precisely known. The sensitivity analysis for some phantom parameters is shown in Fig. 11.24.

According to this analysis, the sensitivity coefficients of the silicone and the tungsten properties were found to be linearly dependent, as they show similar behavior. Thus, it is not possible to estimate both simultaneously.

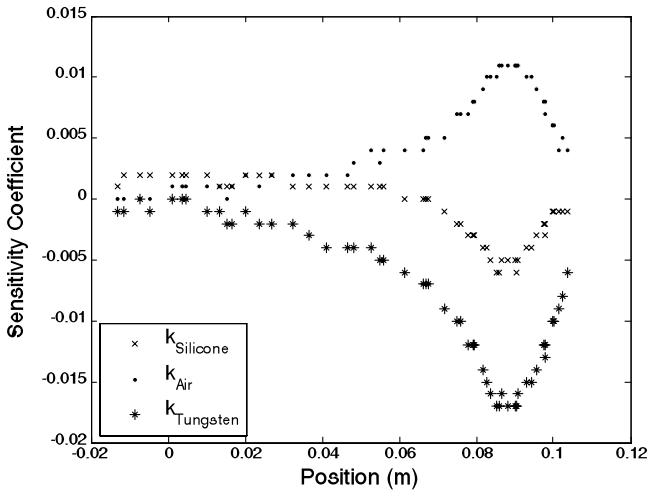

Figure 11.24 Sensitivity analysis for the phantom parameters.

However, as the sensitivity coefficients of silicone conductivity and air conductivity are not linearly dependent, they could be estimated simultaneously. The sensitivity coefficients for thermal conductivities are, in practical terms, null up to position 0.06 m. At this position, these sensitivity coefficients vary. This is due to the presence of the lamp in this region. Table 11.6 presents the actual and estimated parameters, in which, in this case, a very small error was obtained for all parameters. The so-called actual values provided in the table for the thermophysical parameters are those found in the literature.

The conclusion may be drawn that an estimate can be made of the thermophysical parameters using the maximum temperature measured by the IR image. The maximum error was 1.28%. Thereby, this procedure could be used to estimate the thermophysical properties of the nodules of the human breast.

11.3.3.3 Cases analyzed

Next, some results are presented for three patients selected from the database described in Section 11.2.2. The first patient (Patient #01, medical record: 1301345-4) was a 34-year-old woman. Her ultrasound and

Table 11.6 Thermophysical parameters of the phantom.

Design variables (W/m°C)	Actual	Estimated	Error
$k_{silicone}$	0.21	0.2127	1.28%
k_{air}	0.0242	0.0241	0.41%
$k_{tungsten}$	174	174.0372	0.021%

mammography exams showed a fibroadenoma in the lateral lower external quadrant of the left breast. In order to calculate the temperature, the data from the ultrasound exam was used to locate the nodule inside the breast volume. The nodule has a radius of about 1.3 cm, is about 0.6 cm away from the skin surface, and is near the nipple. For the simulation, the tumor was modeled by a sphere with a radius of 1.3 cm. The procedure presented in Section 11.3.1 was applied, and external prosthesis #04 was selected. The unstructured tetrahedral mesh adopted for Patient #01 had 15,282 nodes, 86,624 cells, and 175,943 faces.

The boundary conditions involved were: heat exchange by convection from the breast surface to the environment at a temperature of 27.4 °C. The region of the chest was considered to be at a fixed temperature of 37 °C. The value of the metabolic heat used for the nodule with a diameter of 1.3 cm was 18,907.76 W/m^3.

In Fig. 11.25 it can be seen that the maximum temperature captured by the thermogram was 34.7 °C, and the maximum temperature value obtained by the numerical simulation was 34.69 °C, which represents a relative error of 0.029% when these values are compared. On first analysis this good agreement might have occurred because the patient is a young woman and has dense breasts, with a large amount of glandular tissue.

The sensitivity analysis for some thermophysical parameters is shown in Fig. 11.26. The sensitivity coefficients for the density and the specific heat are null; thus, these properties cannot be estimated. This was expected because it is a steady state problem that is being addressed, and any value assigned to these properties does not influence the final profile of the temperature. It can also be seen that the blood perfusion of the tumor could not be estimated due to its sensitivity coefficient being very small.

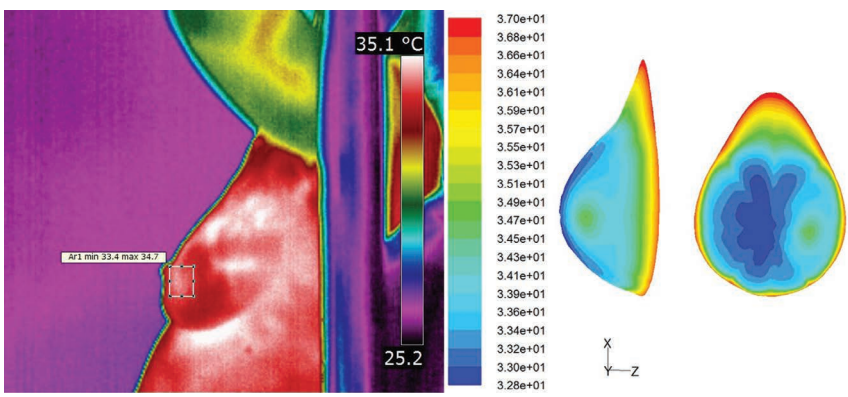

(a) (b)

Figure 11.25 (a) Thermogram of the left breast of Patient #01. (b) Calculated distribution of temperature on the breast surface.

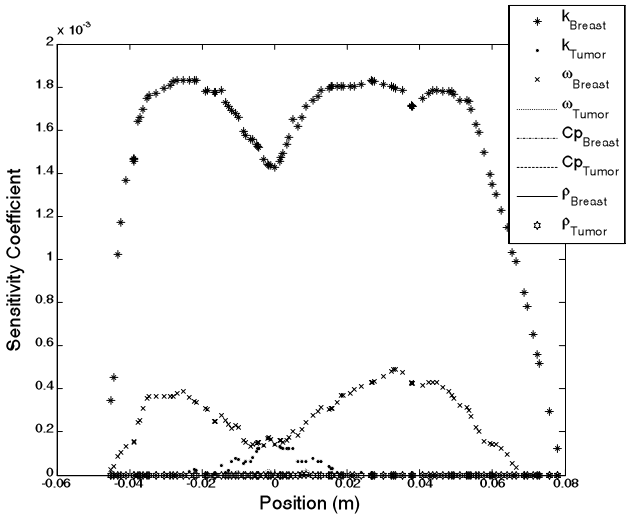

Figure 11.26 Sensitivity analysis for Patient #01.

Figure 11.26 also demonstrates that, in this problem, the sensitivity coefficients of the breast properties are linearly dependent. Thus, it is not possible to estimate both simultaneously. The sensitivity coefficients of the thermal conductivity of the tumor and of the breast are linearly independent. Therefore, they could be estimated simultaneously. The sensitivity of the breast thermal conductivity shows that this parameter causes the most significant effects on the temperature. The results of the estimated parameters are shown in Table 11.7.

As a final validation, the temperature profile was calculated again using all of the estimated parameters from Table 11.7. The maximum temperature obtained was then 34.71 °C. This represents a relative error of 0.0029% if compared with the maximum temperature measured by the thermogram.

Using the whole process already described, two other patients were analyzed. Patient #02 (medical record: 1776566-3) was 54 years old and was diagnosed by clinical examination, ultrasound, and mammography exams. Additionally, her biopsy led to a diagnosis of malignant tumors (invasive ductal carcinoma) in the left breast. The patient had two malignant tumors

Table 11.7 Thermophysical breast parameters for Patient #01.

Design variables	Actual	Estimated	Error
k_{breast} (W/m°C)	0.48	0.4853	1.10%
k_{tumor} (W/m°C)	0.48	0.4815	0.31%
ω_{breast} (s^{-1})	0.00018	0.0001833	1.83%

Table 11.8 Thermophysical parameters of the breast for Patient #02.

Design variables	Actual	Estimated	Error
k_{breast} (W/m°C)	0.48	0.4503	6.18%
k_{tumor} (W/m°C)	0.48	0.5107	6.39%
ω_{breast} (s^{-1})	0.00018	0.000106	41.1%
ω_{tumor} (s^{-1})	0.009	0.007937	11.81%

in the upper outer quadrant of her left breast. Using the data provided by the ultrasound exam, it was possible to locate the tumors in the volume used for the calculations.

The maximum temperature obtained by the numerical simulation was 34.33 °C. This temperature is slightly above the thermogram temperature, with a relative error of 0.97%. The sensitivity coefficient analysis indicated that the thermal conductivities of the breast and tumor can be estimated simultaneously. The same occurs with the blood perfusion. Table 11.8 provides estimated values of the considered parameters.

At this point, a new simulation was conducted considering the estimated values of the thermophysical properties. The value of the maximum temperature at the point analyzed was 34.06 °C, giving a relative error of 0.17% when compared to the maximum measured value by the thermography.

Then, Patient #03 (medical record: 1309087-4) was studied. She is a 69 year-old patient who was diagnosed by means of clinical examination, ultrasound, and mammography exams and, finally, a biopsy. The ultrasound examination indicated a solid nodule. Also, her biopsy led to a diagnosis of lymphangioma, which is a benign tumor, in the subcutaneous layer.

The analysis of the sensitivity coefficients was performed and showed a linear independence between the sensitivity coefficients of the thermophysical properties of the breast. Therefore, these properties could be estimated simultaneously. The sensitivity coefficients of the thermal conductivity and blood perfusion of the tumor are very small, indicating an insensitivity of the temperature to these parameters. Hence, only the breast thermal conductivity and the breast blood perfusion were estimated.

The maximum temperature obtained by the numerical simulation was 34.8 °C, which is greater than that measured by the thermogram, and had a relative error of 1.45%.

Once again, the temperature profile was calculated using all of the estimated parameters from Table 11.9. The maximum temperature obtained was then 34.28 °C. This represents a relative error of 0.058% when compared with the maximum temperature measured by the thermogram.

Table 11.9 Thermophysical parameters of the breast for Patient #03.

Design variables	Actual	Estimated	Error
k_{breast} (W/m°C)	0.48	0.375	21.87%
ω_{breast} (s^{-1})	0.00018	0.0001352	24.88%

As can be seen from Tables 11.8 and 11.9, the values of the estimated parameters for Patient #02 and Patient #03 were worse than those obtained for Patient #01 and for the phantom. Several other analyses are in the course of being made in an attempt to find an explanation for these differences. At this moment, it is thought that they are probably related to the patient's age and to the simplified physical model that is used for the breast. These assumptions are supported by the fact that the phantom breast consists of a homogeneous medium, silicone rubber, which does not have the internal structures present in the human breast. The physical properties for this material are well known. Patient #01 is a young woman. The physical properties of the breast used in the numerical simulations are those of a glandular tissue, the only tissues for which values of physical parameters were found in the literature. The young breast actually consists of this type of tissue. These properties were used also for Patient #02 and Patient #03. By the time patients reach the age of Patient #02 and #03, breast tissue partially or totally consists of fat. This fact has not yet been taken into account in the calculations. Also, the nature of the diseases (two malignant tumors) presented by Patient #02 can substantially affect the value of the blood perfusion rate used in the numerical simulations.

11.4 Conclusions

The main innovation presented in this chapter is to make links between complementary subjects so as to help analyze IR images, the goal being to detect breast cancer earlier. Furthermore, the chapter considers the computer vision aspects while also numerically modeling the problems involved when analyzing these images. This study considered the development of the IR image from the acquisition protocol to the inverse problem of estimating breast and tumor thermophysical parameters. The main contribution presented by this study is that of linking these subjects and encouraging a public database of the results achieved. A database for benchmarking the segmentation of breast tissue is presented, and some comparisons between pattern recognition algorithms are also made.

The whole idea was implemented by following four steps. In the first, the segmentation of the ROIs from the surrounding background was carried out by using a semi-automatic technique. The second step deals with extracting features from the ROIs using a large number of possible

features, ranging from simple statistical ones to very complex features based on fractal geometry. The third step interpreted the values of the features based on knowledge from database methods. The fourth considers the use of a CFD software program and other programs specifically developed to evaluate some internal states of the breast by analyzing IR images. This is an inverse problem, which should link up the simulation and measurement strategies proposed with prior information. The further development of a CAD system relies on the existence of good input data images and prior knowledge of the diagnosis related to these images. This system could be used as a second-opinion tool by physicians.

The continuation of this study is related to using the geometry of the patient's real breast in conjunction with a linear mapping of the temperatures measured over the breast volume. A more realistic model that considers the heterogeneity of the breast tissue should also be considered. Furthermore, the complete distribution of surface temperature obtained by texture mapping will be used to estimate some thermophysical parameters of the breast that would then be more realistic and reliable. Also, advanced statistical analyses will be improved in the database, and this might well lead to physicians providing individual, fast, and customized diagnosis.

References

1. N. Diakides, M. Diakides, J. Lupo, J. L. Paul, and R. Balcerak, "Advances in Medical Infrared Imaging," *Medical Devices and Systems*, The Biomedical Engineering Handbook, J. D. Bronzino, Ed., 3rd edition, pp. 9-1–19-14, CRC Press, Boca Raton, FL (2006).
2. L. L. Leape and D. M. Berwick, "Five years after to err is human: What have we learned?" *JAMA* **293**(19), 2384–2390 (2005).
3. T. H. Payne, P. J. Hoey, P. Nichol, and C. Lovis, "Preparation and use of preconstructed orders, order sets, and order menus in a computerized provider order entry system," *J. Am. Med. Inform. Assoc.* **10**(4), 322–329 (2003).
4. H. Lindgren, "Decision Support in Dementia Care: Developing Systems for Interactive Reasoning," Ph. D. thesis, Umea University, Sweden (2007).
5. E. S. Berner, *Clinical Decision Support Systems: Theory and Practice*, Springer, Birmingham (2007).
6. M. L. Giger, H. P. Chan, and J. Boone, "History and status of CAD and quantitative image analysis: The role of medical physics and AAPM," *J. Med. Phys.* **35**(12), 5799–5820 (2008).

7. M. M. Oliveira, "Development of a Protocol and Construction of a Mechanical Apparatus for Standardizing the Acquisition of Breast Thermographic Images," Master's thesis, Federal University of Pernambuco, Brazil, (2012) (*In Portuguese*).
8. E. Y. K. Ng, "A review of thermography as promising non-invasive detection modality for breast tumor," *Int. J. Therm. Sci*. **48**, 849–859 (2009).
9. W. C. Amalu, W. B. Hobbins, J. F. Head, and R. L. Elliot, "Infrared Imaging of the Breast – An Overview," *Medical Devices and Systems*, The Biomedical Engineering Handbook, J. D. Bronzino, Ed., 3rd edition, pp. 25-1–25-20, CRC Press, Boca Raton, FL (2006).
10. M. L. Brioschi, M. J. Teixeira, F. M. R. M. Silva, and D. Colman, *Medical Thermography Textbook: Principles and Applications*, 1st edition, Andreoli, São Paulo (2010) (*In Portuguese*).
11. J. D. Haberman, T. J. Love, and J. E. Francis, "Screening a rural population for breast cancer using thermography and physical examination techniques: Methods and results – a preliminary report," *Ann. N. Y. Acad. Sci.* **335**, 492–500 (1980).
12. E. Ring and K. Ammer, "The technique of infra red imaging in medicine, Review," *Thermol. Int.* **10**(1), 7–14 (2000).
13. K. Ammer and E. F. Ring, "Standard Procedures for Infrared Imaging in Medicine," *Medical Devices and Systems*, The Biomedical Engineering Handbook, J. D. Bronzino, Ed., 3rd edition, pp. 36-1–36-14, CRC Press, Boca Raton, FL (2006).
14. W. Cockburn, *Breast Thermal Imaging. The Paradigm Shift*, International Academy of Clinical Thermography (2002). (reprint) original published in *Thermologie Oesterreich*, pp. 1021–4356 (April 1995).
15. J. Koay, C. Herry, and M. Frize, "Analysis of breast thermography with an artificial neural network," *Conf. Proc. IEEE Eng. Med. Biol. Soc.* **2**, 1159–1162 (2004).
16. J. Wang, K. J. Chang, C. Y. Chen, K. L. Chien, Y. S. Tsai, Y. M. Wu, Y. C. Teng, and T. T. F. Shih, "Evaluation of the diagnostic performance of infrared imaging of the breast: A preliminary study," *BioM. Eng. OnLine* **9**(3), 1–14 (2010).
17. J. Wang, T. T. F. Shih, R. F. Yen, Y. S. Lu, C. Y. Chen, T. L. Mao, C. H. Lin, W. H. Kuo, Y. S. Tsai, K. J. Chang, and K. L. Chien. "The association of infrared imaging findings of the breast with hormone receptor and human epidermal growth factor receptor 2 status of breast cancer," *Acad. Radiol.* **18**, 212–219 (2011).

18. Y. R. Parisky, A. Sardi, R. Hamm, K. Hughes, L. Esserman, S. Rust, and K. Callahan, "Efficacy of computerized infrared imaging analysis to evaluate mammographically suspicious lesions," *Am. J. Roentgenol.* **180**(1), 263–269 (2003).

19. M. C. Araújo, "Use of the Infrared Camera to Evaluate Different Diseases in Tropical Climates and Using It Together with a Database System So as to Detect Breast Cancer," Master's thesis, Federal University of Pernambuco, Brazil (2009) (*In Portuguese*).

20. L. A. Bezerra, "The Use of Thermographic Images of Breast Tumors to Validate Computer Simulation," Master's thesis, Federal University of Pernambuco, Brazil (2007) (*In Portuguese*).

21. M. J. A. Viana, "Simulating the Temperature Profile in the Breast Using Surrogate Geometry Obtained from an External Breast Prosthesis," Master's thesis, Federal University of Pernambuco, Brazil (2010) (*In Portuguese*).

22. L. S. Motta, "Automatic Retrieval of the Region of Interest in Frontal Breast Thermograms to aid Early Detection of Diseases," Master's thesis, Federal Fluminense University, Brazil (2010) (*In Portuguese*).

23. *FLIR Systems*, ThermaCAM™S45. Operator's manual, FLIR Systems (2004).

24. L. A. Bezerra, R. N. T. Silva, F. S. Magnani, and J. R. Henriquez, "Study of the influence of parameters when taking measurements using thermography," *An. IV Congr. Nac. Eng. Mec.* (2006) (*In Portuguese*).

25. E. F. Ring and B. F. Jones, "The historical development of thermometry and thermal imaging in medicine," *Medical Devices and Systems*, The Biomedical Engineering Handbook, J. D. Bronzino, Ed., 3rd edition, pp. 20-1–20-5, CRC Press, Boca Raton, FL (2006).

26. M. C. Araújo, R. C. F. Lima, and F. G. S. Santos, "Development of a database as an auxiliary tool in earlier diagnosis of breast cancer," *XXX Iber. Lat. Am. Congr. on Comput. Meth. in Eng.* **1**, 1–15 (2009) (*In Portuguese*).

27. C. J. Date, *An Introduction to Database Systems*, 8th edition, Addison Wesley Longman, Reading, MA (2003).

28. K. J. Maxwell, "Human-Computer Interaction Design," in *Biomedical Engineering Fundamentals,* J. D. Bronzino, Ed., 3rd edition, CRC Press, Boca Raton, FL (2006).

29. T. A. Pryor, "Hospital Information Systems: Their Function and State," in *Biomedical Engineering Fundamentals,* J. D. Bronzino, Ed., 3rd edition, CRC Press, Boca Raton, FL (2006).

30. Institute of Medicine, *Patient Safety: Achieving a New Standard for Care*, National Academic Press, Washington, D. C. (2003).

31. Health Level Seven, *Health Level-7 Standards Website*: <http://www.hl7.org/>, (03/2012).

32. I. N. Bankman, *Handbook of Medical Imaging: Processing and Analysis*, 3rd edition, Academic Press, San Diego (2009).

33. S. V. Rocha, G. Braz Júnior, A. C. Silva, and A. C. Paiva, "Mammography mass detection and diagnosis: a survey", *Cad. de Pesquisa PPPG – UFMA* **18**, 26–38 (2011) (*In Portuguese*).

34. R. C. Gonzalez, R. E. Woods, and E. L. Eddins, *Digital Image Processing Using Matlab*, Pearson Prentice Hall, Upper Saddle River, NJ (2004).

35. A. R. Backes and O. M. Bruno, "Segmenting textures by means of complexity analysis" <http://www.dcc.ufla.br/infocomp/artigos/v5.1/art11.pdf> (04/2010) (*In Portuguese*).

36. R. C. Serrano, A. Conci, M. Zamith, and R. C. F. Lima, "About the feasibility of Hurst coefficient in thermal images for early diagnosis of breast diseases," *11th Pan-Am. Congr. Appl. Mec. - PACAM XI*, Paraná, Brazil (2010).

37. R. H. C. Melo, E. A. Vieira, and A. Conci, "Comparing two approaches to compute lacunacity of mammograms," *13th Int. Conf. Syst., Signal. Imag. – IWSSIP*, Budapest, Hungary (2006).

38. R. H. C. Melo, E. A. Vieira, and A. Conci, "Characterizing the lacunarity of objects and image sets and its use as a technique for the analysis of textural patterns, Advanced Concepts for Intelligent Vision Systems," Lecture Notes in *Comput. Sci*., *ACIVS - IEEE* Benelux Signal Processing Chapter, **4179**, 208–219, Springer Berlin/Heidelberg, Antwerp, Belgium (2006).

39. C. Allain and M. Cloitre, "Characterizing the lacunarity of random and deterministic fractal sets," *Phys. Rev. A.* **44**, 3552–3558 (1991).

40. R. C. Serrano, J. Ulysses, S. Ribeiro, and R. C. F. Lima, "Using Hurst coefficient and lacunarity to diagnosis early breast diseases," *Proc. 17th Int. Confer. Systems, Signals and Image Processing*, Rio de Janeiro, Brazil, pp. 550–553 (2010).

41. T. Holden, G. Tremberger, E. Cheung, R. Subramaniam, R. Sullivan, P. Schneider, A. Flamholz, D. Lieberman, and T. Cheung, "Fractal analysis of Creutzfeld-Jakob disease frontal horn brain magnetic resonance image," *3rd Int. Conf. Bioinform. and Biom. Eng. - ICBBE*, pp. 1–3 (2009).

42. S. Shekar and H. Xiong, *Encyclopedia of GIS*, Springer Verlag, Berlin (2008).

43. T. B. Borchartt, R. Resmini, A. Conci, A. Martins, A. C. Silva, E. M. Diniz, A. Paiva, and R. C. F. Lima, "Thermal feature analysis to aid on breast diseases," *Proc. 21st Braz. Congr. Mec. Eng. - COBEM*, Natal, Brazil, pp. 1–8 (2011).

44. T. B. Borchartt, R. Resmini, L. S. Motta, E. W. G. Clua, A. Conci, M. J. A. Viana, L. C. Santos, R. C. F. Lima, and A. Sanchez, "Combining approaches for early diagnosis of breast diseases using thermal imaging," to appear in *Int. J. of Innov. Comp. and Appl.*, Special Issue on Intelligent Image and Signal Processing (In Press; Vol. and pages not yet released) (2012).

45. PROENG, "Image processing and image analyses applied to mastology," available at: <http://visual.ic.uff.br/en/proeng/> (01/2012).

46. M. Hall, E. Frank, G. Holmes, B. Pfahringer, P. Reutemann, and I. H. Witten, "The WEKA data mining software: An update," *SIGKDD Explorations*, **11**(1), 10–18 (2009).

47. R. P. Pereira, A. Plastino, B. Zadrozny, L. H. C. Merschmann, and A. A. Freitas, "Lazy attribute selection: Choosing attributes at classification time," *Intel. Data Analysis J.* **15**(5) 715–732 (2011).

48. R. E. Fan, P. E. Chen, and C. J. Lin, "Working set selection using the second order information for training SVM," *J. Machine Learn. Res.* **6**, 1889–1918 (2005).

49. C. C. Chang and C. J. Lin, "LIBSVM: a library for support vector machines," *ACM Trans. Intel. Systems Technology* **2**(3), 27.1–27.27 (2001).

50. E. Y. K. Ng and E. C. Kee, "Integrative computer-aided diagnostic with breast thermogram," *J. Mec. Med. and Biol.* **7**(1), 1–10 (2007).

51. G. Schaefer, M. Zavisek, and T. Nakashima, "Thermography based breast cancer analysis using statistical features and fuzzy classification," *Pattern Recognition* **42**(6), 1133–1137 (2009).

52. U. R. Acharya, E. Y. K. Ng, J. H. Tan, and S. V. Sree, "Thermography based breast cancer detection using texture features and support vector machine," *J. Med. Syst.* **36**(3) 1503–10 (2010).

53. R. Resmini, T. B. Borchartt, A. Conci, and R. C. F. Lima, "Assisting the early diagnosis of pathologies of the breast using thermal images and data mining techniques," *Computer on the Beach 2012: Anais do Evento* **1**, 305–314 (2012) (*In Portuguese*).

54. M. C. Koch, B. Adamietz, S. M. Jud, P. A. Fasching, L. Haeberle, S. Karbacher, K. Veit, R. Schulz-Wendtland, M. Uder, M. W. Beckmann,

M. R. Bani, K. Heusinger, C. R. Loehberg, and A. Cavallaro, "Breast volumetry using a three-dimensional surface assessment technique," *Aesthetic Plastic Surgery* **35**(5), 847–55, Epub (2011).

55. P. Huang, L. Gu, J. Yan, H. Xu, and J. Dong, "Virtual surgery planning of breast reconstruction using deformation modeling and curve shape approximation," *6th International Special Topic Conference on Information Technology Applications in Biomedicine 2007*, pp. 127–130 (2007).
56. O. M. Tepper, K. Small, L. Rudolph, M. Choi, and N. Karp, "Virtual 3-dimensional modeling as a valuable adjunct to aesthetic and reconstructive breast surgery," *Am. J. Surgery* **192**, 548–551 (2006).
57. F. J. Gonzalez, "Thermal simulation of breast tumors," *Mexican Magazine of Physics* (*in Spanish*: *Revista Mexicana de Física*) **53** (4), 323–326 (2007).
58. E. Y. K. Ng and N. M. Sudharsan, "Computer simulation in conjunction with medical thermography as an adjunct tool for early detection of breast cancer," *BMC Cancer* **4** (17), 6 (2004).
59. T. L. Rolim, "Procedures for the Coordinate Measuring Machine Calibration Method," Doctorate thesis, Federal University of Paraíba, Brazil (2003) (*in Portuguese*).
60. F. Wäldele and J. Ni, "Coordinate Measuring Machines," *Coordinate Measuring Machine and Systems*, J. A. Bosch, Ed., Marcel Dekker, Inc., New York, pp. 39–74 (1995).
61. S. V. Silva, "Reconstruction of the Geometry of the Breast Using Thermographic Imaging, Thesis, Fluminense Federal University, Brazil (2010) (*In Portuguese*).
62. E. Azevedo, A. Conci, and F. Leta, *Graphics Computer: Theory and Practices*, Vol. II, 3rd edition, Campus, Brazil (2007) (*In Portuguese*).
63. S. P. Timoshenko and J. M. Gere, *Mechanics of Solids*, 1st edition, Livros Técnicos e Científicos, Rio de Janeiro, Brazil (1994) (*In Portuguese*).
64. S. Chapra and R. P. Canale, *Numerical Methods for Engineers*, 3rd edition, WCB McGraw-Hill, Columbus, OH (1998).
65. M. A. G. Ruggiero and V. L. da Rocha, *Numerical Calculus: Theoretical and Computational Aspects*, 1st edition, McGraw-Hill, São Paulo, Brazil, pp. 96–107 (1988) (*in Portuguese*).
66. M. Gautherie, "Thermobiological assessment of benign and malignant breast diseases," *Am. J. Obstet. Gynecol*. **147**, 861–869 (1983).
67. E. Y. K. Ng and N. Sudarshan, "An improved three-dimensional direct numerical modelling and thermal analysis of a female breast with tumour," *Proc. Instn. Mech. Enghs.* **215**, 25–36 (2001).

68. M. Gautherie, "Thermopathology of breast cancer: measurements and analysis of in vivo temperature and blood flow," *Ann. N.Y. Acad. Sci.* **335**, 383–415 (1980).

69. S. Mitra and C. Balaji, "A neural network based estimation of tumor parameters from a breast thermogram," *Int. J. Heat and Mass Transf.* **53**, 4714–4727 (2010).

70. D. W. Milles, L. L. Thomsen, L. Happerfield, L. G. Bobrow, R. G. Knowles, and S. Moncada, "Nitric oxide synthase activity in human breast cancer," *J. of Cancer* **72**, 41–44 (1995).

71. L. C. dos Santos, M. J. A. Viana, T. L. Rolim, P. R. M. Lyra, R. C. F. de Lima, and A. Conci, "Estimating the height of a breast abnormality through comparisons between simulated temperature profile and thermogram," *Proc. 21st Brazilian Congress of Mechanical Engineering–COBEM,* p. 6, Natal Brazil (2011).

72. L. C. dos Santos, *"*Development of a Computational Tool for the Parametric Analysis of the Influence of the Position and of the Size of a Breast Tumor in Temperature Profiles," M.Sc. Thesis, Federal University of Pernambuco, Brazil (2009) *(in Portuguese)*.

73. C. Yang, W. Jianh, D. H. Chen, U. Adiga, and W. Chiu, "Estimating contrast transfer function and associated parameters by constrained nonlinear optimization," *J. Microsc.* **233**(3), 391–403 (2009).

74. B. M. Nicolai, J. A. Egea, N. Scheerlinck, J. R. Banga, and A. K. Datta, "Fuzzy finite element analysis of heat conduction problems with uncertain parameters," *J. Food Engin*. **103**, 38–46 (2011).

75. M. L. Teles and H. M. Gomes, "Genetic algorithms and sequential quadratic programming comparisons for optimizing engineering problems," *Theory and Practice in Civil Engineering*, pp. 29–39 (2010), *(In Portuguese)*.

76. J. Nocedal and S. J. Wright, "Numerical Optimization," 2nd edition, Springer, New York (2006).

77. *Optimization Toolbox for uses with MATLAB - User's Guide*, The Mathworks, version 2 (2001).

78. N. H. Thomson, "Theoretical-Experimental Analysis for Identifying Thermophysical Properties using the Probe-Linear TSechnique," M.Sc. thesis, Federal University of Rio de Janeiro, Brazil (2005). (*In Portuguese*).

79. B. F. Blackwell, "Sensitivity analysis and uncertainty propagation of computational models," *Handbook of Numerical Heat Transfer*, 2nd

edition, W. J. Minkowywcz, E. M. Sparrow, and J. Y. Murthy, Eds., Kluwer Academic, Dordrecht, Netherlands, pp. 53–71 (1989).

80. M. N. Özisik and H. R. B. Orlande, *Inverse Heat Transfer Fundamentals and Applications*, Taylor & Francis, New York (2000).
81. M. C. Araújo, L. A. Bezerra, L. C. Santos, T. L. Rolim, T. B. Santos, P. R. M. Lyra, and R. C. F. Lima, "Instrumentation and acquisition of the three-dimensional geometry of the breast of a phantom: Comparison of temperatures calculated numerically and measured by thermographic imaging," *Annals of XXIX Iberian Latin-American Congress on Computational Methods in Engineering*, Maceió, Brazil (2008). (*In Portuguese*).
82. F. P. Incropera and D. P. DeWitt, *Fundamentals of Heat and Mass Transfer*, 6th edition, John Wiley, New York, (2007).

Luciete A. Bezerra is a doctoral student in Mechanical Engineering at Federal University of Pernambuco (UFPE), Brazil. She received a Master's degree in mechanical engineering from UFPE in 2007. Her main areas of interest include breast cancer, medical thermography, numerical simulation, heat transfer, and inverse heat transfer problems.

Marília M. Oliveira received a Master's degree in Mechanical Engineering in the area of thermal sciences in 2012 from UFPE, Brazil, working with standardization in the acquisition of breast thermography images. She is interested in research in the domain of biomedical engineering, especially in thermography. She was directly involved in undergraduate research at UFPE in biomedical instrumentation, photogrammetry, and image processing. She did an internship in international trade in Paris and another in nuclear metrology in Recife, Brazil. After she received her engineering degree, she worked in the field of clinical engineering.

Marcus C. Araújo is a substitute professor in the Mechanical Engineering Department of UFPE, Brazil. He is currently a doctoral student in Mechanical Engineering at UFPE. He received a Master's degree in Mechanical Engineering from UFPE in 2009 and a degree in biomedical engineering in 2006. His main areas of interest include medical thermography, medical imaging, clinical engineering, biomedical engineering, and heat transfer in biological tissues.

Mariana J. A. Viana received a Master's degree in Mechanical Engineering from UFPE, Brazil in 2010, and a PG diploma in teaching higher education from Cândido Mendes University, Brazil (UCAM) in 2004. She is teaching at the Federal Institute of Education, Science and Technology of Pernambuco (IFPE), Brazil. She is currently a doctoral student in mechanical engineering at the UFPE. Her current research is focused on breast cancer, breast modeling, IR images, and numerical simulation.

Ladjane C. Santos is a doctoral student at UFPE, Brazil. She received a Master's degree in Mechanical Engineering from UFPE (2009). Her areas of interest include medical thermography and texture mapping.

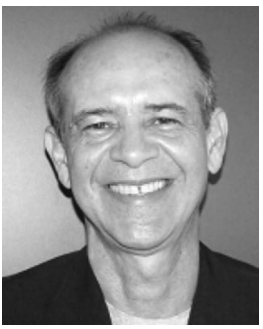

Francisco G. S. Santos received his M.D. from the UFPE. He works in mastology at Hospital das Clínicas of UFPE and is also the coordinator of the Mastology Department at the Gynecology Clinic at the same hospital. He is an expert in evidence-based medicine, teaching undergraduates and interns at the Gynecology Department. He is also a member of a research group on breast cancer.

Tiago L. Rolim is Chief of the Coordinate Measure Technology section in the Mechanical Engineering Department of UFPE, Brazil. Dr. Rolim joined UFPE in 1985 as mechanical engineer, received his doctorate from the Federal University of Paraíba in 2004, and was promoted to his current position in 2005. The theme of Dr. Rolim's research is a proposed system that is capable of indicating a method for calibrating the moving bridge of small and medium-sized coordinate measure machines. Dr. Rolim has one patent and is well known for his work in the area of coordinate metrology.

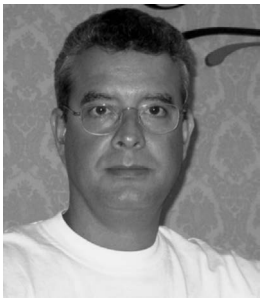

Paulo R. M. Lyra is an associate professor in the Department of Mechanical Engineering at UFPE, where he is the Leader of the High Performance Computing on Computational Mechanics (PADMEC) group. He is a Civil Engineer from UFPE (1984) and holds a M.Sc. (1988) from COPPE-UFRJ, and a Ph.D. (1994) from University of Wales at Swansea (UWS), with a postdoctoral assignment at UWS (1995) and at MIT (2002–2003) in Computational Mechanics. He has coauthored more than 150 research publications in referred journals and in conference proceedings on different subjects. His main research areas of interest are CFD and high-performance computing (HPC).

Rita C. F. Lima received her M.Sc. degree in Nuclear Sciences in 1984 from UFPE, Brazil and her doctorate degree in Nuclear Technology in 1997 from the Federal University of São Paulo, Brazil. She is an associate professor in the mechanical engineering Department of UFPE. Her research areas of interest are medical applications of IR images, numerical simulations of hyperthermic medical processes, and breast cancer. She is a supervisor to graduate students in those areas. She is coauthor of more than 70 research publications in referred journals and conference proceedings.

Tiago B. Borchartt is a Ph.D. student at the Computer Institute of Federal Fluminense University (UFF), Rio de Janeiro, Brazil. He has a Master's degree in Computer Science from the Federal University of Santa Maria (UFSM), Brazil. He currently works in the VisualLab of UFF and performs research in the analysis and processing of biomedical images. He is participating in two projects: Processing and Analysis of Mastologic Images and Image Analysis for Mastologic Applications.

Roger Resmini obtained a Master's degree in Computer Science from UFF, where he is a doctoral student in computer science. He received financial support from CAPES to do his research for his Master and Doctorate degrees. His main research areas are medical thermography, medical imaging, pattern recognition, computer vision, computer graphics, and education.

Aura Conci works in the area of computer vision and image processing. She received M.Sc. and D.Sc. degrees in Civil Engineering from Pontifícia Universidade Católica do Rio de Janeiro (PUC-Rio), Brazil, in 1983 and 1988, respectively. From 1988 to 1995 she was a lecturer in the Mechanical Engineering Department of PUC-Rio. Since 1994 she has been a full professor at UFF, Brazil, in the Computer Science Department. She has published two books and has made more than 100 contributions to international journals and conferences. She was the editor of international conference proceedings and invited editor of the journal special issues. She has successfully supervised 87 students in M.Sc. and D.Sc. programs.

Chapter 12
Diffuse Optical Imaging of the Breast: Recent Progress

Jun Hui Ho, Jing Dong, and Kijoon Lee
School of Chemical and Biomedical Engineering, Nanyang Technological University, Singapore

12.1 Introduction

Breast cancer is the most frequently diagnosed cancer in women, with an estimated number of 226,870 new cases of invasive breast cancer occurring among women in the US during 2012. In addition, breast cancer also ranks second as a cause of cancer death in women (after

lung cancer).[1] Thus, even modest improvements in breast cancer screening, diagnosis, and therapy monitoring can have a significant impact in improving women's health. Accurate detection and characterization of breast tumors is required for breast cancer screening and diagnosis, whereas therapy monitoring provides valuable information about cancer treatment efficacy. X-ray mammography, a common breast cancer screening technique, has high false negative rates in women under fifty[2] and also uses harmful ionizing x-ray radiation. Techniques such as ultrasound and MRI are sometimes employed in addition to x-ray mammography but have limitations such as high cost, low throughput, limited specificity (MRI) and low sensitivity (ultrasound).[3] Thus, new methods are required to detect earlier stages of cancers and cancers missed by mammography,[4] and to monitor tumor growth during cancer therapy. Diffuse optical imaging (DOI) is an emerging noninvasive medical imaging modality that is especially suitable for breast imaging. It can be divided into several categories, namely diffuse correlation spectroscopy (DCS), diffuse optical spectroscopy (DOS), and diffuse optical tomography (DOT). In terms of spectroscopic techniques, DCS is typically used to measure relative blood flow in deep tissues, whereas DOS can provide information about absorption and scattering properties within tissues. On the other hand, DOT makes use of optical transmission measurements on the sample surface to reconstruct 3D maps of optical properties within the sample, namely the absorption and scattering coefficients. In addition, low tissue absorption in the 650- to 900-nm wavelength range allows us to convert optical property maps into concentration maps of intrinsic chromophores, such as oxy- (HbO_2) and deoxy-haemoglobin (Hb), water and lipid, and extrinsic agents such as fluorescent dyes. 3D maps of the parameters mentioned above can aid in tumor detection and characterization. For instance, tumor position has been shown to be strongly correlated with total haemoglobin concentration via angiogenesis.[5,6] This is especially valuable in breast cancer imaging, since the breast is a relatively homogeneous tissue. Thus, DOI provides physiological information directly related to tumor oxygenation and vasculature, while utilizing cost-effective, nonionizing, rapid, portable and noninvasive instrumentation at the same time.

This review gives an overview of the recent DOI developments in breast cancer imaging, in terms of instrumentation and clinical applications. In addition, the theoretical framework behind DOI is also highlighted to provide background knowledge to the reader, and potential future research directions are also presented. This review is not meant to be comprehensive; thus, for further details on theory and instrumentation, please refer to earlier reviews by Choe et al.,[7] Durduran et al.,[8] and Lee.[9]

12.2 Theory

This section provides the theoretical framework behind DOI, which is based on the photon propagation model in tissues. Equations and calculations required to obtain optical parameters are presented for the various diffuse optical techniques.

12.2.1 Photon propagation model

Light propagation through human tissue has been successfully described via the photon diffusion equation. It can be derived from the radiation transport equation (RTE), which is a conservation equation for the radiance in each infinitesimal volume element within the sample;[8] i.e.,

$$\begin{aligned}\frac{1}{v}\frac{\partial L(r,\hat{\Omega},t)}{\partial t}+\hat{\Omega}\cdot\nabla L(r,\hat{\Omega},t)&=-(\mu_a+\mu_s)L(r,\hat{\Omega},t)\\&+Q(r,\hat{\Omega},t)+\mu_s\int_{4\pi}L(r,\hat{\Omega}',t)f(\hat{\Omega},\hat{\Omega}')d\Omega',\end{aligned}\tag{12.1}$$

where $L(r, \hat{\Omega}, t)$ is the light intensity traveling in the $\hat{\Omega}$ direction at position r and time t, $f(\hat{\Omega}, \hat{\Omega}')$ is the normalized differential cross section for single light scattering events in the medium, and $Q(r, \hat{\Omega}, t)$ is the power per volume emitted by sources.

Equation (12.1) can be reduced to the photon diffusion equation:

$$\nabla\cdot\left[D(r)\nabla\phi(r,t)\right]-v\mu_a(r)\phi(r,t)-\frac{\partial\phi(r,t)}{\partial t}=-vS(r,t),\tag{12.2}$$

where μ_a is the absorption coefficient, μ_s' is the reduced scattering coefficient (i.e., the reciprocal of the "photon random walk step length"), D is the diffusion coefficient defined as $D(r) = v/3[\mu_a(r) + \mu_s'(r)]$, v represents the speed of light in the turbid medium, $S(r, t)$ is an isotropic source term, and $\phi(r, t)$ is the light intensity. The photon diffusion model is valid only when the source is isotropic and scattering is much higher than absorption. This assumption is not valid at locations near the surface or near the source.

12.2.2 Diffuse optical spectroscopy

DOS is a noninvasive spectroscopic technique that can provide relatively accurate quantification of absorption μ_a and reduced scattering μ_s' coefficients in thick tissues of up to several centimeters. In turn, such near-infrared (NIR) absorption spectra can offer further insight into the concentrations of key tissue chromophores, i.e., oxy- and deoxy-haemoglobin, total

haemoglobin concentration, water, and lipid. In particular, the wavelength-dependent absorption coefficient is given by the Beer–Lambert law:

$$\mu_a(\lambda) = \sum_i \varepsilon_i(\lambda) c_i, \tag{12.3}$$

where $\varepsilon_i(\lambda)$ is the wavelength-dependent extinction coefficient, and c_i is the concentration of i-th chromophore. By measuring μ_a at different wavelengths, the unknown chromophore concentrations can be obtained by solving the Beer–Lambert equation in an inverse manner. Generally, in order to estimate the number N of chromophores, at least N different wavelengths are necessary for the determination of wavelength-dependent μ_a. Therefore, in the case where the main absorbers considered are oxy- and deoxy-haemoglobin in the NIR range, two wavelengths are sufficient for determining haemoglobin concentration. However, more wavelengths permit the inclusion of other chromophores such as water and lipid. Also, the use of more wavelengths improves the accuracy of the concentration measurements since random errors can be reduced via multiple measurements.

The most common configuration of DOS is the reflection geometry, in which a homogenous semi-infinite (also called half-space) model is employed to approximate human tissue. In this situation, the photon diffusion equation [Eq. (12.2)] can be solved by providing an additional source, as shown in Fig. 12.1. The solution of the diffusion equation is of the form[10]

$$G_0(\rho) = \frac{1}{4\pi D}\left(\frac{e^{-kr_1}}{r_1} - \frac{e^{-kr_2}}{r_2}\right). \tag{12.4}$$

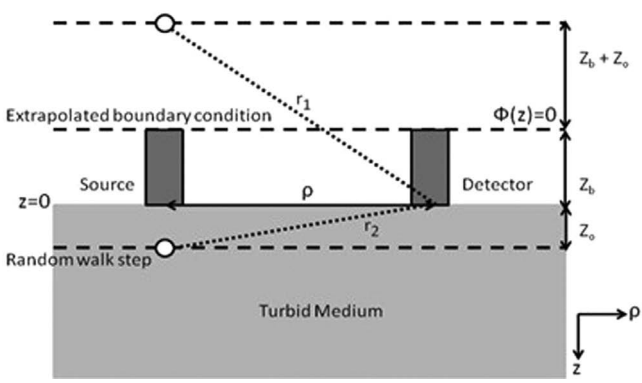

Figure 12.1 The source detector pair in a semi-infinite medium.

Here, $k^2 = \sqrt{(\mu_a v - iw)/D}$, ρ is the distance between the source and the detector, $r_1 = \sqrt{\rho^2 + z_0^2}$, and $r_2 = \sqrt{\rho^2 + (z_0 + 2z_b)^2}$. In addition, D refers to the diffusion coefficient defined as $1/3\mu_s'$, and $z_b = (2/3\mu_s')(1 - R_{eff}/1 + R_{eff})$ is defined as the random walk step $1/\mu_s'$, where R_{eff} represents the effective reflectance, and z_0 is defined as the random-walk step $1/\mu_s'$.

In many cases, people are more interested in the temporal variations of physiological quantities; thus, we need to look into the changes in optical properties, namely $\Delta\mu_a$ and $\Delta\mu_s'$, respectively. The differential pathlength approach can be applied directly to obtain these relative changes and is defined as

$$d_a = \frac{\partial OD(\mu_a, \mu_s')}{\partial \mu_a}. \tag{12.5}$$

According to the modified Beer–Lambert law, and assuming that $\Delta\mu_s' = 0$ and $d_a(\rho, \lambda) = DPF(\lambda)\rho$,

$$\begin{aligned} \Delta OD(\lambda, t) &\approx \sum_i [\varepsilon_i(\lambda)\Delta c_i(t)]\, d_a(\rho, \lambda) + \Delta\mu_s'(\lambda, t) d_s(\rho, \lambda) \\ &\approx \sum_i [\varepsilon_i(\lambda)\Delta c_i(t)] DPF(\lambda)\rho, \end{aligned} \tag{12.6}$$

where $\Delta OD(\lambda, t, \rho) = -\ln[I(r_d, t)/I(r_d, t = 0)]$, and ε_i is the extinction coefficient of the i-th chromophore at a given wavelength. By measuring ΔOD at multiple wavelengths, we can determine the changes in chromophore concentrations by inverting the above equation.

12.2.3 Diffuse correlation spectroscopy

DCS is another promising spectroscopic technique for noninvasive measurement of relative blood flow in deep tissues. It provides continuous measurements of blood flow with high temporal but limited spatial resolution in tissues. Essentially, when a laser beam with constant intensity shines on the surface of a turbid sample, the emerging photons at the detector will form speckles due to constructive or destructive interference caused by migration through different path lengths through the medium. The speckle fluctuations are sensitive to the motions of scattering particles, such as red blood cells. It is straightforward to show that the electric field temporal autocorrelation function $G_1(\tau)$, which is defined as $G_1(\tau) = \langle E(r, t)E^*(r, t + \tau)\rangle$, satisfies the correlation diffusion equation;[11,12] i.e.,

$$\left(-\frac{1}{3\mu_s'}\nabla^2 + \mu_a + \frac{1}{3}\alpha\mu_s' k_0^2 \langle \Delta r^2(\tau)\rangle \right) G_1(\tau) = S(t), \tag{12.7}$$

where k_0 represents the wavenumber of the light diffusing through the medium, $\langle \Delta r^2(\tau) \rangle$ refers to the mean-square displacement of the moving scatterers, and α represents the fraction of photon scattering events resulting from moving particles in the medium. The angle bracket $\langle ... \rangle$ denotes an ensemble average that is experimentally assumed to be equivalent to the time average in most situations. Two models can be used to describe the dynamics of blood flow, namely the Brownian motion model and the random flow model. In the former model (the mean-square displacement of moving particles), $\langle \Delta r^2(\tau) \rangle = 6D_B\tau$,[13,14] where D_B is the effective diffusion coefficient of red blood cells. In the latter model, $\langle \Delta r^2(\tau) \rangle = \langle V^2 \rangle \tau^2$,[15,16] where both the speed and direction of the flow at any point in space are random, and $\langle V^2 \rangle$ represents the mean-square velocity of the scatterers. The Brownian motion model is more commonly used in analysis because it fits the experimental autocorrelation curves quite well over a broad range of tissue types.[17–19] One should notice that changes in αD_B are proportional to the changes in tissue blood flow; therefore, blood flow is characterized by αD_B [also called blood flow index (BFI)], which can be obtained from the exponential decay rate of the correlation functions.

The Green's function solution of the correlation diffusion equation has a similar form to that presented in the previous section for DOS. For a point light source with unit intensity impinging upon a homogeneous semi-infinite medium, the solution is as follows:

$$G_1(\rho,\tau) = \frac{3\mu_s'}{4\pi}\left(\frac{e^{-k_D r_1}}{r_1} - \frac{e^{-k_D r_2}}{r_2}\right), \tag{12.8}$$

where $k_D = \sqrt{3\mu_s'\mu_a + 6\mu_s'^{\,2}k_0^2\alpha D_B\tau}$, and the other variables are defined in Fig. 12.1.

Practically, one can only measure the normalized intensity temporal autocorrelation function $g_2(\tau)$, which is defined as $g_2(\tau) = \langle I(t)I(t+\tau)\rangle / \langle I(t)\rangle^2$, where $I(t)$ is the detected diffusing light intensity at time t. By applying the Siegert relation,

$$g_2(\tau) = 1 + \beta\left|G_1(\tau)\right|^2 \Big/ \langle I(t)\rangle^2, \tag{12.9}$$

the electric field autocorrelation function $G_1(\tau)$ can be obtained. β is a numerical factor related to detector geometry, number of detected speckles, and other experimental parameters, and can be set to one in the ideal case. Hence, quantitative particle motion information can be extracted by measuring the temporal intensity fluctuations of scattered light.

12.2.4 Diffuse optical tomography

The goal of DOT is to reconstruct the spatial distribution of optical/physiological properties at each point (or volume element) in the tissue from measurements of light transmission between many points on the tissue surface. This image-reconstruction procedure is typically known as solving the inverse problem. In contrast, the forward problem refers to the calculation of the fluence rate on the tissue surface, given a forward model (radiative transport/photon diffusion equation) and prior knowledge of the sources and internal optical properties.[20] The forward problem can be solved using numerical finite-difference methods (FDMs), finite-element methods (FEMs), boundary-element methods (BEMs),[21] or Monte Carlo simulations.[22]

On the other hand, inversion approaches are classified as linear or nonlinear, as well as analytical or numerical. In terms of quantification, nonlinear methods are preferred, since the DOT inverse problem is inherently nonlinear. However, nonlinear methods are computationally intensive. In the limit that the optical properties of the volume elements are close to those of the background, the inverse problem is approximately linear and, thus, can be solved using linearized methods. Over the years, many linearized methods have been employed for inverting the ill-posed Jacobian matrix, including singular value decomposition (SVD), algebraic reconstruction technique (ART), and simultaneous iterative reconstruction technique (SIRT).[23,24] These methods have been used in optical mammography applications, wherein optical properties change in response to external stimuli such as compression.

In addition, symmetry in some systems has been exploited by some researchers in an attempt to boost the speed and efficiency in solving the inverse problem. These include translational symmetry in a slab and rotational symmetry in a cylinder or sphere. Such initiatives have been developed for Green's functions, which are analytical inversion kernels for solving the inverse problem. Markel[25,26] and Markel and Schotland[27] have demonstrated that the symmetry of the slab geometry can be used to transform the original 3D integral equation into a series of 1D integral equations in Fourier space. These linear equations are then merged to form a final solution, which can be transformed into image space via inverse Fourier Transform. Similar schemes can be employed for cylindrical and spherical geometries as well, in which Fourier and spherical harmonic waves form the integral components respectively.[25–27] For instance, Konecky et al. [28] used the same linearized analytic inversion method to reconstruct the optical properties of complex targets in turbid medium. In this experiment, datasets corresponding to 10^7 source–detector pairs obtained with a CW instrument required only approximately one minute for image reconstruction on a 1.3-GHz workstation.

On the other hand, when the optical properties of the volume elements are substantially different from those of the background, the linearized approach becomes inappropriate as an inversion model. In order to circumvent this problem, nonlinear iterative methods, such as Jacobian- and gradient-based schemes are required. In essence, nonlinear Jacobian-based schemes involve comparing calculated fluence rates with measured fluence rates and updating the calculated optical properties iteratively until convergence,[23] whereas gradient-based schemes encompass finding the optical properties that minimize an objective function along a search direction and updating them repeatedly as well until convergence.[29,30] Since the gradient-based approach does not involve direct inversion of the Jacobian matrix, it is computationally less intensive than the Jacobian-based scheme. Both the gradient-based and Jacobian-based schemes are primarily written in MATLAB® and are utilized in popular DOT reconstruction packages such as TOAST[31] and NIRFAST.[32]

Besides the various image reconstruction techniques mentioned above, there are other critical aspects that can also affect the quality of reconstructed images. In general, when solving the inverse problem, experimental noise in data may lead to image artifacts, which can be reduced via regularization methods.[33] In addition, various research groups are also combining DOT with other imaging modalities such as MRI and ultrasound in order to incorporate prior information into the inversion process. This improves the accuracy and resolution of the reconstructed images. Recently, Dehghani et al.[34] published a comprehensive review focusing on the incorporation of prior information into DOT.

12.3 Instrumentation

This section gives a brief outline of breast DOI system configurations, such as measurement domain and geometry, for the various diffuse optical methods.

12.3.1 Diffuse optical spectroscopy

DOS, also called diffuse reflectance spectroscopy (DRS), is a powerful technique that can provide functional information about the tissue under investigation via the measurement of optical properties. DOS has been used to assist in the detection of breast cancer, as well as to monitor and assess therapeutic responses. By the measurement of the intrinsic absorption coefficient μ_a and reduced scattering coefficient μ_s' with multiwavelength light sources, physiological variables of the breast can be obtained, such as oxy- and deoxy-haemoglobin concentration, total haemoglobin concentration, oxygen saturation, etc. Unlike conventional x-ray mammography, DOS is noninvasive and nonionizing, as it employs only NIR light to resolve spectroscopic information and generate images. Based on

the instruments employed, DOS can be categorized into continuous wave (CW), frequency domain (FD) and time domain (TD).

CW systems require a source with constant intensity or modulation at a low frequency of a few kilohertz, in order to provide high sensitivity inherent in phase-locked detection methods. These systems also offer the advantages of fast data acquisition and simple instrumentation. However, they are unable to resolve both absorption and scattering contrasts simultaneously, due to only a single amplitude measurement for each source–detector pair.

FD systems involve modulating the source amplitude at high frequencies in the order of a few hundred megahertz, and measuring the corresponding change in amplitude and phase shift of the transmitted signal. At a given source–detector separation, both the amplitude and phase of the diffusing wave are measured, from which simultaneous determination of absorption and scattering properties becomes possible.

Tromberg and coworkers developed a white-light-based broadband DOS system.[35–37] The light sources include a CW 650- to 1000-nm halogen lamp and several FD amplitude-modulated diode lasers, whereas the detectors comprise a fiber-coupled spectrometer and an avalanche photodiode (APD). The inclusion of FD components provides separation of absorption and scattering. In addition, the broadband spectra also provide information about other absorbers besides oxy- and deoxy-haemoglobin, such as water and fat.

TD systems measure the temporal point spread function (TPSF), which is defined as the photon distribution generated as a function of time when an ultrashort light pulse of a few picoseconds is shone through a highly scattering medium.[38] The TPSF contains the most information content per source–detector pair among the three domains, since it is equivalent to intensity-modulated sources scanned over the wide range of modulation frequencies present in the pulse, via the Fourier transform. However, there is a tradeoff between instrument complexity and information content, as TD systems also require complicated instrumentation and have high implementation costs. Bassi and coworkers[39] developed the first portable and clinically compatible TD-DOS system, using a photonic crystal fiber (PCF)-pumped laser as the source and a single-photon avalanche diode (SPAD) as the detector.

12.3.2 Diffuse correlation spectroscopy

DCS is an emerging optical method that is very sensitive to the blood cell motion in microvasculature, namely capillaries, arterioles, and venules. It offers high temporal (~100 ms) and moderate spatial (~1 mm) resolution in tissues. DCS has been studied extensively as a potential noninvasive probe of blood flow in deep tissue due to its portability and cost effectiveness compared to existing techniques. The first direct validation of relative blood flow (rBF) measurement by DCS in a human was recently performed.[40]

Moreover, DCS has been successfully used over a wide range of tissue types such as the brain,[17] human skeletal muscle,[18] and skin,[12] as well as the breast.[41] In addition, blood flow is a key physiological parameter that can provide information about tumor metabolism and the micro-environment. Therefore, DCS can also serve as an alternative method for bedside monitoring of tumor therapies such as chemotherapy in human breast cancer and photodynamic therapy in patients with head and neck tumors.

The typical DCS system includes the CW laser with a long coherence length as the source, as well as an APD, a photomultiplier tube (PMT), or a charge-coupled device (CCD) as the detector. The detected signals need to be connected to either a hardware or a software[68] autocorrelator to compute the autocorrelation function. The APD and PMT are extremely sensitive detectors with relatively high acquisition speed, when compared to the CCD. Therefore, in APD- or PMT-based DCS systems, single-mode fibers are always employed, and a time-averaged light intensity autocorrelation function is also calculated for increased accuracy. On the other hand, the multispeckle nature of CCD detection enables parallel detection at multiple spatial positions so that a position-averaged light intensity can be performed in this case.[42] However, the CCD-based system has not been validated in clinical settings.

12.3.3 Diffuse optical tomography

DOT can be regarded as an extension of DOS, using a large number of source–detector pairs, thereby enabling 3D image reconstruction. In a fashion similar to DOS instruments, DOT devices for breast imaging can also be classified under analogous categories, based on the measurement domain (CW, FD, TD) or the measurement geometry (reflection, transmission, ring). The measurement domain determines the source modulation and detection techniques, whereas the measurement geometry is defined by the relative positions of the sources and detectors.

As an example of a multidomain instrument, a hybrid CW/FD DOT developed at the University of Pennsylvania is noteworthy. It combines the benefits of speed and low cost of CW systems, with the ability of FD measurements to simultaneously resolve absorption and scattering.[43,44] The system uses four amplitude-modulated laser diodes operating at four different wavelengths (690, 750, 786, and 830 nm), and diffusely reflected light is detected simultaneously by APDs via nine detector fibers distributed among the source fibers. Additional CW lasers at 650 and 905 nm are included to improve the separation of optical parameters, from which transmitted CW data are collected by a lens-coupled CCD camera.

On the other hand, DOT devices can also be sorted based on measurement geometry. In reflection geometry, light sources and detectors are placed in the same plane,[36] rendering the sensitivity volume to be banana-shaped

with a depth of roughly half the source–detector distance. In transmission geometry, the breast is positioned between the two different source and detector planes.[43] This geometry provides benefits in terms of high SNRs and parallel CCD data acquisition. Frequency-domain measurement is also possible using a gain-modulated image intensifier.[69] In ring geometry, the breast is surrounded by the light sources and detectors, which are evenly spaced along the circumference.[45] Although the symmetry of ring geometry provides increased image stability, a large dynamic range in the detectors is required, due to vast differences in the source–detector separation.

12.4 Clinical Applications

This section gives a general overview of DOI applications in various clinical settings, namely in the detection and characterization of breast cancer and neoadjuvant chemotherapy monitoring. System configurations and clinical results are briefly presented.

12.4.1 Breast cancer detection/characterization

Diffuse optical techniques can offer potential alternatives to current breast imaging modalities such as x-ray mammography, ultrasound, and MRI because they provide physiological information directly related to tumor oxygenation and vasculature, while simultaneously utilizing cost-effective, nonionizing, rapid, portable, and noninvasive instrumentation. Among the various physiological parameters accessible to DOI, high total haemoglobin concentration (THC) in malignant tumors has been unequivocally reported. This high THC is most likely due to malignant tumor growth accompanied by angiogenesis.[5,6] In addition, the rapid proliferation of tumor cells can also give rise to an increase in the number density of subcellular organelles (e.g., mitochondria, nucleolus), an increase that in turn affects tissue scattering properties.[46] On the other hand, tissue oxygenation (StO_2) is useful for predicting the treatment efficacy in cancer therapy. However, reports on StO_2 in cancerous tissue have been contradictory, with either a decrease,[47] increase,[48] or no change[44] in StO_2 in the tumor. This discrepancy may be due to the dependence of cancer oxygen metabolism on the cancer stage and type, as well as biochemical pathways, or variations in detection accuracy and sensitivity among systems.

12.4.1.1 Endogenous contrast

Cancerous cells can be differentiated from normal cells via the optical property and fluorescence contrast from endogenous chromophores (oxy- and deoxy-haemoglobin, water, and lipid) and fluorophores (protoporphyrin IX), respectively. This endogenous contrast can have significant value in breast cancer detection and characterization.

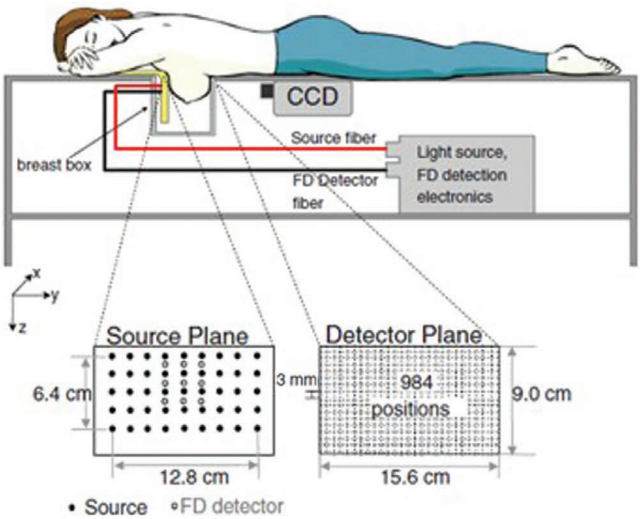

Figure 12.2 Schematic of the parallel-plate diffuse optical tomography instrument. (Reprinted with permission from Ref. 44.)

Choe and coworkers[44] built a parallel-plate DOT system (Fig. 12.2) for *in vivo* 3D imaging of breast cancer. A female subject lies in prone position on a bed with her breasts inside the breast box filled with an intralipid/ink fluid. CW transmission and FD reflection data are acquired simultaneously by a CCD camera and nine APDs connected by fibers on the source plate for 45 source positions at multiple wavelengths. With this system, Choe and coworkers[44] demonstrated that benign and malignant lesions can be distinguished by quantitative 3D DOT. This system was validated on 47 patients with benign and malignant tumors, where corresponding images of tumor-to-normal ratios (Fig. 12.3) of oxy- ($rHbO_2$) and deoxy- (rHb) haemoglobin, total haemoglobin concentration (rTHC), blood oxygen saturation ($rStO_2$), and tissue scattering ($r\mu_s'$) were reconstructed. In addition, an optical index ($OI = rTHC \times r\mu_s'/rStO_2$) was proposed to increase the tumor contrast. Results indicated that malignant cancers show statistically significant higher total haemoglobin, oxy-haemoglobin concentration, scattering, and optical index compared to normal tissue, whereas benign tumors do not exhibit statistical significance in the tumor-to-normal ratios of any parameter.[44]

Flexman and coworkers[49] also investigated the dynamic hemodynamic changes due to a breath hold in a digital optical breast imaging system and its potential for use in breast cancer detection. The system is used to image both breasts simultaneously over the course of a breath hold in both a healthy volunteer and a breast cancer patient. Preliminary results support the potential use of a breath hold to detect breast lesions. Specifically, during the recovery period of the breath hold, the tumor can be identified by

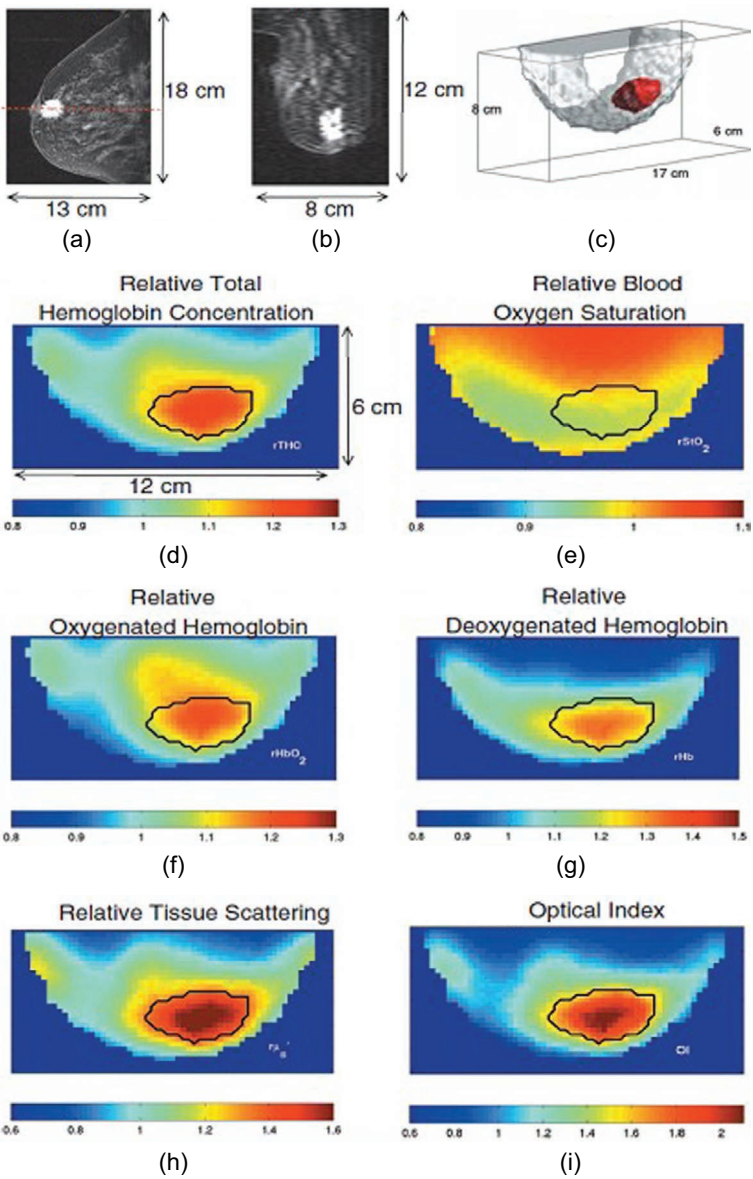

Figure 12.3 MR image and DOT images of a 2.2-cm invasive ductal carcinoma in the right breast of a 53-year-old woman. (a) Sagittal dynamic-contrast-enhanced MRI (DCE-MRI) containing the tumor center.(b) Axial DCE-MRI slice along the red horizontal line in (a). (c) Tumor region (in red) determined based on MRI-guided optical data in 3D space. (d)–(i): DOT images of (d) rTHC, (e) $rStO_2$, (f) $rHbO_2$, (g) rHb, (h) $r\mu_s'$ at 786 nm, and (i) OI. High tumor-to-normal contrast is visible within the tumor region (black solid line) in all of the DOT images. (Reprinted with permission from Ref. 44.)

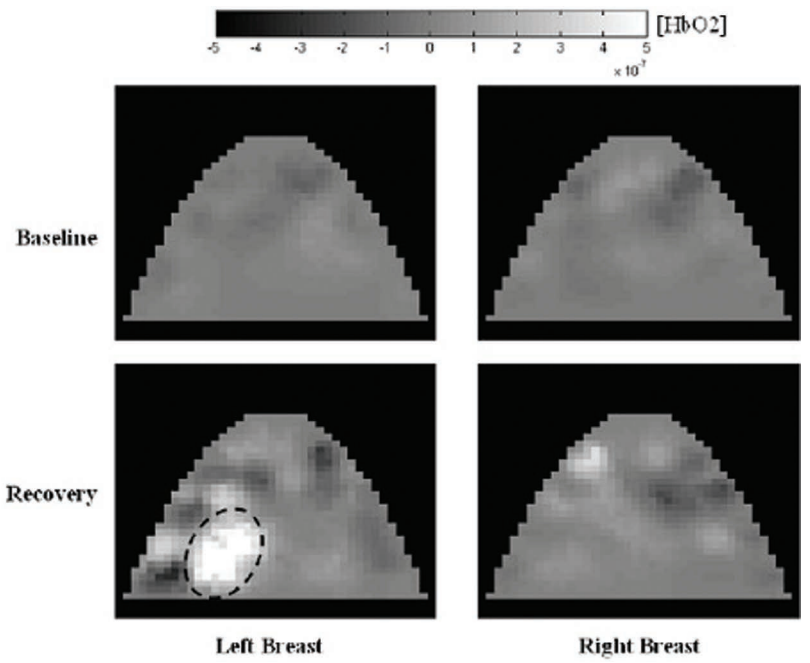

Figure 12.4 Oxy-haemoglobin axial maps of the left and right breast taken during the baseline prior to a 30-sec breath hold, and during the recovery period 15 sec following the end of the breath hold. The tumor region is identified by the dashed line. (Reprinted with permission from Ref. 49.)

an increase in haemoglobin levels (Fig. 12.4). During the breath hold, the increase in venous return pressure results in an increase in haemoglobin levels in the breast. Upon recovery, the haemoglobin levels return to their baseline values. However, the convoluted vasculature of the tumor region is more sluggish in responding to the end of the breath hold. This creates a time window (15 sec immediately after the breath hold) where the increased haemoglobin levels in the tumor distinguish it from the background tissue.[49]

Alternatively, endogenous fluorophores, such as protoporphyrin IX (PPIX), can also be used for breast cancer detection and characterization. PPIX is an endogenous fluorophore involved in the synthesis of heme, which is normally produced at low levels in tissue. However, the rate of PPIX production and accumulation can be dramatically enhanced with the systemic or topical administration of 5-aminolevulinic acid (ALA). ALA-induced PPIX is typically utilized in photodynamic therapy and exploited as a tumor marker in various kinds of cancers, including breast cancer. Recently, Davis et al.[51] demonstrated MRI-coupled PPIX fluorescence tomography in the breast of a patient undergoing chemotherapy for breast cancer. The fibro-glandular tissue shows the highest level of fluorescence

activity, followed by the tumor region and adipose tissue, and chemotherapy is likely to affect PPIX production in breast cancer cells. Such preliminary results will require further validation, which may allow PPIX fluorescence tomography to be used for breast cancer diagnosis and chemotherapy monitoring in the future.[50]

12.4.1.2 Exogenous contrast

In breast cancer imaging, exogenous contrast dyes can be exploited to improve tumor contrast via the spatial distribution of their concentrations and lifetimes within the tissue. This offers higher sensitivity and specificity in terms of detection and also provides additional information about the tissue micro-environment, such as pO_2, pH, and intracellular calcium concentration. At present, indocynanine-green (ICG) is the only FDA-approved dye suitable for DOT, since it has both absorption and fluorescence spectra in the NIR region (650–900 nm). Previously, Godavarty et al. conducted fluorescence imaging using ICG in breast phantoms,[51] and Reynolds et al. used fluorescent contrast agents to image canine breast cancer,[52] while Corlu et al. also demonstrated the first 3D ICG-based fluorescence DOT of breast cancer in humans.[53]

12.4.2 Therapy monitoring

Neoadjuvant chemotherapy is commonly used to treat women with locally advanced breast cancer, and therapeutic monitoring is essential for treatment efficacy. In the past, DCE-MRI and positron emission tomography (PET) have always been used to monitor changes in both tumor size and vasculature following neoadjuvant chemotherapy in breast cancer patients. However, such methods are costly and, thus, impractical for frequent monitoring. To circumvent this problem, a more cost-effective alternative, diffuse optical imaging, has been developed and applied successfully in similar clinical settings, using imaging instruments[6,54] and hand-held probes.[5,37]

In recent development, Srinivasan and coworkers[55] proposed using the boundary element method (BEM) in an image-guided NIR spectroscopy (IG-NIRS) setting in order to quantitatively reconstruct THC, StO_2, water, and scattering coefficient during neoadjuvant chemotherapy treatment. The BEM was used to model light propagation in 3D based on surface discretization, and a dual-modality MRI-NIR system was used to acquire light reflectance data from breast tissue. For clinical validation, this technique was applied to six healthy individuals and one breast cancer patient. Results showed that healthy breast tissues exhibited higher THC and water in fibroglandular tissue than in adipose tissue. In the cancer patient, the tumor exhibited higher THC compared to the background and was reduced by 9 μM during treatment (Fig. 12.5). Thus, this method provides

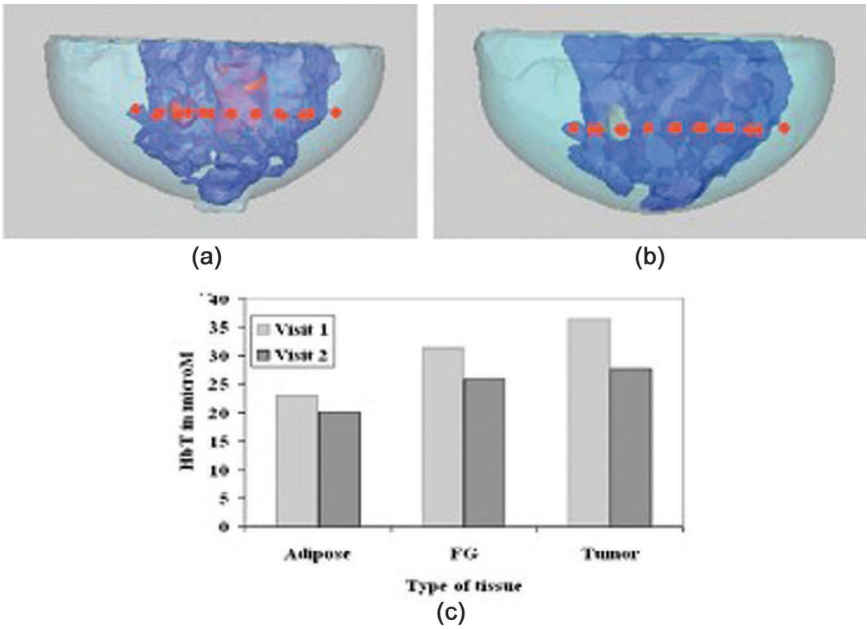

Figure 12.5 Rendered surfaces of adipose, FG, and lesions segmented from T1-weighted MRI and DCE-MRI of subject undergoing neoadjuvant chemotherapy for (a) visit 1 and (b) visit 2. The red markers indicate optical fiber locations. (c) Reconstructed IG-NIRS values for HbT in adipose, fibrograndular (FG), and tumor tissues for both visits. The subject underwent a therapeutic response. (Reprinted with permission from Ref. 55.)

potentially complementary information to DCE-MRI for tumor characterization, as well as hemodynamic responses to therapeutic treatment.[55]

Li and coworkers[56,57] also built a dual-wavelength dual-modality (MR-NIR) tomography system that has the ability to image through thick breast tissue at 20 Hz. In the system, both MR and NIR images were acquired simultaneously and coregistered, during which the MR images provided prior structural information for NIR reconstruction. In addition, acquisition of the finger pulse oximeter (PO) plethysmogram was also synchronized with the system, in order to offer a frequency-locked reference. The fast Fourier transform of the output signal sequence indicated that the heart rate of the subject was between 1.1 and 1.4 Hz during imaging. The blood flow signal in breast tissue had a small peak sharing the same temporal frequency range of 1.1 to 1.4 Hz as the PO output. Thus, these results demonstrated the ability of this multimodality design to recover small pulsatile variations in absorption within breast tissue due to the heartbeat. This capability can be useful for breast tissue characterization and evaluation of treatment response to neoadjuvant chemotherapy. Moreover, the results also demonstrated the system's ability to image fast-flowing signals in deep tissue.[56,57]

Gioux et al.[58] designed a novel spatial frequency-domain multispectral NIR oxygenation imaging device and performed the first *in vivo* skin flap oxygenation imaging for patients undergoing breast reconstruction after mastectomy. The system employs a novel laser diode light source capable of providing six different wavelengths, a digital micromirror device (DMD)-based projector to project light patterns, and a three-camera system capable of simultaneously collecting two NIR spectral bands with a color image. This study lays the foundation for the clinical translation of endogenous contrast imaging in surgery, providing useful intraoperative feedback to surgeons.[58]

12.5 Future of DOI of the Breast

Although diffuse optical tomography (DOT) and fluorescence diffuse optical tomography (fDOT) are powerful in-vivo optical imaging techniques for imaging the breast as well as other tissues, they are normally limited by slow data acquisition and low accuracy. In addition, possible new optically accessible physiological parameters can be added, which can serve as tumor markers. In this section, we present novel techniques and approaches that have been recently developed, in order to overcome current shortcomings.

12.5.1 Structural illumination

Recently, the use of spatially modulated light has been proposed in order to reduce the acquisition time and computational complexity of the inverse problem. Additionally, the measured datasets can be compressed to further boost the image reconstruction speed. Konecky et al.[59] demonstrated the use of structured illumination to reconstruct 3D images of absorption contrast in turbid media, via analytic and finite-element-based reconstruction (Fig. 12.6). In addition, a novel correction to the diffusion approximation for increased accuracy near boundaries was also introduced.[59]

Belanger et al.[60] designed a novel optical acquisition scheme based on a pair of DMDs that was able to perform high-resolution quantitative volumetric imaging of absorbing targets within turbid media. In addition, the reconstruction algorithm was implemented on a graphical processor unit to provide optical reconstructions at a frame rate of 2 Hz. This proposed method has significant cost advantages over camera systems, since only a single detector is required. Moreover, it also has the potential to increase frame rate, moving toward real-time DOT.[60]

Mazhar et al.[61] showed that oxy- and deoxy-haemoglobin concentrations in tissues can be measured accurately via acquiring spatial-frequency-domain imaging data at only two wavelengths (670 and 850 nm), as long as proper assumptions for water and lipid fractions are made in the fitting process. The quality of *in vivo* fitting for both oxy- (HbO_2) and deoxy-haemoglobin (Hb)

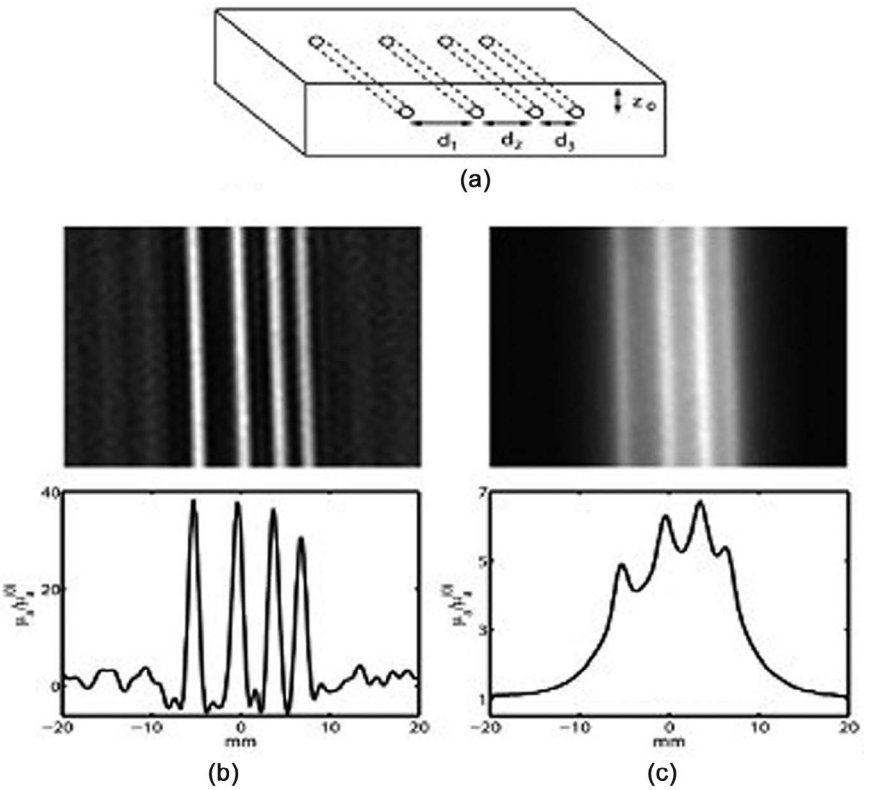

Figure 12.6 (a) Schematic of tissue simulating phantom with four absorbing tubes located at a depth of $z_0 = 2$ mm, and with lateral separations of $d_1 = 5$ mm, $d_2 = 4$ mm, and $d_3 = 3$ mm. (b) Image and line profile of the reconstructed image using the tomographic method. (c) Image and line profile of the image produced by fitting to a homogeneous model. (Reprinted with permission from Ref. 59, © 2009 OSA.)

is dependent on wavelength selection, fitting parameters, and acquisition rate. Wavelength optimization enables dynamic imaging of arterial occlusions with improved spatial resolution due to reduction of motion artifacts.[61]

Structured illumination can also be applied to fluorescence imaging. Ducros and coworkers[62,63] experimentally demonstrated a fast finite-element-based reconstruction algorithm for structured illumination in fDOT, for both slab and cylindrical geometries. The approach consists of illuminating the medium with a few wavelet patterns and compressing the acquired images via wavelet transform. Compared to the classical raster-scanning method, the proposed technique is able to reduce both acquisition and reconstruction times dramatically while maintaining high image quality, thus making it suitable for *in vivo* applications.[62,63]

In addition, Mazhar and coworkers[64] introduced a noncontact imaging method utilizing multifrequency structured light for improving lateral and axial resolution and contrast of fluorescent molecular probes in turbid

media. They demonstrated that by increasing the spatial frequency, fluorescence from deeper structures is suppressed, while signals from more superficial objects are enhanced. By measuring the fluorescence dependence on spatial frequency, the background can be reduced by localizing the signal to a buried fluorescent object. This method improves localization and SNRs, when compared to planar imaging techniques.[64]

12.5.2 Spectral derivative

Dehghani and coworkers[65,66] proposed the concept of using spectral derivative data in NIR diffuse optical spectroscopy and tomography, whereby the difference between adjacent spectral measurements is utilized instead of using discrete measurements at certain wavelengths. In terms of spectroscopy, reflectance measurements from 650 to 850 nm at 2-nm intervals are acquired on the forearms of three human subjects. The collected data is then utilized together with the spectral derivative technique for calculation of physiological parameters, such as THC, StO_2, water content, and scattering properties. In addition, this technique is also extended to full tomographic image reconstruction, where it can provide better image quality via eliminating image artifacts and improving contrast, as well as reducing cross-talk. As a whole, this method is proven to be independent of the tissue type and fiber contact coupling coefficients, thus providing significantly higher accuracy when compared to traditional techniques. Moreover, its self-calibrating capability also improves its robustness in clinical settings, as demonstrated by simulation and experimental results.[65,66]

12.5.3 New parameters

In the search for optical contrast to enhance differentiation between tumor and normal tissues, research groups are employing broader wavelength ranges to explore other endogenous parameters. Chung et al.[67] developed a bound water index (BWI) from quantitative tissue water absorption spectra in the NIR region. The accuracy of BWI as a water state index was validated by comparing broadband DOS to MR spectroscopy, diffusion-weighted MRI, and conductivity in bound water phantoms. Noninvasive DOS measurements of malignant and normal breast tissues performed in 18 subjects showed a significantly higher fraction of free water in malignant tissues compared to normal tissues (Figs. 12.7 and 12.8). These results highlight broadband DOS sensitivity to tissue water content and state, and demonstrate the potential of BWI as a noninvasive *in vivo* index that correlates with tissue pathology.[67]

12.6 Conclusion

In summary, DOI makes use of diffuse light to probe deep tissues by taking advantage of low tissue absorption within the NIR wavelength range

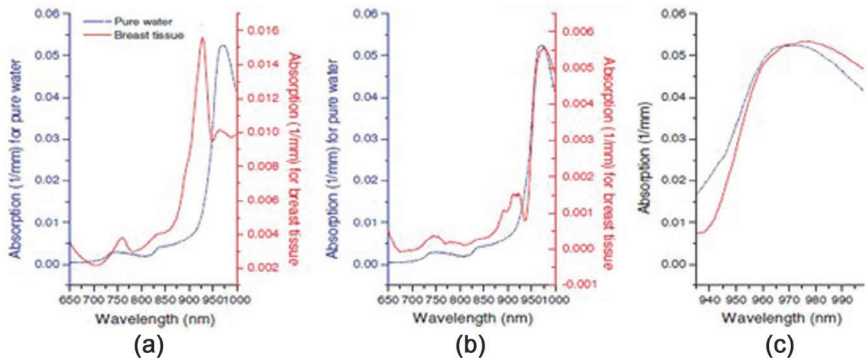

Figure 12.7 (a) *In vivo* tissue absorption spectrum (solid line) from normal breast tissue. (b) Tissue water spectrum after subtracting other tissue components' spectra (solid line). (c) Normalized tissue water spectrum at 935–998 nm (solid line). The pure water spectrum at 36 °C is shown in each panel (a, b and c, dashed lines) for comparison. (Reproduced with permission from Ref. 67, © 2008 Institute of Optics.)

(650–900 nm). The optical measurements obtained can be used to calculate optical properties, namely absorption and scattering, within tissues. This, in turn, can provide information about physiological parameters within tissues (such as oxy- and deoxy- haemoglobin, water, and lipid) that can be utilized in the detection, characterization, and therapy monitoring of breast cancer.

Currently, the future of DOI is bright. Many excellent research groups worldwide are actively developing new technologies, and we are

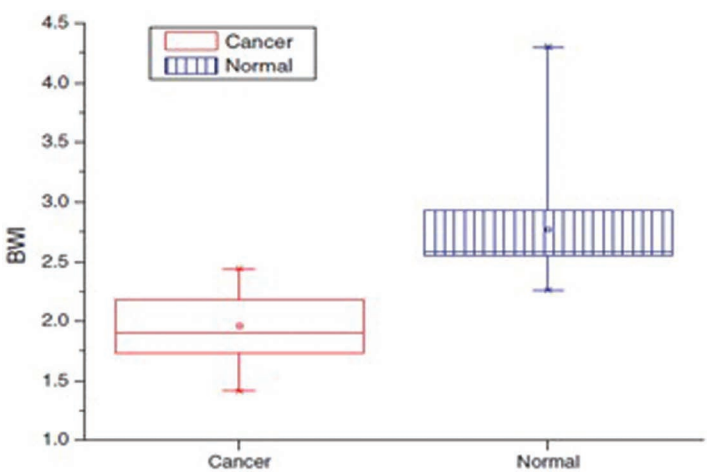

Figure 12.8 Box plots of BWI of malignant (1.96 ± 0.3) and normal (2.77 ± 0.47) breast tissues for 18 subjects. Tumor and normal tissues were differentiated with statistical significance with $p < 0.0001$ (Wilcoxon ranked-sum test). (Reproduced with permission from Ref. 67, © 2008 Institute of Optics.)

witnessing fast translation from table-top experiments to clinical trials. We believe that it will not be too long before inexpensive and safe optical mammography systems are widely introduced in all the breast clinics.

References

1. American Cancer Society, "Cancer Facts & Figures 2012" http://www.cancer.org.
2. K. Kerlikowske, J. Barclay, D. Grady, E. A. Sickles, and V. Ernster, "Comparison of risk factors for ductal carcinoma in situ and invasive breast cancer," *J. Natl. Cancer Inst.* **89**, 76–82 (1997).
3. A. Karellas and S. Vedantham, "Breast cancer imaging: A perspective for the next decade," *Med. Phys.* **35**(11), 4878–4897 (2008).
4. J. Wang, T. T. Shih, J. C. Hsu, and Y. W. Li, "The evaluation of false negative mammography from malignant and benign breast lesions," *J. Clin. Imaging* 24, 96–103 (2000).
5. D. B. Jakubowski, A. E. Cerussi, F. Bevilacqua, N. Shah, D. Hsiang, J. Butler, and B. J. Tromberg, "Monitoring neoadjuvant chemotherapy in breast cancer using quantitative diffuse optical spectroscopy: A case study," *J. Biomed. Optics* **9**, 230–238 (2004).
6. R. Choe, A. Corlu, K. Lee, T. Durduran, S. D. Konecky, M. Grosicka-Koptyra, S. R. Arridge, B. J. Czerniecki, D. L. Fraker, A. DeMichele, B. Chance, M. A. Rosen, and A. G. Yodh, "Diffuse optical tomography of breast cancer during neoadjvant chemotherapy: a case study with comparison to MRI," *Med. Phys.* **32**, 1128–1139 (2005).
7. R. Choe and A. G. Yodh, "Diffuse optical tomography of the breast," *Emerging Technologies in Breast Imaging and Mammography*, J. S. Suri, R. M. Rangayyan, amd S. Laxminarayan, Eds., American Scientific, Valencia, CA, pp. 317–342 (2008).
8. T. Durduran, R. Choe, W. B. Baker, and A. G. Yodh, "Diffuse optics for tissue monitoring and tomography," *Rep. Prog. Phys.*, **73**(7), 0076701 (2010).
9. K. Lee, "Optical mammography: Diffuse optical imaging of breast cancer," *World J. Clin. Oncol.* **1**, 64–72 (2011).
10. D. A. Boas, *Diffuse Photon Probes of Structural and Dynamical Properties of Turbid Media: Theory and Biomedical Applications*, University of Pennsylvania Press, Pennsylvania (1996).
11. D. A. Boas, L.E. Campbell, and A. G. Yodh, "Scattering and imaging with diffusing temporal field correlations," *Phys. Rev. Lett.* **75**(9), 1855–1858 (1995).

12. D. A. Boas and A. G. Yodh, "Spatially varying dynamical properties of turbid media probed with diffusing temporal light correlation," *J. Opt. Soc. Am. A* **14**(1), 192–215 (1997).

13. G. Maret and P. E. Wolf, "Multiple light scattering from disordered media: The effect of Brownian motion of scatterers," *Zeitschrift für Physik B Condensed Matter* **65**(4), 409–413 (1987).

14. D. J. Pine, D. A. Weitz, P. M. Chaikin, and E. Herbolzheimer, "Diffusing wave spectroscopy," *Phy. Rev. Lett.* **60**(12), 1134 (1988).

15. R. Nossal, S. H. Chen, and C. C. Lai, "Use of laser scattering for quantitative determinations of bacterial motility," *Opt. Comm.* **4**(1), 35–39 (1971).

16. R. Bonner and R. Nossal, "Model for laser Doppler measurements of blood flow in tissue," *Appl. Opt*. **20**(12), 2097–2107 (1981).

17. C. Cheung, J. P. Cilver, K. Takahashi, J. H. Greenberg, and A. G. Yodh, "In vivo cerebrovascular measurement combining diffuse near-infrared absorption and correlation spectroscopies," *Phys. Med. Biol.* **46**(8), 2053–2065 (2001).

18. G. Yu, T. Durduran, G. Lech, et al., "Time-dependent blood flow and oxygenation in human skeletal muscles measured with noninvasive near-infrared diffuse optical spectroscopies," *J. Biomed. Opt.* **10**(2), 024027 (2005) [doi: 10.1117/1.1884603].

19. G. Yu, T. Durduran, C. Zhou, et al., "Noninvasive monitoring of murine tumor blood flow during and after photodynamic therapy provides early assessment of therapeutic efficacy," *Clin. Cancer Res.* **11**(9), 3543–3552 (2005).

20. S. Arridge and J. Schotland, "Optical tomography: Forward and inverse problems," *Inverse Problems* **25**(123010) (2009).

21. S. Srinivasan, B. W. Pogue., C. Carpenter, P. K. Yalavarthy, and K. Paulsen, "A boundary element approach for image-guided near-infrared absorption and scatter estimation," *Med. Phys.* **34**, 4545–57 (2007).

22. L. Wang and S. L. Jacques, "Hybrid model of Monte Carlo simulation diffusion theory for light reflectance by turbid media," *J. Opt. Soc. Am. A* **10**, 1746–52 (1993).

23. S. R. Arridge, "Optical tomography in medical imaging," *Inverse Problems* **15**, R41–R93 (1999).

24. A. B. Gibson, J. C. Hebden, and S. R. Arridge, "Recent advances in diffuse optical imaging," *Phys. Med. Biol.* **50**, R1–43 (2005).

25. V. A. Markel and J. C. Schotland, "Inverse problem in optical diffusion tomography: I. Fourier-Laplace inversion formulas," *J. Opt. Soc. Am. A* **18**, 1336–47 (2001).

26. V. A. Markel and J. C. Schotland, "Inverse problem in optical diffusion tomography: II. Role of boundary conditions*." J. Opt. Soc. Am. A* **19**, 558–66 (2002).

27. V. A. Markel, V. Mital, and J. C. Schotland, "Inverse problem in optical diffusion tomography: III. Inversion formulas and singular-value decomposition," *J. Opt. Soc. Am. A* **20**, 890–902 (2003).

28. S. D. Konecky, G. Y. Panasyuk, K. Lee, V. Markel, A. G. Yodh, and J. C. Schotland, "Imaging complex structures with diffuse light," *Opt. Express* **16**, 5048–60 (2008).

29. S. Arridge and M. Schweiger, "A gradient-based optimisation scheme for optical tomography," *Opt. Express* **2**, 213–26 (1998).

30. A. H. Hielscher, A. D. Klose, and K. M. Hanson, "Gradient-based iterative image reconstruction scheme for time-resolved optical tomography," *IEEE Trans. Med. Imaging* **18**(3), 262–71 (1999).

31. http://web4.cs.ucl.ac.uk/research/vis/toast/.

32. H. Dehghani, M. E. Eames, P. K. Yalavarthy, S. C. Davis, S. Srinivasan, C. M. Carpenter, B. W. Pogue, and K. D. Paulsen, "Near infrared optical tomography using NIRFAST: Algorithm for numerical model and image reconstruction," *Commun. Numer. Methods Eng.* **25**(6), 711–732 (2008).

33. B. W. Pogue, T. O. McBride, J. Prewitt, U. L. Österberg, and K. D. Paulsen, "Spatially variant regularization improves diffuse optical tomography," *Appl. Opt.* **38**(13), 2950–61 (1999).

34. H. Dehghani, S. Srinivasan, B. W. Pogue, and A. Gibson, "Numerical modelling and image reconstruction in diffuse optical tomography." *Phil. Trans. R. Soc. A* **367**(1900), 3073–3093 (2009).

35. F. Bevilacqua, A. J. Berger, A. E. Cerussi, D. Jakubowski, and B. J. Tromberg, "Broadband absorption spectroscopy in turbid media by combined frequency-domain and steady-state methods," *Appl. Opt.* **39**(34), 6498–6507 (2000).

36. A. Cerussi, N. Shah, D. Hsiang, A. Durkin, J. Butler, and B. J. Tromberg, "*In vivo* absorption, scattering, and physiologic properties of 58 malignant breast tumors determined by broadband diffuse optical spectroscopy," *J. Biomed. Opt.* **11**(4), 044005 (2006) [doi: 10.1117/1.2337546].

37. A. Cerussi, D. Hsiang, N. Shah, R. Mehta, A. Durkin, J. Butler, and B. J. Tromberg, "Predicting response to breast cancer neoadjuvant chemotherapy using diffuse optical spectroscopy," *Proc. Natl. Acad. Sci. (US)* **104**(10), 4014–4019 (2007).

38. X. Intes, "Time-domain optical mammography SoftScan: Initial results," *Acad. Radiol.* **12**(8), 934–947 (2005).

39. A. Bassi, A. Farina, C. D'Andrea, A. Pifferi, G. Valentini, and R. Cubeddu, "Portable, large-bandwidth time-resolved system for diffuse optical spectroscopy," *Opt. Express* **15**(22), 14482–14487 (2007).

40. G. Yu, T. F. Floyd, T. Durduran, C. Zhou, J. Wang, J. A. Detre, and A. G. Yodh, "Validation of diffuse correlation spectroscopy for muscle blood flow with concurrent arterial spin labeled perfusion MRI," *Opt. Express* **15**(3), 1064–1075 (2007).

41. R. Choe, "Diffuse optical tomography & spectroscopy in breast cancer characterization & therapy monitoring at UPENN," *Conf. Proc. IEEE Eng. Med. Biol. Soc.* **2009**, 6335–6337 (2009).

42. V. Viasnoff, F. Lequeux, and D. J. Pine, "Multispeckle diffusing-wave spectroscopy: A tool to study slow relaxation and time-dependent dynamics," *Rev. Sci. Instruments* **73**(6), 2336–2344 (2002).

43. J. P. Culver, R. Choe, M. J. Holboke, L. Zubkov, T. Durduran, A. Slemp, A. G. Yodh, V. Ntziachristos, and B. Chance, "Three-dimensional diffuse optical tomography in the parallel plane transmission geometry: Evaluation of a hybrid frequency domain/continuous wave clinical system for breast imaging," *Med. Phys.* **30**, 235–247 (2003).

44. R. Choe, S. D. Konecky, A. Korlu, et al., "Differentiation of benign and malignant breast tumors by in-vivo three-dimensional parallel-plate diffuse optical tomography," *J. Biomed. Opt.* **14**(2), 024020 (2009) [doi: 10.1117/1.3103325].

45. H. Dehghani, M. M. Doyley, B. W. Pogue, S. Jiang, J. Geng, and K. D. Paulsen, "Breast deformation modelling for image reconstruction in near infrared optical tomography," *Phys. Med. Biol.* **49**, 1131–1145 (2004).

46. B. W. Pogue, S. P. Poplack, T. O. McBride, W. A. Wells, K. S. Osterman, U. L. Osterberg, and K. D. Paulsen, "Quantitative hemoglobin tomography with diffuse near-infrared spectroscopy: Pilot results in the breast," *Radiol.* **218**, 261–266 (2001).

47. L. C. Enfield, A. P. Gibson, N. L. Everdell, et al.," Three-dimensional time-resolved optical mammography of the uncompressed breast." *Appl. Opt.* **46**, 3628–3638 (2007).

48. H. Dehghani, B. W. Pogue, S. P. Poplack, and K. D. Paulsen, "Multiwavelength three-dimensional near-infrared tomography of the breast: Initial simulation, phantom, and clinical results," *Appl. Opt*. **42**, 135–145 (2003).

49. M. L. Flexman, M. A. Khalil, R. M. Al Abdi, et al., "Optical tomographic imaging of the hemodynamic response to a breath hold in breast cancer patients," *Proc. SPIE* **7896**, 78962J (2011) [doi: 10.1117/12.875461].

50. S. C. Davis, M. A. Mastanduno, B. W. Pogue, and K. D. Paulsen, "MRI-guided fluorescence tomography of PPIX in the breast: a case study." *Proc. SPIE* **7892**, 78920M (2011) [doi: 10.1117/12.875775].

51. A. Godavarty, M. J. Eppstein, C. Zhang, S. Theru, A. B. Thompson, M. Gurfinkel, and E. M. Sevick-Muraca, "Fluorescence-enhanced optical imaging in large tissue volumes using a gain-modulated ICCD camera," *Phys. Med. Biol.* **48**, 1701–20 (2003).

52. J. S. Reynolds, T. L. Troy, R. H. Mayer, A. B. Thompson, D. J. Waters, K. K. Cornell, P. W. Snyder, and E. M. Sevick-Muraca, "Imaging of spontaneous canine mammary tumors using fluorescent contrast agents," *Photochem. Photobiol*. **70**, 87–94 (1999).

53. A. Corlu, R. Choe, T. Durduran, et al., "Three-dimensional in vivo fluorescence diffuse optical tomography of breast cancer in humans," *Opt. Express* **15**(11), 6696-6716 (2007).

54. S. D. Jiang, B. W. Pogue, C. M. Carpenter, et al., "Evaluation of breast tumor response to neoadjuvant chemotherapy with tomographic diffuse optical spectroscopy: Case studies of tumor region-of-interest changes," *Radiol*. **252**(2), 551–560 (2009).

55. S. Srinivasan, C. M. Carpenter, H. R. Ghadyani, et al., "Image guided near-infrared spectroscopy of breast tissue in vivo using boundary element method," *J. Biomed. Opt.* **15**(6), 061703 (2010) [doi: 10.1117/1.3499419].

56. Z. Li, V. Krishnaswamy, S. Jiang, et al., "Rapid magnetic resonance-guided near-infrared mapping to image pulsatile hemoglobin in the breast," *Opt. Lett.* **35**(23), 3964–3966 (2010).

57. Z. Li, S. Jiang, V. Krishnaswamy, et al. "High frame-rate MR-guided near-infrared tomography system to monitor breast hemodynamics," *Proc. SPIE* **7896**, 78962M (2011) [doi: 10.1117/12.875839].

58. S. Gioux, A. Mazhar, B. T. Lee, et al. "Preclinical and clinical validation of a novel oxygenation imaging system," *Proc. SPIE* **7896**, 78961R (2011) [doi: 10.1117/12.875603].

59. S. D. Konecky, A. Mazhar, D. Cuccua, et al., "Quantitative optical tomography of sub-surface heterogeneities using spatially modulated structured light," *Opt. Express* **17**(17), 14780–14790 (2009).

60. S. Belanger, M. Abran, X. Intes, C. Casanova, and F. Lesage, "Real-time diffuse optical tomography based on structured illumination," *J. Biomed. Opt.* **15**(1), 016006 (2010) [doi: 10.1117/1.3290818].

61. A. Mazhar, S. Dell, D. J. Cuccia, et al., "Wavelength optimization for rapid chromophore mapping using spatial frequency domain imaging," *J. Biomed. Opt.* **15**(6), 061716 (2010) [doi 10.1117/1.3523373].

62. N. Ducros, C. D'andrea, G. Valenti, et al., "Full-wavelet approach for fluorescence diffuse optical tomography with structured illumination," *Opt. Lett.* **35**(21), 3676–3678 (2010).

63. N. Ducros, A. Bassi, G. Valentini, et al., "Multiple-view fluorescence optical tomography reconstruction using compression of experimental data." *Opt. Lett.* **36**(8), 1377–1379 (2011).

64. A. Mazhar, D. J. Cuccia, S. Gioux, et al., "Structured illumination enhances resolution and contrast in thick tissue fluorescence imaging," *J. Biomed. Opt.* **15**(1), 010506 (2010). [doi:10.1117/1.3299321].

65. H. Dehghani, F. Leblond, B. W. Pogue, and F. Chauchard, "Application of spectral derivative data in visible and near-infrared spectroscopy," *Phys. Med. Biol*. **55**(12), 3381–3399 (2010).

66. H. Dehghani, F. Leblond, B. W. Pogue, and F. Chauchard, "Application of spectral derivative data in spectral near infrared tomography," *Proc. SPIE* **7896**, 78960I (2011) [doi: 10.1117/12.873940].

67. S. H. Chung, A. E. Cerussi, C. Klifa, et al., "In vivo water state measurements in breast cancer using broadband diffuse optical spectroscopy," *Phys. Med. Biol*. **53**(23), 6713–6727 (2008).

68. J. Dong, R. Bi, J. H. Ho, P. S. P. Thong, K. C. Soo, and K. Lee, "Diffuse correlation spectroscopy with a fast Fourier transform-based software autocorrelator," *J. Biomed. Opt*. **17**(9), 097004 (2012) [doi: 10.1117/1.JBO.17.9.097004].

69. J. H. Ho, H. L. Chin, J. Dong, and K. Lee, "Multi-harmonic homodyne approach for optical property measurement of turbid medium in transmission geometry," *Opt. Comm*. **285**, 2007–2011 (2012).

Jun Hui Ho is currently a postdoctoral researcher at Singapore Bioimaging Consortium (SBIC), Agency for Science, Technology and Research (A*STAR), in Singapore. He received a Bachelor's degree in Bioengineering and a Ph.D. in Bioengineering from Nanyang Technological University (NTU), Singapore in 2006 and 2012, respectively. His Ph.D. research focused on developing novel imaging and spectroscopic techniques, as well as image processing and reconstruction algorithms in the context of diffuse optics and fluorescence lifetime imaging. His research interests include the application of surface-enhanced Raman spectroscopy and photoacoustic techniques in the diagnosis of diseases.

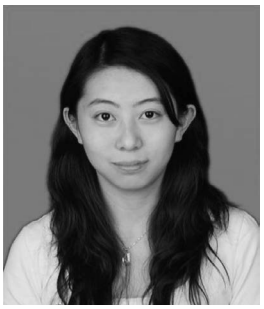

Jing Dong is currently a Ph.D. student in the School of Chemical and Biomedical Engineering at Nanyang Technological University, Singapore. She received her B.S. degree from Xi'an Jiaotong University, Shaanxi, China in 2008. Her research is focused on developing a multimodal noninvasive system on the brain by using diffuse optical and correlation spectroscopic, as well as electroencephalographic techniques.

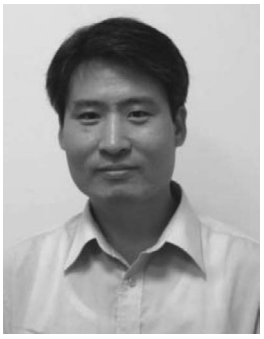

Kijoon Lee has a Ph.D. degree in physics from Brown University, RI, USA, and worked at the University of Pennsylvania as a postdoctoral researcher before joining the School of Chemical and Biomedical Engineering in Nanyang Technological University as an assistant professor. His expertise includes instrumentation and image reconstruction in diffuse optical tomography, and noninvasive flow measurement using diffuse correlation spectroscopy. His research is focused on developing a fast optical tomography system and a noninvasive multimodal functional imaging system in the breast and brain.

Chapter 13
Computer Vision Theoretic Approach for Breast Cancer Diagnosis: Commonly Perceived Diagnostic Significance of Cytological Features and Feature Usability Analysis of an Existing Breast Cancer Database

Hrushikesh Garud
School of Medical Science and Technology, Indian Institute of Technology Kharagpur, Kharagpur, India and Texas Instruments (I) Pvt. Ltd., Bangalore, India

Debdoot Sheet, Jyotirmoy Chatterjee, and Manjunatha Mahadevappa
School of Medical Science and Technology, Indian Institute of Technology Kharagpur, Kharagpur, India

Ajoy Kumar Ray
Department of Electronics and Electrical Communication Engineering, Indian Institute of Technology Kharagpur, Kharagpur, India and Bengal Engineering and Science University, Shibpur, India

Arindam Ghosh
Sub-Divisional Hospital, Kharagpur, India

13.1 Introduction

Cytopathology is a branch of pathology that studies and diagnoses diseases on the cellular level using samples of free cells or tissue fragments. The tissue fragments can be collected by exfoliation or by intervention techniques such as fine-needle aspiration (FNA). FNA is widely used for evaluation of a variety of breast abnormalities. It has been shown in numerous studies to be a good screening tool for diagnosis of breast lumps in symptomatic patients. Microscopic appearance of the nuclei, cells, cellular arrangement in clusters, and background elements in the smeared aspirates provide clues for evaluation and diagnosis. Several visual clues (features) relevant for the diagnosis of benign or malignant conditions of the breast abnormality as obtained via microscope have been reported in the literature and are used by experts in the decision-making process. A list of eighteen such adequate cytological features is given in Table 13.1. The list was prepared with the help of scholarly texts in clinical pathology.[1–5] The list is subdivided in the four categories (1) aggregate properties, (2) background properties, (3) nuclear properties, and (4) cellular properties according to the elements whose features are used as evidence for diagnosis.

Currently, cytological diagnosis of the breast lump is based on the subjective assessment of the microscopic appearance of the aspirate. As a result, difficulties in maintaining consistency and reproducibility are inevitable. A review of the literature[2,3] served to highlight the following limitations of fine-needle aspiration cytology (FNAC) leading to equivocal diagnosis: (1) inadequate or nonrepresentative sampling, and (2) the overlap of cytological features of benign and malignant lesions due to the nature of the lesion. Image analysis of breast FNAC slides by computer vision techniques is helpful in overcoming some of these limitations.[5] Incorporating the practice of FNA with an expert system embedded in a microscope aids pathologists/cytopathologists (experts) in a speedy and accurate assessment of the slides through the use of quantitative and objective feature assessment for diagnostic decision making.

Table 13.1 List of cytological features used in breast FNAC diagnosis.

Aggregate properties
1. Overall cell yield
2. Presence or absence of bimodal pattern of aggregates of epithelial cells
3. Size and shape of aggregates
4. Cohesiveness of epithelial cells in the aggregates
5. Presence/absence or count of myoepithelial cell nuclei in aggregates
Background properties
6. Presence/absence of bare nuclei
7. Presence/absence of single cells with intact cytoplasm
8. Nature of background
Nuclear properties
9. Nuclear size
10. Nuclear shape
11. Nuclear membrane
12. Nuclear chromatin
13. Prominence of nucleoli
14. Number of nucleoli
15. Mitosis
Cellular properties
16. Cellular pleomorphism
17. Volume and color of cytoplasm
18. Nucleus–cytoplasmic ratio

Computer vision techniques that use histological or cytological images for computer-aided cancer diagnosis have been in development for some time now.[6] These approaches use image processing, image segmentation, feature quantification, and pattern recognition to perform quantitative and objective feature assessment. These approaches essentially try to mimic an expert's bottom-up manner of diagnostic reasoning from evidence to hypothesis.[7]

Development of such computer vision systems entails the following:

- identification of diagnostic procedures and features used by experts;
- selection of aspects that are well suited to computer-aided analysis;
- selection/development of feature enhancement, delineation, and extraction techniques;
- statistical analysis of feature data and feature selection; and
- selection/development of pattern-recognition techniques for decision making.

There exists differential preference for clinico-pathological procedures and discordance among experts in morphometric diagnosis. Experts either do not use the same criteria for diagnosis or apply the

same criteria differently from one another.[8] Alternatively, it has been observed that, globally, experts see the same, but, locally, they see different things and with different levels of appreciation.[9] Also, for individual experts, reliance on explicit features is dynamic.[10] Thus, it is necessary to develop a meticulous and methodical understanding of the practices and perceptions of domain experts to identify useful and necessary features for computer-aided analysis.

Here we present commonly perceived significance levels for cytological features used in breast FNAC obtained through an India-wide survey of experts' opinions. This information can be used for selecting the cytological features for computer-aided analysis, selecting feature extraction and quantification techniques, and for combining experts' acumen with learning algorithms to improve their performance. Further, we also present the feature ranking and selection analysis of the Wisconsin Diagnostic Breast Cancer (WDBC) database.[5] Findings of this analysis are discussed in the context of the survey findings to highlight the fact that the class discrimination ability of cytological criteria is different from the class discrimination ability of the objective/mathematical features used to quantify and represent the state of cytological features. Findings of this analysis are also discussed in the context of the need for selection of optimal feature-extraction techniques.

13.2 Commonly Perceived Significance of Cytological Features in Breast FNAC

Essentially, there exists a difference of opinion among experts on the absolute and relative diagnostic significance of the cytological features in breast lesion diagnosis. This work has been initiated with the belief that the commonly perceived diagnostic significance of a cytological feature represents its true ability in discriminating between benign and malignant conditions of a breast lump. This ability of the cytological criteria is different from class discrimination ability of the objective/mathematical features used to quantify and represent the state of cytological features. Linguistic features visually identified by a domain expert can each be quantified using multiple techniques. Every method of quantification has a different aptitude to represent underlying physical evidence[11] and thus has different discriminatory power.[12]

To identify the commonly perceived diagnostic significance of cytological features for diagnosis of benign or malignant condition of breast lesions, an India-wide questionnaire-based survey of cytopathologists' opinions was conducted. The findings of this survey are presented here. The following subsection describes the methodology of the survey.

Subsection 13.2.2 explains how individual opinions of the participants were combined and presents the survey findings.

13.2.1 Overview of the survey

As mentioned earlier, identification of the commonly perceived diagnostic significance of cytological features was the primary goal of the survey; however, the survey also served to identify the common clinico-pathological practices followed by experts. Accordingly, the survey questionnaire was prepared with help from scholarly texts in clinical pathology.[1–4] To complement the set goals, participants were asked to specify the importance level they attach to each cytological feature during diagnosis of benign or malignant conditions. For each cytological feature, the participants selected one of the five predefined linguistic significance levels defined as not significant (0), slightly significant (1), moderately significant (2), significant (3), and most significant (4). Here numerical values in the brackets represent corresponding numerical values used to combine individual opinions in finding common perception. The sample question in the questionnaire is given in Fig. 13.1, where the experts specified the importance (significance) they attach to the *nuclear size* along with the microscope objective magnification they use for observation. The information on objective magnifications used can help design the imaging protocol for computer-aided analysis.

We received responses from 51 cytopathologists/pathologists from renowned medical education institutes (52%), oncological tertiary care centers (28%), and primary care centers/private diagnostic pathology laboratories (20%) spread over 13 states (marked in pink in Fig. 13.2) of India. Individual reporting experiences of the participants are in the range of 2 to 41 years with an average reporting experience of 17 years. An overview of the survey is provided in Fig. 13.3.

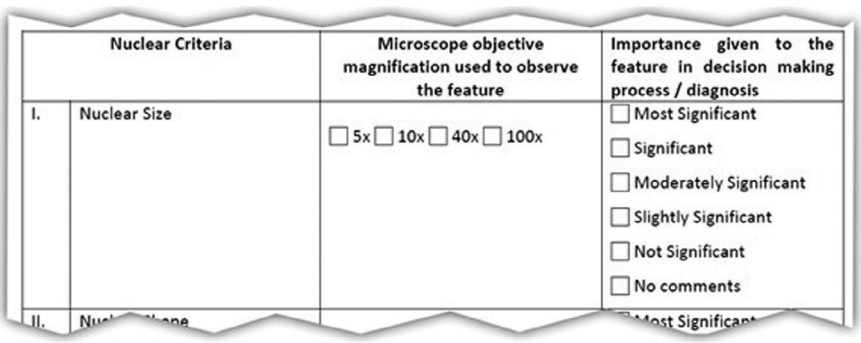

	Nuclear Criteria	Microscope objective magnification used to observe the feature	Importance given to the feature in decision making process / diagnosis
I.	Nuclear Size	☐ 5x ☐ 10x ☐ 40x ☐ 100x	☐ Most Significant ☐ Significant ☐ Moderately Significant ☐ Slightly Significant ☐ Not Significant ☐ No comments
II.	Nuc[illegible]hape		[illegible]Most Significant

Figure 13.1 Sample question in the survey.

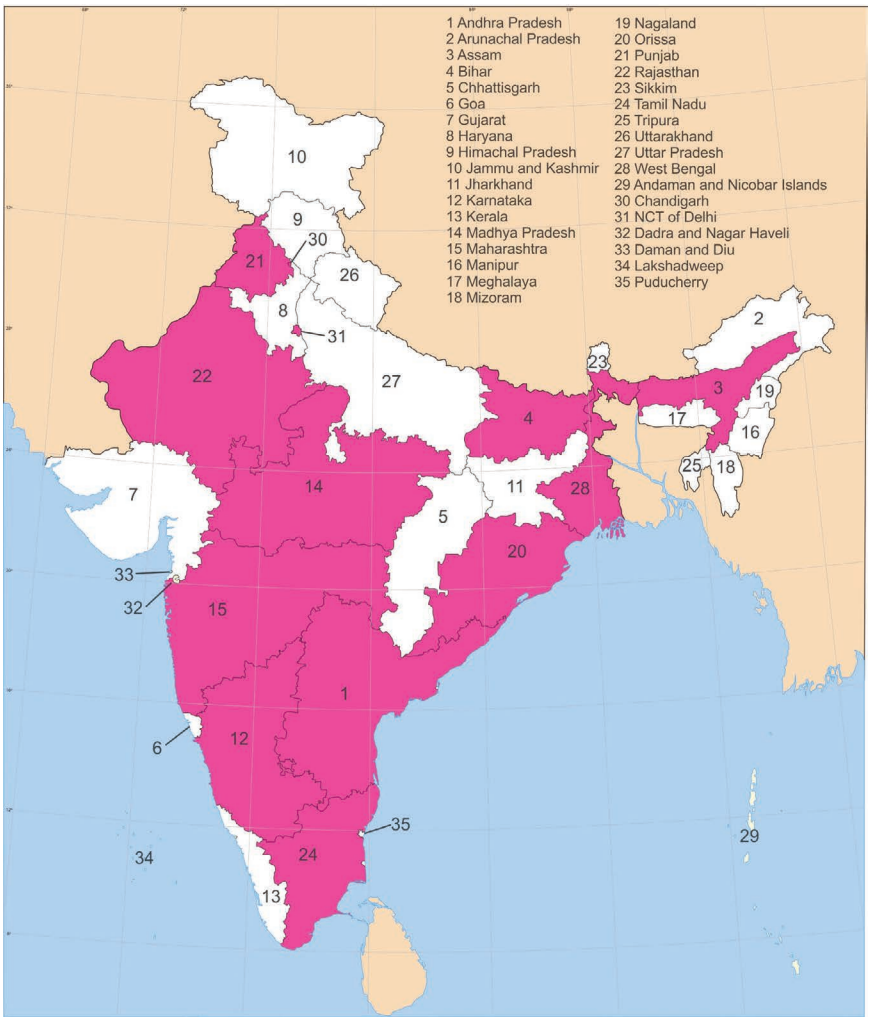

Figure 13.2 Map of India with states from which responses were received highlighted in pink.

13.2.2 Opinion of the experts

Participants' percentage opinion on significance levels of the cytological features is given in Fig. 13.4. Though there exists a considerable degree of agreement among the participants on diagnostic significance of most of the cytological criteria, there exists varying levels of concordance among the experts for different cytological features. For four criteria, namely, size and shape of aggregates, nature of background, number of nucleoli, and volume and color of cytoplasm, participants exhibit a relatively higher degree of disagreement.

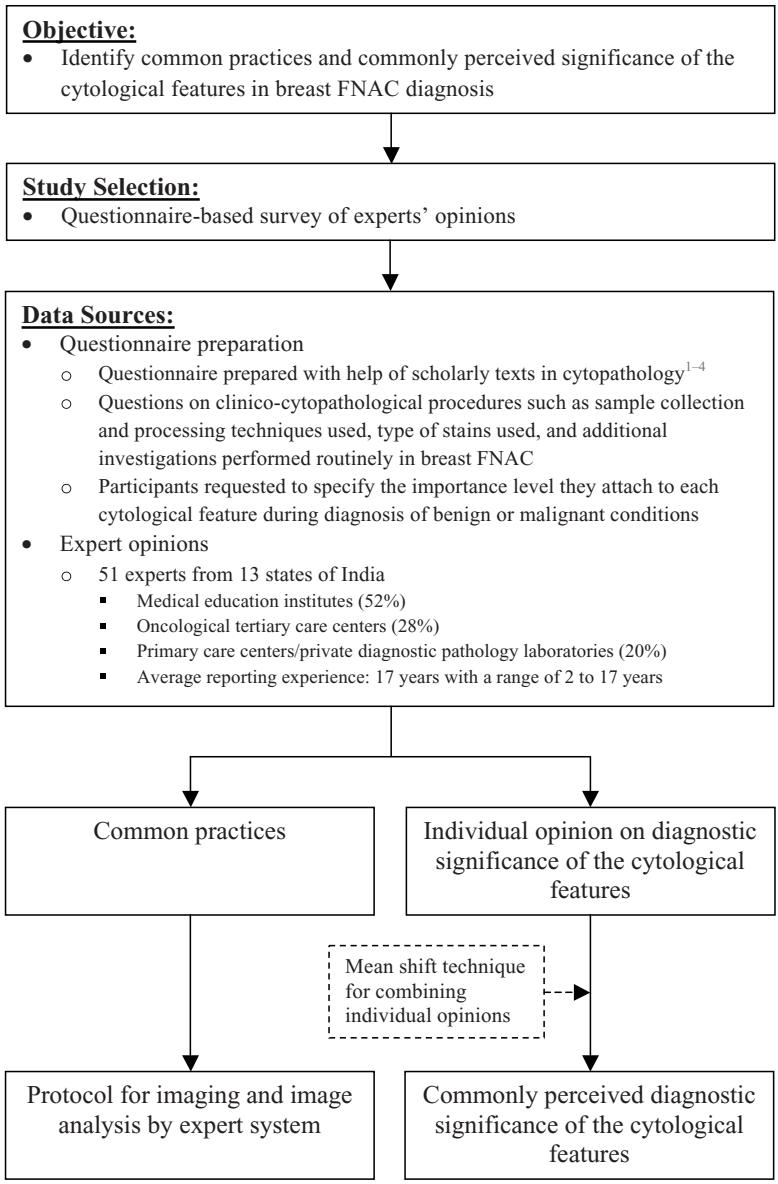

Figure 13.3 Overview of the survey. Details of the survey and its findings are available in Ref. 17.

Compilation of the responses to identify the commonly perceived relative significance of the cytological features has been performed by use of a mean shift technique.[13] The process treats each participant's opinion on 18 cytological features as a vector (opinion vector (X_i)) and iteratively computes the weighted mean significance vector (X^j). Each opinion is weighted

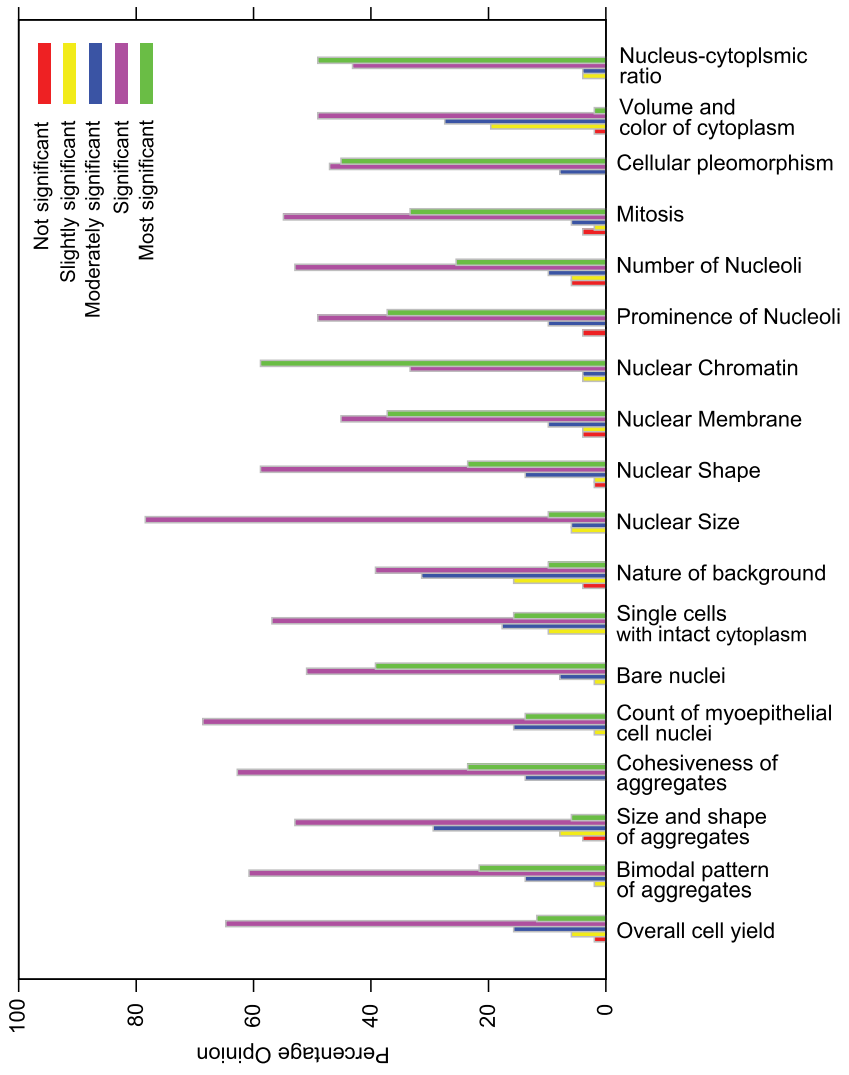

Figure 13.4 Percentage opinion of the participants on significance levels of different cytological features.

Input: Set of N opinion vectors $\{\mathbf{X}_i\}$
Output: Weighted mean of the expert opinions $\{\mathbf{X}^{term}\}$
Initialization: Obtain initial estimate $\mathbf{X}^0$ as

$$\mathbf{X}^0 = \frac{1}{N}\sum\nolimits_{i=1,\ \ ,N} \mathbf{X}_i$$

do:

Compute weight for individual opinions using the kernel function, defined as

$$\mathrm{K}(\mathbf{X}_i - \mathbf{X}^{j-1}) = \exp\left\{\frac{-\left\|\mathbf{X}_i - \mathbf{X}^{j-1}\right\|^2}{\alpha}\right\},$$

$$\mathbf{X}^j = \frac{\sum_{i=1,\ \ ,N} \mathrm{K}(\mathbf{X}_i - \mathbf{X}^{j-1})\mathbf{X}_i}{\sum_{i=1,\ \ ,N} \mathrm{K}(\mathbf{X}_i - \mathbf{X}^{j-1})},$$

while $(\mathbf{X}^j \neq \mathbf{X}^{j-1})$
$\mathbf{X}^{term} = \mathbf{X}^j$

Algorithm 13.1 Mean shift technique.

as a function $[K(\bullet)]$ of the distance of participant's opinion vector and the mean significance vector, such that highly discordant and inconsistent opinions receive smaller weights than receive the consistent opinions. The mean shift technique as applied is represented in Algorithm 13.1.

The mean significance scores obtained by the cytological features are presented in Table 13.2. The plot of significance values of features is given in Fig. 13.5. The x axis of the plot presents the features arranged in nonincreasing order of their mean significance score, starting from the feature having the highest mean significance score. The y axis shows the corresponding mean significance scores for the features. From overall mean significance scores, it can be observed that nuclear chromatin is the only most-significant feature; nature of background and volume and color of cytoplasm are a moderately significant category; whereas, all other cytological features belong to the significant category.

From overall mean significance scores it can be observed that nuclear chromatin is the only most-significant feature; nature of background and volume and color of cytoplasm are in the moderately significant category, while all other cytological features belong in the significant category. We believe that features ranked significant and most-significant must be used in a computer vision technique to match experts' skills.

Table 13.2 Mean significance scores obtained by the cytological features.

Cytological feature	Mean significance score	Rank
Overall cell yield	2.7822	14
Presence or absence of bimodal pattern of aggregates of epithelial cells	3.068	9
Size and shape of aggregates	2.5261	16
Cohesiveness of epithelial cells in the aggregates	3.0864	8
Presence/absence or count of myoepithelial cell nuclei in aggregates	2.9265	13
Presence or absence of bare nuclei	3.2789	4
Presence or absence of single cells with intact cytoplasm	2.7807	15
Nature of background	2.4477	17
Nuclear size	2.9533	12
Nuclear shape	3.0526	10
Nuclear membrane	3.1789	7
Nuclear chromatin	3.548	1
Prominence of nucleoli	3.2388	5
Number of nucleoli	2.9731	11
Mitosis	3.2228	6
Cellular pleomorphism	3.4159	3
Volume and color of cytoplasm	2.3729	18
Nucleus/cytoplasmic ratio	3.4475	2

13.3 Analysis of the Wisconsin Diagnostic Breast Cancer (WDBC) Database

Wisconsin Diagnostic Breast Cancer (WDBC)[5] is an open-source database of features computed from the digitized images of FNA of the breast mass. These attributes describe characteristics of the cell nuclei present in an image. Ten real-valued attributes are computed for manually selected cell nuclei and combined to compute the mean, standard error, and "worst" or largest (mean of the three largest values) of these nuclear attributes for each image. Thus, a set of 30 real-valued attributes is formed for each image. The data are divided in two classes, namely, benign and malignant with 357 and 212 instances respectively.

The mapping of WDBC attributes used to describe nuclear characteristics and the cytological nuclear features that are quantified by them are given in Table 13.3. This mapping is as reported by developers of the database. We believe that derived features such as standard error of area implicitly quantify a larger number of cytological features. A detailed description of the feature extraction methods are detailed by Wolberg et al.[5]

Here it can be observed that the experts use far more cytological features for diagnosis than those quantified in the WDBC database. Some of the excluded features are considered diagnostically more significant than those quantified.

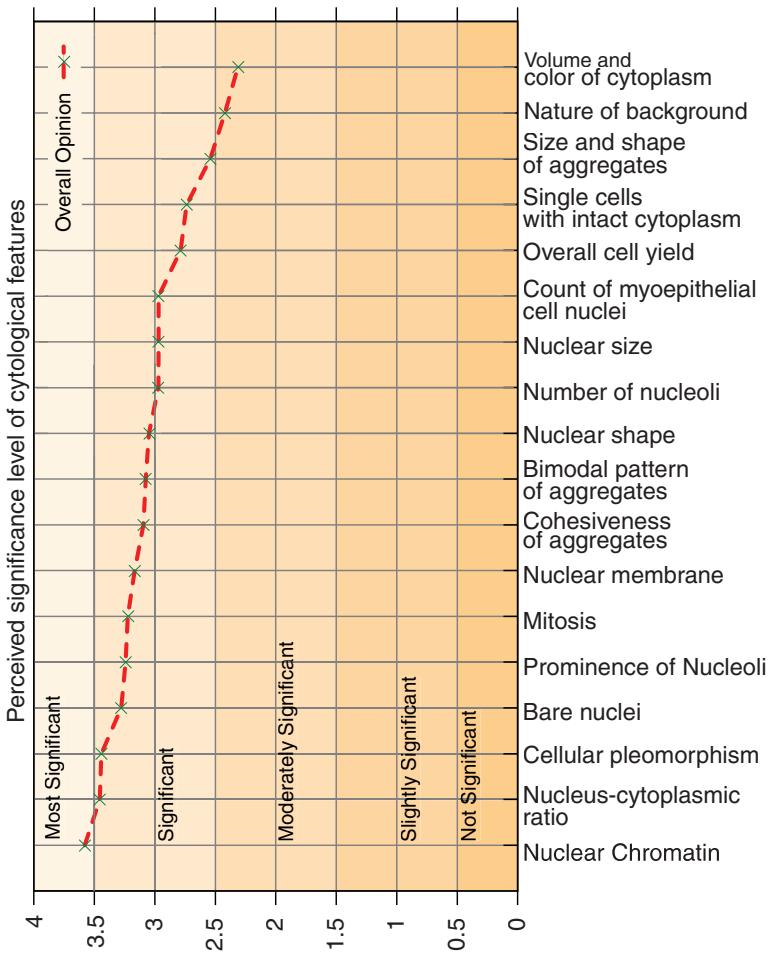

Figure 13.5 Commonly perceived significance levels for different cytological features.

Table 13.3 Mapping between WDBC features and cytological features.

WDBC attribute	Feature number			Corresponding cytological feature
	Mean	Standard error	Worst	
Radius	1	11	21	Nuclear size
Texture	2	12	22	Nuclear chromatin
Perimeter	3	13	23	Nuclear size, nuclear shape
Area	4	14	24	Nuclear size
Smoothness	5	15	25	Nuclear shape
Compactness	6	16	26	Nuclear shape
Concavity	7	17	27	Nuclear shape
Concave points	8	18	28	Nuclear shape
Symmetry	9	19	29	Nuclear shape
Fractal dimension	10	20	30	Nuclear shape

In Section 13.3.1 we perform ranking and selection analysis of the database features. Here, ranking of the attributes is based on their class discrimination ability, which is evaluated using feature usability index (FUI),[14] whereas, classifier-dependent feature selection using a ranked feature set is performed by the wrapper method[15] to identify an optimal feature set that maximizes the classification accuracy. The block diagrammatic representation of the feature ranking and selection procedure applied is given in Fig. 13.6, and the ensuing subsections describe the feature ranking and selection procedure in detail.

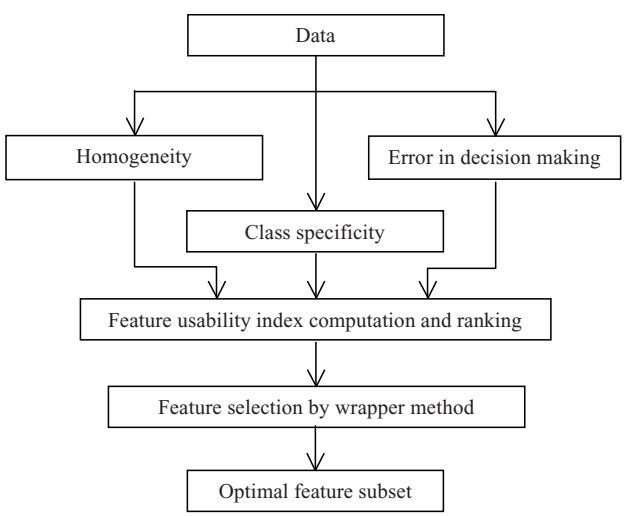

Figure 13.6 Block diagrammatic representation of feature ranking and selection procedure.

13.3.1 Ranking of features using feature usability index

Given an object, its feature is expressed in an attribute vector $\mathbf{Y}= [y^{(1)}, y^{(2)}, \ldots, y^{(d)}, \ldots, y^{(D)}]$, where each element $y^{(d)}$ of $\mathbf{Y}$ is an analytical value contributed by the d^{th} feature extraction technique $F^{(d)}$. We assume that the N samples of $\mathbf{Y}$ are $\mathbf{Y}_1, \mathbf{Y}_2, \ldots, \mathbf{Y}_N$ and their corresponding class labels are $C_1, C_2, \ldots, C_N$. These class labels are finite, and $C_n \in \{\omega_1, \omega_2, \ldots, \omega_K\}$ for a K-class classification problem. Then FUI evaluates the classification efficacy of an attribute $F^{(d)}$ in a classification problem and is computed using measures of homogeneity ($O^{(d)}$), class specificity ($S^{(d)}$), and error in decision making ($R^{(d)}$). The FUI of the d^{th} feature is thus expressed as

$$f^{(d)} = \frac{S^{(d)}}{O^{(d)} \times R^{(d)}}. \tag{13.1}$$

The measures of homogeneity, class specificity, and error in decision making are explained further in the following subsections.

13.3.1.1 Homogeneity

Homogeneity measures the density of outlying observations in the K classes. For the d^{th} feature, it is computed as

$$O^{(d)} = \frac{card\left\{\left(\left|s_n^{(d)} - 1\right|\right) > 0.01\right\}}{card\left\{\left(\left|s_n^{(d)} - 1\right|\right) \le 0.01\right\}} \quad n = 1, 2, \ldots, N, \tag{13.2}$$

where *card* $\{\bullet\}$ denotes the set cardinality, and $s_n = a^{(d)}/|a_n^{(d)}|$ is the one-outlier scatter ratio of a sample, with $|a^{(d)}|$ being the internal scatter of samples belonging to each of the K classes, and $|a_n^{(d)}|$ being the analogous quantity with the n^{th} observation omitted.

13.3.1.2 Class specificity

Class specificity of observations for a particular feature indicates its discrimination potential. It is generally associated with a high value of *between* class scatter and a low value of *within* class scatter. Class specificity of a feature for a multiclass problem is expressed as the minimum of the ratio of between class scatter to within class scatter of the observations analyzed over all classes. For the d^{th} feature, it is expressed as

$$S^{(d)} = \min_{(C_j, C_k)} \left\{ \frac{\left(\mu_{C_j}^{(d)} - \mu_{C_k}^{(d)}\right)^2}{\left(\sigma_{C_j}^{(d)}\right)^2 + \left(\sigma_{C_j}^{(d)}\right)^2} \right\} \; j \neq k, \tag{13.3}$$

where $(C_j, C_k) \in \{\omega_1, \omega_2, \ldots, \omega_k\}$, and $\mu_{C_k}^{(d)}$ and $\sigma_{C_k}^{(d)}$ are the *mean* and *standard deviation*, respectively, of the observations corresponding to the *d*-th feature having class label C_k.

13.3.1.3 Error in decision making

Error in decision making generally arises due to overlap in the *a posteriori* decision boundary. Here, class overlap in the Bayesian *a posteriori* decision boundary to the strength of the decision making that involves the *d*-th feature is expressed as a risk factor and is quantified accordingly:

$$R^{(d)} = \frac{\int_{y^{(d)}} P_{\min}\left(C_k \left| y^{(d)} \right.\right) dy^{(d)}}{\int_{y^{(d)}} P_{\max}\left(C_k \left| y^{(d)} \right.\right) dy^{(d)}} \quad k = 1, 2, \ldots, K, \tag{13.4}$$

where $P_{\min}(C_k|y^{(d)}) = \min_{C_k \in \{\omega_1, \omega_2, \ , \omega_K\}} (P(C_k|y^{(d)}))$, $P_{\max}(C_k|y^{(d)}) = \max_{C_k \in \{\omega_1, \omega_2, \ , \omega_K\}} (P(C_k|y^{(d)}))$, and $P(C_k|y^{(d)})$ is the Bayesian *a posteriori* probability of belongingness of an observation $y^{(d)}$ to a class with label $C_k \in \{\omega_1, \omega_2, \ldots, \omega_K\}$.

FUI as defined in Eq. (13.1) has an expression bound of $[0; \infty)$, with minimum corresponding to the worst feature and *vice versa*. Here we compute FUI for the features in the WDBC database and rank them in nonincreasing order of their FUI value to obtain an ordered feature set $\{F_{ordered}^{(d)}\}$. The ranked features are accordingly available based on their classification efficacy (Table 13.4). A plot illustrating FUI for the features is given in Fig. 13.7. The *x* axis of the plot presents the features arranged in nonincreasing

Table 13.4 Ranks of the WDBC attributes in an ordered feature set. The attribute names can be retrieved from Table 13.3.

WDBC attribute number	Rank	WDBC attribute number	Rank	WDBC attribute number	Rank
1	16	11	13	21	9
2	5	12	28	22	6
3	11	13	15	23	7
4	8	14	4	24	3
5	1	15	27	25	22
6	21	16	26	26	19
7	17	17	14	27	18
8	12	18	10	28	2
9	25	19	30	29	20
10	29	20	24	30	23

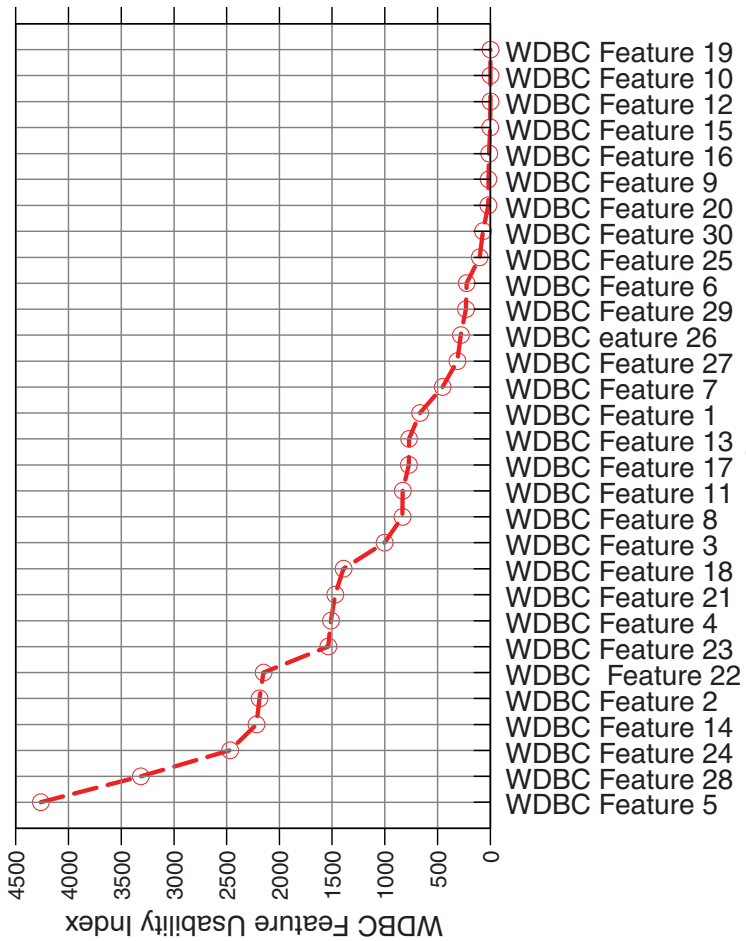

Figure 13.7 Plot illustrating feature usability index for WDBC features.

order of their FUI values and starting from the best ranked feature. The y axis shows the corresponding FUI value.

At this point, comparing the ranks of the attributes in the WDBC database to the ranks of the corresponding cytological features in the experts' opinion, an evident mismatch between the ranks of the features can be observed. Also, of the multiple feature extraction techniques used to quantify a cytological characteristic, each technique results in different FUI values and secures considerably different ranks.

13.3.2 Feature selection

The wrapper model of optimal feature subset selection presented here is specific to the classifier used. This method includes subset generation by sequential forward selection from the ordered feature set $\{F^{(d)}_{ordered}\}$ and classifier accuracy evaluation by experimentation. The sequential forward selection procedure assumes that, with an ordered feature set as an input, the classification accuracy levels achieved increase monotonically to reach the global maxima, and any further additions to the subset deteriorate the classifier performance Algorithm 13.2 illustrates the wrapper model used in this application.

Here, experimentation to estimate classification accuracy for a subset of features is based on an exhaustive experimentation strategy. In order to avoid experimental bias in randomized trials, multiple experiments are conducted, with randomly chosen training and testing samples. One trial consists of 1,000 randomized experiments performed in order to avoid

Input: Ordered feature set $\{F^{(d)}_{ordered}\}$ with D features
Output: Optimal feature subset $\{G^{(d)}\}$ specific to a classifier
Initialization: Empty set $\{G^{(d)}\}$, $A_0 = 0$ and $k = 1$;
do
    Shift k^{th} top element of $\{F^{(d)}_{ordered}\}$ to $\{G^{(d)}\}$;
    Compute the classifier accuracy A_k with the features in $\{G^{(d)}\}$;
    $k = k + 1$;
while ($A_k \geq A_{k-1}$ and $k \leq D$)
if ($k \leq D$) **then**
    Remove $(k-1)^{th}$ element from $\{G^{(d)}\}$;
end
/* $\{G^{(d)}\}$ is the classifier specific optimal subset */

Algorithm 13.2 Sequential forward selection procedure of optimal feature subset selection.

Table 13.5 Optimal subsets and corresponding accuracies for classifiers.

	Naïve Bayesian classifier	**Support vector machine**
Features forming the optimal subset	Mean smoothness Worst concave points Worst area Standard error of area Mean texture Worst texture	Mean smoothness Worst concave points Worst area Standard error of area Mean texture Worst texture Worst perimeter
Corresponding accuracy	96.2%	96.5%

experimental bias. Then the expected accuracy with a feature subset for a particular classifier is the mean of the accuracy obtained from all of the experiments. Here we present the findings of our experiments conducted with naïve Bayesian classifier (NBC)[16] and support vector machine (SVM)[16] with a radial basis function as kernel. The mean accuracies obtained for each candidate subset are plotted in Fig. 13.8. The x axis of the plot presents the constituent features in a subset formed by incremental inclusion of ranked features starting from the best ranked feature. The y axis shows the corresponding mean accuracy achieved by the classifiers in the randomized experiments.

It can be observed that the accuracy levels achieved increase monotonically for the first K iterations to reach the global maxima, and any further additions to the subset give lower accuracy. In the case of the NBC, the global maxima is reached with *six* top-ranked features in the subset. Thus, they form the optimal subset for the classifier. Similarly, for SVM, the top *seven* features form the optimal subset. The list of features and corresponding accuracies achieved are reported in Table 13.5.

13.4 Conclusions

We presented the commonly perceived significance of 18 cytological features used in breast FNAC evaluation. We believe that commonly perceived diagnostic significance of a cytological feature represents its true ability in discriminating benign and malignant condition of a breast lump. This ability of the cytological criteria is different from the class discrimination ability of the objective/mathematical features used to quantify and represent the state of cytological features. Currently available databases use a much smaller number of visual cues for diagnosis than those used by experts. However, here it is important to note that the derived features such as standard error of the nuclear size and shape features effectively quantify the cytological feature; cellular pleomorphism and WDBC attributes such as smoothness and concave points effectively quantify the

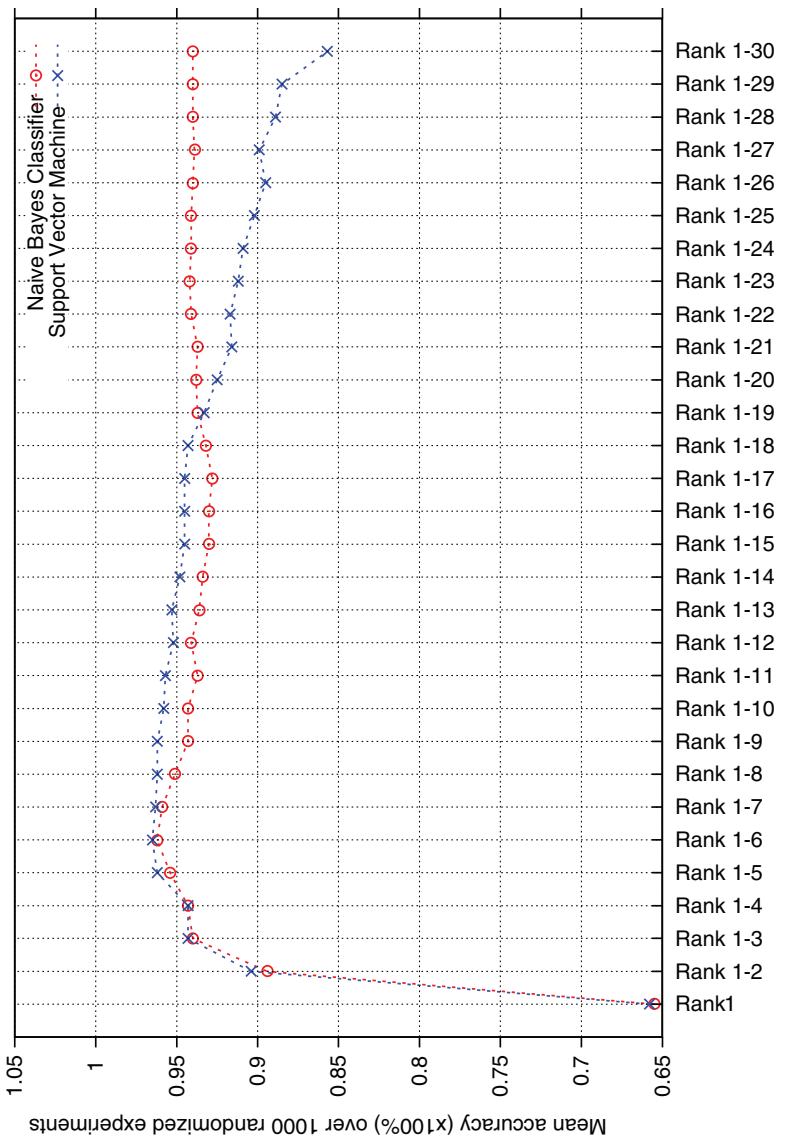

Figure 13.8 Expected classification accuracy for different candidate subsets.

state of nuclear membrane rather than the overall shape of the nucleus. The commonly perceived significance of the features can act as a reference point, while selection of cytological features for computer-aided analysis and those features ranked significant and most-significant must be used by the computer vision technique to match an expert's skills.

Ranking of the WDBC features according to their FUI scores shows that, of the multiple-feature-extraction techniques used to quantify cytological characteristics, each one results in a different FUI value and secures considerably different ranks in the ordered feature set. This verifies that every method and technique of feature quantification has a different aptitude for representing underlying physical evidence and thus different discriminatory power. Results of the experiments conducted on classifier dependant feature selection show that WDBC attributes quantifying nuclear membrane, nuclear size, pleomorphism, and nuclear chromatin form the optimal subset for both NBC and SVM. Attributes such as compactness, symmetry, and fractal dimension along with their derivative features that quantify shape of the nucleus are not members of the optimal subsets that maximize classifier accuracy, rendering cytological shape features weakly preferred in the decision-making process. Thus, in order to maximize translation of a cytological features' class discrimination ability to quantified features, special attention should be paid while selecting feature quantification techniques and methods. Along with reducing dimensionality of the data, feature ranking and selection techniques discussed here can also be used in selection of optimal feature extraction techniques. This has been demonstrated by Sheet et al.[11]

References

1. S. R. Orell, G. F. Sterrett, M. N. Walters, D. Whitaker, and K. Lindholm, *Manual and Atlas of Fine Needle Aspiration Cytology*, 3rd edition, Churchill Livingstone, London, pp. 145–200 (2006).
2. G. Kocjan, *Fine Needle Aspiration Cytology: Diagnostic Principles and Dilemmas*, Springer, Berlin, pp. 214–223 (2006).
3. B. S. Ducatman and H. H. Wang, *Cytology: Diagnostic Principles and Clinical Correlates*, 3rd edition, Saunders Elsevier, Philadelphia, pp. 221–254 (2009).
4. R. Sharma, *Textbook of Pathology*, 4th edition, Jaypee, New Delhi, pp. 891–907 (2002).
5. W. H. Wolberg, W. N. Street, D. M. Heisey, and O. L. Mangasarian, "Computer-derived nuclear features distinguish malignant from benign breast cytology," *Hum. Pathol.* **26**, 792–796 (1995).

6. C. Demir and B. Yener, "Automated cancer diagnosis based on histopathological images: A systematic survey," Rensselaer Polytechnic Institute, Troy, NY, Technical Report TR-05-09 (2005).
7. V. L. Patel and G. J. Groen, "Knowledge-based solution strategies in medical reasoning," *Cognit. Sci.* **10**(1), 91–116 (1986).
8. A. B. Ackerman, "Discordance among expert pathologists in diagnosis of melanocytic neoplasms," *Hum. Pathol.* **27**(11), 1115–1116 (1996).
9. N. Crus-Ramírez, H. G. Acosta-Mesa, H. Carrillo-Calvet, L. A. Nava-Fernández, and R. E. Barrientos-Martínez, "Diagnosis of breast cancer using Bayesian networks: A case study," *Comput. Biol. Med.* **37**, 1553–1564 (2007).
10. R. S. Crowley, G. J. Naus, J. Stewart III, and C. P. Friedman, "Development of visual diagnostic expertise in pathology: An information processing study," *J. Am. Med. Inform. Assoc.* **10**, 39–51 (2003).
11. D. Sheet, V. Venkatraghavan, A. Suveer, H. Garud, J. Chatterjee, M. Mahadevappa, and A. K. Ray, "Statistical tools for evaluating classification efficacy of feature extraction techniques," *Proc. SPIE* **7546**, 75461B (2010) [doi: 10.1117/12.853168].
12. T. Acharya and A. K. Ray, *Image Processing: Principles and Applications*, Wiley-Interscience, Hoboken, NJ (2005).
13. Y. Cheng, "Mean shift, mode seeking, and clustering," *IEEE Trans. Pattern Anal. Mach. Intel*. **17**, 790–799 (1995).
14. D. Sheet, J. Chatterjee, and H. Garud, "Feature usability index and optimal feature subset selection," *Int. J. Comp. Appl.* **12**(2), 29–36 (2010).
15. L. Mathembu and T. Marwala, "A note on the separability index," *ArXiv* e-print 0812.1107 (2008).
16. R. O. Duda, P. E. Hart, and D. G. Stork, *Pattern Classification*, 2nd edition, John Wiley & Sons Asia. Pte. Ltd., Singapore (2007).
17. H. Garud, D. Sheet, M. Mahadevappa, J. Chatterjee, A. K. Ray, and A. Ghosh, "Breast fine needle aspiration cytology practices and commonly perceived diagnostic significance of cytological features: A pan- India survey," *J. Cytol*. **29**(3), 183–189 (2012).

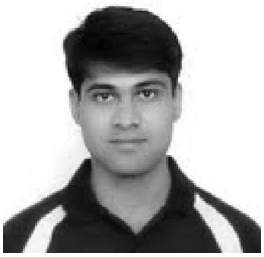

Hrushikesh Garud received his B.E. degree in Electronics Engineering from Dr. Babasaheb Ambedkar Marathwada University, Aurangabad, India in 2005 and his M.Tech degree in Electronics and Electrical Communication from Indian Institute of Technology (IIT) Kharagpur, India in 2008. He is currently a doctoral research scholar at IIT Kharagpur, on leave from Texas Instruments (I) Pvt. Ltd., Bangalore, India where he served as a design engineer. Garud is a graduate student member of IEEE. His research interests include image and multidimensional signal processing, medical imaging, pattern analysis and machine intelligence, fuzzy systems, and consumer electronics.

Debdoot Sheet received his B.Tech degree in Electronics and Communication Engineering from the Institute of Engineering and Management, West Bengal University of Technology, Kolkata, India in 2008, and his M.S. degree in Medical Science and Technology from IIT Kharagpur, India in 2010. He is currently working toward his Ph.D. degree at the same institute. Sheet's work focuses on early diagnosis of breast cancer using smart image analysis techniques for interpretation of sonomammography. He is also co-inventor of four related disclosures filed with the US Patents and Trademarks Office. His current research interests include image and multidimensional signal processing, pattern analysis and machine intelligence, and social implications of technology. Sheet is currently undertaking part of his research at Technische Universität München (TU Munich), Germany on a DAAD fellowship.

Jyotirmoy Chatterjee received his M.Sc. degree in Cytology and Molecular Genetics and Ph.D. degree in Radiation Biology from University of Burdwan, India in 1984 and 1990, respectively. He received a Senior Research Fellowship from the Indian Council of Medical Research for postdoctoral research from 1992 to 1995. He is currently an associate professor at IIT Kharagpur, India, where he is also investigator on five sponsored research projects. He has authored more than twenty research papers and is a member of IEEE and the Engineering in Medicine and Biology Society. His current research interests include medical imaging, image analysis and system biology for regenerative medicine, cancer diagnosis, and radiation toxicology.

Manjunatha Mahadevappa received his B.E. and M.Tech degrees from University of Mysore, India in 1990 and 1994, respectively, and his Ph.D. degree in Biomedical Engineering from IIT Madras, India in 2001. In 2001, he joined Doheny Eye Institute at the University of Southern California, as a postdoctoral Fellow. During 2004–2005, he worked as a postdoctorate scholar at Wenner-Gren Research Lab, University of Kentucky, Lexington, KY. He is currently an associate professor at the IIT Kharagpur, India. He is a member of IEEE, the Engineering in Medicine and Biology Society, Biomedical Engineering Society of India, Institute of Engineers (India), and MISTE. His current research interests include biosignal processing, biomedical image processing, biomedical instrumentation and biosensors, retinal and neural prosthesis, electrical retinal stimulation, and rehabilitation engineering.

Ajoy Kumar Ray joined Bengal Engineering and Science University, Shibpur as its Vice Chancellor in 2009. Prior to this assignment he was a professor of electronics and electrical communication engineering and Head of the School of Medical Science and Technology at IIT Kharagpur. Ray received his B.Eng. degree from Bengal Engineering College, Shibpur, followed by his M.Tech and Ph.D. from IIT Kharagpur. He joined IIT Kharagpur as a faculty member in 1980. Ray was associated with the University of Southampton as a senior research Fellow from 1989 to 1990 and led the research group on 'Image and Video Processing' of Avisere Inc., USA from 2004 to 2005. He has coauthored more than 80 research papers in international journals and conferences and has authored 5 books, including one in Chinese, published by international publishing houses.

Arindam Ghosh is currently a pathologist with Sub-Divisional Hospital of Department of Health and Family Welfare at Kharagpur, India. He completed his M.D. from the Institute of Post Graduate Medical Education and Research, Kolkata, India in 2005. Ghosh has coauthored more than five research papers and patents.

Chapter 14
Radiofrequency Ablation of Breast Neoplasms

José Luis del Cura
Basurto University Hospital, Basque Country University, Bilbao, Spain

14.1 Introduction

Breast surgery maintains a central role in achieving local disease control in the management of breast cancer. After the introduction of radical mastectomy as a standard treatment technique, there has been a continuing shift toward decreasing the amount of tissue removed during surgery, especially for the treatment of small cancers. Breast conservative treatment has been increasingly used because it has demonstrated survival rates similar to those of the more radical treatments. These treatments also have the added advantage of resulting in a more-natural appearing breast after cosmetic surgery. In fact, the current standard treatment for T1N0M0 tumors is lumpectomy followed by radiation therapy.[1,2]

Over the past decade, a number of new, minimally invasive image-guided techniques have been developed that allow the insertion of needle-shaped devices into the tumor to completely and percutaneously destroy, or ablate, the cells using cold or heat. These techniques have demonstrated their efficacy and are being routinely used in the treatment of diverse tumors, especially in liver, kidney, lung, or bone.[3–8]

Ablative techniques allow parenchyma-sparing treatment of tumors. In addition, in patients who are not candidates for surgery, percutaneous ablation allows local treatment with lower morbidity and mortality. Therefore, this approach could increase the number of patients who are candidates for treatment. Ablative techniques may be considered alone or in conjunction with resection. Radiofrequency (RF) ablation is the most widely used of these techniques.[3–8]

14.2 Radiofrequency

14.2.1 Concept

RF ablation induces a thermal injury to the tumor through electromagnetic energy deposition. In this context, the term radiofrequency does not refer to an emitted wave but to an alternating electric current that oscillates in the range of high frequency (200–1,200 kHz). The patient becomes a part of an electric circuit that includes a generator, grounding pads attached to the skin of the patient (usually on the thighs), and an electrode needle inserted into the tumor. When the generator is switched on, an alternating electric field is created within the tissue of the patient. Following the changes in direction of alternating electric current, the ions in the tissue that surrounds the electrode are alternately attracted and rejected. This ionic agitation creates friction within the surrounding tissue and provokes heating around the electrode.[3]

The thermal damage caused by RF depends both on the tissue temperature achieved and the duration of the heating. Heating of tissue at 50–55 °C for 4–6 min produces irreversible cellular damage. At temperatures between 60 and 100 °C, tissue immediately coagulates, causing irreversible damage to mitochondrial and cytosolic enzymes of the cells. At more than 100–110 °C, tissue vaporizes and carbonizes.[3]

To ensure destruction of the tumor, it is necessary to submit the whole tumor to cytotoxic temperatures for a period of time. A minimum may be to maintain a 50–100 °C temperature throughout the entire tumor for at least 6 min. Given the relatively slow thermal conduction from the electrode through the tissues, usually the application should be maintained during a minimum of 12–30 min, depending of the size of the tumor to be treated.[3]

The goal of the procedure is to create a necrotic region that includes the tumor and a safety margin surrounding the target. Most authors recommend a safety margin of 1 cm beyond the boundaries of the tumor.[3] However, this is a controversial issue.

14.2.2 Technical issues

The main problems with RF ablation are the relatively slow thermal conduction from the electrode surface through the tissues and the need to

avoid carbonization and vaporization around the tip of the electrode due to excessive heating. Both carbonized tissue and vapor act as insulators, blocking the transmission of the electric current.

Two strategies have been used to increase the volume of ablation: preventing overheating of the surrounding tissue, and increasing the number of active heads for treatment. Application of these strategies has resulted in different kinds of electrodes, as listed below:

- Internally cooled electrodes: the tip of the electrode is cooled by an inner circuit of circulating fluid to minimize carbonization around the needle tip. In this way, the transmission of the electric current is not blocked, and a larger volume of tissue can be ablated.
- Multiple electrodes: several electrodes (usually up to three) work simultaneously to increase the total volume of ablation.
- Multitined expandable electrodes: these electrodes have several prongs that are deployed once the tip of the needle is in the tumor. The ablation volumes of each of these prongs combine to produce a larger total ablation volume. Some of these modified electrodes can ablate an area over 7 cm in diameter.
- Multitined perfused electrode: in this kind of electrode, a small volume of a saline solution is continuously injected through the tip into the surrounding tissues during the ablation. This fluid increases the conductivity of the treated tissue, allowing the RF current to penetrate farther into the tissue, increasing tissue heating and necrosis.

Inadequate coagulation can also be due to the cooling effect of blood flow that can reduce the extent of thermal damage (the "heat sink effect").

14.3 Radiofrequency Ablation in the Breast

During the last decade a number of articles have been published describing studies on the treatment of breast cancer with RF ablation. Most of these studies were performed using ultrasound (US) as the technique of guidance.[9–19]

The first report of the use of RF ablation in breast was made by Jeffrey et al.[9] It was a feasibility study in which the authors treated a small series of five patients scheduled for surgical excision. All of the tumors were locally advanced and larger than 5 cm, and some of them underwent preoperative chemotherapy. After performing RF ablation on a part of the tumors, the patients underwent standard surgical treatment, and the specimens were studied to detect viable tumor cells in the areas of RF treatment. Although nonviable tumors were found in the areas of treatment, there was a focus of viable cells in the treated area in one of the tumors.[9]

Following this study, several studies were performed in patients with tumors scheduled for surgical excision, but this time most of them included only small tumors (<3 cm in diameter), and the aim was a complete ablation of the tumor cells. In some of these studies, those patients with a suspicion of multifocal disease or intraductal spreading were excluded. The results have been encouraging with success rates ranging from 63% to 100%.[10–16]

Only a few studies have been carried out without removing the ablated tissue. Two of them were reports of small series of cases,[17,18] but Oura et al.[19] published a series of 52 patients with localized breast cancers below 2 cm in diameter treated with RF ablation in which no surgical treatment was performed after the ablation. Multifocal or multicentric tumors were carefully excluded using MRI. After a mean followup of 18 months, no recurrences were reported.[19] These later results have been especially encouraging and have driven interest in the potential use of RF ablation in the management of breast cancer.

14.4 Technique of Ablation

In most of the studies published, RF ablation was performed under general anesthesia. However, sedation has also been used with excellent results.[9–19] Our own experience indicates that RF ablation can be performed under conscious sedation, especially in patients with high surgical risk. One of the groups initially performed the procedure using an intercostal block, but they found that the placement of the block was highly painful for most patients and finally stopped using it.[12]

Several types of electrodes have been used for breast ablations, including internally cooled electrodes and multitined expandable electrodes. In an *ex vivo* study performed in breast and liver models, Quaranta et al.[20] found that cool-tip RF breast ablation assured better performance than multiprobe RF breast ablation in terms of temperature distribution and length of the procedure. However, they used multitined electrodes that were different from the electrodes used in the other studies of breast RF, and the potential effects of blood perfusion and body temperature were not considered in this study.[20] No significant differences in performance between electrodes have been observed in the clinical setting.[9–19]

Some authors excluded the treatment of breast tumors that do not have a minimum distance of 1 cm from the skin and from the chest wall, to avoid thermal damage to these structures.[12,13,16] However, some authors used the technique of hydrodissection, subcutaneously injecting a solution of 5% dextrose to insulate the skin and avoid thermal damage.[19,21] We have also used this technique in two cases in which the tumor was located close to the skin with excellent results. The application of ice pads to the skin over the tumor is also helpful.

Ultrasound is the imaging technique used to guide the placement of the electrodes in the tumors and to follow the process of ablation during the procedure. The type of electrodes and the time of ablation should be selected to achieve the ablation of the tumor plus a margin of at least 0.5 cm around the tumor. The protocol used to deliver energy to the electrodes and the time of ablation was dependent on the type of electrodes and generators used. Every supplier of RF systems has its own recommended algorithm for ablation. The time of application of RF depends in some systems on the appearance of the "roll-off" phenomena (a sudden increase in tissue impedance caused by desiccation and tissue coagulation around the electrode). In other systems, a specific time of ablation is settled before the procedure. A time of 15 min. is considered enough to achieve complete ablation of the tumor in most cases.[9–21]

During the ablation procedure several changes can be observed in the tumor on US. The echogenicity of the area under treatment progressively increases, and the boundaries of the tumor and the tumor itself became fuzzy and finally disappear (Figs. 14.1–14.3). At the end of the RF ablation

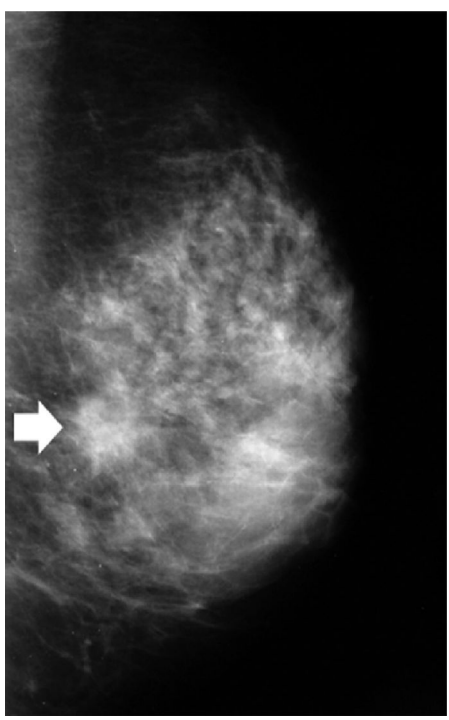

Figure 14.1 83-year-old woman with a symptomatic breast carcinoma in the left breast detected on mammography (arrow). The tumor was also visible on US and was 2 cm in diameter.

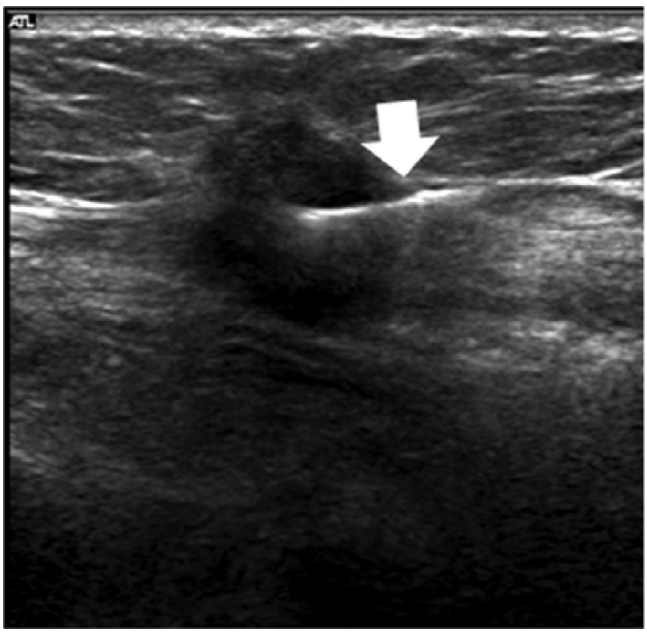

Figure 14.2 Same patient as in Fig. 14.1. A multitined RF electrode (arrow) was placed in the tumor before starting the application of RF.

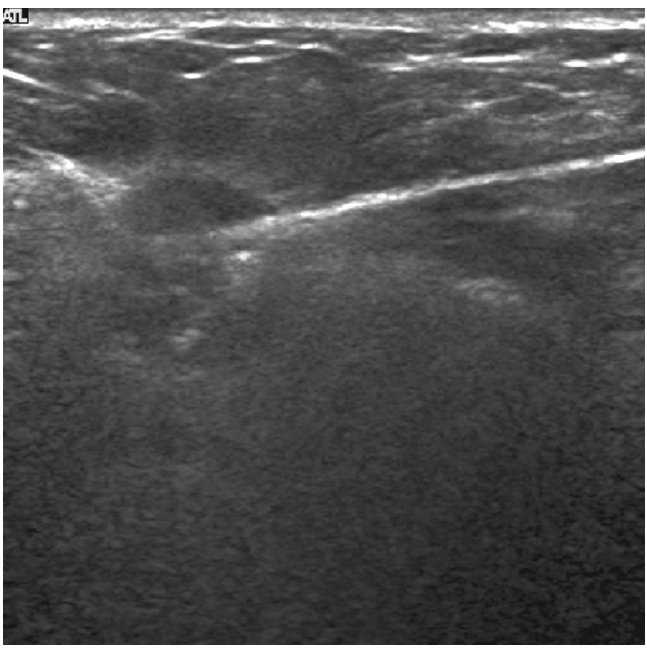

Figure 14.3 Same patient as in Fig. 14.1. After a few minutes of RF application, the limits of the tumor appear fuzzy, and the echogenicity in the area of treatment increases.

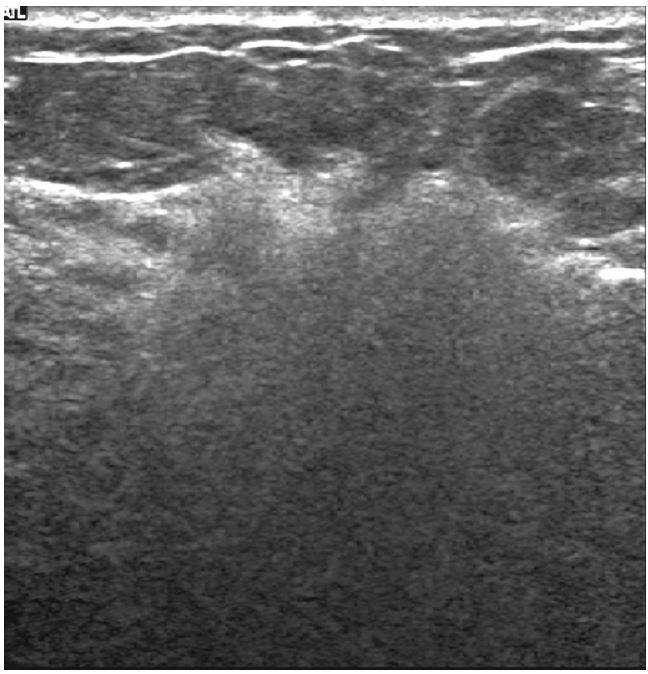

Figure 14.4 Same patient as in Fig. 14.1. At the end of the treatment the tumor is no longer visible on US, and a diffuse hyperechogenicity occupies the entire treated area.

(Fig. 14.4) the tumor is no longer distinguishable on US, and only a diffuse shadow can be seen in the treated area.[9–21]

In the publications in which the tumors were not removed after ablation, patient followups were performed every three months during the first year. This followup included clinical examination, breast imaging (US, mammogram, and MRI in some cases), and also a percutaneous biopsy of the treated area in the first three months after RF ablation.[17–19] Presence of the tumor on US or mammography and the evidence of contrast enhancement on MRI are used as signs of recurrence in these imaging techniques.

14.5 Outcomes

The objective of the application of RF ablation in the treatment of breast tumors is to achieve local control of the disease. In this context, RF ablation appears as a potential substitute for surgery. The studies performed in cases in which RF ablation was followed by surgical excision cast some doubt over the possibility of this substitution. In these trials, the surgical specimen showed that some residual tumor was present in 11% of the cases.[22] The causes of the failures described include the presence of a cyst

within the treated area, suboptimal placement of the electrode, pretreatment underestimation of the tumor extent, or distant tumors not detected prior to RF ablation but found on final histopathology.

However, some of the published trials were in fact preliminary or feasibility studies in which the technique was not yet sufficiently tested and developed, and the conclusions obtained cannot be considered definitive. The real test for the performance of a technique is the clinical test in which several additional factors can play a role in the final outcome. As an example, the addition of radiotherapy has been demonstrated to significantly improve local control after RF ablation.[23] Also, experimental studies suggest that adjuvant chemotherapy may also increase the ablation volume.[24]

In the studies performed in patients in whom no surgical excision was performed after RF ablation, only 1.6% of the cases recurred.[22] From our own experience, five cases also treated without posterior excision showed no relapse after ablation. Although this is an encouraging result, the length of the follow-up periods in the published studies is still too short to make definitive conclusions (Figs. 14.5–14.9).

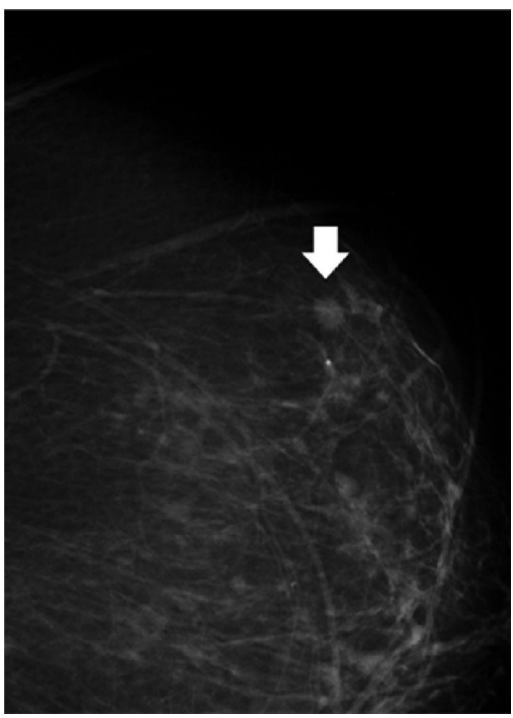

Figure 14.5 73-year-old woman with a ductal invasive carcinoma of 0.5 cm in diameter. The lesion was clearly visible on mammography (arrow).

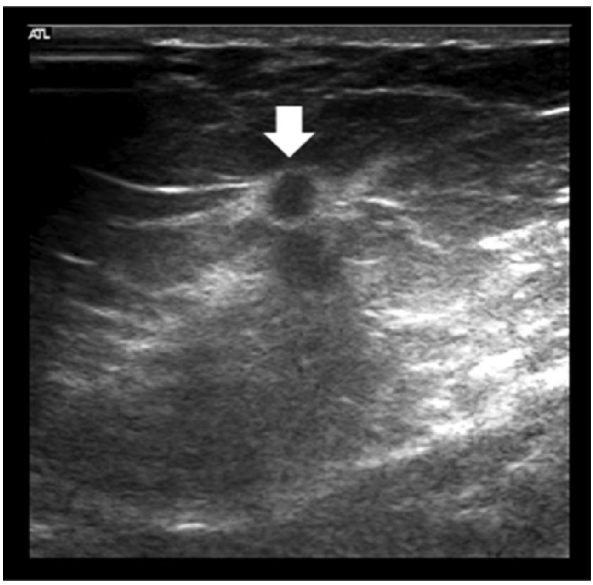

Figure 14.6 Same patient as in Fig. 14.5. The lesion was also visible on US (arrow).

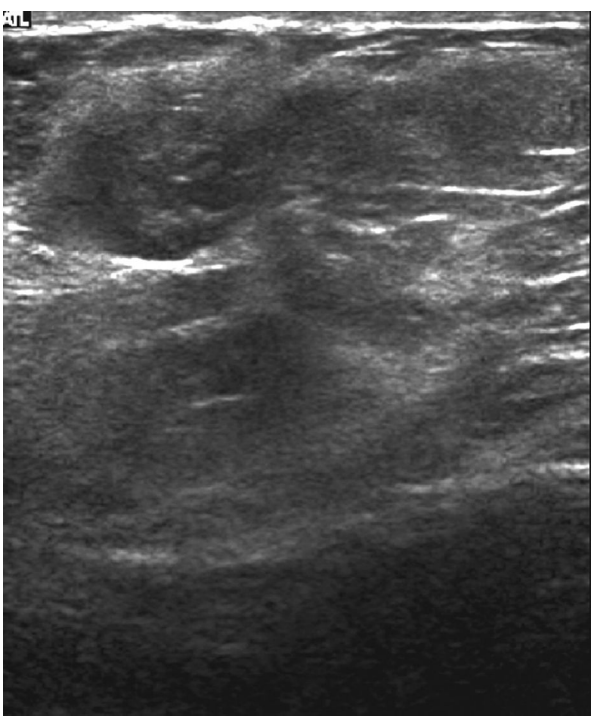

Figure 14.7 Same patient as in Fig. 14.5. One month after RF ablation the tumor is not visible, and the area of treatment appears diffusely hyperechoic.

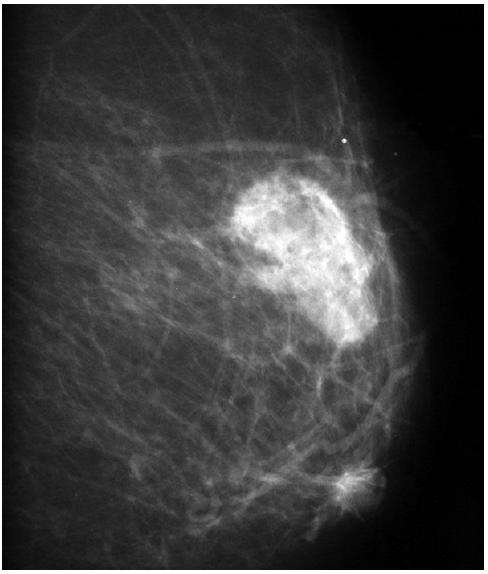

Figure 14.8 Same patient of Fig. 14.5. Six months after RF ablation, a focal ill-defined radiodense opacity can be seen on mammograms in the area of treatment.

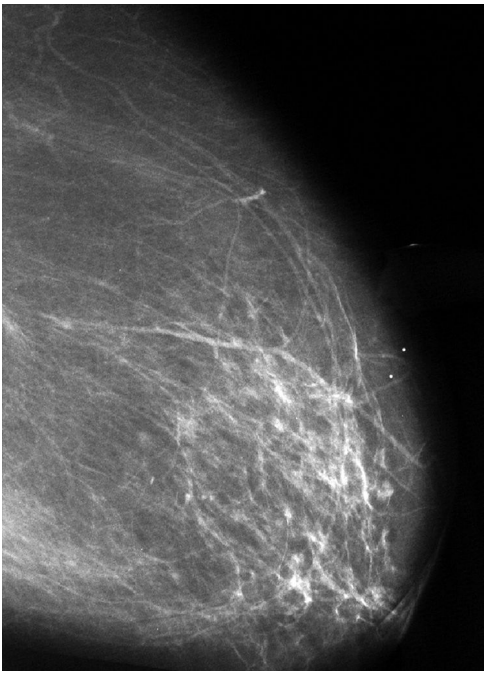

Figure 14.9 Same patient of Fig. 14.5. Two years after RF ablation, the lesion has completely disappeared.

Cosmetic results have been evaluated as well. Most of the patients had a cosmesis that rated as excellent after treatment. Mass formation because of electrocoagulation in the area of treatment and hyperpigmentation due to mild superficial skin burning have been reported in a small number of cases.[16,19]

One of the problems with breast RF ablation is the current lack of standardization of the procedure. The electrode type has been described to affect the outcome of the ablation. Different types of electrodes, such as multitined electrodes or internally cooled devices, produce different shapes of ablation.[20] Ablation time is highly variable among the different studies published, depending mainly on the system of ablation used. More studies are needed to establish specific algorithms to be applied in each system of RF ablation in order to achieve the highest effectiveness.

14.6 Complications

The complication rate is very low in breast RF ablation. Besides the recurrences and cosmetic changes discussed above, the more frequently described complications have been skin and muscle burns in tumors located close to the skin or to the chest wall.[12,19,21] Injection of a solution of 5% dextrose between the skin and the tumor or the chest wall (Fig. 14.10) has proved

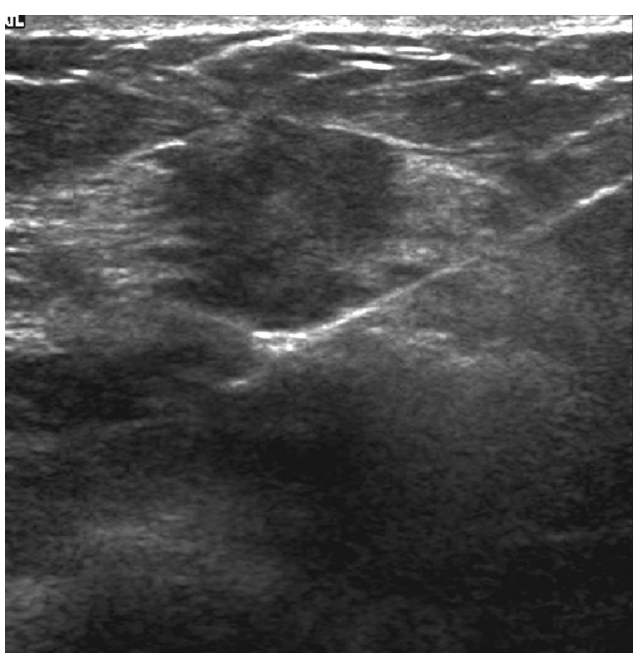

Figure 14.10 Same patient as in Fig. 14.1. A needle has been placed between the nodule and chest wall to inject a solution of 5% dextrose.

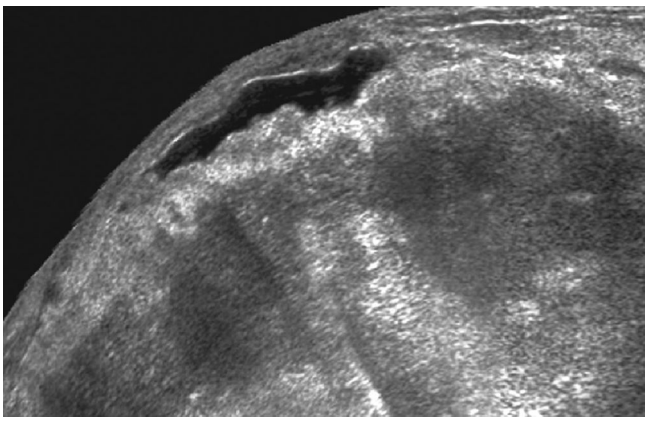

Figure 14.11 Subcutaneous abscess after RF ablation of a breast tumor. The lesion was successfully treated using percutaneous aspiration.

very effective in protecting the skin from thermal damage.[21] Using ice pads in the skin over the ablated area is also useful in our own experience.

Another very infrequent complication is an infection in the area of ablation, usually appearing as an abscess. This complication has been exceptionally described, and we have also observed a case among our patients.[17] A US-guided percutaneous drain can easily solve this problem (Fig. 14.11).

RF ablation procedures in other organs have had other complications such as bleeding, tumor seeding, or grounding pad burns. These particular complications have not been reported in breast RF ablation to date. The shortness of the procedure and the lack of solid organs in the surroundings make breast RF a very safe technique.

14.7 Conclusions and Future Trends

Only a small number of studies have been published on breast RF ablation, and most of them have included the posterior surgical excision of the treated breast. The studies in which treated tumors have been submitted to the test of time are limited to three, and the number of patients treated and the length of the followup are too short yet. Thus, there is currently not enough evidence to support or even glimpse at a future change in the standard of care from surgery to RF ablation for local control in breast cancer. The time has come to conduct some clinical trials with long follow-up times to study the performance of RF in breast cancer treatment.

However, the preliminary studies and especially the series of Oura et al. are encouraging concerning the possibility of a future inclusion of RF ablation among the standard techniques of treatment of breast cancer.[19] The future trends in breast cancer RF ablation will be dependent on the development of

more specific RF algorithms for breast to improve the results, the setting of the specific indications for the technique, and the study of long-term results and survival. Currently, RF ablation appears as an excellent alternative to achieve local control in patients for whom surgery is not indicated or contraindicated, and especially in receptor-negative tumors.

References

1. B. Fisher, C. Redmond, R. Poisson, et al., "Eight-year results of a randomized clinical trial comparing total mastectomy and lumpectomy with or without irradiation in the treatment of breast cancer," *N. Engl. J. Med*. **320**, 822–828 (1989).
2. U. Veronesi, N. Cascinelli, L. Mariani, et al., "Twenty-year follow-up of a randomized study comparing breast-conserving surgery with radical mastectomy for early breast cancer," *N. Engl. J. Med*. **347**, 1227–1232 (2002).
3. R. Lencioni, L. Crocetti, M. C. Pina, and D. Cioni, "Percutaneous image-guided radiofrequency ablation of liver tumors," *Abdom. Imaging* **34**, 547–556 (2009).
4. J. L. del Cura, R. Zabala, I. Iriarte, and M. Unda, "Treatment of renal tumors by percutaneous ultrasound-guided radiofrequency ablation using a multitined electrode: Effectiveness and complications," *European Urology* **57**, 459–465 (2010).
5. T. J. Vogl, N. N. Naguib, T. Gruber-Rouh, et al., "Microwave ablation therapy: Clinical utility in treatment of pulmonary metastases," *Radiolog*. **261**, 643–651 (2011).
6. R. Lencioni, L. Crocetti, R. Cioni, et al., "Radiofrequency ablation of lung malignancies: Where do we stand?" *Cardiovasc. Intervent. Radiol*. **27**, 581–590 (2004).
7. E. Rimondi, A. F. Mavrogenis, G. Rossi, et al., "Radiofrequency ablation for non-spinal osteoid osteomas in 557 patients," *Eur. Radiol*. **22**, 181–188 (2012).
8. H. Rhim, G. D. Dodd, K. N. Chintapalli, et al., "Radiofrequency thermal ablation of abdominal tumors: Lessons learned from complications," *Radiographics* **24**, 41–52 (2004).
9. S. S. Jeffrey, R. L. Birdwell, D. M. Ikeda, et al., "Radiofrequency ablation of breast cancer: First report of an emerging technology," *Arch. Surg*. **134**, 1064–1068 (1999).
10. F. Izzo, R. Thomas, P. Delrio, et al., "Radiofrequency ablation in patients with primary breast carcinoma: A pilot study in 26 patients," *Cancer* **92**, 2036–2044 (2001).

11. W. E. Burak, D. M. Agnese, S. P. Povoski, et al., "Radiofrequency ablation of invasive breast carcinoma followed by delayed surgical excision," *Cancer* **98**, 1369–1376 (2003).
12. A. H. Hayashi, S. F. Silver, N. G. van der Westhuizen, et al., "Treatment of invasive breast carcinoma with ultrasound-guided radiofrequency ablation," *Am. J. Surg*. **185**, 429–435 (2003).
13. B. D. Fornage, N. Sneige, M. I. Ross, et al., "Small (< or = 2-cm) breast cancer treated with US-guided radiofrequency ablation: Feasibility study," *Radiol.* **231**, 215–224 (2004).
14. M. Earashi, M. Noguchi, A. Motoyoshi, and H. Fujii, "Radiofrequency ablation therapy for small breast cancer followed by immediate surgical resection or delayed mammotome excision," *Breast Cancer* **14**, 39–47 (2007).
15. V. P. Khatri, J. P. McGahan, R. Ramsamooj, et al., "A phase II trial of image-guided radiofrequency ablation of small invasive breast carcinomas: Use of saline-cooled tip electrode," *Ann. Surg. Oncol*. **14**, 1644–1652 (2007).
16. G. Manenti, F. Bolacchi, T. Perretta, et al., "Small breast cancers: In vivo percutaneous US-guided radiofrequency ablation with dedicated cool-tip radiofrequency system," *Radiol*. **251**, 339–346 (2009).
17. P. Y. Marcy, N. Magné, P. Castadot, et al., "Ultrasound-guided percutaneous radiofrequency ablation in elderly breast cancer patients: Preliminary institutional experience," *Br. J. Radiol*. **80**, 267–273 (2007).
18. T. Susini, J. Nori, S. Olivieri, et al., "Radiofrequency ablation for minimally invasive treatment of breast carcinoma. A pilot study in elderly inoperable patients," *Gynecol Oncol*. **104**, 304–310 (2007).
19. S. Oura, T. Tamaki, I. Hirai, et al., "Radiofrequency ablation therapy in patients with breast cancers two centimeters or less in size," *Breast Cancer* **14**, 48–54 (2007).
20. V. Quaranta, G. Manenti, F. Bolacchi, et al., "FEM analysis of RF breast ablation: Multiprobe versus cool-tip electrode," *Anticancer Res*. **27**, 775–784 (2007).
21. T. Kinoshita, E. Iwamoto, H. Tsuda, and K. Seki, "Radiofrequency ablation as local therapy for early breast carcinomas," *Breast Cancer* **18**, 10–17 (2011).
22. M. Kontos, E. Felekouras, and I. S. Fentiman, "Radiofrequency ablation in the treatment of primary breast cancer: No surgical redundancies yet," *Int. J. Clin. Pract*. **62**, 816–820 (2008).

23. C. Horkan, K. Dalal, J. A. Coderre, et al., "Reduced tumor growth with combined radiofrequency ablation and radiation therapy in a rat breast tumor model," *Radiol*. **235**, 81–88 (2005).
24. M. Ahmed, Z. Liu, A. N. Lukyanov, et al., "Combination radiofrequency ablation with intratumoral liposomal doxorubicin: Effect on drug accumulation and coagulation in multiple tissues and tumor types in animals," *Radiol*. **235**, 469–477 (2005).

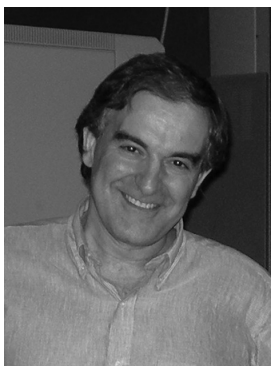

José Luis del Cura is associate professor of radiology at the Basque Country University and director of postgraduate medical education and head of the Section of Radiology at the Basurto University Hospital in Bilbao, Spain. He received his Ph.D. at Basque Country University in 2000. He has published more than 200 papers, including international refereed journals (23), international conference proceedings (42), text book chapters (13), books (7 including in press), with h-index 7. He is on the editorial board, has served as Guest Editor, or is a reviewer for several radiological journals. He is or has been a member of the board of several radiological scientific organizations.

Chapter 15
Minimally Invasive Thermal Ablation for Breast Cancer

Feng Wu
Institute of Ultrasonic Engineering in Medicine, Chongqing Medical University, Chongqing, China; Nuffield Department of Surgical Sciences, University of Oxford and Oxford University Hospitals, Oxford, United Kingdom

15.1 Introduction

Breast cancer is the most frequently occurring female cancer, and ranks second overall when cancers of both sexes are considered together. It is still the leading cause of mortality from cancer in women (the 411,000 deaths reported annually represent 14% of all female deaths from cancer worldwide), and is the fifth cancer-related cause of death overall. There were an estimated 1.15 million new breast cancer cases in 2002, of which more than half were in industrialized countries—about 361,000 in Europe (27.3% of female cancers) and 230,000 in North America (31.3%).[1] Incidence rates are highest in the most developed areas, with the highest age-standardized incidence being in North America (99.4 per 100,000).[2] The prognosis from breast cancer is generally good, with the average survival rate in developed countries being 73% and in developing countries 57%. This favorable survival rate in the West is probably a consequence of the introduction of screening programs.

Radical mastectomy has been accepted as an appropriate therapy for breast cancer for a long time. This treatment involves extensive removal of surrounding healthy normal tissue, and often requires a skin graft. However, since the 1970s, an increased understanding of the natural history of breast cancer has led to the consequent use of preservative surgery in the treatment of small breast tumors. Today, breast conservation surgery, combined with radiotherapy, chemotherapy, and/or hormonal therapy, is performed increasingly often in patients with early-stage breast cancer. The move from mastectomy to breast conservation therapy has not affected the long-term survival rates of patients.[3–6]

In the context of this background, nonsurgical minimally invasive therapies, such as radiofrequency,[7,8] laser,[9,10] microwave,[11,12] cryoablation,[13,14] and high-intensity focused ultrasound (HIFU),[15,16] have been explored with the intention of achieving equivalent efficacy to that achieved with breast conservation therapy, but with improved cosmesis. Using either a percutaneous or an extracorporeal approach, these therapies employ various kinds of physical energy to raise the temperature between 56 and 100 °C, or to drop the temperature to a freezing point in a targeted tumor, and thus induce complete destruction, instead of local tumor removal. Compared with a surgical procedure, the main advantages of the alternative is that it is less invasive with no incision, leaves less scarring, is less costly and less painful, and has shorter recovery time. These advantages result in an associated reduction in mortality, morbidity, hospital stay length, and cost, and improved quality of life for cancer patients.[17–22] In addition, they may lead to better cosmetic results since there is less disruption to the contour of the breast.[23,24] The purpose of this chapter is to introduce recent developments

in the use of thermal ablation techniques for breast cancer, and to discuss their potential in this application.

15.2 Methods of Thermal Ablation Technique

Local tumor destruction occurs while destructive energy is transmitted into a breast lesion, and all of the targeted breast cancer cells are completely destroyed. Minimally invasive thermal techniques rely on heat as the major mode of tumor ablation. These thermal techniques vary based on the processes involved in heat generation and its delivery. Due to differences in energy sources, these techniques can be classified into five categories as follows: radiofrequency ablation (RFA), laser ablation (LA), microwave ablation (MWA), cryoablation, and high-intensity focused ultrasound (HIFU) ablation. Each method has unique characteristics for breast tissue ablation, according to the method of energy delivery through the skin, conduction of energy and length of time required, real-time imaging for targeting/monitoring, and a variety of other specific issues. A summary comparing the varied methods is shown in Table 15.1.

15.2.1 Radiofrequency ablation (RFA)

RFA uses an electromagnetic energy source with frequencies less than 900 kHz to generate heat.[25] An electrode probe is percutaneously placed into a targeted breast cancer. Through the probe, transmission of low-voltage alternating current creates ionic agitation and heating.[26] Ablation temperatures reach 50 to 100 °C, resulting in the coagulation necrosis of the targeted tumor.[27] When the tissue surrounding the tip of the probe reaches more than 100 °C, it will vaporize and char. This decreases the absorption of the energy, and reduces the ablative size of the surrounding tissue.[28]

15.2.2 Laser ablation (LA)

Laser ablation (LA) is also referred to as laser photocoagulation or laser interstitial thermal therapy.[29] LA employs the energy of infrared light to produce heat, and ablates a targeted breast cancer. The light energy is transmitted through an optical fiber with a bare tip and thus induces coagulation necrosis of the targeted tumor while it diffuses through the target.[30] The Nd-YAG (neodymium:yttrium aluminum garnet) laser with a wavelength of 1064 nm, and diode laser with shorter wavelengths (800–980 nm) are the most widely used devices for laser ablation of solid tumors. Both of these lasers can induce tissue photocoagulation at low power or vaporization and cavitation at a higher output. The extent of tissue necrosis is typically limited, depending on the amount of deposited

Table 15.1 Comparison of thermal ablation methods for breast cancer.

Thermal ablation methods	Energy conduction & ablation	Energy delivery through skin	Imaging guidance	Ablation time (varies with tumor size)	Complete ablation	Side-effects after ablation	Required anesthesia	Ablation expense	Published clinical data
Radiofrequency ablation	Heat, not conformal	Percutaneous, with an electrode probe	Ultrasound	10–30 min	76–100%	Moderate discomfort, skin burn	IV sedation, general, local	Inexpensive device, but probe is expensive	Much
Laser ablation	Heat, not conformal	Percutaneous, with an optical fiber	Ultrasound, MRI	25–30 min	13–76%	Moderate discomfort, skin burn	IV sedation, general, local	Expensive device with probe charge	Moderate
Microwave ablation	Heat, not conformal	Percutaneous, with an electrode antenna	Ultrasound	20–60 min	0–8%	Pain, skin burn	IV sedation	Expensive device with probe charge	Little
Cryoablation	Cold, not conformal	Percutaneous with an applicator	Ultrasound	15–30 min	36–83%	Minimal discomfort,	Local	Inexpensive device, but applicator is expensive	Much
HIFU ablation	Heat, conformal	Transcutaneous with no probe insertion	Ultrasound, MRI	30–120 min	20–100%	Moderate discomfort, skin burn	IV sedation, general	Expensive device, but no probe charge	Moderate

energy. Thus, multiple fiber applicators are necessary in clinical application for ablation of larger lesions.[31]

15.2.3 Microwave ablation (MWA)

MWA employs electromagnetic energy to ablate a targeted tumor via an electrode antenna placed within the lesion.[32] While electromagnetic microwaves (900–3,000 kHz) travel through the tissues, they evoke agitation and vibration of ionic molecules such as water molecules within cells. The rapid motion of these ionic molecules causes frictional heating and raises the local temperature ranging from 60 to 100 °C in the cellular environment, resulting in tissue coagulation necrosis.[33] Compared to RFA, MWA can cause a much larger zone of active heating with less effect on heat sink, and no tissue boiling or charring occurs during the ablation procedure.[34]

15.2.4 Cryoablation

Cryoablation is an alternative technique that uses extreme cold to freeze a targeted tumor in the form of an "ice ball." It is one of the oldest ablation methods, with less peri- and postprocedural pain.[35] Cryoablation has recently gained increasing interest due to the use of an argon-gas cryotherapy technique, which induces controlled tissue freezing by inserting a percutaneous applicator into a targeted lesion.[36] A typical cryoablation session involves a freeze–thaw–freeze cycle. The argon and helium gases are alternately delivered to achieve extra- and intracellular ice-crystal formation and tissue osmosis. This process causes protein denaturation, rupture of cell membranes, and cellular death.[37]

15.2.5 High-intensity focused ultrasound (HIFU) ablation

Of all of the minimally invasive therapies, HIFU ablation is the only noninvasive approach proposed to date.[38] It employs extracorporeal ultrasound energy to ablate a targeted tumor at depth, without any needle insertion, so there is no damage to the skin and overlying tissues. Ultrasound is a high-frequency pressure wave. It can be brought to a tight focus at a distance from its source while propagating through tissues. If the concentrated energy is sufficient, energy absorption by the living tissue causes measurable temperature rises (56–100 °C), resulting in coagulation necrosis of the tissue solely within the focal volume.[39] In addition, nonthermal effects such as cavitation can induce local destruction of the tissue due to cavitation-induced high pressures and temperatures.[40] The ablation zone by a single exposure (1–3 sec) is ellipsoidal and small, approximately 1.5×15 mm under normal exposure parameters at 1.6 MHz. By placing numerous individual ablation zones side by side, conformal confluent volumes of ablation of clinically relevant sizes can be achieved.[41] While HIFU ablation

only takes 1–3 sec per exposure, the total time can be substantial, longer than other minimally invasive therapies.

15.3 Scientific Principles of Thermal Ablation

The absorption of the physical energy delivered by the thermal ablation technique can result in a measurable temperature elevation in living tissue. The thermal effects on tissue are directly dependent on how heat interacts with tissue. When temperatures are increased to 42–45 °C for a period of 30–60 min, cells become more subject to damage by other agents such as radiotherapy and chemotherapy.[42] Increasing the temperature can obviously shorten the exposure time for therapeutic effects. If the temperature is increased a few degrees to 50–52 °C and maintained for 4–6 min, irreversible cellular damage is induced.[43] Between 60 and 100 °C, instantaneous induction of protein coagulation occurs, resulting in the permanent destruction of key mitochondrial enzymes and nucleic acid–histone complexes.[44] Temperatures greater than 105 °C can cause tissue vaporization and carbonization.[28]

Thermal ablation is a different therapy from hyperthermia, which has been applied by physical heating technology to elevate targeted regions to temperatures in the 42–45 °C range. This "conventional" hyperthermia usually maintains uniform temperature distributions in a narrow therapeutic range for a period of 30–60 min and is applied once or twice a week.[45] However, the temperature distributions induced *in vivo* are usually nonuniform because of tissue cooling by blood flow, and it is extremely difficult to avoid local cold spots that do not reach the required therapeutic temperature level.[46] The efficacy of hyperthermia is highly dependent on the ability to localize and control the effective temperature distributions, which are often influenced by tissue heterogeneities and blood flow. As a result, hyperthermia cannot be used alone in its clinical application but can be implemented only as an adjuvant method in combination with either radiation therapy or chemotherapy in the treatment of malignant tumors.[47] Two types of mechanisms are commonly involved to explain the rationale for this combined therapy. Heat is a radiosensitizer that increases radiation damage and prevents subsequent repair. Hyperthermia can also produce biological effects on targeted tumors, including direct cellular toxicity, hypoxia, low pH, and indirect deprivation of blood perfusion in the tumor indirectly.[48]

15.4 Mechanisms of Thermal Ablation

Thermal ablation can cause direct and indirect damage to a targeted tumor. Direct heat injury occurs during the period of heat deposition and is predominately determined by the total energy delivered to the targeted

tumor.[49] Indirect heat injury usually occurs after thermal ablation, which produces a progression in tissue damage. It may involve a balance of several factors including microvascular damage, cellular apoptosis, Kupffer cell activation, and altered cytokine release.[50] Direct injury is generally better defined than the secondary indirect effects.

15.4.1 Direct thermal and nonthermal effects on tumors

The effects of thermal ablation on a targeted tumor are determined by increased temperatures, thermal energy deposited, rate of removal of heat, and the specific thermal sensitivity of the tissue. As the tissue temperature rises, the time required to achieve irreversible cellular damage decreases exponentially. At temperatures between 50 and 55 °C, cellular death occurs instantaneously in cell culture.[51] Protein denaturation, membrane rupture, cell shrinkage, pyknosis and hyperchromasia occur *ex vitro* between 60 and 100 °C, leading to immediate coagulation necrosis.[52] Tissue vaporization and boiling are superimposed on this process when the temperature is greater than 105 °C. Carbonization, charring, and smoke generation occur when the temperature is over 300 °C.[53]

In addition, acoustic cavitation, one of mechanical effects induced by HIFU ablation, is the most important nonthermal mechanism for tissue disruption in the ultrasound field.[54] The presence of small gaseous nuclei existing in subcellular organelles and fluid in tissue are the source of cavitation, which can expand and contract under the influence of the acoustic pressure. During the collapse of bubbles, the acoustic pressure is more than several thousand pascals, and the temperatures reach several thousand degrees Celsius, resulting in the local destruction of the tissue.[55,56]

Histological changes are evident in tumor tissue after thermal ablation.[57] In addition to HIFU ablation, four zones of cellular changes are described in the liver after thermal ablation. The four zones are as follows: application, central, transition, and reference tissue zones.[58–60] The application zone is where the heat source contacts the tissue. The central zone immediately surrounds the application zone and consists of damaged tissue. The transition zone contains apparently undamaged tissue but exhibits signs of subacute hemorrhage. The reference zone refers to normal tissue surrounding the transition zone.

15.4.2 Thermal effects on tumor vasculature

Structural and functional changes are directly observed in tumor vasculature after thermal ablation. These changes are not as well described as thermal effects on the tissues, but they rely on varying temperatures. At temperatures between 40 and 42 °C, there is no significant change in tumor blood flow after a 30–60-min exposure.[61] Beyond 42 to 44 °C, there is an irreversible

decrease in tumor blood flow, with vascular stasis and thrombosis, resulting in heat trapping and progressive tissue damage.[62] When temperatures exceed 60 °C, immediate destruction of tumor microvasculature occurs.[63] These temperatures cut the blood supply to the tumor directly through the cauterization of the tumor feeder vessels, leading to deprivation of nutrition and oxygen. Thus, tissue destruction can be enhanced by the damage caused by thermal ablation to tumor blood vessels.

15.4.3 Indirect effects on tumor

Indirect injury is a secondary damage to tissue that progresses after the cessation of thermal ablation stimulus.[50] It is based on histological evaluation of tissue damage at various time points after thermal ablation.[59] The full extent of the secondary tissue damage becomes evident one to seven days after thermal ablation, depending on the model and energy source used.[64,65] The exact mechanism of this process is still unknown. However, it may represent a balance of several promoting and inhibiting mechanisms, including induction of apoptosis, Kupffer cell activation, and cytokine release.

Cellular apoptosis may contribute to the progressive injury of tissue after thermal ablation. It is well established that apoptosis increases in a temperature-dependent manner, and temperatures between 40 and 45 °C cause inactivation of vital enzymes, thus initiating apoptosis of tumor cells.[66,67] Thermal ablation creates a temperature gradient that progressively decreases away from the site of probe insertion. The induction of apoptosis at a distance from the heat source may potentially contribute to the progression of injury. An increased rate of apoptosis is observed in the liver 24 hours after microwave ablation.[59] The stimulation of apoptosis may be directly induced by temperature elevations, alterations in tissue microenvironment, and the release of various cytokines after thermal ablation.

Kupffer cell activity may be one of the major factors involved in progressive injury after thermal ablation.[50] Heat induces Kupffer cells to secrete IL-1[68] and tumor necrosis factor-α (TNF-α),[69] which are known to have *in vivo* antitumor activity[70] and to increase apoptosis in cancer cells.[67] Kupffer cells also induce the production of interferon, which augments the liver-associated natural killer cell activity.[71]

Thermal ablation may induce both regional and systemic production of cytokines through activation of inflammatory cells. Compared with controls, the circulating level of interferon-γ (IFN-γ) and vascular endothelial growth factor levels markedly increase after RFA.[72,73] The increased level of IL-1 and TNF-α is also observed after RFA.[74] These cytokines may have direct cytotoxic effects such as inducing tumor endothelial injury and causing tumor cells to become more sensitive to heat-induced damage.[75,76]

However, contrasting results are obtained for the TNF-α level in two studies[77,78] and IL-1 level in one study[78] in which the IL-1 level remains unchanged after thermal ablation.

Cryoablation may cause pathophysiological changes similar to those observed after endotoxin administration.[79,80] These changes cause important increases in capillary permeability in the lung, leading to the secondary injury.[81] It is generally believed that all alterations may be associated with postcryosurgery activation in the lungs of the nuclear factor-κB and derived cytokines including TNF-α and macrophage inflammatory protein-2, and with an increase in serum thromboxane levels.[82,83]

15.5 Clinical Studies on Thermal Ablation of Breast Cancer

The final goal of breast cancer ablation is to demonstrate oncologic efficacy and aesthetic outcomes without surgical lumpectomy. Two types of clinical studies have been performed to support thermal ablation as a local therapy of breast cancer. The first type of study is designed to investigate the ability of thermal ablation to adequately destroy a targeted breast cancer. These studies are phase I and II clinical trials for assessing the feasibility and safety of thermal ablation. Surgical excision usually follows the ablation, and histological techniques are used to confirm the completeness of ablation and the accurate identification of a unifocal cancer. Most forms of thermal ablation currently under use serve the purpose of this first category.

The second type of clinical study focuses on identifying what happens to breast tumors after ablation in terms of survival benefit and local appearance. Ablated breast tissue remains as a necrotic tissue within the breast and then resorbs over time. Phase III clinical trials investigate the long-term survival and cosmetic outcomes of breast cancer patients who are treated with thermal ablation, in combination with chemotherapy, radiation, endocrine, and biological therapies. Clinical studies for long-term follow-up results are still underway.

15.5.1 Radiofrequency ablation

RFA has been widely used to ablate liver tumors for a long time in clinical practice. It is the most studied form of thermal ablation for breast cancer. The first study of RFA in human breast cancer was performed in 1999 by Jeffrey and colleagues.[84] Five patients with locally advanced breast cancer underwent the ablation, immediately followed by mastectomy. Complete ablation was found in four of these patients, with the fifth showing a small area of viable cells lining a cyst. No complications related to RFA were observed in these patients.

Subsequently, several investigators reported feasibility studies of RFA for small breast cancer.[85–92] The tumor was removed immediately or 1–4 weeks after RF ablation, and tumor viability was evaluated on histological examinations with hematoxylin and eosin (H&E) and nicotinamide adenine dinucleotide plus hydrogen (NADH) staining, a standard assessment for tumor cell viability. The results of these studies are summarized in Table 15.2, and the rates of complete coagulation necrosis ranged from 76 to 100% in this series. Thus, preliminary experiences of RFA for small breast cancer followed by surgical excision were encouraging.

Several pilot studies were performed to investigate the effectiveness of RFA for treatment of breast cancer in elderly patients, and all patients were followed up after the ablation, without any surgical excision. Susini and colleagues[98] reported the first short-term result of RFA in three elderly patients with inoperable breast cancer, and no evidence of local recurrence was found by MRI and core-needle biopsy after 18 months of followup. RFA was also performed after hormone therapy in four elderly inoperable patients, and there was no breast recurrence in three patients who received breast radiation with a mean followup of 29.4 months.[99] Oura and colleagues[100] performed RFA, followed by breast radiation therapy in 52 patients, and reported no breast cancer recurrence with a mean followup of 15 months.

Breast cosmetic results after RF ablation was excellent in 43 patients (83%), good in 5 (12%), and fair in 3 (6%). Brkljacic and colleagues[101] used RF ablation to treat six patients with inoperable breast cancer who were at high-risk for general anesthesia and surgery because of severely impaired cardiac function, advanced age, or associated diseases (acute myeloid leukemia, diabetes, hypertension, depression), and/or who refused surgery. They had core-biopsy-proven T1-2N0 M0, grade I or II, 1.0–2.7-cm sized invasive ductal cancers. Four tumors measured greater than 2 cm, and three were 1.0–1.2 cm in diameter. Follow-up results showed that six tumors in five patients were completely ablated, without recurrence during followup (range: 9–49 months). One patient had a partial ablation, and died two months later from myocardial infarction. One patient with acute myeloid leukemia presented an infection of the treated breast after four months. She received postponed mastectomy with no signs of malignancy in histopathology but finally died of leukemia 42 months after RFA. Thus, based on these early results, this technique is promising as a local treatment for small breast cancer. However, the follow-up periods are too short to allow investigation of tumor recurrence and survival rates, and the long-term cosmetic appearance of the ablated area of the breast is still unknown. Further studies, particularly in randomized clinical trials, are necessary to determine whether the use of RFA can produce local recurrence and survival rates equivalent to those obtainable with conventional breast conserving therapy.

Table 15.2 Results of feasibility studies using RFA for breast cancer.

	No. of patients	Tumor size (cm)	Histological staining	Complete ablation	Complication	Resection
Jeffrey[84]	5	4–7	H&E, NADH staining	80%	Nil	Immediate
Izzo[85]	26	0.7–3.0 (mean: 1.8)	H&E, NADH staining	96%	Full thickness skin burn (4%)	Immediate
Burak[86]	10	0.8–1.6 (mean: 1.2)	H&E staining	90%	Nil	1–3 weeks
Hayashi[87]	22	0.5–2.6 (mean: 0.9)	H&E, NADH staining	86%	Skin burn at puncture site (5%)	1–2 weeks
Fornage[88]	21	0.6–2.0 (mean: 1.2)	H&E, NADH staining	95%	Nil	Immediate
Earashi[89]	24	0.5–2.4 (mean: 1.1)	H&E, NADH staining	100%	Nil	Immediate, 1–7 months
Imoto[90]	30	0.9–2.4 (mean: 1.7)	H&E, NADH staining	92%	Skin burn (7%), muscle burn (23%)	Immediate
Medina-Franco[91]	25	0.9–3.8 (mean: 2.08)	H&E, NADH staining	76%	Nil	Immediate
Manenti[92]	34	1.65–1.96 (mean: 1.89)	H&E, NADH staining	97%	Skin burn (3%)	4 weeks
Hung[93]	20	<2 (mean: 1.4)	H&E, NADH staining	89%	Nil	Immediate
Kinoshita[94]	49	0.5–3 (mean: 1.7)	H&E, NADH staining	61%	Skin burn (4%) muscle burn (6%)	Immediate
Yamamoto[95]	29	0.5–1.9 (mean: 1.28)	H&E, NADH staining	92%	Skin burn (10%)	3–4 weeks
Tsuda[96]	28	0.6–5 (mean: 2.21)	H&E, NADH staining	79%	Not clear	Immediate
Wiksell[97]	31	<1.6	H&E, NADH staining	84%	Nil	Immediate

15.5.2 Laser ablation

Almost all of the studies on laser ablation were designed to investigate the safety and feasibility of LA for the treatment of breast cancer. Surgical resection was followed 0–70 days after LA. Either H&E staining, or H&E combined with NADH staining, was used to determine the extent of coagulation necrosis in the targeted tumor. The results of these studies are summarized in Table 15.3. Although four studies did not mention the complete ablation rate, tissue damage was clearly seen in 90–100% of ablated breast cancer.[102–105] Three studies showed that complete ablation of breast cancer was achieved in 13–70% of the patients with T1–T3 tumors.[106–108]

Apart from small skin burns, a gaseous rupture of the tumor was noted as a serious complication of LA.[104] The largest clinical experience with LA for breast cancer was reported by Dowlatshahi and colleagues.[106] Fifty-four patients were enrolled in this study, and the LA procedure was performed under local anesthesia, followed by surgical excision one to eight weeks after thermal ablation. The results showed that the complete ablation rate was 70%, whereas 96% complete ablation was observed in the most recent series of 28 patients. In addition, he reported a 70-year-old woman who underwent LA for a 7-mm low-grade invasive breast cancer without surgery. The patient was placed on tamoxifen (20 mg/day), and followed up closely at three- to six-month intervals. There was no evidence of recurrence three years after LA.[110] Based on promising results in the feasibility study, Akimov and colleagues[104] followed up seven patients who underwent LA. Among them, three were stage IV patients, and LA was intended for palliative treatment. The remaining four patients were diagnosed as stage I–III breast cancer, and LA was used as an alternative to surgery in the primary treatment. The results showed that local tumor control was achieved in five patients, and disease-free survival was 19–60 months in three patients with stage I–III breast cancer.

Recently, Klimberg and colleagues[111] reported preliminary results of using image-guided vacuum-assisted excisional biopsy for lesion removal, followed by either LA or RFA for residual breast cancer, in order to achieve both fresh naïve tissue for histological investigation and better negative margins. Eighteen patients were enrolled onto the study, including 15 for RFA and 3 for LA. They all received lumpectomy immediately after ablation, and treated tissues were histologically investigated for the assessment of thermal destruction. The results showed that complete ablation was achieved in all of the RFA-treated patients with negative tumor margins. However, there was unpredictability of the ablation zone with residual tumor cells in all of the LA-treated patients. This study may provide a novel approach to minimally invasive therapy in combination with percutaneous excision for effective cytoreduction with RF ablation of margins for the treatment of residual breast cancer.

Table 15.3 Results of feasibility studies using LA for breast cancer. (PCNA = proliferating cell nuclear antigen.)

	No. of patients	Tumor size (cm)	Histological staining	Complete ablation	Complication	Resection
Harries[102]	44	1.0–5.0 (mean: unknown)	H&E staining	Unclear, but ablation seen in 91% of tumors	Nil	1–34 days
Mumtaz[103]	20	0.4–3.3 (mean: 2.0)	H&E, NADH staining	Unclear, but ablation seen in 90% of tumors	Nil	1–15 days
Akimov[104]	28	1.0–6.0 (mean: 3.0)	H&E staining	Unclear, but ablation seen in all tumors	Gaseous rupture of tumor (4%), skin burn (7%)	1–11 days
Bloom[105]	40	0.5–2.3 (mean: 0.95)	H&E staining	Unclear, but ablation seen in all tumors	Not mentioned	Immediate, mean 14.5 days
Dowlatshahi[106]	54	0.5–2.2 (mean: 1.2)	H&E staining	70%	Skin burns (4%)	1–8 weeks
Korourian[107]	29	1.8–4.0 (mean: 2.6)	H&E staining, PCNA immunohistochemistry	76%	Skin burn (7%)	Immediate
Haraldsdóttir[108]	24	0.5–3.5 (mean: 1.4)	H&E staining	13%	Skin burn (8%)	4–23 days
van Esser[109]	14	0.8–3.7 (mean: 1.7)	H&E, NADH staining	50%	Skin burn (7%), pneumothorax (7%)	Immediate

15.5.3 Microwave ablation

Clinical experiences of using MWA for breast cancer are limited, and only a few clinical studies have been published so far. Gardner and colleagues[112] reported the first pilot study in which 10 patients with biopsy-proven invasive breast cancer underwent focused MWA. Mastectomy was performed 5–27 days after the ablation in all patients, and surgical specimens were analyzed using histopathologic examinations. Tumor necrosis was noted in 4 of 10 specimens and apoptosis in 6, but no complete ablation was observed. A significant tumor response on the basis of reduction in tumor size or significant tumor cell kill occurred in 8 (80%) of 10 patients. Complications included skin burn in one patient and skin flap necrosis in three patients after mastectomy.

The same group also published another article focusing on sentinel lymph node mapping after thermal ablation.[113] Twenty-one patients with invasive breast cancer received MWA. The sentinel lymph node was found in 91% patients, and axillary metastases were detected in 42% of the patients. Histological evidence of MWA-induced tumor necrosis was present in 68% of the patients. Complications were not mentioned in this study. In addition, this group reported a prospective, nonrandomized dose-escalation study.[114] Twenty-five women with invasive breast cancers underwent MWA, and H&E staining showed pathological necrosis in 17 patients (68%), including 2 patients with complete ablation. However, margins of the ablated tissue were not evaluated in this study. Complications mentioned were mild pain during treatment, skin burn, and short-lived erythema of the skin. Finally, the authors performed a prospective, randomized, multicenter study of preoperative focused MWA for patients with T1, T2 invasive breast cancer with two treatment arms (MWA followed by surgery within 60 days after ablation, and surgery alone as the control arm).[115,116] Outcomes measured were pathologic margin status, surgical re-excision rates including second incisions, excised tissue volume, pathologic tumor necrosis, and side effects. Interim statistical data were analyzed on a study group of 75 patients, consisting of 34 patients treated with thermotherapy prior to surgery and 41 patients who received surgery alone. At enrollment based on ultrasound measurements, mean tumor diameter was 1.7 cm in the thermotherapy arm versus 1.6 cm in the control arm. Three patients receiving MWA had a skin burn, and one patient presented moderate abscess caused by necrotic tissue surrounding the tumor. After treatments were completed, in the MWA arm 0 of 34 (0%) patients had positive margins and in the surgery-alone arm 4 of 41 (9.8%) patients had positive margins, suggesting that MWA could reduce the rate of positive margins compared with breast conservation surgery alone.

15.5.4 Cryoablation

Almost all of the clinical trials using cryoablation for breast cancer are both pilot and feasibility studies, as shown in Table 15.4. All patients receive surgical excision five days to four weeks after cryoablation. Complete ablation of the tumor, which is confirmed by histopathological examinations, ranges from 36 to 83%. No serious complications are observed after cryoablation. Ultrasound guidance is used in three studies but shows only the surface of the ice ball; the area beyond the surface is not clearly visible on ultrasound imaging. This makes ultrasound more difficult as a real-time monitoring tool for ablative procedures. MRI guidance in an open configuration is also used in two of the studies, and the results demonstrate that MRI correctly predicts the cryosurgery results in most patients.

The first breast cancer patient treated with cryoablation was presented in 1997 by Rabin and colleagues.[117] Two invasive lobular tumors were frozen in the same quadrant under ultrasound guidance. No surgical excision was performed. However, core needle biopsy showed no residual or persistent disease 4 to 12 weeks after the well-tolerated procedure. Sabel and colleagues[118] reported a multi-institutional study of cryoablation for early-stage breast cancer. Twenty-nine women were treated with cryoablation, followed by surgical resection 1–4 weeks later. The results showed that cryoablation successfully destroyed 100% of cancers in all patients with tumors less than 1 cm in diameter. For tumors between 1.0 and 1.5 cm, this success rate was achieved only in patients with invasive ductal carcinoma without a significant ductal carcinoma *in situ* component. For tumors greater than 1.5 cm, cryoablation was not reliable with this technique in terms of complete ablation.

Similar results were observed in cryoablation when the breast lesion was less than 15 mm, and complete ablation was achieved in 24 (83%) of 29 patients with small breast cancer.[121] Cryoablation was also performed under MRI guidance in two studies, but complete ablation achieved was low, ranging from 36% (4/11) to 52% (13/25) in patients with invasive breast cancer.[119,122] Cryotherapy seems more successful in treating invasive than *in situ* disease. Roubidoux and colleagues[120] reported their clinical experience with cryoablation for small breast cancers. With ultrasound guidance, seven of nine treated patients had no residual disease, which was confirmed by histopathologic examinations. However, a higher complete ablation rate was achieved when cryoablation was performed for patients with small subclinical breast cancer (mean tumor size: 0.8 ± 0.4 cm). In 14 of the 15 patients a complete necrosis of the cryoablated lesion both in postprocedural MRI followup and anatomo-pathological evaluation after surgical resection was observed.[123] Recently, Littrup and colleagues[124] reported a long-term follow-up result of using cryoablation for the

Table 15.4 Results of feasibility studies using cryoablation for breast cancer.

	No. of patients	Tumor size (cm)	Image guidance	Histological staining	Complete ablation	Complication	Resection
Sabel[118]	29	1.0–5.0 (mean: unknown)	Ultrasound	H&E staining	Unclear, but 100% seen in patients with a tumor <1.0 cm	None mentioned	1–4 weeks
Morin[119]	25	1.2–6.0 (mean: 2.98)	MRI	H&E staining	52%	Skin burn at probe entry site	4 weeks
Roubidoux[120]	9	0.8–1.8 (mean: 1.2)	Ultrasound	H&E staining	78%	Nil	14–23 days
Pfleiderer[121]	29	0.5–1.5 (mean: 1.2)	Ultrasound	H&E staining	83%	Nil	5 days–6 weeks
Pusztaszeri[122]	11	0.5–2.5 (mean:1.3)	MRI	H&E staining	36%	Skin ulceration and necrosis (45%)	4–5 weeks
Manenti[123]	15	mean: 0.8 ± 0.4	US	H&E staining	93%	Nil	35–40 days

treatment of breast cancer. Twenty-two breast cancer foci (stages I–IV) were treated in 11 patients who refused surgery by using multiple 2.4-mm cryoprobes. Five patients had recurrent disease and six had new diagnoses. The mean pretreatment breast tumor diameter was 1.7 cm ± 1.2 (range: 0.5–5.8 cm). Tumor size from MRI and/or clinical followup were available for up to 72 months after ablation. No significant complications, retraction, or scarring were noted. Biopsies at the margins of the cryoablation site immediately after cryoablation and at followup were all negative. No local recurrences have been noted at an average imaging followup of 18 months.

15.5.5 High-intensity focused ultrasound ablation

Two types of HIFU devices, using either MRI or ultrasound as an imaging guidance tool, were used clinically to treat breast cancer. Table 15.5 shows a summary of the clinical results of their use for the treatment of breast cancer. The first HIFU-treated case was reported by Hüber and colleagues.[125] This case involved a woman with invasive ductal carcinoma, on which MRI-guided HIFU ablation was performed, followed by lumpectomy five days later for histological examination. The results revealed lethal and sublethal tumor ablation, which corresponded well with the outlined region on the preprocedural MR images. Gianfelice and colleagues[126] reported the initial use of MRI-guided HIFU followed by segmental resection in the treatment of 17 patients with invasive breast cancer. Histopathologic analysis showed that complete ablation was observed in 4 (24%) of the patients. Some residual tumor was identified predominantly at the periphery of the tumor mass. Similar results were also found in another feasibility study, and complete ablation was histologically confirmed in 2 (20%) of 10 patients with infiltrating breast cancer.[127] Furusawa and colleagues[129] reported the safety and feasibility of MRI-guided HIFU followed by wide surgical excision or mastectomy for the treatment of 30 women with biopsy-proven breast cancer. They found that 15 (53.5%) of 28 evaluable patients had 100% necrosis of the ablated tumor, 10 (35.8%) had 95–97%, and 3 (10.7%) had less than 95% necrosis. Similar results were also observed by Kim and colleagues,[131] and MRI and histological examinations showed that complete ablation was achieved in 3 (50%) of 6 patients with invasive ductal breast cancer. These results were very promising, indicating that MRI-guided HIFU may be considered as a potential noninvasive replacement for lumpectomy in the treatment of breast cancer.

Wu and colleagues[130] undertook a randomized clinical trial of ultrasound-guided HIFU ablation for patients with localized breast cancer. Forty-eight women with biopsy-proven breast cancer were randomly allocated to either a control group (mastectomy alone), or an HIFU group (HIFU ablation followed by mastectomy one to two weeks later). The mean tumor size in the HIFU group was 3.1 cm (2.0–4.7 cm). Pathological examination showed

Table 15.5 Results of feasibility studies using HIFU ablation for breast cancer.

	No. of patients	Tumor size (cm)	Image guidance	Histological staining	Complete ablation	Complication	Resection
Gianfelice[126]	17	<3.5 (mean: unknown)	MRI	H&E staining	24%	None mentioned	3–21 days
Zippel[127]	10	<3.0 (mean: 2.2)	MRI	H&E staining	20%	Skin burn (10%)	7–10 days
Gianfelice[128]	24	0.6–2.5 (mean: 1.51)	MRI	H&E staining (core biopsy)	58.3% (1 session) 79% (2 sessions)	Skin burn (4%)	None
Furusawa[129]	30	0.5–2.5 (mean: 1.3)	MRI	H&E staining	53.5%	Skin burn (3%)	5–23 days
Wu[130]	23	2.0–4.7 (mean: 3.1)	Ultrasound	H&E, NADH staining	100%	Skin burn (4%), moderate pain (17%)	1–2 weeks
Kim[131]	6	1.2–3.7 (mean: 2.56)	MRI	H&E staining (biopsy & surgery)	50%	None mentioned	2–4 weeks

wide local ablation of the target, covering both the tumor and a mean margin of 1.80 ± 0.58 cm of surrounding normal breast tissue. Complete ablation was observed in all patients. The authors concluded that HIFU is effective, safe, and feasible for the treatment of localized breast cancer.

The majority of current studies were phase I and II clinical trials that showed HIFU to be a promising ablative treatment for small breast cancer. While the results were very encouraging, the obvious weakness of the trials was the lack of intermediate and long-term followup. Wu and colleagues[132] reported long-term survival data from a prospective phase-III clinical trial. Twenty-two patients with breast cancer (TNM classification: stage I in 4 patients, stage II in 17 and stage II_A in 1) underwent ultrasound-guided HIFU ablation with conservative intent for the primary lesions, followed by chemotherapy, radiation therapy, and tamoxifen therapy. At a median followup of 54.8 months (range, 36–72 months), 2 of the 22 patients had local recurrence, 1 patient had died, 1 was lost to followup, and 20 were still alive. The five-year disease-free survival and recurrence-free survival rates were 95% and 89%, respectively. The cosmetic result was judged to be good to excellent by 94% of patients.

Gianfelice and colleagues[128] used an MRI-guided HIFU device to treat 24 women with biopsy-proven invasive breast cancer. Before HIFU, all patients had undergone a chemotherapeutic regimen consisting of oral tamoxifen citrate for varying periods of time. After HIFU ablation, they were followed up for 13–39 months (mean: 20.2 months), and core biopsy was performed to histologically assess the tumor response. The results showed that 14 of the 24 patients (58.3%) had no residual tumor, while the remaining 10 patients had varying amounts of residual tumor in biopsy specimens. A second HIFU treatment session rendered five of these 10 patients tumor free on post-treatment biopsy. In total, 19 of 24 patients (79%) had negative biopsy results after 1 or 2 HIFU sessions. The mean follow-up period was 20.2 months (13–39 months). The authors concluded that MRI-guided HIFU could be used as an adjuvant to tamoxifen therapy in high-risk surgical patients with breast cancer. Furusawa and colleagues[133] reported 21 patients undergoing MRI-guided HIFU treatment, including 17 patients treated once and 4 patients twice. They followed up the patients for 3–26 months (mean, 14 months). One case had local recurrence, but no evidence of recurrence was detected through MRI in the remaining 20 patients.

15.6 Antitumor Immune Response after Thermal Ablation

It has been noted that large amounts of tumor debris remain *in situ* after thermal ablation. As a normal process of the healing response, the tumor debris is gradually reabsorbed by the individual patient during a period ranging from months to few years. It is still unclear what

kind of biological significance may exist during the absorption of the ablated tumor. However, some studies have shown that active immune response to the treated tumor could be developed after thermal ablation, and the host immune system could become more sensitive to the tumor cells.[134–137] This may lead to a potential procedure that reduces or perhaps eliminates metastases and prevents local recurrence in cancer patients who have had original dysfunction of antitumor immunity before treatment. In this chapter we review the studies that focused on the host immune responses after thermal ablation of a tumor and analyze experimental and clinical data available to assess whether these studies provide potential for a better understanding of this complex phenomenon. In addition, we compare the various ablation techniques in terms of ablative mechanisms, advantages and disadvantages, and their relevance for the treatment of solid tumors.

15.6.1 Antitumor immune response after RFA

Of the minimally invasive therapies, RFA is only one technique that has been widely used in the clinical management of solid tumors, particularly in hepatocellular carcinoma (HCC). As coagulative necrosis is immediately induced in a targeted tumor after thermal ablation, necrotic cell death can be recognized by the immune system as a result of dangerous events, according to the "danger" model of immunity by Matzinger.[138,139] Necrotic cell death is also accompanied by the release of "danger signals" from the heat-stressed cells such as acute phase proteins, pro-inflammatory cytokines, and heat shock proteins (HSPs), thus developing a temporary inflammatory stress. This stress may be associated with positive processes similar to the healing of injured tissues but could also lead to the stimulation of tumor growth.[140] After RFA treatment, a moderate and temporary systemic inflammatory response has been observed in cancer patients, as demonstrated by the increase in plasma levels of pro-inflammatory cytokines and acute phase reactants.[141–145]

HSPs are families of highly conserved proteins that are involved in the mechanisms of cell repair. They are intracellular molecular chaperones that physiologically bind tumor peptide antigens and enhance tumor cell immunogenicity.[146] Antigen-presenting cells (APCs) take up HSP–tumor-peptide complex and present the chaperoned peptides directly to tumor-specific T lymphocytes with high efficiency, resulting in potent cellular immune responses against tumor cells.[147] Around the necrotic ablated area, RFA produces sublethal injury in the zone of transition that shows apoptosis and increased HSP70 expression in the liver of normal swine.[148] Schueller and colleagues found that there was an increased synthesis and cell surface expression of HSPs (HSP70, 90) after RFA in nude rats bearing human hepatocellular carcinoma.[149] In addition, large amounts

of tumor debris can induce local infiltration of activated dendritic cells (DCs), the most potent APC for induction of adaptive immunity against cancer.[150] Activating signals including necrotic tumor cells and HSPs can induce the progression of infiltrating DCs from an immature to a mature stage, resulting in the matured DCs presenting tumor antigens to naïve T lymphocytes in an MHC-restricted fashion.[151] (Note: MHC stands for major histocompatibility complex.)

Ali and colleagues demonstrated that a transient function of myeloid DCs can be activated in HCC patients 7–14 days after RFA, with an increased ability to stimulate $CD4^+$ T cells.[152] Up to 7% of DCs present in the draining lymph nodes contained tumor antigens in the ablated tumor after RFA. Compared to untreated HCC and normal liver tissue, expression of costimulatory molecules such as CD80 and CD86 was significantly enhanced by incubation with RFA-treated HCC.[153] Similar results were also demonstrated by Zerbini and colleagues in HCC patients,[154] indicative that local tumor ablation can lead to efficient antigen loading, and migration and maturation of APCs including DCs and monocytes. Direct evidence has recently shown that RFA can induce APC infiltration and amplification of weak tumor-induced immunity in a murine tumor model, and that enhanced systemic antitumor T-cell immune responses and tumor regression are associated with increased infiltration of DCs after subtotal RF ablation.[155] These results suggest that the generation of heat-altered tumor antigens, in combination with the "danger signals," may help to overcome immune tolerance or anergy toward the remaining tumor.

The effects of RFA on antitumor T-cell responses have been studied in animal models. A local influx of immune cells was observed after RFA in tumor-free domestic pigs and in the livers of rabbits implanted with epithelial tumors.[156] The influx of immune cells was located in the periphery of the coagulated area and consisted of lymphocytic and plasma cell infiltrates. Concomitantly, a specific T-cell proliferative response to the tumor cells was also detected in the peripheral blood of RFA-treated animals.[157] den Brok and colleagues[158] found that a weak but detectable immune response was present after RFA in mice bearing ovalbumin-transfected melanoma. This antitumor immunity was mediated by antigen-specific $CD8^+$ T cells, and adoptive transfer of splenocytes could induce partial protection against tumor challenge in syngeneic mice. Compared to surgical resection and control groups, RFA could efficiently stimulate activation and proliferation of splenocytes in mice bearing H22 tumors, and the cytotoxicity of splenocytes to tumor cells was significantly enhanced in RFA-treated animals, with an increased secretion of IL-2 and IFN-γ.[159] After *in situ* RFA of liver tumors, resistance to local and systemic tumor rechallenge was increased in mice bearing CC531 colon carcinoma.[160]

However, no inhibitory effect on tumor growth was observed in the nearby untreated liver tumors.

Similar results have been also demonstrated in cancer patients treated with RFA. Zerbini and colleagues[161] showed convincing evidence that RFA can activate a systemic antitumor T-cell response in 20 HCC patients. Using an ELISPOT assay, the reactivity of circulating T cells to autologous HCC lysate was assessed before and after RFA treatment. (Note: ELISPOT stands for enzyme-linked immunosorbent spot.) The researchers found that the specific T-cell response was increased from zero to three patients immediately after RFA. Importantly, this boosting effect still persisted at four weeks after RFA, and the number of the patients showing the same T-cell response increased to nine. These data were confirmed by another study where both HCC and colorectal liver metastasis were treated with RFA.[162] After RFA treatment, both HCC and colorectal cancer cells could significantly stimulate a specific immune response in patients, resulting in an increase of circulating $CD4^+$ and $CD8^+$ T cells, and cytotoxic activity. In contrast, one study observed a decrease of circulating $CD3^+$ and $CD4^+$ T cells after RFA treatment in metastatic cancer patients, together with no change in HCC patients. However, RFA-induced trafficking of naïve and memory $CD62L^+$ T cells from circulation to tissues enhanced the function of T cells, including *in vitro* responses to phytohaemagglutinin (PHA) and tumor-associated MUC1 antigen.[163]

In order to improve the RFA-induced weak immune response, the combination of RFA with immunotherapy has been investigated in laboratory settings. RFA can be efficiently combined with immune modulation by anti-CTLA-4 antibodies or regulatory T-cell depletion. These combination treatments protected mice from the outgrowth of tumor challenges and led to *in vivo* enhancement of tumor-specific T-cell numbers, which produced more IFN-γ upon activation.[153] Saji and colleagues[164] demonstrated that RFA *plus* intratumoral injection of naïve DCs can induce DC migration to regional lymph nodes and adoptive antitumor immunity in a mouse tumor model. The combination of RFA with IFN injection could significantly increase antitumor effects in an orthotopic murine model with squamous cell carcinoma, as compared to single therapy and control groups.[165] RFA stimulated tumor-specific T cells to move to tumor sites, whereas IFN activated DC and enhanced antigen presentation. All of the mice survived for 50 days in the combined-therapy group. Using both neu-overexpressing mouse mammary carcinoma in FVBN202 transgenic mice and 4T1 tumors in Balb/c mice, RFA followed by the administration of intratumor IL-7 and IL-15 induced immune responses to tumors, inhibited tumor development and lung metastasis, and reduced myeloid-derived suppressor cells.[166]

15.6.2 Antitumor immune response after LA

In addition to local destruction with thermal energy, LA can induce an immunogenic effect on cancer in both animal tumor models and cancer patients. Compared to surgical resection, LA can reduce metastatic spread of liver tumors in rats bearing a liver adenocarcinoma.[167] Furthermore, with HSP70 shifts from cytoplasm to nucleus in LA-treated liver cancer cells, an increase of HSP70 immunoreactivity in tumors was observed, leading to increased numbers of tumor-infiltrating macrophages and an increased presence of HSP70 in the membrane and cytoplasm of these macrophages.[168] LA can also induce a significant increase of HSP70 expression in the murine mode of colorectal liver metastasis[169] and prostate cancer.[170,171] While two independent adenocarcinomas were implanted into both lobes of the liver in rats (one as a control in the right lobe and one treated with LA in the left lobe), the control tumor volumes were significantly smaller in the LA group than those in hepatic resection group, and the expression of CD8 and B7-2 (CD86) was significantly higher in the control tumor after LA.[172] Moreover, compared with surgical extirpation, complete eradication of reimplanted tumors and increased local infiltration of ED1 macrophages and CD8 lymphocytes were observed in the LA group 48 days after tumor challenge,[173] suggesting that LA can enhance antitumor immune response to eradicate a challenging tumor. This enhanced response might be associated with increased numbers of tumor-infiltrating macrophages and CD8 lymphocytes.

Immunological assays followed by the LA procedure for cancer patients are still limited in the clinical setting. An early systemic inflammatory reaction was observed after LA in patients with malignant liver tumors.[174] The serum levels of IL-6, TNFRI, and CRP increased significantly up to 72 h after LA procedure, while the TNF-α, IL-1β, and IL-10 levels remained unchanged. Using an IFN-γ secretion assay and flow cytometry, Volg and colleagues[175] studied peripheral T lymphocyte ($CD3^+$, $CD4^+$, $CD8^+$) activation against autologous tumor tissue, and T-cell cytotoxicity against allogenic colorectal cancer (CaCo) cells before and after LA in patients with liver metastasis of colorectal cancer. They found that tumor-specific cytotoxic T-cell stimulation was detected after LA treatment, with a significant increase of cytolytic activity against CaCo cells, indicative that LA can trigger T-lymphocyte-mediated antitumor immune response against autologous tumor tissue in patients.

15.6.3 Antitumor immune response after cryoablation

In the early introduction of cryoablation to clinical practice, there were occasional reports of patients with spontaneous regression of tumor metastases after ablation of a primary tumor, suggesting a potential systemic benefit

to a local therapy.[176] However, the mechanisms behind the existence of a cryo-immunologic response were unclear because immunologic assays were limited at the time of many of these observations. Subsequently, an immune response induced by cryoablation was investigated using a variety of animal tumor models. The results revealed that tumor-specific immunity, as measured by resistance to rechallenge in tumor-bearing animals undergoing cryoablation of a primary tumor, was significantly greater in the cryoablation-treated animals compared with surgical excision or naïve animals.[177–179] In addition, cryoablation could significantly inhibit the growth of contralateral tumors[180,181] and reduce metastatic deposits in the lung and liver in tumor-bearing animals.[182,183]

On the contrary, some studies found that cryoablation failed to induce antitumor immune responses. There was no significant inhibition on secondary tumor growth after rechallenge in cryo-treated rats.[184] Cryoablation alone couldn't directly cause a tumor-specific cytotoxic T lymphocyte (CTL) response and a protective antimetastatic impact compared to cryotherapy combined with subsequent *in situ* injection of immature DCs.[185,186] Moreover, immunosuppressive effects induced by cryoablation on host antitumor immunity was also observed in tumor-bearing animals, resulting in a decreased resistance to a secondary tumor challenge and an increase of pulmonary metastases after cryoablation.[181,187,188] This has led to a controversy over whether a cryo-immunologic response would exist after cryoablation of malignant tissue.

Recently, due to a better understanding of the relationships between the innate and adaptive arms of the immune response, more detailed studies of the mechanism behind cryo-immunology have offered insight into why cryoablation may alternate between immune enhancement and immune suppression. It is evident that several changes induced by cryoablation, such as cytokine profile, the availability of tumor antigens processed by APCs, the mechanism of cell death by either apoptosis or necrosis, and the subsets of phagocytic cells (DCs or macrophages) responsible for clearing the ablated cells, may impact the immune response either positively or negatively.[176] For instance, although apoptosis and necrosis are the primary mechanisms of tumor cell death, they have a significantly different impact on the immune response.[189] Apoptosis results in the uptake of cellular debris without causing inflammation or releasing the intracellular contents. APCs that take up the apoptotic cells not only do not generate an immune response but can lead to clonal deletion and anergy.[189–192] In contrast, necrotic cell death is characterized by cellular breakdown and release of intracellular contents, many of which are danger signals. These signals promote cross-presentation, maturation of the DCs, and ultimately the activation of antigen-specific T cells.[193–195] As both necrosis and apoptosis play a role in tumor cell death after cryoablation, the relative

contribution of necrosis and apoptosis in the death of the tumor cells may shift the immune response from stimulatory to suppressive. Cryoablative techniques that result in large areas of apoptotic cell death, as opposed to necrosis, may result in immunosuppression. However, some studies have suggested that apoptotic tumor cells may be superior to necrotic cells in stimulating an antitumor immune response.[196–198]

In addition to animal models, some clinical studies have recently attempted to reveal how cryoablation has profound effects on the immune system in cancer patients. Osada and colleagues[199] measured serum levels of IL-2, IL-4, IL-6, IL-10, TNF-α, and IFN-γ in 13 patients with unresectable hepatic tumors before and after cryoablation. Decreased levels of serum tumor markers and local tumor necrosis detected on CT scan were observed in all patients, including five cases who presented evidence of necrosis in metastatic tumors away from the treated lesions. Serum IL-6 level was increased in all patients after cryoablation, but no change was made in the IL-2 level. There was a significant increase of serum TNF-α level and Th1/Th2 ratio in the patients showing the necrosis of secondary tumors. The effects of cryoablation on humoral immune compartments were also analyzed by Ravindranath and colleagues in 35 patients with liver metastases originated from colon cancer.[200] They found an increase in the production of IgM antibodies against tumor-released gangliosides. Interestingly, these antibodies were not significantly increased in patients undergoing RFA or routine surgery. Si and colleagues[201] observed a specific cytotoxic T-cell response induced by cryoablation in 20 patients with high-risk prostate cancer. Four weeks after cryoablation, there was a significant increase of serum TNF-α and IFN-γ levels and in the Th1/Th2 ratio compared with the values before cryoablation, but no changes were observed in the serum level of IL-4 or IL-10. Tumor-specific T-cell responses were significantly increased four weeks after cryoablation when peripheral blood mononuclear cells were co-incubated with human prostate cancer (LNCaP) cells, indicating that cryoablation could improve tumor-specific cytolytic activity of CTLs in prostate cancer patients. This immune response was sufficiently maintained only for a period of four weeks. However, when cryoablation was combined with granulocyte macrophage colony-stimulating factor (GM-CSF) administration to treat metastatic hormone refractory prostate cancer, the response lasted for at least eight weeks.[202]

In the case of freezing large tumors, cryoablation may cause a serious complication known as cryoshock, a syndrome of coagulopathy, disseminated intravascular coagulation, and multi-organ failure.[203] As these reactions are similar to those observed after endotoxin administration and other systemic inflammatory stimuli, cryoshock is believed to be caused by the systemic release of inflammatory cytokines including IL-1,

IL-6, and TNF-α after cryoablation.[204–206] This is different from the RFA-treated liver tissue where there is coagulative destruction of the hepatocyte organelles within an intact plasma membrane.[207] Cryoshock rarely appears in the cryoablation of renal and prostate tumors and is a more common side effect of hepatic cryoablation.

15.6.4 Antitumor immune response after MWA

The effect of microwaves on immune cells was initially investigated in murine B16 melanoma models. Microwave hyperthermia in combination with an ethanol injection can significantly prolong the survival of tumor-bearing mice with an increased infiltration of T lymphocytes and NK cells in the ablated melanoma.[208,209] Whole-body microwave hyperthermia can cause a significant enhancement of TNF-α secretion in murine peritoneal macrophages and splenic T lymphocytes.[210] Yao and colleagues[211] found that a murine CT-26 tumor treated with MWA could sensitize immature DCs, subsequently inducing *in vitro* proliferation of T cells and activating the cytotoxicity of CTLs. In addition, the sensitized DCs could significantly inhibit *in vivo* growth of the tumor and prolong the survival of the mice.

Clinical studies related to the immune response were initially conducted on prostate cancer treated by microwave energy. A significant, transient increase of the $CD4^+/CD8^+$ ratio and of the PHA and concanavalin-A transformation indices was observed after microwave hyperthermia in 15 prostate cancer patients, and the peak effect of this immune response was noted at 2 months with a subsequent decrease.[212] Fan and colleagues[213] treated 58 patients with malignant bone tumors with a surgical procedure in combination with microwave hyperthermia and adjuvant immunotherapy, and the immune response, including T-cell subsets, IL-2, and sIL-2, was monitored 3–38 months (mean 19 months) after the combined therapies. The immune function was significantly improved in the majority of the patients, though oncologic outcome was similar to that obtained by the limb-saving procedure.

MWA-induced immune response was mostly observed by Dr. Dong and colleagues in 78 patients with hepatocellular carcinoma, and ultrasound-guided core needle biopsy was performed after treatment for determining the local infiltration of immunocytes within the treated lesion. The results demonstrated a significantly increased infiltration of T lymphocytes, memory T lymphocytes, NK cells, and monocytes in the ablated tumor, with no change in B lymphocytes, suggesting that MWA could only enhance cellular immune response in HCC patients.[214–216] This response was maximal on the third day after thermal ablation but persisted to day 30. The extent of infiltration was negatively related to serum α-fetoprotein and tumor size.[216] But interestingly, patients with a high degree of immune cell infiltration

in the treated tumor had lower recurrence rates than those with low levels of infiltration, and there is a statistically significant correlation between survival outcome and the extent of immunocyte infiltration.[215] In addition, serum levels of IL-6, IL-1ra, and C-reactive protein were significantly elevated one day after laparoscopic MWA and returned to the preoperative levels at day seven postoperatively.[217] Furthermore, MWA combined with either a local injection of staphylococin or oral uptake of Shenqi (a Chinese herb) mixture, could enhance cellular immune response, improve survival time, and reduce local recurrence in HCC patients compared with the control group.[218,219]

15.6.5 Antitumor immune response after HIFU ablation

Animal studies have suggested that HIFU might modulate host antitumor immunity. Yang and colleagues[220] used HIFU to treat C1300 neuroblastoma implanted in mouse flanks, followed by the rechallenge of the same tumor cells. A significantly slower growth of re-implanted tumors was observed in these mice when compared with the controls. After HIFU treatment, the cytotoxicity of peripheral blood T lymphocytes was significantly increased in the H22-tumor-bearing mice treated with HIFU, and adoptive transfer of the activated-lymphocytes could provide better long-term survival and lower metastatic rates in the mice that were rechallenged by the same tumor cells. Similar results were confirmed in the mice implanted with MC-38 colon adenocarcinoma after HIFU ablation. HIFU treatment could also induce enhanced CTL activity *in vivo*, thus providing protection against subsequent tumor rechallenge.[221]

After HIFU ablation, large amounts of tumor debris remain *in situ,* and the host gradually reabsorbs the debris as part of the normal process of a healing response. Using a murine hepatocelluar carcinoma model, Zhang and colleagues[222] demonstrated that the remaining tumor debris induced by HIFU could be immunogenic as an effective vaccine to elicit tumor-specific immune responses, including induction of CTL cytotoxic activity and protection against a lethal tumor challenge in naïve mice. When the tumor debris was loaded with immature DCs, it could significantly induce maturation of DCs, as well as increased cytotoxocity and TNF-α and IFN-γ secretion by CTL, thus initiating a host-specific immune response after the H22 challenge in the vaccinated mice.[223] Immediately after HIFU exposure to MC-38 colon adenocarcinoma cells *in vitro*, the release of endogenous danger signals including HSP60 was observed from the damaged cells. These signals could subsequently activate APCs, leading to an increased expression of costimulatory molecules and enhanced secretion of IL-12 by the DCs, and elevated secretion of TNF-α by the macrophages.[224] In addition, HIFU could upregulate *in vitro* and *ex vitro* molecular expression of Hsp70,[225,226] which is an intracellular molecular chaperone that can

enhance tumor cell immunogenicity, resulting in potent cellular immune responses.

The potency of APC activation from mechanical lysis and a sparse-scan HIFU was much stronger than that from thermal necrosis and a dense-scan HIFU exposure, suggesting that optimization of an HIFU ablation strategy may help to enhance immune response after treatment.[227] Heat and acoustic cavitation are two major mechanisms involved in HIFU-induced tissue damage, and cavitation is a unique effect of HIFU when compared with other thermal ablation techniques. Cavitation causes membranous organelles (including mitochondria and endoplasmic reticulum cells and nuclear membranes) to collapse. This breaks up tumor cells into small pieces, on which the tumor antigens may remain intact, or leads to the exposure of an immunogenic moiety that is normally hidden in tumor antigens. Zhou and colleagues[228] used either heat- or HIFU-treated H22 tumor vaccine to inoculate naïve mice. The vaccination times were in four sessions, once a week for four consecutive weeks, and each mouse was challenged with H22 tumor cells one week after the last vaccination. The researchers found that the HIFU-treated tumor vaccine could significantly inhibit tumor growth and increase survival rates in the vaccinated mice, suggesting that acoustic cavitation can play an important role in stimulating the host antitumor immune system.

Emerging clinical results revealed that a systemic cellular immune response was observed in cancer patients after HIFU treatment. Rosberger and colleagues[229] reported five consecutive cases of posterior choroidal melanoma treated with HIFU. Three patients had abnormal, and two patients had normal CD4/CD8 ratios before treatment. One week after treatment, the ratio in two patients reverted to normal, while another was noted to have a 37% increase in his CD4 T cells relative to his CD8 cells. Wang and Sun[230] used multiple-session HIFU to treat 15 patients with late-stage pancreatic cancer. Although there was an increase in the average values of NK cells, T lymphocytes, and subsets in 10 patients after HIFU treatment, a significant statistical difference was observed in only NK-cell activity before and after HIFU treatment ($p < 0.05$). We[231] observed changes in circulating NK cells, T lymphocytes, and subsets in 16 patients with solid malignancy before and after HIFU treatment. The results showed a significant increase in the population of $CD4^+$ lymphocytes ($p < 0.01$) and the ratio of $CD4^+/CD8^+$ ($p < 0.05$) after HIFU treatment. The abnormal levels of $CD3^+$ lymphocytes returned to normal in two patients, as did the $CD4^+/CD8^+$ ratio in three, the $CD19^+$ lymphocytes in one, and the NK cells in one, respectively, in comparison to the values in the control group. In addition, serum levels of immunosuppressive cytokines including VEGF, TGF-β1, and TGF-β2 were significantly decreased in the peripheral blood of cancer patients after HIFU

treatment, indicating that HIFU may lessen tumor-induced immunosuppression and renew host antitumor immunity.[232]

Clinical evidence suggests that HIFU treatment may also enhance local antitumor immunity in cancer patients. Kramer and colleagues[233] found that HIFU treatment could alter the presentation of tumor antigens in prostate cancer patients and was was most likely to be stimulatory. Histological examination showed significantly upregulated expression of Hsp72, Hsp73, and glucose-regulated protein (GRP) 75 and 78 at the border zone of the HIFU treatment in prostate cancer. Heated prostate cancer cells exhibited increased Th1-cytokine (IL-2, IFN-γ, TNF-α) release but decreased Th2-cytokine (IL-4, -5, -10) release of tumor-infiltrating lymphocytes (TILs). The upregulated expression of Hsp70 was confirmed in the tumor debris of breast cancer after HIFU ablation,[234] indicating that HIFU may modify tumor antigenicity to produce a host immune response. We[235] found that the number of tumor-infiltrating APCs including DCs and macrophages increased significantly along the margin of HIFU-treated human breast cancer with an increased expression of HLA-DR, CD80, and CD86 molecules. Activated APCs may take up the HSP–tumor-peptide complex that remains in the tumor debris and present the chaperoned peptides directly to tumor-specific T lymphocytes with high efficiency, resulting in potent cellular immune responses against tumor cells after HIFU treatment. Furthermore, HIFU could induce significant infiltration of TILs in human breast cancer, including CD3, CD4, CD8, B lymphocytes, and NK cells. The numbers of activated CTLs expressing $FasL^+$, $granzyme^+$, and $perforin^+$ significantly increased in the HIFU-treated tumor, suggesting that specific cellular antitumor immunity can be locally triggered after HIFU treatment.[236]

15.7 Summary

Breast conserving therapy is the gold-standard option for patients with early-stage breast cancer. Current techniques include surgical excision, chemotherapy, radiation therapy, and endocrine therapy. The goal of surgical excision is to remove the entire tumor with a negative surgical margin, and to preserve the breast tissue as far as possible. Minimally invasive ablative techniques may offer complete tumor ablation with less psychological morbidity, better cosmetic results, and shorter hospital stay.

Several drawbacks are encountered in thermal ablation for breast cancer. Successful thermal ablation is a function of appropriate patient selection, and breast lesions close to the skin and chest wall, as well as multiple lesions, should be excluded from thermal ablation. As pathological samples are not obtainable for assessing the tumor-free margins of the ablated tissue after thermal ablation, the lack of pathologic method to directly

examine the tumor margins is still a major argument against this thermal approach for breast cancer. Recently, innovative techniques for the detection of residual disease have been examined in the fields of breast imaging. These techniques include 3D rotating delivery of excitation off (3D RODEO), MRI, and positron emission tomography (PET), for which preliminary results are very encouraging.[237] Determination of the status of the sentinel node in breast cancer is important in breast conserving therapy. As lymph drainage may be disturbed after local tumor ablation, it is preferable to perform the sentinel node biopsy before the ablation. Finally, some of the ablation devices, such as the HIFU device, are currently expensive. With technical developments underway, we are optimistic that device cost will decrease in the future.

Until now, thermal ablation of early-stage breast cancer has been conducted in research settings for the assessment of technical safety and feasibility, and none of those described herein have been used alone in clinical practice. Where clinically appropriate, thermal ablation techniques should give at least the same results as surgical excision, with the extent of the negative surgical margins being determined by imaging. Although recent results have been very encouraging, further trials are essential to evaluate the long-term efficacy, cosmetic outcome, and cost effectiveness of thermal ablation in early-stage breast cancer. Not until these issues have been resolved, and the results from prospective, randomized clinical trials worldwide become available, can minimally invasive ablative techniques be considered as candidates for conventional therapy for widespread clinical application.

However, some of the minimally invasive thermal therapies can already be offered as options for the treatment of some carefully selected breast cancers. The less-invasive nature of these therapies may make them attractive options for the elderly woman with early-stage breast cancer. The rationale for this is the evidence for increased incidence and poorer outcomes in the elderly breast-cancer patient who is undertreated.[238] As the population grows and ages, there will be a large population of elderly candidates for appropriate treatments, and thermal ablation may become the treatment of choice for improving the currently poor outcome of treatment for early-stage breast cancer in elderly women. Thermal ablation may also be performed as a local treatment to eradicate small primary tumors or any residual tumor that persists after the completion of systemic therapy. Finally, these therapies can be used as a salvage method to treat local recurrence after breast conservation therapy.

It is clear that minimally invasive thermal therapies should be undertaken when there is precise knowledge not only of the number and location of the lesions, but also of the biological characteristics and natural history of the tumor. For patients with breast cancer, the treatment strategy must

be multidisciplinary and should include surgery, radiotherapy, chemotherapy, and/or tamoxifen therapy. As a local treatment, thermal ablation may provide an alternative to open breast surgery in the future. However, it should be used in combination with other conventional therapies.

References

1. D. M. Parkin, F. Bray, J. Ferlay, and P. Pisani, "Global cancer statistics, 2002," *CA Cancer J. Clin.* **55**, 74–108 (2005).
2. A. Jemal, L. X. Clegg, E. Ward, L. A. Ries, X. Wu, P. M. Jamison, P. A. Wingo, H. L. Howe, R. N. Anderson, and B. K. Edwards, "Annual report to the nation on the status of cancer, 1975–2001, with a special feature regarding survival," *Cancer* **101**, 3–27 (2004).
3. B. Fisher, S. Anderson, C. K. Redmond, N. Wolmark, D. L. Wickerham, and W. M. Cronin, "Reanalysis and results after 12 years of follow-up in a randomized clinical trial comparing total mastectomy with lumpectomy with or without irradiation in the treatment of breast cancer," *N. Engl. J. Med.* **333**, 1456–1461 (1995).
4. J. A. Jacobson, D. N. Danforth, K. H. Cowan, T. d'Angelo, S. M. Steinberg, L. Pierce, M. E. Lippman, A. S. Lichter, E. Glatstein, and P. Okunieff, "Ten-year results of a comparison of conservation with mastectomy in the treatment of stage I and II breast cancer," *N. Engl. J. Med.* **332**, 907–911 (1995).
5. J. A. van Dongen, A. C. Voogd, I. S. Fentiman, C. Legrand, R. J. Sylvester, D. Tong, E. van der Schueren, P. A. Helle, K. van Zijl, and H. Bartelink, "Long-term results of a randomized trial comparing breast-conserving therapy with mastectomy: European Organization for Research and Treatment of Cancer 10801 trial," *J. Natl. Cancer Inst.* **92**, 1143–1150 (2000).
6. U. Veronesi, N. Cascinelli, L. Mariani, M. Greco, R. Saccozzi, A. Luini, M. Aguilar, and E. Marubini, "Twenty-year follow-up of a randomized study comparing breast-conserving surgery with radical mastectomy for early breast cancer," *N. Engl. J. Med.* **347**, 1227–1232 (2002).
7. A. H. Hayashi, S. F. Silver, N. G. van der Westhuizen, J. C. Donald, C. Parker, S. Fraser, A. C. Ross, and I. A. Olivotto, "Treatment of invasive breast carcinoma with ultrasound-guided radiofrequency ablation," *Am. J. Surg.* **185**, 429–435 (2003).
8. F. Izzo, R. Thomas, P. Delrio, M. Rinaldo, P. Vallone, A. DeChiara, G. Botti, G. D'Aiuto, P. Cortino, and S. A. Curley, "Radiofrequency ablation in patients with primary breast carcinoma: A pilot study in 26 patients," *Cancer* **92**, 2036–2044 (2001).

9. K. Dowlatshahi, D. S. Francescatti, and K. J. Bloom, "Laser therapy for small breast cancers," *Am. J. Surg.* **184**, 359–363 (2002).
10. K. J. Bloom, K. Dowlat, and L. Assad, "Pathologic changes after interstitial laser therapy of infiltrating breast carcinoma," *Am. J. Surg.* **182**, 384–388 (2001).
11. R. A. Gardner, H. I. Vargas, J. B. Block, C. L. Vogel, A. J. Fenn, G. V. Kuehl, and M. Doval, "Focused microwave phased array thermotherapy for primary breast cancer," *Ann. Surg. Oncol.* **9**, 326–332 (2002).
12. H. I. Vargas, W. C. Dooley, R. A. Gardner, K. D. Gonzalez, R. Venegas, S. H. Heywang-Kobrunner, and A. J. Fenn, "Focused microwave phased array thermotherapy for ablation of early-stage breast cancer: Results of thermal dose escalation," *Ann. Surg. Oncol.* **11**, 139–146 (2004).
13. E. D. Staren, M. S. Sabel, L. M. Gianakakis, G. A. Wiener, V. M. Hart, M. Gorski, K. Dowlatshahi, B. F. Corning, M. F. Haklin, and G. Koukoulis, "Cryosurgery of breast cancer," *Arch. Surg.* **132**, 28–33 (1997).
14. M. Caleffi, D. D. Filho, K. Borghetti, M. Graudenz, P. J. Littrup, L. A. Freeman-Gibb, V. J. Zannis, M. J. Schultz, C. S. Kaufman, D. Francescatti, J. S. Smith, R. Simmons, L. Bailey, C. A. Henry, and L. H. Stocks, "Cryoablation of benign breast tumors: Evolution of technique and technology," *Breast* **13**, 397–407 (2004).
15. F. Wu, Z. B. Wang, Y. D. Cao, W. Z. Chen, J. Bai, J. Z. Zou, and H. Zhu, "A randomised clinical trial of high-intensity focused ultrasound ablation for the treatment of patients with localised breast cancer," *Br. J. Cancer* **89**, 2227–2233 (2003).
16. D. F. Kacher and F. A. Jolesz, "MR imaging-guided breast ablative therapy," *Radiol. Clin. N. Am.* **42**, 947–962 (2004).
17. G. Cabibbo, F. Latteri, M. Antonucci, and A. Craxì, "Multimodal approaches to the treatment of hepatocellular carcinoma," *Nat. Clin. Pract. Gastroenterol. Hepatol.* **6**, 159–169 (2009).
18. R. D. Timmerman, C. S. Bizekis, H. I. Pass, Y. Fong, D. E. Dupuy, L. A. Dawson, and D. Lu, "Local surgical, ablative, and radiation treatment of metastases," *CA Cancer J. Clin.* **59**, 145–170 (2009).
19. E. Liapi and J. F. Geschwind, "Transcatheter and ablative therapeutic approaches for solid malignancies," *J. Clin. Oncol.* **25**, 978–986 (2007).
20. K. Hong, C. S. Georgiades, and J. F. Geschwind, "Technology insight: Image-guided therapies for hepatocellular carcinoma—Intra-arterial and ablative techniques," *Nat. Clin. Pract. Oncol.* **3**, 315–324 (2006).

21. J. Hafron and J. H. Kaouk, "Ablative techniques for the management of kidney cancer," *Nat. Clin. Pract. Urol.* **4**, 261–269 (2007).
22. B. Decadt and A. K. Siriwardena, "Radiofrequency ablation of liver tumours: Systematic review," *Lancet Oncol.* **5**, 550–560 (2004).
23. T. L. Huston and R. M. Simmons, "Ablative therapies for the treatment of malignant diseases of the breast," *Am. J. Surg.* **189**, 684–701 (2005).
24. S. E. Singletary, "Minimally invasive surgery in breast cancer treatment," *Biomed. Pharmacother.* **55**, 510–514 (2001).
25. B. Decadt and A. K. Siriwardena, "Radiofrequency ablation of liver tumours: Systematic review," *Lancet Oncol.* **5**, 550–560 (2004).
26. W. Y. Lau and E. C. Lai, "The current role of radiofrequency ablation in the management of hepatocellular carcinoma: A systematic review," *Ann. Surg.* **249**, 20–25 (2009).
27. S. A. Curley, "Radiofrequency ablation of malignant liver tumors," *Oncologist* **6**, 14–23 (2001).
28. S. N. Goldberg, G. S. Gazelle, E. F. Halpern, W. J. Rittman, P. R. Mueller, and D. I. Rosenthal, "Radiofrequency tissue ablation: Importance of local temperature along the electrode tip exposure in determining lesion shape and size," *Acad. Radiol.* **3**, 212–218 (1996).
29. S. N. Goldberg, C. J. Grassi, J. F. Cardella, J. W. Charboneau, G. D. Dodd III, D. E. Dupuy, D. Gervais, A. R. Gillams, R. A. Kane, F. T. Lee, Jr., T. Livraghi, J. McGahan, D. A. Phillips, H. Rhim, and S. G. Silverman, "Image-guided tumor ablation: Standardization of terminology and reporting criteria," *Radiol.* **235**, 728–739 (2005).
30. A. L. Gough-Palmer and W. M. Gedroyc, "Laser ablation of hepatocellular carcinoma: A review," *World J. Gastroenterol.* **14**, 7170–7174 (2008).
31. T. Sabharwal, K. Katsanos, X. Buy, and A. Gangi, "Image-guided ablation therapy of bone tumors," *Semin. Ultrasound CT MR* **30**, 78–90 (2009).
32. G. Carrafiello, D. Laganà, M. Mangini, F. Fontana, G. Dionigi, L. Boni, F. Rovera, S. Cuffari, and C. Fugazzola, "Microwave tumors ablation: Principles, clinical applications and review of preliminary experiences," *Int. J. Surg.* **6**, S65–69 (2008).
33. C. J. Simon, D. E. Dupuy, and W. W. Mayo-Smith, "Microwave ablation: Principles and applications," *Radiographics* **25**, S69–83 (2005).
34. M. Beland, P. R. Mueller, and D. A. Gervais, "Thermal ablation in interventional oncology," *Semin. Roentgenol.* **42**, 175–190 (2007).

35. L. D. Rybak, "Fire and ice: Thermal ablation of musculoskeletal tumors," *Radiol. Clin. North Am.* **47**, 455–469 (2009).

36. J. A. Dumot and B. D. Greenwald, "Argon plasma coagulation, bipolar cautery, and cryotherapy: ABC's of ablative techniques," *Endoscopy* **40**, 1026–1032 (2008).

37. R. J. Babaian, B. Donnelly, D. Bahn, J. G. Baust, M. Dineen, D. Ellis, A. Katz, L. Pisters, D. Rukstalis, K. Shinohara, and J. B. Thrasher, "Best practice statement on cryosurgery for the treatment of localized prostate cancer," *J. Urol.* **180**, 1993–2004 (2008).

38. J. E. Kennedy, "High-intensity focused ultrasound in the treatment of solid tumours," *Nat. Rev. Cancer* **5**, 321–327 (2005).

39. C. Chaussy, S. Thuroff, X. Rebillard, and A. Gelet, "Technology insight: High-intensity focused ultrasound for urologic cancers," *Nat. Clin. Pract. Urol.* **2**, 191–198 (2005).

40. F. Wu, "Extracorporeal high intensity focused ultrasound in the treatment of patients with solid malignancy," *Minim. Invasive Ther. Allied. Technol.* **15**, 26–35 (2006).

41. G. ter Haar, "Therapeutic applications of ultrasound," *Prog. Biophys. Mol. Biol.* **93**, 111–129 (2007).

42. C. R. Hill and G. R. ter Haar, "Review article: High intensity focused ultrasound—Potential for cancer treatment," *Br. J. Radiol.* **68**, 1296–1303 (1995).

43. S. Thomsen, "Pathologic analysis of photothermal and photomechanical effects of laser-tissue interactions," *Photochem. Photobiol.* **53**, 825–835 (1991).

44. S. N. Goldberg, G. S. Gazelle, and P. R. Mueller, "Thermal ablation therapy for focal malignancy: A unified approach to underlying principles, techniques, and diagnostic imaging guidance," *Am. J. Roentgen.* **174**, 323–331 (2000).

45. C. J. Diederich and K. Hynynen, "Ultrasound technology for hyperthermia," *Ultrasound Med. Biol.* **25**, 871–887 (1999).

46. A. S. Lubb and C. Bergemann, "Ultrasound therapy for malignant tumors: A conceptual assessment," *J. Clin. Ultrasound* **22**, 113–117 (1994).

47. W. C. Dewey, "Arrhenius relationships from the molecule and cell to the clinic," *Int. J. Hyperthermia* **10**, 457– 483 (1994).

48. J. Overgaard, "The current and potential role of hyperthermia in radiotherapy," *Int. J. Radiation Oncol. Biol. Phys.* **16**, 537–549 (1989).

49. M. Nikfarjam, C. Malcontenti-Wilson, and C. Christophi, "Focal hyperthermia produces progressive tumor necrosis independent of the initial thermal effects," *J. Gastrointest. Surg.* **9**, 410–417 (2005).

50. M. Nikfarjam, V. Muralidharan, and C. Christophi, "Mechanisms of focal heat destruction of liver tumors," *J. Surg. Res.* **127**, 208–223 (2005).

51. D. N. Wheatley, C. Kerr, and D. W. Gregory, "Heat-induced damage to HeLa-S3 cells: Correlation of viability, permeability, osmosensitivity, phase-contrast light-, scanning electron- and transmission electron-microscopical findings," *Int. J. Hyperthermia* **5**, 145–162 (1989).

52. J. Heisterkamp, R. van Hillegersberg, E. Sinofsky, and J. N. IJzermans, "Heat-resistant cylindrical diffuser for interstitial laser coagulation: Comparison with the bare-tip fiber in a porcine liver model," *Lasers Surg. Med.* **20**, 304–309 (1997).

53. C. T. Germer, A. Roggan, J. P. Ritz, C. Isbert, D. Albrecht, G. Muller, and H. J. Buhr, "Optical properties of native and coagulated human liver tissue and liver metastases in the near infrared range," *Lasers Surg. Med.* **23**, 194–203 (1998).

54. H. Maris and S. Balibar, "Negative pressures and cavitation in liquid helium," *Phys. Today* **53**, 29–32 (2000).

55. C. R. Hill, G. R. ter Haar, "Review article: High intensity focused ultrasound—Potential for cancer treatment," *Br. J. Radiol.* **68**, 1296–1303 (1995).

56. G. T. Clement, "Perspectives in clinical uses of high-intensity focused ultrasound," *Ultrasonics* **42**, 1087–1093 (2004).

57. T. Ozaki, K. Tabuse, T. Tsuji, Y. Nakamura, K. Kakudo, and I. Mori, "Microwave cell death: Enzyme histochemical evaluation for metastatic carcinoma of the liver," *Pathol. Int.* **53**, 837–845 (2003).

58. C. Germer, C. M. Isbert, D. Albrecht, J. P. Ritz, A. Schilling, A. Roggan, K. J. Wolf, G. Muller, and H. Buhr, "Laser-induced thermotherapy for the treatment of liver metastasis. Correlation of gadolinium-DTPA-enhanced MRI with histomorphologic findings to determine criteria for follow-up monitoring," *Surg. Endosc.* **12**, 1317–1325 (1998).

59. T. Ohno, K. Kawano, A. Sasaki, M. Aramaki, T. Yoshida, and S. Kitano, "Expansion of an ablated site and induction of apoptosis after microwave coagulation therapy in rat liver," *J. Hepatobiliary Pancreat. Surg.* **8**, 360–366 (2001).

60. T. Ozaki, I. Mori, M. Nakamura, H. Utsunomiya, K. Tabuse, K. Kakudo, "Microwave cell death: Immunohistochemical and enzyme histochemical evaluation," *Pathol. Int.* **53**, 686–692 (2003).
61. B. Emami and C. W. Song, "Physiological mechanisms in hyperthermia: A review," *Int. J. Radiat. Oncol. Biol. Phys.* **10**, 289–298 (1984).
62. K. G. Tranberg, "Percutaneous ablation of liver tumours," *Best Pract. Res. Clin. Gastroenterol.* **18**, 125–45 (2004).
63. V. Muralidharan, M. Nikfarjam, C. Malcontenti-Wilson, and C. Christophi, "Effect of interstitial laser hyperthermia in a murine model of colorectal liver metastases: Scanning electron microscopic study," *World J. Surg.* **28**, 33–37 (2004).
64. R. Matsumoto, A. M. Selig, V. M. Colucci, and F. A. Jolesz, "Interstitial Nd:YAG laser ablation in normal rabbit liver: Trial to maximize the size of laser-induced lesions," *Lasers Surg. Med.* **12**, 650–658 (1992).
65. W. J. Wiersinga, M. C. Jansen, I. H. Straatsburg, P. H. Davids, J. M. Klaase, D. J. Gouma, and T. M. van Gulik, "Lesion progression with time and the effect of vascular occlusion following radiofrequency ablation of the liver," *Br. J. Surg.* **90**, 306–312 (2003).
66. R. Benndorf and H. Bielka, "Cellular stress response—stress proteins: Physiology and implications for cancer," *Recent Results Cancer Res.* **143**, 129–144 (1997).
67. M. A. Barry, C. A. Behnke, and A. Eastman, "Activation of programmed cell death (apoptosis) by cisplatin, other anticancer drugs, toxins and hyperthermia," *Biochem. Pharmacol.* **40**, 2353–2362 (1990).
68. K. Hori, E. Mihich, and M. J. Ehrke, "Role of tumor necrosis factor and interleukin 1 in gamma-interferon-promoted activation of mouse tumoricidal macrophages," *Cancer Res.* **49**, 2606–2614 (1989).
69. T. Decker, M. L. Lohmann-Matthes, U. Karck, T. Peters, and K. Decker, "Comparative study of cytotoxicity, tumor necrosis factor, and prostaglandin release after stimulation of rat Kupffer cells, murine Kupffer cells, and murine inflammatory liver macrophages," *J. Leukoc. Biol.* **45**, 139–146 (1989).
70. D. O. Adams and T. A. Hamilton, "The cell biology of macrophage activation," *Annu. Rev. Immunol.* **2**, 283–318 (1984).
71. A. Kirn, A. Bingen, A. M. Steffan, M. T. Wild, F. Keller, and J. Cinqualbre, "Endocyticcapacities of Kupffer cells isolated from the human adult liver," *Hepatol.* **2**, 216–222 (1982).

72. C. Napoletano, F. Taurino, M. Biffoni, A. De Majo, G. Coscarella, F. Bellati, H. Rahimi, S. Pauselli, I. Pellicciotta, J. M. Burchell, L. A. Gaspari, L. Ercoli, P. Rossi, and A. Rughetti, "RFA strongly modulates the immune system and anti-tumor immune responses in metastatic liver patients," *Int. J. Oncol.* **32**, 481–90 (2008).

73. S. Evrard, C. Menetrier-Caux, C. Biota, V. Neaud, S. Mathoulin-Pélissier, J. Y. Blay, and J. Rosenbaum, "Cytokines pattern after surgical radiofrequency ablation of liver colorectal metastases," *J. Gastroenterol. Clin. Biol.* **31**, 141–145 (2007).

74. M. Y. Ali, C. F. Grimm, M. Ritter, L. Mohr, H. P. Allgaier, R. Weth, W. O. Bocher, K. Endrulat, H. E. Blum, and M. Geissler, "Activation of dendritic cells by local ablation of hepatocellular carcinoma," *J. Hepatol.* **43**, 817–822 (2005).

75. N. Watanabe, Y. Niitsu, H. Umeno, H. Kuriyama, H. Neda, N. Yamauchi, M. Maeda, and I. Urushizaki, "Toxic effect of tumor necrosis factor on tumor vasculature in mice," *Cancer Res.* **48**, 2179–2183 (1988).

76. C. Isbert, J. P. Ritz, A. Roggan, D. Schuppan, M. Ruhl, H. J. Buhr, and C. T. Germer, "Enhancement of the immune response to residual intrahepatic tumor tissue by laser-induced thermotherapy (LITT) compared to hepatic resection," *Lasers Surg. Med.* **35**, 284–292 (2004).

77. S. Evrard, C. Menetrier-Caux, C. Biota, V. Neaud, S. Mathoulin-Pélissier, J. Y. Blay, and J. Rosenbaum, "Cytokines pattern after surgical radiofrequency ablation of liver colorectal metastases," *Gastroenterol. Clin. Biol.* **31**, 141–145 (2007).

78. S. R. Schell, F. J. Wessels, A. Abouhamze, L. L. Moldawer, and E. M. Copeland III, "Pro- and anti-inflammatory cytokine production after radiofrequency ablation of unresectable hepatic tumors," *J. Am. Coll. Surg.* **195**, 774–781 (2002).

79. W. C. Chapman, J. P. Debelak, T. S. Blackwell, K. A. Gainer, J. W. Christman, C. W. Pinson, K. L. Brigham, and R. E. Parker, "Hepatic cryoablation, but not radiofrequency ablation, results in lung inflammation," *Arch. Surg.* **135**, 667–672 (2000).

80. L. J. Wudel, Jr., T. M. Allos, M. K. Washington, J. R. Sheller, and W. C. Chapman, "Multi-organ inflammation after hepatic cryoablation in BALB/c mice," *J. Surg. Res.* **112**, 131–137 (2003).

81. K. Washington, J. P. Debelak, C. Gobbell, D. R. Sztipanovits, Y. Shyr, S. Olson, and W. C. Chapman, "Hepatic cryoablation-induced acute lung injury: Histopathologic findings," *J. Surg. Res.* **95**, 1–7 (2001).

82. J. K. Seifert, M. P. France, J. Zhao, E. J. Bolton, I. Finlay, T. Junginger, and D. L. Morris, "Large volume hepatic freezing: Association with significant release of the cytokines interleukin-6 and tumor necrosis factor a in a rat model," *World J. Surg.* **26**, 1333–1341 (2002).

83. R. T. Sadikot, L. J. Wudel, D. E. Jansen, J. P. Debelak, F. E. Yull, J. W. Christman, T. S. Blackwell, and W. C. Chapman, "Hepatic cryoablation-induced multisystem injury: Bioluminescent detection of NF-kappaB activation in a transgenic mouse model," *J. Gastrointest. Surg.* **6**, 264–270 (2002).

84. S. S. Jeffrey, R. L. Birdwell, D. M. Ikeda, B. L. Daniel, K. W. Nowels, F. M. Dirbas, and S. M. Griffey, "Radiofrequency ablation of breast cancer: First report of an emerging technology," *Arch. Surg.* **134**, 1064–1068 (1999).

85. F. Izzo, R. Thomas, P. Delrio, M. Rinaldo, P. Vallone, A. DeChiara, G. Botti, G. D'Aiuto, P. Cortino, and S. A. Curley, "Radiofrequency ablation in patients with primary breast carcinoma: A pilot study in 26 patients," *Cancer* **92**, 2036–2044 (2001).

86. W. E. Burak, Jr., D. M. Agnese, S. P. Povoski, T. L. Yanssens, K. J. Bloom, P. E. Wakely, and D. G. Spigos, "Radiofrequency ablation of invasive breast carcinoma followed by delayed surgical excision," *Cancer* **98**, 1369–1376 (2003).

87. A. H. Hayashi, S. F. Silver, N. G. van der Westhuizen, J. C. Donald, C. Parker, S. Fraser, A. C. Ross, and I. A. Olivotto, "Treatment of invasive breast carcinoma with ultrasound-guided radiofrequency ablation," *Am. J. Surg.* **185**, 429–435 (2003).

88. B. D. Fornage, N. Sneige, M. I. Ross, A. N. Mirza, H. M. Kuerer, B. S. Edeiken, F. C. Ames, L. A. Newman, G. V. Babiera, and S. E. Singletary, "Small (< or = 2-cm) breast cancer treated with US-guided radiofrequency ablation: Feasibility study," *Radiol.* **231**, 215–224 (2004).

89. M. Earashi, M. Noguchi, A. Motoyoshi, and H. Fujii, "Radiofrequency ablation therapy for small breast cancer followed by immediate surgical resection or delayed mammotome excision," *Breast Cancer* **14**, 39–47 (2007).

90. S. Imoto, N. Wada, N. Sakemura, T. Hasebe, and Y. Murata, "Feasibility study on radiofrequency ablation followed by partial mastectomy for stage I breast cancer patients," *Breast* **18**, 130–134 (2009).

91. H. Medina-Franco, S. Soto-Germes, J. L. Ulloa-Gómez, C. Romero-Trejo, N. Uribe, C. A. Ramirez-Alvarado, and C. Robles-Vidal, "Radiofrequency ablation of invasive breast carcinomas: A phase II trial," *Ann. Surg. Oncol.* **15**, 1689–1695 (2008).

92. G. Manenti, F. Bolacchi, T. Perretta, E. Cossu, C. A. Pistolese, O. C. Buonomo, E. Bonanno, A. Orlandi, and G. Simonetti, "Small breast cancers: In vivo percutaneous US-guided radiofrequency ablation with dedicated cool-tip radiofrequency system," *Radiol.* **251**(2), 339–346 (2009).
93. W. K. Hung, K. L. Mak, M. Ying, and M. Chan, "Radiofrequency ablation of breast cancer: A comparative study of two needle designs," *Breast Cancer* **18**(2), 124–128 (2011).
94. T. Kinoshita, E. Iwamoto, H. Tsuda, and K. Seki, "Radiofrequency ablation as local therapy for early breast carcinomas," *Breast Cancer* **18**(1), 10–17 (2011).
95. N. Yamamoto, H. Fujimoto, R. Nakamura, M. Arai, A. Yoshii, S. Kaji, and M. Itami, "Pilot study of radiofrequency ablation therapy without surgical excision for T1 breast cancer: Evaluation with MRI and vacuum-assisted core needle biopsy and safety management," *Breast Cancer* **18**(1), 3–9 (2011).
96. H. Tsuda, K. Seki, T. Hasebe, Y. Sasajima, T. Shibata, E. Iwamoto, and T. Kinoshita, "A histopathological study for evaluation of therapeutic effects of radiofrequency ablation in patients with breast cancer," *Breast Cancer* **18**(1), 24–32 (2011).
97. H. Wiksell, L. Löfgren, K. U. Schässburger, H. Grundström, M. Janicijevic, U. Lagerstedt, K. Leifland, R. Nybom, S. Rotstein, A. Saracco, I. Schultz, K. Thorneman, C. Wadström, L. Westman, H. Wigzell, B. Wilczek, G. Auer, and B. Sandstedt, "Feasibility study on the treatment of small breast carcinoma using percutaneous US-guided preferential radiofrequency ablation (PRFA)," *Breast* **19**(3), 219–225 (2010).
98. T. Susini, J. Nori, S. Olivieri, L. Livi, S. Bianchi, G. Mangialavori, F. Branconi, and G. Scarselli, *Gynecol. Oncol*. **26**, 304–310 (2006).
99. P. Y. Marcy, N. Magne, P. Castadot, C. Bailet, and M. Namer, *Br. J. Radiol.* **80**, 267–73 (2007).
100. S. Oura, T. Tamaki, I. Hirai, T. Yoshimasu, F. Ohta, R. Nakamura, and Y. Okamura, *Breast Cancer* **14**, 48–54 (2007).
101. B. Brkljacic, I. Cikara, G. Ivanac, A. Hrkac Pustahija, R. Zic, Z. Stanec, "Ultrasound-guided bipolar radiofrequency ablation of breast cancer in inoperable patients: A pilot study," *Ultraschall. Med.* **31**(2), 156–62 (2010).
102. S. A. Harries, Z. Amin, M. E. Smith, W. R. Lees, J. Cooke, M. G. Cook, J. H. Scurr, M. W. Kissin, and S. G. Bown, "Interstitial laser photocoagulation as a treatment for breast cancer," *Br. J. Surg.* **81**, 1617–1619 (1994).

103. H. Mumtaz, M. A. Hall-Craggs, A. Wotherspoon, M. Paley, G. Buonaccorsi, Z. Amin, I. Wilkinson, M. W. Kissin, T. I. Davidson, I. Taylor, and S. G. Bown, "Laser therapy for breast cancer: MR imaging and histopathologic correlation," *Radiol.* **200**, 651–658 (1996).

104. A. B. Akimov, V. E. Seregin, K. V. Rusanov, E. G. Tyurina, T. A. Glushko, V. P. Nevzorov, O. F. Nevzorova, and E. V. Akimova, "Nd:YAG interstitial laser thermotherapy in the treatment of breast cancer," *Lasers Surg. Med.* **22**, 257–267 (1998).

105. K. J. Bloom, K. Dowlat, and L. Assad, "Pathologic changes after interstitial laser therapy of infiltrating breast carcinoma," *Am. J. Surg.* **182**, 384–388 (2001).

106. K. Dowlatshahi, D. S. Francescatti, and K. L. Bloom, "Laser therapy for small breast cancers," *Am. J. Surg.* **184**, 359–363 (2002).

107. S. Korourian, S. Klimberg, R. Henry-Tillman, D. Lindquist, M. Jones, D. C. Eng, J. C. Helsel, H. Mumtaz, K. Westbrook, and S. Harms, "Assessment of proliferating cell nuclear antigen activity using digital image analysis in breast carcinoma following magnetic resonance-guided interstitial laser photocoagulation," *Breast J.* **9**, 409–413 (2003).

108. K. H. Haraldsdóttir, K. Ivarsson, S. Götberg, C. Ingvar, U. Stenram, and K. G. Tranberg, "Interstitial laser thermotherapy (ILT) of breast cancer," *Eur. J. Surg. Oncol.* **34**, 739–745 (2008).

109. S. van Esser, G. Stapper, P. J. van Diest, M. A. van den Bosch, J. H. Klaessens, W. P. Mali, I. H. Borel Rinkes, and R. van Hillegersberg, "Ultrasound-guided laser-induced thermal therapy for small palpable invasive breast carcinomas: A feasibility study," *Ann. Surg. Oncol.* **16**, 2259–2263 (2009).

110. K. Dowlatshahi, J. J. Dieschbourg, and K. J. Bloom, "Laser therapy of breast cancer with 3-year follow-up," *Breast J.* **10**, 240–243 (2004).

111. V. S. Klimberg, C. Boneti, L. L. Adkins, M. Smith, E. Siegel, V. Zharov, S. Ferguson, R. Henry-Tillman, B. Badgwell, and S. Korourian, "Feasibility of percutaneous excision followed by ablation for local control in breast cancer," *Ann. Surg. Oncol.* **18**(11), 3079–3087 (2011).

112. R. A. Gardner, H. I. Vargas, J. B. Block, C. L. Vogel, A. J. Fenn, G. V. Kuehl, and M. Doval, "Focused microwave phased array thermotherapy for primary breast cancer," *Ann. Surg. Oncol.* **9**, 326–332 (2002).

113. H. I. Vargas, W. C. Dooley, R. A. Gardner, K. D. Gonzalez, S. H. Heywang-Köbrunner, and A. J. Fenn, "Success of sentinel lymph

node mapping after breast cancer ablation with focused microwave phased array thermotherapy," *Am. J. Surg.* **186**, 330–332 (2003).

114. H. I. Vargas, W. C. Dooley, R. A. Gardner, K. D. Gonzalez, R. Venegas, S. H. Heywang-Kobrunner, and A. J. Fenn, "Focused microwave phased array thermotherapy for ablation of early-stage breast cancer: Results of thermal dose escalation," *Ann. Surg. Oncol.* **11**, 139–146 (2004).
115. W. C. Dooley, H. I. Vargas, A. J. Fenn, M. B. Tomaselli, and J. K. Harness, "Randomized study of preoperative focused microwave phased array thermotherapy for early-stage invasive breast cancer," *Cancer Therapy* **6**, 395–408 (2008).
116. W. C. Dooley, H. I. Vargas, A. J. Fenn, M. B. Tomaselli, and J. K. Harness, "Focused microwave thermotherapy for preoperative treatment of invasive breast cancer: A review of clinical studies" *Ann. Surg. Oncol.* **17**(4), 1076–1093 (2010).
117. E. D. Staren, M. S. Sabel, L. M. Gianakakis, G. A. Wiener, V. M. Hart, M. Gorski, K. Dowlatshahi, B. F. Corning, M. F. Haklin, and G. Koukoulis, "Cryosurgery of breast cancer," *Arch. Surg.* **132**, 28–33 (1997).
118. M. S. Sabel, C. S. Kaufman, P. Whitworth, H. Chang, L. H. Stocks, R. Simmons, and M. Schultz, "Cryoablation of early-stage breast cancer: Work-in-progress report of a multi-institutional trial," *Ann. Surg. Oncol.* **11**, 542–549 (2004).
119. J. Morin, A. Traore, G. Dionne, M. Dumont, B. Fouquette, M. Dufour, S. Cloutier, and C. Moisan, "Magnetic resonance-guided percutaneous cryosurgery of breast carcinoma: Technique and early clinical results," *Can. J. Surg.* **47**, 347–351 (2004).
120. M. A. Roubidoux, M. S. Sabel, J. E. Bailey, C. G. Kleer, K. A. Klein, and M. A. Helvie, "Small (< 2.0-cm) breast cancers: Mammographic and US findings at US-guided cryoablation—Initial experience," *Radiol.* **233**, 857–867 (2004).
121. S. O. Pfleiderer, C. Marx, O. Camara, M. Gajda, and W. A. Kaiser, "Ultrasound-guided, percutaneous cryotherapy of small (< or = 15 mm) breast cancers," *Invest. Radiol.* **40**, 472–477 (2005).
122. M. Pusztaszeri, G. Vlastos, K. Kinkel, and M. F. Pelte, "Histopathological study of breast cancer and normal breast tissue after magnetic resonance-guided cryotherapy ablation," *Cryobiol.* **55**, 44–51 (2007).
123. G. Manenti, T. Perretta, E. Gaspari, C. A. Pistolese, L. Scarano, E. Cossu, E. Bonanno, O. C. Buonomo, G. Petrella, G. Simonetti, and S. Masala, "Percutaneous local ablation of unifocal subclinical breast

cancer: Clinical experience and preliminary results of cryotherapy," *Eur. Radiol.* **21**(11), 2344–2353 (2011).

124. P. J. Littrup, B. Jallad, P. Chandiwala-Mody, M. D'Agostini, B. A. Adam, and D. Bouwman, "Cryotherapy for breast cancer: A feasibility study without excision," *J. Vasc. Interv. Radiol.* **20**, 1329–1341 (2009).
125. P. E. Hüber, J. W. Jenne, R. Rastert, I. Simiantonakis, H. P. Sinn, H. J. Strittmatter, D. von Fournier, M. F. Wannenmacher, and J. Debus, "A new noninvasive approach in breast cancer therapy using magnetic resonance imaging-guided focused ultrasound surgery," *Cancer Res.* **61**, 8441–8447 (2001).
126. D. Gianfelice, A. Khiat, M. Amara, A. Belblidia, and Y. Boulanger, "MR imaging-guided focused ultrasound surgery of breast cancer: Correlation of dynamic contrast-enhanced MRI with histopathologic findings," *Breast Cancer Res. Treat.* **82**, 93–101 (2003).
127. D. B. Zippel and M. Z. Papa, "The use of MR imaging guided focused ultrasound in breast cancer patients: A preliminary phase one study and review," *Breast Cancer* **12**, 32–38 (2005).
128. D. Gianfelice, A. Khiat, Y. Boulanger, M. Amara, and A. Belblidia, "Feasibility of magnetic resonance imaging-guided focused ultrasound surgery as an adjunct to tamoxifen therapy in high-risk surgical patients with breast carcinoma," *J. Vasc. Interv. Radiol.* **14**, 1275–1282 (2003).
129. H. Furusawa, K. Namba, S. Thomsen, F. Akiyama, A. Bendet, C. Tanaka, Y. Yasuda, and H. Nakahara, "Magnetic resonance-guided focused ultrasound surgery of breast cancer: Reliability and effectiveness," *J. Am. Coll. Surg.* **203**, 54–63 (2006).
130. F. Wu, Z. B. Wang, Y. D. Cao, W. Z. Chen, J. Bai, J. Z. Zou, and H. Zhu, "A randomised clinical trial of high-intensity focused ultrasound ablation for the treatment of patients with localised breast cancer," *Br. J. Cancer* **89**, 2227–2233 (2003).
131. S. H. Kim, S. E. Jung, H. L. Kim, S. T. Hahn, G. S. Park, and W. C. Park, "The potential role of dynamic MRI in assessing the effectiveness of high-intensity focused ultrasound ablation of breast cancer," *Int. J. Hyperthermia* **26**(6), 594–603 (2010).
132. F. Wu, Z. B. Wang, H. Zhu, W. Z. Chen, J. Z. Zou, J. Bai, K. Q. Li, C. B. Jin, F. L. Xie, and H. B. Su, "Extracorporeal high intensity focused ultrasound treatment for patients with breast cancer," *Breast Cancer Res. Treat.* **92**, 51–60 (2005).
133. H. Furusawa, K. Namba, H. Nakahara, C. Tanaka, Y. Yasuda, E. Hirabara, M. Imahariyama, and K. Komaki, "The evolving non-surgical

ablation of breast cancer: MR guided focused ultrasound (MRg-FUS)," *Breast Cancer* **14**, 55–58 (2007).

134. F. Wu, L. Zhou, and W. R. Chen, "Host antitumour immune responses to HIFU ablation," *Int. J. Hyperthermia* **23**, 165–171 (2007).
135. G. Gravante, G. Sconocchia, S. L. Ong, A. R. Dennison, and D. M. Lloyd, "Immunoregulatory effects of liver ablation therapies for the treatment of primary and metastatic liver malignancies," *Liver Int.* **29**, 18–24 (2009).
136. F. F. Fagnoni, A. Zerbini, G. Pelosi, and G. Missale, "Combination of radiofrequency ablation and immunotherapy," *Front. Biosci.* **13**, 369–381 (2008).
137. M. S. Sabel, "Cryo-immunology: A review of the literature and proposed mechanisms for stimulatory versus suppressive immune responses," *Cryobiol.* **58**, 1–11 (2009).
138. S. Gallucci, M. Lolkema, and P. Matzinger, "Natural adjuvants: Endogenous activators of dendritic cells," *Nat. Med.* **5**, 1249–1255 (1999).
139. P. Matzinger, "The danger model: A renewed sense of self," *Science* **296**, 301–305 (2002).
140. G. Gravante, G. Sconocchia, S. L. Ong, A. R. Dennison, and D. M. Lloyd, "Immunoregulatory effects of liver ablation therapies for the treatment of primary and metastatic liver malignancies," *Liver Int.* **29**,18–24 (2009).
141. S. Evrard, C. Menetrier-Caux, C. Biota, V. Neaud, S. Mathoulin-Pélissier, J. Y. Blay, and J. Rosenbaum, "Cytokines pattern after surgical radiofrequency ablation of liver colorectal metastases," *Gastroenterol. Clin. Biol.* **31**, 141–145 (2007).
142. S. R. Schell, F. J. Wessels, A. Abouhamze, L. L. MoldawerL, and E. M. Copeland III, "Pro- and anti-inflammatory cytokine production after radiofrequency ablation of unresectable hepatic tumors," *J. Am. Coll. Surg.* **195**, 774–781 (2002).
143. K. Meredith, D. Haemmerich, C. Qi, and D. Mahvi, "Hepatic resection but not radiofrequency ablation results in tumor growth and increased growth factor expression," *Ann. Surg.* **245**, 771–776 (2007).
144. G. Schueller, A. Stift, J. Friedl, P. Dubsky, T. Bachleitner-Hofmann, T. Benkoe, R. Jakesz, and M. Gnant, "Hyperthermia improves cellular immune response to human hepatocellular carcinoma subsequent to co-culture with tumor lysate pulsed dendritic cells," *Int. J. Oncol.* **22**, 1397–1402 (2003).

145. A. M. Fietta, M. Morosini, I. Passadore, A. Cascina, P. Draghi, S. Dore R, Rossi, E. Pozzi, and F. Meloni, "Systemic inflammatory response and downmodulation of peripheral CD25+Foxp3+ T-regulatory cells in patients undergoing radiofrequency thermal ablation for lung cancer," *Hum. Immunol.* **70**, 477–486 (2009).

146. A. G. Pockley, "Heat shock proteins as regulators of the immune response," *Lancet* **362**, 469–476 (2003).

147. S. M. Todryk, J. Michael, M. J. Goughy, and A. G. Pockley, "Facets of heat shock protein 70 show immunotherapeutic potential," *Immunol.* **110**, 1–9 (2003).

148. G. Schueller, J. Kettenbach, R. Sedivy, H. Bergmeister, A. Stift, J. Fried, M. Gnant, and J. Lammer, "Expression of heat shock proteins in human hepatocellular carcinoma after radiofrequency ablation in an animal model," *Oncol. Rep.* **12**, 495–499 (2004).

149. R. Rai, C. Richardson, P. Flecknell, H. Robertson, A. Burt, and D. M. Manas, "Study of apoptosis and heat shock protein (HSP) expression in hepatocytes following radiofrequency ablation (RFA)," *J. Surg. Res.* **129**, 147–151 (2005).

150. C. J. Melief, "Cancer immunotherapy by dendritic cells," *Immunity* **29**, 372–383 (2008).

151. M. B. Lutz and G. Schuler, "Immature: Semi-mature and fully mature dendritic cells: Which signals induce tolerance or immunity?" *Trends Immunol.* **23**, 445–449 (2002).

152. M. Y. Ali, C. F. Grimm, M. Ritter, L. Mohr, H. P. Allgaier, R. Weth, W. O. Bocher, K. Endrulat, H. E. Blum, and M. Geissler, "Activation of dendritic cells by local ablation of hepatocellular carcinoma," *J. Hepatol.* **43**, 817–22 (2005).

153. M. H. den Brok, R. P. Sutmuller, S. Nierkens, E. J. Bennink, C. Frielink, L. W. Toonen, O. C. Boerman, C. G. Figdor, T. J. Ruers, and G. J. Adema, "Efficient loading of dendritic cells following cryo and radiofrequency ablation in combination with immune modulation induces antitumour immunity," *Br. J. Cancer* **95**, 896–905 (2006).

154. A. Zerbini, M. Pilli, F. Fagnoni, G. Pelosi, M. G. Pizzi, S. Schivazappa, D. Laccabue, C. Cavallo, C. Schianchi, C. Ferrari, and G. Missale, "Increased immunostimulatory activity conferred to antigen-presenting cells by exposure to antigen extract from hepatocellular carcinoma after radiofrequency thermal ablation," *J. Immunother.* **31**, 271–282 (2008).

155. S. A. Dromi, M. P. Walsh, S. Herby, B. Traughber, J. Xie, K. V. Sharma, K. P. Sekhar, A. Luk, D. J. Liewehr, M. R. Dreher, T. J. Fry,

and B. J. Wood, "Radiofrequency ablation induces antigen-presenting cell infiltration and amplification of weak tumor-induced immunity," *Radiol.* **251**, 58–66 (2009).

156. J. Hänsler, D. Neureiter, D. Strobel, W. Müller, D. Mutter, T. Bernatik, E. G. Hahn, and D. Becker, "Cellular and vascular reactions in the liver to radiofrequency thermo-ablation with wet needle applicators. Study on juvenile domestic pigs," *Eur. Surg. Res.* **34**, 357–363 (2002).

157. T. T. Wissniowski, J. Hänsler, D. Neureiter, M. Frieser, S. Schaber, B. Esslinger, R. Voll, D. Strobel, E. G. Hahn, and D. Schuppan, "Activation of tumorspecific T lymphocytes by radio-frequency ablation of the VX2 hepatoma in rabbits," *Cancer Res.* **63**, 6496–6500 (2003).

158. M. H. den Brok, R. P. Sutmuller, R. van der Voort, E. J. Bennink, C. G. Figdor, T. J. Ruers, and G. J. Adema, "In situ tumor ablation creates an antigen source for the generation of antitumor immunity," *Cancer Res.* **64**, 4024–4029 (2004).

159. J. P. Zhang, H. M. Pan, L. P. Huang, L. P. Huang, and J. M. Wu, "Impact of radiofrequency on splenocyte immunity of mice bearing H22 liver cancer," *Ai Zheng* **25**, 34–39 (2006) (Chinese with English abstract).

160. F. H. van Duijnhoven, R. A. Tollenaar, O. T. Terpstra, and P. J. Kuppen, "Locoregional therapies of liver metastases in a rat CC531 coloncarcinoma model results in increased resistance to tumour rechallenge," *Clin. Exp. Metastasis* **22**, 247–253 (2005).

161. A. Zerbini, M. Pilli, A. Penna, G. Pelosi, C. Schianchi, A. Molinari, S. Schivazappa, C. Zibera, F. F. Fagnoni, C. Ferrari, and G. Missale, "Radiofrequency thermal ablation of hepatocellular carcinoma liver nodules can activate and enhance tumor-specific T-cell responses," *Cancer Res.* **66**, 1139–1146 (2006).

162. J. Hänsler, T. T. Wissniowski, D. Schuppan, A. Witte, T. Bernatik, E. G. Hahn, and D. Strobel, "Activation and dramatically increased cytolytic activity of tumor specific T lymphocytes after radiofrequency ablation in patients with hepatocellular carcinoma and colorectal liver metastases," *World J. Gastroenterol.* **12**, 3716–3721 (2006).

163. C. Napoletano, F. Taurino, M. Biffoni, A. De Majo, G. Coscarella, F. Bellati, H. Rahimi, S. Pauselli, I. Pellicciotta, J. M. Burchell, L. A. Gaspari, L. Ercoli, P. Rossi, and A. Rughetti, "RFA strongly modulates the immune system and anti-tumor immune responses in metastatic liver patients," *Int. J. Oncol.* **32**, 481–490 (2008).

164. H. Saji, W. Song, H. Nakamura, T. Saijo, M. Hosaka, M. Hagiwara, A. Ogata, N. Kawasaki, E. G. Engleman, and H. Kato, "A possibility of overcoming local tumor immune tolerance by radiofrequency ablation in combination with intratumoral injection of naïve dendritic cell," *Gan To Kagaku Ryoho* **33**, 1736–1738 (2006) (Japanese with English abstract).

165. K. Saito, A. Haas, S. Albelda, D. Li, and B. W. O'Malley, Jr., "Combination of immunotherapy with radiofrequency ablation for head and neck cancer," *Otolaryngol. Head Neck Surg.* **133**(Supple), P98–99 (2005).

166. M. Habibi, M. Kmieciak, L. Graham, J. K. Morales, H. D. Bear, and M. H. Manjili, "Radiofrequency thermal ablation of breast tumors combined with intralesional administration of IL-7 and IL-15 augments anti-tumor immune responses and inhibits tumor development and metastasis," *Breast Cancer Res. Treat.* **114**, 423–431 (2009).

167. P. H. Möller, K. Ivarsson, U. Stenram, M. Radnell, and K. G. Tranberg, "Comparison between interstitial laser thermotherapy and excision of an adenocarcinoma transplanted into rat liver," *Br. J. Cancer* **77**, 1884–1892 (1998).

168. K. Ivarsson, L. Myllymäki, K. Jansner, A. Bruun, U. Stenram, and K. G. Tranberg, "Heat shock protein 70 (HSP70) after laser thermotherapy of an adenocarcinoma transplanted into rat liver," *Anticancer Res.* **23**, 3703–3712 (2003).

169. M. Nikfarjam, V. Muralidharan, K. Su, C. Malcontenti-Wilson, and C. Christophi, "Patterns of heat shock protein (HSP70) expression and Kupffer cell activity following thermal ablation of liver and colorectal liver metastases," *Int. J. Hyperthermia* **21**, 319–332 (2005).

170. J. A. Paulus, R. D. Tucker, S. W. Flanagan, P. L. Moseley, S. A. Loening, and J. B. Park, "Heat shock protein response in a prostate tumor model to interstitial thermotherapy: Implications for clinical treatment," *Prostate* **23**, 263–270 (1993).

171. M. N. Rylander, Y. Feng, Y. Zhang, J. Bass, R. J. Stafford, A. Volgin, J. D. Hazle, and K. R. Diller, "Optimizing heat shock protein expression induced by prostate cancer laser therapy through predictive computational models," *J. Biomed. Opt.* **11**(4), 041113 (2006) [doi: 10.1117/1.2241310].

172. C. Isbert, J. P. Ritz, A. Roggan, D. Schuppan, M. Rühl, H. J. Buhr, and C. T. Germer, "Enhancement of the immune response to residual

intrahepatic tumor tissue by laser-induced thermotherapy (LITT) compared to hepatic resection," *Lasers Surg. Med.* **35**, 284–292 (2004).

173. K. Ivarsson, L. Myllymäki, K. Jansner, U. Stenram, and K. G. Tranberg, "Resistance to tumour challenge after tumour laser thermotherapy is associated with a cellular immune response," *Br. J. Cancer* **93**, 435–440 (2005).
174. R. Kallio, R. Sequeiros, H. M. Surcel, P. Ohtonen, H. Kiviniemi, and H. Syrjälä, "Early cytokine responses after percutaneous magnetic resonance imaging guided laser thermoablation of malignant liver tumors," *Cytokine* **34**, 278–283 (2006).
175. T. J. Vogl, T. T. Wissniowski, N. N. Naguib, R. M. Hammerstingl, M. G. Mack, S. Münch, M. Ocker, D. Strobel, E. G. Hahn, and J. Hänsler, "Activation of tumor-specific T lymphocytes after laser-induced thermotherapy in patients with colorectal liver metastases," *Cancer Immunol. Immunother.* **58**, 1557–1563 (2009).
176. M. S. Sabel, "Cryo-immunology: A review of the literature and proposed mechanisms for stimulatory versus suppressive immune responses," *Cryobiol.* **58**, 1–11 (2009).
177. P. Redondo, J. del Olmo, A. Lopez-Diaz de Cerio, S. Inoges, M. Marquina, I. Melero, and M. Bendandi, "Imiquimod enhances the systemic immunity attained by local cryosurgery destruction of melanoma lesions," *J. Invest. Dermatol.* **127**, 1673–1680 (2007).
178. M. H. den Brok, R. P. Sutmuller, S. Nierkens, E. J. Bennink, C. Frielink, L. W. Toonen, O. C. Boerman, C. G. Figdor, T. J. Ruers, and G. J. Adema, "Efficient loading of dendritic cells following cryo and radiofrequency ablation in combination with immune modulation induces anti-tumour immunity," *Br. J. Cancer* **95**, 896–905 (2006).
179. M. S. Sabel, M. A. Nehs, G. Su, K. P. Lowler, J. L. Ferrara, and A. E. Chang, "Immunologic response to cryoablation of breast cancer," *Breast Cancer Res. Treat.* **90**, 97–104 (2005).
180. J. J. Joosten, G. H. Muijen, T. Wobbes, and T. J. Ruers, "In vivo destruction of tumor tissue by cryoablation can induce inhibition of secondary tumor growth: An experimental study," *Cryobiol.* **41**, 49–58 (2001).
181. T. Shibata, T. Yamashita, K. Suzuki, N. Takeichi, M. Micallef, M. Hosokawa, H. Kobayashi, M. Murata, and M. Arisue, "Enhancement of experimental pulmonary metastaseis and inhibition of subcutaneously transplanted tumor growth following cryosurgery," *Anticancer Res.* **18**, 4443–4448 (1998).

182. L. C. Müller, M. Micksche, S. Yamagata, and F. Kerschbaumer, "Therapeutic effect of cryosurgery of murine osteosarcoma—Influence on disease outcome and immune function," *Cryobiol.* **22**, 77–85 (1985).

183. M. Urano, C. Tanaka, Y. Sugiyama, K. Miya, and S. Saji, "Antitumor effects of residual tumor after cryoablation: The combined effect of residual tumor and a protein-bound polysaccharaide on multiple liver metastases in a murine model," *Cryobiol.* **46**, 238–245 (2003).

184. N. E. Hoffmann, J. E. Coad, C. S. Huot, D. J. Swanlund, and J. C. Bischof, "Investigation of the mechanism and the effect of cryoimmunology in the Copenhagen rat," *Cryobiol.* **41**, 59–68 (2001).

185. M. Udagawa, C. Kudo-Saito, G. Hasegawa, K. Yano, A. Yamamoto, M. Yaguchi, M. Toda, I. Azuma, T. Iwai, and K. Kawakami, "Enhancement of immunologic tumor regression by intratumoral administration of dendritic cells in combination with cryoablative tumor pretreatment and bacillus calmetteguerin cell wall skeleton stimulation," *Clin. Cancer Res.* **12**, 7465–7475 (2006).

186. A. Machlenkin, O. Goldberger, B. Tirosh, A. Paz, I. Volovitz, E. Bar-Haim, S. H. Lee, E. Vadai, E. Tzehoval, and L. Eisenbach, "Combined dendritic cell cryotherapy of tumor induces systemic antimetastatic immunity," *Clin. Cancer. Res.* **11**, 4955–4961 (2005).

187. S. Hanawa, "An experimental study on the induction of anti-tumor immunological activity after cryosurgery for liver carcinoma, and the effect of concomitant immunotherapy with OK432," *Nippon Geka Gakkai Zasshi* **94**, 57–65 (1993) (Japanese with English abstract).

188. K. Miya, S. Saji, T. Morita, H. Niwa, K. Sakata, "Experimental study on mechanism of absorption of cryonecrotized tumor antigens," *Cryobiol.* **24**, 135–139 (1987).

189. I. C. B. Viorritto, N. P. Nikolov, and R. M. Siegel, "Autoimmunity versus tolerance: Can dying cells tip the balance?" *Clin. Immunol.* **122**, 125–134 (2007).

190. Y. Peng, D. A. Martin, J. Kenkel, K. Zhang, C. A. Ogden, and K. B. Elkon, "Innate and adaptive immune response to apoptotic cells," *J. Autoimmun.* **29**, 303–309 (2007).

191. J. Savill, I. Dransfield, C. Gregory, and C. Haslett, "A blast from the past: Clearance of apoptotic cells regulates immune responses," *Nat. Rev. Immunol.* **2**, 965–975 (2002).

192. K. Liu, T. Iyoda, M. Saternus, Y. Kimura, K. Inaba, and R. M. Steinman, "Immune tolerance after delivery of dying cells to dendritic cells in situ," *J. Exp. Med.* **196**,1091–1097 (2002).

193. S. Gallucci, M. Lolkema, and P. Matzinger, "Natural adjuvants: Endogenous activators of dendritic cells," *Nat. Med.* **5**, 1249–1255 (1999).

194. B. Sauter, M. L. Albert, L. Francisco, M. Larsson, S. Somersan, and N. Bhardwaj, "Consequences of cell death: Exposure to necrotic tumor cells, but not primary tissue cells or apoptotic cells, induces the maturation of immunostimulatory dendritic cells," *J. Exp. Med.* **191**, 423–434 (2000).

195. M. Skoberne, A. S. Beignon, and N. Bhardwaj, "Danger signals: A time and space continuum," *Trends Mol. Med.* **10**, 251–257 (2004).

196. K. L. Rock, A. Hearn, C. J. Chen, and Y. Shi, "Natural endogenous adjuvants," *Springer Semin. Immunopathol.* **26**, 231–246 (2005).

197. S. R. Scheffer, H. Nave, F. Korangy, K. Schlote, R. Pabst, E. M. Jaffee, M. P. Manns, and T. F. Greten, "Apoptotic, but not necrotic, tumor cell vaccines induce a potent immune response in vivo," *Int. J. Cancer* **103**, 205–211 (2003).

198. M. Schnurr, C. Scholz, S. Rothenfusser, P. Galambos, M. Dauer, J. Röbe, S. Endres, and A. Eigler, "Apoptotic pancreatic tumor cells are superior to cell lysates in promoting cross-priming of cytotoxic T-cells and activate NK and gammadelta T cells," *Cancer Res.* **62**, 2347–2352 (2002).

199. S. Osada, H. Imai, H. Tomita, Y. Tokuyama, N. Okumura, N. Matsuhashi, F. Sakashita, and K. Nonaka, "Serum cytokine levels in response to hepatic cryoablation," *J. Surg. Oncol.* **95**, 491–498 (2007).

200. M. H. Ravindranath, T. F. Wood, D. Soh, A. Gonzales, S. Muthugounder, C. Perez, D. L. Morton, and A. J. Bilchik, "Cryosurgical ablation of liver tumors in colon cancer patients increases the serum total ganglioside level and then selectively augments antiganglioside IgM," *Cryobiol.* **45**, 10–21 (2002).

201. T. Si, Z. Guo, and X. Hao, "Immunologic response to primary cryoablation of high-risk prostate cancer," *Cryobiol.* **57**, 66–71 (2008).

202. T. Si, Z. Guo, and X. Hao, "Combined cryoablation and GM-CSF treatment for metastatic hormone refractory prostate cancer," *J. Immunother.* **32**, 86–91 (2009).

203. J. K. Seifert and T. Junginger, "Cryotherapy for liver tumors: Current status, perspectives, clinical results, and review of literature," *Technol. Cancer Res. Treat.* **3**, 151–163 (2004).

204. W. C. Chapman, J. P. Debelak, T. S. Blackwell, K. A. Gainer, J. W. Christman, C. W. Pinson, K. L. Brigham, and R. E. Parker, "Hepatic

cryoablation-induced acute lung injury: Pulmonary hemodynamic and permeability effects in a sheep model," *Arch. Surg.* **135**, 667–672 (2000).

205. R. T. Sadikot, L. J. Wudel, D. E. Jansen, J. P. Debelak, F. E. Yull, J. W. Christman, T. S. Blackwell, and W. C. Chapman, "Hepatic cryoablation-induced multisystem injury: Bioluminescent detection of NF-kappaB activation in a transgenic mouse model," *J. Gastrointest. Surg.* **6**, 264–270 (2002).

206. J. K. Seifert, M. P. France, J. Zhao, E. J. Bolton, I. Finlay, T. Junginger, and D. L. Morris, "Large volume hepatic freezing: Association with significant release of the cytokines interleukin-6 and tumor necrosis factor a in a rat model," *World J. Surg.* **26**, 1333–1341 (2002).

207. W. C. Chapman, J. P. Debelak, C. Wright Pinson, M. K. Washington, J. B. Atkinson, A. Venkatakrishnan, T. S. Blackwell, and J. W. Christman, "Hepatic cryoablation, but not radiofrequency ablation, results in lung inflammation," *Ann. Surg.* **231**, 752–761 (2000).

208. J. Nakayama, H. Kokuba, J. Kobayashi, Y. Yoshida, and Y. Hori, "Experimental approaches for the treatment of murine B16 melanomas of various sizes. I: Local injection of ethanol with a combination of interleukin-2 or microwaval hyperthermia for B16 melanomas with a size of less than 7 mm in diameter," *J. Dermatol. Sci.* **15**, 75–81 (1997).

209. J. Nakayama, H. Kokuba, J. Kobayashi, Y. Yoshida, and Y. Hori, "Experimental approaches for the treatment of murine B16 melanomas of various sizes. II: Injection of ethanol with combinations of beta-interferon and microwaval hyperthermia for B16 melanomas with a size of greater than 10 mm in diameter," *J. Dermatol. Sci.* **15**, 82–88 (1997).

210. E. E. Fesenko, V. R. Makar, E. G. Novoselova, and V. B. Sadovnikov, "Microwaves and cellular immunity. I. Effect of whole body microwave irradiation on tumor necrosis factor production in mouse cells," *Bioelectrochem. Bioenerg.* **49**, 29–35 (1999).

211. L. C. Yao and R. L. Yang, "Immunotherapy against tumor with dendritic cell sensitized by necrotic tumor tissue after microwave coagulation therapy," *Zhonghua Yi Xue Za Zhi* **87**, 2552–2556 (2007) (Chinese with English abstract).

212. S. Szmigielski, J. Sobczynski, G. Sokolska, B. Stawarz, H. Zielinski, and Z. Petrovich, "Effects of local prostatic hyperthermia on human NK and T cell function," *Int. J. Hyperthermia* **7**, 869–880 (1991).

213. Q. Fan, B. Ma, A. Guo, Y. Li, J. Ye, Y. Zhou, and X. Qiu, "Surgical treatment of bone tumors in conjunction with microwave-induced hyperthermia and adjuvant immunotherapy. A preliminary report," *Chin. Med. J. (Engl.)* **109**, 425–431 (1996).

214. J. Zhang, B. Dong, P. Liang, X. Yu, L. Su, D. Yu, X. Ji, and G. Yu, "Significance of changes in local immunity in patients with hepatocellular carcinoma after percutaneous microwave coagulation therapy," *Chin. Med. J. (Engl.)* **115**, 1367–1371 (2002).

215. B. W. Dong, J. Zhang, P. Liang, X. L. Yu, L. Su, D. J. Yu, X. L. Ji, and G. Yu, "Sequential pathological and immunologic of percutaneous microwave coagulation therapy of hepatocellular carcinoma," *Int. J. Hyperthermia* **19**, 119–133 (2003).

216. B. Dong, J. Zhang, P. Liang, X. Yu, L. Su, D. Yu, X. Ji, G. Yu, and Z. Yin, "Influencing factors of local immunocyte infiltration in hepatocellular carcinoma tissues pre-and post-percutaneous microwave coagulation therapy," *Zhonghua Yi Xue Za Zhi* **82**, 393–397 (2002) (Chinese with English abstract).

217. H. Sadamori, T. Yagi, Y. Kanaoka, Y. Morimoto, M. Inagaki, T. Ishikawa, H. Matsukawa, H. Matsuda, H. Iwagaki, and N. Tanaka, "The analysis of the usefulness of laparoscopic microwave coagulation therapy for hepatocellular carcinoma in patients with poor hepatic reserve by serial measurements of IL-6, cytokine antagonists, and C-reactive protein," *Surg. Endosc.* **17**, 510–514 (2003).

218. J. J. Lin, C. N. Jin, M. L. Zheng, X. N. Ouyang, J. X. Zeng, and X. H. Dai, "Clinical study on treatment of primary hepatocelluar carcinoma by Shenqi mixture combined with microwave coagulation," *Chin. J. Integr. Med.* **11**, 104–110 (2005).

219. X. J. Han, B. W. Dong, P. Liang, X. L. Yu, and D. J. Yu, "Local cellular immune response induced by ultrasound-guided tumor bed superantigen injection after percutaneous microwave coagulation therapy for liver cancer," *Zhonghua Zhong Liu Za Zhi* **31**, 602–606 (2009) (Chinese with English abstract).

220. R. Yang, C. R. Reilly, F. J. Rescorla, N. T. Sanghvi, F. J. Fry, T. D. Franklin, Jr., and J. L. Grosfeld, "Effects of high-intensity focused ultrasound in the treatment of experimental neuroblastoma," *J. Pediatr. Surg.* **27**, 246–250 (1992).

221. Z. Hu, X. Y. Yang, Y. Liu, G. N. Sankin, E. C. Pua, M. A. Morse, H. K. Lyerly, T. M. Clay, and P. Zhong, "Investigation of HIFU-induced anti-tumor immunity in a murine tumor model," *J. Transl. Med.* **5**, 34 (2007).

222. Y. Zhang, J. Deng, J. Feng, and F. Wu, "Enhancement of antitumor vaccine in ablated hepatocellular carcinoma by high-intensity focused ultrasound: A preliminary report," *World J. Gastroenterol.* **16**, 3584–3591 (2010).

223. J. Deng, Y. Zhang, J. Feng, and F. Wu, "Dendritic cells loaded with ultrasound-ablated tumour induce in vivo specific antitumour immune responses," *Ultrasound Med. Biol.* **36**, 441–448 (2010).

224. Z. Hu, X. Y. Yang, Y. Liu, M. A. Morse, H. K. Lyerly, T. M. Clay, and P. Zhong, "Release of endogenous danger signals from HIFU-treated tumor cells and their stimulatory effects on APCs," *Biochem. Biophys. Res. Commun.* **335**, 124–131 (2005).

225. D. E. Kruse, M. A. Mackanos, C. E. O'Connell-Rodwell, C. H. Contag, and K. W. Ferrara, "Short-duration-focused ultrasound stimulation of Hsp70 expression in vivo," *Phys. Med. Biol.* **53**, 3641–3660 (2008).

226. W. Hundt, C. E. O'Connell-Rodwell, M. D. Bednarski, S. Steinbach, and S. Guccione, "In vitro effect of focused ultrasound or thermal stress on HSP70 expression and cell viability in three tumor cell lines," *Acad. Radiol.* **14**, 859–870 (2007).

227. F. Liu, Z. Hu, L. Qiu, C. Hui, C. Li, P. Zhong, and J. Zhang, "Boosting high-intensity focused ultrasound-induced anti-tumor immunity using a sparse-scan strategy that can more effectively promote dendritic cell maturation," *J. Transl. Med.* **8**, 7 (2010).

228. P. Zhou, M. Fu, J. Bai, Z. Wang, and F. Wu, "Immune response after high-intensity focused ultrasound ablation for H22 tumor," *J. Clin. Oncol.* **25**(S18), 21169 (2007).

229. D. F. Rosberger, D. J. Coleman, R. Silverman, S. Woods, M. Rondeau, and S. Cunningham-Rundles, "Immunomodulation in choroidal melanoma: Reversal of inverted CD4/CD8 ratios following treatment with ultrasonic hyperthermia," *Biotechnol. Ther.* **5**, 59–68 (1994).

230. X. Wang and J. Sun, "High-intensity focused ultrasound in patients with late-stage pancreatic carcinoma," *Chin. Med. J. (Engl.)* **115**, 1332–1335 (2002).

231. F. Wu, Z. B. Wang, P. Lu, Z. L. Xu, W. Z. Chen, H. Zhu, and C. B. Jin, "Activated anti-tumor immunity in cancer patients after high intensity focused ultrasound ablation," *Ultrasound Med. Biol.* **30**, 1217–1222 (2004).

232. Q. Zhou, X. Q. Zhu, J. Zhang, Z. L. Xu, P. Lu, and F. Wu, "Changes in circulating immunosuppressive cytokine levels of cancer patients

after high intensity focused ultrasound treatment," *Ultrasound Med. Bio.* **34**, 81–88 (2008).

233. G. Kramer, G. E. Steiner, M. Grobl, K. Hrachowitz, F. Reithmayr, L. Paucz, M. Newman, S. Madersbacher, D. Gruber, M. Susani, and M. Marberger, "Response to sublethal heat treatment of prostatic tumor cells and of prostatic tumor infiltrating T-cells," *Prostate* **58**, 109–120 (2004).
234. F. Wu, Z. B. Wang, Y. D. Cao, Q. Zhou, J. Zhang, Z. L. Xu, X. Q. Zhu, "Expression of tumor antigens and heat-shock protein 70 in breast cancer cells after high-intensity focused ultrasound ablation," *Ann. Surg. Oncol.* **14**, 1237–1242 (2007).
235. Z. L. Xu, X. Q. Zhu, P. Lu, Q. Zhou, J. Zhang, and F. Wu, "Activation of tumor-infiltrating antigen presenting cells by high intensity focused ultrasound ablation of human breast cancer," *Ultrasound Med. Biol.* **35**, 50–57 (2009).
236. P. Lu, X. Q. Zhu, Z. L. Xu, Q. Zhou, J. Zhang, and F. Wu, "Increased infiltration of activated tumor-infiltrating lymphocytes after high intensity focused ultrasound ablation of human breast cancer," *Surgery* **145**, 286–293 (2009).
237. S. E. Singletary, "Surgical margins in patients with early-stage breast cancer treated with breast conservation therapy," *Am. J. Surg.* **184**, 383–393 (2002).
238. S. M. Witherby and H. B. Muss, "Managing early-stage breast cancer in your older patients," *Oncology (Williston Park)* **20**, 1003–1013 (2006).

With a medical degree from China, **Feng Wu** finished his surgical training at Chongqing Medical University (CMU), China. He holds M.D. and Ph.D. degrees and was awarded a permanent professorship of surgery at CMU, where he initiated translational studies using focused ultrasound for noninvasive ablation of tumors. Over the last 20 years, he has focused his scientific interests on topics related to life-threatening disorders including cancer. With his expertise in interventional radiology, high-intensity focused ultrasound (HIFU) therapy, and surgical oncology research, he has established a series of platforms for preclinical and clinical evaluation of diagnostics/therapeutics such as HIFU therapy in both Chongqing, China and Oxford, UK. His main areas of research are the development of HIFU therapeutic systems, therapeutic

strategies, and clinical guidelines for noninvasive treatment of solid tumors, antitumor immunity induced by thermal ablation, ultrasound-enhanced drug delivery, and novel ultrasound surgical devices. He holds international patents, has published numerous SCI journal papers and book chapters, edits/reviews for academic journals, served as a general secretary/board member in international academic societies such as the International Society for Therapeutic Ultrasound, and worked as a guest professor in several universities. He is currently working as an HIFU consultant at the Oxford University Hospitals in Oxford, and also as Senior Clinical Scientist at the Nuffield Department of Surgical Sciences, University of Oxford. Innovative, translational, and longstanding research has been his goal in his academic career.

Chapter 16
Correlated Microwave Acoustic Imaging for Breast Cancer Detection

Yuanjin Zheng, Fei Gao, and Zhiping Lin
School of Electrical & Electronic Engineering, Nanyang Technological University, Singapore

16.1 Introduction

Breast cancer is one of the most common cancers in the world and caused 460,000 deaths in 2008 according to World Health Organization.[1] In Singapore, about 1300 women are diagnosed with breast cancer, causing an average death of 313 every year, and making breast cancer the number one cause of death of women in Singapore.[2] Detection of breast cancer at an early stage is extremely important in determining the effectiveness of consequent treatment and the survival rate of the patient. However, early-stage tumor detection is challenging due to the inefficacy of existing commercial imaging modalities. Although mammography is currently the golden standard imaging method, it still suffers from some limitations, such as

low sensitivity for dense-breast screening, low specificity to differentiate malignant and benign tumors, low-dose ionization, and discomfort during the screening process. Other alternative imaging modalities such as ultrasound imaging and MRI have much lower contrast, especially for early-stage tumor detection. High cost, bulky size, and safety issues also prevent x-ray imaging and MRI from on-site diagnosis in homecare and routine screening.

Microwave-based imaging modalities, which include microwave imaging (MWI)[3–17] and microwave-induced thermo-acoustic imaging (MTAI),[18–32] have been receiving increasing attention in the last decade. By exploring the significant dielectric contrast between tumor and normal tissue,[33–36] microwave-based imaging modalities can potentially provide improved performance, especially in terms of contrast, over conventional imaging modalities. Currently, most of the research on both MWI and MTAI focuses on algorithm design, prototyping, and even clinical trials,[3–32] while little research is focused on correlating these two promising modalities to each other.[37]

In this chapter, we demonstrate the necessity of correlating MWI and MTAI theoretically and propose a simple but efficient algorithm called correlated microwave acoustic imaging (CMAI) to achieve enhanced resolution and contrast. A preliminary experimental setup is also established to simultaneously receive both microwaves and thermo-acoustic waves. Then, an ultrawideband (UWB) transmitter is designed as the microwave source for future prototyping.

16.2 Emerging Microwave-based Imaging Modality

The basic principle behind the microwave-based imaging modality is the interaction between microwave and biological tissue; i.e., when incident microwaves are transmitted into biological tissue, scattered microwaves can be received by an antenna for MWI, and due to thermal expansion, an acoustic signal can also be collected by an ultrasound transducer for MTAI. Unlike the existing microwave-based imaging approach that only collects microwaves or thermo-acoustic waves for imaging (e.g., MWI and MTAI), the CMAI introduced in this chapter aims to simultaneously collect both scattering microwaves and induced thermo-acoustic waves for image reconstruction with improved quality. As shown in Fig. 16.1, both kinds of wave are received for CMAI, in which the dielectric contrast is expected to be further enhanced compared to MWI and TMAI. This section will review the dielectric properties of biological tissue and the principles of the currently existing modalities of MWI and TMAI.

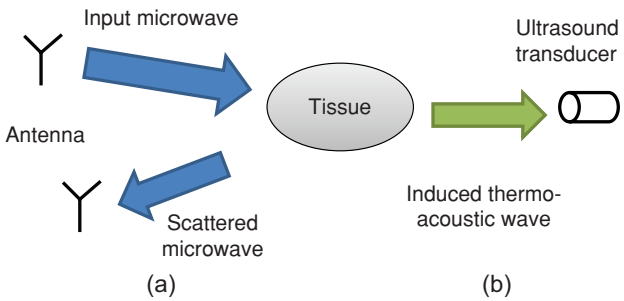

Figure 16.1 Waveform of (a) scattered microwaves and (b) induced thermo-acoustic wave.

16.2.1 Dielectric property of biological tissue

The physical principle behind microwave-based imaging modalities is interactions between the electromagnetic (EM) field (microwave spectrum) and biological tissue. Therefore, the basis of tumor detection by microwave-based imaging modalities is the large dielectric contrast among different biological tissues, which is defined as complex permittivity ε:

$$\varepsilon = \varepsilon' - j\varepsilon'', \tag{16.1}$$

where ε' is the relative permittivity of biological tissue related to the storage of the electric field, and ε'' is the loss factor referring to the EM energy absorption and dissipation inside tissue expressed as

$$\varepsilon'' = \sigma/\varepsilon_0\omega, \tag{16.2}$$

where σ is the total conductivity of tissue, ε_0 is the permittivity of vacuum, and ω is the angular frequency of the EM wave. Previous work has explored the complex permittivity of various biological tissues from 10 Hz to 20 GHz.[34] The mechanism of microwave–tissue interaction relies on α, β, and γ dispersions at different frequency bands. For the microwave-based imaging modality, a band of more than 1 GHz to several GHz is usually utilized, and the γ dispersion is dominant due to the polarization of water molecules. In other words, relative permittivity in the microwave spectrum mainly reveals the water content of different biological tissues. Figure 16.2 shows the relative permittivity and conductivity of muscle and fat tissue in the spectrum from 1 to 10 GHz, the range we are interested in. The figure shows that the dielectric difference between muscle and fat is significant. This difference is the main advantage of microwave-based imaging compared with conventional imaging modalities. Specifically, for breast cancer detection, the

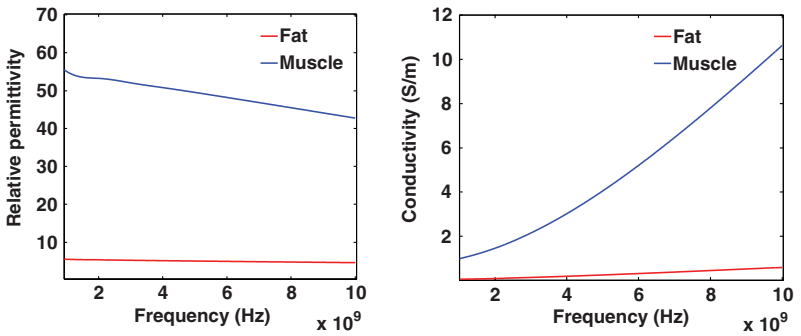

Figure 16.2 Relative permittivity and conductivity of fat and muscle tissue ranging from 1 to 10 GHz.

dielectric difference between tumor and breast fat tissue is up to 5:1 according to previous literature.[36] To make use of the large dielectric contrast of biological tissue for imaging, two kinds of microwave-based imaging modalities have been widely investigated in recent years. As mentioned already, these are MWI and MTAI, which are the subjects of the next two sections.

16.2.2 Microwave imaging

Microwave imaging refers to reconstructing the map dielectric property of the human body through microwave transmitting and receiving at different locations around the body, as shown in Fig. 16.3.

MWI is mainly subdivided into two categories: microwave tomography and confocal microwave imaging (also called radar-based microwave imaging). Microwave tomography reconstructs the dielectric distribution by solving a nonlinear inverse scattering problem. To overcome the limitation of the long microwave wavelength, various iteration algorithms are proposed to achieve super-resolution performance, and a prototype has been built for clinical trial.[16,17] Unlike microwave tomography, which is a narrowband system, confocal microwave imaging utilizes short UWB pulses in the nanosecond range to illuminate the object. The image is reconstructed by beamforming the scattered UWB pulses received at various locations. Instead of obtaining an accurate dielectric image, confocal microwave imaging shows the scattering intensity at every image pixel to localize the tumor area. Many beamforming techniques have also been developed to achieve a better signal-to-clutter ratio (S/C) for tumor detection.[5–9] For the sake of simplicity, the integral equation derived from Maxwell's equations representing the scattered electric field E_{scat} is derived as

$$E_{scat} = \omega^2\mu\left(1+\frac{\nabla\nabla\cdot}{k_b^2}\right)\int_V E(r')g(r,r')[\varepsilon^*(r')-\varepsilon_b^*]dV', \qquad (16.3)$$

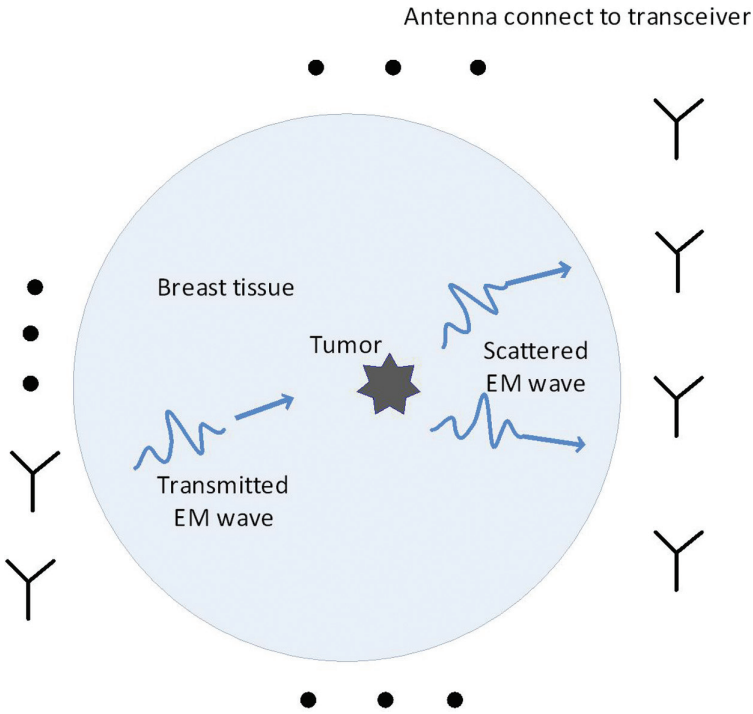

Figure 16.3 Imaging setup for MWI.

where ω and μ are the angular frequency and permeability of the medium, respectively, $\varepsilon^*(r')$ and ε_b^* are the permittivity of the tumor and the surrounding normal tissue, respectively, $E(r')$ is the total electrical field, and $k_b = \omega\sqrt{\mu\varepsilon_b^*}$ and $g(r, r') = \exp(-jk_b|r - r'|)/4\pi|r - r'|$ are Green's function. In microwave tomography, the reconstruction algorithms formulate this mathematical inverse problem as a nonlinear optimization problem that is iteratively solved to obtain the dielectric distribution of the unknown biological object. However, in confocal microwave imaging, the time-of-flight scattered UWB signals are beamformed to obtain the scattering field intensity of the reconstructed image. For both kinds of microwave imaging modalities, the dielectric contrast $\varepsilon^*(r') - \varepsilon_b^*$ is the basis.

16.2.3 Microwave-induced thermo-acoustic imaging

The microwave-induced thermo-acoustic effect refers to the acoustic generation due to EM energy absorption followed by heating and thermal expansion. Based on the thermo-acoustic effect, MTAI receives the induced thermo-acoustic signal after high microwave illumination by ultrasound transducers placed around a biological object and reconstructs

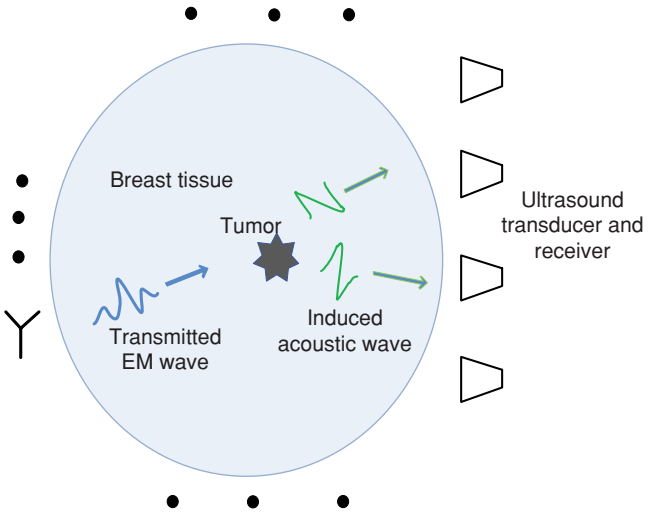

Figure 16.4 Imaging setup for MTAI.

the image representing EM absorption of biological tissue.[18–32] Figure 16.4 illustrates the working principle of MTAI in a 2D configuration, where high peak power up to a kilowatt microwave pulse is usually required to illuminate the biological tissue to induce a sufficiently strong acoustic signal, and the acoustic signal is collected at different locations around the biological object for image reconstruction. The induced thermo-acoustic pressure $p(r, t)$ follows the equation below:

$$\nabla^2 p(r, t) - \frac{1}{c}\frac{\partial^2}{\partial t^2} p(r, t) = -\frac{\beta}{C_p}\frac{\partial}{\partial t} H(r, t), \tag{16.4}$$

where c is the acoustic velocity, β is the isobaric volume expansion coefficient, C_p is the specific heat, and $H(r, t)$ is the heating function defined as the thermal energy per time and volume deposited by the microwave source. Using Green's function method, a general form of the thermo-acoustic pressure can be expressed as

$$p(r, t) = \frac{\beta}{4\pi C_p} \iiint \frac{d^3 r'}{|r - r'|} \frac{\partial H(r', t')}{\partial t'}\bigg|_{t'=t-(|r-r'|/c)}. \tag{16.5}$$

The heating function can be expressed as the product of the spatial absorption function and microwave envelope function:

$$H(r, t) = A(r)I(t). \tag{16.6}$$

Then, $p(r, t)$ is expressed as

$$p(r, t) = \frac{\beta}{4\pi C_p} \iiint \frac{d^3 r'}{|r - r'|} A(r') \frac{dI(t')}{dt'}. \tag{16.7}$$

From Eq. (16.7), the received acoustic signal has an amplitude proportional to the microwave absorption $A(r)$, which is related to the conductivity of biological tissue, and the pulse shape is related to the derivative of the microwave envelope function $I(t)$. A backprojection algorithm aims to reconstruct the microwave absorption by received thermo-acoustic signals at different locations around the biological tissue.

16.3 Correlated Microwave Acoustic Imaging: Numerical Example

According to the analysis in previous sections, both MWI and MTAI reveal the dielectric properties of biological tissue, i.e., relative permittivity and conductivity. Therefore, it is expected that correlating these two microwave-based imaging methods will allow for better performance. CMAI will be introduced in this section as a method to strengthen tumor detection and suppress clutter in both imaging modalities, as verified by numerical simulation. The system setup is shown in Fig. 16.5, which shows an objective breast tissue sample modeled as a circle filled with heterogeneous healthy human tissue with an embedded tumor with a dielectric property that is different from that of the surrounding tissue. Microwave antennas are placed around the breast model to transmit microwaves and receive

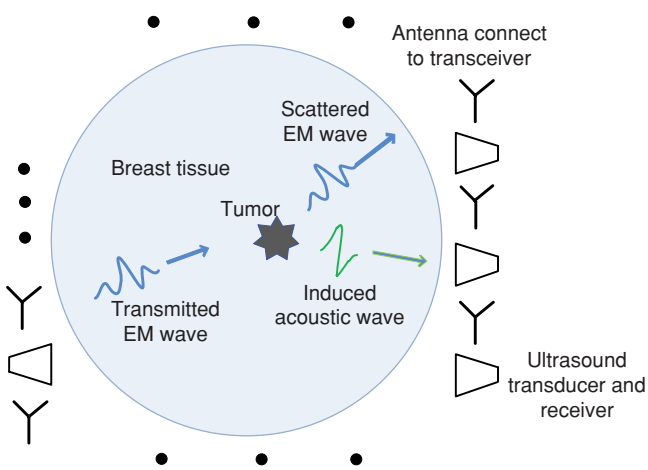

Figure 16.5 Imaging setup for CMAI.

scattered microwave signals. Ultrasound transducers are also placed for acoustic signal detection. This setup allows collection of both microwave and acoustic signals at different locations for image reconstruction.

16.3.1 Image reconstruction algorithm

Although the imaging basis for both MWI and MTAI is the dielectric difference between the tumor and the surrounding healthy tissue, the signal collection methods for the two imaging modalities are completely different: one is scattered microwaves, and the other is thermo-acoustic waves. Due to the different forms of energy (EM waves and acoustic waves), each propagates in separate channels and suffers respective noise sources. Therefore, it is expected that the images from MWI and MTAI are correlated at the tumor location (strong scattering and absorption) and uncorrelated at other locations (different forms of noise source). Thus, CMAI, which combines MWI and MTAI, is expected to achieve better performance.

The signal processing of CMAI is shown in Fig. 16.6. The microwave transmitter generates an input microwave source into biological tissue. Experiencing EM wave scattering and absorption, both scattered microwaves and induced thermo-acoustic waves are processed but in separate channels. Following signal calibration and gain compensation, which are used to remove strong scattering at the skin and to compensate for attenuation in lossy tissue, a delay-and-sum algorithm is applied to the scattered microwaves. After low-pass filtering and gain compensation for induced acoustic signal, a back-projection algorithm is applied to reconstruct the MTAI image. Due to the different reconstruction methods of MWI and MTAI, a

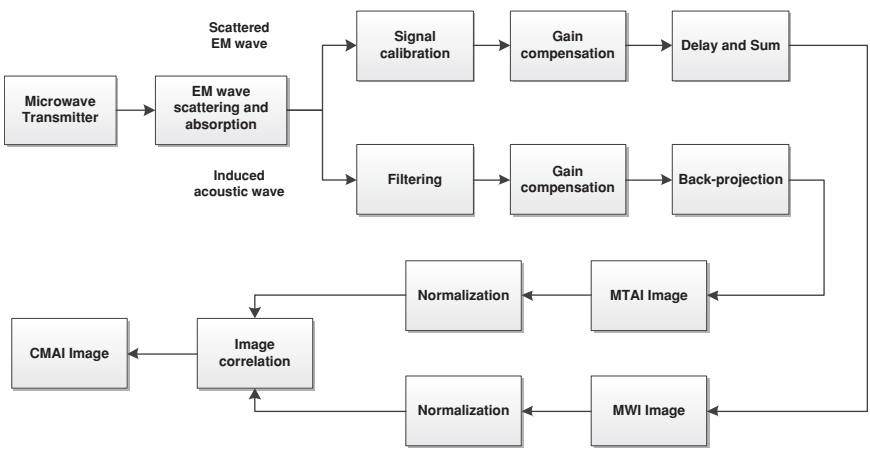

Figure 16.6 Signal-processing flow chart for CMAI.

scaling procedure is applied so that both images have the same scale range, and then the images are shifted by their mean values. This normalization is shown in Eqs. (16.8) and (16.9):

$$MWI: A_{i,j} = \frac{A_{i,j} - \text{mean}[A_{i,j}]}{\max[A_{i,j}]}, \tag{16.8}$$

$$MTAI: B_{i,j} = \frac{B_{i,j} - \text{mean}[B_{i,j}]}{\max[B_{i,j}]}. \tag{16.9}$$

Then image correlation of MWI and MTAI is performed by

$$CMAI: C_{i,j} = \frac{\sum_{m=i-l}^{i+l} \sum_{n=j-s}^{j+s} A_{m,n} B_{m,n}}{(2l+1)(2s+1)}, \tag{16.10}$$

where the correlated image $C_{i,j}$ is obtained by multiplying the corresponding elements of MWI and MTAI images in a rectangular area $(2l+1) \times (2s+1)$, adding together and then averaging. In this way, at the tumor location, the elements of A and B are highly correlated, and multiplication and summation will lead to significant amplification and sharpening of the tumor. For other locations, due to different noise sources and clutter, the elements of A and B are uncorrelated; i.e., since both positive and negative values exist, their multiplication and summation tend to be zero. Therefore, through this kind of image correlation, the tumor will be enhanced, while clutter will be effectively suppressed.

16.3.2 Numerical simulation results

Finite-difference time-domain (FDTD) analysis is utilized for the simulation of EM wave scattering and thermo-acoustic signal propagation.[38] A simulated UWB signal is transmitted into a female breast model, where a tumor is modeled as a circle with a 1.6-mm radius. Scattered microwaves and induced thermo-acoustic waves shown in Fig. 16.7 are collected by microwave receivers and ultrasound transducers placed simultaneously around the breast model.

The grid cell of FDTD simulation is 0.4 mm for the EM field and 0.1 mm for acoustic simulation due to the much smaller wavelength of the acoustic wave. A perfectly matched layer is utilized to terminate the computational region. In EM simulation, scattered microwaves are recorded by the receiver, tumor response is calculated by subtracting the calibration signal recorded without the tumor, and specific absorption rate is calculated at every grid cell and interpolated for the following

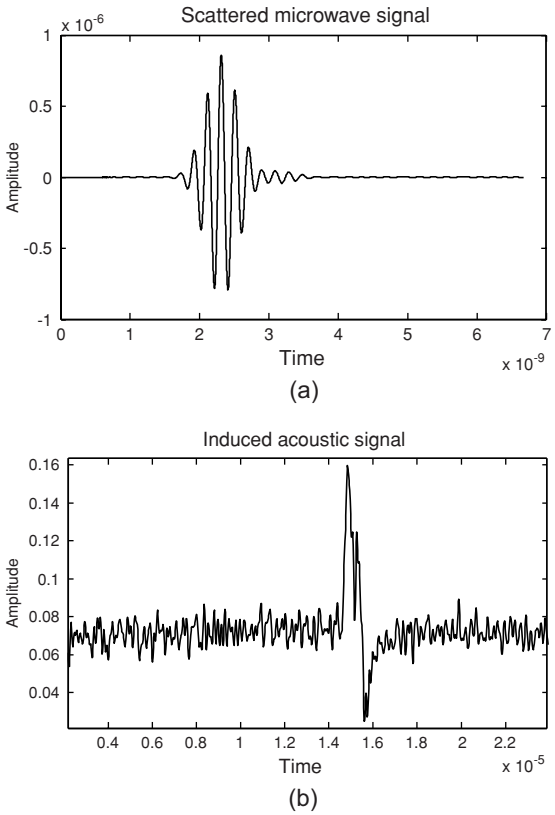

Figure 16.7 Waveform of (a) scattered microwave and (b) induced thermoacoustic wave.

acoustic simulation. We set two scenarios of low contrast and large variation to test the performance of the correlated microwave acoustic imaging. In Table 16.1, three cases for low-contrast scenarios and three cases for large-variation scenarios are simulated, where $\varepsilon_r/\varepsilon_b$ specifies the dielectric contrast ratio of tumor and surrounding fat tissue, and ε_b variation models the heterogeneous properties of fat tissue. Signal-to-clutter ratio

Table 16.1 Dielectric properties of six cases.

Table head	Dielectric properties					
	Low-contrast scenario			High-variation scenario		
$\varepsilon_r/\varepsilon_b$	2.0	1.7	1.4	2.0		
ε_b variation	3%			3%	6%	9%

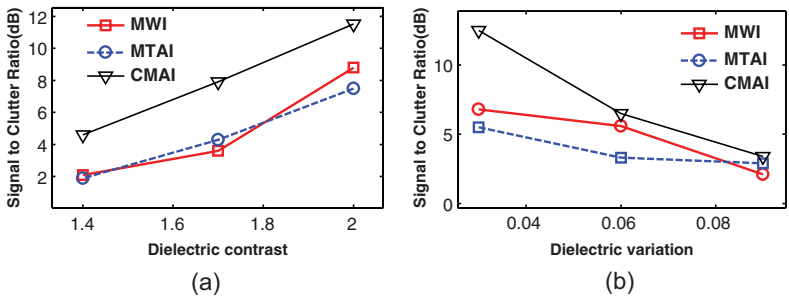

Figure 16.8 Signal-to-clutter ratio decreases with (a) lower contrast and (b) larger variation.

(S/C) for these six cases are shown in Fig. 16.8. The S/C deteriorates when the dielectric contrast decreases and dielectric variation increases. In either case, CMAI outperforms MWI and MTAI with at least 2.5 dB and 0.5 dB improvement, respectively.

Another case is simulated with dielectric contrast as low as 1.4:1 and variation as large as 9%, utilizing the three approaches. Simulated results are shown in Fig. 16.9, which shows that for MWI, a strong clutter caused by multiple scattering of microwaves in the heterogeneous breast tissue model exists, leading to confusion, and in MTAI, the tumor is blurred due to limited contrast. Image reconstructed by CMAI is shown in Fig. 16.9(d)

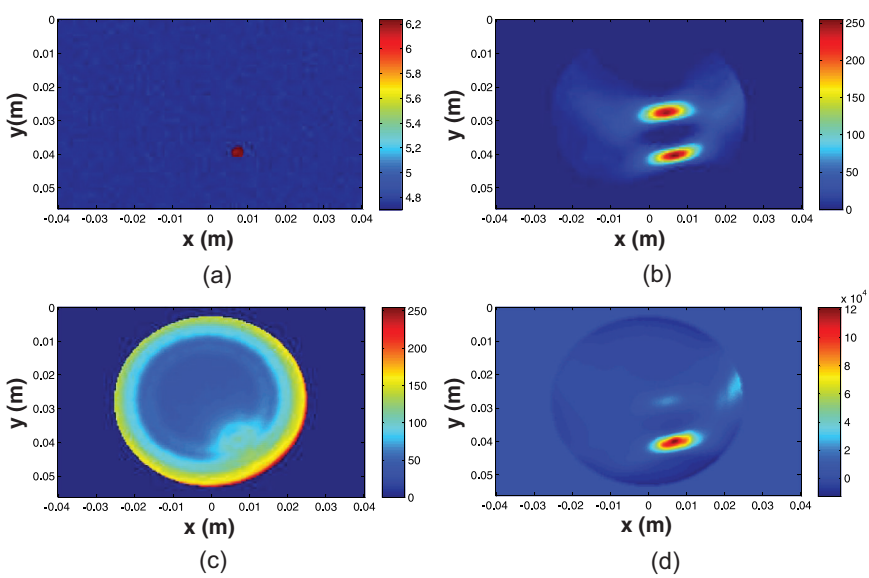

Figure 16.9 (a) Original dielectric distribution and constructed images by (b) MWI, (c) MTAI and (d) proposed CMAI.

with enhanced resolution, contrast, and accuracy; i.e., the tumor is detected clearly by strengthening the correlated location of tumor and suppressing other uncorrelated clutter parts.

16.4 Preliminary Prototyping

Significant improvement of CMAI has been proved by numerical simulation in the previous section. In this section we focus on experimental implementation. Before conducting a correlated microwave acoustic imaging experiment, we first establish a preliminary experimental setup to collect both microwaves and thermo-acoustic waves simultaneously. Then, a UWB transmitter is designed and fabricated using microelectronics technology for imaging system implementation in future work.

16.4.1 Collecting microwaves and acoustic waves simultaneously

The preliminary experimental setup to collect both microwaves and thermo-acoustic waves simultaneously is shown in Fig. 16.10, where a Gaussian modulated microwave pulse is generated and both scattering microwave pulse and induced acoustic signal are collected by oscilloscope. In detail, a microwave generator (Rohde & Schwarz SMBV100A) under amplitude-shift keying configuration is used to provide a modulated Gaussian pulse microwave signal, which is amplified up to 100 W peak power by a microwave power amplifier (Mini-Circuits ZHL-100W-GAN+). Due to the power and bandwidth limit (up to 100 W and 500 MHz, respectively) of the power amplifier, we choose 440 MHz as the carrier frequency and 2-μs pulse width in order to deliver up to 0.2 mJ/pulse into biological

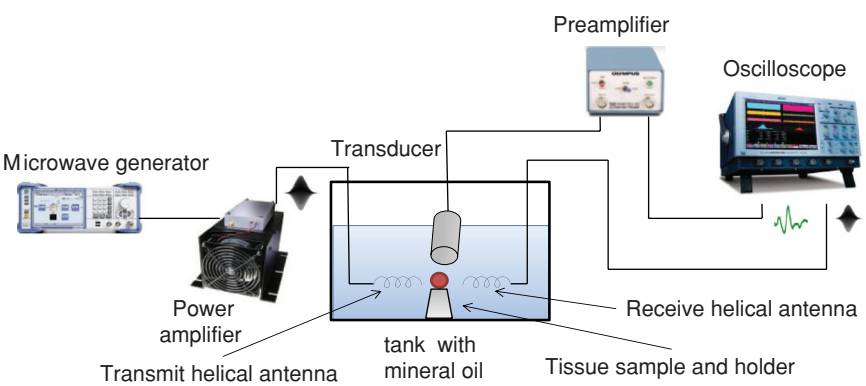

Figure 16.10 Experimental setup capable of collecting both scattering microwaves and induced thermo-acoustic waves simultaneously.

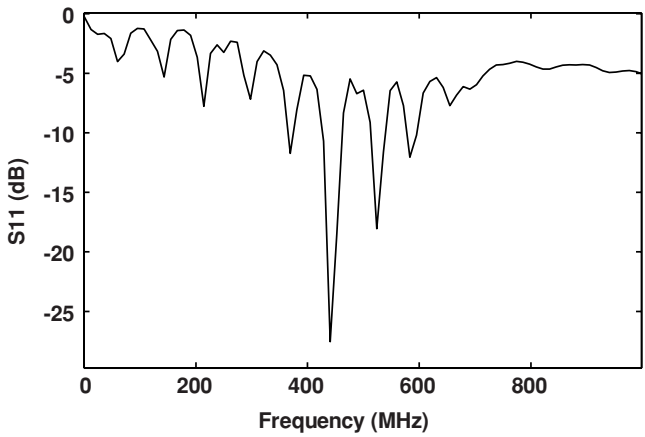

Figure 16.11 Measured S11 of the custom-designed helical antenna.

tissue. The amplified modulated Gaussian microwave is fed into a custom-designed helical antenna operating at 440 MHz. The measured S-parameter of S11 is shown in Fig. 16.11. To receive the scattered microwave signal, another helical antenna is placed at the other side, and meanwhile, thermo-acoustic signal due to microwave absorption is also collected by an ultrasound transducer (Olympus V323-SU) with 2.25-MHz central frequency, followed by an ultrasound preamplifier with 54-dB gain (Olympus 5662). Both scattered microwave and thermo-acoustic signals are recorded with a digital oscilloscope (Lecroy WaveMaster 8000A) at a 5-GHz sample/s rate. In the tank shown in Fig. 16.10, both the microwave antennas and the ultrasound transducer are immersed in mineral oil ($\varepsilon_r = 2.1$, $\sigma \approx 0$), which is a proper medium for microwave and acoustic wave propagation and is used to model female fat tissue.

Porcine muscle tissue with different dielectric contrast ($\varepsilon_r = 54.8$, $\sigma \approx 0.98$) from mineral oil is utilized to model the tumor tissue. Made into a small round shape with a 5-mm diameter, the muscle tissue is placed close to both the antennas and the transducer. Recorded microwaves and thermo-acoustic waves of muscle are shown in Figs. 16.12(a) and (b), respectively. After low-pass filtering, the thermo-acoustic waveforms in time domain and frequency domain are shown in Figs. 16.12(c) and (d), respectively. The central frequency of the thermo-acoustic wave is around 400 kHz due to the long microwave pulse width (2 μs), and the measured microwave follows well with the incident microwave pulse. In this preliminary experiment, we successfully collected both scattering microwave signal and induced thermo-acoustic signal simultaneously, a success that is promising for the implementation of the CMAI prototype in future work.

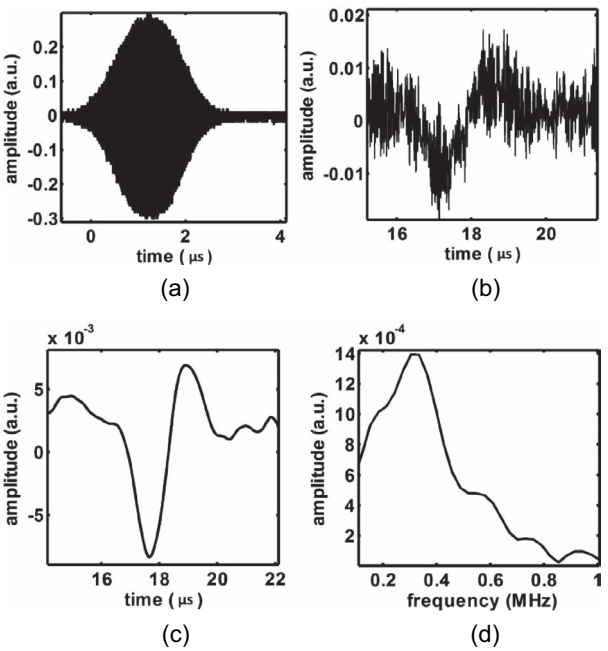

Figure 16.12 (a) Measured scattering microwave signal, (b) thermo-acoustic signal and its low-pass filtered waveform in (c) time domain and (d) frequency domain.

16.4.2 UWB transmitter design

In implementing the CMAI prototype, the microwave source is a very important component in the system. First, for MWI, a short UWB microwave pulse with a higher carrier frequency is highly appreciated for better resolution and localization performance. For the MTAI system, a tunable pulse width is required to meet the different tradeoffs between SNR, penetration depth, and resolution. In this section, we present the design and fabrication of a UWB transmitter using microelectronics technology. This UWB transmitter is ready for implementation in future imaging prototypes.[39]

The UWB transmitter is implemented in a complementary metal-oxide semiconductor 0.18-μm technology with 3.3-V power supply with low complexity and high efficiency. The simple architecture of a switched LC (inductor/capacitor) oscillator is a good option for this UWB transmitter to achieve high energy efficiency and peak power (VDD represents the power supply voltage). The UWB transmitter architecture is shown in Fig. 16.13, and the data flow of the transmitter is shown in Fig. 16.14. As shown in these two figures, the rising edge of input digital data A triggers a digital pulse generator to generate a nanosecond-wide digital pulse B. The pulse train B controls the tail current source of the LC oscillator, and consequently a UWB pulse train is generated at C. After amplification by the driver amplifier, the output pulses D are sent

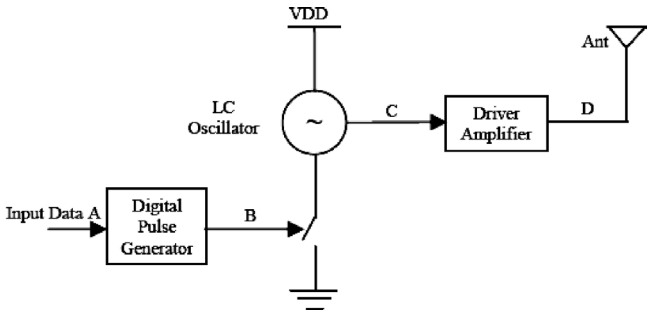

Figure 16.13 UWB transmitter architecture for correlated microwave acoustic imaging prototype.

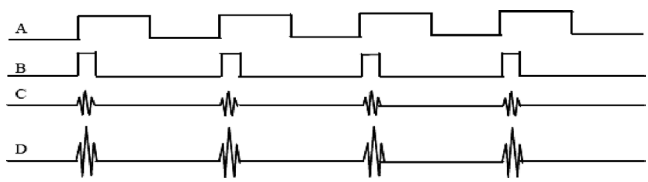

Figure 16.14 Data flow of the UWB transmitter.

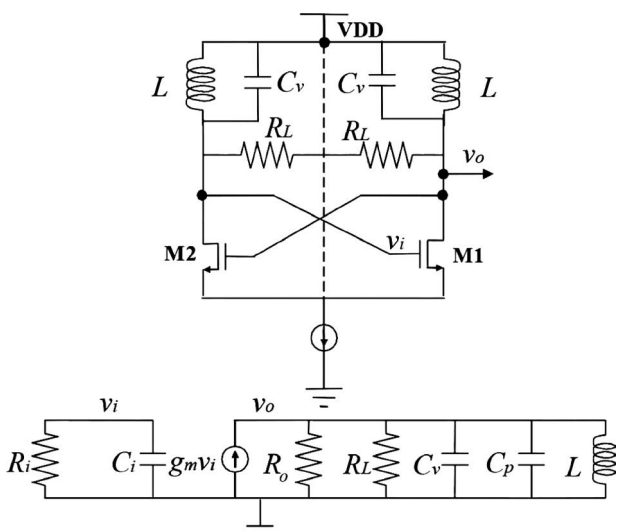

Figure 16.15 LC VCO circuit (upper) and its small-signal equivalent circuit (lower).

to a matched antenna (Ant). A common LC VCO (voltage-controlled oscillator) and its small-signal schematic are shown in Fig. 16.15. Here C_v is the varactor capacitance, and C_p is the parasitic capacitance. R_L is the load resistance. R_i, C_i, and R_o represent the input resistance, input capacitance, and output resistance, respectively, and g_m represents the transconductance of M1.

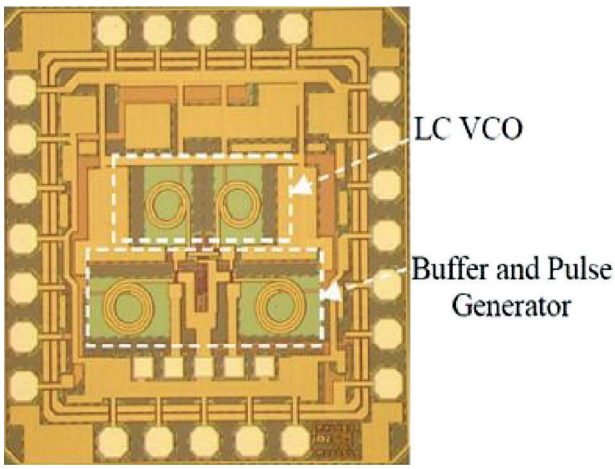

Figure 16.16 Die photography of the UWB transmitter.

The transmitter chip is realized in Chartered Semiconductor's 0.18-μm process and occupies an area of 0.8×0.6 mm (core circuit). A die photo is shown in Fig. 16.16. The chip is mounted on a Rogers Corp. printed circuit board and tested. With 1-Mbps baseband input data, the circuit can generate a pulse with 2-GHz bandwidth.

The entire transmitter circuit structure is shown in Fig. 16.17, which includes a pulse generator, an LC VCO, and a buffer (driver) amplifier. The buffer is switched on and off simultaneously with the VCO through a gate bias (not shown here). The OOK modulation scheme is adopted. The pulse width is tunable by adjusting the current of delay elements. The cross-coupled NMOS pair NM2, NM3 forms a VCO core. The LC tank consists

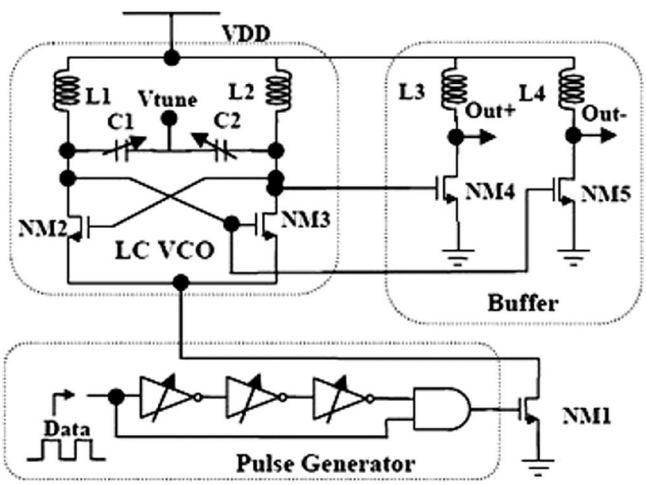

Figure 16.17 The complete circuit architecture of the UWB transmitter for CMAI.

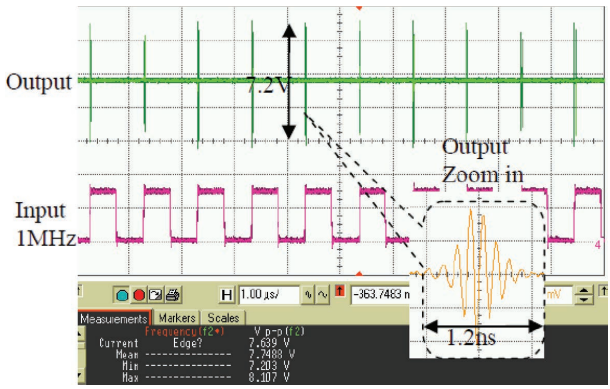

Figure 16.18 Measured UWB pulse in time domain and the input data.

of inductors L1, L2 and varactors C1, C2. An accumulation MOS varactor is used here to achieve 1-GHz tuning range (3.49–4.6 GHz) for calibration purposes. To facilitate fast start up and high output peak power, the sizing of transistors NM2-5 are large. Hence, the parasitic capacitance is quite large—around 0.6 pF. L3, L4, and NM4, NM5 form a buffer. It is used to drive 100-Ω loading and to stabilize the frequency of the LC VCO. The digital data with a certain duty cycle is used to trigger the pulse generator. A narrow pulse will be generated according to the rising edge of the input data. The pulse controls the gate of NM1 to turn on or off the VCO and the buffer circuits. The large size for NM1 is chosen to minimize the drain-source voltage and effectively present a short circuit directly to the ground.

Figure 16.18 shows the output pulse with 1.2-ns width and peak swing of 7.2 V, which is the highest output swing reported for the integrated UWB transmitters. The current consumption is 224 μA at 1 Mbps for the entire transmitter, and around 200-ps start-up time is achieved. The performance is summarized in Table 16.2.

Table 16.2 UWB transmitter summary.

Specifications	Measurement results
Process	CMOS 0.18 μm
Supply voltage	3.3 V
Die area	0.8 × 0.6 mm (core circuit)
Modulation	OOK
Maximum data rate	1 Mbps
Input data duty cycle	0.1%
Current consumption (1 Mbps)	224 μA
Pulse width	1.2 ns (tunable)
Differential output swing	7 V
Center frequency	4 GHz
Frequency band	3–5 GHz
Start up	200 ps

16.5 Conclusion

Microwave-based imaging modality is an emerging noninvasive medical imaging approach that uses the dielectric property of biological tissue and shows great potential in breast cancer detection. Microwave tomography reconstructs the dielectric distribution of the object, while radar-based microwave imaging shows scattering intensity distribution to detect the tumor. On the other hand, microwave-induced thermo-acoustic imaging uses the microwave absorption property (conductivity) of the object. All of these modalities have been receiving much research interest in the recent decade, but few people are working on fusing the emerging microwave-based imaging modalities together. Combining these modalities, we expect an imaging performance that exceeds that of any the single modalities.

In this chapter, the microwave-based imaging modality is introduced, then CMAI is proposed and studied by numerical simulation using FDTD analysis. A preliminary experiment is conducted to collect both scattering microwave and induced thermo-acoustic signals for future imaging prototyping. Then, a UWB microwave transmitter is introduced and implemented with microelectronics technology, providing a pulse-width-tunable microwave signal for CMAI implementation. It is clearly shown that combination of microwave-based imaging modalities is expected to achieve higher performance in terms of resolution, contrast, and robustness. Such a multimodality imaging approach will provide an efficient diagnostic method for breast cancer detection in the future.

References

1. World Health Organization, "Fact sheet No. 297: Cancer," *http://www.who.int/mediacentre/factsheets/fs297/en/index.html.*
2. Breast Cancer Foundation, *http://bcf.org.sg.*
3. E. J. Bond, L. Xu, S. C. Hagness, et al., "Microwave imaging via space-time beamforming for early detection of breast cancer," *IEEE Trans. Antenn. Propag.* **51**(8), 1690–1705 (2003).
4. A. E. Bulyshev, S. Y. Semenov, A. E. Souvorov, et al., "Computational modeling of three-dimensional microwave tomography of breast cancer," *IEEE Trans. Biomed. Eng.* **48**(9), 1053–1056 (2001).
5. M. Converse, E. J. Bond, S. C. Hagness, et al., "Ultrawide-band microwave space-time beamforming for hyperthermia treatment of breast cancer: A computational feasibility study," *IEEE Trans. Microwave Theory Techniques* **52**(8), 1876–1889 (2004).

6. S. K. Davis, H. Tandradinata, S. C. Hagness, et al., "Ultrawideband microwave breast cancer detection: A detection-theoretic approach using the generalized likelihood ratio test," *IEEE Trans. Biomed. Eng.* **52**(7), 1237–1250 (2005).
7. S. K. Davis, B. D. Van Veen, S. C. Hagness, et al., "Breast tumor characterization based on ultrawideband microwave backscatter," *IEEE Trans. Biomed. Eng.* **55**(1), 237–246 (2008).
8. E. C. Fear, S. C. Hagness, P. M. Meaney, et al., "Enhancing breast tumor detection with near-field imaging," *IEEE Microwave Mag.* **3**(1), 48–56 (2002).
9. E. C. Fear, X. Li, S. C. Hagness, et al., "Confocal microwave imaging for breast cancer detection: Localization of tumors in three dimensions," *IEEE Trans. Biomed. Eng.* **49**(8), 812–822 (2002).
10. E. C. Fear, P. M. Meaney, and M. A. Stuchly, "Microwaves for breast cancer detection?" *IEEE Potentials* **22**(1), 12–18 (2003).
11. E. C. Fear, J. Sill, and M. A. Stuchly, "Experimental feasibility study of confocal microwave imaging for breast tumor detection," *IEEE Trans. Microwave Theory Techn.* **51**(3), 887–892 (2003).
12. E. C. Fear and M. A. Stuchly, "Microwave detection of breast cancer," *IEEE Trans. Microwave Theory Techn.* **48**(11), 1854–1863 (2000).
13. S. C. Hagness, A. Taflove, and J. E. Bridges, "Two-dimensional FDTD analysis of a pulsed microwave confocal system for breast cancer detection: Fixed-focus and antenna-array sensors," *IEEE Trans. Biomed. Eng.* **45**(12), 1470–1479 (1998).
14. S. C. Hagness, A. Taflove, and J. E. Bridges, "Three-dimensional FDTD analysis of a pulsed microwave confocal system for breast cancer detection: Design of an antenna-array element," *IEEE Trans. Antenn. Propag.* **47**(5), 783–791 (1999).
15. P. Kosmas and C. M. Rappaport, "Time reversal with the FDTD method for microwave breast cancer detection," *IEEE Trans. Microwave Theory Techn.* **53**(7), 2317–2323 (2005).
16. P. M. Meaney, M. W. Fanning, L. Dun, et al., "A clinical prototype for active microwave imaging of the breast," *IEEE Trans. Microwave Theory Techn.* **48**(11), 1841–1853 (2000).
17. Q. H. Luo, Z. Q. Zhang, T. T. Wang, et al., "Active microwave imaging. I. 2-D forward and inverse scattering methods," *IEEE Trans. Microwave Theory Techn.* **50**(1), 123–133 (2002).

18. M. A. Anastasio, Z. Jin, P. Xiaochuan, et al., "Half-time image reconstruction in thermoacoustic tomography," *IEEE Trans. Med. Imaging* **24**(2), 199–210 (2005).
19. P. Burgholzer, C. Hofer, G. Paltauf, et al., "Thermoacoustic tomography with integrating area and line detectors," *IEEE Trans. Ultrason. Ferroelect. Freq. Control* **52**(9), 1577–1583 (2005).
20. Z. Guangran, M. Popovic, and F. Qianqian, "Microwave-induced thermoacoustics: Assisting microwave tomography," *IEEE Trans. Magnetics* **45**(3), 1654–1657 (2009).
21. Z. Jin, M. A. Anastasio, P. Xiaochuan, et al., "Weighted expectation maximization reconstruction algorithms for thermoacoustic tomography," *IEEE Trans. Med. Imaging* **24**(6), 817–820 (2005).
22. R. A. Kruger, W. L. Kiser, D. R. Reinecke, G. A. Kruger, and R. L. Eisenhart, "Thermoacoustic computed tomography of the breast at 434 MHz," *Microwave Symp. Digest, 1999 IEEE MTT-S International* **2**, 591–594 (1999).
23. X. Minghua and L. V. Wang, "Time-domain reconstruction for thermoacoustic tomography in a spherical geometry," *IEEE Trans. Med. Imaging* **21**(7), 814–822 (2002).
24. X. Minghua, X. Yuan, and L. V. Wang, "Time-domain reconstruction algorithms and numerical simulations for thermoacoustic tomography in various geometries," *IEEE Trans. Biomed. Eng.* **50**(9), 1086–1099, 2003.
25. S. K. Moore, "Better breast cancer detection," *IEEE Spectrum* **38**(5), 50–54 (2001).
26. L. Nie, D. Xing, D. Yang, et al., "Detection of foreign body using fast thermoacoustic tomography with a multielement linear transducer array," *Appl. Phys. Lett.* **90**(17), 174109 (2007).
27. L. V. Wang, "Tutorial on photoacoustic microscopy and computed tomography," *IEEE J. Sel. Topics Quantum Electron.* **14**(1), 171–179 (2008).
28. M. Xu, and L. V. Wang, "Photoacoustic imaging in biomedicine," *Rev. Scient. Instrum.* **77**(4), 041101 (2006).
29. X. Yao, G. Bin, L. Jian, et al., "Adaptive and robust methods of reconstruction (ARMOR) for thermoacoustic tomography," *IEEE Trans. Biomed. Engin.* **55**(12), 2741–2752 (2008).
30. X. Yuan, F. Dazi, and L. V. Wang, "Exact frequency-domain reconstruction for thermoacoustic tomography. I. Planar geometry," *IEEE Trans. Med. Imaging* **21**(7), 823–828 (2002).
31. X. Yuan, X. Minghua, and L. V. Wang, "Exact frequency-domain reconstruction for thermoacoustic tomography. II. Cylindrical geometry," *IEEE Trans. Med. Imaging* **21**(7), 829–833 (2002).

32. X. Yuan and L. V. Wang, "Rhesus monkey brain imaging through intact skull with thermoacoustic tomography," *IEEE Trans. Ultrason. Ferroelect. Freq. Control* **53**(3), 542–548 (2006).
33. C. Gabriel, S. Gabriel, and E. Corthout, "The dielectric properties of biological tissues. 1. Literature survey," *Phys. Med. Biol.* **41**(11), 2231–2249 (1996).
34. S. Gabriel, R. W. Lau, and C. Gabriel, "The dielectric properties of biological tissues. 2. Measurements in the frequency range 10 Hz to 20 GHz," *Phys. Med. Biol.* **41**(11), 2251–2269 (1996).
35. S. Gabriel, R. W. Lau, and C. Gabriel, "The dielectric properties of biological tissues. 3. Parametric models for the dielectric spectrum of tissues," *Phys. Med. Biol.* **41**(11), 2271–2293 (1996).
36. M. Lazebnik, D. Popovic, L. McCartney, et al., "A large-scale study of the ultrawideband microwave dielectric properties of normal, benign and malignant breast tissues obtained from cancer surgeries," *Phys. Med. Biol.* **52**(20), 6093–6115 (2007).
37. E. Kirshin, B. Oreshkin, K. G. Zhu, et al., "Fusing microwave radar and microwave-induced thermoacoustics for breast cancer detection," *2011 IEEE Int. Symp. Biomedical Imaging: From Nano to Macro,* 113–116 (2011).
38. A. Taflove and S. C. Hagness, *Computational Electrodynamics: The Finite-Difference Time-Domain Method*, 3rd edition, Artech House, Boston (2005).
39. S. Diao and Y. Zheng, "An ultra low power and high efficiency UWB transmitter for WPAN applications," *IEEE 34th European Conference on Solid State Circuits 2008: ESSCIRC 2008*, 334–337 (2008).

Yuanjin Zheng received the B.Eng. and M.Eng. degrees from Xi'an Jiaotong University, Xi'an, China, in 1993 and 1996, respectively, and the Ph.D. degree from Nanyang Technological University (NTU), Singapore, in 2001. From July 1996 to April 1998, he was with the National Key Laboratory of Optical Communication Technology, University of Electronic Science and Technology of China. In 2001, he joined the Institute of Microelectronics (IME), Agency for Science, Technology and Research (A*STAR), Singapore, as a Senior Research Engineer, and was then promoted to a Principle Investigator. With the IME, he has led and developed various projects on CMOS RF

transceivers, baseband system-on-a-chip (SoC) for wireless local area networks (WLANs), WCDMA, ultra-wideband (UWB), and low-power medical radio, etc. In July 2009, he joined NTU as an assistant professor. His research interests are gigahertz RFIC and SoC design, UWB systems and circuits, biomedical sensors and imaging, SAW/BAW/MEMS, and application-specific integrated circuits (ASICs). He has authored or coauthored over 90 international journal and conference papers, 13 filed/granted patents, and two book chapters. He has successfully led and contributed to numerous publically funded research and industry projects.

Fei Gao received the B.S. degree from Xi'an Jiaotong University in China and has been pursuing his Ph.D. at Nanyang Technological University, Singapore since 2010. His areas of research interest include system design and prototyping of microwave-based medical imaging modalities for breast cancer detection, and integrated circuit (IC) design for biomedical applications.

Zhiping Lin received the B.Eng. degree in Control Engineering from South China Institute of Technology, Canton, China, in 1982 and the Ph.D. degree in information engineering from the University of Cambridge, United Kingdom, in 1987. He was with the University of Calgary, Canada from 1987 to 1988, Shantou University, China, from 1988 to 1993, and DSO National Laboratories, Singapore, from 1993 to 1999. Since February 1999, he has been an associate professor at Nanyang Technological University (NTU), Singapore. He is also the Program Director of Bio-Signal Processing, Valens Centre of Excellence, NTU. Dr. Lin is currently serving as the Editor-in-Chief of *Multidimensional Systems and Signal Processing* after being on its editorial board since 1993. He was an Associate Editor of *Circuits, Systems and Signal Processing* from 2000 to 2007 and an Associate Editor of *IEEE Transactions on Circuits and Systems II* from 2010 to 2011. He also serves as a reviewer for *Mathematical Reviews*. His research interests include multidimensional systems and signal processing, statistical signal processing, biomedical signal processing, and machine learning. He is a coauthor of the 2007 Young Author Best Paper Award from the IEEE Signal Processing Society. He was a Distinguished Lecturer of the IEEE Circuits and Systems Society in 2007–2008, and the Chair of the IEEE Circuits and Systems Singapore Chapter in 2007–2008.

Chapter 17
Diagnostic Sensing of Specific Proteins in Breast Cancer Cells Using Hollow-Core Photonic Crystal Fiber

Vadakke Matham Murukeshan, Vengalathunadakal Kuttinarayanan Shinoj, and Saraswathi Padmanabhan
School of Mechanical and Aerospace Engineering, Nanyang Technological University, Singapore

Parasuraman Padmanabhan
Laboratory of Molecular Imaging, Singapore BioImaging Consortium (SBIC), Singapore

17.1 Introduction

The recent drive in biomedical research has been mainly focused on detection, diagnosis, treatment, and prevention of diseases in order to ultimately foster better health. Detection of cancerous tissue or relevant

cancer-causing entities using an extremely low sample volume and at an early stage is another targeted objective of researchers in the recent past. From that perspective, ultrasensitive detection and imaging methods are treated as enablers for the advancement of diagnostic methodologies to the next level. The steady progress in biology, engineering, and medicine toward diagnostics based on molecular markers leads to the exploration of high-throughput methods for the detection of biomolecules and their interactions in a biological system. Fluorescence-based bioassays are novel diagnostic tools available to clinicians for deciding on further treatment and to researchers for monitoring biological functions that lead to novel investigations.

Protein microarrays are an essential tool in proteomics research and are also used in biomedical applications to determine the presence and/or amount of proteins in a biological sample.[1] In recent years, fluorescence assay technologies have played a pivotal role in the high-throughput analysis of proteins and protein interactions. The precise measurement of a fluorescence signal is a prime parameter in analyzing the functional responses of the biological samples.[2] Diagnostics or detection at the molecular level using reporter assays or expression studies are led by improved techniques using fluorescent proteins as biomarkers.[3]

It is known that breast cancer, the fifth most common cancer, leads to approximately 502,000 deaths worldwide per year and has already been linked with the steroid hormone estrogen.[4] Further, it is well reported that many human breast cancers are initially hormone dependent. This knowledge led to the utilization of anti-estrogens in the treatment of breast cancer.[5,6] Discovery of the estrogen receptor (ER) has given the medical community a powerful diagnostic and predictive marker that is employed as a proficient target for the treatment of hormone-dependent breast cancer.[7,8] Several techniques are available for the specific detection of the said protein. The immune-sensing technique is a powerful and flexible tool, used to identify a targeted antigen with desired specific antibodies.[9–11] Even though enzyme-linked immunosorbent assay (ELISA) is an old method, it is still in use to detect proteins[12–13] but has the disadvantage of showing nonspecific interaction leading to false positives. The gel shift assay is another approach for detecting the ER protein. Its intracellular localization and expression levels are reported elsewhere.[14] Immunohistochemistry is another technique for assessing the ER status of breast cancers.[15,16] However, it is reported that this method has a disadvantage in determining the level of expression.

The use of optical fibers for various sensing purposes has been reported heavily in the recent past.[17,18] The emergence of microstructured optical fibers (MOFs) opens up new opportunities for novel fluorescent detection and relevant biosensor design, both of which can solve the problems encountered in conventional biosensors.[19–21] MOFs are characterized as

having a plurality of air holes running along the entire length of the fiber.[22] The optical properties of this class of fibers are determined by their geometry, size, and relative position of the air holes. Photonic crystal fibers (PCFs) are one of the most prominent MOFs that have emerged in recent years that could be engineered to have vastly different properties compared to conventional fibers.[23,24]

17.2 Photonic Crystal Fibers

Photonic crystal fibers are fundamentally 2D photonic crystals in the transverse geometry that extend longitudinally along the length of the fiber. Their guiding mechanism is based on the photonic bandgap (PBG) formed due to its high index contrast (commonly silica and air in the optical region) and from the wavelength-scale microstructure. The mode propagation properties strongly depend on wavelength, which in turn depends on the design, configuration, and geometry of the air holes.[24–26] The transmission bands, or transmission windows, of the hollow-core photonic crystal fiber (HC-PCF) is decided by the spacing between the holes of the capillaries (pitch), the hole diameters of the capillaries, and/or the air-filling content within the inner cladding. In 1996, Russell and his coworkers demonstrated the first PCF,[27] compromising fine silica fibers with an array of air holes running down their length with the central region where an air hole is absent acting as the guiding core. Since then, the field of PCF has developed rapidly and has attracted attention from research communities from around the world. A common way to classify PCFs is based on the guiding mechanism.

Holey fibers consist of a central solid core surrounded by a cladding region laced with air holes, which acts as index-decreasing elements. In this case, light is guided by a modified form of total internal reflection, since the refractive index (RI) of the core is greater than effective index of the surrounding cladding region. Another class of fibers is the abovementioned HC-PCFs, where light within certain wavelength bands is prevented from propagating through the cladding region due to bandgap effects.[26] HC-PCFs are formed by introducing a low-index effect in a 2D photonic crystal structure; hence, they are able to support guidance in air.[24–26] Illustrations of the guiding mechanisms in hollow and solid core fiber are shown in Fig. 17.1. Unlike conventional fibers, PCFs are made of pure silica glass (SiO_2) without any doping. Hence, they are biocompatible and chemically inert. Furthermore, the capillary tubes present in PCFs have a good surface-to-volume ratio. A high light–matter interaction cross section of the field energy and the sample material can be achieved with HC-PCFs. Hence, an HC-PCF-based sensor utilizes the available sample volume much more effectively than fiber optic sensors based on conventional optical fibers.

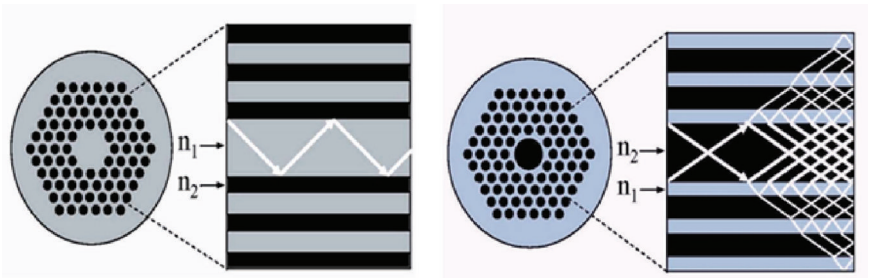

Figure 17.1 Illustration of (a) index guidance and (b) bandgap guidance in photonic crystal fibers, where $n_1 = 1.45$ (silica) and $n_2 = 1$ (air).

In the recent past, HC-PCFs have been widely used for evanescent wave sensing or highly efficient sensing of biomolecules, such as DNA, enzymes, antigens, antibodies, and proteins.[28–31] Of late, optical manipulation and detection of the fluorescent sample inside the core of HC-PCFs is also explored.[32,33] When the holey regions of HC-PCFs are filled with aqueous solution, the transmission window shows a blue shift.[34,35] This approach is analogous with the well-known scaling laws that describe the shift in the PBG edge that is derived from scalar waveguide approximation.[34] By means of the scalar-wave approximation, simple RI scaling laws have been derived to predict the manner in which the photonic states of the fiber scale with changes in the RI contrast. An experimental demonstration of the shift in the PBG edge due to RI scaling is considered, and an efficient fluorescence sensing scheme using HC-PCFs has been illustrated.[36] In this context, this chapter describes an efficient fluorescence sensing approach to developing a technique to recognize specific proteins in an extremely low volume of sample based on immune binding.

17.2.1 Refractive-index scaling law

In general, the wave equation for the scalar field distribution in microstructured index-contrast structures is given by[35]

$$\nabla_{\perp}^{2}\Psi(x,y) + (k^{2}n_{0}^{2} - \beta^{2})\Psi(x,y) = 0, \tag{17.1}$$

where k is a free-space wave number, n_0 is the transverse distribution of the RI of the structure, β is the propagation constant of the mode, and $\nabla_{\perp}$ is the transverse Laplacian operator.

The scalar wave equation is valid for very small index contrast. However, it is found to roughly explain light propagation in high-index-contrast microstructures such as HC-PCFs, as well.[37] Figure 17.2 represents the

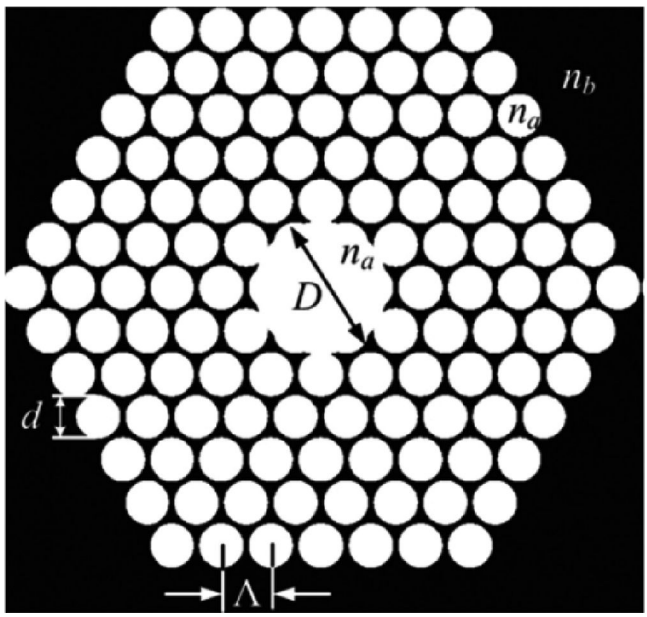

Figure 17.2 HC-PCF with air holes arranged in a triangular lattice (white regions correspond to air).

cross section of a representative HC-PCF. It consists of a hollow-core of diameter D surrounded by cladding holes in a triangular lattice. The separation between the holes is represented as Λ (pitch), and the air-hole diameter is d. The important characteristics of HC-PCFs are the positions and the bandwidths of the PBG, which in turn depend on the fiber geometry and the RI contrast between the ambient and background media. In scalar approximation for a photonic crystal structure comprising a material with a high index n_1 and a material with low index n_2 with pitch Λ, the photonic states scale so that the quantities such as ν^2 and ω^2 remain invariant with any changes of parameters k, Λ, n_1 and n_2,[37] where

$$\nu^2 = k^2\Lambda^2(n_1^2 - n_2^2), \tag{17.2}$$

and

$$\omega^2 = \Lambda^2(\beta^2 - k^2 n_2^2). \tag{17.3}$$

Equations (17.2) and (17.3) provide the RI scaling laws, which can describe the extent to which the frequency of the photonic state of fiber can shift on changing the index contrast of the fiber materials. Specifically, consider the case where the low-index material (n_2) in an HC-PCF is altered while the high-index material remains unchanged. The initial

RI contrast [$N_0 = (n_1/n_2)$] changes to N. From Eqs. (17.2) and (17.3), the bandgap at wavelength λ_0 will shift to a new wavelength λ, given by[35,37]

$$\lambda = \lambda_0 \left[\frac{1 - N^{-2}}{1 - N_0^{-2}} \right]^{1/2}. \tag{17.4}$$

17.2.2 Selection of fibers

As shown in Fig. 17.2, in HC-PCFs, the ambient RI n_a represents the RI of the holey region that consists of both core and cladding holes. The RI of the background material (in general, silica) is symbolized as n_b. The shift in central wavelength from wavelength λ_0 to a new wavelength λ can be expressed as

$$\lambda = \lambda_0 \left[\frac{\left(n_b^2 - n_m^2\right)}{\left(n_b^2 - n_a^2\right)} \right]^{1/2}. \tag{17.5}$$

In Eq. (17.5), n_a represents the ambient index inside the holey region, which includes the core and the holes inside the cladding. The RI of the background material and infiltrated material is denoted as n_b and n_m, respectively. Also, λ_0 represents the central wavelength of the fiber in air medium (n_0). This RI scaling law is particularly applicable where the entire air region of the HC-PCF needs to be filled with gases or liquids. Filling the holes with different fluid media results in a shift in bandgaps and a shift in their corresponding bandwidths. This shift in central wavelength and bandwidth can be evaluated using the RI scaling law [Eq. (17.5)].

Hence, for hollow-core fibers with similar geometry profile, when the RI of the filling material changes from n_0 to n_m, the corresponding wavelength shift of the PBG edge varies from λ_0 to λ. Most HC-PCFs have cladding made of pure fused silica ($n_b = 1.45$) with array of air holes ($n_a = 1$) running along the entire length of the fiber. Based on the RI scaling law, for a particular filling material, the shifted wavelength λ is proportional to central wavelength λ_0 of the HC-PCF. The variation of λ with λ_0 is plotted in Fig. 17.3 for different filling-material index values ranging from 1.3 to 1.4. It can be seen that on increasing the filling material indices, the central wavelength of a particular HC-PCF is shifted to the lower-wavelength region.

This shift in central wavelength should be a significant parameter to be considered in HC-PCF-based fluorescent sensors where fluorescent sample solutions are infiltrated into the fiber holes. For efficient fluorescent sensing, when filling the aqueous sample, the selection of HC-PCF should satisfy the condition that the emitted fluorescence wavelength is centered at the shifted wavelength of the HC-PCF. Hence, based on the RI scaling law,

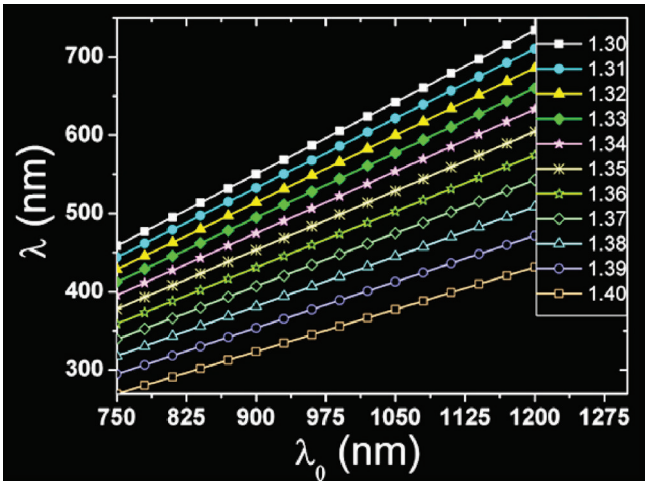

Figure 17.3 The shift in central wavelength λ_0 of HC-PCFs to the new wavelength λ at various filling material indices (adapted from Ref 36).

two HC-PCFs such as one with central wavelength at 830 nm (HC-800) and another with central wavelength at 1060 nm (HC-1060) are selected for the detection of green and red fluorescent dye respectively. The scanning electron microscope (SEM) images of these two fibers are given in Fig. 17.4.

The HC-800 has an approximate core diameter of 9.3 μm surrounded by a 40-μm diameter microstructured cladding. It exhibits full PBG (high transmission range) extending from approximately 770 to 890 nm. The attenuation over this range is less than 0.5 dB/m. In HC-1060, the PBG presents a band larger than 100 nm centered at 1060 nm. The hollow core has a center core size of diameter 10 ± 1 μm surrounded by a microstructure

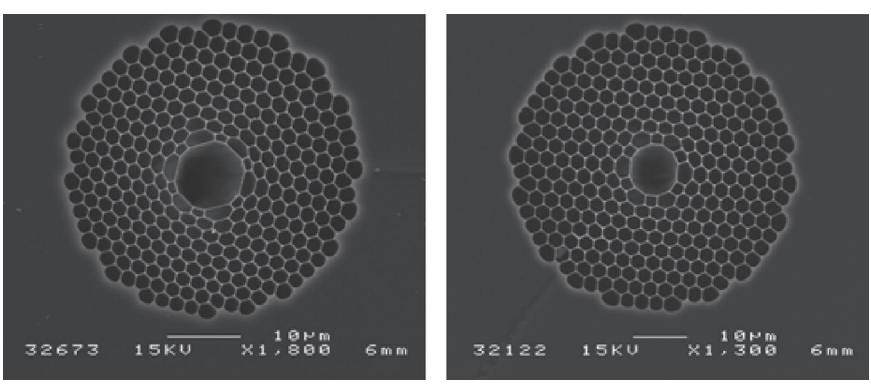

(a) (b)

Figure 17.4 SEM images of an HC-PCF with (a) central wavelength of 830 nm (HC-800) and (b) central wavelength of 1060 nm (HC-1060).

comprising eight periods of hexagonally packed cylinders with a period of 2.75 μm and a filling fraction of around 90%. The cladding diameter is 123 ± 5 μm. Both of the hollow-core fibers are cut into segments of ≈10-cm length, and one end of the fiber is cleaved carefully (approximately 1.5–2.0-cm length) using a fiber cleaver to produce a flat surface.

17.3 Sensing Mechanism Based on Evanescent Waves

A majority of the optical sensing methods are based on the existence of evanescent waves (EWs) in the region where the chemical species to be sensed is placed. Evanescent waves occur when there is a confinement region in which a majority of the optical density exists; however, outside this region, a tail of the optical field exists, forming the EWs.

Typically, an EW field is created when light undergoes total internal reflection at the boundary between two dielectric media. The evanescent optical field that decays exponentially from the waveguide interface has been used in a variety of sensing schemes. The sensitivity of an EW-based sensor depends on both the amplitude of the EW in the region where the sample is located and the length of the region that has the target species within the EW field. But the drawback of this type of sensor is that the sensitivity is reliant on the mode distribution and hence on launching conditions and external disturbances.

17.3.1 Conventional-fiber-based evanescent wave sensing

Optical-fiber-based evanescent sensors, which make use of the interaction of an EW with analytes in the field along an optical waveguide, have been widely used. This sensing technique relies on the penetration of the EW of a totally internally reflected light into the fiber cladding, where a chemical species absorbs/scatters the EWs or is excited by the EWs to give a sensing signal. In conventional EW-based fiber sensors, commercially available silica optical fibers or silver halogenide fibers are used. In order to create an EW field in this sort of fiber, one needs to remove the optical fiber's jacket as well as the cladding. This removal will make such fibers fragile and difficult to handle, especially when a fiber of small diameter, such as a single-mode optical fiber, is used to fabricate the sensor. Moreover, in most reported EW-based optical fiber sensors, only a few centimetres of the cladding can be replaced, limiting the sensitivity of the sensors.

17.3.2 Evanescent wave sensing using HC-PCF

HC-PCF is characterized as having a hollow core (of diameter D) surrounded by a pattern of air holes (of diameter d) running along the entire length of the fiber. As indicated by their name, HC-PCFs guide light in the air core within certain bandgaps, which manifest as transmission

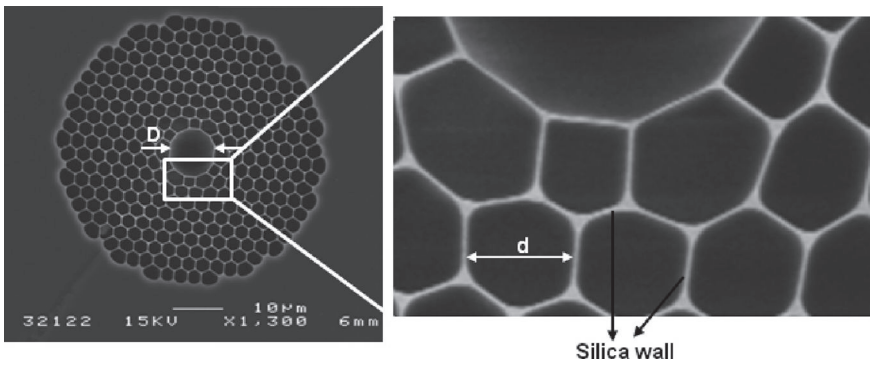

Figure 17.5 SEM image of an HC-PCF (a) end face and (b) enlarged view of the region enclosed by the rectangular box in (a).

windows in the transmission spectrum. The SEM image of a fiber end face and an enlarged view of the region enclosed by the rectangular box are shown in Fig. 17.5. When the entire section of the fiber is illuminated/excited with a laser light source from one end, the electromagnetic field from light propagating through the fiber is mostly confined to the silica walls (the area between the neighboring air holes). However, due to the wave nature of electromagnetic waves, an exponential tail of the optical field will penetrate into the holes of the HC-PCF (core and cladding holes) and thereby probe any sample placed there. The strong evanescent field interaction with the fluorescent sample over several centimeters ensures efficient usage of the entire sample volume, and the emitted fluorescence is guided along the fiber for subsequent detection at the other end.

17.4 Materials and Methods

The method is based on antibody-based immunoassay technology[38] that makes use of the binding between an antigen and its homologous antibody in order to identify and quantify the specific antigen in a sample. ER-positive MCF-7 breast carcinoma cells and ER-negative MDA-MB-231 cells were chosen for the study. ER-positive and ER-negative cell lysates immobilized inside HC-PCFs were detected using an anti-ER primary antibody with either Alexa Fluor® 488 (green fluorescent dye) or 555 (red fluorescent dye) labeled goat anti-rabbit IgG as the secondary antibody.

17.4.1 Cell culture and sample preparation

Both MCF-7 and MDA-MB-231 cells were grown to confluence in Dulbecco's Modified Eagle Medium (high glucose) supplemented with 10% fetal bovine serum (FBS) and 1% penicillin and streptomycin. The media

were removed from the 12-well culture plates in which the cells were grown, and the cells were washed twice with phosphate-buffered saline (PBS). These cells were lysed (200 μL) in the buffer (1×) and kept at 4 °C in a rotator for 1 h. After incubation, 5 μL of 200-mM phenylmethylsulfonyl fluoride was added, and the sample solution was centrifuged at 10,000 rpm for 15 min. The supernatant-containing protein was extracted and stored at −70 °C until it was used.

17.5 Results and Discussion

The concentration of proteins in the cell lysates are quantified using the Bradford method.[39] The estimated amount of protein in MCF-7 and MDA-MB-231 cell lysates is found to be 1 μg/μL. The amounts of ER-α protein immobilized in the fibers are calculated according to the protein quantity in the cell lysate. The western blot is used as an analytical technique to detect specific proteins in the given sample. The endogenous ER levels in the positive cells are detected using the antibody raised against ER-α. To confirm the ER protein signal, the cells are analyzed using anti-ER-α antibody for cellular ER, and anti-β-actin antibody for β-actin. As the β-actin is the housekeeping gene, it acts as an internal standard protein. Hence, it gives a signal in both MCF-7 and MDA-MB 231 cell lines. It is also noted that only the MCF-7 cell line gives a signal that corresponds to ER-α. The absence of signal in MDA-MB-231 cell lines confirms the lack of ER-α receptor in it.

17.5.1 HC-PCF-based fluorescence detection

The different steps involved in the process are schematically represented in Fig. 17.6. The binding of protein mainly depends on efficient surface attachment procedures, which are crucial for biosensor applications. Hence, the primary step of the experiment is to activate the silica inner core of the fiber to facilitate the detection of the ER protein. Poly-L-lysine is used to precoat the inner wall of the fiber. The activated surface of the inner core provides a base for appending the targeted protein to achieve this goal. The tip of the fiber is dipped in the 0.01% poly-L-lysine solution for 3 min, and the solution is allowed to get into the fiber by simple capillary force. The fiber is permitted to dry out at room temperature for approximately 1 h. After drying, it is washed twice with PBS for 5 min. Thus, the inner core is prepared for further processing.

In the next step, ER-α positive (MCF-7) and negative (MDA-MB-231) cell lysates are allowed to stick inside different PCFs for protein binding (3 min.). After that, the fibers are incubated at 4 °C for 2 h, then washed thrice briefly in TBST buffer. The primary antibody (Acris Antibodies,

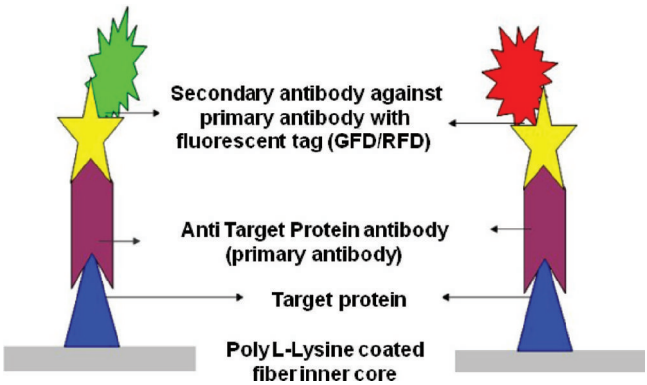

Figure 17.6 Drawing showing specific protein binding by the developed protocol. (GFD = green fluorescent dye, RFD = red fluorescent dye.) (Adapted from Ref. 31.)

GmbH, Germany) binding is performed using anti-estrogen-α solution diluted to a final concentration of 1:1000 (14 mg/ml) in TBS for 5–10 min and incubated for 3 h at 4 °C. Concurrently, sodium iodide symporter antibody (NIS primary antibody, Whatman Ltd.) is also used to check the nonspecific binding of the ER-α protein. This is followed by TBST buffer wash (thrice) for 10 min. and drying at 4 °C for 1 h. The experiment is completed by adding a secondary antibody solution made in TBS containing Alexa Fluor 488 and/or 555 red fluorescent dye labeled goat anti-rabbit IgG diluted to 1:100, in same way as in the earlier step. Appropriate controls are performed simultaneously for both green and red dye detections. Now the immuno binding of the protein is completed inside the fiber core, and the fiber is ready for imaging/sensing. The fibers are stored in dark ambience at 4 °C.

The fluorescence fingerprints of the ER-α protein are observed under a fluorescence microscope, and their optical characteristics are also analyzed using a spectrophotometer. The cleaved end of the fiber carrying immobilized protein is focused under the microscope (Olympus America Inc. fluorescence microscope CKX41) and checked for the fluorescence signal. Both the control fiber and sample fiber are analyzed for the emission signal. An abundant fluorescence signal is noticed in the center core due to the large size that allows fast and easy flow of a larger quantity of samples inside, compared to the surrounding holes in the case of a fiber immobilized with ER-α positive (MCF-7) cell lysate. The fluorescence signal is found to be linearly increased with the concentration of cell lysate as a result of the larger number of binding surfaces inside. The control fibers (MDA-MB-231 cell lysate immobilized) showed literally no fluorescence signal [see Figs. 17.7(b) and 17.8(b)], whereas the green [see Fig. 17.7(a)] and red [see Fig. 17.8(a)] signals are observed for sample fibers

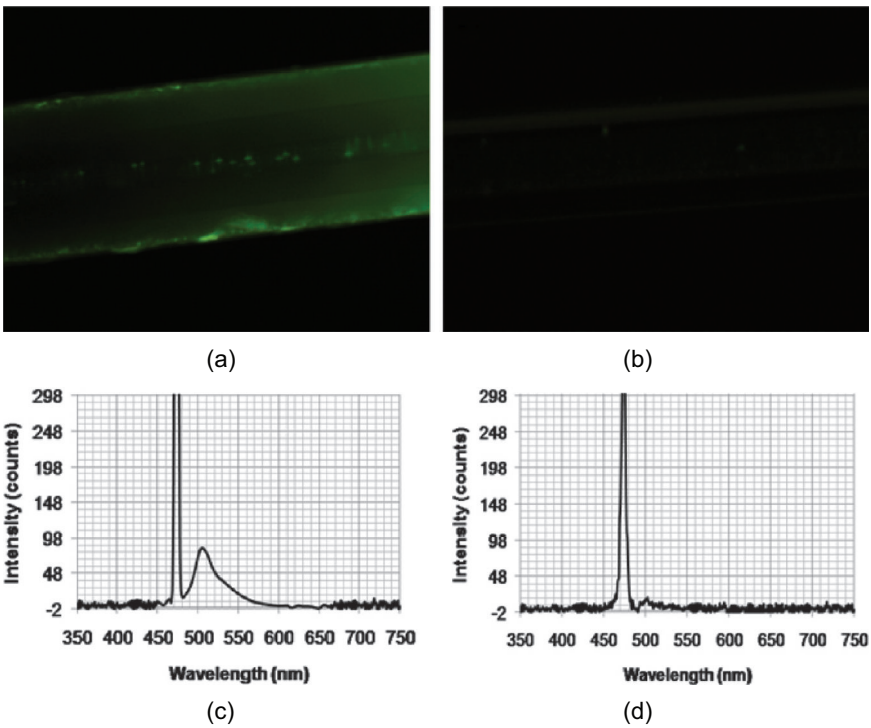

Figure 17.7 (a) and (b) Fluorescence microscopy images of (a) sample fiber with green fluorescent dye and (b) control fiber. (c) and (d) Spectral signatures showing (c) protein binding inside the fiber immobilized with ER-α positive (MCF-7) cell lysate (sample fiber) and (d) ER-α negative (MDA-MB-231) cell lysate (control fiber). (Adapted from Ref. 31.)

(MCF-7 cell lysate immobilized) with secondary antibodies such as green (Alexa Fluor 488) and red (Alexa Fluor 555) dyes.

17.5.1.1 Spectroscopic analysis

The presence of ER-α protein inside the hollow core is further confirmed through the spectroscopic method. The schematic setup used for the spectral analysis of fluorescent proteins is shown in Fig. 17.9. A CW diode-pumped solid state (DPSS) laser (output power ≈ 10 mW) is coupled to the proximal end of the sample-immobilized PCF using a high-precision single-mode fiber coupling (FC) unit (Melles Griot Pte Ltd.) with a microscope objective [20X, 0.65NA (L_1)]. The diverging beam emerging from the distal end of the sample-immobilized fiber is allowed to pass though a 2-*f* lens system, which is configured using two microscope objective lenses [Newport M-20X, 0.4 (L_2) and Olympus UMPLAN FI 50X/0.8 (L_3)]. The 2-*f* lens system focuses the beam into a high-quantum-efficiency spectrophotometer (Ocean Optics QE65000). The spectrometer is coupled to a

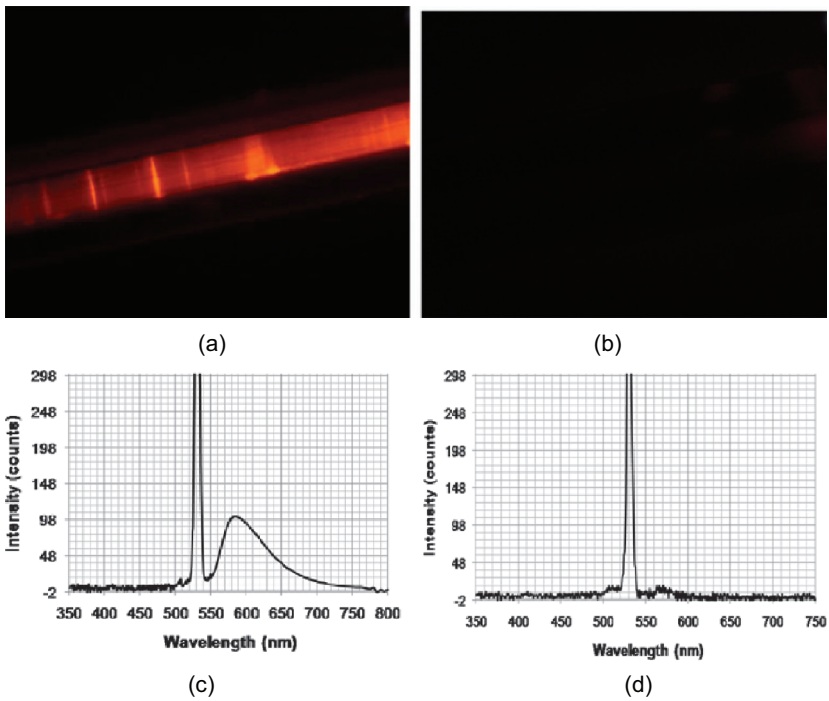

Figure 17.8 (a) and (b) Fluorescence microscopy images of (a) sample fiber with red fluorescent dye and (b) control fiber. (c) and (d) Spectral signatures showing (c) protein binding inside the fiber immobilized with ER-α positive (MCF-7) cell lysate (sample fiber) and (d) ER-α negative (MDA-MB-231) cell lysate (control fiber). (Adapted from Ref. 31.)

PC that displays the spectrum. In our study, lasers with wavelengths of 473 and 532 nm were used for the green fluorescent dye and red fluorescent dye analysis, respectively. Green emission is obtained at around 515 nm for sample fibers (MCF-7 cell lysate immobilized) [see Fig. 17.7(c)] with Alexa

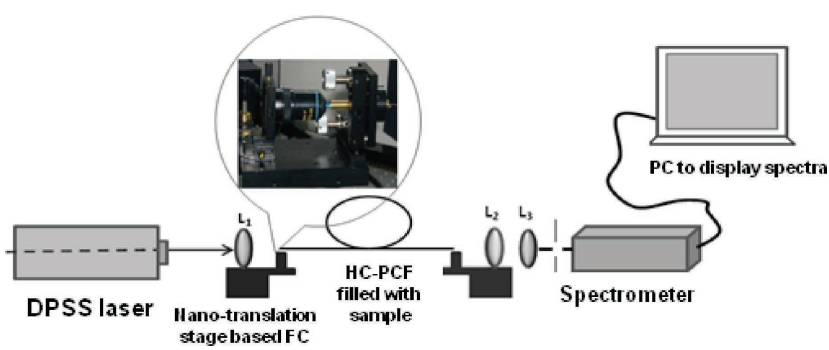

Figure 17.9 Schematic diagram of the setup used for PCF-based EW sensing of samples (adapted from Ref. 36).

Fluor 488 as the secondary antibody. Similarly, red emission at around 585 nm is obtained for sample fibers with Alexa Fluor 555 as the secondary antibody as shown in Fig. 17.8(c). However, in the both cases, control fibers failed to show any fluorescence signals [Figs. 17.7(d) and 17.8(d)]. These spectral signatures authenticate the strong binding of ER-α protein inside the HC-PCF.

17.5.1.2 Image processing method

The distribution of fluorescence in the fiber and the localized presence of protein are investigated by image processing means. In order to understand the distribution of fluorescence inside the fiber, the image is processed with ImageJ, a Java-based program developed at the National Institutes of Health. The wavelengths corresponding to the red dye (Alexa Fluor 555) are extracted from the obtained fluorescence image. The distribution of the extracted intensity along the length of the sample fiber has been normalized and plotted, as given in Fig. 17.10(b). It is clear that the fluorescence

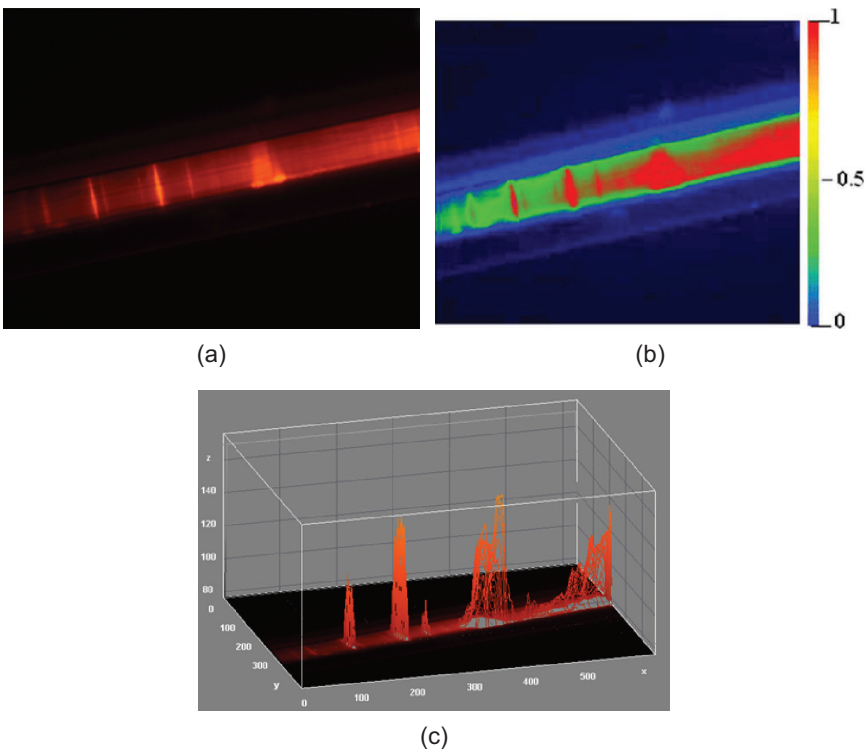

Figure 17.10 (a) Fluorescence microscopic image of Alexa-Fluor-555-labeled MCF-7 cell immobilized inside the HC-PCF. (b) Normalized fluorescence intensity distribution along the length of fiber and (c) its corresponding interactive 3D surface plot.

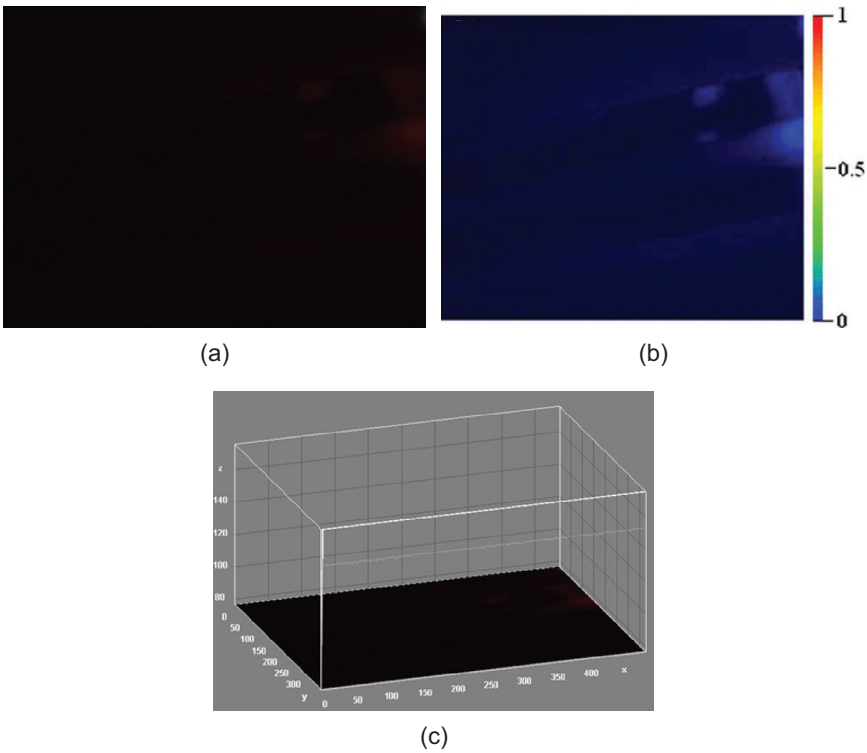

Figure 17.11 (a) Fluorescence microscopic image of Alexa-Fluor-555-labeled MDA-MB-231 cell immobilized inside the HC-PCF. (b) Normalized fluorescence intensity distribution along the length of fiber and (c) its corresponding interactive 3D surface plot.

is distributed along the central hollow core where the cells are immobilized. The fluorescence has concentrated toward the right end facet of the fiber through which the sample is adsorbed inside the fiber. The interactive 3D surface plot of the fluorescence images has been plotted using ImageJ in Fig.17.10(c), which further confirms the presence of localized protein inside the hollow core. These results strongly confirm the specific binding of ER-α protein inside the hollow core. The respective fluorescence microscopic image, normalized fluorescence intensity distribution along the length of fiber, and interactive 3D surface plot of the control fiber (negative cell line-MDA-MB-231 immobilized) are given in Fig. 17.11. The control fiber has failed to produce fluorescence signal due to the lack of a receptor.

17.6 Conclusion

The different aspects of PCF, its guiding mechanism, the RI scaling law, etc. are analyzed and explained in this chapter. In order to recognize the ER-α protein, an antigen–antibody reaction method is employed. The distribution

of fluorescence inside the PCF immobilized with an ER-positive cell and the localization of protein across the length of the fiber have been investigated. The proposed methodology is implemented in array format with immuno recognition of specific proteins using an HC-PCF. The primary step of the experiment is to activate the silica inner core of the fiber to facilitate the detection of ER protein. Poly-L-lysine is used to precoat the inner wall of the fiber to create an activated surface that can effectively bind the targeted protein. In the second step, ER-α positive (MCF-7) and negative cell (MDA-MB-231) lysates are allowed to stick inside different HC-PCFs in order to bind with specified antibodies. The primary antibody raised against ER-α protein (anti-rabbit) is subsequently used to recognize the biomolecule (even in fragments), which is available on the core surface. It is illustrated that the Alexa Fluor 488 (green fluorescent dye) and/or 555 (red fluorescent dye) as a secondary antibody compatible to the anti ER-α protein can be employed. Fluorescence signal is observed inside the fiber core under a microscope in the case of MCF-7-cell-immobilized HC-PCF, whereas MDA-MB-231-cell-immobilized fiber shows literally no signal. This result confirms the possible application of HC-PCF in specifically detecting the presence of protein at a very low sample volume. This method has an additional advantage that the immobilized sample can be analyzed spectroscopically using a simple optical set up. By using a laser with wavelengths such as 473 and 532 nm, the fluorescence spectrum can be obtained for both positive- and negative-cell-immobilized HC-PCF, which further confirms the ability of HC-PCF for specific protein detection. The developed technique enables recognition of ≈20 pg of ER-α protein specifically in a 50-nL sample volume. This method holds great promise in that the HC-PCF can be used as a potential biosensor for medical diagnosis and therapeutics. In general, this sensor can be applied for any other protein of interest, too.

Acknowledgments

Part of the work presented in this chapter was performed when Dr. Saraswathi was working as a Research Fellow with Prof. Murukeshan at the School of MAE, NTU and when Dr. Padmanabhan was with SBIC, Singapore. Dr. Padmanabhan acknowledges SBIC for the support provided when he was there to perform the relevant analysis. The authors MVM and VKS acknowledge the various financial support received through AcRF and NTU-RSS.

References

1. E. Phizicky, P. I. H. Bastiaens, H. Zhu, M. Snyder, and S. Fields, "Protein analysis on a proteomic scale," *Nature* **422**(6928), 208–215 (2003).

2. W. Chen, "Nanoparticle fluorescence based technology for biological applications," *J. Nanosci. Nanotechnol.* **8**(3), 1019–1051 (2008).
3. R. Y. Tsien, "The green fluorescent protein," *Annu. Rev. Biochem.* **67**(1), 509–544 (1998).
4. WHO, "Fact Sheet No. 297: Cancer 2006," Cancer Information Center, USA (2006), http://www.cancer-sos.com/content.php.
5. P. Picard, G. Bunone, J. W. Liu, and O. Donze, "Steroid-independent activation of steroid receptors in mammalian and yeast cells in breast cancer," *Biochem. Soc. Trans.* **25**, 597–602 (1997).
6. V. J. Elwood, "Steroid hormones, receptors, and antagonists," *Ann. N.Y. Acad. Sci.* **784**, 1–17 (1996).
7. D. R. J. Snead, "Methodology of immunohistological detection of oestrogen receptor in human breast carcinoma in formalin-fixed, paraffin-embedded tissue: A comparison with frozen section methodology," *Histopathol.* **23**(3), 233–238 (1993).
8. S. M. Thorpe, "Prognostic value of steroid hormone receptors: Multivariate analysis of systemically untreated patients with node negative primary breast cancer," *Cancer Res.* **47**(22), 6126–6133 (1987).
9. A. P. F. Turner, "Biosensors—sense and sensitivity," *Science* **290**(5495), 1315–1317 (2000).
10. T. Vo-Dinh, "Biosensors and biochips: Advances in biological and medical diagnostics," *J. Anal. Chem. USSR* **366**(6–7), 540–551 (2000).
11. R. I. Stefan, "Immunosensors in clinical analysis," *J. Anal. Chem. USSR* **366**(6–7), 659–668 (2000).
12. H. J. Geerligs, "The influence of pH and ionic strength on the coating of peptides of herpes simplex virus type 1 in an enzyme-linked immunosorbent assay," *J. Immunol. Methods* **106**(2), 239–244 (1988).
13. J. Yang, H. Wang, Y. Jiang, Y. Sun, K. Pan, H. Lei, Q. Wu, Y. Shen, Z. Xiao, and Z. Xu, "Development of an enzyme-linked immunosorbent assay (ELISA) method for carbofuran residues," *Molecules* **13**(4), 871–881 (2008).
14. Y. Chien, M. Ito, Y. Park, T. Tagami, B. D. Gehm, and J. L. Jamsen, "A fusion protein of the estrogen receptor (ER) and nuclear receptor corepressor (NCoR) strongly inhibits estrogen-dependent responses in breast cancer cells," *Mol. Endocrinol.* **13**(12), 2122–2136 (1999).
15. J. M. Harvey, G. M. Clark, C. K. Osborne, and D. C. Alfred, "Estrogen receptor status by immunohistochemistry is superior to the ligand-binding assay for predicting response to adjuvant endocrine therapy in breast cancer," *J. Clin. Oncol.* **17**(5), 1474–1481 (1999).

16. H. Gobbi, "Predictive factors of breast cancer evaluated by immunohistochemistry," *J. Brasil. Patologia Med. Lab.* **44**(2), 131–140 (2008).

17. Y. Zhao and Y. Liao, "Discrimination methods and demodulation techniques for fiber Bragg grating sensors," *Optic Laser Eng.* **41**(1), 1–18 (2004).

18. J. I. Peterson and G. G. Vurek, "Fiber-optic sensors for biomedical applications," *Science* **224**, 123–127 (1984).

19. J. Jensen, P. Hoiby, G. Emiliyanov, O. Bang, L. Pedersen, and A. Bjarklev, "Selective detection of antibodies in microstructured polymer optical fibers," *Opt. Express* **13**(15), 5883–5889 (2005).

20. C. Cordeiro, M. Franco, G. Chesini, E. Barretto, R. Lwin, C. Brito Cruz, and M. Large, "Microstructured-core optical fibre for evanescent sensing applications," *Opt. Express* **14**(26), 13056–13066 (2006).

21. A. S. Webb, F. Poletti, D. J. Richardson, and J. K. Sahu, "Suspended-core holey fiber for evanescent-field sensing," Opt. Eng. **46**, 010503 (2007) [doi: 10.1117/1.2430505].

22. M. van Eijkelenborg, M. Large, A. Argyros, J. Zagari, S. Manos, N. Issa, I. Bassett, S. Fleming, R. McPhedran, and C. de Sterke, "Microstructured polymer optical fibre," Opt. Express **9**(7), 319–327 (2001).

23. P. Russell, "Review: Photonic crystal fibers," Science **299**, 358–362 (2003).

24. J. C. Knight, J. Broeng, T. A. Birks, and P. S. J. Russell, "Photonic band gap guidance in optical fibers," Science **282** (5393), 1476–1478 (1998).

25. D. Mogilevtsev, T. A. Birks, and P. S. J. Russell, "Group-velocity dispersion in photonic crystal fibers," Opt. Lett. **23** (21), 1662–1664 (1998).

26. R. F. Cregan, B. J. Mangan, J. C. Knight, T. A. Birks, P. S. J. Russell, P. J. Roberts, and D. C. Allan, "Single-mode photonic band gap guidance of light in air," *Science* **285**(5433), 1537–1539 (1999).

27. J. C. Knight, T. A. Birks, P. S. J. Russell, and D. M. Atkin. "All-silica single-mode optical fiber with photonic crystal cladding," *Opt. Lett.* **21**(19), 1547–1549 (1996).

28. J. B. Jensen, L. H. Pedersen, P. E. Hoiby, L. B. Nielsen, T. P. Hansen, J. R. Folkenberg, J. Riishede, D. Noordegraaf, K. Nielsen, and A. Carlsen, "Photonic crystal fiber based evanescent-wave sensor for

detection of biomolecules in aqueous solutions," *Opt. Lett.* **29**(17), 1974–1976 (2004).

29. L. Rindorf, P. E. Høiby, J. B. Jensen, L. H. Pedersen, O. Bang, and O. Geschke, "Towards biochips using microstructured optical fiber sensors." *Anal. Bioanal. Chem.* **385**(8), 1370–1375 (2006).
30. S. Smolka, M. Barth, and O. Benson, "Highly efficient fluorescence sensing with hollow core photonic crystal fibers," *Opt. Exp.* **15**(20), 12783–12791 (2007).
31. S. Padmanabhan, V. K. Shinoj, V. M. Murukeshan, and P. Padmanabhan, "Highly sensitive optical detection of specific protein in breast cancer cells using micro structured fiber in extremely low sample volume," *J. Biomed. Opt.* **15**, 017005 (2010) [doi:10.1117/1.3302810].
32. V. K. Shinoj and V. M. Murukeshan, "An integrated hollow-core photonic crystal fiber transverse optical trapping system for optical manipulation and detection," *J. Appl. Phy.* **111**, 023106 (2012).
33. V. K. Shinoj and V. M. Murukeshan, "An HC-PCF based multifunctional optical system for trapping, position sensing and detection of fluorescent particles," *Opt. Lett.* **37**(10), 1607–1609 (2012).
34. T. Birks, D. Bird, T. Hedley, J. Pottage, and P. Russell, "Scaling laws and vector effects in bandgap-guiding fibres," *Opt. Express* **12,** 69–74 (2004).
35. G. Antonopoulos, F. Benabid, T. A. Birks, D. M. Bird, J. C. Knight, and P. S. J. Russell, "Experimental demonstration of the frequency shift of bandgaps in photonic crystal fibers due to refractive index scaling," *Opt. Express* **14,** 3000–3006 (2006).
36. V. K. Shinoj and V. M. Murukeshan, "An HC-PCF fluorescence spectroscopy for detection of microsphere samples based on refractive index scaling law," *Opt. Photon. J.* **1**(2), 85–90 (2011).
37. T. Birks, D. Bird, T. Hedley, J. Pottage, and P. Russell. "Scaling laws and vector effects in bandgap-guiding fibres," *Opt. Express* **12**(1), 69–74 (2004).
38. P. B. Luppa, L. J. Sokoll, and D. W. Chan. "Immunosensors: Principles and applications to clinical chemistry," *Clin. Chim. Acta*, **314**(1–2), 1–26 (2001).
39. M. M. Bradford, "A rapid and sensitive method for the quantitation of microgram quantities of protein utilizing the principle of protein-dye binding," *Anal. Biochem.* **72**(1–2), 248–254 (1976).

Vadakke Matham Murukeshan has been with the School of Mechanical and Aerospace Engineering, Nanyang Technological University (NTU), Singapore, since 1997, where he works as an associate professor. His major research interests are optical interferometric and plasmonic lithography, biomedical optics, MEMS and waveguide optics, speckle metrology, fiber optic sensors, and optofluidics. He has guest edited international journal special issues and currently serves on the editorial boards of the *International Journal of Optomechatronics* and the *Journal of Holography and Speckle*. He has published over 220 international journal and conference proceedings papers and 3 book chapters. He also holds four patents in the areas of applied optics, laser speckle, and bio-optics for medical and forensic applications. He leads research teams working in the areas of optics and metrology, nanoscale optics, and biomedical optics. He is currently the deputy director of the Center for Optical & Laser Engineering (COLE) of NTU.

Vengalathunadakal Kuttinarayanan Shinoj completed his Ph.D. at the School of Mechanical & Aerospace Engineering, NTU, Singapore, in 2012. He received his M.Sc. degree in Physics from Cochin University of Science and Technology, India, in 2006. Dr. Shinoj is currently a Research Associate at Singapore Eye Research Institute (SERI), Singapore. His main research interests include microstructured photonic crystal fiber and biomedical optical imaging and sensors.

Saraswathi Padmanabhan was a Research Fellow at Mechanical and Aerospace Engineering, NTU, Singapore. She was a biologist by training at NEERI-CSIR, India and Cornell University, USA and currently conducts research at the Singapore Eye Research Institute. Her main research interests are biomedical optical imaging and clinical microbiology.

Parsuraman Padmanabhan was a research manager at the Singapore BioImaging Consortium (SBIC) where he performed multimodality molecular imaging research and development. He received postdoctoral training at Cornell University, USA and Stanford University, USA. He has 20 years of experience in biological research and is currently with Biopharma Training Institute Pte Ltd., Singapore.

Chapter 18
Quality Assurance in Digital Mammography

Kwan-Hoong Ng
Department of Biomedical Imaging, University of Malaya, Kuala Lumpur, Malaysia

Tânia Aparecida Correia Furquim
Instituto de Eletrotécnica e Energia da Universidade de São Paulo, São Paulo, Brazil

Noriah Jamal
Malaysian Nuclear Agency, Kajang, Malaysia

18.1 Introduction

18.1.1 Scope

The chapter is intended to provide overviews of the following:

- quality assurance (QA) programs for digital mammography,
- quality control (QC) test procedures based on the American College of Radiology (ACR) and the International Atomic Energy Agency (IAEA),
- the role of medical physicists in mammography QA programs, including acceptance, annual, and regular QC testing, and
- the role of technologists/radiographers in mammography QA programs, including regular QC testing.

Recent advances in digital detector technology have paved the way to full-field digital mammography (FFDM) systems. The performance of these systems has evolved to the point where replacement of screen-film mammography (SFM) systems is becoming realistic. FFDM has several inherent advantages, such as wide dynamic range, reduction in recall rates, potential for reduction in radiation dose, increased patient throughput, postprocessing capability, and digital acquisition.[1,2] There is an urgent

need to implement an effective QA program for ensuring optimum diagnostic information and patient safety.

18.2 Technical Quality Control

A high-quality digital mammogram must meet clinical requirements to ensure that the radiologist can identify the following five features:[3]

(1) the characteristic morphology of a mass,
(2) the shape and spatial configuration of calcifications,
(3) distortion of the normal architecture of the breast tissue,
(4) asymmetry between images of the left and right breast, and
(5) the development of anatomically definable new densities when compared to prior studies.

In order to produce a high-quality digital mammogram, a quality assurance program (QAP) should be implemented. Thus, a QAP can be defined as a program that ensures the soundness of the entire mammography process, including image production, radiography technique, and technical components, as well as the administrative and personnel aspects.

The QAP follows several steps to obtain good results, such as determining who will be responsible for possible corrective actions, complemented by administrative procedures, which include conducting acceptance testing of equipment and facility, conducting routine QC testing, and taking continuing education courses.

Routine testing is periodic and must be conducted in accordance with specific procedures for different types of equipment, accessories, image viewers, printers, conference reports, and examinations. These tests need to be recorded and monitored on an on-going basis.

In the *Quality Control Manual*[4] (ACR/1999) on mammography screen-film system, it is specified that tests should be performed by technologists and medical physicists. Even with the transition to digital mammography, many ACR/1999 tests remain valid, such as kVp Accuracy and Reproducibility, beam quality assessment [half-value layer (HVL) measurement], and radiation output rate. However, many more tests have been added depending on the type of detector being used. For accreditation with the ACR, the facilities must follow the quality control procedures provided by the manufacturers' manuals.

In the IAEA mammography quality assurance publication,[5] which provides the QAP for dedicated digital mammography, the methods of measurement are integrated, differing from the ACR QAP (see Appendices 18.1 and 18.2). However, the division of tasks between medical physicists and technologists is still maintained. The tests to be performed by medical physicists and technologists are shown in Table 18.1. For QA to produce

Table 18.1 Tasks of a quality assurance program QAP for medical physicists and technologists according to American College of Radiology (ACR) and International Atomic Energy Agency (IAEA) documents. (SNDR is signal-difference-to-noise ratio.)

Tests	Performed by	
	ACR	**IAEA**
Mammography unit assembly	Medical Physicist	Medical Physicist
Compression force and thickness	Technologist	Medical Physicist
Site technique factors for SDNR (radiographer baseline)	Medical Physicist	Medical Physicist
Automatic exposure control evaluation	Medical Physicist	Medical Physicist
Baseline detector performance	Medical Physicist	Medical Physicist
Spatial linearity and geometric distortion of the detector	Medical Physicist	Medical Physicist
Detector ghosting	Medical Physicist	Medical Physicist
Detector uniformity and artifact evaluation	Medical Physicist	Medical Physicist
Modulation transfer function	Medical Physicist	Medical Physicist
Limiting spatial resolution	Medical Physicist	Medical Physicist
Beam quality assessment (HVL)	Medical Physicist	Medical Physicist
Incident air kerma at the entrance surface of PMMA slabs	Medical Physicist	Medical Physicist
Mean glandular dose (MGD)	Medical Physicist	Medical Physicist
Collimation system	Medical Physicist	Medical Physicist
Image display quality	Medical Physicist	Medical Physicist
Laser printer (where applicable)	Technologist	Medical Physicist
Phantom image quality	Technologist (monthly)	Medical Physicist
Monitor inspection, cleaning, and viewing conditions	Technologist	Technologist
Digital mammography equipment daily checklist	Technologist	Technologist
Daily flat-field phantom image	Technologist	Technologist
Visual inspection for artifacts (CR systems only)	Technologist	Technologist
Laser printer sensitometry and artifacts	Technologist	Technologist
Image plate erasure (CR systems only)	Technologist	Technologist
Monitor QC	Technologist	Technologist
View box cleanliness	Technologist	Technologist
Weekly QC test object and full-field artifacts	Technologist	Technologist
Safety and function checks of examination room and equipment	Technologist	Technologist

(*continued on next page*)

Table 18.1 (*Continued*)

Tests	Performed by	
	ACR	IAEA
Full-field artifacts	Technologist	Technologist
Printed image quality	Technologist	Technologist
Repeat image analysis	Technologist	Technologist
Spatial resolution test (CR and scanning systems only)	Technologist	Technologist

good results, these tests must rely on administrative procedures to ensure corrective actions where necessary.

Although many tests are the same as with screen-film mammography, special attention should be given to equipment that produces digital images. If there is no image quality and dose optimization, the detectors can introduce new types of artifacts, and the dose may be higher than that emitted by screen-film equipment.

18.3 Testing by Medical Physicists and Equipment Performance

Medical physicists must perform the acceptance tests to ensure that the equipment is able to carry out the clinical routine with the highest quality. Some equipment, such as GE Senographe Essential or DS and Hologic Selenia®, require special attention in the selection of technical parameters by automatic exposure control (AEC). Two tables can be selected for the equipment according to expected response in entrance surface air kerma (ESAK); an example of calibration using slabs of PMMA (45- and 63-mm thickness) is presented in Fig. 18.1. Calibration should be carried out during the installation of equipment before the acceptance test.

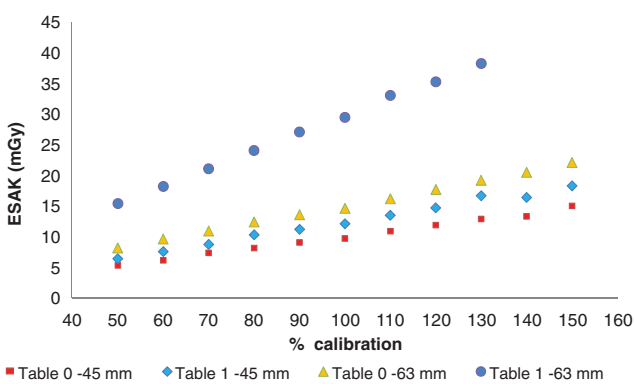

Figure 18.1 Selenia detector response to a selection of Table 0 or 1 according to the expected response to ESAK. The percentage of calibration varies and can be chosen from within each table.

18.3.1 Mammography unit assembly evaluation

The mammography unit requires care in all its mechanical components and accessories, since they can be damaged by the intense use. A common problem is compression plate crack, which can be harmful to the patient. In addition, special attention must be given to the control room temperature due to the sensitivity of the detector, which may stop working if the temperature is not in the proper range. These issues and other items as shown in Appendix 18.3 checklist must be checked frequently (semi-annually is desirable; annually is essential) to ensure that the examinations can be carried out without problems.

18.3.2 Compression force and thickness accuracy

18.3.2.1 Compression force

Compression force is one factor that makes the mammography exam painful and uncomfortable for a patient. However, compression is critical for the exam because it reduces the thickness of the breast and serves several key functions:[5]

- reduces scattered radiation,
- increases contrast,
- reduces radiation exposure to the breast,
- improves image sharpness,
- minimizes focal spot blurring of structures in the image,
- minimizes patient motion, and
- results in more-uniform image densities.

As the compressed breast thickness determines the choice of technical factors for exposure, it is important that the compression parameter is calibrated. It is necessary that both modes of compression are evaluated, namely powered and manual.

To check the compression force, use an analog bathroom scale and bath towels or blocks of rubber foam. Place the bathroom scale on the bucky resting on a towel for protection, and place another towel (or blocks of foam rubber) on top, properly centered, and set the bathroom scale to zero. Using the power drive, activate the compression paddle and allow it to operate and stop automatically at the maximum available powered force. Some equipment has staged compression, in which case, compress several times until it ceases. Record the values of compression force shown on the bathroom scale and equipment. Release the compression and then check the manual mode. Move the compression paddle until it stops. Record the maximum compressive force F and make sure that the values are within the limits. For ACR, 111 N $\leq F \leq$ 200 N; for IAEA, 150 N $< F <$ 200 N, and for powered compression, $F <$ 300 N, where displayed value accuracy is ±20 N.

18.3.2.2 Thickness accuracy

As thickness must be considered in the choice of technical factors, this parameter needs to be calibrated. To check the thickness accuracy, use blocks of PMMA with thicknesses of 20, 45 and 70 mm, ideally with the size of 18 cm × 24 cm (to avoid deformation of the compression paddle).

Centralize the PMMA blocks laterally, align them with the chest wall edge, and activate the compression paddle until the clinically used compression force is achieved. The performance criteria are:

ACR: According to manufacturers' manuals. For example, for Hologic Selenia, the displayed thickness is within ±5 mm of the slab thickness.

IAEA: Acceptable: The displayed thickness is within ±8 mm of slab thickness.
Achievable: The displayed thickness is within ±5 mm of slab thickness.

18.3.3 Site technique factors for SDNR (radiographer baseline)

An imaging system is designed to give the observer an image containing a signal that can be recognized on a background of noise. Noise is one of the image parameters that can produce more problems, since it can lead to nonidentification of findings. Noise is produced by all systems and by various sources, from electronic signals generated by background noise detector electronics to the structure of a normal breast tissue. When an electronic detector is at rest waiting for an x-ray exposure, it produces signals that come from random background noise, and many sources cannot be eliminated. Thus, the noise must be constantly evaluated to ensure that the image quality of the system is maintained at optimal levels.

This test should be performed by a medical physicist during acceptance testing to obtain a baseline of technical parameters, while the routine test should be performed weekly by a technologist. According to the IAEA, the test consists of placing a 45-mm-thick PMMA test object, centered and laterally aligned with the chest wall edge of the digital image receiver, with a 1-mm-thick contrast object of placed 40 mm from the chest wall. The compression force should be recorded, including the thickness shown by the equipment, the position of the AEC sensor (where applicable), target, filter, kV, grid, density control position, and operating mode (automatic or semiautomatic). This test should be performed routinely by a technologist, always under the same conditions. The image obtained from this phantom should be analyzed in the DICOM image format "for presentation." The window width and window level used to analyze the image will also be used for routine testing by the technologist.

According to the IAEA publication,[5] this part of the test is subjective, and is designed to check for artifacts. The expected results should be the absence of:

- blotches or regions of altered texture appearance,
- observable lines or structural artifacts, and
- "bright" or "dark" pixels that are evident.

18.3.4 Automatic exposure control evaluation

The AEC evaluation aims to verify whether the automatic choice of technical parameters by the equipment ensures quality images in different compressed breast thicknesses, associating with an acceptable level of SNR. This test is performed in two parts: (1) to verify that the AEC compensates for the compressed breast thickness, and (2) to check the variations of density control (where applicable).

18.3.4.1 Thickness behavior

To verify the compressed breast thickness, it is necessary to use slabs of PMMA or BR12, with thickness of 20 to 70 mm. If using PMMA, one should consider that the thickness of PMMA and typical breasts are not equal; thus, to achieve the same thickness read by the equipment, spacer thicknesses should be placed (method shown in Table 18.2[6]).

Place the contrast disk or square of 1-mm thickness positioned 40-mm from the chest wall on the upper surface of PMMA (Fig. 18.2). Compress with the force used clinically (if using the protocol for GE equipment, as

Table 18.2 Spacer thicknesses used for attaining thickness equivalence between PMMA and typical breasts.[6]

Equivalent breast thickness (mm)	PMMA thickness (mm)	Spacer thickness (mm)
21	20	0
53	45	8
90	70	20

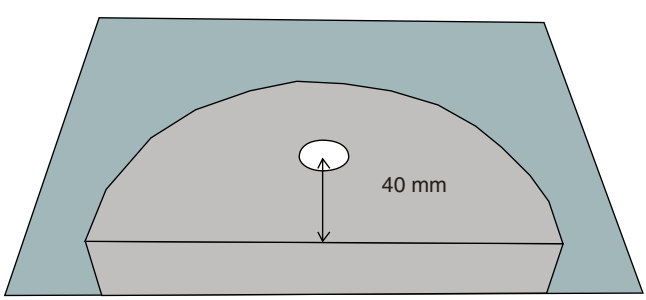

Figure 18.2 Slabs of PMMA with a 1-mm-thick contrast object positioned 40 mm from the edge of the chest wall.

per ACR, compress to 50 N). Choose the exposure mode used clinically; however, if conducting the acceptance test, all modes should be tested.

After exposure, record the technical parameters, which will be used to determine the incident air kerma. The incident air kerma, in turn, is used to calculate the mean MGD. This test should be performed for the three thicknesses, which vary according to the protocol to be followed:

IAEA: for thickness shown in Table 18.2.
ACR: GE Senographe: 25 mm, 50 mm, 60 mm.
Hologic Selenia: 20 mm, 40 mm, 60 mm, 80 mm.

In unprocessed images taken at all thicknesses, place a region of interest (ROI) in the contrast object area and another outside it. Calculate the SDNR according to

$$SDNR = \frac{|A - B|}{C}, \tag{18.1}$$

where A and B are the mean pixel value (MPV) of the ROIs placed in the areas of image background and the object contrast, respectively, and C is the ROI value of the background standard deviation.

The methods to analyze the results differ according to the protocol being used:

IAEA: The SDNR values for images of 20, 45, and 70 mm of PMMA should exceed the acceptable values given in Tables 18.3 and 18.4 for the aluminum and PMMA contrast object, respectively.
ACR: One should follow manufacturers' recommendations:

- GE Senographe DS or Essential: The expected results are presented in Table 18.5. SNR values must be assessed from a baseline.
- Hologic Selenia: The pixel value of each individual image corresponding to a breast thickness between 20 and 80 mm at any operating mode should not vary more than 10% of the mean value recorded from all tested breast thickness and operating modes.[7]
- In the Mammography Quality Standards Act (MQSA) form, "Medical Physicist's Mammography QC Test Summary: Full-Field Digital – Hologic or GE," the results should only be recorded as "pass" or "fail."

18.3.4.2 Density control

In the case of equipment that controls the variation in densities, allowing adjustments to the mAs (milliampere × second), test all of the possible steps of change. Use the 40-mm thickness and vary the steps from –3 to +4, or vary the steps for the particular equipment. Evaluate the SDNR of each image "for processing" and calculate the time from mAs for each

Table 18.3 Acceptable and achievable values for SDNR for AEC evaluation 0.2-mm-thick aluminum contrast object (used with permission from IAEA[5]).

	PMMA thickness (mm)					
	20		45		70	
System	Acceptable	Achievable	Acceptable	Achievable	Acceptable	Achievable
Agfa CR (MM3.0)	13.8	20.1	12.4	18.0	10.8	15.8
Agfa CR (HM5.0)	10.2	15.0	8.9	13.0	8.0	11.7
Fuji CR	9.8	14.2	8.8	12.8	7.7	11.2
Fuji Amulet	6.1	8.7	5.5	7.8	4.8	6.8
GE 2000D	8.9	12.9	7.9	11.5	6.9	10.0
GE DS	8.9	12.9	7.9	11.5	6.9	10.0
GE Essential	12.7	18.4	11.3	16.5	9.9	14.4
Hologic Selenia	4.8	7.0	4.3	6.3	3.8	5.5
IMS Giotto	7.8	11.3	7.0	10.1	6.1	8.8
Carestream CR (M2 plate)	9.5	13.9	8.5	12.5	7.5	10.9
Carestream CR (M3 plate)	11.7	17.0	10.2	14.8	9.1	13.3
Konica CR (RP-6M)	11.4	16.6	10.2	14.8	8.9	13.0
(RP-7M)	8.7	12.8	7.8	11.4	6.8	10.0
(CP-1M)	6.6	9.5	5.9	8.5	5.1	7.5
Planmed Nuance	6.3	9.1	5.0	7.2	4.3	6.2
Sectra D40	3.6	5.3	3.2	4.7	2.8	4.1
Sectra L30	3.6	5.3	3.2	4.7	2.8	4.1
Siemens Novation DR	5.1	7.4	4.5	6.6	4.0	5.8
Siemens Inspiration	4.4	6.3	3.9	5.7	3.4	5.0

exposure. Calculate the variation in pixel value with respect to the mean value computed for the zero-exposure compensation step. The results should be evaluated according to the protocol adopted as follows:

IAEA: The techniques chosen should not result in an exposure time greater than 5.0 s for 70 mm of PMMA, and the exposure time should be less than 2.5 s for a 45-mm PMMA slab. These time limits do not apply to scanning-type systems.

ACR: The MQSA form does not go into detail, but the manufacturer's manual, particularly for the Hologic Selenia, gives the criteria shown in Table 18.6.

18.3.5 Baseline for detector performance

The baseline must be established for the response and noise characteristics of the image acquisition system under standard radiation exposure conditions. Therefore, one should use the contrast object (0.2-mm aluminum

Table 18.4 Acceptable and achievable values for SDNR used for AEC evaluation of 1-mm-thick PMMA contrast object (used with permission from IAEA[5]).

	PMMA thickness (mm)					
	20		45		70	
System	Acceptable	Achievable	Acceptable	Achievable	Acceptable	Achievable
Agfa CR (MM3.0)	5.8	8.7	5.1	7.8	4.3	6.7
Agfa CR (HM5.0)						
Fuji CR	3.9	6.5	3.4	5.8	2.9	4.8
Fuji Amulet	2.1	3.4	1.8	2.9	1.5	2.5
GE 2000D	3.4	5.61	3.0	5.0	2.5	4.1
GE DS	3.4	5.61	3.0	5.0	2.5	4.1
GE Essential	5.2	7.9	4.6	7.0	3.9	6.0
Hologic Selenia	1.5	2.6	1.3	2.2	1.0	1.8
IMS Giotto	2.9	4.6	2.6	4.0	2.1	3.4
Carestream CR (M2 plate)	3.8	5.8	3.3	5.1	2.8	4.4
Carestream CR (M3 plate)						
Konica CR (RP-6M)	4.6	7.1	4.1	6.2	3.5	5.4
(RP-7M)	3.4	5.3	2.9	4.6	2.5	4.0
(CP-1M)	2.3	3.8	2.0	3.3	1.7	2.8
Planmed Nuance	1.2	2.0	1.6	2.7	2.4	3.9
Sectra D40	0.9	1.7	0.8	1.5	0.6	1.2
Sectra L30	0.9	1.7	0.8	1.5	0.6	1.2
Siemens Novation DR	1.6	2.7	1.4	2.4	1.1	2.0
Siemens Inspiration	1.3	2.2	1.1	1.9	0.9	1.6

or 1-mm PMMA) over 45-mm PMMA, with the center at a distance of 60 mm from the chest wall. One compresses and images in AEC mode and then reproduces these parameters in manual mode, but with mAs values as close as possible to those achieved in automatic mode. One obtains images for three different values of mAs. The incident air kerma without backscatter is measured using a dosimeter appropriate for mammography in mAs values obtained above. Calculate the SDNR [Eq. (18.1)] with the values

Table 18.5 Expected results for the verification of the STD mode in equipment GE.[7]

PMMA thickness (mm)	Exposure parameters for standard mode only			SNR
	Track/filter	mAs	kV	
25	Mo/Mo	20–60	26	>50
50	Rh/Rh	40–90	29	
60	Rh/Rh	16–120	30 or 31	

Table 18.6 The exposure compensation step should result in the following changes in pixel value when dividing the pixel value at a given step by the MPV at step 0.[8]

Step	Change in pixel value
–3	0.50 to 0.61
–2	0.63 to 0.77
–1	0.77 to 0.94
+1	1.04 to 1.27
+2	1.17 to 1.43
+3	1.31 to 1.60
+4	1.44 to 1.76

obtained in ROI 1 and 2, as shown in Fig. 18.3, for each image, and plot the values of MPV (B), the variance (C^2), and SDNR versus mAs.

For linear systems, perform a linear fit to obtain the slope, intercept, and correlation coefficients (R^2). For logarithmic systems, it may be necessary to plot the MPV and variance against 1/mAs to obtain a straight line. Some manufacturers intentionally add a pixel value offset (B_0) to their image data, obtained from the manufacturer's technical documentation or the intercept obtained. To calculate the average value of this quantity, use the following equation:

$$\frac{B - B_0}{mAs}. \tag{18.2}$$

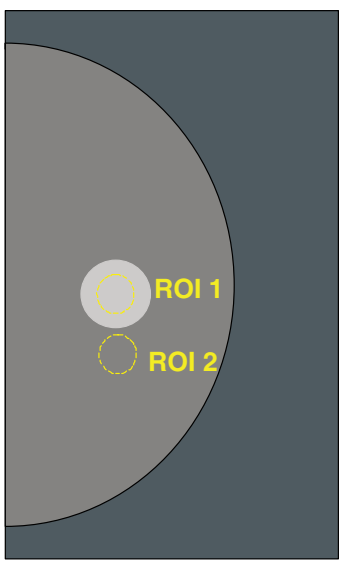

Figure 18.3 Obtaining values in ROIs for calculating SDNR.

Table 18.7 Detector response and noise tolerance (used with permission from IAEA[5]).

System type	Parameter	Acceptable tolerance
Nominally linear (DR)	MPV (B–B_0)	(B–B_0) ≤ 10%
	Standard deviation (C)	C ≤ 5%
	SDNR	SDNR ≤ 5%
Nonlinear (CR)	Fuji, Philips, Konica—S#	S# ≤ 10%
	Agfa—SAL/SALlog/PVIlog	±5%/±430/±580
	Carestream—EI	EI ≤ 40 units

For CR systems without ROI capability, compare the values of the exposure index (EI) at each mAs value with the baseline and the results of previous tests. The results using IAEA standards should agree with the detector response and noise tolerances (Table 18.7), and

- For linear [digital radiology (DR)] systems: The plot of MPV (B) and variance (C^2) versus mAs should be linear with $R^2 \geq 0.95$. All values of (B–B_0)/mAs should be within 10% of the mean value of this ratio.
- For logarithmic (CR) systems: EI versus mAs should be linear with $R^2 \geq 0.95$.

18.3.6 Spatial linearity and geometric distortion of the detector

A test that checks for distortion in straight lines in both contact and magnification mode is performed as follows. Place a geometric distortion test tool (with parallel lines at 20 mm spacing and lines angled at 45 deg to the edges of the tool) on the breast support plate and center it. Analyze the image of the distortion phantom acquired in automatic mode using appropriate window width and window level settings such that the lines are clearly visible. Examine the image for uniformity of sharpness across the image and for any distortion in the regular pattern. Calculate the effective detector element (del) size referenced to the breast support table measuring vertical and horizontal distances, which must be obtained in pixels. The results should agree with the following criteria for IAEA:

- The effective del width and length (x and y) dimensions should be within 5% of each other.
- The image size (in cm) in each dimension should be within 10% of the manufacturer's stated nominal image size.
- The distances measured using the annotation tool should be within 5% of the true size.
- There should be less than 2% deviation from a straight line over a 100-mm length in the center of the field.

18.3.7 Detector ghosting

This measurement aims to assure that the level of detector ghosting does not interfere with image quality. The goal of the test is to cause a ghost image to appear in the detector in order to quantify it. Place a PMMA slab of 45 mm on the support of the breast, and select a technique that is clinically used for a standard breast. Turn the slab 90 deg so that it covers one-half of the useful area of the detector, as shown in Fig. 18.4. Make an exposure with the same technique twice, with the minimal time between acquisitions allowed by the equipment. Use the image "for processing," if possible, to visualize the ghost. Calculate according to Eq. (18.3), obtaining the data of ROI, as shown in Fig. 18.4.

$$Ghost\,image\,SDNR = \left| \frac{A - B}{C} \right|. \tag{18.3}$$

This factor can have values described as follows:

IAEA: Acceptable: ghost image SDNR ≤ 2.0.

ACR: Manufacturers (more precisely Hologic) describe a slightly different method, where instead of taking two images with the PMMA half of the detector, it takes only one. Place a 0.1-mm sheet of aluminum over the PMMA, in the position that covers the entire detector. Thus, the calculation will be as is shown in the following equation and in Fig 18.5:

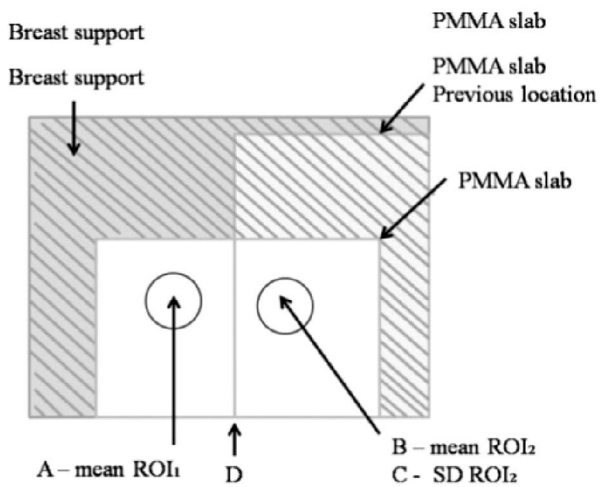

Figure 18.4 Analysis of the ghost image obtained with PMMA in different positions.

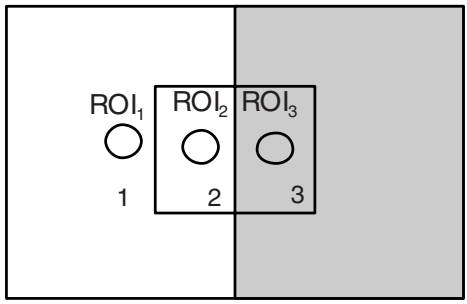

Figure 18.5 Position of ROI to calculate the ghost image factor.

$$Ghost\,image\,factor = \frac{mean_3 - mean_2}{mean_1 - mean_2}. \tag{18.4}$$

In this method, the recommendation is that the ghost image factor value should be within ±0.3.

18.3.8 Detector uniformity and artifact evaluation

A qualitative assessment of uniformity and artifacts in the detector is performed as follows. Use a 45-mm-thick slab of PMMA or a sheet of aluminum, 2–3-mm thick. Apply a compression force and make an exposure turning off any image enhancements or postprocessing options. Images should be acquired for all target–filter combinations. In the magnification mode, image using a 25-mm-thick slab of PMMA or a sheet of aluminum, 1–2 mm thick. Examine the unprocessed images and select a window width and window level that allows artifact severity assessment without accentuating the noise excessively. The analysis is performed according to the following protocols:

IAEA, none of the following should be visible:

- dead pixels, missing lines, or missing columns of data at a level that could interfere with the detection of anatomical structures or could mimic structures that do not actually exist in the breast;
- distracting structured noise patterns in a uniform phantom image;
- regions of discernibly different density on an unprocessed image of a uniform phantom; and
- unexpected variation in apparent texture or magnitude of the noise across the uniform image. If necessary, calculate the SNR from ROIs placed in regions of nonuniformity and compare them.

Table 18.8 Artifact evaluation exposure techniques for Hologic Selenia.

X-ray tube	Mode	kVp	Filter 1st image	Filter 2nd image	Focal Spot
Mo	Auto-time	28	Mo	Rh	Large
W	Auto-time	28	Rh	Ag	Large

ACR: Manufacturers apply this test, but each requests a different thickness of PMMA:

- GE: a 25-mm-thick uniform sheet of PMMA. The image must be analyzed with window width in the range of about 400 to 450 and a window level that allows visualization of artifacts. The qualitative analysis is the same as that presented by IAEA.
- Hologic Selenia: a 40-mm-thick uniform sheet of PMMA. The image must be acquired without compression paddle. The artifact evaluation exposure techniques are presented in Table 18.8. The window width is suggested to be set at 500 and window level at 350. The qualitative analysis is the same as that presented by IAEA.

18.3.9 Modulation transfer function

The spatial resolution of the imaging system or component can be described by modulation transfer function (MTF) in terms of its ability to transfer the signal from its input to output as a function of the spatial frequency of the signal.[9] Thus, MTF quantifies how an imaging system reproduces high-contrast objects with varying size. It represents the relationship between contrast and spatial resolution.[10] This is a fundamental parameter in the analysis of image quality and is easy to quantify. Two different methods can be used: one employs the linear edge of high contrast, and the second employs the high-contrast resolution pattern. The first method was adopted by IAEA,[5] and the second was adopted by equipment manufacturers in their quality control manuals.[7,8]

18.3.9.1 High-contrast edge

The first method for determining the MTF of a system is to measure its edge spread function (ESF) using an opaque object with a straight edge.[11] To measure, use a square piece of metal foil with very straight edges, 20–50 mm on a side, and provide a high contrast in the mammography energy range. Place the foil over the 45-mm-thick slab of PMMA, which is slightly angled (2–5 deg) with respect to the chest wall edge of the breast support table. Make an exposure using manual mode and use the proper techniques for the uniform image region without reaching the minimum

Table 18.9 Acceptable frequencies at which the MTF falls to 50% and 20% (cycles/mm) (used with permission from IAEA[5]).

	Contact mode	
System	**50%**	**20%**
Agfa CR (MM3.0)	2.0/2.0	4.5/3.5
Agfa CR (HM5.0)	2.5/2.0	5.5/4.5
Carestream CR (EHR-M3)	2.0/2.0	4.5/4.0
Carestream CR (EHR-M2)	1.5/1.5	3.5/3.0
Konica CR (RP-6M)	2.5/2.0	5.0/3.5
(RP-7M)	3.0/2.0	6.0/4.0
(CP-1M)	3.5/2.0	7.5/4.0
Fuji Amulet	4.5/4.5	7.5/4.5
Fuji Profect (HR-BD)	3.0/2.0	6.0/4.0
GE 2000D	2.5/2.5	5.0/5.0
GE DS	3.5/3.5	6.0/6.0
GE Essential	2.5/2.5	4.5/4.5
Hologic Selenia	6.5/6.5	9/9
IMS Giotto	4.0/4.0	6.5/6.5
Philips PCREleva	5.0/5.0	9.0/8.0
Planmed Nuance	4.5/5.5	9.0/8.0
Sectra L30	4.0/5.5	6.0/8.0
Siemens Novation DR	5.0/5.0	8.0/8.0
Siemens Inspiration	5.0/5.0	9.0/8.0

or maximum pixel values for the system. Analyze the image "for processing" with MTF software provided by http://humanhealth.iaea.org.

According to IAEA,[5] the tolerances are for spatial frequencies where the MTF:

- has fallen to 50% and 20% and should not be less than the values specified in Table 18.9 for the relevant model of digital mammography equipment.
- at 2.5, 5.0, and 7.5 cycles/mm should not change more than 10% from the value established at acceptance tests of the equipment.

18.3.9.2 High-contrast resolution pattern

The second method uses a high-contrast resolution pattern with frequencies of 2.09 and 3.93 lp/mm over 45 mm of PMMA. If the equipment used is GE Senographe 2000D, DS, or Essential, disable the "fine view" mode. Remove the compression paddle and orient the resolution pattern parallel to the anode-cathode axis (perpendicular to the chest wall edge of the bucky). Image the pattern in manual exposure mode and set the

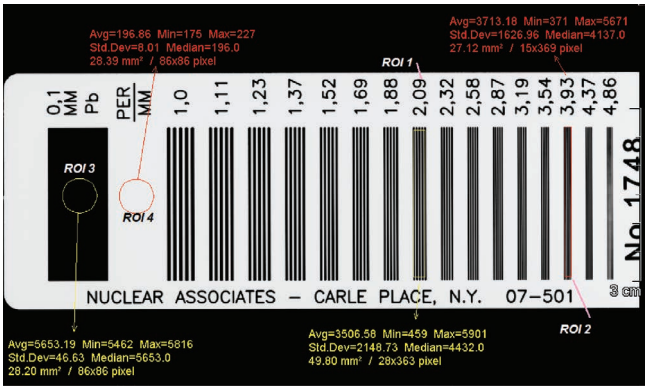

Figure 18.6 MTF analysis for a high-contrast resolution pattern for large focal spot.

following parameters: Mo-Mo, 30 kVp and 140 mAs. Image the pattern again with the technical parameters: Rh-Rh, 30 kVp and 140 mAs. Repeat this procedure with the resolution pattern perpendicular to the anode-cathode axis.

Analyze the images "for processing" obtained by adjusting the window width and window level for optimum visibility of the bar pattern image. Place the ROI of 1 to 4, as shown in Fig. 18.6. Equation (18.5) below shows how to calculate MTF in the desired frequency $M(f)$, $f = 2.09$ and 3.93 lp/mm for large focal spot and 5 and 8 lp/mm for the small focal spot, considering the parameters mean value (S_i) and standard deviation (N_i) in an ROI, with $i = 1$ to 4:

$$M_0 = \frac{\sqrt{2}}{\pi}(S_3 - S_4) = 0.45(S_3 - S_4), \qquad N^2 = \frac{N_3^2 + N_4^2}{2},$$
$$M(f) = \frac{\sqrt{N^2(f) - N^2}}{M_0}. \tag{18.5}$$

The MTF values for GE Senographe 2000D, DS, and Essential equipment must exceed the action limits specified in Table 18.10.

18.3.10 Limiting spatial resolution

In a screen-film system, checking the size of the focal spot is sufficient to indicate the system resolution, based on the results of the line-pair test object. In a digital system, as the detector resolution is limited by the del size, this measurement is not appropriate.[12] To evaluate the spatial resolution of a digital system, it is recommended to calculate the MTF. However, if this is not possible, an alternative is to measure the limiting spatial resolution. This test is similar to that recommended for screen-film systems, using

Table 18.10 Action limits to MTF values in GE equipment.

		Large Focal		Small focal spot	
Track	**Axis**	**Frequency (lp/mm)**	**Action limit**	**Frequency (lp/mm)**	**Action limit**
Mo	Width	2.09	0.58	5	0.34
Rh	Width	2.09	0.58	5	0.34
Mo	Length	2.09	0.58	5	0.34
Rh	Length	2.09	0.58	5	0.34
Mo	Width	3.93	0.26	8	0.11
Rh	Width	3.93	0.26	8	0.11
Mo	Length	3.93	0.26	8	0.11
Rh	Length	3.93	0.26	8	0.11

a star or bar resolution pattern covering at least the range 5–12 lp/mm. Thus, the recommended values for the system performance are:

IAEA: Baseline value: Achievable—The limiting spatial resolution (in line pairs per millimeter) should not fall below the values listed under the 20% column in Table 18.9. In routine tests, the variation should be <10% from the baseline value.

ACR: The MSQA form asks for results of MTF measurement only, for GE equipment. For Hologic Selenia, the form asks for results of evaluation of system resolution. In this case, the system spatial resolution must be >7 lp/mm when the bars are at 45 deg to the anode-cathode axis.

18.3.11 Half-value layer

The purpose of this test is to ensure that the half-value layer (HVL) of the x-ray beam is adequate to minimize patient breast dose.[4] It is necessary to calculate the MGD in order to know the HVL, and it is appropriate to measure it with the compression paddle in the beam and for the same technical parameters related to MGD calculation. Measurements are performed following the ACR,[4] with the compression paddle in the beam. Both IAEA and ACR publications evaluate the result according to the following equation:

$$\frac{\text{kV}}{100} + 0.03 \leq HVL \leq \frac{\text{kW}}{100} + C, \tag{18.6}$$

where $C = 0.12$ for Mo/Mo,
0.19 for Mo/Rh,
0.22 for Rh/Rh,
0.30 for W/Rh,
0.32 for W/Ag, and
0.25 for W/Al.

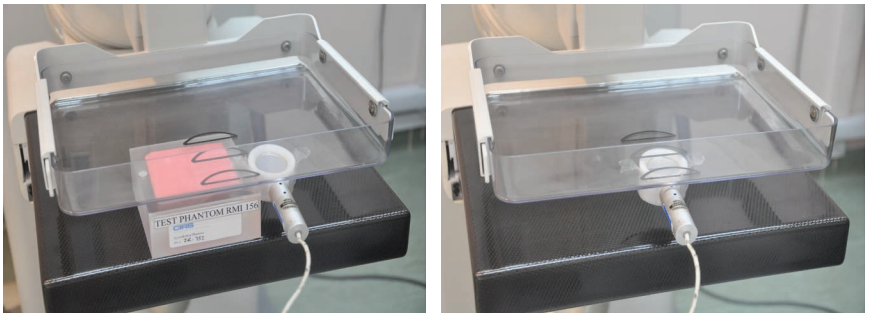

(a) (b)

Figure 18.7 Estimating the incident air kerma (a) with and (b) without backscatter.

18.3.12 Incident air kerma at the entrance surface of PMMA slabs

This measurement aims to estimate the incident air kerma at the position corresponding to the entrance surface of PMMA (IAEA) with thickness of 20, 45, and 70 mm or phantom image quality (ACR) (see Fig. 18.7) to calculate the MGD. The IAEA publication refers to this measurement without backscatter (without the PMMA) and ACR publication with backscatter (with the dosimeter beside the phantom). In the first method, place the desired thickness of PMMA and use automatic mode to acquire the technical parameters. Then, in manual mode and without the PMMA, measure the incident air kerma.

If the mAs of manual exposure (mAs_{M1}) does not correlate with the mAs automatic mode (mAs_{AEC}), make a correction to the measurement M of air kerma, as follows:

$$M_{AEC} = \frac{\mathrm{mAs}_{AEC}}{\mathrm{mAs}_{M_1}} M_1. \tag{18.7}$$

Then, the incident air kerma K is

$$K_{i,45\mathrm{mm}} = M_{AEC} \cdot N_{mammo} \cdot k_{TP}, \tag{18.8}$$

where k_{TP} is the dosimeter correction factor for temperature and pressure, and N_{mammo} is the value of the calibration factor for beam quality.

18.3.13 Mean glandular dose

As breast cancer appears predominantly in the glandular tissue and this tissue is very sensitive to radiation, doses in mammography should be routinely monitored. Thus, the measurement of MGD is essential both for monitoring the doses given to patients and for evaluating the system performance. MGD can be derived from incident air kerma.

18.3.13.1 IAEA method

We use Eq. (18.9) for each thickness of PMMA studied and obtain the MGD:[13]

$$MGD = g_t \cdot c_t \cdot s \cdot K_{i,t}, \tag{18.9}$$

where:

$K_{i,t}$ is the incident air kerma at the surface of PMMA [Eq. (18.8)],
g_t is the factor that converts from air kerma to MGD for a breast having 50% fibroglandular/50% adipose composition with a thickness of t mm,
c_t is the conversion factor that corrects for any difference in breast composition from 50% glandularity, and
s is the factor related to different x-ray spectra that gives a correction that depends on the target–filter combination.

The factors g_t, c_t, and s are tabulated and can be found in the IAEA publication.[5] Acceptable and achievable levels for MGD are presented in Table 18.11.

18.3.13.2 ACR method

Wu[14] defined the normalized MGD D_{gN} as MGD D_g per unit entrance skin exposure X_{ese}. D_{gN} is assumed to be a function of beam quality (HVL), x-ray tube target material, breast thickness, and breast composition. From D_{gN} and X_{ese}, the D_g can be calculated using

$$D_g = D_{gN} \cdot X_{ese}. \tag{18.10}$$

The measurement of X_{ese} is performed with a compression paddle and backscatter.

The ACR publication presents tabulated values of D_{gN} as a function of target–filter combination, kVp and HVL, to a 42-mm breast thickness—50% adipose, 50% glandular breast tissue. Other combinations of tissue

Table 18.11 Acceptable and achievable levels for MGD.[5]

Thickness of PMMA (mm)	Thickness of equivalent breast (mm)	Acceptable level of MGD for equivalent breast (mGy)	Achievable level of MGD for equivalent breast (mGy)
20	21	1.0	0.6
30	32	1.5	1.0
40	45	2.0	1.6
45	53	2.5	2.0
50	60	3.0	2.4
60	75	4.5	3.6
70	90	6.5	5.1

composition, target–filter combination, kVp and HVL, can be obtained using the method of parameterization published by Sobol and Wu.[15] The MGD to 42-mm compressed breast must not exceed 3 mGy per view. This ACR recommendation refers to screen-film system.

18.3.14 Collimation system

The positioning of the patient is very important for obtaining a high-quality image. It is important to include as much of the breast tissue as possible in the image to increase the possibility of detecting breast cancer. As the positioning is directed by the light beam, it must be appropriately aligned with the x-ray beam and with the detector. Therefore, the objective of this test is to check for proper alignment and to determine the amount of breast tissue at the chest wall that is excluded in obtaining the image.

For CR systems, it is possible to perform the tests that are recommended by the ACR[4] and the IAEA[16] using two sizes of cassettes (18 cm × 24 cm and 24 cm × 30 cm) and coins to delineate the edge of the light field. The smallest cassette is placed in the image receptor holder and the large cassette on top of the bucky.

In this method, the tolerance for coincidence between light field and radiation field is achievable for ≤1% of the source-to-image distance (SID) on any side. The tolerance for coincidence between detector and radiation field is as follows. It is achievable when the beam completely irradiates the image receptor but can only extend to the chest wall side of <5 mm. It is acceptable when the beam is inside the breast support by ≤2% of the SID for the three sides other than at the chest wall, which is <5 mm. The tolerance between the compression paddle and detector is acceptable for 1% of the SID.

For DR systems, two radiographic rulers, five phosphorescent screen pieces, opaque material, and slabs of PMMA totaling 45 mm in thickness are placed as shown in Fig. 18.8.

In this method the tolerance is as follows for:

- missing tissue at the chest wall:
  - achievable: ≤5 mm;
  - acceptable: ≤7 mm.
- coincidence between active detector edge and radiation field:
  - achievable: The beam completely irradiates the active area of the detector but does not extend beyond the breast support.
  - acceptable: The beam completely irradiates the active area of the detector and does not extend beyond the breast support (for a chest wall of <5 mm).

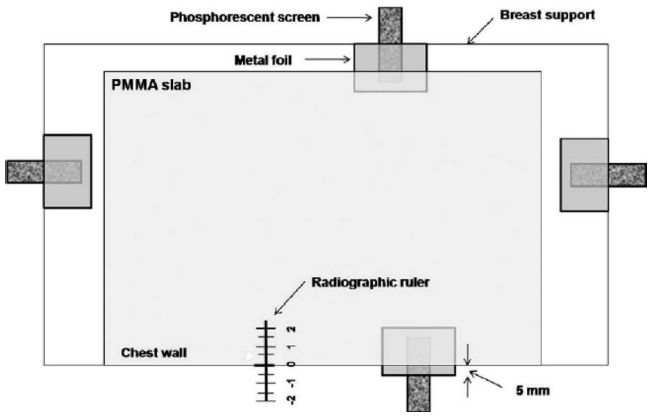

Figure 18.8 Arrangement that suggests evaluating the x-ray field alignment with light field and missing tissue.

- the extent of the compression paddle in the chest wall edge of <5 mm. The chest wall edge of the paddle must not be visible in the image.

18.3.15 Image display quality

It is widely accepted that, compared to film, digital mammograms have many advantages related to image quality, efficiency, handling of image information, manipulation of images, and parameter remote viewing. However, these improvements cannot be completely appreciated without monitors that are suitable for the format of the displayed image.[17] The monitors should provide information that represents small differences in attenuation of x rays or small differences in thickness of any anatomical ROI. This information should also result in small differences in luminance of an image represented. Therefore, a monitor should have specific characteristics such as spatial resolution and contrast, noise, luminance, geometric distortion, and reflection appropriate for enabling the observer to make an assessment that will lead to better diagnosis.[18]

Thus, to ensure a better response, the quality of the image must be periodically assessed, both with the software provided by some manufacturers and, externally, to evaluate the performance of the internal monitor calibration. With continual use, a monitor can undergo degradation of luminance or uniformity and degradation of the definition of edges or variations of some parameters that characterize them. Additionally, the monitor's output must be verified.[19]

The performance of display devices plays a significant role in the overall image quality of a digital mammographic system. In a filmless environment, it is necessary to implement acceptance and constancy tests on

monitors used for interpretation of medical images.[20] To check the monitor, use the TG18 test pattern series.[21]

18.3.15.1 Geometric distortions

The geometric distortion test is to be performed only in cathode ray tube monitors, since liquid crystal monitors have a fixed matrix and will not deform the image. However, this test can determine the proportion of images, that is, whether the monitor displays flattened images, which can result if the resolution is not correctly configured on the video card. Use the pattern TG18-QC (Fig. 18.2) test measuring square with a flexible ruler. The variation between the horizontal and vertical measures may not exceed 2%.

18.3.15.2 Luminance uniformity

The luminance uniformity of the test checks for the region of the screen where the light intensity varies with a same shade of gray. Use the pattern TG18-UNL80 (80% of maximum luminance) and TG18-UNL10 (10% of maximum luminance), Fig. 18.9. With a photometer, measure the four regions of the edges and the center. These measures cannot vary by more than 30%.

18.3.15.3 Luminance response and contrast

This test indicates whether the maximum luminance L_{max} of the monitor is sufficient for viewing medical images ($L_{max} > 170$ cd/m^2) and whether the contrast level is consistent with the DICOM grayscale standard display function (GSDF). In addition, it is also important to check the variation of the maximum luminance when workstations with dual screens are used, as this variation cannot be greater than 10%. The relationship between the maximum and minimum luminance assigns the parameter contrast response (CR), which cannot be <250.

This check is done by measuring with a photometer luminance of 18 gray levels with the test patterns TG18-LN. The evaluation is performed by means of a graph that relates the variation of luminance with the index JND (just noticeable difference) and luminance (level contrast) with the index JND. Both curves cannot exceed the 10% difference compared to standard DICOM GSDF.

18.3.15.4 Ambient lighting

The room where the monitor is installed should be maintained in adequate lighting to prevent any glare on the monitor screen and to exclude daylight. The ambient lighting should be measured and should be <10 lux and, ideally, <5 lux.

18.3.16 Laser printer (where applicable)

In a facility, usually the laser printer is used for all imaging modalities, and each modality has an appropriate lookup table (LUT) that should be

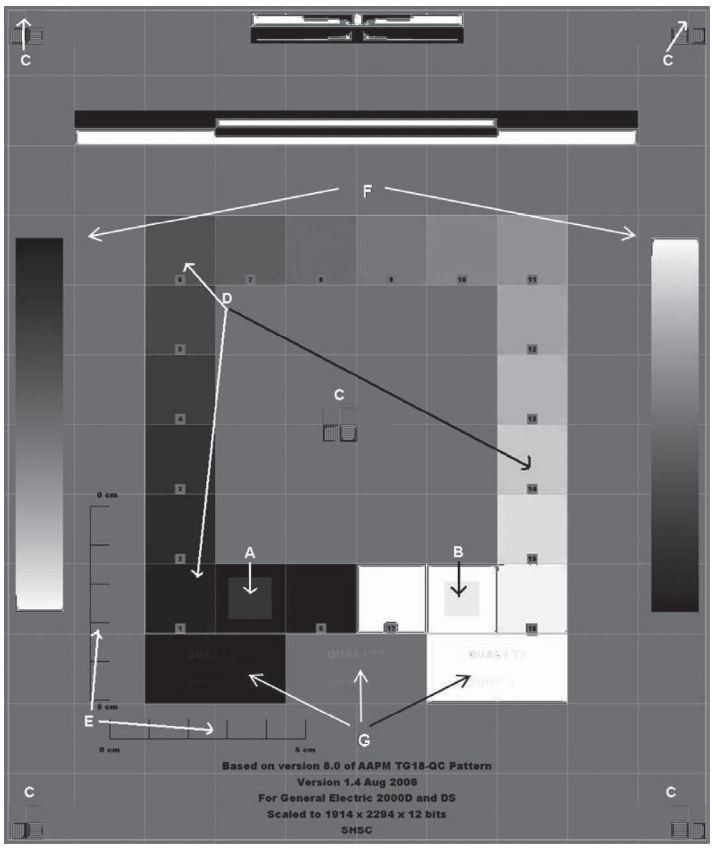

(a)

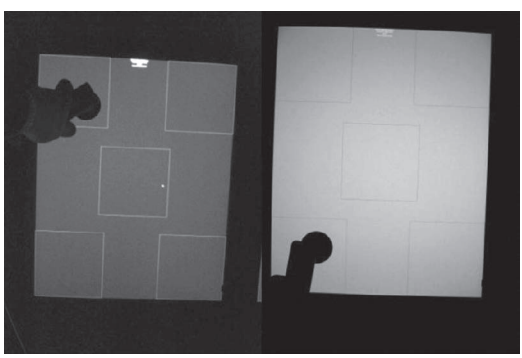

(b)

Figure 18.9 (a) Modified TG18-QC test pattern with test objects indicated: A marks the 0%–5% contrast square, B the 95%–100% contrast square, C the horizontal and vertical line pairs, D the squares going from black to white, E the 5-cm line, F the grayscale ramp, and G the 'quality control' subjective test. (b) TG18-UNL10 e UNL80.

automatically selected by the printer. Thus, to ensure the correct functioning, the laser printer should be evaluated by a medical physicist during acceptance testing, annually, and after servicing the printer or printing software.

The test is simple and requires the printing of an image of the test pattern TG18-QC (Fig. 18.9). The following should be visible:

- all density steps,
- squares in the corners of the grayscale patches,
- the 5% squares at both bright and dark,
- all line-pair patterns, and
- the letters 'QUALITY CONT.'

The measured lengths of the horizontal and vertical should be within 5% of actual values for the rulers on the TG18-QC pattern and for the annotation lines on the film.

18.3.17 Phantom image quality

The verification of image quality is similar to that performed for screen-film systems, where the medical physicist establishes the baseline for the technologist in routine testing. A breast phantom containing structures such as fiber, specks, and masses is used. The phantom image evaluation and identification of structures must be made both on the film that is printed on laser printer and on the workstation.

The tolerance for this test for IAEA requires establishment of baseline for degradation of image quality, exposure factors, and the identification of structures. The tolerance for this test using the ACR phantom should identify, as a minimum, the numbers of structures shown in Table 18.12.

18.4 Technologist Testing

Technologists play an important role in the implementation of the QAP in mammography. They are involved with all routine examinations and are aware of the problems that can affect the equipment. Therefore, they can implement many quick and easy routine checks.

Table 18.12 Minimum required number of identified structures for the tolerance of the ACR breast phantom image quality test.

	Fibers	Masses	Speck groups
GE 2000D, DS, Essential	4	3	3
Hologic Selenia	5	4	4
Siemens Mammomat Inspiration	5	4	4

18.4.1 Inspection, cleaning, and viewing conditions of monitors and view boxes

Dust, fingerprints, and other marks on the monitor screens can interfere with image interpretation. Therefore, the monitor must be inspected and cleaned daily. For the same reasons, view boxes must be kept clean and maintained with a luminance of 3000 cd/m^2. The uniformity of the luminance should also be checked. The viewing conditions should be kept as initially measured by a medical physicist, as explained in Section 18.3.15.

18.4.2 Laser printer

18.4.2.1 Sensitometry

The technologist must obtain a TG18-CQ image (Fig. 18.2) daily for wet processing and monthly for dry processing, and compare these with the baseline [reference operating levels (ROLs)] as established by a medical physicist. It is recommended that this image confirm the visibility of objects and the measurements made in acceptance testing. When performing sensitometry, the densities on the step wedge pattern should be obtained in accordance with the following parameters:

- maximum density D_{max}—the darkest step;
- density difference (DD)—the step closest to an optical density of 2.20 (DD1) minus the step closest to but not less than 0.45 (DD2);
- mid-density (MD)—the step closest to but not below an optical density of 1.20 or the working optical density; and
- base + fog (B + F)—the lightest step.

The tolerances provided by the IAEA publication are presented in Table 18.13.

18.4.2.2 Artifacts

In addition to tests already carried out in the laser printer, this test checks whether there are any artifacts in the film printed. An image of the test

Table 18.13 Tolerance for laser print sensitometry (used with permission from IAEA[5]).

Parameter	Acceptable tolerance	Achievable tolerance
D_{max2}	≥ROL – 0.15 or 3.50, whichever is less	≥ROL – 0.10 or 3.50, whichever is less
DD	ROL ± 0.15	ROL ± 0.10
MD	ROL ± 0.15	ROL ± 0.10
B + F	≤ROL + 0.03	—

pattern TG18-UNL80 (Fig. 18.2) must be printed with a window level that gives an optical density of between 1.5 and 2.0. The window width should be set to maximum. The resulting film must display an image with uniform optical density, and with no streaks, lines, specks, or blotches.

18.4.2.3 Printed image quality

An image of the test pattern TG18-CQ should be obtained quarterly to ensure that the printed image quality is consistently high. The visibility of the different test objects on the printed image quality should be evaluated according to the following IAEA criteria:[5]

- The 0%–5% contrast square and 95%–100% contrast square should be distinguishable.
- The finest horizontal and vertical line pairs should be visible in all four corners.
- The squares of different shades from black to white should be distinct.
- Lines should appear straight and even, without apparent distortions.
- There should be no distracting artifacts.
- The 5-cm lines should be between 4.7 and 5.3 cm long on the printed image.

18.4.3 Phantom image quality

The technologist must obtain an image of the phantom and confirm the baseline established by a medical physicist. The tolerance for the parameters evaluated in this image comprises the following:

- mAs is $\leq \pm 10\%$ of the baseline mAs value if the kV and filter have not changed.
- For CR systems, the tolerance for the EI is not be exceeded.
- No significant degradation of image quality from the baseline image occurs.
- No blotches or regions of altered noise appearance, observable lines or structural artifacts, and 'bright' or 'dark' pixels are evident.
- The baseline to fibers, masses, and specks is maintained.

18.4.4 Digital mammography equipment daily checklist

Assessment of the mammography equipment must be carried out to ensure that all parts and accessories are working properly. Checks should be made on items listed in Table 18.14.

18.4.5 Daily and monthly flat-field phantom image test

The implementation of this test is important to eliminate the possibility that the image has artifacts. For this evaluation, the technologist uses a

Table 18.14 Digital mammography (DM) checklist for the technologist.

Daily and weekly tests	Monthly, quarterly, and semi-annual tests
Monitor inspection and cleaning (daily)	Laser printer sensitometry (dry) (monthly)
Monitor viewing conditions (daily)	Safety and function checks of examination
DM equipment daily checklist (daily)	room and equipment (monthly)
Daily flat-field image (daily)	Full-field artifacts (monthly)
Visual inspection for artifacts (CR systems only) (daily)	Laser printer artifacts (monthly)
Laser printer sensitometry (wet) (daily)	Printed image quality (quarterly)
Image plate erasure (CR systems only) (daily)	Repeat image analysis (quarterly)
Monitor QC (weekly)	Spatial resolution test (CR and scanning
Viewbox cleanliness (weekly)	systems) (quarterly)
QC test object and full-field artifacts (weekly)	CR plate sensitivity matching and plate
Image quality with breast-mimicking phantom	artifacts (semi-annually)
(weekly)	

phantom of 45-mm PMMA covering the entire detector area, applies a compression force typically used clinically, acquires an image, and analyzes it in "for processing" mode.

This image should not contain:

- blotches or regions of altered texture appearance,
- observable lines or structural artifacts, or
- evident 'bright' or 'dark' pixels.

On a monthly basis, the test is extended to include all applicable focal spots, filters, and magnification modes; however, the tests for MPV and SDNR are not required.

18.4.6 Visual inspection for artifacts (CR systems only)

This test for CR systems is similar to that described in Section 18.4.5, to check whether the image is free of artifacts. All clinical images should be inspected during the day for excessive artifacts attributable to dust on the imaging plates or in the readout system, defects on the imaging plates, or dirt on the breast support plate or compression paddle.

18.4.7 Image plate erasure (CR systems only)

One of the advantages of using the imaging plate instead of film is the ability to reuse it. However, residual latent image signals or signals arising from ionizing radiation are retained on the phosphor plate after readout.[22] These signals can cause image ghosting. The erasure of the plate is a function of the overall exposure. To ensure the absence of residual signals, the erasure test evaluates the ability of the read–erase cycle to remove ghosting artifacts. This erasure is repeated before clinical exposures on plates that have not been used for more than eight hours.

18.4.8 Monitor QC

This test consists of evaluating the monitors using a TG18-QC (or SMPTE) test pattern and to ensure the following:

- Viewing conditions for the radiologist workstation are as recommended by the medical physicist.
- There are no noticeable diagonal lines, flickering, blotches, nonuniform grayscale ramps, curved 'straight' lines, and bright or dark pixels in the evaluated image.
- All 16 luminance patches are distinct from each other.
- 5% contrast squares are visible in both the dark (0%–5%) and light (95%–100%) squares.
- The letters 'QUALITY CONT' are visible.
- The images on all radiologists' workstations appear with the same brightness and contrast.

The TG18-QC image must be evaluated in the ambient condition presented in the Section 18.3.15.4.

18.4.9 Weekly QC test object and full-field artifacts

The technologist will monitor the consistency of imaging performance from the baseline image of the test object obtained in a previous physicist's test. The acquisition and image evaluation is performed in the same manner as described in Section 18.3.5, and the results should be evaluated and maintained as specified in Table 18.15.

18.4.10 Safety and function checks of examination room and equipment

The mammography unit must operate mechanical and electrical operations in a way that ensures that the image acquisition is correct. For this, attention and verification should be performed on the items shown in Table 18.16.

Table 18.15 Tolerances for imaging weekly QC test object (used with permission from IAEA[5]).

Parameter	Acceptable tolerance with respect to baseline values
mAs	±10%*
MPV	±10%
SDNR	±10%
CR systems: EI	
Fuji, Philips and Konica (S#)	±10%
Agfa (SAL/SALlig/PVIlog)	±5%/±430/±580
Carestream (EI)	±40 units

*Provided that the anode/filter and kV used are identical.

Table 18.16 Items to be checked for corrective actions.

Items requiring immediate action before any further patients are imaged:	**Items requiring action within 30 days of first identified failure:**
1. Room temperature not controlled	4. Angulation indicator not functioning
2. Loose parts present, paddles damaged or bucky not clean	6. Gantry motion not smooth
3. Hoses or cables kinked or damaged	7. Problems in panel switches, indicator lights, and meters
5. Interlocks faulty	8. Field light inoperative
10. Time, date, and facility ID incorrect or not present on images	9. Current technique chart not posted
13. Automatic and/or manual compression release not working	11. Breast thickness indicator inaccurate
15. Cleaning solution not available	12. Face guard absent or damaged
	14. Operator radiation shield damaged
	16. Overall integrity questionable

18.4.11 Repeat image analysis

The repeat image analysis is very important for an assessment to identify problems in the production of the image. This method shows the cause of the repeat image, and the analysis of the data will help to identify ways to improve system performance. After identifying the cause of rejection, one should discern which equipment was involved and which technician received the rejected radiography. With these results, the particular malfunction in the imaging chain can be seen, or it may be determined that the technologist requires training.

The tolerance according to the IAEA publication[5] is:

- Acceptable repeat rate: <5%,
- Achievable repeat rate: ≤2%.

18.4.12 Spatial resolution test (CR and scanning systems only)

Spatial resolution in CR systems can be checked with a bar resolution pattern as is used to calculate the MTF or limiting spatial resolution. The technologist monitors the system to ensure that there is no degradation in spatial resolution over time. Thus, the value should not vary from the baseline.

Appendix 18.1 ACR Summary of Medical Physicist's and Technologist's QC Tests: General Electric

MEDICAL PHYSICIST'S MAMMOGRAPHY QC TEST SUMMARY
Full-Field Digital – General Electric

Site Name		**Report Date**	
Address		**Survey Date**	
Medical Physicist's Name		**Signature**	
X-Ray Unit Manufacturer	*General Electric*	**Model**	*Senographe 2000D*
Date of Installation		**Room ID**	

QC Manual Version: *(check one; **must** use version applicable to unit tested; contact mfr if questions)* ☑ 2000D 2371472-100 Rev 0, 2003

☐ DS 5133453-4-1EN, Rev 1, 2007 ☐ ESSENTIAL 5305863-3-S-1EN Rev 1, 2008 ☐ OTHER (write in):

Accessory Equipment:	Manufacturer	Model	Location	QC Manual Version
Review Workstation*			☐ On-site ☑ Off-site	SmFit and 2000D 2371472-100 Rev0, 2003
Laser Film Printer*			☑ On-site ☐ Off-site	ACR Stereotactic breast biopsy QC Manual

**FDA recommends that only monitors and printers specifically cleared for FFDM use by FDA's Office of Device Evaluation (ODE) be used. See FDA's Policy Guidance Help System www.fda.gov/CDRH/MAMMOGRAPHY/robohelp/START.HTM.*

Survey Type: ☐ Mammo Eqpt Evaluation of new unit (include MQSA Rqmts for Mammo Eqpt checklist) ☑ Annual Survey

Medical Physicist's QC Tests

("Pass" means all components of the test pass; indicate "Fail" if any component fails)

		PASS/FAIL
1.	**Flat Field**	Pass
2.	**Phantom Image Quality**	

	Fibers	Specks	Masses	
Phantom IQ Test on AWS	6,0	4,0	5,0	Pass
Phantom IQ Test on Printer	5,0	4,0	5,0	Pass

3. **CNR Measurement** *(NA for **DS or Essential** if Sub-System MTF test done)*
   CNR 3,895 *(Required for both new unit Mammography Equipment Evaluations and Annual Surveys)*
   Change in CNR ≤0.2 *(NA for Mammography Equipment Evaluations)* — Pass
4. **MTF Measurement** *(NA for **2000D, DS or Essential** if Sub-System MTF test done)* — Pass
5. **AOP Mode and SNR** — Pass
6. **Collimation Assessment**

	Mammo Equipment Evaluation			Annual Survey			
	Essential	DS	2000D	Essential	DS	2000D	
24 cm × 30.7 cm	x	NA	NA	x	NA	NA	Pass
19 cm × 23 cm tests	x	x	x	NA	x	x	Pass

7. **Evaluation of Focal Spot Performance** *(NA for **2000D, DS or Essential** if Sub-System MTF test done)* — Pass
8. **Sub-System MTF** *(NA for **2000D** if MTF and Focal Spot Performance tests done; NA for **DS or Essential** if CNR, MTF and Focal Spot Performance tests done)* — NA
9. **Breast Entrance Exposure, Average Glandular Dose and Reproducibility**
   Average glandular dose for average breast is ≤3 mGy (300 mrad) — 163 mrad — Pass
   Exposure reproducibility (CV) for air kerma (R) and mAs is ≤0.05 — Pass
10. **Artifact Evaluation and Flat Field Uniformity** — Pass
11. **kVp Accuracy and Reproducibility** — Pass
12. **Beam Quality Assessment (Half-Value Layer Measurement)** — Pass
13. **Radiation Output**
    Radiation output is ≥800 mR/s — 880 mR/s — Pass
14. **Mammographic Unit Assembly Evaluation**
    Meets requirements for motion of tube-image receptor assembly — Pass
    Meets requirements for compression paddle decompression — Pass
15. **Review Workstation (RWS) Tests** *(for all RWS, even if located offsite)*
    Overall Results *("Pass" means all tests pass; indicate "Fail" if any test fails)* — Pass

MEDICAL PHYSICIST'S MAMMOGRAPHY QC TEST SUMMARY
(*General Electric, continued*)

Evaluation of Site's Technologist QC Program

New units: Medical physicists must review the site's technologist QC program within 45 days of installation and complete this section so that the facility may submit this form along with the entire Mammography Equipment Evaluation report to the ACR.
Renewing units: Medical physicists must complete this section as part of the unit's annual survey.

	FREQUENCY	PASS/FAIL
1. Monitor Cleaning	Daily	**Pass**
2. Darkroom Cleanliness *(if applicable)*	Daily	**NA**
3. Processor QC *(if applicable)*	Daily	**NA**
4. Flat Field	Weekly	**Pass**
5. Phantom Image Quality	Weekly	**Pass**
6. CNR	Weekly	**Pass**
7. Viewbox and Viewing Conditions *(NA if no hardcopy interpreted or compared)*	Weekly	**NA**
8. MTF Measurement	DS/Essential-Weekly; 2000D-Monthly	**Pass**
9. AOP Mode and SNR	Monthly	**Pass**
10. Visual Checklist	Monthly	**Pass**
11. Repeat Analysis	Quarterly	**Pass**
12. Analysis of Fixer Retention *(if applicable)*	Quarterly	**NA**
13. Compression Force	Semi-annually	**Pass**
14. Darkroom Fog *(if applicable)*	Semi-annually	**NA**
15. Review Workstation QC-Overall	See FDA guidance	**Pass**
16. Laser Film Printer QC *(GE requires laser printer mfr's manual)*	Printer mfr recommendations	**Pass**
17. Mobile Unit Quality Control *(if applicable)*	After every move	**NA**

Medical Physicist's Recommendations for Quality Improvement

Important:
1. The facility's "quality assurance program shall be ***substantially the same*** as the quality assurance program recommended by the ***image receptor [digital detector] manufacturer***." This is required by the FDA.
2. Use the QC manual version provided.

Appendix 18.2 ACR Summary of Medical Physicist's and Technologist's QC Tests: Hologic

MEDICAL PHYSICIST'S MAMMOGRAPHY QC TEST SUMMARY

(Lorad, continued)

Evaluation of Site's Technologist QC Program

New units: Medical physicists ***must*** review the site's technologist QC program within 45 days of installation and complete this section so that the facility may submit this form along with the entire Mammography Equipment Evaluation report to the ACR with t

Renewing units: Medical physicists ***must*** complete this section as part of the unit's annual survey.

	FREQUENCY	PASS/FAIL
1. DICOM Printer Quality Control	Weekly	Pass
2. Viewboxes and Viewing Conditions	Weekly	Pass
3. Artifact Evaluation	Weekly	Pass
4. Signal-To-Noise and Contrast-To-Noise Measurements	Weekly	Pass
5. Phantom Image	Weekly	Pass
6. Detector Flat-Field Calibration	Weekly	Pass
7. Compression Thickness Indicator	Bi-weekly	Pass
8. Visual Checklist	Monthly	Pass
9. Reject Analysis	Quarterly	Pass
10. Compression	Semi-annually	NA
11. Review Workstation QC-Overall	See FDA guidance	Pass

Medical Physicist's Recommendations for Quality Improvement

Important:

1. The facility's "quality assurance program shall be ***substantially the same*** as the quality assurance program recommended by the ***image receptor [digital detector] manufacturer***." This is required by the FDA.
2. Use the QC manual version provide

Appendix 18.3 IAEA* Safety and Function Checklist of Examination Room and Equipment

SAFETY AND FUNCTION CHECKLIST OF EXAMINATION ROOM AND EQUIPMENT

Facility:		Room/Unit:	
Manufacturer:		Model:	
Year:			

Checkmark (✓) = Pass/Adequate; × = Fail; Initial when complete

Year												
Month	Jan	Feb	Mar	Apr	May	Jun	Jul	Aug	Sep	Oct	Nov	Dec
Date												
Initials												
Room temperature												
No loose parts												
Cleanliness												
No cracks in paddle												
Automatic compression release												
Compression release on power failure												
Overall integrity												
Hoses and cabling unobstructed												
Angulation indicator												
Locks (all)												
Field light												
Smoothness of motion												
Breast thickness indicator accuracy												
Face guard integrity												
Panel switches/lights/meters												
Technique charts												
Time and date on images correct												
Facility ID on images correct												
Operator radiation shield												
Cleaning solution												

If a failure of a test listed above is noted, document corrective action:

*Based on the checklist in the IAEA publication.[5]

References

1. M. Mahesh, "AAPM/RSNA physics tutorial for residents: Digital mammography—An overview," *Radiographics* **24**, 1747–1760 (2004).
2. K. H. Ng and M. Muttarak, "Advances in mammography have improved early detection of breast cancer," *J. HK Coll. Radiol.* **6**, 126–131 (2003).
3. American College of Radiology (ACR), American Association of Physics in Medicine (AAPM), Society for Imaging Informatics in Medicine (SIIM), *Practice Guideline for Determinants of Image Quality in Digital Mammography* – Resolution 35, (2007). http://www.acr.org/SecondaryMainMenuCategories/quality_safety/guidelines/breast/image_quality_digital_ mammo.aspx.
4. American College of Radiology, *Manual of Quality Assurance* (1999).
5. International Atomic Energy Agency (IAEA), "Quality Assurance Programme for Digital Mammography," *IAEA Human Health Series* No. 17, Vienna (2011).
6. D. R. Dance, C. L. Skinner, K. C. Young, J. R. Beckett, and C. J. Kotre, "Additional factors for the estimation of mean glandular breast dose using the UK mammography dosimetry protocol," *Phys. Med. Biol*. **45**, 3225–3240 (2000).
7. GE Healthcare, "Senographe DS—Quality Control Manual Revision 1," General Electric Company Inc., BucCedex, France (2009).
8. Hologic Lorad Selenia, "Selenia Quality Control Manual Part Number MAN-01476, Revision 001," Hologic, Bedford, MA (2009).
9. M. B. Williams, M. J. Yaffe, A. D. A. Maidment, M. C. Martin, J. A. Seibert, and E. D. Pisano, "Image quality in digital mammography: Image acquisition," *J. Am. Coll. Radiol.* **3**, 589–608 (2006).
10. L. A. Lança Silva, "Digital radiography detectors - A technical overview: Part 2," *Radiography* **15**, 134–138 (2009).
11. E. Samei, E. and M. J. Flynn, "A method for measuring the presampled MTF of digital radiographic systems using an edge test device," *Med. Phys*. **25**(1), 102–113 (1998).
12. I. D. Mclean, J. C. P. Heggie, J. Herley, F. J., Thomson, and R. K. Grewal, "Interim recommendations for a digital mammography quality assurance program," *Australas. Phy. Eng. Sci. Med.* **30**(2), 65–100 (2007).
13. D. R. Dance, C. L. Skinner, K. C. Young, J. R. Beckett, and C. J. Kotre, "Additional factors for the estimation of mean glandular breast

dose using the UK mammography dosimetry protocol," *Phys. Med. Biol.* **45**, 3225–3240 (2000).

14. X. Wu, G. T. Barnes, and D. M. Tucker, "Spectral dependence of tissue glandular dose in screen-film mammography, *Radiol.* **179**, 143–148 (1991).
15. W. T Sobol and X. Wu, "Parametrization of mammography normalized average glandular dose tables," *Med. Phys.* **24**(4), 547–554 (1997).
16. International Atomic Energy Agency, "Quality Assurance Programme for Screen Film Mammography," *IAEA Human Health Series* No. 2, Vienna (2009).
17. L. D. Ribeiro and T. A. C. Furquim, "Estudo do desempenho de monitores LCD utilizados em radiologia digital," *Rev. Imagem.* **2**(1/2), 7–12 (2010).
18. H. Roehrig, E. A. Krupinski, A. S. Chawla, et al., "Noise of LCD display systems," *International Congress Series* **1256**, 162–168 (2003).
19. M. Li, D. Wilson, M. Wong, and A. Xthona, "The evolution of display technologies in PACS applications," *Comput. Med. Imaging Graph.* **27**, 175–184 (2003).
20. L. D. Ribeiro and T. A. C. Furquim, "Study of performance of LCD display devices in radiology with digital imaging," *Revista Brasileira de Física Médica* **4**(2), 27–30 (2010).
21. E. Samei, A. Badano, D. Chakraborty, et al., "Assessment of display performance for medical imaging systems: Executive summary of AAPM TG18 report, *Med. Phys*. **32**(4), 1205–1225 (2005).
22. Association of Physicists in Medicine, "Acceptance Testing and Quality Control of Photostimulable Storage Phosphor Imaging Systems," AAPM Report No. 93 (2006).

Kwan-Hoong Ng is a Senior Professor at the Department of Biomedical Imaging and a Senior Consultant of the University of Malaya Medical Center, Kuala Lumpur, Malaysia. He received his M.Sc. (Medical Physics) from University of Aberdeen and Ph.D. (Medical Physics) from University of Malaya, Malaysia. He is also a certified by the American Board of Medical Physicists. He has authored/coauthored more than 180 papers in peer-reviewed journals and 15 book chapters. He has presented over 400 scientific papers, more than

200 of which were invited lectures. He has directed several workshops on radiology quality assurance, digital imaging, and scientific writing. He is the cofounder and coeditor in chief of the *Biomedical Imaging and Intervention Journal*. His main research contribution has been in the biophysical characterization of breast diseases and developing computer methods as tools to improve the diagnostic capability of mammography. He has also been directing research initiatives in digital imaging, radiological protection, and radiation dosimetry. Dr. Ng has been serving as an IAEA expert and is a member of International Advisory Committee of the World Health Organization. He also serves as a consulting expert for the International Commission on Non-Ionizing Radiation Protection (ICNIRP).

Tânia Aparecida Correia Furquim works at the Electrotechnical and Energy Institute of University of São Paulo, São Paulo, Brazil. She received her M.Sc. in biophysics from the Physics Institute of the University of São Paulo and her Ph.D. in medical physics from Nuclear and Energy Research Institute associated with the University of São Paulo. She is a radiodiagnostic specialist certified by the Brazilian Association of Medical Physics. Regarding her main activities, she is responsible for quality control program implementation in five reference hospitals in São Paulo city. Her main publications are in the area of mammography and digital radiology.

Noriah Jamal graduated with B.Sc. (Hons) in nuclear science from the National University of Malaysia in 1984. She obtained a postgraduate diploma in radiation and environmental protection from University of Surrey, UK in 1988 and a Master's degree in medical physics from University of Aberdeen, Scotland in 1992. She obtained her Ph.D. in medical physics from University of Malaya, Malaysia in 2005. Dr. Jamal is currently a director at the Malaysian Nuclear Agency. She is actively involved in Medical physics activities in the country and the region, covering radiation protection, diagnostic radiology, radiation therapy, and nuclear medicine. She has authored and coauthored more than 40 publications at both international and national levels.

Index

Multimodality Breast Imaging
Diagnosis and Treatment

E. Y. K. Ng, U. Rajendra Acharya,
Rangaraj M. Rangayyan, Jasjit S. Suri, *Editors*

Breast cancer is an abnormal growth of cells in the breast, usually in the inner lining of the milk ducts or lobules. It is currently the most common type of cancer in women in developed and developing countries. The number of women affected by breast cancer is gradually increasing and remains as a significant health concern. Researchers are continuously working to develop novel techniques to detect early stages of breast cancer. This book covers breast cancer detection, diagnosis, and treatment using different imaging modalities such as mammography, magnetic resonance imaging, computed tomography, positron emission tomography, ultrasonography, infrared imaging, and other modalities. The information and methodologies presented will be useful to researchers, doctors, teachers, and students in biomedical sciences, medical imaging, and engineering.

E. Y. K. Ng received his Ph.D. from Cambridge University (UK) and is an associate professor at Nanyang Technological University (Singapore). He serves as editor for six international journals and as Editor-in Chief for two. His research interests are in thermal imaging, biomedical engineering, breast cancer detection, and computational fluid dynamics and heat transfer.

U. Rajendra Acharya is a visiting faculty member at Ngee Ann Polytechnic (Singapore), an adjunct faculty member at Singapore Institute of Technology-University of Glasgow (Singapore) and Singapore Institute of Management, and an adjunct professor at University of Malaya (Malaysia). He received his Ph.D. from National Institute of Technology Karnataka (India) and D.Engg. from Chiba University (Japan). He is on the editorial board and has served as guest editor of many journals. His research interests are in biomedical signal processing, bio-imaging, data mining, visualization, and biophysics for better healthcare design, delivery, and therapy.

Rangaraj M. Rangayyan is a professor at the University of Calgary (Canada). His research interests are in digital signal and image processing, biomedical signal analysis, biomedical image analysis, and computer-aided diagnosis. His research productivity was recognized with the 1997 and 2001 Research Excellence Awards of the Department of Electrical and Computer Engineering, and the 1997 Research Award of the Faculty of Engineering, both from the University of Calgary.

Jasjit S. Suri is an innovator, scientist, and an internationally known world leader in biomedical engineering. He has worked for more than 20 years in the field of biomedical engineering/sciences and its management. He earned his doctorate from the University of Washington (USA) and his MBA from Case Western Reserve University (USA). Suri was awarded the President's Gold medal in 1980 by India's Directorate General National Cadet Corps and was named a Fellow of the AIMBE for his outstanding contributions.

ISBN 978-0-8194-9294-4
90000
9 780819 492944

SPIE

P.O. Box 10
Bellingham, WA 98227-0010

ISBN: 9780819492944
SPIE Vol. No.: PM227

SPIE PRESS

Multimodality Breast Imaging: Diagnosis and Treatment

NG
ACHARYA
RANGAYYAN
SURI